Physique du Higgs au-delà du Modèle Standard

Jérémie Quevillon

UNIVERSITÉ PARIS SUD

Comprendre le monde, construire l'avenir®

LPT Orsay

THÈSE DE DOCTORAT

École Doctorale Physique en Île-de-France - ED 564

Présentée pour obtenir

LE GRADE DE DOCTEUR EN SCIENCES
DE L'UNIVERSITÉ PARIS-SUD XI

Spécialité: Physique Théorique

par

Jérémie QUEVILLON

Higgs Physics Beyond the Standard Model

Soutenue le 19 Juin 2014 devant le jury composé de:

Dr.	Abdelhak DJOUADI	(Directeur de thèse)
Dr.	Emilian DUDAS	(Rapporteur)
Pr.	John ELLIS	(Examinateur)
Pr.	Ulrich ELLWANGER	(Président du jury)
Dr.	Louis FAYARD	(Examinateur)
Dr.	Sabine KRAML	(Rapporteur)
Dr.	Pietro SLAVICH	(Examinateur)

Thèse préparée au
Laboratoire de Physique Théorique d'Orsay (UMR 8627), Bât. 210
Université Paris-Sud 11
91 405 Orsay CEDEX

La Physique du Higgs au delà du Modèle Standard

Résumé

Le 4 Juillet 2012, la découverte d'une nouvelle particule scalaire avec une masse de $\sim$ 125 GeV a été annoncée par les collaborations ATLAS et CMS. Une nouvelle ère s'annonce : celle au cours de laquelle il faudra déterminer précisément les propriétés de cette nouvelle particule. Cela est crucial afin d'établir si cette particule est bien la trace du mécanisme responsable de la brisure de la symétrie du secteur électro-faible. Cela permettrait aussi de repérer tout élément susceptible d'être associé à une "nouvelle physique" dans le cas où le mécanisme de brisure ferait intervenir des ingrédients autres que ceux prédits par le Modèle Standard. Dans cette thèse, nous avons essayé de comprendre et de caractériser jusqu'à quel point ce nouveau champ scalaire est le boson de Higgs prédit par le Modèle Standard. Nous avons établi les implications d'une telle découverte dans le contexte de théories supersymétriques et de modèles décrivant la matière noire. Dans une première partie consacrée au Modèle Standard de la physique des particules, nous étudions après une courte introduction au domaine, le processus de production d'une paire de bosons de Higgs au LHC. Un résultat majeur est que ce mode de production permettra de mesurer le couplage trilinéaire du Higgs qui est un paramètre essentiel à mesurer afin de reconstruire le potentiel du Higgs et donc représente la dernière vérification à effectuer pour confirmer l'origine de la brisure spontanée de la symétrie électro-faible. La deuxième partie traite des théories supersymétriques. Après une introduction au sujet, un de nos importants résultats est d'avoir fortement contraint un certain nombre de modèles supersymétriques après la découverte du boson de Higgs. Nous avons aussi introduit une nouvelle approche qui permet aux physiciens expérimentateurs de rechercher de manière efficace les bosons de Higgs supersymétriques dans les expériences actuelles et futures du LHC. La troisième partie concerne la matière noire. Nous présentons des résultats qui établissent d'importantes limitations sur des modèles où la matière noire interagirait avec le boson de Higgs. Nous discutons aussi de scénarios alternatifs qui font intervenir de la matière noire hors équilibre avec le bain thermique. Dans un premier temps nous démontrons qu'il existe un lien étroit entre la température de réchauffement de l'univers et le schéma de brisure du groupe de jauge du Modèle Standard et dans un deuxième temps nous étudions la genèse de matière noire par l'intermédiaire de nouveaux bosons Z'.

Mots-clefs : Modèle Standard, Boson de Higgs, Supersymétrie, LHC, Matière noire.

Abstract

On the 4^{th} of July 2012, the discovery of a new scalar particle with a mass of ~ 125 GeV was announced by the ATLAS and CMS collaborations. An important era is now opening: the precise determination of the properties of the produced particle. This is of extreme importance in order to establish that this particle is indeed the relic of the mechanism responsible for the electroweak symmetry breaking and to pin down effects of new physics if additional ingredients beyond those of the Standard Model are involved in the symmetry breaking mechanism. In this thesis we have tried to understand and characterize to which extent this new scalar field is the Standard Model Higgs Boson and set the implications of this discovery in the context of supersymmetric theories and dark matter models. In a first part devoted to the Standard Model of particle physics, we discuss the Higgs pair production processes at the LHC and the main output of our results is that they allow for the determination of the trilinear Higgs self–coupling which represents a first important step towards the reconstruction of the Higgs potential and thus the final verification of the Higgs mechanism as the origin of electroweak symmetry breaking. The second part is about supersymmetric theories. After a review of the topics one of our result is to set strong restrictions on supersymmetric models after the Higgs discovery. We also introduce a new approach which would allow experimentalists to efficiently look for supersymmetric heavy Higgs bosons at current and next LHC runs. The third part concerns dark matter. We present results which give strong constraints on Higgs-portal models. We finally discuss alternative non-thermal dark matter scenario. Firstly, we demonstrate that there exists a tight link between the reheating temperature and the scheme of the Standard Model gauge group breaking and secondly we study the genesis of dark matter by a Z' portal.

Keywords : Standard Model, Higgs boson, Supersymmetry, LHC, Dark matter.

Remerciements

Ces trois années de thèse au sein du Laboratoire de Physique Théorique d'Orsay ont été extraordinaires. C'est tout naturellement que je remercie les directeurs successifs Henk Hilhorst et Sébastien Descotes-Genon pour m'avoir offert la possibilité de m'épanouir par mes recherches dans un cadre idyllique. Mon enchantement n'aurait pas été celui qu'il est sans la présence et le soutien de l'ensemble des chercheurs du laboratoire.

Le CERN a toujours été mon endroit de pèlerinage préféré depuis déjà 7 années, je tiens à remercier cette incroyable institution, exemple à suivre dans bien des domaines.

Je souhaiterais aussi remercier l'ensemble de mes collaborateurs dont notamment Marco Battaglia, Oleg Lebedev, Luciano Maiani, Gregory Moreau, Keith Olive et Géraldine Servant pour leur temps, leur confiance et de m'avoir tant appris !

J'ai également une pensée pour tous les doctorants du laboratoire et les discussions passionnantes, ou pas, que nous avons eues, qu'elles aient été scientifiques ou non. En particulier, je remercie ceux qui ont partagé mon bureau : Bertrand Ducloué, Hermès Belusca-Maito et Antoine Gérardin. Cette thèse m'a aussi offert la possibilité de rencontrer et de collaborer avec des personnes fantastiques, merci à Florian Lyonnet, Christine Hartmann et Bryan Zaldivar.

Je remercie également l'ensemble des membres de mon jury pour leur disponibilité et leur soutient, merci à John Ellis, Ulrich Ellwanger, Louis Fayard, Pietro Slavich et mes rapporteurs, qui m'ont été d'une grande aide, Emilian Dudas et Sabine Kraml, merci pour toutes les remarques, suggestions et corrections qui ont contribuées à améliorer la qualité de ce manuscrit.

Mon succès n'aurait pas été celui qu'il est sans les incroyables personnalités d'Adam Falkowski et de Yann Mambrini qui m'ont enseigné un nombre faramineux de choses, qui ont toujours été là pour moi durant ces trois dernières années et le seront toujours j'en suis sûre. Merci encore pour tout cela ainsi que pour l'organisation du Magic Monday Journal Club, véritable lieu d'échange scientifique, un modèle !

Je remercie aussi un grand nombre de mes professeurs de la petite classe en passant par le Lycée, les classes préparatoires, l'Ecole Nationale Supérieure des Mines et de l'Ecole Normale Supérieure pour avoir participé à me donner goût aux sciences, et pour m'avoir transmis cette volonté de savoir et de comprendre.

Enfin tous les superlatifs vont à celui qui m'a chapeauté, éduqué, cocooné, exposé, protégé, épuisé, motivé, bref, qui m'a fait devenir un physicien théoricien qui a les pieds sur terre et qui a tout ce qu'il faut faut pour voler de ses propres ailes. Merci à Abdelhak Djouadi pour m'avoir forgé à sa manière, pour tous ses enseignements, sa patience et d'être en plus d'un physicien exceptionnel une personne si éblouissante !

Mes derniers remerciements iront naturellement à ma famille qui m'a toujours supporté, sans qui rien aurait été possible mais au contraire grâce à qui tout m'a été possible. Merci de m'avoir transmis le goût de l'effort, l'équilibre et la stabilité nécessaire pour pouvoir penser et avoir l'existence de mon choix. J'espère faire honneur à ceux qui nous ont quittés en cours de jeu, je dédie ce manuscrit à mon père.

Contents

List of Figures

List of Tables

Liste des publications

Les papiers suivants ont été écrits durant les trois années de ma thèse.
The following papers were written during the three years of my PhD.

Articles publiés (published papers) :

"Implications of a 125 GeV Higgs for supersymmetric models",
A. Arbey, M. Battaglia, A. Djouadi, F. Mahmoudi, J. Quevillon.
Phys. Lett. B708 (2012) 162-169, arXiv:1112.3028 [hep-ph]

"Implications of LHC searches for Higgs–portal dark matter",
Abdelhak Djouadi, Oleg Lebedev, Yann Mambrini, Jérémie Quevillon.
Phys. Lett. B709 (2012) 65-69, arXiv:1112.3299 [hep-ph]

"Direct detection of Higgs-portal dark matter at the LHC",
Abdelhak Djouadi, Adam Falkowski, Yann Mambrini, Jérémie Quevillon.
Eur. Phys. J. C73 (2013) 2455, arXiv:1205.3169 [hep-ph]

"The measurement of the Higgs self-coupling at the LHC: theoretical status",
J. Baglio, A. Djouadi, R. Gröber, M.M. Mühlleitner, J. Quevillon, M. Spira.
JHEP 1304 (2013) 151, arXiv:1212.5581 [hep-ph]

"Gauge coupling unification and non-equilibrium thermal dark matter",
Yann Mambrini, Keith A. Olive, Jérémie Quevillon, Bryan Zaldivar.
Phys. Rev. Lett. 110, 241306 (2013), arXiv:1302.4438 [hep-ph]

"The MSSM Higgs sector at a high M_{SUSY}: reopening the low $\tan\beta$ regime and heavy Higgs searches",
Abdelhak Djouadi, Jérémie Quevillon.
JHEP 10 (2013) 028, arXiv:1304.1787 [hep-ph]

"More on the hypercharge portal into the dark sector",
Florian Domingo, Oleg Lebedev, Yann Mambrini, Jérémie Quevillon, Andreas Ringwald.
JHEP 09 (2013) 020, arXiv: 1305.6815 [hep-ph]

"Thermal and non-thermal production of dark matter via Z'-portal(s)",
Xiaoyong Chu, Yann Mambrini, Jérémie Quevillon, Bryan Zaldivar.
JCAP 140 (2014) 034 arXiv: 1306.4677 [hep-ph]

"The post-Higgs MSSM scenario: Habemus MSSM?",
A. Djouadi, L. Maiani, G. Moreau, A. Polosa, J. Quevillon, V. Riquer.
Eur. Phys. J. C73 (2013) 2650, arXiv: 1307.5205 [hep-ph]

Comptes–rendus de conférences (proceedings) :

"Simplified description of the MSSM Higgs sector",
Jérémie Quevillon.
XLIX^{e} Rencontres de Moriond, EW interactions & unified theories,
arXiv: 1405.2241[hep-ph]

Introduction

In the last decades, the Standard Model of particle physics passed successfully the experimental tests at colliders. Before the year 2012, one crucial piece was missing: the Higgs boson. Since 1983 and the discovery of the massive W and Z gauge bosons, we knew that the electroweak symmetry was broken, but the discovery of the Higgs boson was necessary in order to check if the generation of mass relates on the spontaneous electroweak symmetry breaking, the Higgs mechanism. On the 4^{th} of July 2012, the discovery of a new particle with a mass of ~ 125 GeV was announced by the ATLAS and CMS collaborations. Many questions arise since this incredible experimental success, among them: is it the Standard Model scalar Higgs boson? Is it a supersymmetric Higgs boson i.e is it compatible with supersymmetric theories? Does it couple to the dark matter i.e does it connect us with a new sector?

Is it the Standard Model Higgs boson? Part I is devoted to an overview of the Standard Model of particle physics. In Section 1 we will immerse in the paradigm of gauge theories and shortly describe the construction of the electroweak theory. We will present the concept of spontaneous symmetry breaking which motivates the elaboration of the Higgs mechanism. Some of the properties of the scalar discovered by ATLAS and CMS still need to be checked, but it is very likely to be the Higgs scalar boson. If it is so, the Standard Model is complete and inside its framework it does not exist anymore unknown parameter. This closes the first era of the probing of the mechanism that triggers the breaking of the electroweak symmetry and generates the fundamental particle masses. Another equally important era is now opening: the precise determination of the properties of the produced particle. This is of extreme importance in order to establish that this particle is indeed the relic of the mechanism responsible for the electroweak symmetry breaking and, eventually, to pin down effects of new physics if additional ingredients beyond those of the Standard Model are involved in the symmetry breaking mechanism. To do so, besides measuring the mass, the total decay width and the spin–parity quantum numbers of the particle, a precise determination of its couplings to fermions and gauge bosons is needed in order to verify the fundamental prediction that they are indeed proportional to the particle masses.

Furthermore, it is of prime importance to measure the Higgs self–interactions. This is the only way to reconstruct the scalar potential of the Higgs doublet field, responsible for spontaneous electroweak symmetry breaking. Then in Section 2, we discuss the various processes which allow for the measurement of the trilinear Higgs coupling. We first evaluate the production cross sections for these processes at the Large Hadron Collider (LHC) and discuss their sensitivity to the trilinear Higgs coupling. We then discuss the various channels which could allow for the detection of the double Higgs production signal at the LHC and estimate their potential to probe the trilinear Higgs coupling.

Despite its enormous success, the Standard Model is widely believed to be an effective theory valid only at the presently accessible energies since it has several issues. For example, it does not provide a true unification of the electroweak and strong interactions. Furthermore, the Standard Model fails to explain dark matter, whose existence is unambiguously proven by observational cosmology. In addition, the scalar Higgs mass is highly unstable through radiative corrections: assuming the Standard Model to be valid

up to a very large scale, like the Planck scale, it would require an incredible amount of fine tuning between this scale and the bare Higgs mass in order to get a physical mass of ~ 125 GeV. This asks for a mechanism to protect the Higgs mass and more generally the electroweak scale. All those issues call for application of new physics beyond the Standard Model.

Is it a supersymmetric Higgs boson? Part II is devoted to supersymmetric extension of the Standard Model which is commonly assumed to be the most elegant way to ensure gauge coupling unification, a dark matter candidate and naturalness of the electroweak scale. In Section 3 we will motivate supersymmetry and give an introduction to its theoretical structure in Section 4 . We will move on to the Minimal Supersymmetric extension of the Standard Model (MSSM) that we will describe in details in Section 5 mainly focusing on the Higgs sector.

We will see in Section 6 that the $\sim$ 125 GeV Standard Model like Higgs boson discovered by ATLAS and CMS has extremely important consequences in the context of the MSSM. We have shown during this PhD that several unconstrained and constrained MSSM scenarios are now excluded, while the parameters of some others such as Split or high-scale supersymmetry are severely restricted.

One of the main implications of the LHC discovery, together with the non-observation of superparticles, is that the scale of supersymmetry-breaking might be rather high. This previous fact led us to study in particular the rich low $\tan\beta$ region, in Section 7. In Section 8 we will present a new model independent approach which would allow experimentalists to efficiently look for supersymmetric heavy Higgs bosons at current and next LHC runs.

Does it couple to the dark matter? Part III entirely deals with the dark matter issue. In section 9 we review the basics concerning dark matter and the early universe. In Section 10 we study the implications of a 125 GeV Standard Model like scalar for Higgs-portal models of dark matter in a model independent way. Their impact on the cosmological relic density and on the direct detection rates are studied in the context of generic scalar, vector and fermionic thermal dark matter particles. Possible observation of these particles in collider searches are discussed.

We also consider the process in which a Higgs particle is produced in association with jets and we show that monojet searches at the LHC already provide interesting constraints on the invisible decays of a 125 GeV Higgs boson. We also compare these direct constraints on the invisible rate with indirect ones based on measuring the Higgs rates in visible channels. We then discuss how the LHC limits on the invisible Higgs branching fraction impose strong constraints on the dark matter scattering cross section on nucleons probed in direct detection experiments.

An interesting alternative to the Higgs portal models is if the hidden sector contains more than one $U(1)$ groups. Consequently additional dim-4 couplings between the massive $U(1)$ fields and the hypercharge generally appear and the hidden vector fields could play the role of dark matter. In Section 11 we study this hypercharge portal into the dark sector.

The last two sections 12 and 13 are devoted to models where the dark matter particle is not in kinetic equilibrium with the thermal bath as usually assumed. In the first

one, we introduce a new mechanism that allows for gauge coupling unification, fixes reasonably the value of the universe reheating temperature and naturally provides a dark matter candidate. In the second section, we analyze the genesis of dark matter in the primordial universe for representative classes of Z′-portals models.

Finally, we summarize the results which have been obtained during this PhD thesis.

Part I

The Standard Model of particle physics

Summary

1 Introduction to the electroweak theory

1.1 Quantum electrodynamics or the paradigm of gauge theories

If a physical free field in particle physics is invariant under a global symmetry then an interacting theory is obtained by promoting the global symmetry to a local one (defining the gauge group). This can be done by introducing new vector boson fields, called the gauge fields, that interact in a gauge invariant way to the originally free field. The Standard Model of particle physics has been built mostly from this gauge principle since it is based on particle interactions invariant under the gauge group $SU(3)_C \times SU(2)_L \times U(1)_Y$.

Let us consider a free Dirac fermion field ψ with mass m and electric charge eQ, its associated Lagrangian reads

$$\mathcal{L}_D = \overline{\psi}(x)(i\partial_\mu\gamma^\mu - m)\psi(x) \; . \tag{1.1}$$

This Lagrangian is then invariant under a global $U(1)$ transformation which modifies the field as $\psi \to e^{iQ\theta}\psi$ with θ the parameter of the induced global phase. This symmetry invariance implies some conservation laws in accordance to the Noether's theorem. The $U(1)$ symmetry is responsible for the conservation of the electromagnetic current $J_\mu = \overline{\psi}\gamma_\mu eQ\psi$, and the electromagnetic charge $eQ = \int d^3x J_0(x)$. If the parameter of the transformation depends on the space-time (θ(x)) then the transformation is not anymore global but local and the previous Lagrangian is not anymore invariant under such transformations. By introducing the interacting photon field $A_\mu(x)$ which transforms under the $U(1)$ gauge transformation as

$$A_\mu \to A_\mu - \frac{1}{e}\partial_\mu\theta(x) \; , \tag{1.2}$$

one re-establishes the invariance which becomes local. Consequently, the Lagrangian invariant under $U(1)$ gauge transformations is the Quantum Electrodynamics (QED) Lagrangian

$$\mathcal{L}_{\rm QED} = \overline{\psi}(x)(i\partial D_\mu\gamma^\mu - m)\psi(x) - \frac{1}{4}F_{\mu\nu}(x)F^{\mu\nu}(x) \tag{1.3}$$

where we have introduced the covariant derivative $D_\mu \equiv \partial_\mu - ieQA_\mu$ and the field strength tensor $F_{\mu\nu} = \partial_\mu A_\nu - \partial_\nu A_\mu$ which has been useful to build the kinetic term associated to the photon propagation. The new interaction term between the Dirac fermion and the photon is $\overline{\psi}eQA_\mu\gamma^\mu\psi$.

Some fermion fields, the quarks, are charged (called color) under an other gauge symmetry group. The Quantum Chromo Dynamics (QCD) is a non abelian gauge symmetry build on the group $SU(3)$. QCD is the fondamental theory that describes the strong interactions between quarks and gluons in a similar way that QED describes the electromagnetic interactions between the electrons and photons. In the next discussions we will mostly focus on an other gauge symmetry associated to the weak interactions.

1.2 Toward the electroweak theory

A new weak strength interaction has been imagined in order to explain measurements of long lifetimes in the decays of well known particles such as the neutron or the muon

$$\begin{aligned} n &\rightarrow (\overline{\nu}_e)e^- p \quad [\tau_n = 920s] \,, \\ \mu^- &\rightarrow (\nu_\mu \overline{\nu}_e)e^- \quad [\tau_n = 2.2 \times 10^{-6} s] \,. \end{aligned} \tag{1.4}$$

These lifetimes are indeed much more longer than decays mediated by the electromagnetic interaction, as for instance

$$\pi^0 \rightarrow \gamma\gamma \quad [\tau_{\pi^0} = 10^{-16} s] \,, \tag{1.5}$$

or the one involving the strong interaction as

$$\Delta \rightarrow \pi p \quad [\tau_{\pi^0} = 10^{-23} s] \,. \tag{1.6}$$

We will shortly review the main theories elaborated to describe the weak interactions before the formulation of the electroweak theory of the Standard Model, namely the Fermi Theory, the Feynman and Gell-Mann $V-A$ theory and the Lee, Yang and Glashow intermediate vector boson theory.

1.2.1 Fermi theory of weak interactions

In order to explain the neutron β-decay process $n \rightarrow \overline{\nu}_e e^- p$, Fermi introduced in 1934 a theory with four-fermion interactions [1]

$$\mathcal{L}_{\text{Fermi}} = -\frac{G_F}{\sqrt{2}} \left[\overline{p}\gamma_\mu n\right] \left[\overline{e}\gamma^\mu \nu e\right] + h.c. \tag{1.7}$$

with p, n, e, ν the fermion fields and the dimensional Fermi constant $G_F = 1.167 \times 10^{-5}$ GeV^{-2}. Fermi contracted two vectorial currents, the hadronic current $J_\mu^{(had)}(x) = \overline{p}(x)\gamma_\mu n(x)$ and the leptonic current $J_\mu^{(lep)}(x) = \overline{e}(x)\gamma_\mu \nu_e(x)$, at the same space-time point.

1.2.2 Parity violation and the $V - A$ theory of charged weak interactions

In 1956, Lee and Yang claimed that the weak interactions did not respect the parity symmetry (if the experimental apparatus is mirror-reversed the results are unchanged) [2]. This argument was motivated by the observation of Kaon decays in two distinct final states with opposite parities $K^+ \rightarrow \pi^+\pi^+\pi-$ and $K^+ \rightarrow \pi^+\pi^0$. Parity violation was observed a year later, in 1957, by Wu and collaborators [3] in the beta decay of cobalt ^{60}Co $\rightarrow \overline{\nu}_e e^{-\,60}$Ni* where they established that charged currents produce electrons which are only left-handed and antineutrinos which are only right-handed. This is a clear evidence of parity violation, and therefore, the charged weak current cannot be only vectorial but should contain axial vector contribution $J_\mu = \alpha V_\mu + \beta A_\mu$. We remind that vector and axial vector currents transform under parity transformation as

$$\begin{aligned} V^\mu = \overline{\psi}\gamma^\mu\psi &\underset{P}{\rightarrow} (\overline{\psi}\gamma^0\psi, -\overline{\psi}\gamma^i\psi) \,, \\ A^\mu = \overline{\psi}\gamma^\mu\gamma^5\psi &\underset{P}{\rightarrow} (-\overline{\psi}\gamma^0\gamma^5\psi, +\overline{\psi}\gamma^i\gamma^5\psi) \,. \end{aligned} \tag{1.8}$$

Thus, the product $V_\mu A^\mu$ is not invariant under parity transformation so a current of the form $J_\mu = \alpha V_\mu + \beta A_\mu$, will induce parity violation in the theory because of the Lagrangian term $\mathcal{L}_{\not P} \propto J_\mu J^{\dagger\mu}$.

The fact that the weak current couples only to the left-handed fermions and only to the right-handed anti-fermions is a clear evidence of maximal parity violation that can be obtained with

$$J_\mu = V_\mu - A_\mu \ . \tag{1.9}$$

For example, the leptonic current reads in terms of the chiral fields

$$J_\mu^{(lep)} \propto V_\mu - A_\mu = \overline{\nu}_{e,R}\gamma_\mu(1-\gamma_5)e = 2\overline{\nu}_{e,R}\gamma_\mu e_L \ . \tag{1.10}$$

In 1958, Feynman and Gell-Mann added to the Theory of Fermi the charged weak current of the form $V-A$ in order to cure the parity non conservation issue [4]. The Lagrangian for the two first generations is now

$$\begin{aligned} \mathcal{L}_{V-A} &= -\frac{G_F}{\sqrt{2}} J_\mu^{c.c.}(x) J^{c.c.\dagger\mu}(x) \ , \\ J_\mu^{c.c.} &= 2\overline{\nu}_{e,R}\gamma_\mu e_L + 2\overline{\nu}_{\mu,R}\gamma_\mu \mu_L + 2\overline{u}_R\gamma_\mu d'_L \ . \end{aligned} \tag{1.11}$$

An other anomaly concerned the ratio between the kaon ($\bar{u}s$) and the pion ($\bar{u}d$) decay rates and was experimentally measured around 1/20 and not 1 as naively expected. In 1963, Cabibbo had the idea to relate the weak interaction d-quark eigenstate (noted d$'$) with the d-quark mass eigenstate noted d and the strange quark mass eigenstate noted s [5]. He introduced the Cabibbo angle θ_c through the rotation

$$d' = \cos\theta_c d + \sin\theta_c s \ . \tag{1.12}$$

Then in the $V-A$ theory assuming $\theta_c \approx 13$ one can accommodate the previous anomaly

$$\frac{\Gamma(K^- \to \mu\overline{\nu}_\mu)}{\Gamma(\pi^- \to \mu\overline{\nu}_\mu)} = \frac{\sin^2\theta_c}{\cos^2\theta_c} \approx \frac{1}{20} \ . \tag{1.13}$$

The Fermi constant was determined by measuring the muon lifetime

$$\tau_\mu = \frac{192\pi^3}{G_F^2 m_\mu^5} \ . \tag{1.14}$$

However in 1973, the discovery of the neutral current [6] was not in agreement with the $V-A$ theory which does not include any currents of this type. On the top of that the $V-A$ theory is also non-renormalizable and violates unitarity. Thus this is a low energy effective theory and it certainly needs more refinements.

1.2.3 The intermediate vector boson theory of weak interactions

The Intermediate Vector Boson theory (IVB) stipules that the weak interaction is mediated through massive vector bosons. Charged vector bosons were introduced to explain charged weak currents [7] and one neutral vector boson to explain the weak neutral current [8].The Lagrangian of such interactions reads

$$\mathcal{L} \ = \ \frac{g}{\sqrt{2}}\left(J_\mu^{c.c.}W^{+\mu} + J_\mu^{c.c.\dagger}W^{-\mu}\right) + \frac{g}{\cos\theta_w} J_\mu^{n.c.\dagger} Z^\mu \tag{1.15}$$

with the weak angle θ_w that will be discussed later on and the newly introduced neutral current for a generic fermion f

$$J_\mu^{n.c} = g_L^f \overline{f} \gamma_\mu \left(\frac{1-\gamma_5}{2} \right) f + g_R^f \overline{f} \gamma_\mu \left(\frac{1+\gamma_5}{2} \right) f \ . \tag{1.16}$$

The current interactions are not local anymore due to the propagation of the vector bosons. The neutral current discovery at CERN was a great success for this IVB theory. Nevertheless this is still an effective theory which is non-renormalizable and violate unitarity as the $V-A$ theory. Furthermore, it does not include vector bosons self-interactions. As we will see, non-abelian gauge theory will fix these major issues.

1.3 The electroweak theory

1.3.1 A short historical overview

In 1961, Glashow introduced the electroweak theory gauge group $SU(2)_L \times U(1)_Y$ [8]. His goal was to unify the weak interactions with the electromagnetic interactions in a group which contains $U(1)_{em}$. His model already contains the four vector bosons $\mathrm{W}^\pm$, Z and γ obtained from the weak eigenstates. The $\mathrm{W}^\pm$ and Z boson were not yet considered as gauge bosons and their masses were just parameters. An important ingredient for the electroweak theory is the Goldstone theorem which is largely due to the work of Nambu in 1960, Goldstone in 1961, and by Goldstone, Salam and Weinberg in 1962 [9–11]. The theorem introduces scalar massless fields that emerge from spontaneous symmetry breaking of global symmetries. The spontaneous symmetry breaking of local/gauge symmetries, a necessary step in order to break the electroweak sector $SU(2)_L \times U(1)_Y$, was investigated starting the year 1964 by Higgs, Brout, Englert, Guralnik, Hagen and Kibble [12–16]. This spontaneous breakdown of gauge symmetries is called the Higgs mechanism and it was inspired from the work on superconductivity of Jona-Lasinio and Nambu [17, 18] and those of Schwinger in 1962 [19] and Anderson in 1963 [20]. The modern formulation of the electroweak theory is the one of Weinberg in 1967 [21] and Salam in 1968 [22] which makes use of the unification principle of Glashow [8]. This Glashow-Weinberg-Salam theory or the Standard Model of particle physics is a gauge theory based on the gauge symmetry of the electroweak interactions $SU(2)_L \times U(1)_Y$.The massive gauge bosons result from the Higgs mechanism. In 1971, 't Hooft proved the renormalizability of gauge theories without and with spontaneous symmetry breaking [23, 24]. The first strong evidence in favor of the SM was the discovery at CERN of the weak neutral current in 1973 [6] allowing to measure the Weinberg angle for the first time providing estimate for the weak gauge bosons masses. Ten years later, in 1983, the UA1 and UA2 experiments at the SPS proton-antiproton collider at CERN, which were leaded by Van der Meer and Rubbia, discovered directly the $W^\pm$ and Z gauge bosons. Another characteristic of the SM is its three family duplication and mixing between quarks. Indeed, as we have seen, Cabibbo introduced mixing between the d and s quarks [5]. The partner of the strange quark in charged weak current, the charm quark, c, was introduced by Bjorken and Glashow in 1964 [25]. In 1970, Glashow, Iliopoulos and Maiani predicted the existence of the charm quark in order to suppress Flavor (originally strangeness) Changing Neutral Currents, this is the GIM mechanism. In 1974, the discovery of the $J-\Psi$ particle which is a $\bar{c}c$ bound state, proved the existence

of the c quark [26]. When one adds the discovery of the b quark [27] and the lepton τ and ν_τ [28] the three family generation is well established. The last piece, the top quark, was discovered in 1994 [29–31]. Finally, the mixing between these three families is given by the Cabibbo-Kobayashi-Maskawa (CKM) matrix [32] which introduces the SM CP-violation phase.

1.3.2 Why $SU(2)_L \times U(1)_Y$?

For simplicity we will concentrate on the case of the first lepton family, namely e^- and ν_e. As we have seen, for this family, the charged and neutral weak currents only involve the left-handed component of the fields. Let us gather these left-handed components in the same lepton doublet

$$\begin{aligned} l_L &= \begin{pmatrix} \nu_L \\ e_L \end{pmatrix} , \\ \overline{l_L} &= \begin{pmatrix} \overline{\nu_L} & \overline{e_L} \end{pmatrix} . \end{aligned} \tag{1.17}$$

We can then write the charged currents derived above and some neutral weak currents as

$$\begin{aligned} J_\mu &= \overline{l_L}\gamma_\mu\sigma_+ l_L \; ;, \\ J_\mu^\dagger &= \overline{l_L}\gamma_\mu\sigma_- l_L \; , \\ J_\mu^3 &= \overline{l_L}\gamma_\mu\frac{\sigma_3}{2} l_L \; , \end{aligned} \tag{1.18}$$

where we have introduced the Pauli matrices σ_i defined as

$$\sigma_1 = \begin{pmatrix} 0 & 1 \\ 1 & 0 \end{pmatrix} \quad , \quad \sigma_2 = \begin{pmatrix} 0 & -i \\ i & 0 \end{pmatrix} \quad , \quad \sigma_3 = \begin{pmatrix} 1 & 0 \\ 0 & -1 \end{pmatrix} \tag{1.19}$$

with the definition $\sigma_\pm = (\sigma_1 \pm \sigma_2)/2$. In fact the three Pauli matrices (more exactly $T_i = \sigma_i/2$) generate the $SU(2)$ group transformations defined by its algebra

$$[\sigma_i, \sigma_j] = i\epsilon_{ijk}\sigma_k \tag{1.20}$$

with the Levi-Civita symbols ϵ_{ijk}. This new symmetry which concerns left-handed chiral fields (that explains the notation $SU(2)_L$) is associated (cf. Noether's theorem) to three conserved charges, called weak charges. The one associated to J_0^3 is called the weak isospin and is noted T_3. Nevertheless, the neutral weak current we are considering is not the physically known electromagnetic current neither the measured neutral current. In order to unify the weak interactions with electromagnetism, Glashow introduces the hypercharge $U(1)_Y$ group associated to a new neutral current J_μ^Y and a new conserved charge, the hypercharge Y. The electromagnetic group is then a subgroup of the electroweak group $SU(2)_L \times U(1)_Y$. Since $U(1)$ commutes with $SU(2)$, the electromagnetic current simply reads

$$J_\mu^{em} = J_\mu^3 + J_\mu^Y \tag{1.21}$$

and the electric charge, Q, is linked to the weak charge T_3 by the intermediate of the hypercharge through the Gell-Mann-Nishijima like formula

$$Q = T_3 + \frac{Y}{2} \; . \tag{1.22}$$

Knowing the expression of J_μ^3 and for example the physical current associated to the photon A_μ, J_μ^{em}, one can compute J_μ^Y and afterwards the physical neutral current associated to Z_μ, $J_\mu^{n.c.}$, which is a combination of J_μ^3 and J_μ^Y orthogonal to J_μ^{em}. The weak angle parametrizes this rotation which can be written as

$$J_\mu^{n.c.} = \cos^2\theta_w J_\mu^3 - \sin^2\theta_w \frac{J_\mu^Y}{2} \tag{1.23}$$

In full generality, one can write the neutral currents for all leptons and quarks of all the generations as

$$\begin{aligned}
J_\mu^3 &= \sum_f T_3^f \overline{f_L}\gamma_\mu f_L \ , \\
J_\mu^Y &= \sum_f Y^{fL}\overline{f_L}\gamma_\mu f_L + \sum_f Y^{fR}\overline{f_R}\gamma_\mu f_R \ , \\
J_\mu^{em} &= \sum_f Q^f \overline{f_L}\gamma_\mu f_L + \sum_f Q^f \overline{f_R}\gamma_\mu f_R \ , \\
J_\mu^{n.c.} &= \sum_f g_L^f \overline{f_L}\gamma_\mu f_L + \sum_{f\neq\nu} g_R^f \overline{f_R}\gamma_\mu f_R \ ,
\end{aligned} \tag{1.24}$$

with weak chiral couplings defined as $g_L^f = T_3^f - Q^f \sin^2\theta_w$ and $g_R^f = -Q^f \sin^2\theta_w$. Consequently, we have everything to write the Lagrangian describing the electroweak interactions

$$\begin{aligned}
\mathcal{L}_{int} &= \mathcal{L}_{em} + \mathcal{L}_{n.c.} + \mathcal{L}_{c.c.} \ , \\
\mathcal{L}_{em} &= e J_\mu^{em} A^\mu \ , \\
\mathcal{L}_{n.c.} &= \frac{g}{\cos\theta_w} J_\mu^{n.c.} Z^\mu \ , \\
\mathcal{L}_{c.c.} &= \frac{g}{\sqrt{2}}\left(J_\mu W^{+\mu} + J^{\dagger\mu} W^{-\mu}\right) \ .
\end{aligned} \tag{1.25}$$

1.3.3 Gauging the electroweak theory

In the previous paragraph we used the symmetry group in order to write the interactions of the electroweak sector. Nevertheless, the introduced bosons are not yet promoted to gauge bosons. Let us gauge the electroweak theory, i.e upgrade $SU(2)_L \times U(1)_Y$ to a local symmetry. One has to proceed as in any gauge theory, that is to say, replace the field derivatives by the corresponding covariant derivatives. The electroweak covariant derivative of a generic fermion f reads

$$D_\mu f = \left(\partial_\mu - ig\frac{\sigma_i}{2}W_\mu^i - ig'\frac{Y}{2}B_\mu\right) f \tag{1.26}$$

where W^i are the three $SU(2)_L$ weak bosons and B_μ is the $U(1)_Y$ hypercharge boson. The terms which generate the electroweak interactions come, as usual, from $\overline{f}\gamma^\mu D_\mu f$ and one can recover easily the electroweak interaction Lagrangian of Eq.1.25. Finally one obtains the full Electroweak Lagrangian by adding the fermion kinetic terms (which

include gauge interactions), the boson kinetic terms (including boson self interactions), the electroweak symmetry breaking terms and the Yukawa terms

$$\begin{aligned} \mathcal{L}_{SM} &= \mathcal{L}_f + \mathcal{L}_B + \mathcal{L}_{EWSB} + \mathcal{L}_Y \ , \\ \mathcal{L}_f &= \sum_{f=l,q} i\overline{f}\gamma^\mu D_\mu f \ , \\ \mathcal{L}_B &= -\frac{1}{4}W^i_{\mu\nu}W_i^{\mu\nu} - \frac{1}{4}B_{\mu\nu}B^{\mu\nu} + (\mathcal{L}_{GF+FP}) \end{aligned} \tag{1.27}$$

with $B_{\mu\nu}$ the usual field strength associated to the $U(1)_Y$ symmetry, and $W^i_{\mu\nu}$ is the field strength associated to the non-abelian $SU(2)_L$ group

$$W^i_{\mu\nu} = \partial_\mu W^i_\nu - \partial_\nu W^i_\mu + g\epsilon^{ijk}W^j_\mu W^k_\nu \ . \tag{1.28}$$

For completeness we should mention the Gauge Fixing (GF) procedure and the Faddeev Popov (FP) terms. The SM Lagrangian is by construction invariant under $SU(2)_L \times U(1)_Y$ gauge transformations and we recall the different fields transformations

$$\begin{aligned} f_L &\to e^{iT_i\theta^i(x)}f_L \ , \\ f_R &\to f_R \ , \\ W^i_\mu &\to W^i_\mu - \frac{1}{g}\partial\theta^i(x) + \epsilon^{ijk}\theta^j W^k_\mu \ , \\ f &\to e^{i\frac{Y}{2}\alpha(x)}f \ , \\ B_\mu &\to B_\mu - \frac{1}{g'}\partial\alpha(x) \ . \end{aligned} \tag{1.29}$$

Before discussing the two last Lagrangian contributions, notice that the physical gauge bosons $W^\pm_\mu, Z_\mu$ and A_μ mass eigenstates are obtained from the interaction eigenstates as follows

$$\begin{aligned} W^\pm_\mu &= \frac{1}{\sqrt{2}}\left(W^1_\mu \mp W^2_\mu\right) \ , \\ Z_\mu &= \cos\theta_w W^3_\mu - \sin\theta_w B_\mu \ , \\ A_\mu &= \sin\theta_w W^3_\mu + \cos\theta_w B_\mu \ . \end{aligned} \tag{1.30}$$

By identification with our adopted approach before gauging the electroweak theory, one finds $g = e/\sin\theta_w$ and $g' = e/\cos\theta_w$. Notice that the mass terms of the gauge bosons $M^2_W W^\mu W_\mu$, $\frac{1}{2}M^2_Z Z^\mu Z_\mu$ and of fermions $m_f\overline{f}f$ are not present in $\mathcal{L}_B$ nor $\mathcal{L}_f$ because there are not gauge invariant under the electroweak symmetry group: they break the $SU(2)_L \times U(1)_Y$ gauge symmetry. The gauge boson masses will be generated by the Electroweak Symmetry Breaking Lagrangian term and the fermion masses will be generated by the Yukawa term. However these masses must be realized in a gauge invariant way. We will now focus on the Spontaneous Electroweak Symmetry breaking which can be performed by the Higgs mechanism that provides a gauge invariant mass generation.

1.4 From spontaneous symmetry breaking to the Higgs mechanism

1.4.1 Spontaneous symmetry breaking and the Goldstone theorem

A physical system has a symmetry which is spontaneously broken if the interactions controlling its dynamics has such a symmetry and its ground state does not. A crucial implication of spontaneously symmetry breaking is the existence of massless modes. This effect is stated by the Goldstone theorem [9–11]: "If a Theory has a global symmetry of the Lagrangian which is not a symmetry of the vacuum then there must exist one massless boson, scalar or pseudoscalar, associated to each generator which does not annihilate the vacuum and has the same quantum numbers. These modes are referred to as Goldstone bosons". In Quantum Field Theory, spontaneously symmetry breaking is equivalent to the scenario where a field gets a non-vanishing vacuum expectation value. However, the Goldstone theorem only applies for theories with spontaneously global symmetry breaking, so it does not apply for gauge theories. The Brout-Englert-Higgs mechanism (shortly the Higgs mechanism) is the realization of spontaneously gauge symmetry breaking [12–16]. "The would-be Goldstone bosons associated to the global symmetry breaking do not manifest explicitly in the physical spectrum but instead they combine with the massless gauge bosons and as a result, once the spectrum of the theory is built up on the asymmetrical vacuum, there appear massive vector particles. The number of vector bosons that acquire a mass is precisely equal to the number of these would-be Goldstone bosons".

We expect from the Higgs mechanism, when applied to the electroweak sector of the Standard Model, to generate masses for the three gauge bosons $W^{\pm}, Z$ but not for the photon γ. It will require three Goldstone bosons that will combine with three massless bosons associated to the $SU(2)_L \times U(1)_Y$ symmetry. We should not forget that the SM is invariant under this last group transformations, thus the Higgs mechanism should preserve it. In addition, since only $U(1)_{em}$ is not broken, the vacuum should never break it. Let us now spontaneously break the electroweak symmetry, $SU(2)_L \times U(1)_Y \rightarrow U(1)_{em}$.

1.4.2 The Higgs mechanism

Let us consider Φ as the field system which will ensure this breaking. If we want that this breaking preserves Lorentz invariance then Φ has to be a scalar field. A priori, if we want the Lagrangian to be Hermitian Φ should be a complex field. If we want to break $SU(2)_L \times U(1)_Y$ with it, Φ has to be charged under $SU(2)_L$ and $U(1)_Y$. The choices of its quantum numbers and of its representation are various. However we can classify its possible representations in two categories, one type will impose that Φ will not transform linearly under $SU(2)_L \times U(1)_Y$, and the other type will ensure linear transformations. For this second scenario, the minimal set up is one complex $SU(2)_L$ doublet but a priori a complex triplet or two complex doublets as in the Minimal Supersymmetric extension of the Standard Model (that will be discussed in details in the following) are possible. The non-vanishing vacuum expectation value, $\langle 0|\Phi|0\rangle \neq 0$, should result from the self-interaction of this field. Furthermore as we do not want to break $U(1)_{em}$ only the electromagnetically neutral component of Φ should get a non-vanishing vacuum

expectation value. Obviously we do not want to spoil good features of gauge theories i.e the nice high energy behavior and the renormalizability. Taking into account all these requirements and simplifications, the breaking system will be a complex scalar field, $SU(2)_L$ doublet with hypercharge $Y = 1$ written as

$$\Phi = \begin{pmatrix} \phi^+ \\ \phi^0 \end{pmatrix} \tag{1.31}$$

The Lagrangian which will break spontaneously the electroweak symmetry is the following

$$\begin{aligned} \mathcal{L}_{EWSB} &= (D_\mu \Phi)^\dagger (D^\mu \Phi)^\dagger - V(\Phi) \,, \\ V(\Phi) &= -\mu^2 \Phi^\dagger \Phi + \lambda \left(\Phi^\dagger \Phi\right)^2 \,. \end{aligned} \tag{1.32}$$

This choice of scalar potential introduces two parameters μ and λ. Requiring an extremum somewhere and more precisely a minimum energy state which defines the vacuum, offers two possibilities

- One trivial solution is to set $\langle 0|\Psi|0\rangle = 0$ then the ground state is a global minimum if $(-\mu^2) > 0$. But this is not what we planned to do since the vacuum does not break the $SU(2)_L \times U(1)_Y$ symmetry.
- The other solution, that we are looking for, occurs with

$$|\langle 0|\Psi|0\rangle| = \begin{pmatrix} 0 \\ \frac{v}{\sqrt{2}} \end{pmatrix} \tag{1.33}$$

  with the extremum requirement that $v \equiv \sqrt{\frac{\mu^2}{\lambda}}$. This implies that $(-\mu^2) < 0$ and it leads to an infinite number of degenerate vacua distinguished by a complex phase and all of them preserve $U(1)_{em}$ and break $SU(2)_L$ and $U(1)_Y$. As soon as a particular phase is privileged i.e the vacuum is set, the breaking $SU(2)_L \times U(1)_Y \to U(1)_{em}$ occurs.

The physical particles result from small fluctuations of this field around its vacuum. Because the $U(1)_{em}$ symmetry is preserved one can always performed a $SU(2)_L$ rotation of the field Φ (which corresponds to a particular gauge choice) and write it around its vacuum as

$$\Phi = \begin{pmatrix} 0 \\ \frac{1}{\sqrt{2}}(v + H(x)) \end{pmatrix} \tag{1.34}$$

If we rotate also the weak boson interaction eigenstates to their mass eigenstates which are defined by Eq.1.30, we can easily obtain their newly introduced mass terms by looking at

$$(D_\mu \Phi)^\dagger (D^\mu \Phi)^\dagger \supset \left(\frac{g^2 v^2}{4}\right) W_\mu^+ W^{\mu -} + \frac{1}{2}\left(\frac{(g^2 + g'^2)v^2}{4}\right) Z_\mu Z^\mu \tag{1.35}$$

then we get the SM tree level mass $M_W = gv/2$ and $M_Z = \sqrt{g^2 + g'^2}v/2$. The two scalar degrees of freedom that compose ϕ^+ played the role of the Goldstone bosons and

have been "eaten" by $W^{\pm}$ and represent their longitudinal polarization i.e their mass. The same process happens for one of the scalar component of ϕ^0 relatively to Z. The remaining scalar degree of freedom corresponds in our notation to the fluctuation H. After that electroweak symmetry breaking happens the extra physical scalar, the Brout-Englert-Higgs boson (in short the BEH boson or traditionally the Higgs boson) gets a mass from the scalar potential

$$-V(\Phi) \supset \frac{1}{2}(-2\mu^2)H^2 \tag{1.36}$$

the tree level SM prediction is then $M_H^2 = -2\mu^2$. The only missing ingredient is the fermion masses. The fermions of the SM also couple to the Higgs field and these terms are collected in the Yukawa Lagrangian of Eq.1.28 which reads

$$\mathcal{L}_Y = -Y_e\overline{L}\Phi e_R - Y_d\overline{Q}\Phi d_R - Y_u\overline{Q}(i\tau_2\Phi^*)u_R \tag{1.37}$$

where we have for simplicity only written the first family Yukawa terms and we have left out the CKM coefficients in the quark sector. When the Higgs field acquires a non-vanishing v.e.v. its oscillations around the ground state will also produce massive fermions. The Yukawa Lagrangian then reads

$$\begin{aligned}\mathcal{L}_Y = & -\left(\frac{Y_e v}{\sqrt{2}}\right)\overline{e}e - \left(\frac{Y_d v}{\sqrt{2}}\right)\overline{d}d - \left(\frac{Y_u v}{\sqrt{2}}\right)\overline{u}u \\ & -\left(\frac{Y_e}{\sqrt{2}}\right)\overline{e}He - \left(\frac{Y_d}{\sqrt{2}}\right)\overline{d}Hd - \left(\frac{Y_u}{\sqrt{2}}\right)\overline{u}Hu\end{aligned} \tag{1.38}$$

with fermion masses $m_{e/d/u} = Y_{e/d/u}v/\sqrt{2}$, the second line corresponds to the Higgs-fermion-fermion couplings.

Notice that at tree level, all the boson masses depend on v and their gauge coupling g, g' and the fermion masses depend only on v and their Yukawa coupling. At the end of the day, all the physical massive particles get a mass thanks to the Higgs mechanism.

For completeness we should also collect all the interaction terms with the Higgs field. From the previous formulas we get ($\mathcal{L}_H^{int} \subset \mathcal{L}_{EWSB} + \mathcal{L}_Y$)

$$\begin{aligned}\mathcal{L}_H^{int} = & -\frac{m_f}{v}fH\overline{f} \\ & +M_W^2 W_\mu^+ W^{\mu-}\left(\frac{v}{2}H + \frac{1}{v^2}H^2\right) \\ & +\frac{1}{2}M_Z^2 Z_\mu Z^\mu\left(\frac{v}{2}H + \frac{1}{v^2}H^2\right) \\ & -\frac{M_H^2}{v}H^3 - \frac{M_H^2}{4v^2}H^4\,.\end{aligned} \tag{1.39}$$

The three first lines correspond to the Higgs couplings to fermion and gauge bosons. We should mention that v is determined experimentally from μ-decay, the identification of the SM μ-decay width to the predicted one in the $V-A$ theory gives

$$\frac{G_F}{\sqrt{2}} = \frac{g^2}{8M_W^2} = \frac{1}{2v^2} \tag{1.40}$$

Numerically $v = (\sqrt{2}G_F)^{-1/2} \approx 246$ GeV. Then the previous Higgs couplings with fermions or gauge bosons are entirely proportional to the gauge coupling and the interacting particle mass. The last line corresponds to the Higgs-self couplings, namely the trilinear self-coupling and the quartic self-coupling. The self-coupling λ is entirely determined by the Higgs mass through the relation $\lambda = M_H^2/v^2$.

Now that the Higgs boson has been observed by the ATLAS and CMS experiments at the LHC with a mass of ≈ 125 GeV, this self-coupling is a priori known but it still remains to be verified experimentally since Beyond the Standard Model physics should modify it (examples of typical expected deviations are given in Ref. [33]). Therefore the next important step would be to measure accurately the Higgs self–coupling in order to establish the details of the electroweak symmetry breaking mechanism. The determination of the Higgs self–coupling can be done by looking at processes where the Higgs boson is produced in pairs.

In the following section, we discuss the various processes that allow for the measurement of the trilinear Higgs coupling: double Higgs production in gluon fusion, vector boson fusion, double Higgs–strahlung and associated production with a top quark pair. We first evaluate the production cross sections for these processes at the LHC with center–of–mass energies ranging from the present $\sqrt{s} = 8$ TeV to $\sqrt{s} = 100$ TeV, and discuss their sensitivity to the trilinear Higgs coupling. We include the various higher order QCD radiative corrections, at next–to–leading order for gluon and vector boson fusion and at next–to–next–to–leading order for associated double Higgs production with a gauge boson. The theoretical uncertainties on these cross-sections are estimated. Finally, we discuss the various channels which could allow for the detection of the double Higgs production signal at the LHC and estimate their potential to probe the trilinear Higgs coupling.

2 The measurement of the Higgs self-coupling at the LHC

2.1 Preliminaries

A bosonic particle with a mass of about 125 GeV has been observed by the ATLAS and CMS Collaborations at the LHC [34, 35] and it has, *grosso modo*, the properties of the long sought Higgs particle predicted in the Standard Model (SM) [12–14, 21, 36]. This closes the first chapter of the probing of the mechanism that triggers the breaking of the electroweak symmetry and generates the fundamental particle masses. Another, equally important chapter is now opening: the precise determination of the properties of the produced particle. This is of extreme importance in order to establish that this particle is indeed the relic of the mechanism responsible for the electroweak symmetry breaking and, eventually, to pin down effects of new physics if additional ingredients beyond those of the SM are involved in the symmetry breaking mechanism. To do so, besides measuring the mass, the total decay width and the spin–parity quantum numbers of the particle, a precise determination of its couplings to fermions and gauge bosons is needed in order to verify the fundamental prediction that they are indeed proportional to the particle masses. Furthermore, it is necessary to measure the Higgs self–interactions. This is the only way to reconstruct the scalar potential of the Higgs doublet field Φ, that is responsible for spontaneous electroweak symmetry breaking, Rewriting the Higgs potential in terms of a physical Higgs boson leads to the trilinear Higgs self–coupling λ_{HHH}, which in the SM is uniquely related to the mass of the Higgs boson,

$$\lambda_{HHH} = \frac{3M_H^2}{v}\,. \tag{2.41}$$

This coupling is only accessible in double Higgs production [37–45]. One thus needs to consider the usual channels in which the Higgs boson is produced singly [46–50], but allows for the state to be off mass–shell and to split up into two real Higgs bosons. At hadron colliders, four main classes of processes have been advocated for Higgs pair production:

a) the gluon fusion mechanism, $gg \to HH$, which is mediated by loops of heavy quarks (mainly top quarks) that couple strongly to the Higgs boson [51–54, 54];

b) the WW/ZZ fusion processes (VBF), $qq' \to V^*V^*qq' \to HHqq'$ ($V = W, Z$), which lead to two Higgs particles and two jets in the final state [52, 55–59];

c) the double Higgs–strahlung process, $q\bar{q}' \to V^* \to VHH$ ($V = W, Z$), in which the Higgs bosons are radiated from either a W or a Z boson [60];

d) associated production of two Higgs bosons with a top quark pair, $pp \to t\bar{t}HH$ [61].

As they are of higher order in the electroweak coupling and the phase space is small due to the production of two heavy particles in the final state, these Standard Model processes have much lower production cross sections, at least two orders of magnitude

smaller, compared to the single Higgs production case [1]. In addition, besides the diagrams with $H^* \to HH$ splitting, there are other topologies which do not involve the trilinear Higgs coupling, e.g. with both Higgs bosons radiated from the gauge boson or fermion lines, and which lead to the same final state. These topologies will thus dilute the dependence of the production cross sections for double Higgs production on the λ_{HHH} coupling. The measurement of the trilinear Higgs coupling is therefore an extremely challenging task and very high collider luminosities as well as high energies are required. We should note that to probe the quadrilinear Higgs coupling, $\lambda_{HHHH} = 3M_H^2/v^2$, which is further suppressed by a power of v compared to the triple Higgs coupling, one needs to consider triple Higgs production processes [37–39, 62–64]. As their cross sections are too small to be measurable, these processes are not viable in a foreseen future so that the determination of this last coupling seems hopeless.

In Refs. [42–44], the cross sections for the double Higgs production processes and the prospects of extracting the Higgs self-coupling have been discussed for the LHC with a 14 TeV center–of–mass (c.m.) energy in both the SM and its minimal supersymmetric extension (MSSM) where additional channels occur in the various processes.

In the present section, we update the previous analysis. In a sense, the task is made easier now that the Higgs boson mass is known and can be fixed to $M_H \approx 125$ GeV. However, lower c.m. energies have to be considered such as the current one, $\sqrt{s} = 8$ TeV. In addition, there are plans to upgrade the LHC which could allow to reach c.m. energies of about 30 TeV [65] and even up to 100 TeV. These very high energies will be of crucial help to probe these processes.

Another major update compared to Refs. [42–44] is that we will consider all main processes beyond leading order (LO) in perturbation theory, i.e. we will implement the important higher order QCD corrections. In the case of the gluon fusion mechanism, $gg \to HH$, the QCD corrections have been calculated at next-to–leading-order (NLO) in the low energy limit in Ref. [66]. They turn out to be quite large, almost doubling the production cross section at $\sqrt{s} = 14$ TeV, in much the same manner as for single Higgs production [67–73]. In fact, the QCD corrections for single and double Higgs productions are intimately related and one should expect, as in the case of $gg \to H$, a further increase of the total cross section by $\approx 30\%$ once the next-to-next-to-leading (NNLO) corrections are also included [74–76].

It is well known that for single Higgs production in the vector boson fusion process $qq' \to Hqq'$ there is no gluon exchange between the two incoming/outgoing quarks as the initial and final quarks are in color singlet states at LO. Then the NLO QCD corrections consist simply of the known corrections to the structure functions [77–79]. The same can be said in the case of double Higgs production $qq' \to HHqq'$, and in this section we will implement the NLO QCD corrections to this process in the structure function approach. The NNLO corrections in this approach turn out to be negligibly small for single Higgs production [80, 81] and we will thus ignore them for double Higgs production.

In the single Higgs–strahlung process, $q\bar{q}' \to V^* \to VH$, the NLO QCD corrections can be inferred from those of the Drell–Yan process $q\bar{q}' \to V^*$ [82–84]. This can be extended to NNLO [74, 85, 85, 86] but, in the case of ZH production, one needs to

[1] Notice that these cross sections might be different in Beyond the Standard Model physics. For an example inside the framework of composite Higgs models see Ref. [45].

include the gg initiated contribution, $gg \to ZH$ [86–88] as well as some additional subleading corrections [89]. The same is also true for double Higgs–strahlung and we will include in this section the Drell–Yan part of the corrections up to NNLO. In the case of ZHH final states, we will determine the additional contribution of the pentagon diagram $gg \to ZHH$ which turns out to be quite substantial, increasing the total cross section by up to 30% at $\sqrt{s} = 14$ TeV.

In the case of the $pp \to t\bar{t}HH$ process, the determination of the cross section at LO is already rather complicated. We will not consider any correction beyond this order (that, in any case, has not been calculated) and just display the total cross section without further analysis. We simply note that the QCD corrections in the single Higgs case, $pp \to t\bar{t}H$, turn out to be quite modest. At NLO, they are small at $\sqrt{s} = 8$ TeV and increase the cross section by less than $\approx 20\%$ at $\sqrt{s} = 14$ TeV [90–92]. We also note that this channel is plagued by huge QCD backgrounds.

In addition, the electroweak radiative corrections to these double Higgs production processes have not been calculated yet. Nevertheless, one expects that they are similar in size to those affecting the single Higgs production case, which are at the few percent level at the presently planned LHC c.m. energies [93–102] (see also Ref. [103] for a review). They should thus not affect the cross sections in a significant way and we will ignore this issue in our analysis.

After determining the K–factors, i.e. the ratios of the higher order to the lowest order cross sections consistently evaluated with the value of the strong coupling α_s and the parton distribution functions taken at the considered perturbative order, a next step will be to estimate the theoretical uncertainties on the production cross sections in the various processes. These stem from the variation of the renormalization and factorization scales that enter the processes (and which gives a rough measure of the missing higher order contributions), the uncertainties in the parton distribution functions (PDF) and the associated one on the strong coupling constant α_s and, in the case of the $gg \to HH$ process, the uncertainty from the use of an effective approach with an infinitely heavy virtual top quark, to derive the NLO corrections (see also Refs. [104, 105]). This will be done in much the same way as for the more widely studied single Higgs production case [103, 106].

Finally, we perform a preliminary analysis of the various channels in which the Higgs pair can be observed at the LHC with a c.m. energy of $\sqrt{s} = 14$ TeV assuming up to 3000 fb^{-1} collected data, and explore their potential to probe the λ_{HHH} coupling. Restricting ourselves to the dominant $gg \to HH$ mechanism in a parton level approach[2], we first discuss the kinematics of the process, in particular the transverse momentum distribution of the Higgs bosons and their rapidity distribution at leading order. We then evaluate the possible cross sections for both the signal and the major backgrounds. As the Higgs boson of a mass around 125 GeV dominantly decays into b–quark pairs with a branching ratio of $\approx 60\%$ and other decay modes such as $H \to \gamma\gamma$ and $H \to WW^* \to 2\ell 2\nu$ are rare [115, 116], and as the production cross sections are already low, we will

[2]Early and more recent parton level analyses of various detection channels have been performed in Refs. [107–112] with the recent ones heavily relying on jet–substructure techniques [113]. However, a full and realistic assessment of the LHC to probe the trilinear coupling would require the knowledge of the exact experimental conditions with very high luminosities and a full simulation of the detectors which is beyond the scope of this section. Only the ATLAS and CMS Collaborations are in a position to perform such detailed investigations and preliminary studies have already started [114].

focus on the three possibly promising detection channels $gg \to HH \to b\bar{b}\gamma\gamma, b\bar{b}\tau\bar{\tau}$ and $b\bar{b}W^+W^-$. Very high luminosities, $\mathcal{O}(\text{ab}^{-1})$ would be required to have some sensitivity on the λ_{HHH} coupling.

The rest of the section is organized as follows. Firstly, we discuss the QCD radiative corrections to double Higgs production in the gluon fusion, vector boson fusion and Higgs–strahlung processes (the $t\bar{t}HH$ process will be only considered at tree–level) and how they are implemented in the programs `HPAIR` [117], `VBFNLO` [118] and a code developed by us to evaluate the inclusive cross sections in Higgs–strahlung processes. Secondly, we evaluate the various theoretical uncertainties affecting these cross sections and collect at $M_H = 125$ GeV the double Higgs production cross sections at the various LHC energies. We also study the sensitivity in the different processes to the trilinear Higgs self–coupling. The third section will be devoted to a general discussion of the channels that could allow for the detection of the two Higgs boson signal at a high–luminosity 14 TeV LHC, concentrating on the dominant $gg \to HH$ process, together with an analysis of the major backgrounds.

2.2 Higgs pairs at higher orders in QCD

Generic Feynman diagrams for the four main classes of processes leading to double Higgs production at hadron colliders, gluon fusion, WW/ZZ fusion, double Higgs–strahlung and associated production with a top quark pair, are shown in Fig. 1. As can be seen in each process, one of the Feynman diagrams involves the trilinear Higgs boson coupling, $\lambda_{HHH} = 3M_H^2/v$, which can thus be probed in principle. The other diagrams involve the couplings of the Higgs boson to fermions and gauge bosons and are probed in the processes where the Higgs particle is produced singly.

In this section we will discuss the production cross sections for the first three classes of processes, including the higher order QCD corrections. We will first review the gluon channel and then we will move on to the higher–order corrections in the weak boson fusion and Higgs–strahlung channels.

2.2.1 The gluon fusion process

The gluon fusion process is – in analogy to single Higgs production – the dominant Higgs pair production process. The cross section is about one order of magnitude larger than the second largest process which is vector boson fusion. As can be inferred from Fig. 1a) it is mediated by loops of heavy quarks which in the SM are mainly top quarks. Bottom quark loops contribute to the total cross section with less than 1% at LO.

The process is known at NLO QCD in an effective field theory (EFT) approximation by applying the low energy theorem (LET) [67–73, 119–121] which means that effective couplings of the gluons to the Higgs bosons are obtained by using the infinite quark mass approximation. The hadronic cross section at LO is given by

$$\sigma_{\text{LO}} = \int_{\tau_0}^1 d\tau \; \hat{\sigma}_{\text{LO}}(\hat{s} = \tau s) \; \int_\tau^1 \frac{dx}{x} f_g(x;\mu_F^2) f_g\left(\frac{\tau}{x};\mu_F^2\right) , \tag{2.42}$$

with s being the hadronic c.m. energy, $\tau_0 = 4M_H^2/s$, and f_g the gluon distribution

(a) gg double-Higgs fusion: $gg \to HH$

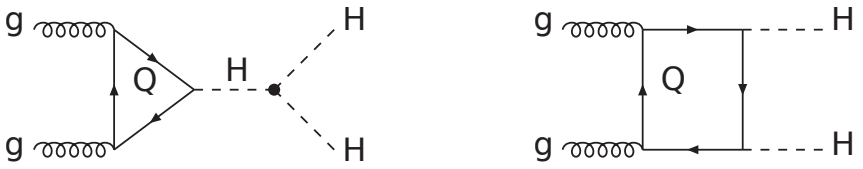

(b) WW/ZZ double-Higgs fusion: $qq' \to HHqq'$

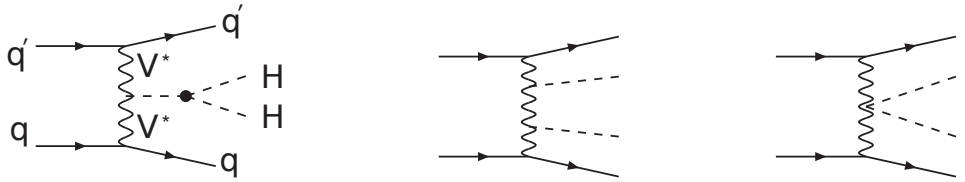

(c) Double Higgs-strahlung: $q\bar{q}' \to ZHH/WHH$

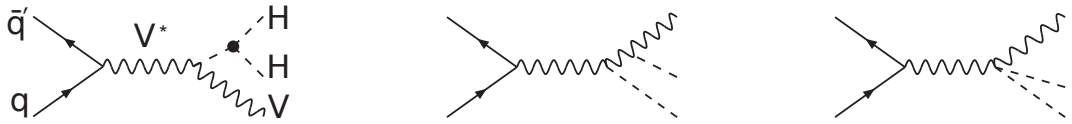

(d) Associated production with top-quarks: $q\bar{q}/gg \to t\bar{t}HH$

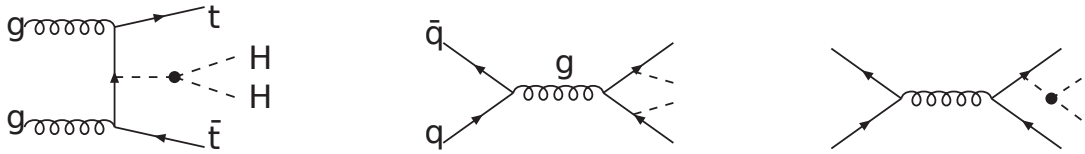

Figure 1: Some generic Feynman diagrams contributing to Higgs pair production at hadron colliders.

function taken at a typical scale μ_F specified below. The partonic cross section at LO, $\hat{\sigma}_{\rm LO}$, can be cast into the form

$$\hat{\sigma}_{\rm LO}(gg \to HH) = \int_{\hat{t}_-}^{\hat{t}_+} d\hat{t}\, \frac{G_F^2 \alpha_s^2(\mu_R)}{256(2\pi)^3} \left\{ \left| \frac{\lambda_{HHH}\, v}{\hat{s} - M_H^2 + iM_H\Gamma_H} F_\triangle + F_\square \right|^2 + |G_\square|^2 \right\} , \tag{2.43}$$

where

$$\hat{t}_\pm = -\frac{\hat{s}}{2}\left(1 - 2\frac{M_H^2}{\hat{s}} \mp \sqrt{1 - \frac{4M_H^2}{\hat{s}}}\right) , \tag{2.44}$$

with $\hat{s}$ and $\hat{t}$ denoting the partonic Mandelstam variables. The triangular and box form factors $F_\triangle$, $F_\square$ and $G_\square$ approach constant values in the infinite top quark mass limit,

$$F_\triangle \to \frac{2}{3}, \quad F_\square \to -\frac{2}{3}, \quad G_\square \to 0\,. \tag{2.45}$$

The expressions with the complete mass dependence are rather lengthy and can be

found in Refs. [54, 54] as well as the NLO QCD corrections in the LET approximation in Ref. [66].

The full LO expressions for $F_\triangle, F_\square$ and $G_\square$ are used wherever they appear in the NLO corrections in order to improve the perturbative results, similar to what has been done in the single Higgs production case where using the exact LO expression reduces the disagreement between the full NLO result and the LET result [46–50, 67–73].

For the numerical evaluation we have used the publicly available code `HPAIR` [117] in which the known NLO corrections are implemented. As a central scale for this process we choose

$$\mu_0 = \mu_R = \mu_F = M_{HH} \ , \tag{2.46}$$

where M_{HH} denotes the invariant mass of the Higgs boson pair. This is motivated by the fact that the natural scale choice in the process $gg \to H$ is $\mu_0 = M_H$. Extending this to Higgs pair production naturally leads to the scale choice of Eq. (2.46). The motivation to switch to $\mu_0 = 1/2\, M_H$ in single Higgs production comes from the fact that it is a way to acccount for the $\sim +10\%$ next–to–next–to–leading logarithmic (NNLL) corrections [103, 122–124] in a fixed order NNLO calculation. It also improves the perturbative convergence from NLO to NNLO [125]. Still NNLO and NNLL calculations for $gg \to HH$ process are not available at the moment, not to mention an exact NLO calculation that would be the starting point of further improvements. It then means that there is no way to check wether these nice features appearing in single Higgs production when using $\mu_0 = 1/2\, M_H$ would still hold in the case of Higgs pair production when using $\mu_0 = 1/2\, M_{HH}$. We then stick to the scale choice of Eq. (2.46). The K–factor, describing the ratio of the cross section at NLO using NLO PDFs and NLO α_s to the leading order cross section consistently evaluated with LO PDFs and LO α_s, for this process is

$$K \sim 2.0\ (1.5) \quad \text{for } \sqrt{s} = 8\ (100)\ \text{TeV} \ . \tag{2.47}$$

2.2.2 The vector boson fusion process

The structure of the Higgs pair production process through vector boson fusion [55–58] is very similar to the single Higgs production case. The vector boson fusion process can be viewed as the double elastic scattering of two (anti)quarks with two Higgs bosons radiated off the weak bosons that fuse. In particular this means that the interference with the double Higgs–strahlung process $qq' \to V^* HH \to qq' HH$ is negligible and this latter process is treated separately. This is justified by the kinematics of the process with two widely separated quark jets of high invariant mass and by the color flow of the process. This leads to the structure function approach that has been applied with success to calculate the QCD corrections in the vector boson fusion production of a single Higgs boson [77–81]. Generic diagrams contributing at NLO QCD order are shown in Fig. 2. For simplicity only the diagrams with the QCD corrections to the upper quark line are shown. The calculation involving the second quark line is identical. The blob of the vertex $VVHH$ is a shortcut for the diagrams depicted in Fig. 3, which include charged currents (CC) with $W^\pm$ bosons and neutral currents (NC) with a Z boson exchange. As can be seen only one of the three diagrams involves the trilinear Higgs coupling. The other diagrams act as irreducible background and lower the sensitivity of the production process to the Higgs self–coupling.

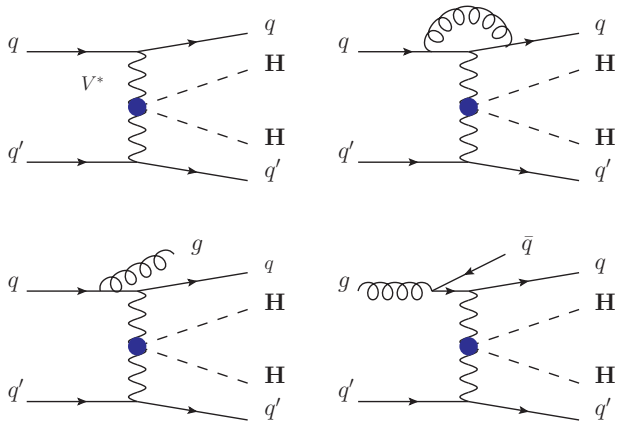

Figure 2: Generic diagrams contributing to the NLO corrections to $qq' \to HHqq'$. Shown are the LO diagram (upper left) and the NLO corrections for the upper quark line. The blob of the $VVHH$ vertex is a shortcut for the three diagrams shown in Figs. 1b) and 3.

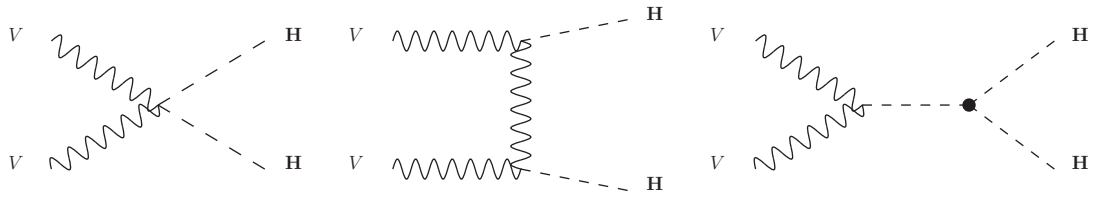

Figure 3: Diagrams contributing to the $VVHH$ vertex.

We have calculated the NLO QCD corrections in complete analogy to the single Higgs VBF process [78]. The real emission contributions are given by a gluon attached to the quark lines either in the initial or the final state and from the gluon–quark initial state. As we are working in the structure function approach, the corrections of the upper and lower quark lines do not interfere and are simply added incoherently. The amplitudes have the following structure,

$$\mathcal{A}_{HHqq'} \propto T^{\mu\nu}_{V^*V^*} J^q_\mu J^{q'}_\nu \,, \tag{2.48}$$

where $T^{\mu\nu}_{V^*V^*}$ stands for the tensor structure of the diagrams depicted in Fig. 3 and $J^{q,q'}_\mu$ are the quark currents of the upper and lower lines, respectively, with four-momenta q, q'. The calculation is done numerically using the *Catani-Seymour* dipole subtraction method [126] to regularize the infrared divergencies. The formulae for the subtraction terms as well as the finite corrections are identical to the ones for single Higgs VBF production as only the quark currents are involved. They can be found in Ref. [78].

We have implemented this calculation in the `VBFNLO` code [118] in which we have provided the tensor structure depicted in Fig. 3 which has been calculated with MadGraph [127]. Up to now the `VBFNLO` implementation only involves on–shell Higgs pairs. We have found an increase of $\sim +7\%$ of the total cross section compared to the LO result when using the central scale

$$\mu_0 = \mu_R = \mu_F = Q_{V^*}, \tag{2.49}$$

with Q_{V^*} being the momentum of the exchanged weak bosons ($V^* = W^*, Z^*$)[3]. This result is in agreement with a previous calculation done in the context of the two Higgs doublet model [128].

2.2.3 The Higgs–strahlung process

The production of a Higgs pair in association with a vector boson has been calculated for the first time quite a while ago [60] and shares common aspects with the single Higgs–strahlung process. The NLO corrections can be implemented in complete analogy to single Higgs-strahlung [82–84]. We will update in this section the former results and present the NNLO corrections to the WHH and ZHH inclusive production cross sections. These calculations have been implemented in a code which shall become publicly available.

At LO the process $pp \to VHH$ ($V = W, Z$) is given by quark–antiquark annihilations in s–channel mediated processes involving three Feynman diagrams, see Fig. 1c). As can be seen only one of the three diagrams involves the trilinear Higgs coupling. The sensitivity to this coupling is then diluted by the remaining diagrams. After integrating over the azimuthal angle we are left with the following partonic differential cross section with $\hat{s}$ being the partonic c.m. energy (see also Refs. [42–44]),

$$\begin{aligned}\frac{d\hat{\sigma}^{\rm LO}_{VHH}}{dx_1 dx_2} &= \frac{G_F^3 M_V^6 (a_q^2+v_q^2)}{1149\sqrt{2}\pi^3 \hat{s}(1-\mu_V^2)}\left[\frac{1}{8} f_0 C_{HHH}^2 + \frac{1}{4\mu_V(1-x_1+\mu_H-\mu_V)}\times\right.\\ &\left.\left(\frac{f_1}{1-x_1+\mu_H-\mu_V} + \frac{f_2}{1-x_2+\mu_H-\mu_V} + 2\mu_V f_3 C_{HHH}\right) + \{x_1 \leftrightarrow x_2\}\right] \quad (2.50)\end{aligned}$$

where we use of the following notation,

$$\mu_V = \frac{M_V^2}{\hat{s}}, \quad \mu_H = \frac{M_H^2}{\hat{s}}, \quad x_1 = \frac{2E_H}{\sqrt{\hat{s}}}, \quad x_2 = \frac{2E_V}{\sqrt{\hat{s}}}, \quad (2.51)$$

and the reduced couplings of the quarks to the vector bosons, $a_q = v_q = \sqrt{2}$ for $V = W$ and any quark q, $a_u = 1$ and $v_u = 1 - 8/3 \sin^2\theta_W$ for $q = u, s$ and $V = Z$, $a_d = -1$ and

[3] In order to stay within the perturbative regime a cut $Q_{V^*} \geq 2$ GeV has to be imposed, see Ref. [77].

$v_d = -1 + 4/3 \sin^2\theta_W$ for $q = d, c, b$ and $V = Z$. The coefficients f_i as well as C_{HHH} are

$$\begin{aligned}
f_0 &= \mu_V \left[(2 - x_1 - x_2)^2 + 8\mu_V\right], \\
f_1 &= x_1^2 (\mu_V - 1 + x_1)^2 - 4\mu_H (1 - x_1)(1 - x_1 + \mu_V - \mu_V x_1 - 4\mu_V) \\
&\quad + \mu_V (\mu_V - 4\mu_H)(1 - 4\mu_H) - \mu_V^2, \\
f_2 &= (2\mu_V + x_1 + x_2)\left[\mu_V (x_1 + x_2 - 1 + \mu_V - 8\mu_H)\right. \\
&\quad \left. - (1 - x_1)(1 - x_2)(1 + \mu_V)\right] + (1 - x_1)^2 (1 - x_2)^2 \\
&\quad + (1 - x_1)(1 - x_2)\left[\mu_V^2 + 1 + 4\mu_H (1 + \mu_V)\right] \\
&\quad + 4\mu_H \mu_V (1 + \mu_V + 4\mu_H) + \mu_V^2, \\
f_3 &= x_1 (x_1 - 1)(\mu_V + x_1 - 1) - (1 - x_2)(2 - x_1)(1 - x_1 + \mu_V) \\
&\quad + 2\mu_V (\mu_V + 1 - 4\mu_H),
\end{aligned}$$

$$\begin{aligned}
C_{HHH} &= \frac{v}{M_V^2} \frac{\lambda_{HHH}}{x_1 + x_2 - 1 + \mu_V - \mu_H} + \frac{2}{1 - x_1 + \mu_H - \mu_V} \\
&\quad + \frac{2}{1 - x_2 + \mu_H - \mu_V} + \frac{1}{\mu_V}\,.
\end{aligned} \tag{2.52}$$

The coefficient C_{HHH} includes the trilinear Higgs coupling λ_{HHH}.

In order to obtain the full hadronic section, the differential partonic cross section of Eq. (2.50) is convoluted with the quark parton distribution functions, $f_q, f_{q'}$ taken at a typical scale μ_F specified below:

$$\sigma(pp \to VHH) = \sum_{q,q'} \int_{\tau_0}^1 d\tau \int_\tau^1 \frac{dx}{x} f_q(x; \mu_F^2)\, f_{\bar{q}/\bar{q}'}\left(\frac{\tau}{x}; \mu_F^2\right) \hat{\sigma}_{VHH}(\hat{s} = \tau s)\,, \tag{2.53}$$

where s stands for the hadronic c.m. energy and $\tau_0 = (2M_H + M_V)^2/s$. The total partonic cross section $\hat{\sigma}_{VHH}$ has been obtained after the integration of Eq.(2.50) over x_1, x_2.

The calculation of the NLO QCD corrections is similar to the single Higgs–strahlung case. In fact, this process can be viewed as the Drell-Yan production $pp \to V^*$ followed by the splitting process $V^* \to VHH$. The off–shell vector boson can have any momentum k^2 with $(2M_H + M_V)^2 \leq k^2 \leq \hat{s}$. This factorization is in principle valid at all orders for the Drell–Yan like contributions and leads, after folding with the PDF, to

$$\sigma(pp \to VHH) = \int_{\tau_0}^1 d\tau \sum_{(ij)} \frac{d\mathcal{L}^{ij}}{d\tau} \int_{\tau_0/\tau}^1 dz\, \hat{\sigma}^{\rm LO}(z\tau s) \Delta_{ij}(ij \to V^*)\,, \tag{2.54}$$

with

$$\frac{d\mathcal{L}^{ij}}{d\tau} = \int_\tau^1 f_i(x; \mu_F^2) f_j\left(\frac{\tau}{x}; \mu_F^2\right) \frac{dx}{x}\,. \tag{2.55}$$

In the expressions above ij stands for any initial partonic subprocess, Δ_{ij} is the Drell–Yan correction, $z = k^2/\hat{s}$ and $\hat{\sigma}^{\rm LO}$ stands for the LO partonic cross section of the process $q\bar{q}' \to V^* \to VHH$. At LO we have $\Delta_{ij}^{\rm LO} = \delta_{iq}\delta_{j\bar{q}/\bar{q}'}\delta(1 - z)$. In Fig. 4 the generic diagrams which contribute at NLO to the Drell–Yan process $q\bar{q}' \to V^*$ are depicted. The NLO QCD corrections increase the total cross section by $\sim +17\%$ at 14 TeV for $M_H = 125$ GeV.

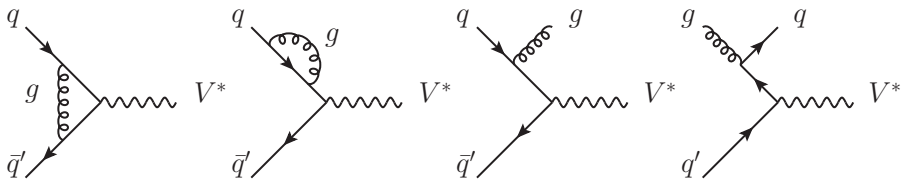

Figure 4: Feynman diagrams contributing to the NLO QCD corrections for Drell–Yan production.

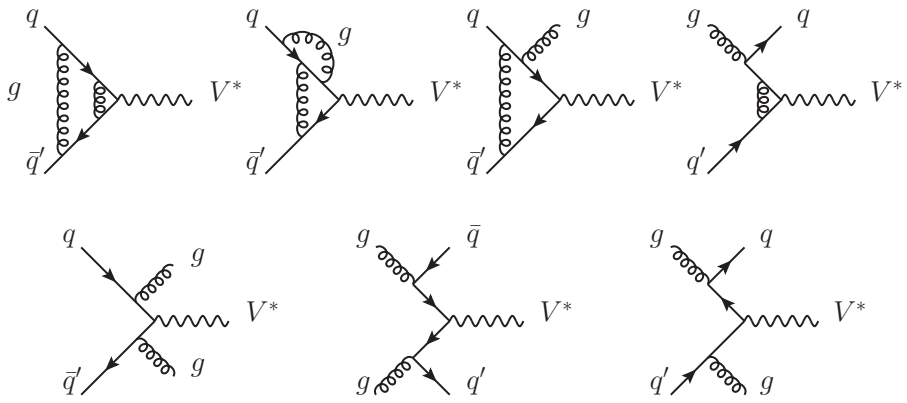

Figure 5: Some Feynman diagrams contributing at NNLO QCD to Drell–Yan production.

We have calculated the NNLO corrections, which have not been available so far, in the same way except for the process involving a Z boson. In fact there are additional contributions that are specific to the case of a Z boson, involving an effective Zgg vertex. Similar to what is stated in Ref. [86] for the single Higgs production case, only the specific gluon fusion initiated process will be of non–negligible contribution and will be described below. Let us start with the NNLO QCD Drell–Yan contribution. Some generic diagrams contributing to the NNLO corrections to $q\bar{q}' \to V^*$ are shown in Fig. 5. We apply the procedure as described by Eq. (2.54) and the expression is then given by

$$\begin{aligned} \sigma^{\mathrm{NNLO}}(pp \to VHH) &= \sigma^{\mathrm{LO}} + \Delta\sigma_{q\bar{q}/\bar{q}'} + \Delta\sigma_{qg} + \Delta\sigma_{qq'} + \\ &\quad \Delta\sigma_{qq} + \Delta\sigma_{gg} + \delta_{VZ}\Delta\sigma_{gg\to ZHH}, \end{aligned} \tag{2.56}$$

with $\delta_{VZ} = 1(0)$ for $V = Z(W)$ and

$$\begin{aligned}
\sigma^{\rm LO} &= \sum_{q,q'} \int_{\tau_0}^1 d\tau \, \frac{d\mathcal{L}^{q\bar{q}/\bar{q}'}}{d\tau} \, \hat{\sigma}^{\rm LO}(\tau s), \\
\Delta\sigma_{q\bar{q}/\bar{q}'} &= \sum_{q,q'} \left(\frac{\alpha_s(\mu_R)}{\pi}\right) \int_{\tau_0}^1 d\tau \, \frac{d\mathcal{L}^{q\bar{q}/\bar{q}'}}{d\tau} \, \times \\
&\quad \int_{\tau_0/\tau}^1 \hat{\sigma}^{\rm LO}(z\tau s) \left(\Delta^{(1)}_{q\bar{q}}(z) + \left(\frac{\alpha_s(\mu_R)}{\pi}\right) \Delta^{(2)}_{q\bar{q}}(z)\right), \\
\Delta\sigma_{qg} &= \sum_{i=q,\bar{q}} \left(\frac{\alpha_s(\mu_R)}{\pi}\right) \int_{\tau_0}^1 d\tau \, \frac{d\mathcal{L}^{ig}}{d\tau} \, \times \\
&\quad \int_{\tau_0/\tau}^1 \hat{\sigma}^{\rm LO}(z\tau s) \left(\Delta^{(1)}_{qg}(z) + \left(\frac{\alpha_s(\mu_R)}{\pi}\right) \Delta^{(2)}_{qg}(z)\right), \\
\Delta\sigma_{qq'} &= \sum_{i=q,\bar{q},j=q',\bar{q}'} \left(\frac{\alpha_s(\mu_R)}{\pi}\right)^2 \int_{\tau_0}^1 d\tau \, \frac{d\mathcal{L}^{ij}}{d\tau} \, \int_{\tau_0/\tau}^1 \hat{\sigma}^{\rm LO}(z\tau s) \Delta^{(2)}_{qq'}(z), \\
\Delta\sigma_{qq} &= \sum_{i=q,\bar{q}} \left(\frac{\alpha_s(\mu_R)}{\pi}\right)^2 \int_{\tau_0}^1 d\tau \, \frac{d\mathcal{L}^{ii}}{d\tau} \, \int_{\tau_0/\tau}^1 \hat{\sigma}^{\rm LO}(z\tau s) \Delta^{(2)}_{qq}(z), \\
\Delta\sigma_{gg} &= \left(\frac{\alpha_s(\mu_R)}{\pi}\right)^2 \int_{\tau_0}^1 d\tau \, \frac{d\mathcal{L}^{gg}}{d\tau} \, \int_{\tau_0/\tau}^1 \hat{\sigma}^{\rm LO}(z\tau s) \Delta^{(2)}_{gg}(z), \\
\Delta\sigma_{gg\to ZHH} &= \int_{\tau_0}^1 d\tau \, \frac{d\mathcal{L}^{gg}}{d\tau} \, \hat{\sigma}_{gg\to ZHH}(\tau s) \, . \qquad (2.57)
\end{aligned}$$

The expressions for the coefficients $\Delta^{(i=1,2)}(z)$ refer to the NLO and NNLO corrections, respectively. As they are too lengthy to be reproduced here, we refer the reader to the appendix B of Ref. [85] and to Ref. [74]. The expressions given there have to be rescaled by a factor of $(\pi/\alpha_s)^i$, and $M \equiv \mu_F$, $R \equiv \mu_R$. In our calculation we have included the full CKM matrix elements in the quark luminosity as well as the initial bottom quark contribution. We use the central scale

$$\mu_0 = \mu_R = \mu_F = M_{VHH} \, , \qquad (2.58)$$

where M_{VHH} denotes the invariant mass of the VHH system.

The Drell–Yan NNLO QCD corrections Eq. (2.57) turn out to be very small. They typically increase the cross section by a few percent at 14 TeV.

The last contribution $\Delta\sigma_{gg\to ZHH}$, see diagrams in Fig. 6, is only present in the case of Higgs pair production in association with a Z boson. It stems from the process $gg \to ZHH$ which is loop–mediated already at LO. Being of order α_s^2 it contributes to the total cross section $pp \to ZHH$ at NNLO QCD. The process is mediated by quark loops in triangle, box and pentagon topologies. In the latter two topologies, only top and bottom quarks contribute as the Yukawa couplings to light quarks can be neglected. At the LHC the contribution of the gluon fusion channel is substantial in contrast to the single Higgs production case. Indeed, while in the latter the contribution is of order $\sim +5\%$ compared to the NNLO QCD Drell–Yan contribution, in the case of Higgs pair production it contributes with $\sim +20 \cdots +30\%$ depending on the c.m. energy. This enhancement can be explained by the additional pentagon topology which a) involves two

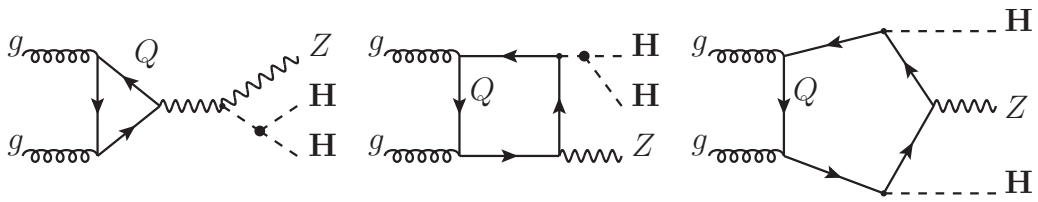

Figure 6: Some generic diagrams contributing to $gg \to ZHH$. For the triangle+box topologies, only those involving the trilinear Higgs couplings are depicted.

top Yukawa couplings and b) softens the destructive interference between the triangle and box diagrams that is present in the single Higgs production case. Furthermore, the suppression by a power $(\alpha_s/\pi)^2$ is partly compensated by the increased gluon luminosity at high energies. This explains why this channel, which has been calculated using FeynArts/FormCalc [129–132], should be taken into account. It also implies that the scale variation in $pp \to ZHH$ will be worse than in $pp \to WHH$ because of the $\mathcal{O}(\alpha_s^2)$ gluon fusion mechanism appearing at NNLO.

2.3 Cross sections and sensitivity at the LHC

In this section we will present the results for the calculation of the total cross sections including the higher–order corrections discussed in the previous section as well as the various related theoretical uncertainties. We will use the MSTW2008 PDF set [133] as our reference set. We choose the following values for the W, Z and top quark masses and for the strong coupling constant at LO, NLO and NNLO,

$$M_W = 80.398 \text{ GeV}, \quad M_Z = 91.1876 \text{ GeV}, \quad M_t = 173.1 \text{ GeV},$$

$$\alpha_s^{\rm LO}(M_Z^2) = 0.13939, \quad \alpha_s^{\rm NLO}(M_Z^2) = 0.12018, \quad \alpha_s^{\rm NNLO}(M_Z^2) = 0.11707.$$

The electromagnetic constant α is calculated in the G_μ scheme from the values of M_W and M_Z given above. For the estimate of the residual theoretical uncertainties in the various Higgs pair production processes we considered the following uncertainties:

1. the scale uncertainty, stemming from the missing higher order contributions and estimated by varying the renormalization scale μ_R and the factorization scale μ_F in the interval $\frac{1}{2}\mu_0 \leq \mu_R, \mu_F \leq 2\mu_0$ with some restrictions on the ratio μ_R/μ_F depending on the process;

2. the PDF and related α_s errors. The PDFs are non–perturbative quantities fitted from the data and not calculated from QCD first principles. It is then compulsory to estimate the impact of the uncertainties on this fit and on the value of the strong coupling constant $\alpha_s(M_Z^2)$ which is also fitted together with the PDFs;

3. in the case of the gluon fusion process there is a third source of uncertainties which comes from the use of the effective field theory approximation to calculate the NLO QCD corrections, where top loops are taken into account in the infinite top mass approximation and bottom loops are neglected.

In the following we will present results for $M_H = 125$ GeV. Note that the results for the total cross sections and uncertainties are nearly the same for $M_H = 126$ GeV. The total cross sections at the LHC for the four classes of Higgs pair production processes are shown in Fig. 7 as a function of the c.m. energy. For all processes the numerical uncertainties are below the permille level and have been ignored. The central scales which have been used are ($\mu_R = \mu_F = \mu_0$)

$$\mu_0^{gg\to HH} = M_{HH}, \;\; \mu_0^{qq'\to HHqq'} = Q_{V^*}, \;\; \mu_0^{q\bar{q}'\to VHH} = M_{VHH}, \;\; \mu_0^{q\bar{q}/gg\to t\bar{t}HH} = M_t + \frac{1}{2}M_{HH}. \tag{2.59}$$

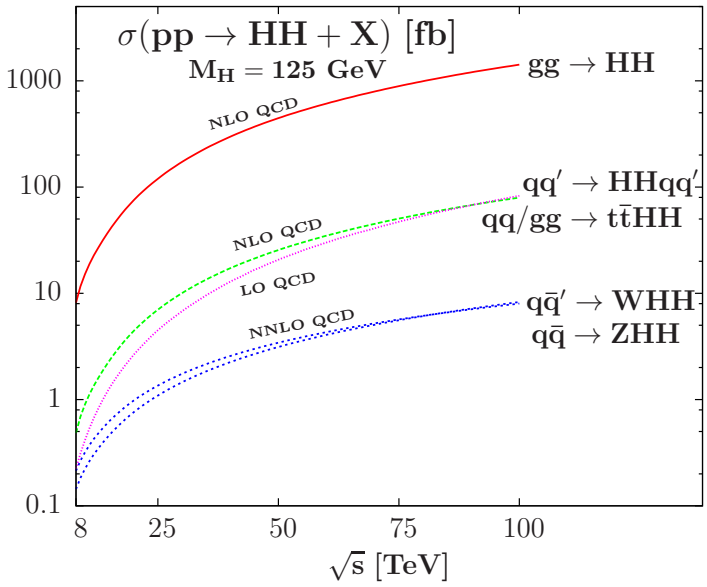

Figure 7: The total cross sections for Higgs pair production at the LHC, including higher-order corrections, in the main channels – gluon fusion (red/full), VBF (green/dashed), Higgs-strahlung (blue/dotted), associated production with $t\bar{t}$ (violet/dotted with small dots) – as a function of the c.m. energy with $M_H = 125$ GeV. The MSTW2008 PDF set has been used and higher–order corrections are included as discussed in the text.

As can be inferred from the figure and also seen in Table 1 the largest cross section is given by the gluon fusion channel which is one order of magnitude larger than the vector boson fusion cross section. All processes are $\sim$ 1000 times smaller than the corresponding single Higgs production channels, implying that high luminosities are required to probe the Higgs pair production channels at the LHC.

2.3.1 Theoretical uncertainties in the gluon channel

Theoretical uncertainty due to missing higher order corrections

The large K–factor for this process of about $1.5 - 2$ depending on the c.m. energy shows that the inclusion of higher order corrections is essential. An estimate on the size of the uncertainties due to the missing higher order corrections can be obtained by a variation of the factorization and renormalization scales of this process. In analogy to single Higgs production studies [103, 106] we have estimated the error due to missing

$\sqrt{s}$ [TeV]	$\sigma^{\rm NLO}_{gg\to HH}$ [fb]	$\sigma^{\rm NLO}_{qq'\to HHqq'}$ [fb]	$\sigma^{\rm NNLO}_{q\bar{q}'\to WHH}$ [fb]	$\sigma^{\rm NNLO}_{q\bar{q}\to ZHH}$ [fb]	$\sigma^{\rm LO}_{q\bar{q}/gg\to t\bar{t}HH}$ [fb]
8	8.16	0.49	0.21	0.14	0.21
14	33.89	2.01	0.57	0.42	1.02
33	207.29	12.05	1.99	1.68	7.91
100	1417.83	79.55	8.00	8.27	77.82

Table 1: The total Higgs pair production cross sections in the main channels at the LHC (in fb) for given c.m. energies (in TeV) with $M_H = 125$ GeV. The central scales which have been used are described in the text.

higher order corrections by varying μ_R, μ_F in the interval

$$\frac{1}{2}\mu_0 \leq \mu_R = \mu_F \leq 2\,\mu_0\ . \tag{2.60}$$

As can be seen in Fig. 8 we find sizeable scale uncertainties Δ^μ of order $\sim +20\%/-17\%$ at 8 TeV down to $+12\%/-10\%$ at 100 TeV. Compared to the single Higgs production case the scale uncertainty is twice as large [103, 106]. However, this should not be a surprise as there are NNLO QCD corrections available for the top loop (in a heavy top mass expansion) in the process $gg \to H$ while they are unknown for the process $gg \to HH$.

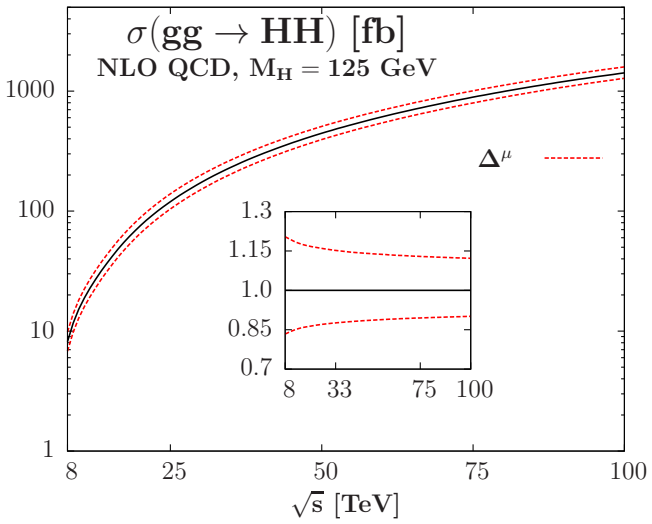

Figure 8: Scale uncertainty for a scale variation in the interval $\frac{1}{2}\mu_0 \leq \mu_R = \mu_F \leq 2\mu_0$ in $\sigma(gg \to HH)$ at the LHC as a function of $\sqrt{s}$ at $M_H = 125$ GeV. In the insert the relative deviations to the results for the central scale $\mu_0 = \mu_R = \mu_F = M_{HH}$ are shown.

2.4 The PDF and α_S errors

The parametrization of the parton distribution functions is another source of theoretical uncertainty. First there are pure theoretical uncertainties coming from the assumptions made on the parametrization, e.g. the choice of the parametrization, the set of input parameters used, etc. Such uncertainties are rather difficult to quantify. A possibility might be to compare different parameter sets, such as MSTW [133], CT10 [134],

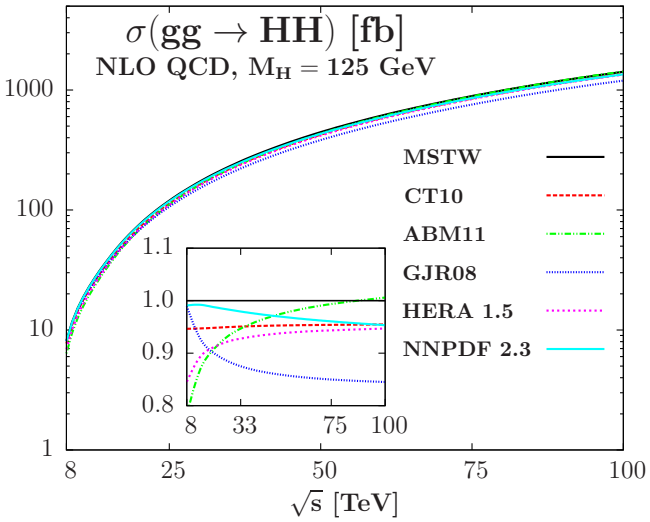

Figure 9: The NLO cross section $\sigma(gg \to HH + X)$ at the LHC as a function of the c.m. energy for $M_H = 125$ GeV, when using different NLO PDF sets. In the insert the cross sections normalized to the cross section calculated with the MSTW PDF set are shown.

ABM11 [135], GJR08 [136], HERA 1.5 [137] and NNPDF 2.3 [138]. This is exemplified in Fig. 9 where the predictions using the six previous PDF sets are displayed. As can be seen there are large discrepancies over the whole considered c.m. energy range. At low energies the smallest prediction comes from ABM11 which is $\sim 22\%$ smaller than the prediction made with the MSTW set while at high energies ABM11 and MSTW lead to similar results whereas the result obtained with the GJR08 set deviates by $\sim -15\%$. The CT10 predictions show about -5% difference over the whole energy range with respect to the cross section obtained with MSTW while the HERA prediction starts from lower values and eventually reaches the CT10 result. Finally the cross sections calculated with the NNPDF set decrease over the energy range, starting from being very similar to the MSTW result to reach at $\sqrt{s} = 100$ TeV the one calculated with CT10.

Another source of uncertainty due to the PDF sets comes from the experimental uncertainties on the fitted data. The so-called Hessian method, used by the MSTW collaboration, provides additional PDF sets next to the best-fit PDF. Additional $2N_{PDF}$ sets reflect the $\pm 1\sigma$ variation around the minimal χ^2 of all N_{PDF} parameters that enter the fit. Using the 90% CL error PDF sets provided by the MSTW collaboration a PDF error of about 6% is obtained for $\sqrt{s} = 8$ TeV. The uncertainty shrinks to $\sim 2\%$ for $\sqrt{s} = 100$ TeV.

In addition to the PDF uncertainties, there is also an uncertainty due to the errors on the value of the strong coupling constant α_s. The MSTW collaboration provides additional PDF sets such that the combined PDF+α_s uncertainties can be evaluated [139]. At NLO the MSTW PDF set uses

$$\alpha_s(M_Z) = 0.12018^{+0.00122}_{-0.00151}(\text{at } 68\% \text{ CL}) \text{ or } {}^{+0.00317}_{-0.00386} \text{ (at } 90\% \text{ CL)} . \tag{2.61}$$

As the LO process is already $\mathcal{O}(\alpha_s^2)$, uncertainties in α_s can be quite substantial.

The combined PDF and α_s error is much larger than the pure PDF error. At 8 TeV the PDF error of $+5.8\%/-6.0\%$ rises to a combined error of $+8.5\%/-8.3\%$. At 33 TeV

the rise is even larger – from the pure PDF error of $+2.5\%/-2.7\%$ to the combined PDF+α_s error of $+6.2\%/-5.4\%$.

There is also a theoretical uncertainty on α_s stemming from scale variation or ambiguities in the heavy flavour scheme definition. The MSTW collaboration estimates this uncertainty for α_s at NLO to $\Delta\alpha_s(M_Z) = \pm 0.003$ [139]. However this uncertainty is already included in the scale uncertainty on the input data sets used to fit the PDF and has been taken into account in the definition of the PDF+α_s uncertainty. Thus, it does not have to be taken into account separately and the combined PDF+α_s error calculated with the MSTW 2008 PDF set will be our default PDF+α_s uncertainty.

However, even if all these uncertainties for the MSTW PDF set are taken into account, the different PDF set predictions do not agree. There might be agreement if also uncertainties of the other PDF sets are taken into account, as done in Ref. [106] for the case of single Higgs production. This means that the PDF uncertainty might be underestimated, but this issue is still an open debate (see for example Ref. [140] for a new discussion about theoretical issues in the determination of PDFs) and improvements may come with the help of new LHC data taken into account in the fits of the various PDF collaborations.

The effective theory approach

The last source of theoretical errors that we consider is the use of the LET for the calculation of the NLO corrections. At LO it was found in Ref. [52] that for $\sqrt{s} = 16$ TeV the LET underestimates the cross section by $\mathcal{O}(20\%)$. Furthermore this can be even worse for different energies, not to mention the fact that the LET approximation produces incorrect kinematic distributions [107–110]. The reason is that the LET is an expansion in $m_{top} \gg \sqrt{\hat{s}}$. Such an expansion works very well for single Higgs production, since $\sqrt{\hat{s}} = M_H$ (at LO) for the production of an on–shell Higgs boson whereas in Higgs pair production we have

$$2M_H \leq \sqrt{\hat{s}} \leq \sqrt{s}\,. \tag{2.62}$$

This means that for Higgs pair production $m_{top} \gg \sqrt{\hat{s}}$ is never fulfilled for $M_H = 125$ GeV so that the LET approximation is not valid at LO [104].

At NLO, however, the LET approximation works much better in case the LO cross section includes the full mass dependence. The reason is that the NLO corrections are dominated by soft and collinear gluon effects. They factorize in the Born term and in the NLO correction contributions, meaning that the K–factor is not strongly affected from any finite mass effects. Based on the results for the single Higgs case [72] where the deviation between the exact and asymptotic NLO results amounts to less than 7% for $M_H < 700$ GeV, we estimate the error from applying an effective field theory approach for the calculation of the NLO corrections to 10%.

Total uncertainty

In order to obtain the total uncertainty we follow the procedure advocated in Ref. [141]. Since quadratic addition is too optimistic (as stated by the LHC Higgs Cross Section Working Group, see Ref. [103]), and as the linear uncertainty might be too conservative, the procedure adopted is a compromise between these two ways of combining the individual theoretical uncertainties. We first calculate the scale uncer-

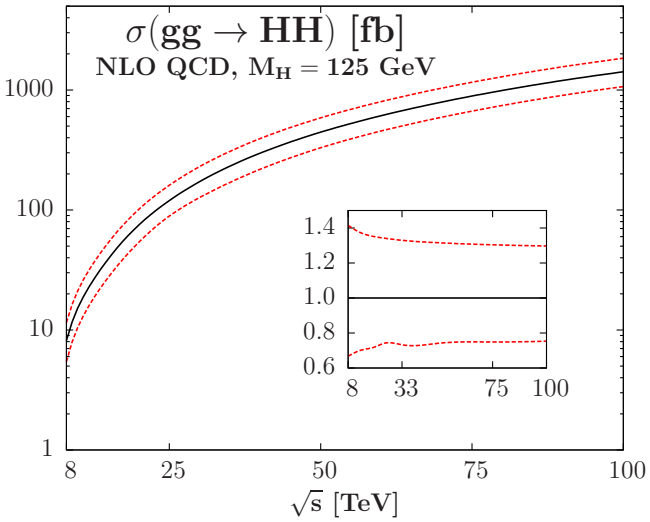

Figure 10: The total cross section (black/full) of the process $gg \to HH + X$ at the LHC for $M_H = 125$ GeV as a function of $\sqrt{s}$ including the total theoretical uncertainty (red/dashed). The insert shows the relative deviation from the central cross section.

tainty and then add on top of that the PDF+α_s uncertainty calculated for the minimal and maximal cross sections with respect to the scale variation. The LET error is eventually added linearly. This is shown in Fig. 10 where we display the total cross section including the combined theoretical uncertainty. It is found to be sizeable, ranging from $\sim +42\%/-33\%$ at 8 TeV down to $\sim +30\%/-25\%$ at 100 TeV. The numbers can be found in Table 2.

$\sqrt{s}$ [TeV]	$\sigma^{\rm NLO}_{gg\to HH}$ [fb]	Scale [%]		PDF [%]		PDF+α_s [%]		EFT [%]	Total [%]	
8	8.16	+20.4	−16.6	+5.8	−6.0	+8.5	−8.3	±10.0	+41.5	−33.3
14	33.89	+18.2	−14.7	+3.9	−4.0	+7.0	−6.2	±10.0	+37.2	−29.8
33	207.29	+15.2	−12.4	+2.5	−2.7	+6.2	−5.4	±10.0	+33.0	−26.7
100	1417.83	+12.2	−9.9	+2.0	−2.7	+6.2	−5.7	±10.0	+29.7	−24.7

Table 2: The total Higgs pair production cross section at NLO in the gluon fusion process at the LHC (in fb) for given c.m. energies (in TeV) at the central scale $\mu_F = \mu_R = M_{HH}$, for $M_H = 125$ GeV. The corresponding shifts due to the theoretical uncertainties from the various sources discussed are shown as well as the total uncertainty when all errors are added as described in the text.

2.4.1 VBF and Higgs–strahlung processes

We will not repeat the detailed description of the previous uncertainties in this subsection and only summarize how they affect the VBF and Higgs–strahlung inclusive cross sections. In both channels, only the scale uncertainties and the PDF+α_s errors are taken into account, the calculation being exact at a given order.

The VBF channel

As stated previously, we use the central scale $\mu_0 = \mu_R = \mu_F = Q_{V^*}$, that is the

momentum transfer of the exchanged weak boson. Note that a cut of $Q_{V^*} \geq 2$ GeV has to be applied as stated in the previous section. The scale uncertainty is calculated in exactly the same way as for the gluon fusion mechanism, exploring the range $\mu_0/2 \leq \mu_R, \mu_F \leq 2\mu_0$. We have checked that imposing the restriction $1/2 \leq \mu_R/\mu_F \leq 2$ does not modify the final result. We obtain very small scale uncertainties ranging from $\sim \pm 2\%$ at 8 TeV down to $\sim \pm 1\%$ and even lower at 33 TeV as can be seen in Fig. 11 (left). This is in sharp contrast with the $\pm 8\%$ uncertainty obtained at LO at 8 TeV for example, which illustrates the high level of precision already obtained with NLO QCD corrections.

The 90% CL PDF+α_s uncertainties are calculated following the recipe presented in the gluon fusion subsection. The PDF+α_s uncertainty dominates the total error, ranging from $+7\%/-4\%$ at 8 TeV down to $+5\%/-3\%$ at 100 TeV.

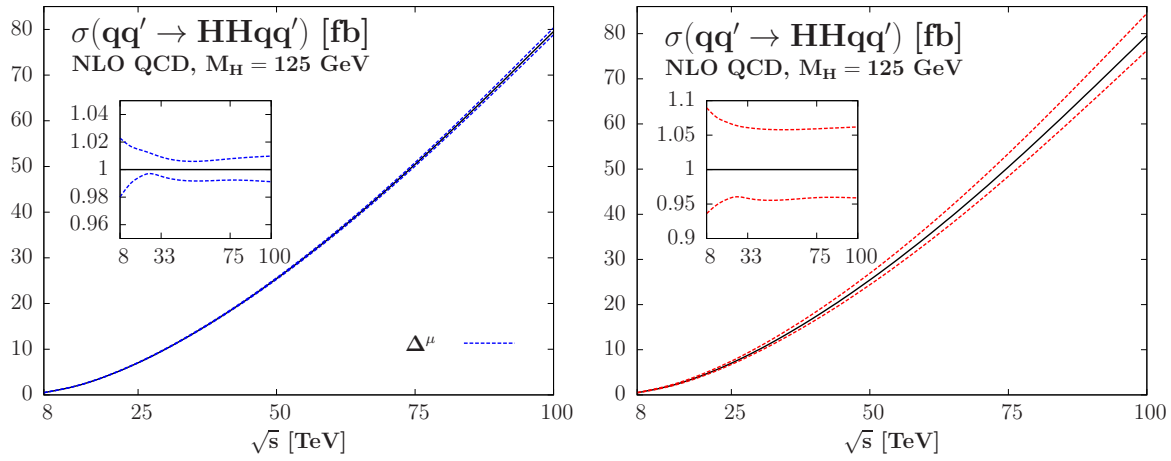

Figure 11: Scale uncertainty for a scale variation in the interval $\frac{1}{2}\mu_0 \leq \mu_R, \mu_F \leq 2\mu_0$ (left) and total uncertainty bands (right) in $\sigma(qq' \to HHqq')$ at the LHC as a function of $\sqrt{s}$ at $M_H = 125$ GeV. The inserts show the relative deviations to the cross section evaluated at the central scale $\mu_0 = \mu_R = \mu_F = Q_{V^*}$.

The total error has been obtained by adding linearly the scale and PDF+α_s uncertainties, given the small variation of the cross section with respect to the choice of the scale. This process has a total theoretical uncertainty which is always below 10%, from $+9\%/-6\%$ at 8 TeV to $+6\%/-4\%$ both at 33 and 100 TeV as can be read off Table 3. The total uncertainty is displayed in Fig. 11 (right) as a function of the c.m. energy. The QCD corrections drastically reduce the residual theoretical uncertainty.

The associated Higgs pair production with a vector boson

The cross section is calculated with the central scale $\mu_0 = \mu_R = \mu_F = M_{VHH}$ which is the invariant mass of the W/Z + Higgs pair system. The scales are varied in the interval $\mu_0/2 \leq \mu_R = \mu_F \leq 2\mu_0$. The factorization and renormalization scales can be chosen to be the same as the impact of taking them differently is totally negligible, given the fact that the scale μ_R only appears from NLO on and that we have a NNLO calculation which then reduces any non-negligible contribution arising from the difference between renormalization and factorization scales. As noticed previously, the scale uncertainty is expected to be worse in the ZHH channel because of the significant impact of the gluon fusion contribution. This is indeed the case as we obtain a scale uncertainty below $\pm 0.5\%$ in the WHH channel whereas the uncertainty in the ZHH channel is $\Delta^\mu \sim \pm 3\%$

$\sqrt{s}$ [TeV]	$\sigma^{\rm NLO}_{qq'HH}$ [fb]	Scale [%]		PDF [%]		PDF+α_s [%]		Total [%]	
8	0.49	$+2.3$	-2.0	$+5.2$	-4.4	$+6.7$	-4.4	$+9.0$	-6.4
14	2.01	$+1.7$	-1.1	$+4.6$	-4.1	$+5.9$	-4.1	$+7.6$	-5.1
33	12.05	$+0.9$	-0.5	$+4.0$	-3.7	$+5.2$	-3.7	$+6.1$	-4.2
100	79.55	$+1.0$	-0.9	$+3.5$	-3.2	$+5.2$	-3.2	$+6.2$	-4.1

Table 3: The total Higgs pair production cross section at NLO in the vector boson fusion process at the LHC (in fb) for given c.m. energies (in TeV) at the central scale $\mu_F = \mu_R = Q_{V^*}$ for $M_H = 125$ GeV. The corresponding shifts due to the theoretical uncertainties from the various sources discussed are also shown as well as the total uncertainty when all errors are added linearly.

at 8 TeV and slightly more at higher energies to reach $\sim \pm 5\%$ at 33 TeV, as can be seen in Fig. 12 (left).

The total PDF+α_s error that we obtain is very similar for the two channels WHH and ZHH. It varies from $\sim \pm 4\%$ at 8 TeV down to $\sim \pm 3\%$ at 33 TeV, with a slightly higher uncertainty at 100 TeV.

The total error has been obtained exactly as in the VBF case, given the very small variation of the cross section with respect to the scale choice. It is dominated by the PDF+α_s uncertainty and amounts to $+5\%/-4\%$ ($+4\%/-4\%$) at 8 (100) TeV in the WHH channel and $+7\%/-5\%$ ($+8\%/-8\%$) at 8 (100) TeV in the ZHH channel. The total theoretical uncertainty in the Higgs–strahlung channels is less than 10%. The numbers are given in Tables 4 and 5. The total uncertainty bands for the WHH and ZHH channels are displayed in Fig. 12 (right).

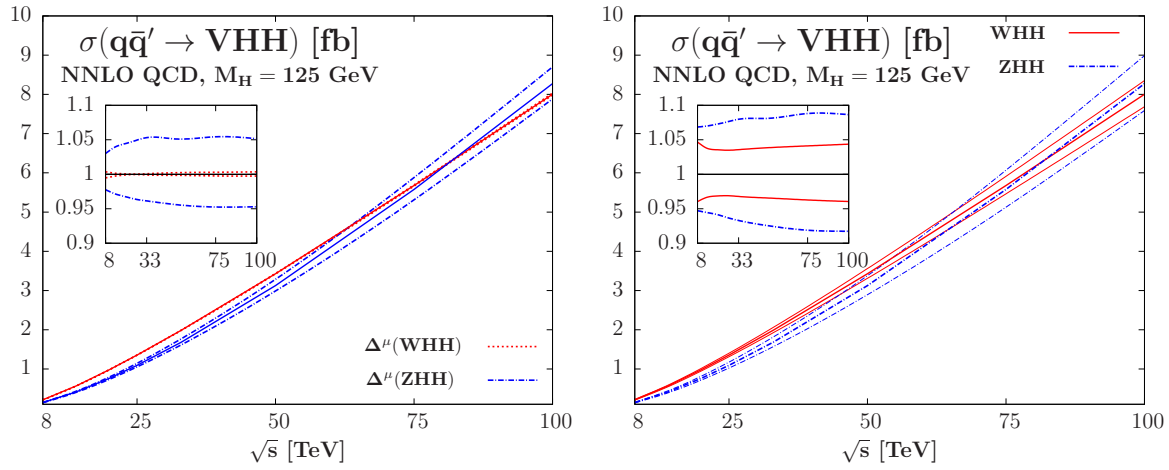

Figure 12: Scale uncertainty for a scale variation in the interval $\frac{1}{2}\mu_0 \leq \mu_R, \mu_F \leq 2\mu_0$ (left) and total uncertainty bands (right) in Higgs pair production through Higgs–strahlung at NNLO QCD at the LHC as a function of $\sqrt{s}$ for $M_H = 125$ GeV. The inserts show the relative deviations to the cross section evaluated at the central scale $\mu_0 = \mu_R = \mu_F = M_{VHH}$.

$\sqrt{s}$ [TeV]	$\sigma^{\rm NNLO}_{WHH}$ [fb]	Scale [%]		PDF [%]		PDF+α_s [%]		Total [%]	
8	0.21	+0.4	−0.5	+4.3	−3.4	+4.3	−3.4	+4.7	−4.0
14	0.57	+0.1	−0.3	+3.6	−2.9	+3.6	−3.0	+3.7	−3.3
33	1.99	+0.1	−0.1	+2.9	−2.5	+3.4	−3.0	+3.5	−3.1
100	8.00	+0.3	−0.3	+2.7	−2.7	+3.8	−3.4	+4.2	−3.7

Table 4: The total Higgs pair production cross sections at NNLO in the $q\bar{q}' \to WHH$ process at the LHC (in fb) for different c.m. energies (in TeV) at the central scale $\mu_F = \mu_R = M_{WHH}$ for $M_H = 125$ GeV. The corresponding shifts due to the theoretical uncertainties from the various sources discussed are also shown as well as the total uncertainty when all errors are added linearly.

$\sqrt{s}$ [TeV]	$\sigma^{\rm NNLO}_{ZHH}$ [fb]	Scale [%]		PDF [%]		PDF+α_s [%]		Total [%]	
8	0.14	+3.0	−2.2	+3.8	−3.0	+3.8	−3.0	+6.8	−5.3
14	0.42	+4.0	−2.9	+2.8	−2.3	+3.0	−2.6	+7.0	−5.5
33	1.68	+5.1	−4.1	+1.9	−1.5	+2.7	−2.6	+7.9	−6.7
100	8.27	+5.2	−4.7	+1.9	−2.1	+3.2	−3.2	+8.4	−8.0

Table 5: Same as Table 4 for ZHH production using the central scale $\mu_F = \mu_R = M_{ZHH}$.

2.4.2 Sensitivity to the trilinear Higgs coupling in the main channels

We end this section by a brief study of the sensitivity of the three main channels to the trilinear Higgs coupling that we want to probe. Indeed, as can be seen in Fig. 1, all processes do not only involve a diagram with the trilinear Higgs couplings but also additional contributions which then dilute the sensitivity. In order to study the sensitivity within the SM, we rescale the coupling λ_{HHH} in terms of the SM trilinear Higgs coupling as $\lambda_{HHH} = \kappa\lambda^{\rm SM}_{HHH}$. This is in the same spirit as the study done in Refs. [42–44] and its goal is to give a way to estimate the precision one could expect in the extraction of the SM trilinear Higgs coupling from HH measurements at the LHC. In particular the variation of the trilinear Higgs coupling should not be viewed as coming from some beyond the SM physics model and it should be noted that quite arbitrary deviations of the trilinear Higgs couplings emerge from non-vanishing higher-dimension operators starting with dimension 6.

In Fig. 13 the three main Higgs pair production cross sections are displayed as a function of κ for three different c.m. energies $\sqrt{s} = 8, 14$ and 33 TeV. The left panels show the total cross sections while the right panels show the ratio between the cross sections at a given $\lambda_{HHH} = \kappa\lambda^{\rm SM}_{HHH}$ and the SM cross section with $\kappa = 1$.

As can be seen, the most sensitive channel is by far the VBF production mode, in particular for low and high values of κ. The shapes of the cross sections with respect to a variation of κ are the same in all channels and at all energies with a minimum reached at $\kappa \sim -1$, 2 and 3 for Higgs–strahlung, VBF and gluon fusion, respectively. The right panels of Fig. 13 also show that the sensitivity decreases when $\sqrt{s}$ increases. This is to be expected as the diagrams involving the trilinear Higgs self–coupling are mediated by

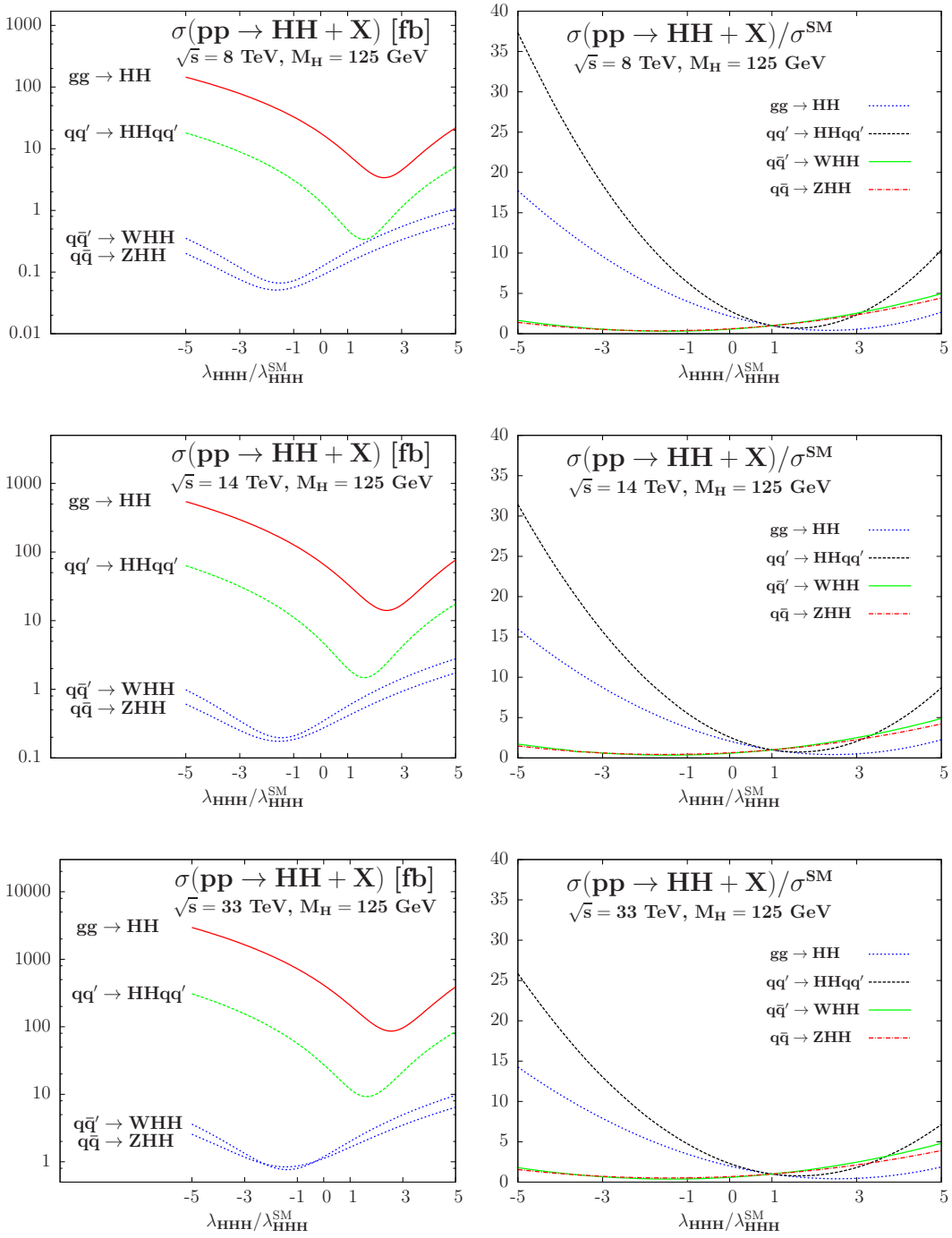

Figure 13: The sensitivity of the various Higgs pair production processes to the trilinear SM Higgs self–coupling at different c.m. energies. The left panels display the total cross sections, the right panels display the ratio between the cross sections at a given $\kappa = \lambda_{HHH}/\lambda^{\rm SM}_{HHH}$ and the cross sections at $\kappa = 1$.

s-channel propagators which get suppressed with increasing energy, so that the relative importance of these diagrams with respect to the remaining ones is suppressed.

Again it is important to note that the sensitivity tested here does not give information on the sensitivity to Higgs self–couplings in models beyond the SM. It only tests within the SM how accurately the respective Higgs pair production process has to be measured

in order to extract the SM trilinear Higgs self–coupling with a certain accuracy. For example the gluon fusion cross section has to be measured with an accuracy of $\sim 50\%$ at $\sqrt{s} = 8$ TeV in order to be able to extract the trilinear Higgs self–coupling with an accuracy of 50%, as can be inferred from Fig. 13 upper left. Similar discussions can be found in Refs. [42–44, 66].

2.5 Prospects at the LHC

As shown in the previous section, inclusive Higgs boson pair production is dominated by gluon fusion at LHC energies. Other processes, such as weak boson fusion, $qq' \to qq'HH$, associated production with heavy gauge bosons, $q\bar{q}' \to VHH$ ($V = W$, Z), or associated production with top quark pairs, $gg/q\bar{q} \to t\bar{t}HH$, yield cross sections which are factors of 10 – 30 smaller than that for $gg \to HH$. Since at the LHC Higgs boson pair production cross sections are small, we concentrate on the dominant gluon fusion process. In the following, we examine channels where one Higgs boson decays into a b quark pair and the other Higgs boson decays into either a photon pair, $gg \to HH \to b\bar{b}\gamma\gamma$, into a τ pair, $gg \to HH \to b\bar{b}\tau\bar{\tau}$, or into an off–shell W boson pair, $gg \to HH \to b\bar{b}W^*W^*$. Following the Higgs Cross Section Working Group recommendations [103], we assume a branching ratio of 57.7% for a 125 GeV Higgs boson decaying into b quarks, 0.228% for the Higgs boson decaying into a photon pair, 6.12% for the Higgs boson decaying into a τ pair and 21.50% for the Higgs boson decaying into off–shell W^* bosons.

At the time of the analysis, no generator existed for the signal process, but the matrix element for Higgs pair production in the gluon fusion channel was available in the Fortran code `HPAIR` [66,117]. In parallel to the approach used by the program described in [142,143], the `HPAIR` matrix element was added to `Pythia 6` [144]. It has been checked that the cross sections produced by `HPAIR` and by the `Pythia 6` implementation are consistent.

All tree–level background processes are calculated using `Madgraph 5` [145]. Signal and background cross sections are evaluated using the MSTW2008 parton distribution functions [133] with the corresponding value of α_s at the investigated order in perturbative QCD. The effects of QCD corrections are included in our calculation via multiplicative factors which are summarized in the following subsections and have been introduced previously for the signal cross sections.

2.5.1 Kinematical distributions of $gg \to HH$

In this subsection the characteristic distributions of the gluon fusion process $gg \to HH$ are studied for several observables. In Fig. 14, we show for each of the two final state Higgs bosons the normalized distributions of the transverse momentum $P_{T,H}$ and the pseudorapidity η_H, as well as the invariant mass M_{HH}, the helicity angle $\theta^\star_{HH}$ which is the angle between the off-shell Higgs boson, boosted back into the Higgs boson pair rest frame, and the Higgs boson pair direction, and the rapidity y_{HH} of the Higgs boson pair. The distributions of each observable are shown for different values of the trilinear Higgs coupling $\lambda/\lambda_{SM} = 0$ (green curve), 1 (red curve) and 2 (blue curve). We also include in the plots the typical background $q\bar{q} \to ZH$ coming from the Higgs boson itself (black curve), the Z boson faking a Higgs boson.

The Higgs bosons from inclusive Higgs pair production are typically boosted, as we can see in the upper left plot of Fig. 14 where the $P_{T,H}$ distributions reach their maximum for $P_{T,H} \sim 150$ GeV. For $\lambda/\lambda_{SM} = 2$, the triangle diagram interferes destructively with the box diagram, which explains the dip in the $P_{T,H}$ distribution. This high transverse momentum spectrum can also be interpreted in terms of the low pseudorapidity of the two Higgs bosons which have a typical symmetric distribution with the maximum around zero, see Fig. 14 upper right. The $q\bar{q} \to ZH$ background has a completely different topology with less boosted Higgs and Z bosons, $P_{T,H/Z} \sim 50$ GeV, with pseudorapidity of order $|\eta_{H/Z}| \sim 2$ as can be seen in the upper left and right plots of Fig. 14. The middle left plot of Fig. 14 displays the distributions of the invariant mass of the Higgs boson pair. For the signal the typical value is $M_{HH} \gtrsim 400$ GeV to be compared to a lower value of $M_{ZH} \gtrsim 250$ GeV for the ZH background. Also note that an important depletion appears in the signal for $\lambda/\lambda_{SM} = 2$ caused by the destructive interference between the triangle and box contribution. Due to the Higgs boson scalar nature a known discriminant observable is the angle $\theta^{\star}_{HH}$ [146]. The middle right plot in Fig. 14 shows that signal and ZH background have similar distributions thus making this observable less discriminant than others described before but still efficient for some specific backgrounds, as we will see in the following. From the bottom plot of Fig. 14, it can be inferred that the rapidity distribution of the Higgs pair is narrower for the signal than for the ZH background.

In the following the different decay channels $HH \to b\bar{b}\gamma\gamma$, $HH \to b\bar{b}\tau\bar{\tau}$ and $HH \to b\bar{b}W^+W^-$ will be investigated in more detail.

2.5.2 The $b\bar{b}\gamma\gamma$ decay channel

In this subsection, the $b\bar{b}\gamma\gamma$ final state for the production of two Higgs bosons with a mass of 125 GeV at $\sqrt{s} = 14$ TeV is investigated. Earlier studies can be found in Refs. [107–110]. The calculation of the signal, $pp \to HH \to b\bar{b}\gamma\gamma$, is performed as described above by incorporating the matrix element extracted from the program `HPAIR` into `Pythia 6`. We include the effects of NLO QCD corrections on the signal by a multiplicative factor, $K_{NLO} = 1.88$, corresponding to a 125 GeV Higgs boson and a c.m. energy of 14 TeV. Here we set the factorization and renormalization scales equal to M_{HH}. The generated background processes are the QCD process $b\bar{b}\gamma\gamma$ and the associated production of a Higgs boson with a $t\bar{t}$ pair, $t\bar{t}H$, with the Higgs boson subsequently decaying into a photon pair and the top quarks decaying into a W boson and a b quark, as well as single Higgs-strahlung ZH with the Higgs boson decaying into $\gamma\gamma$ and the Z boson decaying into $b\bar{b}$. The QCD corrections have been included by a multiplicative K–factor applied to the respective LO cross section. All K–factors are taken at NLO except for the single Higgs–strahlung process which is taken at NNLO QCD and the case of $b\bar{b}\gamma\gamma$ in which no higher order corrections are taken into account. The various K–factors are given in Table 6 and taken from Ref. [103]. The factorization and renormalization scales have been set to M_{HH} for the signal and to specific values for each process for the backgrounds.

In this analysis, the signal and background processes are generated with exclusive cuts. The basic acceptance cuts are motivated by the fact that the b quark pair and the photon pair reconstruct the Higgs mass according to the resolutions expected for ATLAS and CMS. Note that starting from this section all the plots include the decays and the acceptance cuts specific to each final state.

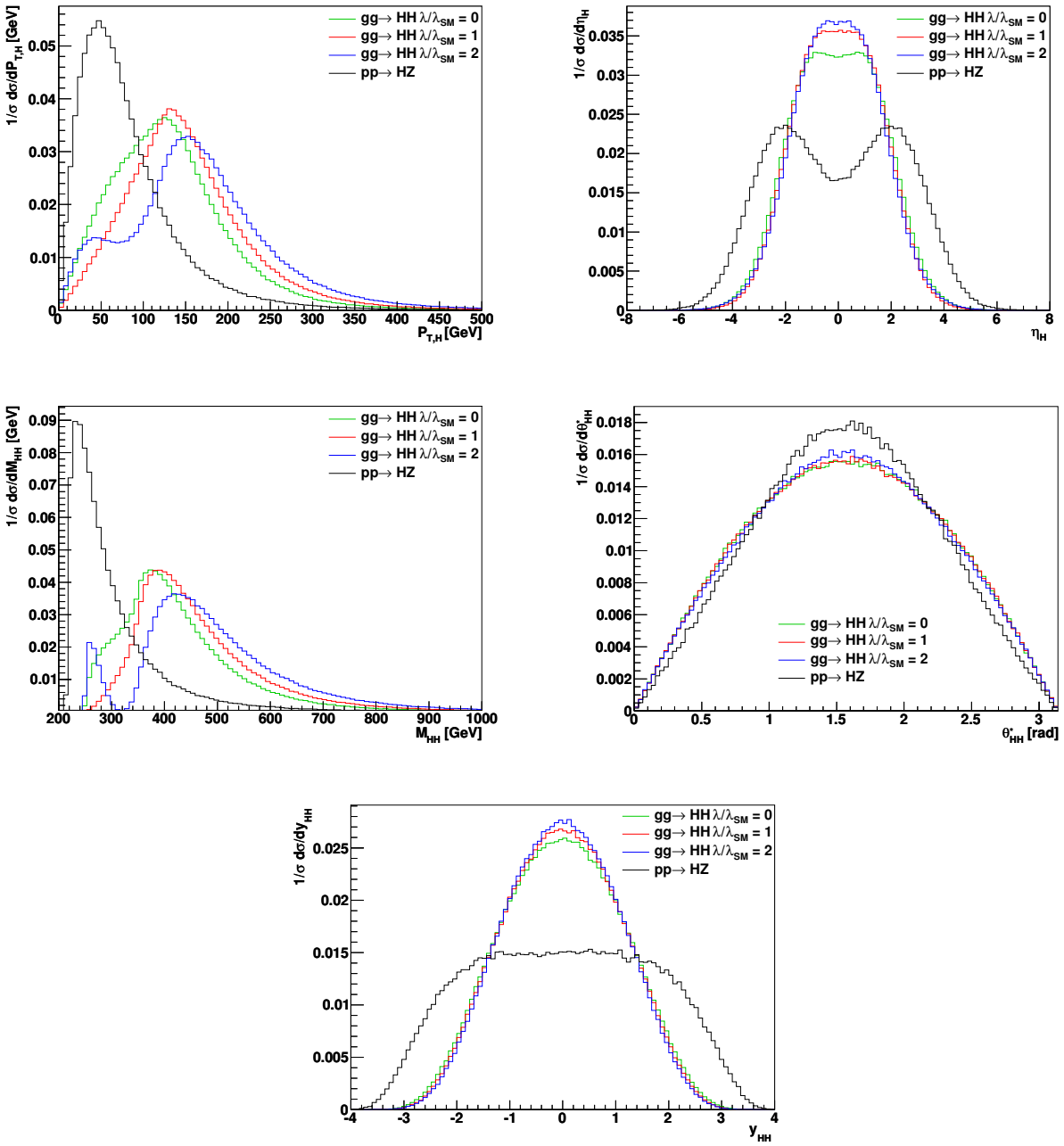

Figure 14: Normalized distributions of $P_{T,H}$, η_H, M_{HH}, $\theta^{\star}_{HH}$ and y_{HH} for different values of the trilinear Higgs coupling in terms of the SM coupling, $\lambda/\lambda_{SM} = 0, 1, 2$.

In detail, we veto events with leptons having soft transverse momentum $p_{T,\ell} > 20$ GeV and with a pseudorapidity $|\eta_\ell| < 2.4$ in order to reduce the $t\bar{t}H$ background. Furthermore we also veto events with QCD jets $p_{T,jet} > 20$ GeV and with a pseudorapidity $|\eta_{jet}| < 2.4$ to further reduce the $t\bar{t}H$ background. We require exactly one b quark pair and one photon pair. The b quark pair is restricted to have $p_{T,b} > 30$ GeV, $|\eta_b| < 2.4$ and $\Delta R(b,b) > 0.4$, where $\Delta R(b,b)$ denotes the isolation of the two b quarks defined by the distance $\Delta R = \sqrt{(\Delta\eta)^2 + (\Delta\phi)^2}$ in the pseudorapidity and azimuthal angle plane (η, ϕ). We consider the b–tagging efficiency to be 70%. The photon pair has to fulfill $p_{T,\gamma} > 30$ GeV, $|\eta_\gamma| < 2.4$ and $\Delta R(\gamma,\gamma) > 0.4$. The two reconstructed Higgs bosons, from the b quark pair and from the photon pair, have to reproduce the Higgs

$\sqrt{s}$ [TeV]	HH	$b\bar{b}\gamma\gamma$	$t\bar{t}H$	ZH
14	1.88	1.0	1.10	1.33

Table 6: K–factors for $gg \to HH$, $b\bar{b}\gamma\gamma$, $t\bar{t}H$ and ZH production at $\sqrt{s} = 14$ TeV [103]. The Higgs boson mass is assumed to be $M_H = 125$ GeV.

boson mass within a window of 25 GeV, 112.5 GeV $< M_{b\bar{b}} <$ 137.5 GeV, and a window of 10 GeV, 120 GeV $< M_{\gamma\gamma} <$ 130 GeV, respectively. We require additional isolations between the b quarks and the photons being $\Delta R(\gamma, b) > 0.4$.

Based on the distributions shown in Fig. 15, apart from the acceptance cuts we have applied more advanced cuts for this parton level analysis. We first require the reconstructed invariant mass of the Higgs pair to fulfill $M_{HH} > 350$ GeV. Furthermore we remove events which do not satisfy $P_{T,H} > 100$ GeV. We also constrain the pseudorapidity of the two reconstructed Higgs bosons, $|\eta_H| < 2$, and the isolation between the two b jets to be $\Delta R(b, b) < 2.5$.

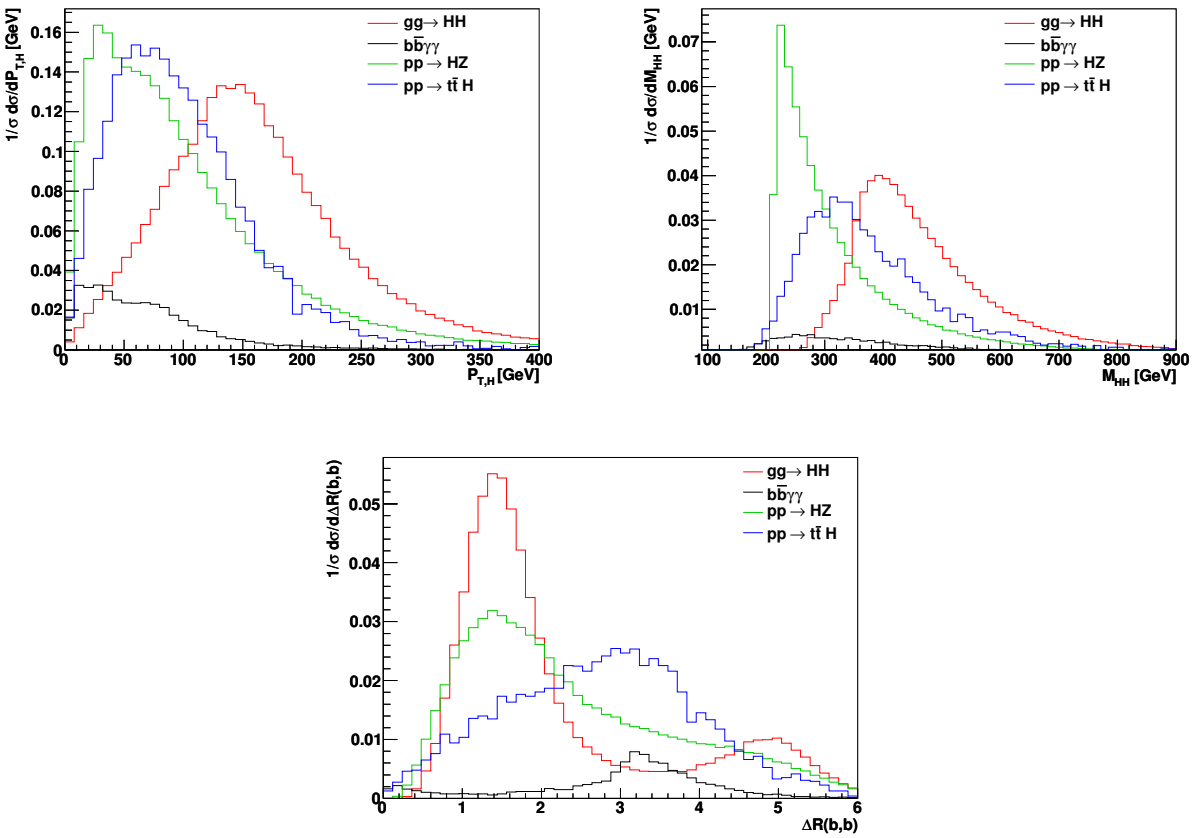

Figure 15: Normalized signal and backgrounds distributions of $P_{T,H}$, M_{HH} and R_{bb} in the $b\bar{b}\gamma\gamma$ channel.

The results are collected in Table 7. The local decrease of the sensitivity between the cut on M_{HH} and the cut on $P_{T,H}$ is explained by the fact that we accept to have a reduced sensitivity locally during the chain of cuts in order to enhance the final significance. In the case described in this section a cut on $P_{T,H}$ alone reduces the sensitivity as does a cut on η_H alone, but the first cut actually improves the discrimination between the

signal and the background in the pseudorapidity distribution, hence allowing for a larger improvement when applying the η_H cut just after the $P_{T,H}$ cut. Eventually all the cuts allow for an improvement of the significance by two orders of magnitude, that is the ratio of signal events S over the square root of background events B, $S/\sqrt{B}$. The final value for $S/\sqrt{B}$ is 16.3 for an integrated luminosity of $\int\mathcal{L} = 3000$ fb^{-1}, corresponding to 51 signal events. Therefore this channel seems promising.

	HH	$b\bar{b}\gamma\gamma$	$t\bar{t}\gamma\gamma$	ZH	S/B	$S/\sqrt{B}$
Cross section NLO [fb]	8.92×10^{-2}	5.05×10^{3}	1.39	3.33×10^{-1}	1.77×10^{-5}	6.87×10^{-2}
Reconstructed Higgs from bs	4.37×10^{-2}	4.01×10^{2}	8.70×10^{-2}	1.24×10^{-3}	1.09×10^{-4}	1.20×10^{-1}
Reconstructed Higgs from γs	3.05×10^{-2}	1.78	2.48×10^{-2}	3.73×10^{-4}	1.69×10^{-2}	1.24
Cut on M_{HH}	2.73×10^{-2}	3.74×10^{-2}	7.45×10^{-3}	1.28×10^{-4}	6.07×10^{-1}	7.05
Cut on $P_{T,H}$	2.33×10^{-2}	3.74×10^{-2}	5.33×10^{-3}	1.18×10^{-4}	5.44×10^{-1}	6.17
Cut on η_H	2.04×10^{-2}	1.87×10^{-2}	3.72×10^{-3}	9.02×10^{-5}	9.06×10^{-1}	7.45
Cut on $\Delta R(b,b)$	1.71×10^{-2}	0.00	3.21×10^{-3}	7.44×10^{-5}	5.21	16.34
"Detector level"	1.56×10^{-2}	0.00	8.75×10^{-3}	8.74×10^{-3}	8.92×10^{-1}	6.46

Table 7: Cross section values of the HH signal and the various backgrounds expected at the LHC at $\sqrt{s} = 14$ TeV, the signal to background ratio S/B and the significance $S/\sqrt{B}$ for $\int\mathcal{L} = 3000$ fb^{-1} in the $b\bar{b}\gamma\gamma$ channel after applying the cuts discussed in the text.

A realistic assessment of the prospects for measuring the signal in the $b\bar{b}\gamma\gamma$ final state depends mostly on a realistic simulation of the diphoton fake rate due to multijet production, which is the dominant background in such an analysis. Our first parton level study gives a rough idea of how promising the $b\bar{b}\gamma\gamma$ channel is.

In the following we perform a full analysis including fragmentation and hadronization effects, initial and final state radiations by using `Pythia 6.4` in order to assess more reliably whether the promising features of this channel survive in a real experimental environment. All the events are processed through `Delphes` [147], the tool which is used for the detector simulation. For the jet reconstruction we use the anti-k_T algorithm with a radius parameter of $R = 0.5$. We still consider a b–tagging efficiency of 70%. We keep the same acceptance cuts as before except for the transverse momentum of the reconstructed b jet and photon which we increase up to $p_{T,b/\gamma} > 50$ GeV. We also enlarge the window for the reconstructed Higgs boson coming from the b quark pair, by requiring 100 GeV $< M_{b\bar{b}} <$ 135 GeV. We select events with exactly two reconstructed b jets and two photons.

The final result is displayed in the last line of Table 7. The final significance $S/\sqrt{B}$ for this simulation has decreased to 6.5 for an integrated luminosity of 3000 fb^{-1}, corresponding to 47 events. Though low, the significance nevertheless is promising enough to trigger a real experimental analysis as can be performed only by the experimental collaborations and which is beyond the scope of this work.

$\sqrt{s}$ [TeV]	HH	$b\bar{b}\tau\bar{\tau}$	$t\bar{t}$	ZH
14	1.88	1.21	1.35	1.33

Table 8: K–factors for $gg \to HH$, $b\bar{b}\tau\bar{\tau}$ [149], $t\bar{t}$ [150–162] and ZH production [103] at $\sqrt{s} = 14$ TeV. The Higgs boson mass is assumed to be $M_H = 125$ GeV.

2.5.3 The $b\bar{b}\tau\bar{\tau}$ decay channel

The $b\bar{b}\tau\bar{\tau}$ decay channel is promising for low mass Higgs boson pair production at the LHC and has been previously studied in Refs. [107–111]. An important part of this analysis will depend on the ability to reconstruct the b quark pair and the τ pair. As the real experimental assessment of such a reconstruction is beyond the scope of our work we will perform in the following a parton level analysis, assuming a perfect τ reconstruction[4]. The analysis thus represents an optimistic estimate of what can be done at best to extract the trilinear Higgs self–coupling in the $b\bar{b}\tau\bar{\tau}$ channel.

We consider the two QCD–QED continuum background final states $b\bar{b}\tau\bar{\tau}$ and $b\bar{b}\bar{\tau}\nu_\tau\tau\bar{\nu}_\tau$ calculated at tree–level. The $b\bar{b}\bar{\tau}\nu_\tau\tau\bar{\nu}_\tau$ final state background dominantly stems from $t\bar{t}$ production with the subsequent top quark decays $t \to bW$ and $W \to \bar{\tau}\nu_\tau$. We also include backgrounds coming from single Higgs production in association with a Z boson and the subsequent decays $H \to \tau\bar{\tau}$ and $Z \to b\bar{b}$ or $H \to b\bar{b}$ and $Z \to \tau\bar{\tau}$. The effects of QCD corrections are included in our calculation via multiplicative K–factors which are summarized in Table 8. All K–factors are taken at NLO except for the single Higgs–strahlung process which is taken at NNLO QCD. The factorization and renormalization scales have been taken at M_{HH} for the signal and at specific values for each background process.

Concerning the choice of our cuts, we demand exactly one b quark pair and one τ pair. The b quark pair is required to fulfill $p_{T,b} > 30$ GeV and $|\eta_b| < 2.4$. We assume the b–tagging efficiency to be 70% and the τ–tagging efficiency to be 50% and we neglect fake rates in both cases. The τ pair has to fulfill $p_{T,\tau} > 30$ GeV and $|\eta_\tau| < 2.4$. The reconstructed Higgs boson from the b quark pair is required to reproduce the Higgs mass within a window of 25 GeV, 112.5 GeV $< M_{b\bar{b}} <$ 137.5 GeV. The reconstructed Higgs boson from the τ pair needs to reproduce the Higgs mass within a window of 50 GeV, 100 GeV $< M_{\tau\bar{\tau}} <$ 150 GeV or within a window of 25 GeV, 112.5 GeV $< M_{\tau\bar{\tau}} <$ 137.5 GeV, in a more optimistic scenario. In addition to these acceptance cuts we also add more advanced cuts for this parton level analysis, based on the distributions shown in Fig. 16 and in a similar way as what has been done in the previous $b\bar{b}\gamma\gamma$ analysis. We first demand the invariant mass of the reconstructed Higgs pair to fulfill $M_{HH} > 350$ GeV. In addition, we remove events which do not satisfy $P_{T,H} > 100$ GeV. We do not use a cut on the pseudorapidity of the reconstructed Higgs bosons in this analysis as it would reduce the significance.

The different results of our parton level analysis are summarized in Table 9. The cuts allow for an improvement of two orders of magnitude in the significance $S/\sqrt{B}$. The final $S/\sqrt{B}$ is 6.71 for an integrated luminosity of $\int \mathcal{L} = 3000$ fb^{-1}, corresponding

[4]There have been improvements over the last years to reconstruct the invariant mass of a τ pair. In particular, the use of the Missing Mass Calculator algorithm offers very promising results [148]. It is used by experimental collaborations at the LHC in the $H \to \tau\bar{\tau}$ search channel.

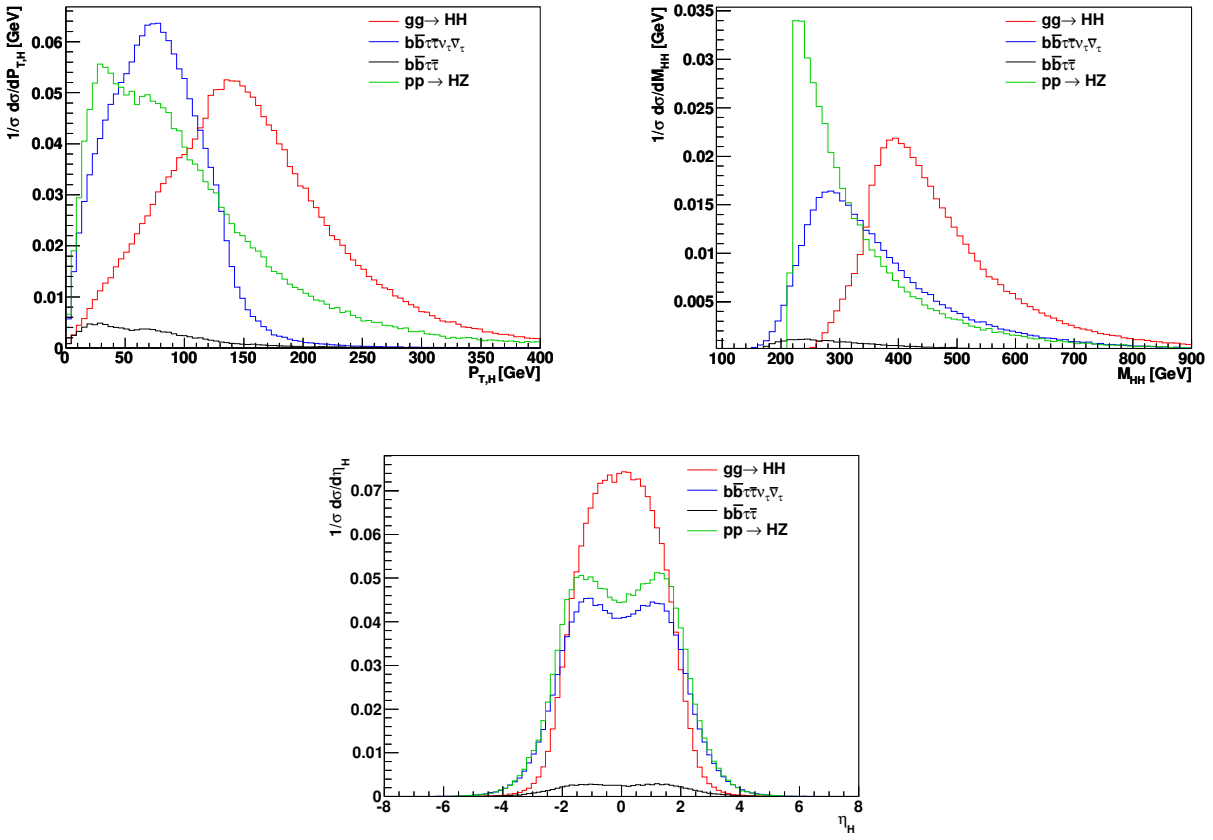

Figure 16: Normalized distributions of $P_{T,H}$, M_{HH} and η_H for signal and backgrounds in the $b\bar{b}\tau\bar{\tau}$ channel.

to 330 signal events. We then conclude that this channel is promising. In the last line we reproduce our result for the optimistic requirement of 112.5 GeV $< M_{\tau\tau} <$ 137.5 GeV leading to the final significance $S/\sqrt{B} = 9.36$ for an integrated luminosity of 3000 fb^{-1}. Already for a planned mid–term integrated luminosity of 300 fb^{-1} at 14 TeV the expectations are promising with 33 signal events and a significance $S/\sqrt{B} = 2.96$ in the optimistic scenario.

2.5.4 The $b\bar{b}W^+W^-$ decay channel

The analysis in this channel is difficult as the leptonic W boson decays lead to missing energy in the final state. Consequently, one of the two Higgs bosons cannot *a priori* be reconstructed equally well as the other Higgs boson, thus reducing our capability to efficiently remove the background with the canonical acceptance cuts previously applied in the other decay channels. This channel with one lepton plus jets final state has been studied in [111, 112]. We only consider here the decay $W \to \ell\nu_\ell$ ($\ell = e, \mu$) with a branching ratio of 10.8%.

We take into account the continuum background which contains all processes with the $b\bar{b}\ell\nu_\ell\ell\nu_\ell$ final states at tree–level, for example $qq/gg \to b^*\bar{b}^* \to \gamma bZ\bar{b} \to b\bar{b}\ell\ell Z$ with the subsequent splitting $Z \to \nu_\ell\bar{\nu}_\ell$. We proceed in a similar manner as in the previous analyses. We generate the signal and the backgrounds with the following parton-level

	HH	$b\bar{b}\tau\bar{\tau}$	$b\bar{b}\tau\bar{\tau}\nu_\tau\bar{\nu}_\tau$	ZH	S/B	$S/\sqrt{B}$
Cross section NLO [fb]	2.47	2.99×10^4	8.17×10^3	2.46×10^1	6.48×10^{-5}	6.93×10^{-1}
Reconstructed Higgs from τs	2.09×10^{-1}	8.35×10^1	1.58×10^2	5.70×10^{-1}	8.63×10^{-4}	7.36×10^{-1}
Reconstructed Higgs from bs	1.46×10^{-1}	6.34×10^{-1}	1.43×10^1	3.75×10^{-2}	9.75×10^{-3}	2.07
Cut on M_{HH}	1.30×10^{-1}	1.37×10^{-1}	1.74	1.26×10^{-2}	6.88×10^{-2}	5.18
Cut on $P_{T,H}$	1.10×10^{-1}	7.80×10^{-2}	7.17×10^{-1}	1.15×10^{-2}	1.36×10^{-1}	6.71
With 112.5 GeV $< M_{\tau\bar{\tau}} <$ 137.5 GeV	1.10×10^{-1}	3.41×10^{-2}	3.76×10^{-1}	3.15×10^{-3}	2.67×10^{-1}	9.37

Table 9: Cross section values of the of HH signal and the various backgrounds expected at the LHC at $\sqrt{s} = 14$ TeV, the signal to background ratio S/B and the significance $S/\sqrt{B}$ for $\int \mathcal{L} = 3000$ fb^{-1} in the $b\bar{b}\tau\bar{\tau}$ channel after applying the cuts discussed in the text.

cuts. We require that the b quarks fulfill $p_{T,b} > 30$ GeV and $|\eta_b| < 2.4$. We consider the b–tagging efficiency to be 70%. The leptons have to fulfill $p_{T,\ell} > 20$ GeV and $|\eta_\ell| < 2.4$. The reconstructed Higgs boson from the b quark pair has to reproduce the Higgs boson mass within a window of 25 GeV, 112.5 GeV $< M_{b\bar{b}} <$ 137.5 GeV. We also require that the missing transverse energy respects $E_T^{miss} > 20$ GeV.

As done in the previous subsections, we also add more advanced cuts for this parton level analysis, based on the distributions shown in Fig. 17. The distributions on the upper left of Fig. 17 correspond to the transverse mass of the lepton pair, being defined as $M_T = \sqrt{2p_T^{\ell\ell} E_T^{miss}(1 - \cos\Delta\phi(E_T^{miss}, \ell\ell))}$, where $\Delta\phi(E_T^{miss}, \ell\ell)$ is the angle between the missing transverse momentum and the transverse momentum of the dilepton system. The distribution of the signal has an endpoint at the value of M_H. The distributions on the upper right of Fig.17 represent the angle between the two leptons projected on the transverse plane, $\Delta\phi_{\ell_1\ell_2}$. The angle is reduced for the signal compared to the broad distribution of the background. The last distributions on the bottom of Fig. 17 display the projected missing transverse energy $\tilde{E}_T^{miss} = E_T^{miss} \sin\Delta\phi(E_T^{miss}, \ell)$ for $\Delta\phi(E_T^{miss}, \ell) \leq \pi/2$, where $\Delta\phi(E_T^{miss}, \ell)$ is the angle between the missing transverse momentum and the transverse momentum of the nearest lepton candidate. If $\Delta\phi(E_T^{miss}, \ell) > \pi/2$, then $\tilde{E}_T^{miss} = E_T^{miss}$. The signal distribution is shifted to the left compared to the background distribution.

We first require the transverse mass of the lepton pair to be $M_T < 125$ GeV. We then remove events which do not satisfy $\Delta\phi_{\ell_1\ell_2} < 1.2$ and we also add a constraint on the angle between the two leptons, $\Delta\theta_{\ell_1\ell_2} < 1.0$. We demand the missing transverse energy to fulfill $E_T^{miss} > 120$ GeV and the projected energy to satisfy $\tilde{E}_T^{miss} < 80$ GeV. Note that the $\tilde{E}_T^{miss}$ distribution displayed in Fig. 17 is obtained after the acceptance cuts having been applied but before the advanced cuts. The cuts on M_T, $\Delta\phi_{\ell_1\ell_2}$, $\Delta\theta_{\ell_1\ell_2}$ and $\tilde{E}_T^{miss}$ modify this distribution and explain why the $\tilde{E}_T^{miss}$ cut, which would seem not to be efficient, actually improves the significance.

The results for the LHC at $\sqrt{s} = 14$ TeV are summarized in Table 10. While the cuts allow for an improvement of the significance $S/\sqrt{B}$ by about one order of magnitude, we are still left with a very small signal to background ratio. Thus, this channel using the final states considered here is not very promising.

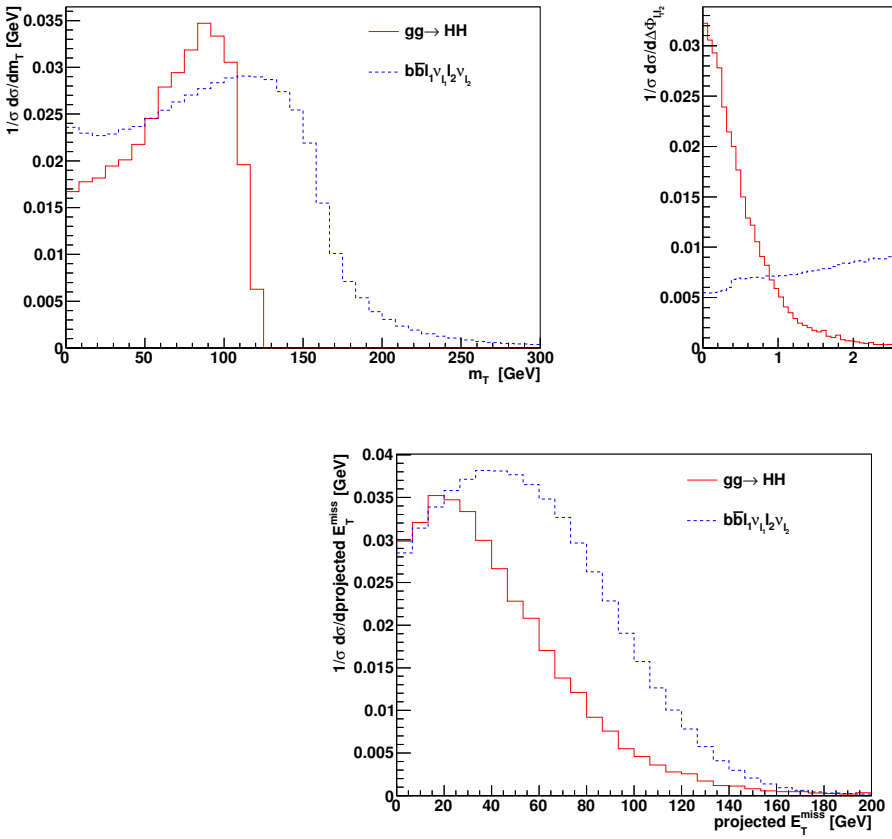

Figure 17: Normalized distributions of M_T, $\Delta\phi_{l_1 l_2}$ and projected missing transverse energy $\tilde{E}_T^{miss}$ for signal and background channels in the $b\bar{b}l_1\nu_{l_1}l_2\nu_{l_2}$ final states of the $b\bar{b}W^+W^-$ channel.

	HH	$b\bar{b}l_1\nu_{l_1}l_2\nu_{l_2}$	S/B	$S/\sqrt{B}$
Cross section NLO [fb]	3.92×10^{-1}	2.41×10^{4}	1.63×10^{-5}	1.38×10^{-1}
Reconstructed Higgs from bs	6.18×10^{-2}	1.89×10^{2}	3.27×10^{-4}	2.46×10^{-1}
Cut on M_T	$6.18. \times 10^{-2}$	1.19×10^{2}	5.19×10^{-4}	3.10×10^{-1}
Cut on $\Delta\phi_{\ell_1\ell_2}$	5.37×10^{-2}	6.96×10^{1}	7.72×10^{-4}	3.53×10^{-1}
Cut on $\Delta\theta_{\ell_1\ell_2}$	5.17×10^{-2}	5.65×10^{1}	9.15×10^{-4}	3.77×10^{-1}
Cut on E_T^{miss}	8.41×10^{-3}	3.77×10^{-1}	2.22×10^{-2}	7.50×10^{-1}
Cut on $\tilde{E}_T^{miss}$	4.59×10^{-3}	2.70×10^{-2}	1.70×10^{-1}	1.53

Table 10: Cross section values of the HH signal and the considered background expected at the LHC at $\sqrt{s} = 14$ TeV, the signal to background ratio S/B and the significance $S/\sqrt{B}$ for $\int\mathcal{L}$=3000 fb^{-1} in the $b\bar{b}W^+W^-$ channel after applying the cuts discussed in the text.

2.6 Conclusions on the Higgs self-coupling measurement at the LHC

In this section we have discussed in detail the main Higgs pair production processes at the LHC, gluon fusion, vector boson fusion, double Higgs–strahlung and associated

production with a top quark pair. They allow for the determination of the trilinear Higgs self–coupling λ_{HHH}, which represents a first important step towards the reconstruction of the Higgs potential and thus the final verification of the Higgs mechanism as the origin of electroweak symmetry breaking. We have included the important QCD corrections at NLO to gluon fusion and vector boson fusion and calculated for the first time the NNLO corrections to double Higgs–strahlung. It turns out that the gluon initiated process to ZHH production which contributes at NNLO is sizeable in contrast to the single Higgs-strahlung case. We have discussed in detail the various uncertainties of the different processes and provided numbers for the cross sections and the total uncertainties at four c.m. energies, i.e. 8, 14, 33 and 100 TeV. It turns out that they are of the order of 40% in the gluon fusion channel while they are much more limited in the vector bosons fusion and double Higgs–strahlung processes, i.e. below 10%. Within the SM we also studied the sensitivities of the double Higgs production processes to the trilinear Higgs self–coupling in order to get an estimate of how accurately the cross sections have to be measured in order to extract the Higgs self–interaction with sufficient accuracy.

In a second part we have performed a parton level analysis for the dominant Higgs pair production process through gluon fusion in different final states which are $b\bar{b}\gamma\gamma$, $b\bar{b}\tau\bar{\tau}$ and $b\bar{b}W^+W^-$ with the W bosons decaying leptonically. Due to the smallness of the signal and the large QCD backgrounds the analysis is challenging. The $b\bar{b}W^+W^-$ final state leads to a very small signal to background ratio after applying acceptance and selection cuts so that it is not promising. On the other hand, the significances obtained in the $b\bar{b}\gamma\gamma$ and $b\bar{b}\tau\bar{\tau}$ final states after cuts are ~ 16 and ~ 9, respectively, with not too small event numbers. They are thus promising enough to start a real experimental analysis taking into account detector and hadronization effects, which is beyond the scope of our work. Performing a first simulation on the detector level for the $b\bar{b}\gamma\gamma$ state shows, however, that the prospects are good in case of high luminosities. Taking into account theoretical and statistical uncertainties and using the sensitivity plot, Fig. 13, the trilinear Higgs self-coupling λ_{HHH} can be expected to be measured within a factor of two. In order to improve the precision of this measurement, one will certainly need new experimental facilities. It has been reported [33] that a 50% measurement is expected from HL-LHC and 13% from linear e^-e^+ colliders at 1 TeV. One would need even higher collision energies to improve these last results, with CLIC achieving 10% at 3 TeV and VLHC achieving 8% at 100 TeV.

These conclusions put an end to the first part of this thesis devoted to the study of the Higgs boson within the Standard Model of particle physics. There are many reasons to look for physics Beyond the Standard Model. We now turn to the most motivated ones, the Supersymmetric Theories.

Part II

The Higgs bosons in the Minimal Supersymmetric Standard Model

Summary

3 Introduction to supersymmetry

3.1 A brief historical overview

In the 1960's there was some effort to merge external symmetries such as Lorentz invariance with internal symmetries such as flavor isospin or SU(3) in order to extend the Poincaré algebra with internal transformations. Nevertheless in 1967, Coleman and Mandula [163] proved that it is impossible to combine these two kinds of symmetries assuming only bosonic (integer spin) generators. However, in 1971, Gol'fand and Likhtman [164] found a way to avoid this no-go theorem, extending the Poincaré algebra with fermionic (half integer spin) generators. Supersymmetry was born. Few months later, Ramond and both Neveu and Schwarz [165, 166] succeeded in includind fermions in string theories, in order to explain the origin of baryons. These were the first two dimensional supersymmetric models. Four dimensional supersymmetric fields theories were introduced by Volkov and Akulov [167] in 1973, in a non-linear realization (they attempted to apply supersymmetry to neutrinos, but it has been shown experimentally that their theory did not describe correctly interactions at low energy). In the same year, Wess and Zumino [168] proposed the first linear realization of a supersymmetric field theory in four dimensions, which is now used in most model-building. Then, Wess, Zumino, Iliopoulos and Ferrara [169, 170] discovered that many divergencies, inherent to some four-dimensional field theories, go away when we include supersymmetry. Supersymmetry became even more attractive thanks to this last feature. Later in 1976, two independent groups, Freedman, van Nieuwenhuizen and Ferrara [171] on one side and Deser and Zumino [172] on the other side, discovered by analogy with gauge theories that local supersymmetry could include a description of the gravity, the so-called supergravity.

As a consequence, phenomenological studies of supersymmetry have been extensively studied and supersymmetric theories are nowadays considered as the most motivated ones to look for physics Beyond the Standard Model.

3.2 Quadratic divergence and naturalness

Inspired by the fact that local supersymmetry deals with gravity, many theorists tried to unify in supergravity models all the particles and interactions. Nevertheless, there is no evidence for the supersymmetry breaking scale, and no one knows if the new supersymmetric states (sparticles) should not be as heavy as the Planck scale, $M_P \sim 10^{19}$ GeV, where one expects to describe gravity. This energy range is commonly accepted to be the fundamental mass scale in physics, but it is attached to the so called mass hierarchy problem : why $M_P \gg M_W$? Since the Gravitational constant and the Fermi constant, $G_{N/F}$, scale as $1/M^2_{P/W}$, the latter interrogation translates into : why $G_N \ll G_F$? And again since in the atom the Newton potential is proportional to $G_N m_e^2/r$ and the Coulomb potential is proportional to e^2/r, why the Newton potential is much smaller than the Coulomb potential? A non-answer is because $M_P \gg M_W$, but why? One could try to live with it, which means, assume that $M_P \gg M_W$ and accept our ignorance of what is happening at very large energy scales. Doing so we can for example compute the bare mass of the electron $m^0\bar{\psi}\psi$. When we start to include radiative corrections at

one-loop level, the renormalized theoretical mass reads $m^{ren} = m^0 + \delta m$, where δm is the one-loop corrections. This new contribution is in fact divergent due to Ultra-Violet (UV) singularities in loop integrals. δm contains a $1/\epsilon$ pole if we consider dimensional regularization ($D = 4 - 2\epsilon$). Clearly, the physical explanation of this divergence is the non validity of our field theory at large energy since gravity is not incorporated. We then absorb our ignorance into δm and m^0 which are infinite in order to make m^{ren} finite, that is associated to an experimentally measured value. For the electron, $m^{exp} \equiv m^{ren} = m^0 + \delta m = 0.51$ MeV. Thus we need an infinite fine tuning between the bare mass and the loop corrections.

Nevertheless, we may avoid this infinite fine tuning issue if we trigger the scale Λ which bounds the breakdown of our theory. This can be done if we replace our dimensional regularization approach by a more physical one which introduces in the loop integrals the cutoff scale Λ. So let us do that, still considering our example of the electron. The correction to the electron mass, δm_F, induced by photon loop as depicted by Fig. 18(a) is

$$\delta m_F \sim \int^{\Lambda} d^4k \frac{1}{k^3} \sim \Lambda + m_F \ln \frac{\Lambda}{m_F} \ . \tag{3.63}$$

In fact we know that in the limit of zero mass, a new symmetry appears : chiral symmetry. Then the associated transformation $\psi \to \exp(i\alpha\gamma_5)\psi$ prevents mass terms from being generated at loop level. So indeed chiral symmetry is broken but in such a way that this symmetry is restored in the limit where all the fermion masses go to zero. As a consequence, in this limit, we expect the one-loop mass to be zero, i.e the linear divergence of Eq. (3.63) should not be there. Radiative corrections are continuously connected to the chiral sector and consistency in the unbroken limit calls for a purely logarithmic divergence. So $\delta m_F \sim m_F \ln \Lambda/m_F$ and even for large values of Λ, loop correction is of the order of m_F, $\delta m_F \lesssim m_F$, so there is no infinite fine tuning. In that sense, chiral symmetry protects fermion masses.

What about one-loop radiative correction to gauge boson masses? If we denote by m_{loop} the mass of fermions and gauge bosons which propagate in the loops, as shown in Fig. 18(b),(c), we can write the correction as

$$\delta m_G^2 \sim \int^{\Lambda} d^4k \frac{1}{k^2} \sim \Lambda^2 + m_{loop}^2 \ln \frac{\Lambda}{m_{loop}} \ . \tag{3.64}$$

Again there is a symmetry which cancels the divergence, quadratic here. Gauge symmetry, unbroken or spontaneously broken, guarantees that quadratic divergences vanish.

Problems start when we consider radiative corrections to the scalar masses, and for example the Standard Model Higgs boson mass correction δm_H^2. Each one-loop diagram allowed in the Standard Model, as the ones of Fig. 18(d)-(g), gives the same divergent contributions than in the previous case of gauge bosons loop corrections, except there is no particular symmetry which cancels the quadratic divergence, thus they remain and

$$\delta m_H^2 \sim \int^{\Lambda} d^4k \frac{1}{k^2} \sim \Lambda^2 + m_{loop}^2 \ln \frac{\Lambda}{m_{loop}} \tag{3.65}$$

If we set $\Lambda \sim M_P$, the 125 GeV Higgs boson mass becomes much smaller than the quantum correction (in fact as soon as $\Lambda \gtrsim 1$ TeV). As we have seen, this is not an important problem for renormalization theory since it is always possible to have an

infinite fine tuning between the divergence and the bare mass. Nevertheless, this finely-tuned cancellation would have to be repeated order by order in perturbation theory and this feature is commonly assumed to be unnatural.

The hope is to protect naturally small boson masses $m_H^2 \gtrsim \delta m_H^2$ due to a symmetry principle in analogy to gauge symmetry or chiral symmetry. This symmetry which cancels quadratic divergence to scalar masses exists, this is supersymmetry. It exploits the fact that fermion loop diagrams have an opposite sign contribution to the scalar mass compared to the scalar loop diagrams. The one-loop quantum correction to the Higgs mass due to fermion is

$$\delta^{(\mathrm{f})} m_H^2 = \frac{\lambda_F^2}{8\pi^2}\left[-\Lambda^2 + 6m_F^2 \ln\frac{\Lambda}{m_F} - 2m_F^2\right] + \mathcal{O}\left(\frac{1}{\Lambda^2}\right) , \tag{3.66}$$

to be compared to the scalar particle contribution which is

$$\delta^{(\mathrm{s})} m_H^2 = \frac{\lambda_S}{16\pi^2}\left[-\Lambda^2 + 2m_S^2 \ln\left(\frac{\Lambda}{m_S}\right)\right] - \frac{\lambda_S^2}{16\pi^2} v^2 \left[-1 + 2\ln\left(\frac{\Lambda}{m_S}\right)\right] + \mathcal{O}\left(\frac{1}{\Lambda^2}\right) \tag{3.67}$$

Consequently, in a supersymmetric theory with twice more scalars than fermions and with Yukawa couplings satisfying $\lambda_S = -\lambda_F^2$, the Higgs boson mass quadratic divergences vanish. Only remains logarithmic (naturally) small corrections

$$\delta^{(\mathrm{f+s})} m_H^2 = \frac{\lambda_S^2}{4\pi^2}\left[(m_F^2 - m_S^2)\ln\left(\frac{\Lambda}{m_S}\right) + 3m_F^2 \ln\left(\frac{m_S}{m_F}\right)\right] + \mathcal{O}\left(\frac{1}{\Lambda^2}\right) . \tag{3.68}$$

The hierarchy and the naturalness problems are practically solved. In the case of exact supersymmetry, $m_S = m_F$ there is no divergence at all since the logarithmic divergences also cancel.

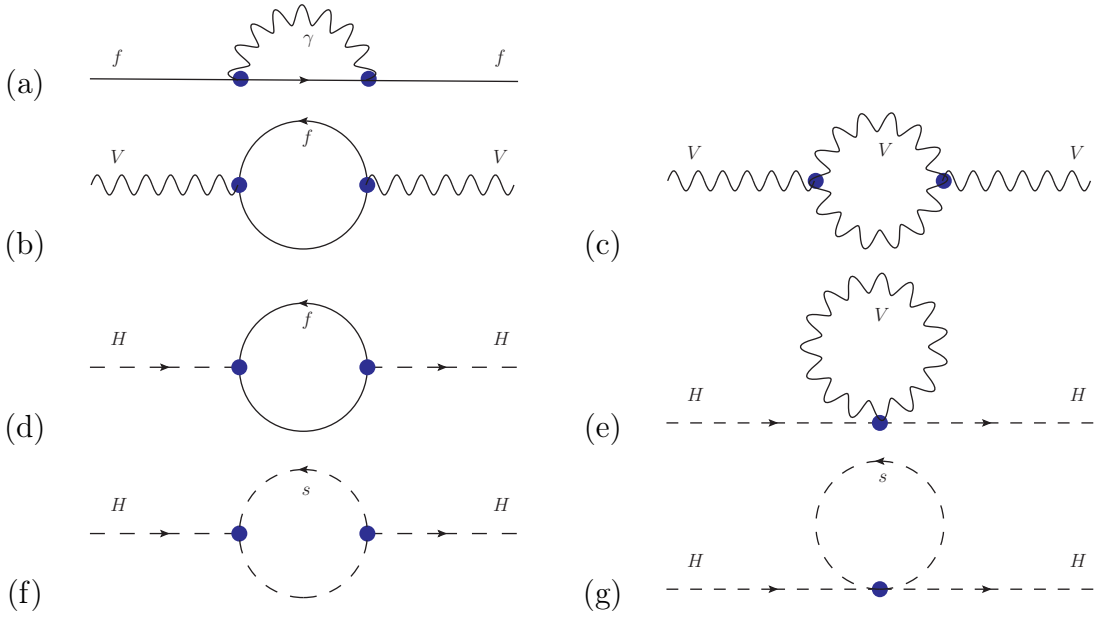

Figure 18: One-loop quantum corrections to fermion, gauge boson and scalar mass.

3.3 The gauge coupling unification

In the Standard Model all the interactions, strong, weak and electromagnetic are described through a symmetry group which introduces a coupling constant. At the beginning of this manuscript, when we introduced the electroweak theory, we have seen that the weak interactions and the electromagnetic interactions are partially unified since the electroweak interactions are described by the gauge group $SU(2)_L \times U(1)_Y$ but we still need two coupling constants. In the paradigm of Grand Unified Theory (GUT), the SM gauge group would be a subset of a higher symmetry (for example SU(5), SO(10) or E(6)) realized at higher energies. In this framework all the SM gauge couplings could converge toward a common value at high energies, this is the gauge coupling unification.

Gauge couplings are renormalized quantities consequently they run with the energy scale. The running proceeds through quantum loop corrections and is described by the Renormalization Group Equations. At the one-loop level, the evolution of the coupling constants $g_{SU(3)_C}$, $g_{SU(2)_L}$ and $g_{U(1)_Y}$ are given by

$$\beta_X \equiv \frac{d}{dt} g_X = \frac{1}{16\pi^2} b_X g_X^3 \tag{3.69}$$

with $t \equiv \ln Q$, Q being the renormalization scale. Historically, the $g_{U(1)_Y}$ coupling is rescaled in order to match with the covariant derivative of the grand unification gauge group $SU(5)$ or $SO(10)$ i.e $g_{U(1)_Y} = \sqrt{5/3} g'$. The b_X coefficients are

$$(b_{U(1)_Y}, b_{SU(2)_L}, b_{SU(3)_C}) = \left(\frac{41}{10}, -\frac{19}{6}, -7\right) . \tag{3.70}$$

It is useful to express the previous equations in terms of $\alpha_X \equiv g_X^2/(4\pi)$

$$\beta_X = \frac{d}{dt} \alpha_X^{-1} = -\frac{b_X}{2\pi} \tag{3.71}$$

In the left panel of Fig.11 we show the running of the SM coupling constants between the weak scale and the Planck scale, and we note that there is no accidental unification of the gauge couplings. However in the Minimal Supersymmetric extension of the Standard Model the larger particle spectrum will induce new quantum loop effects and then modifications of the SM gauge coupling runnings. Within the MSSM the b_X coefficients read

$$(b_{U(1)_Y}, b_{SU(2)_L}, b_{SU(3)_C}) = \left(\frac{33}{5}, 1, -3\right) . \tag{3.72}$$

In the right panel of Fig.11 we show the running of the SM coupling constants between the weak scale and the Planck scale in the framework of the MSSM and they do unify at an energy scale, the GUT scale, of $M_{GUT} \approx 2 \times 10^{16}$ GeV.

In the next part of this thesis we will come back to this Grand Unified Theory paradigm in the context of Non-Thermal-Dark Matter (NETDM) model which has been elaborated during this PhD thesis.

3.4 The dark matter

We should not close the motivation paragraph for supersymmetry without mentioning its dark matter solution. Even if the dark matter subject will be largely covered in the

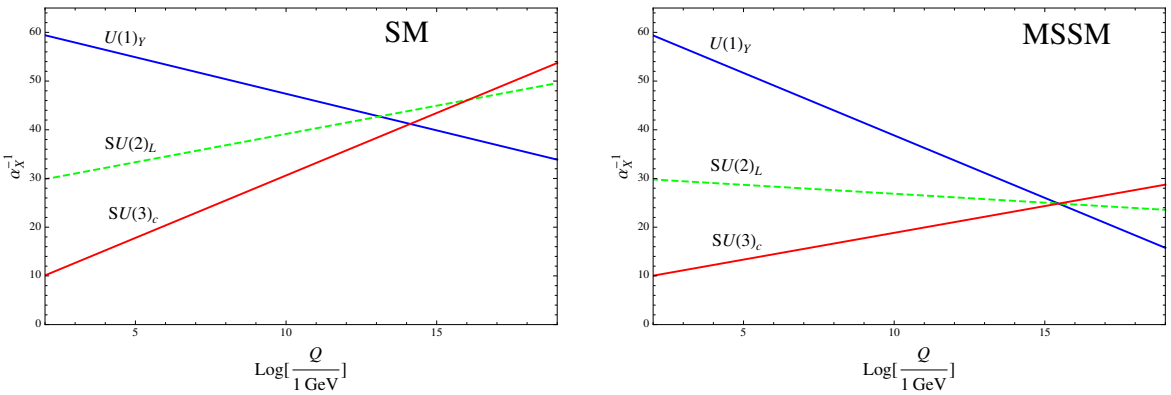

Table 11: Standard Model gauge couplings running from the weak scale up to the Planck scale within the SM (left) and within the MSSM framework (right).

next part, we should advocate here that Supersymmetric Theories offer interesting dark matter candidates. The WMAP satellite measured that the baryonic luminous matter represents only $\sim 5\%$ of the matter of the universe, $\sim 23\%$ being dark matter and the remaining $\sim 72\%$ is what is called the dark energy. This dark matter component of the universe could correspond to a new particle species which is electrically neutral, weakly interacting and stable. Furthermore, in order to be compatible with the formation of the Astrophysical structures as the galaxies, this particle should be relatively massive. In the Minimal Supersymmetric extension of the Standard Model, if one imposes a new conservation law being the R-parity (in order to ensure the proton stability) a natural dark matter candidate arises. It corresponds to the Lightest Supersymmetric Particle or LSP and it is a mixture of the superpartners of the weak bosons and the Higgs bosons, it is called the neutralino. Even if it is the most popular supersymmetric dark matter candidate we should also mention others as the sneutrino and the graviton in models of supergravity.

4 Theoretical structure of a supersymmetric theory

4.1 From symmetries in physics to the Poincaré superalgebra

For a given system, a symmetry is a group of transformations that leaves its Lagrangian invariant. For example in electrodynamics the Dirac Lagrangian

$$\mathcal{L}_D = \bar{\psi}(x)(i\gamma^\mu \partial_\mu - m)\psi(x) \tag{4.73}$$

is invariant under the U(1) global symmetry which acts on the vectorial space composed by the physical states as follow

$$\begin{aligned} \psi(x) \to \psi'(x) &= e^{-i\alpha}\psi(x)\ , & (4.74)\\ \bar{\psi}(x) \to \bar{\psi}'(x) &= e^{i\alpha}\bar{\psi}(x)\ . & (4.75) \end{aligned}$$

Here the global U(1) symmetry does not depend on the time-space, the symmetry is called an internal symmetry. The reason why symmetries are crucial is that each continuous symmetry is associated to a conserved quantity (Noether theorem) and nature follows many of them. Many systems respect rotational and translational symmetry in our apparent three-dimensional space i.e their Lagrangian is invariant under the transformation

$$\vec{x} \to \vec{x}' = R(\vec{\theta}).\vec{x} + \vec{a} \tag{4.76}$$

with $R(\vec{\theta}) \in SO(3)$ and $\vec{a}$ is a translational vector. In quantum physics, a wave function transforms under a spatial transformation R, as

$$\psi'(\vec{x}) = \psi(R\vec{x}) = \mathcal{R}\psi(\vec{x}) \qquad \begin{array}{ccccc} & & \overset{R}{} & & \\ & \vec{x} & \longrightarrow & \vec{x}' & \\ \psi & \downarrow & & \downarrow & \psi \\ & \psi(\vec{x}) & \underset{\mathcal{R}}{\longrightarrow} & \psi(\vec{x}') & \end{array} \tag{4.77}$$

And more explicitly for a particular order of the transformations

$$\psi(\vec{x}) \to \psi'(\vec{x}) = e^{-i\vec{a}.\vec{P}}.e^{-i\vec{\theta}.\vec{J}}.\psi(\vec{x}) \tag{4.78}$$

with $\vec{P}$ and $\vec{J}$ generators respectively of the translations and the rotations which satisfy the commutation relations

$$\begin{aligned} [P_i, P_j] &= 0\ , \\ [J_i, J_j] &= i\epsilon_{ijk}J_k\ , \\ [P_i, J_j] &= i\epsilon_{ijk}P_k\ . & (4.79) \end{aligned}$$

But in fact we know that we can enlarge this last symmetry group. Quantum Field Theory is built on the Poincaré group which consists of mixture of Lorentz transformations and translations defined by

$$x^\mu \to x'^\mu = x^\mu + \omega^{\mu\nu}x_\nu + a^\mu \tag{4.80}$$

where now $x^\mu = (t, \vec{x})$ are the coordinates in the Minkowski space-time. In order to fully define an arbitrary Poincaré transformation we need the following ingredients

$$\left\{ \begin{array}{l} \text{6 Lorentz parameters:} \quad \left\{ \begin{array}{l} \text{- 3 boost parameters} \\ \text{- 3 rotation angles} \end{array} \right\} \text{antisymmetric tensor : } \omega^{\mu\nu} = -\omega^{\nu\mu} \\ \\ \text{4 translation parameters:} \quad a^\mu \end{array} \right\}$$

The Lorentz transformations involve six generators that we write in terms of an antisymmetric tensor $M^{\sigma\rho}$. The translation involves four generators P^ρ, one for each direction. $M^{\sigma\rho}$ is only, the generalization in four-dimensions of the angular momentum $\vec{J}$ and P^ρ is the natural generalization of the classical momentum. Of course, the explicit form of the generators depends on the nature of the field they act on :

$$\begin{aligned} \text{for 0 spin field : } & M^{\rho\sigma} = i(x^\rho \partial^\sigma - x^\sigma \partial^\rho), \qquad P^\rho = i\partial^\rho \ , \\ \text{for 1/2 spin field : } & M^{\rho\sigma} = i(x^\rho \partial^\sigma - x^\sigma \partial^\rho) + \frac{i}{4}\left[\gamma^\rho, \gamma^\sigma\right], P^\rho = i\partial^\rho \ . \end{aligned} \tag{4.81}$$

We can write down the transformation (assuming here a specific ordering) of a field as

$$\Psi(x) \to \Psi'(x) = e^{ia^\rho P_\rho} e^{\frac{i}{2}\omega^{\rho\sigma} M_{\rho\sigma}} \Psi(x) \tag{4.82}$$

The Poincaré algebra is thus defined by the commutation relations between the generators $M^{\rho\sigma}$ and P^ρ and by the metric $g^{\rho\sigma}$ (with the $(+,-,-,-)$ signature)

$$\begin{aligned} [P^\rho, P^\sigma] &= 0 \ , \\ [M^{\mu\nu}, M^{\rho\sigma}] &= -i(g^{\mu\rho} M^{\nu\sigma} + g^{\nu\sigma} M^{\nu\rho} - g^{\nu\sigma} M^{\nu\rho} - g^{\nu\rho} M^{\mu\sigma}) \ , \\ [P^\rho, M^{\nu\sigma}] &= i(g^{\rho\nu} P^\sigma - g^{\rho\sigma} P^\nu) \ . \end{aligned} \tag{4.83}$$

Finally, what have we really done to enlarge our primordial symmetry group to the Poincaré group? In fact, we have increased the number of dimension of our classical three-dimensional vectorial space by introducing a fourth coordinate, the time t. In doing so, we have enlarged the symmetry group of the spatial rotations and translations composed of 6 generators to a symmetry group of 10 generators that take now into account space and time. A natural question appears, could we enlarge this new symmetry group in order to find a more fundamental symmetry group respected by nature? The symmetry can indeed be extended and it is exactly what gauge theories do. For example, in the case of a $SU(N)$ gauge group ($N^2 - 1$ generators noted T^a), we can write a gauge transformation as

$$\psi(x) \to \psi'(x) = e^{i\omega_a T^a} \psi(x) \ . \tag{4.84}$$

So, we can add these new generators to the Poincaré algebra but such an extension is trivial since all the gauge generators commute with the Poincaré algebra generators

$$\begin{aligned} \left[T^a, T^b\right] &= i f^{abc} T^c \ , \\ [T^a, M^{\rho\sigma}] &= 0 \ , \\ [T^a, P^\rho] &= 0 \ . \end{aligned} \tag{4.85}$$

This means that we can write the new extended symmetry group as the extended direct product

$$\text{Extended symmetry group} = \text{Poincaré group} \otimes \text{Gauge group} \tag{4.86}$$

Such extensions are quite limited but not less successful to describe particle interactions. Could we extend the Poincaré symmetry in a non trivial way, such that the added generators do not commute with (i.e mix) with the Poincaré algebra ones? The Coleman-Mandula no-go theorem [163] concludes that the most general Lie algebra of symmetries, in interacting relativistic Quantum Field Theory, contains the Poincaré algebra ($M^{\sigma\rho}$ and P_ρ) in direct product with a finite number of Lorentz scalar operators (such as those of a gauge symmetry). P^ρ, $M^{\rho\sigma}$ and T^a do not change the spin of the state they act on, so they are bosonic type of generators. We can indeed imagine generators, Q_α , which change the spin of the state they act on by $\frac{1}{2}$. These spinors would then introduce supersymmetry transformation which turns a bosonic state into a fermionic state and vice-versa, schematized by

$$Q_\alpha|\text{boson}\rangle = |\text{fermion}\rangle_\alpha, \quad Q_\alpha|\text{fermion}\rangle^\alpha = |\text{boson}\rangle \ . \tag{4.87}$$

These spinors are anticommutating since they follow the Fermi-Dirac statistics. Furthermore it is possible to avoid the Coleman-Mandula theorem by generalizing the notion of a Lie algebra to include algebraic systems which are defined by usual Lie commutators but also anticommutators: these new algebras are called graded Lie algebras or superalgebras. This result constitutes the Haag-Lopuszanski-Sohnius theorem [173]. We can then extend the Poincaré algebra in a non-trivial way assuming that we have one Majorana spinor which respects the following superalgebra

$$\begin{aligned} \{Q_\alpha, \bar{Q}_{\dot\beta}\} &= 2(\sigma^\rho)_{\alpha\dot\beta} P_\rho \ , \\ \{Q_\alpha, Q_\beta\} &= \{\bar{Q}_{\dot\alpha}, \bar{Q}_{\dot\beta}\} = 0 \ , \\ [Q_\alpha, P^\rho] &= 0 \ , \\ [M^{\rho\sigma}, Q_\alpha] &= -i(\sigma^{\rho\sigma})_\alpha{}^\beta Q_\beta \ , \end{aligned} \tag{4.88}$$

with $\sigma^{\sigma\nu} = \frac{1}{4}(\sigma^\mu\bar\sigma^\nu - \sigma^\nu\bar\sigma^\mu)$ and σ^μ the usual Pauli matrices.

We understand here, why supersymmetry is a nice candidate for physics beyond the SM. It is the only way to increase the Poincaré symmetry as known to be respected by nature. This is historically the first motivation for supersymmetry, the solution to the hierarchy problem being a consequence.

In order to study the phenomenology of such theories we need to learn how to build a Lagrangian which is invariant under supersymmetric transformations.

4.2 Superfields in superspace

Let us review what we have done so far. We have added the new supersymmetric generators Q_α and $\bar{Q}_\alpha$ to enlarge the Poincaré algebra. By introducing these new generators we automatically introduce new associate coordinates called Grassmann (anticommuting) variables θ^α and $\bar\theta^{\dot\alpha}$. So before the Poincaré algebra was the symmetry group of the vectorial space composed of vectors that we call fields, and generically write $\psi(x)$ with $x = x^\mu$ quadri-vector. Now the super Poincaré algebra is the symmetry group of the vectorial superspace of coordinate $(x^\mu, \theta^\alpha, \bar\theta^{\dot\alpha})$ populated with vectors that we call superfields, and that we generically write $\Phi(x, \theta, \bar\theta)$.

In order to build a supersymmetric invariant Lagrangian, we first need to find a representation of the generators. Schematically $\{Q, \bar{Q}\} \sim P$ i.e Q^2 is a translation in

space-time and thus it might be possible to express Q in terms of differential operators since $P_\mu = i\partial_\mu$. To make things clear, let us consider a pure supersymmetric transformation

$$G(0,\zeta,\bar{\zeta}) \equiv e^{i(\zeta^\alpha Q_{\dot{\alpha}} + \bar{\zeta}_{\dot{\alpha}}\bar{Q}\alpha)} \tag{4.89}$$

If we combine two of such transformations, we obtain, after using the Baker-Campbell-Hausdorff formula

$$G(0,\zeta,\bar{\zeta})G(0,\theta,\bar{\theta}) = G(i\zeta\sigma^\mu\bar{\theta} - i\theta\sigma^\mu\bar{\zeta}, \zeta+\theta, \bar{\zeta}+\bar{\theta}) \tag{4.90}$$

This last supersymmetric transformation transforms the superspace as

$$(x,\theta,\bar{\theta}) \rightarrow (x^\mu + i\zeta\sigma^\mu\bar{\theta} - i\theta\sigma^\mu\bar{\zeta}, \zeta+\theta, \bar{\zeta}+\bar{\theta}) \tag{4.91}$$

and transforms a vector of this superspace, a superfield, as

$$\begin{aligned} \Phi(x,\theta,\bar{\theta}) &\rightarrow e^{-i(\zeta^\alpha \mathcal{Q}_\alpha + \bar{\zeta}_{\dot{\alpha}}\bar{\mathcal{Q}}^{\dot{\alpha}})}\Phi(x,\theta,\bar{\theta}) \\ &= \Phi(x^\mu + i\zeta\sigma^\mu\bar{\theta} - i\theta\sigma^\mu\bar{\zeta}, \zeta+\theta, \bar{\zeta}+\bar{\theta}) \end{aligned} \tag{4.92}$$

if we make a Taylor expansion around $(x,\theta,\bar{\theta})$

$$\Phi + (i\zeta\sigma^\mu\bar{\theta} - i\theta\sigma^\mu\bar{\zeta})\partial_\mu\Phi + \zeta^\alpha\partial_\alpha\Phi - \bar{\zeta}_{\dot{\alpha}}\bar{\partial}^{\dot{\alpha}}\Phi = \Phi - i(\zeta^\alpha\mathcal{Q}_\alpha + \bar{\zeta}_{\dot{\alpha}}\bar{\mathcal{Q}}\dot{\alpha})\Phi \tag{4.93}$$

We obtain by identification of the two sides what we were looking for, i.e differential expressions of the fermionic charges

$$\begin{aligned} \mathcal{Q}_\alpha &= i\partial_\alpha - \sigma^\mu_{\alpha\dot{\alpha}}\bar{\theta}^{\dot{\alpha}}\partial_\mu \ , \\ \bar{\mathcal{Q}}_{\dot{\alpha}} &= -i\bar{\partial}_{\dot{\alpha}} + \theta^\alpha\sigma^\mu_{\alpha\dot{\alpha}}\partial_\mu \ . \end{aligned} \tag{4.94}$$

We can expand the most general superfield $\Phi(x,\theta,\bar{\theta})$ in θ and $\bar{\theta}$

$$\begin{aligned} \Phi(x,\theta,\bar{\theta}) &= C(x) + \theta\psi(x) + \bar{\theta}\bar{\psi}'(x) + (\theta\theta)F(x) + (\bar{\theta}\bar{\theta})F'(x) + \theta\sigma^\mu\bar{\theta}v_\mu(x) \\ &\quad + (\theta\theta)\bar{\theta}\bar{\lambda}'(x) + (\bar{\theta}\bar{\theta})\theta\lambda(x) + (\theta\theta)(\bar{\theta}\bar{\theta})D(x) \ . \end{aligned} \tag{4.95}$$

Notice that any product of θ,$\bar{\theta}$ which contains more than three $\theta/\bar{\theta}$ terms vanishes because of Grassmann variable properties ans as a consequence the expansion stops at finite order. We have now everything to compute superfield transformation under the previously defined supersymmetric operation

$$\begin{aligned} \delta\Phi &= \Phi(i\zeta\sigma^\mu\bar{\theta} - i\theta\sigma^\mu\bar{\zeta}, \zeta+, \theta, \bar{\zeta}+\bar{\theta}) - \Phi(0,\theta,\bar{\theta}) \ , \\ \delta\Phi &= -i(\zeta^\alpha\mathcal{Q}_\alpha + \bar{\zeta}_{\dot{\alpha}}\bar{\mathcal{Q}}^{\dot{\alpha}})\Phi \ . \end{aligned} \tag{4.96}$$

As a remark, the newly introduced anticommuting numbers ζ,$\bar{\zeta}$ (or θ,$\bar{\theta}$) play an important role since they allow to express the supersymmetric algebra entirely in terms of commutators, we can re-write non commuting part of Eq. (4.88) as

$$\begin{aligned} \left[\zeta^\alpha Q_\alpha, \bar{\zeta}^{\dot{\beta}}\bar{Q}_{\dot{\beta}}\right] &= 2\zeta^\alpha(\sigma^\rho)_{\alpha\dot{\beta}}\bar{\zeta}^{\dot{\beta}}P_\rho \\ \left[\zeta^\alpha Q_\alpha, \zeta^\beta Q_\beta\right] &= \left[\bar{\zeta}^{\dot{\alpha}}\bar{Q}_{\dot{\alpha}}, \bar{\zeta}^{\dot{\beta}}\bar{Q}_{\dot{\beta}}\right] = 0 \end{aligned} \tag{4.97}$$

Or in field theory, global continuous symmetry are generated by such transformation

$$\delta\Phi = \left[\zeta^\alpha \mathcal{Q}_\alpha + \bar{\zeta}_{\dot{\alpha}}\bar{\mathcal{Q}}^{\dot{\alpha}}, \Phi\right] \tag{4.98}$$

and operators acting on the Hilbert space are linked to the differential operators in the Heisenberg picture as

$$\left[\zeta^\alpha \mathcal{Q}_\alpha + \bar{\zeta}_{\dot{\alpha}}\bar{\mathcal{Q}}^{\dot{\alpha}}, \Phi\right] = -i(\zeta^\alpha \mathcal{Q}_\alpha + \bar{\zeta}_{\dot{\alpha}}\bar{\mathcal{Q}}^{\dot{\alpha}})\Phi \tag{4.99}$$

which would lead directly to the result of Eq. 4.96.

Coming back to our superfield, we see that the most general superfield contains :

- Four Weyl spinors : ψ, $\bar{\psi}'$, λ and $\bar{\lambda}'$,
- Four scalar fields: C, F, F' and D,
- One vector field : v.

We will not use this supermultiplet as an elementary piece to build a supersymmetric Lagrangian. Smaller particle content superfields might be used as chiral and vector superfields.

4.2.1 Chiral superfieds

A left-handed chiral superfield χ satisfies by definition the condition $\bar{D}_{\dot{\alpha}}\chi = 0$, defining the covariant derivative as

$$\bar{D}_{\dot{\alpha}} \equiv \bar{\partial}_{\dot{\alpha}} - i\theta^\alpha \sigma^\mu_{\alpha\dot{\alpha}}\partial_\mu \ . \tag{4.100}$$

The most general left-handed chiral superfield can be expanded in function of x, θ and $\bar{\theta}$ as

$$\begin{aligned}\chi(x,\theta,\bar{\theta}) &= \varphi(x) + \sqrt{2}\theta\psi(x) - i\theta\sigma^\mu\bar{\theta}\partial_\mu\varphi(x) + \frac{i}{\sqrt{2}}\theta\theta\partial_\mu\psi(x)\sigma^\mu\bar{\theta} \\ &\quad -\frac{1}{4}\theta\theta\bar{\theta}\bar{\theta}\partial^\mu\partial_\mu\varphi(x) - \theta\theta F(x) \ .\end{aligned} \tag{4.101}$$

Generically, it contains :

- One Weyl spinor : ψ
- Two scalar fields: φ, F

The spinor ψ will be the left-handed quarks and leptons of the SM, and the new scalar field φ will be their supersymmetric partners, the squarks and sleptons. We will see later that the F scalar field, which has an unusual mass dimension of two, is not physical.

We can explicit the transformations of these new fields

$$\begin{aligned}\delta\varphi &= \sqrt{2}\zeta\psi \ , \\ \delta\psi_\alpha &= -\sqrt{2}F\zeta_\alpha - i\sqrt{2}\sigma^\mu_{\alpha\dot{\alpha}}\bar{\zeta}^{\dot{\alpha}}\partial_\mu\varphi \ , \\ \delta F &= -i\sqrt{2}\partial_\mu\psi\sigma^\mu\bar{\zeta} = \partial_\mu(-i\sqrt{2}\psi\sigma^\mu\bar{\zeta}) \ .\end{aligned} \tag{4.102}$$

Without any surprises, the variation of the bosonic (fermionic) fields are proportional to the fermionic (bosonic) fields. The scalar field F has the particularity to be proportional to a total derivative. Similarly, we can obtain right-handed chiral field as the hermitian conjugate of the left-handed chiral field.

4.2.2 Vector superfields

In order to describe the gauge bosons of the SM, we also introduce the vector superfield V. By definition it satisfies the supersymmetric invariant constraint

$$V(x,\theta,\bar{\theta}) = V^{\dagger}(x,\theta,\bar{\theta}) \ . \tag{4.103}$$

We can expand it in terms of several constituent fields

$$\begin{aligned} V(x,\theta,\bar{\theta}) &= c(x) + i\theta\kappa(x) - i\bar{\theta}\bar{\kappa}(x) + \theta\sigma^{\mu}\bar{\theta}v_{\mu}(x) + i(\theta\theta)N(x) - i\bar{\theta}\bar{\theta}N^{\dagger}(x) \\ &+ i\theta\theta\bar{\theta}(\bar{\lambda}(x) + \frac{i}{2}\partial_{\mu}\kappa(x)\sigma^{\mu}) - i\bar{\theta}\bar{\theta}\theta(\lambda(x) - \frac{i}{2}\sigma^{\mu}\partial_{\mu}\bar{\kappa}(x)) \\ &+ \frac{1}{2}\theta\theta\bar{\theta}\bar{\theta}(D(x) - \frac{1}{2}\partial^{\mu}\partial_{\mu}c(x)) \end{aligned} \tag{4.104}$$

v is the vector field that we were looking for and represents gauge bosons in supersymmetric prolongation of the SM. We also have scalar fields, c, N and D and fermion fields κ and λ but only κ is physical.

As in the case of the left-handed chiral superfield, the D-term has a total derivative under supersymmetric transformation

$$\delta D = \zeta\sigma^{\mu}\partial_{\mu}\bar{\lambda}(x) + \partial_{\mu}\lambda(x)\sigma^{\mu}\bar{\zeta} = \partial_{\mu}(\zeta\sigma^{\mu}\bar{\lambda}(x) + \lambda(x)\sigma^{\mu}\bar{\zeta}) \ . \tag{4.105}$$

We will explain and use later this important feature.

4.2.3 Particles in superfields

Now, the classical particle physics fields are components of a superfield. Because it contains too much component fields, we have constructed three different superfields that verify three different constraint relations. We have obtained the left-handed chiral superfield, the right-handed chiral superfield and the vector superfield.

If we want to expand, accordingly to supersymmetry, the Quantum Electro Dynamic theory, we should promote the left (right)-handed electron field into a left (right)-handed chiral superfield. By doing so, we automatically introduce the scalar partners called selectrons. We promote also the photon field into a vector superfield which introduces its fermionic partners, the photinos. A priori, we would need the following fields to write a supersymmetric Lagrangian

$$\begin{aligned} \text{Left-handed fermions:} \quad \psi_f \in \chi_f &= (\varphi_f, \psi_f) \\ \text{Right-handed fermions:} \quad \bar{\psi}_f \in \chi_f^{\dagger} &= (\varphi_f^{\dagger}, \bar{\psi}_f) \\ \text{Gauge bosons:} \quad v^{\mu} \in V &= (v^{\mu}, \lambda, \bar{\lambda}) \\ \text{Higgs bosons:} \quad \varphi_h \in \chi_h &= (\varphi_h, \psi_h) \\ \varphi_h^{\dagger} \in \chi_h^{\dagger} &= (\varphi_h^{\dagger}, \bar{\psi}_h) \end{aligned}$$

As a remark, $N = 1$ supersymmetric theories keep the left-handed and the right-handed fermions in separate superfields. For $N > 1$ theories the superfields embed left-handed and right-handed fermions in a same supermultiplet: this is, a priori, a difficulty to solve since these fields transforms differently under the gauge transformation of $SU(2)_L$. Obviously it is still possible to break such realization in order to recover $N = 1$ supersymmetry at lower energy scale. This tells us why $N = 1$ supersymmetric scenario are preferentially used in phenomenology.

We now derive a Lagrangian which is invariant under supersymmetric transformations.

4.3 A simple supersymmetric Lagrangian : The Wess-Zumino model

As we have shown before, the F-term of a chiral superfield and the D-term of a vector superfield transform under supersymmetry as themselves plus a total derivative. Obviously the action is not changed if the Lagrangian switches from a total derivative. Thus using only D and F-terms we would be sure to have a supersymmetric invariant theory.

We will discuss how to build kinetic and interacting terms and build a Lagrangian invariant under supersymmetric transformations with only one chiral superfield, thus one scalar, one fermion and its conjugate field.

Kinetic terms for fermion and scalar fields

We first need terms like $(\partial_\mu\varphi)(\partial^\mu\varphi)^\dagger$ which can only come from combinations of $\chi\chi^\dagger$ term. This last is clearly a vector superfield since $(\chi\chi^\dagger)^\dagger = \chi\chi^\dagger$. The kinetic term we are looking for is in the D-term of $\chi\chi^\dagger$, we get

$$\begin{aligned}\mathcal{L}_{kin} &= \int d^2\theta d^2\bar{\theta}\chi_i\chi_i^\dagger \equiv \left[\chi_i\chi_i^\dagger\right]_{\theta\theta\bar{\theta}\bar{\theta}} \\ &= F^\dagger F + (\partial_\mu\varphi)(\partial^\mu\varphi)^\dagger + \frac{i}{2}\psi\sigma^\mu(\partial_\mu\bar{\psi}) - \frac{i}{2}(\partial_\mu\psi)\sigma^\mu\bar{\psi}\ . \end{aligned} \tag{4.106}$$

As we were expecting it, the D-term contains the propagating term of both the scalar field φ and the fermionic field ψ.

Interacting terms between fermion and scalar fields

An important remark is that a product of left(right)-handed chiral superfield is a left(right)-handed chiral superfield. On that basis, we introduce interactions between component fields of chiral superfields through the superpotential which is defined as

$$W(\chi_i) \equiv a_i\chi_i + \frac{1}{2}m_{ij}\chi_i\chi_j + \frac{1}{3!}y_{ilk}\chi_i\chi_j\chi_k \tag{4.107}$$

with a_i,m_{ij} and y_{ilk} some constants. The F-terms of this superpoptential lead to the interacting lagrangian

$$\mathcal{L}_{int} = \int d^2\theta W(\chi_i) + \int d^2\bar{\theta}W^\dagger(\chi_i^\dagger) \equiv [W(\chi_i)]_{\theta\theta} + \left[W^\dagger(\chi_i^\dagger)\right]_{\bar{\theta}\bar{\theta}}\ . \tag{4.108}$$

We should notice that we cannot add to the superpotential terms with higher power of χ in order to keep renormalizability. In our example (the Wess-Zumino model) of a single chiral superfield, the interacting Lagrangian reads

$$\mathcal{L}_{int} = -aF - m\varphi F - \frac{m}{2}\psi\psi - \frac{y}{2}\varphi\varphi F - \frac{y}{2}\varphi(\psi\psi) + h.c. \tag{4.109}$$

Previously we have stated that the F field was not physical, we notice here that we do not have any kinetic term for this field. Using its Euler-Lagrange equation we can then eliminate this auxiliary field.

Finally, we can express the total Lagrangian as

$$\begin{aligned}\mathcal{L} &= (\partial_\mu\varphi)(\partial^\mu\varphi)^\dagger + \frac{i}{2}\psi\sigma^\mu(\partial_\mu\bar{\psi}) - \frac{i}{2}(\partial_\mu\psi)\sigma^\mu\bar{\psi} \\ &\quad -|m|^2\varphi\varphi^\dagger - \frac{|y|^2}{4}\varphi\varphi\varphi^\dagger\varphi^\dagger - (\frac{m}{2}\psi\psi + \frac{m^*y}{2}\varphi\varphi\bar{\varphi} + \frac{y}{2}\varphi\psi\psi + h.c)\end{aligned} \tag{4.110}$$

and also in function of the superpotential which fixes all the masses (notice that scalar and fermion fields share the same mass) and all the interactions

$$\begin{aligned}\mathcal{L} &= (\partial_\mu\varphi)(\partial^\mu\varphi)^\dagger + \frac{i}{2}\psi\sigma^\mu(\partial_\mu\bar{\psi}) - \frac{i}{2}(\partial_\mu\psi)\sigma^\mu\bar{\psi} \\ &\quad -\Big|\frac{\partial W(\varphi)}{\partial\varphi}\Big|^2 - \frac{\partial^2 W(\varphi)}{\partial\varphi^2}\psi\psi - \frac{\partial^2 W^\dagger(\varphi)}{\partial\varphi^{\dagger 2}}\bar{\psi}\bar{\psi}\,.\end{aligned} \tag{4.111}$$

4.4 Supersymmetric gauge theories

Now that we have a supersymmetric description of matter fields we should generalize the concept of gauge fields. As we have seen before, in order to include vector bosons we will have to introduce vector superfields.

We first study a global $U(1)$ symmetry and remark that the kinetic term of the Wess-Zumino Lagrangian, $\left[\chi_i\chi_i^\dagger\right]_{\theta\theta\bar{\theta}\bar{\theta}}$, studied previously is invariant under a global transformation defined by $\chi \to \chi' = e^{-i\Lambda}\chi$, with Λ a real constant. This asset does not remain correct if Λ depends on the coordinates of the superspace i.e the transformation is local. In usual field theory it is possible to restore local gauge invariance by replacing partial derivatives with covariant derivatives involving gauge fields. In our supersymmetric approach we proceed in a similar way. If we introduce a vector superfield which transforms under the gauge transformation as

$$e^V \to e^{-i\Lambda^\dagger(x)}e^V e^{i\Lambda(x)} \tag{4.112}$$

then the term $\chi^\dagger e^V\chi$ is locally gauge invariant. Finally we simply need to replace our global invariant term, $\left[\chi_i\chi_i^\dagger\right]_{\theta\theta\bar{\theta}\bar{\theta}}$, by $\left[\chi_i e^V\chi_i^\dagger\right]_{\theta\theta\bar{\theta}\bar{\theta}}$ to impose local gauge invariance in addition to supersymmetry.

The last thing we should perform is to introduce the dynamics of the vector superfields. In a specific choice of gauge, which is the generalization of the unitarity gauge and is called the Wess-Zumino gauge, the vector superfield reads

$$V = \theta\sigma^\mu\bar{\theta}v_\mu(x) + i(\theta\theta)\bar{\theta}\bar{\lambda}(x) - i(\bar{\theta}\bar{\theta})\theta\lambda(x) + \frac{1}{2}(\theta\theta)(\bar{\theta}\bar{\theta})D(x)\,. \tag{4.113}$$

In this gauge, the physical fields remain: the gauge field v and the fermionic field (called gaugino) λ. The D-term, D, is the only non physical field which is still present. The equivalent of the standard field strength tensor $v_{\mu\nu} = \partial_\mu v_\nu - \partial_\nu v_\mu$ is defined (in the abelian gauge theory case) through the following left-handed and right-handed chiral superfields

$$\begin{aligned} W_\alpha &\equiv -\frac{1}{4}(\bar{D}_{\dot{\alpha}}\bar{D}^{\dot{\alpha}})D_\alpha V \\ \bar{W}_{\dot{\alpha}} &\equiv -\frac{1}{4}(D_\alpha D^\alpha)\bar{D}_{\dot{\alpha}} V \ . \end{aligned} \tag{4.114}$$

As seen before, the F-terms of $W^\alpha W_\alpha$ and $\bar{W}^{\dot{\alpha}}\bar{W}_{\dot{\alpha}}$ are supersymmetric. We can show that they contain the kinetic terms of the vector fields and the fermion fields that we were looking for

$$\begin{aligned} \mathcal{L} &= \frac{1}{4}\left(W^\alpha W_\alpha\Big|_{\theta\theta} + \bar{W}^{\dot{\alpha}}\bar{W}_{\dot{\alpha}}\Big|_{\bar{\theta}\bar{\theta}}\right) \\ &= \frac{1}{2}D^2 - \frac{i}{2}(\partial_\mu\lambda)\sigma^\mu\bar{\lambda} + \frac{i}{2}\lambda\sigma^\mu(\partial_\mu\bar{\lambda}) - \frac{1}{4}v^{\mu\nu}v_{\mu\nu} \ . \end{aligned} \tag{4.115}$$

As in the chiral case, the auxiliary field D can be eliminated through its equation of motion and contributes to the scalar potential without altering the definite positive asset of the last one.

4.5 Complete supersymmetric Lagrangian

We now have everything to build the most general (renormalizable) supersymmetric Lagrangian which is invariant under a gauge group defined by $\left[T^\alpha, T^\beta\right] = if^{\alpha\beta\gamma}T^\gamma$. Notice that up to now, we have worked with an abelian gauge group, but the generalization to an non abelian group is straightforward. In all generality, we can write

$$\begin{aligned} \mathcal{L} &= \frac{1}{4}([W^\alpha W_\alpha]_{\theta\theta} + \left[\bar{W}^\alpha\bar{W}_\alpha\right]_{\bar{\theta}\bar{\theta}}) \\ &\quad + \left[\chi_i^\dagger(e^{2gV})_{ij}\chi_j\right]_{\theta\theta\bar{\theta}\bar{\theta}} \\ &\quad + [W(\chi_i)]_{\theta\theta} + \left[W^\dagger(\chi_i^\dagger)\right]_{\bar{\theta}\bar{\theta}} \ . \end{aligned} \tag{4.116}$$

We can also express this Lagrangian in terms of the component fields of the chiral superfields $\chi_i = (\varphi_i, \psi_i)$ and the vector superfields $V_\alpha = (v_\alpha, \lambda_\alpha)$

$$\begin{aligned} \mathcal{L} &= -\frac{1}{4}v_{\alpha,\mu\nu}v_\alpha^{\mu\nu} + \left[\frac{i}{2}\lambda_\alpha\sigma^\mu(D_\mu\bar{\lambda}_\alpha) + h.c.\right] \\ &\quad + (D_\mu\varphi_i)^\dagger(D^\mu\varphi_i) + \left[\frac{i}{2}\psi_i\sigma^\mu(D_\mu\bar{\psi}_i) + h.c.\right] - \left[\sqrt{2}ig\bar{\psi}_i\bar{\lambda}_\alpha T_{\alpha,ij}\varphi_j - h.c.\right] \\ &\quad - \left[\frac{1}{2}\frac{\partial^2 W(\varphi_i)}{\partial\varphi_i\partial\varphi_j}\psi_i\psi_j - h.c.\right] - V(\varphi_i, \varphi_j^\dagger) \end{aligned} \tag{4.117}$$

with the most general superpotential

$$W(\varphi_i) = a_i\varphi_i + \frac{1}{2}m_{ij}\varphi_i\varphi_j + \frac{1}{3!}y_{ijk}\varphi_i\varphi_j\varphi_k \tag{4.118}$$

with a_i, m_{ij} and y_{ijk} determined by the gauge invariance. The scalar potential (for completeness we have included the Fayet-Iliopoulos contributions η_α) reads

$$V(\varphi_i, \varphi_j^\dagger) = F_i^\dagger F_i + \frac{1}{2}(D_\alpha)^2 = \sum_i \left| \frac{\partial W(\varphi_i)}{\partial \varphi_i} \right|^2 + \frac{1}{2} \sum_\alpha \left(g \varphi_i^\dagger T_{\alpha,ij} \varphi_j + \eta_\alpha \right)^2 \tag{4.119}$$

and the covariant derivatives are

$$\begin{aligned} D_\mu \lambda_\alpha &= \partial_\mu \lambda_\alpha - igf^{\alpha\beta\gamma} v_{\beta,\mu} \lambda_\gamma \ , \\ D_\mu \varphi_i &= \partial_\mu \varphi_i + igv_{\alpha,\mu} T_{\alpha,ij} \varphi_j \ , \\ D_\mu \psi_i &= \partial_\mu \psi_i + igv_{\alpha,\mu} T_{\alpha,ij} \psi_j \ . \end{aligned} \tag{4.120}$$

We should keep in mind the key role played by the superpotential. Indeed it controls the shape of the scalar potential which is of prime interest when we study the spontaneous electroweak symmetry breaking.

4.6 Supersymmetry breaking

We just have seen that in case of exact supersymmetry, all the physical fields of a given superfield have the same mass. Thus the newly introduced superpartners have the same mass than their corresponding Standard Model particles. Since experimentally it has not been observed accessible superpartners such as the selectron (scalar superpartner of the electron) this means that if supersymmetry is realized in nature, it is broken. We will then study how to break supersymmetry in order to give a larger mass to the superpartners, which would explain why we do not observe them.

4.6.1 Spontaneous supersymmetry breaking

In the Standard Model we already encountered this kind of issue. Indeed gauge symmetries mean that associated vector bosons are massless which is experimentally not the case. As we have already seen, this inconsistency is solved by the spontaneous electroweak symmetry breaking meaning that the vacuum will stop to be invariant under gauge symmetry even if the theory is still gauge invariant. Consequently, the gauge bosons get their mass and "gauge symmetry is preserve". One would also expect that the supersymmetry is spontaneously broken, i.e at one energy scale, only the ground state stops to be invariant under supersymmetry. If we look at the Hamiltonian associated to a supersymmetric algebra

$$H = \frac{1}{4}(Q_\alpha \bar{Q}_{\dot{\alpha}} + \bar{Q}_{\dot{\alpha}} Q_\alpha) \tag{4.121}$$

we realize that this operator is positive definite i.e for any state Ψ, $\langle \Psi | H | \Psi \rangle \geq 0$. Therefore, any state $|0\rangle$ which satisfies $\langle 0|H|0\rangle = 0$ is necessarily a global vacuum and satisfies $Q_\alpha |0\rangle = \bar{Q}_{\dot{\alpha}} |0\rangle = 0$, meaning the state is supersymmetric. Reciprocally, if supersymmetry is exact, the vacuum $|0\rangle$ is invariant under supersymmetry which implies $Q_\alpha |0\rangle = \bar{Q}_{\dot{\alpha}} |0\rangle = 0$ and then $\langle 0|H|0\rangle = 0$. Now, if we spontaneously break supersymmetry the vacuum must have a non-vanishing energy $Q_\alpha |0\rangle \neq 0 \Leftrightarrow \langle 0|H|0\rangle > 0$, which means that if we neglect space-time dependent effects and fermion condensates,

$\langle 0|H|0\rangle = \langle 0|V|0\rangle > 0$, where $V(\varphi_i, \varphi_j^\dagger) = F_i^\dagger F_i + \frac{1}{2}(D_\alpha)^2$ is the scalar potential that we have previously obtained. In conclusion, spontaneous supersymmetry breaking can only occur if all the F-terms and all the D-terms do not vanish simultaneously. A breaking through F-terms is called the O'Raifeartaigh mechanism [174]. A breaking through D-terms is called the Fayet-Iliopoulos mechanism [175]. Only F-terms can spontaneously break non-abelian gauge supersymmetric theories.

4.6.2 The Goldstone fermions problem and the supertrace constraint

We have just seen that in order to spontaneously break supersymmetry we need to break fermionic generators ($Q_\alpha|0\rangle \neq 0$), so in comparison with the Standard Higgs mechanism one should expect the presence of Goldstone which are fermions. Indeed when scalars get a non vanishing value in the vacuum, we can derive the mass matrix of the fermions in the basis $(\psi_i, i\sqrt{2}\lambda_\alpha)$ looking at the fermions couplings

$$\begin{aligned}
&\sqrt{2}ig\langle\varphi_i^*\rangle T_{\alpha,ij}\psi_j\lambda_\alpha - \frac{1}{2}\left.\frac{\partial^2 W}{\partial\varphi_i\partial\varphi_j}\right|_{\langle\varphi_k\rangle}\psi_i\psi_j + h.c. \\
&= -\frac{1}{2}\begin{pmatrix} \psi_i & i\sqrt{2}\lambda_\alpha \end{pmatrix}\begin{pmatrix} \left.\frac{\partial^2 W}{\partial\varphi_i\partial\varphi_j}\right|_{\langle\varphi_k\rangle} & -g\langle\varphi_j^*\rangle T_{\alpha,ji} \\ -g\langle\varphi_i^*\rangle T_{\alpha,ij} & 0 \end{pmatrix}\begin{pmatrix} \psi_j \\ i\sqrt{2}\lambda_\alpha \end{pmatrix} + h.c
\end{aligned} \tag{4.122}$$

However this fermion mass matrix also appears when we express the minimization condition for the scalar potential

$$\frac{\partial V}{\partial\varphi_i} = \left.\frac{\partial^2 W}{\partial\varphi_i\partial\varphi_j}\right|_{\langle\varphi_k\rangle} F^j - g\langle\varphi_j^*\rangle T_{\alpha,ji} D_\alpha = 0\,. \tag{4.123}$$

Adding the fact that the superpotential is gauge invariant ($F_j\left[g\langle\varphi_i^*\rangle T_{\alpha,ij}\right] = 0$) we get the condition

$$\begin{pmatrix} \left.\frac{\partial^2 W}{\partial\varphi_i\partial\varphi_j}\right|_{\langle\varphi_k\rangle} & -g\langle\varphi_j^*\rangle T_{\alpha,ji} \\ -g\langle\varphi_i^*\rangle T_{\alpha,ij} & 0 \end{pmatrix}\begin{pmatrix} F^j \\ D_\alpha \end{pmatrix} = \begin{pmatrix} 0 \\ 0 \end{pmatrix}\,. \tag{4.124}$$

As a matter of fact, if supersymmetry is spontaneously broken, $(F_i, D_\alpha) \neq (0,0)$, then the fermion mass matrix has a vanishing eigenvalue, and the corresponding state, $\psi_G = \langle F_i\rangle\psi_i - \frac{i}{\sqrt{2}}\lambda_\alpha$ is the Goldstone fermion (also called Goldstino), supersymmetric version of the Goldstone boson. This massless fermion, if physical, would be a huge problem. A possible solution would be to gauge supersymmetry, as done in supergravity. Nevertheless these theories which incorporate gravity are not renormalizable.

It also exists another strong constraint which disfavour spontaneously broken supersymmetry. If we inspect the traces of the scalar, fermion and vector squared matrices one can deduce the supertrace sum-rule formula

$$\mathrm{sTr}\left[\mathcal{M}^2\right] \equiv \mathrm{Tr}\left[\mathcal{M}_0^2\right] - 2\mathrm{Tr}\left[\mathcal{M}_{1/2}^2\right] + 3\mathrm{Tr}\left[\mathcal{M}_1^2\right] = -2g^2\mathrm{Tr}(T_\alpha)\langle D^\alpha\rangle \tag{4.125}$$

with the squared mass matrices defined by the following expressions

$$\begin{aligned}
\mathcal{L} &= -\frac{1}{2}\left[\begin{pmatrix}\varphi_i & \varphi_j^*\end{pmatrix}\mathcal{M}_0^2\begin{pmatrix}\varphi_k^*\\ \varphi_l\end{pmatrix}+\begin{pmatrix}\psi_i & \lambda_\alpha\end{pmatrix}\mathcal{M}_{1/2}^2\begin{pmatrix}\psi_k\\ \lambda_\alpha\end{pmatrix}+v_{\alpha\mu}\mathcal{M}_1^{2,\alpha\beta}v_\beta^\mu\right] ,\\
\mathcal{M}_0^2 &= \left.\begin{pmatrix}\frac{\partial^2 V}{\partial\varphi_i\partial\varphi_k^*} & \frac{\partial^2 V}{\partial\varphi_i\partial\varphi_l}\\ \frac{\partial^2 V}{\partial\varphi_j^*\partial\varphi_k^*} & \frac{\partial^2 V}{\partial\varphi_j^*\partial\varphi_l}\end{pmatrix}\right|_{\langle\varphi_m\rangle} ,\\
\mathcal{M}_{1/2}^2 &= \left.\begin{pmatrix}\frac{\partial^2 W}{\partial\varphi_i\partial\varphi_j} & i\sqrt{2}\frac{\partial D_\beta}{\partial\varphi_i}\\ i\sqrt{2}\frac{\partial D_\alpha}{\partial\varphi_j} & 0\end{pmatrix}\right|_{\langle\varphi_m\rangle} ,\\
\mathcal{M}_1^{2,\alpha\beta} &= 2g^2(\varphi^\dagger T^\alpha)_i(T^\beta\varphi)_i\big|_{\langle\varphi_m\rangle} .
\end{aligned} \tag{4.126}$$

This sum-rule imposes that some superparticles are still unacceptably light, therefore we conclude that it is not possible to break supersymmetry directly in the visible sector (supposed to be a supersymmetric standard model). Generally, supersymmetry breaking is assumed to occur at high energy in a hidden sector which couples to the visible sector through messengers. The breaking is then mediated to the standard sector by effective soft-terms at some (TeV ?) scale which affect the low energy theory through loop effects.

4.6.3 Mediation of supersymmetry breaking

In the following we will shortly review the most popular mechanisms used to break supersymmetry in a hidden sector as Gravity Mediated Supersymmetry Breaking, Gauge Mediated Supersymmetry Breaking and Anomaly Mediation Supersymmetry Breaking.

Gravity Mediation

When gravitational effects mediate the breaking of supersymmetry, we deal with Gravity Mediation Supersymmetry Breaking. The hidden sector will be described by a gauge singlet (gravitational) supermultiplet (X, ψ_X, F_X) which will trigger the breaking, and a multiplet which contains the spin 2 graviton together with the spin 3/2 gravitino. On the other side, the visible sector will be described by a set of chiral superfields (φ_i, ψ_i, F_i). When the supersymmetry is not broken the graviton and the gravitino have a vanishing mass. When the supersymmetry is spontaneously broken in the hidden sector we have the analogue of the Higgs mechanism, which is called super-Higgs mechanism. The graviton gets a mass by absorbing the degree of freedom of the goldstino, which is related to the vacuum expectation value of the auxiliary field F_X. In supergravity, we have to add to the superpotential, $W = W_v(\varphi_i) + W_c(X)$ (we distinguish the contribution from the visible sector and the one from the hidden sector), the Käller potential $K = \varphi_i^*\varphi_i + X^*X$. Here we have considered only diagonal kinetic terms for the chiral superfields, $\frac{\partial^2 K}{\partial\varphi_i\partial\varphi_j^\dagger} = \delta_j^i$. This assumption is known as minimal supergravity (mSUGRA). If we have the following relations in the vacuum

$$\langle X\rangle = wM_P, \quad \langle W_c\rangle = xM_P^2, \quad \left\langle\frac{\partial W_c}{\partial X}\right\rangle = x'M_P . \tag{4.127}$$

After imposing $\langle V\rangle = 0$ we get

$$\begin{aligned}
|x' + xw^*|^2 &= 3|x|^2 ,\\
m_{3/2} &= \frac{|\langle F_X\rangle|}{\sqrt{3}M_P} = |x|e^{|w|^2/2} .
\end{aligned} \tag{4.128}$$

One can obtain the lower order in $1/M_P$ expansion of the scalar potential

$$V = \left| \frac{\partial W_v}{\partial \varphi_i}\Big|_{\langle\varphi_k\rangle} \right|^2 + m_{3/2}^2 \varphi_*^i \varphi_i + m_{3/2} \left[\varphi_i \frac{\partial W_v}{\partial \varphi_i}\Big|_{\langle\varphi_k\rangle} + \left(\frac{x'^* w^* + |w|^2 x^*}{x} - 3 \right) W_c + h.c. \right] \tag{4.129}$$

We see that in mSUGRA, $m_{3/2}$ is the only one relevant parameter which triggers the supersymmetry breaking: all the soft-terms are related to this variable. We remark that there is no gaugino mass in mSUGRA at tree-level. They appear with radiative corrections and are proportional to $m_{3/2}$.

Gauge Mediation

Supersymmetry might be broken through messengers which connect the hidden sector and the visible sector by gauge interactions. In Gauge Mediation Supersymmetry Breaking (GMSB), the breaking scale is generally much smaller than the Planck scale and the soft breaking terms will be entirely generated by radiative correction effects. Basically, we introduce a set of chiral superfields charged under the Standard Model gauge group $(SU(3)_C \times SU(2)_L \times U(1)_Y)$, $q(\bar{q})$ which contain the quark-like fermion ψ_q ($\bar{\psi}_q$) and the associated scalar, $l(\bar{l})$ which contain the lepton-like fermion ψ_l ($\bar{\psi}_l$) and the associated scalar. Because we have not discovered such species so far, they have to be quite massive. We can accommodate this if they have couplings with a chiral superfield which is a gauge singlet (we call it S) as

$$W_m = y_q S \bar{\chi}_q \chi_q + y_l S \bar{\chi}_l \chi_l \tag{4.130}$$

where the scalar component of S and its auxiliary field have a non-vanishing value in the vacuum i.e $\langle S\rangle, \langle F_S\rangle \neq 0$. We then obtain mass terms for the fermion messengers $\psi_q, \bar{\psi}_q, \psi_l, \bar{\psi}_l$

$$\mathcal{L}_m = -y_q \langle S\rangle \bar{\psi}_q \psi_q - y_l \langle S\rangle \bar{\psi}_l \psi_l + h.c. \,. \tag{4.131}$$

and for the scalar messengers $q, \bar{q}, l, \bar{l}$

$$\begin{aligned} V_m &= |y_q \langle S\rangle|^2 \left(|q|^2 + |\bar{q}|^2\right) + |y_l \langle S\rangle|^2 \left(|l|^2 + |\bar{l}|^2\right) \\ &\quad -(y_q \langle F_S\rangle \bar{q} q + y_l \langle F_S\rangle \bar{l} l + h.c.) \end{aligned} \tag{4.132}$$

We can then compute the eigenvalues of the several fermion, scalar mass matrices which are obtained from the previous equations. As a consequence of supersymmetry breaking, scalar and fermion masses inside a same messenger multiplet are shifted

$$\begin{aligned} \chi_q : \quad & m_{\psi_q}^2 = |y_q \langle S\rangle|^2, \quad m_q^2 = |y_q \langle S\rangle|^2 \pm |y_q \langle F_S\rangle| \,, \\ \chi_l : \quad & m_{\psi_l}^2 = |y_l \langle S\rangle|^2, \quad m_l^2 = |y_l \langle S\rangle|^2 \pm |y_l \langle F_S\rangle| \,. \end{aligned} \tag{4.133}$$

This mass-splitting will mediate supersymmetry breaking to the visible sector through loop corrections which involve gauge couplings. The gauginos (fermion component of a vector superfield) acquire a mass at one-loop

$$M_g = \frac{\alpha_g \langle F_S\rangle}{4\pi \langle S\rangle} \,. \tag{4.134}$$

The scalars of the visible sector do not have any correction at the one-loop level. The first contributions arise at two-loops, the scalar masses are then

$$m_\phi^2 = 2 \left(\frac{\langle F_S\rangle}{\langle S\rangle} \right)^2 \left[\left(\frac{\alpha_3}{4\pi} \right)^2 C_3^\phi + \left(\frac{\alpha_2}{4\pi} \right)^2 C_2^\phi + \left(\frac{\alpha_1}{4\pi} \right)^2 C_1^\phi \right] \tag{4.135}$$

where C_i^ϕ are the Casimir invariants of the considered gauge group.

Anomaly Mediation

Anomaly Mediation Supersymmetry Breaking (AMSB) occurs when supersymmetry breaking is mediated to the visible sector through loop effects related to anomalous rescaling violations. In particular gaugino masses are directly produced by this mechanism.

4.6.4 Break supersymmetry, but softly

Up to now we have talked about spontaneous supersymmetry breaking in a hidden sector which propagates to the visible sector. We should not forget that one of the main feature of supersymmetric theory was to cure the problem of quadratic divergences as we have seen previously. The breaking terms which arise in the standard sector should not spoil the cancellation of quadratic divergences: such terms are called soft supersymmetry breaking terms. In order to give a general form to these allowed soft terms, let us look at the scalar potential at one loop in function of the cutoff of the theory, Λ

$$\delta V = \frac{\Lambda^2}{32\pi^2}\mathrm{sTr}\mathcal{M}^2(\varphi_i) + \frac{1}{64\pi^2}\mathrm{sTr}\mathcal{M}^4(\varphi_i)\ln\left(\frac{\mathcal{M}^2(\varphi_i)}{\Lambda^2}\right) \tag{4.136}$$

where we reintroduce the definition given in Eq. (4.125), 4.126. If we do not want to add any new divergent contributions to $\mathrm{sTr}\mathcal{M}^2$, here are the acceptable terms

- Scalar mass $\mu^{2,ij}\varphi_i\varphi_j^*$ which gives a constant contribution to $\mathrm{Tr}\mathcal{M}_0^2$.
- Holomorphic polynomial function of scalar fields of the form $V_{soft} = \lambda^i\varphi_i + \frac{m^{ij}}{2}\varphi_i\varphi_j + \frac{y^{ijk}}{3!}\varphi_i\varphi_j\varphi_k + h.c.$ which only gives off-diagonal contributions to $\mathcal{M}_0^2$.
- Gaugino mass $-\frac{1}{2}M^{\alpha\beta}\lambda_\alpha\lambda_\beta$ which only gives constant contribution to $\mathrm{Tr}\mathcal{M}_{1/2}^2$ (contrary to chiral fermion mass terms).

Consequently, we can write the most general soft breaking Lagrangian as

$$\mathcal{L}_{soft} = \mu^{2,ij}\varphi_i\varphi_j^* + \left(\lambda^i\varphi_i + \frac{m^{ij}}{2}\varphi_i\varphi_j + \frac{y^{ijk}}{3!}\varphi_i\varphi_j\varphi_k + h.c\right) - \frac{1}{2}M^{\alpha\beta}\lambda_\alpha\lambda_\beta \tag{4.137}$$

5 The Minimal Supersymmetric Standard Model

5.1 The Lagrangian of the MSSM

A supersymmetric version of the Standard Model has been motivated to naturally set the electroweak scale compared to the Planck scale. The study of the spontaneous supersymmetry breaking told us that new ingredients are needed and that a minimal model can only be an effective description. The Minimal Supersymmetric Standard Model is this effective description.

5.1.1 Field content

A first step is to promote each fermionic field of the Standard Model to a chiral superfield identically charged under the gauge group $(SU(3)_C \times SU(2)_L \times U(1)_Y)$. By doing so, we introduce (in the same representation of the symmetry group) a new scalar partner (a sfermion) to each quark and lepton, that we respectively call squark and slepton. Similarly, each gauge boson of the Standard Model is promoted to a vector superfield. Therefore we introduce (in the adjoint representation of the gauge group) new fermionic partners (gauginos) to the gauge bosons. We call them gluinos in the case of $SU(3)_C$, winos for $SU(2)_L$ and bino for $U(1)_Y$. We should specify that these new fermions are Weyl spinors (or Majorana spinors in four-component notation) contrary to Standard Model fermions which are Dirac spinors. Finally we promote the Higgs boson to not one, but two chiral superfields. Indeed, in the Standard Model it is a coincidence if we only need one Higgs doublet to give rise mass to up and down-type components. This is because the fundamental representation of $SU(2)$ coincides with its adjoint, thus allowing to replace the first Higgs doublet by its conjugate, reducing the a priori required number of Higgs doublets. This reduction is not anymore possible in supersymmetry. Firstly, higgsinos (superpartners of the scalar Higgs) are also $SU(2)_L$ doublet with hypercharge ± 1. If we introduce only one of these two chiral superfields we would not have anymore a vanishing chiral anomaly because of these new fermionic contributions to it. With two Higgs supermultiplets which have opposite hypercharge we keep a vanishing anomaly. Secondly, the fermionic mass terms originate from the superpotential which has the property to be holomorphic i.e it does not depend on both the Higgs field and its conjugate. Again we need two Higgs superfields that couple separately to the up and down-type component, thus with opposite hypercharge. We then have a larger Higgs sector with fermionic partners which will mix with some of the gauginos to produce charginos and neutralinos. We summarize the situation by giving the minimal particle content in Table 12 (for chiral supefields) and in Table 13 (for vector superfields).

5.1.2 The Lagrangian

With our choice of minimal gauge group and of minimal field content, we can write the associated Lagrangian. The kinetic part of these fields can be derived exactly as we have done previously. We will focus here on the interacting part between matter fields of the theory. The most general superpotential i.e at most cubic holomorphic function of the

Multiplet	Notation	scalar	spinor	$(SU(3)_C, SU(2)_L, U_Y(1))$
(s)quarks	Q	$(\tilde{u}_L, \tilde{d}_L)$	(u_L, d_L)	$(3, 2, \frac{1}{3})$
	U	$\tilde{u}_R^\dagger$	$u_R^\dagger$	$(\bar{3}, 1, -\frac{4}{3})$
	D	$\tilde{d}_R^\dagger$	$d_R^\dagger$	$(\bar{3}, 1, \frac{2}{3})$
(s)leptons	L	$(\tilde{\nu}, \tilde{e}_L)$	(ν, e_L)	$(1, 2, -1)$
	E	$(\tilde{e}_R^\dagger)$	$(e_R^\dagger)$	$(1, 1, 2)$
higgs(inos)	H_u	(h_u^+, h_u^0)	$(\tilde{h}_u^+, \tilde{h}_u^0)$	$(1, 2, 1)$
	H_d	(h_d^0, h_d^-)	$(\tilde{h}_d^0, \tilde{h}_d^-)$	$(1, 2, -1)$

Table 12: Chiral superfields of the MSSM with their particle content. For simplicity we do not write explicitly an additional family index

Multiplet	Notation	spinor	vector	$(SU(3)_C, SU(2)_L, U_Y(1))$
gluinos & gluons	G	$\tilde{g}$	g	$(8, 1, 0)$
winos & W-bosons	W	$\tilde{W}^\pm, \tilde{W}^0$	$W^\pm, W^0$	$(1, 3, 0)$
bino & B-boson	B	$\tilde{B}$	B	$(1, 1, 0)$

Table 13: Vector superfields of the MSSM with their particle content. For simplicity we do not explicit their number index.

supermultiplets (higher terms lead to a non-renormalizable theory) invariant under the SM gauge group is

$$\begin{aligned} W &= \mu H_u.H_d + y_u U(Q.H_u) - y_d D(Q.H_d) - y_e E(L.H_d) \\ &\quad + \lambda_{\not L} E(L.L) + \lambda'_{\not L} D(L.Q) + \lambda''_{\not L} L.H_u + \lambda'''_{\not L} E(H_d.H_u) \\ &\quad + \lambda_{\not B} UDD \end{aligned} \tag{5.138}$$

were we drop family and gauge indices. y_u,y_d and y_e, are the Yukawa 3×3 matrices and the product of $SU(2)_L$ doublet "." means $A.B \equiv \epsilon^{ij} A_i B_j$ with ϵ the Levi-Civita symbol. The last two lines are problematic since they violate lepton and baryon numbers. They lead to fast proton decay i.e serious problems. To enforce lepton and baryon conservation number by hand, a simple way is to introduce a quantum discrete multiplicative symmetry called R-parity. It is defined in terms of the lepton number L, the baryon number B and the spin, s, of the particle it acts on

$$R \equiv (-1)^{L+3B+2s} \tag{5.139}$$

All the SM particles have $R = 1$ contrary to all their superpartners which have $R = -1$. An important phenomenological feature is that sparticles are always pair produced, then they always decay in a odd number of sparticles that ensures the lightest one (called LSP) to be absolutely stable. Imposing this new discrete symmetry, we obtain the following MSSM superpotential

$$W_{MSSM} = \mu H_u.H_d + y_u U(Q.H_u) - y_d D(Q.H_d) - y_e E(L.H_d)\ . \tag{5.140}$$

The first μ-term is both a mass term for the Higgs doublets and a mixing mass term for the higgsinos. The last terms include the generic Yukawa couplings for fermions, the new

interactions between the fermions and sfermions and also new contributions to the scalar potential. Finally, we have to introduce the soft supersymmetry breaking terms which explicitly break supersymmetry. As we have seen before, they can be interpreted as quadratically safe reminiscences of spontaneous symmetry breaking which has occurred in a hidden sector after being mediated to the visible sector. In a model independent way we can cast them in the following way

- Mass terms for the gauginos (gluinos, winos and binos)

$$-\mathcal{L}_{\text{gauginos}} = \frac{1}{2}\left(M_3\tilde{g}^\alpha\tilde{g}_\alpha + M_2\tilde{W}^\alpha\tilde{W}_\alpha + M_1\tilde{B}\tilde{B} + h.c.\right) \tag{5.141}$$

  where M_i are real numbers.

- Mass terms for the sfermions ($\tilde{D}$ denotes only the sparticle content of the supermultiplet D)

$$-\mathcal{L}_{\text{sfermions}} = m^2_{\tilde{Q}}\tilde{Q}^\dagger\tilde{Q} + m^2_{\tilde{u}_R}|\tilde{u}_R|^2 + m^2_{\tilde{d}_R}|\tilde{d}_R|^2 + m^2_{\tilde{L}}\tilde{L}^\dagger\tilde{L} + m^2_{\tilde{l}_R}|\tilde{l}_R|^2 \tag{5.142}$$

  where the squared mass parameters represent 3×3 Hermitian matrices in the flavor space (here $H_{u/d}$ represents only the scalar content).

- Mass and bilinear terms for the Higgs bosons

$$-\mathcal{L}_{\text{Higgs}} = m^2_{H_u}H_u^\dagger H_u + m^2_{H_d}H_d^\dagger H_d + B\mu(H_u.H_d + h.c.) \tag{5.143}$$

  where $m_{H_{u/d}}$ and $B\mu$ are real numbers.

- Trilinear couplings between Higgs bosons and sfermions (here $H_{u/d}$ represents only the scalar content)

$$-\mathcal{L}_{\text{tril.}} = A_u y_u \tilde{u}_R(Q.H_u) + A_d y_d \tilde{d}_R(Q.H_d) + A_l y_l \tilde{l}_R(Q.H_d) + h.c. \tag{5.144}$$

  where $A_{u/d/l}$ and $y_{u/d/l}$ are 3×3 complex matrices in generation space.

The soft supersymmetry breaking Lagrangian is the sum of these four last terms

$$\mathcal{L}_{soft} = \mathcal{L}_{\text{gauginos}} + \mathcal{L}_{\text{sfermions}} + \mathcal{L}_{\text{Higgs}} + \mathcal{L}_{\text{tril.}} \tag{5.145}$$

From our four hypotheses, namely minimal gauge group structure, minimal particle content, minimal Yukawa interactions (R-parity) and minimal set of soft supersymmetry breaking terms, we have defined the unconstrained MSSM. The soft supersymmetry breaking Lagrangian adds 109 parameters to the 19 needed to describe the SM. Paradoxically to the aim of supersymmetry, supersymmetry breaking introduces a huge number of arbitrary parameters. This leads to phenomenological incompatibilities such as Flavor Changing Neutral Current (FCNC), unacceptable additional amount of CP-violation, charge and color breaking minima. And needless to say that the parameter space needs to be squeezed in order to perform viable phenomenological studies. We then come to constrained MSSM (cMSSM).

5.1.3 The constrained MSSM

Phenomenological MSSM

It is possible to reduce the number of soft supersymmetry breaking terms by doing the following simplifications

- Suppress the new source of CP-violation (others than the one coming from the CKM matrix) by imposing real soft terms,
- Suppress the FCNC at tree level by imposing diagonal mass matrices and trilinear coupling matrices,
- Evade the $K^0 - \bar{K}^0$ mixing constraint by imposing at low energy that masses and trilinear coupling of the first and second generations are the same.

With these assumptions it remains only 20 parameters which are : the gaugino masses $M_{1/2/3}$; first-second generation sfermion masses $m_{\tilde{q}}, m_{\tilde{u}_R}, m_{\tilde{d}_R}, m_{\tilde{l}}, m_{\tilde{l}_R}$ and trilinear couplings A_u, A_d, A_e; same thing for the third generation $m_{\tilde{Q}}, m_{\tilde{t}_R}, m_{\tilde{b}_R}, m_{\tilde{L}}, m_{\tilde{\tau}_R}$ and A_t, A_b, A_τ; the Higgs mass parameter $m_{H_{u/d}}$ and the ratio of the vacuum expectation values of the two Higgs doublet fields $\tan\beta$. This defines the phenomenological MSSM (pMSSM).

mSUGRA

Most of the problems associated to the unconstrained MSSM disappear if the soft supersymmetric breaking terms obey universal boundary conditions at the GUT scale. We have already seen that generally one has to assume that supersymmetry is broken in a hidden sector and that soft terms are the reminiscence of this breaking in our standard sector. In the case of Minimal Supergravity scenario, mSUGRA, the soft breaking terms arise and the supergravity interactions are flavor blind. Considering the unification scale being $M_{GUT} \approx 2\times10^{16}$ GeV, unification boundary conditions in mSUGRA would consist in unifying the gaugino masses

$$m_{1/2} \equiv M_1(M_{GUT}) = M_2(M_{GUT}) = M_3(M_{GUT}) \tag{5.146}$$

and also the scalar masses

$$\begin{aligned} m_0 &\equiv M_{H_u}(M_{GUT}) = M_{H_d}(M_{GUT}) = m_{\tilde{Q}_i}(M_{GUT}) = m_{\tilde{u}_{Ri}}(M_{GUT}) = m_{\tilde{d}_{Ri}}(M_{GUT}) \\ &= m_{\tilde{L}_i}(M_{GUT}) = m_{\tilde{l}_{Ri}}(M_{GUT}) \end{aligned} \tag{5.147}$$

as well as the trilinear couplings

$$A_0\delta_{ij} \equiv A^u_{ij}(M_{GUT}) = A^d_{ij}(M_{GUT}) = A^l_{ij}(M_{GUT})\ . \tag{5.148}$$

In addition to these three universal parameters $m_{1/2}$, m_0 and A_0 the Higgs sector is described by the Higgs mass parameter μ and the bilinear coupling B. In fact these two parameters can be traded with $\tan\beta$ and the sign of μ (this exchange will become clearer when we will detail the electroweak symmetry breaking process in the MSSM). The mSUGRA model has then only few parameters which are : m_0, $m_{1/2}$, A_0, $\tan\beta$ and sign(μ). All the soft breaking parameters at the weak scale are obtained from this last set of parameters through the RGEs.

In a next section, when we will address the implication of a 125 GeV Higgs on supersymmetric models, we will come back to the mSUGRA scenario but also to other famous constrained MSSM models as the Gauge Mediated and the Anomaly Mediated Supersymmetry breaking alternatives.

But now let us focus on the Higgs sector of the MSSM and the electroweak symmetry breaking mechanism of a two-Higgs doublet model.

5.2 The Higgs sector of the MSSM

5.2.1 Electroweak symmetry breaking: the MSSM Higgs potential

We have determined the full Lagrangian of the MSSM. We will discuss now the electroweak symmetry breaking of the Higgs sector which occurs when the Higgs fields acquire a vacuum expectation value (vev). As we have seen in the previous section, we have two main contributions to the scalar potential: one is invariant under supersymmetric transformation and come from the superpotential and the D-terms, the other is not invariant and come from the soft breaking terms. Then we can write the first contribution as

$$\begin{aligned} V_{SUSY} &= \mu^2 \left(|H_u|^2 + |H_d|^2\right) \\ &\quad + \frac{g^2}{8}\left(|H_d|^2 - |H_u|^2\right)^2 + \frac{g^2}{2}|H_d^\dagger H_u|^2 \\ &\quad + \frac{g_Y^2}{8}\left(|H_d|^2 - |H_u|^2\right)^2 \end{aligned} \tag{5.149}$$

where the first line corresponds to the F-term, the second line to the D-term associated to the $SU(2)_L$ gauge group and the third line to the D-term associated to the $U(1)_Y$ gauge group. The second main contribution coming from the soft breaking Lagrangian can be written as

$$V_{soft} = m_{H_u}^2 H_u^\dagger H_u + m_{H_d}^2 H_d^\dagger H_d + B\mu(H_u.H_d + h.c.)\ . \tag{5.150}$$

When the two Higgs doublet fields

$$H_u = \begin{pmatrix} h_u^+ \\ h_u^0 \end{pmatrix}, \quad H_d = \begin{pmatrix} h_d^0 \\ h_d^- \end{pmatrix} \tag{5.151}$$

will acquire a v.e.v., then the minimum of the scalar potential will have to break the electroweak gauge group $SU(2)_L \times U(1)_Y$ down to $U(1)_{\rm em}$. At this minimum, in all generality, we can perform a $SU(2)_L$ rotation in order to recover the case where $\langle h_u^+ \rangle = 0$. In that situation, the minimization equation $\partial V/\partial h_u^+ = 0$ at the minimum directly implies that $\langle h_d^- \rangle = 0$ i.e we recover that $U(1)_{\rm em}$ is not broken. We are left with the case where only the neutral components get a vev

$$\langle H_u \rangle = \frac{1}{\sqrt{2}} \begin{pmatrix} 0 \\ v_u \end{pmatrix}, \quad \langle H_d \rangle = \frac{1}{\sqrt{2}} \begin{pmatrix} v_d \\ 0 \end{pmatrix}\ . \tag{5.152}$$

v_u and v_d are real and positive numbers as $B\mu$ up to a $U(1)$ rotation of the fields h_u^0 and h_d^0 (the potential conserves CP at tree-level). We can write the two minimization

equations coming from $\left.\frac{\partial V}{\partial h_u^0}\right|_{\rm vev} = \left.\frac{\partial V}{\partial h_d^0}\right|_{\rm vev} = 0$ as

$$\left[m_{H_u^2} + \mu^2 + \frac{g^2+g'^2}{4}\left(v_u^2 - v_d^2\right)\right] v_u - B\mu v_d = 0 \ ,$$
$$\left[m_{H_d^2} + \mu^2 - \frac{g^2+g'^2}{4}\left(v_u^2 - v_d^2\right)\right] v_d - B\mu v_u = 0 \ . \tag{5.153}$$

In order to spontaneously break the electroweak symmetry, the Higgs potential has to be bounded from below. For generic values of the vacuum expectation values v_u, v_d the quartic term of Eq. (5.149) ensures that the potential is always stabilized. Nevertheless, in the situation where $v_u = v_d$ at the minimum the quartic term vanishes (we refer to this case as the D-flat direction since the quartic term originates from the auxiliary D fields). In this case, the minimization conditions Eq.(5.153) are always satisfied but in order to bound the potential from below one has to verify the condition

$$m_{H_u}^2 + m_{H_d}^2 + 2\mu^2 - 2B\mu > 0 \ . \tag{5.154}$$

In order to have a spontaneous symmetry breaking we also have a second condition coming from the fact that one eigenvalue of the mass matrix has to be negative, which is equivalent to require a negative determinant of the Hessian matrix $\left.\frac{\partial V}{\partial h_i^0 \partial h_j^0}\right|_{\rm vev}$ and can be written as

$$\begin{pmatrix} h_u^{0*} & h_d^{0*} \end{pmatrix} \begin{pmatrix} m_{H_u}^2 + \mu^2 & -B\mu \\ -B\mu & m_{H_d}^2 + \mu^2 \end{pmatrix} \begin{pmatrix} h_u^0 \\ h_u^0 \end{pmatrix} \ . \tag{5.155}$$

This last condition reads

$$(m_{H_u}^2 + \mu^2)(m_{H_d}^2 + \mu^2) - (B\mu)^2 < 0 \ . \tag{5.156}$$

An interesting remark is that the two conditions needed in order to have spontaneous symmetry breaking, Eq. (5.153) and Eq. (5.156), cannot be simultaneously satisfied if $m_{H_u}^2 = m_{H_d}^2$. Thus, in order to break the electroweak symmetry, we also need to break supersymmetry. Therefore, radiative corrections through the supersymmetric renormalization group equations drive the evolution of these two parameters from the high scale where supersymmetry is supposed to be broken down to the eletroweak scale. Since the Higgs doublet which gives mass to the up type quark strongly couples to the top quark, $m_{H_u}^2$ is naturally pushed to much smaller values than $m_{H_d}^2$. The running then triggers the electroweak symmetry breaking, this mechanism is commonly denoted as radiative breaking of the symmetry [176–180]. In this framework, gauge symmetry breaking could appear as more natural (elegant) in the context of the MSSM than in the SM because we do not need to rely on the SM hypothesis $\mu^2 < 0$, since we now rely on loop effects.

Electroweak symmetry breaking leads to a mixing between $SU(2)_L$ and $U(1)_Y$ gauge bosons which will acquire a mass in the same way than in the SM. After shifting the neutral component of the scalar Higgs bosons by their vev $h_{u/d}^0 \to \frac{1}{\sqrt{2}}(v_{u/d} + h_{u/d}^0)$, we obtain the squared mass matrix of the neutral gauge bosons B_μ and W_μ^3 by only considering the usual Higgs kinetic Lagrangian

$$\mathcal{L}_{EW} = D_\mu H_u^\dagger D^\mu H_u + D_\mu H_d^\dagger D^\mu H_d \ . \tag{5.157}$$

We can then link the mass matrix in the interaction basis (W^3_μ, B_μ) and in the mass basis (Z_μ, A_μ) in the following way

$$\frac{v_u^2+v_d^2}{8}\begin{pmatrix} W^3_\mu & B_\mu \end{pmatrix}\begin{pmatrix} g^2 & -gg' \\ -gg' & g'^2 \end{pmatrix}\begin{pmatrix} W^{3\mu} \\ B^\mu \end{pmatrix} = \frac{1}{2}\begin{pmatrix} Z_\mu & A_\mu \end{pmatrix}\begin{pmatrix} m_Z^2 & 0 \\ 0 & 0 \end{pmatrix}\begin{pmatrix} Z\mu \\ A^\mu \end{pmatrix},$$

and the link between the two basis is done by an orthogonal transformation defined as

$$\begin{pmatrix} Z^\mu \\ A^\mu \end{pmatrix} = \begin{pmatrix} \cos\theta_w & -\sin\theta_w \\ \sin\theta_w & \cos\theta_w \end{pmatrix}\begin{pmatrix} W^{3\mu} \\ B^\mu \end{pmatrix} \tag{5.158}$$

with

$$\cos\theta_w \equiv \frac{g}{\sqrt{g^2+g'^2}}, \quad \sin\theta_w \equiv \frac{g'}{\sqrt{g^2+g'^2}}, \quad m_Z^2 = \frac{(v_u^2+v_d^2)(g^2+g'^2)}{4}, \quad m_A = 0\,.$$

Concerning the charged weak bosons, the relation between the interaction and mass basis and the physical eigenvalues corresponding to the $W^\pm$ masses are as follow

$$W^\pm_\mu = \frac{1}{\sqrt{2}}(W^1_\mu \mp iW^2_\mu), \quad m_W^2 = \frac{g^2(v_u^2+v_d^2)}{4}\,. \tag{5.159}$$

Afteward, defining the famous parameter

$$\tan\beta \equiv \frac{v_d}{v_u} = \frac{v\sin\beta}{v\cos\beta} \tag{5.160}$$

and using the relation we have just derived: $(v_u^2+v_d^2) = 4m_Z^2/(g^2+g'^2)$, we can express the extremum conditions Eq. (5.153) as

$$\begin{aligned} \mu^2 &= \frac{m^2_{H_u}\sin\beta^2 - m^2_{H_d}\cos\beta^2}{\cos 2\beta} - \frac{m_Z^2}{2}\,, \\ B\mu &= \frac{(m^2_{H_d}-m^2_{H_u})\tan 2\beta + m_Z^2\sin 2\beta}{2}\,. \end{aligned} \tag{5.161}$$

If m_{H_u}, m_{H_d} and $\tan\beta$ are known then the value of B and μ up to its sign are determined.

5.2.2 The masses of the MSSM Higgs bosons

The W and Z bosons get their mass by eating the three Goldstone bosons, $G^\pm$ and G^0, out of the eight real degrees of freedom included in the two Higgs doublets. The remaining degrees of freedom will give after mixing the five physical Higgs states. The Higgs fields and their associated masses are obtained by diagonalizing the pseudoscalar, the charged and the scalar Higgs mass matrices computed from the scalar potential $\mathcal{M}^2_{ab} = \frac{1}{2}\frac{\partial^2 V}{\partial H_a \partial H_b}\Big|_{\text{vev}}$.

Before diagonalizing these matrices, one should expand the two doublet scalar Higgs fields around their vacuum into real component fields in the following way

$$H_u = \frac{1}{\sqrt{2}}\begin{pmatrix} h_u^+ \\ v_u + h_u^0 + iP_u^0 \end{pmatrix}, \quad H_d = \frac{1}{\sqrt{2}}\begin{pmatrix} v_d + h_d^0 + iP_d^0 \\ h_d^- \end{pmatrix} \tag{5.162}$$

- Case of the CP-odd Higgs bosons
  From the scalar potential we can extract the squared matrix in the interaction basis

$$V \supset \frac{1}{2} \begin{pmatrix} P_u^0 & P_d^0 \end{pmatrix} \begin{pmatrix} \frac{B\mu}{\tan\beta} & B\mu \\ B\mu & B\mu \tan\beta \end{pmatrix} \begin{pmatrix} P_u^0 \\ P_d^0 \end{pmatrix} . \tag{5.163}$$

  In the mass basis, the eigenvalues are the neutral Goldstone bosons G^0 (eaten by the Z boson) and the physical CP-odd Higgs boson A. This mass basis is related to the interaction basis through the following transformation

$$\begin{pmatrix} G^0 \\ A \end{pmatrix} = \begin{pmatrix} \cos\beta & -\sin\beta \\ \sin\beta & \cos\beta \end{pmatrix} \begin{pmatrix} P_d^0 \\ P_u^0 \end{pmatrix} . \tag{5.164}$$

  The eigenvalues are

$$M_{G^0}^2 = 0, \quad M_A^2 = \frac{2B\mu}{\sin 2\beta} . \tag{5.165}$$

- Case of the charged Higgs bosons
  From the scalar potential we can extract the squared matrix in the interaction basis

$$V \supset \begin{pmatrix} h_u^+ & h_d^+ \end{pmatrix} \begin{pmatrix} (M_A^2 + m_W^2)\cos^2\beta & (M_A^2 + m_W^2)\cos\beta\sin\beta \\ (M_A^2 + m_W^2)\cos\beta\sin\beta & (M_A^2 + m_W^2)\sin^2\beta \end{pmatrix} \begin{pmatrix} h_u^- \\ h_d^- \end{pmatrix} .$$

  In the mass basis, the eigenvalues are the two charged Goldstone bosons $G^\pm$ (eaten by $W^\pm$) and the two physical charged Higgs $H^\pm$. This mass basis is related to the interaction basis through the following transformation

$$\begin{pmatrix} G^\pm \\ H^\pm \end{pmatrix} = \begin{pmatrix} \cos\beta & -\sin\beta \\ \sin\beta & \cos\beta \end{pmatrix} \begin{pmatrix} h_d^\pm \\ h_u^\pm \end{pmatrix} . \tag{5.166}$$

  The eigenvalues are

$$M_{G^\pm}^2 = 0, \quad M_{H^\pm}^2 = M_A^2 + m_W^2 \tag{5.167}$$

- Case of the CP-even Higgs bosons
  From the scalar potential we can extract the squared matrix in the interaction basis

$$V \supset \frac{1}{2} \begin{pmatrix} h_u^0 & h_d^0 \end{pmatrix} \begin{pmatrix} m_Z^2\sin^2\beta + M_A^2\cos^2\beta & -(m_Z^2 + M_A^2)\cos\beta\sin\beta \\ -(m_Z^2 + M_A^2)\cos\beta\sin\beta & m_Z^2\cos^2\beta + M_A^2\sin^2\beta \end{pmatrix} \begin{pmatrix} h_u^0 \\ h_d^0 \end{pmatrix} .$$

  In the mass basis, the eigenvalues are the lightest neutral Higgs boson, h, and the heaviest neutral Higgs boson, H. This mass basis is related to the interaction basis through the following transformation

$$\begin{pmatrix} h \\ H \end{pmatrix} = \begin{pmatrix} \cos\alpha & -\sin\alpha \\ \sin\alpha & \cos\alpha \end{pmatrix} \begin{pmatrix} h_u^0 \\ h_d^0 \end{pmatrix} . \tag{5.168}$$

  The eigenvalues are

$$M_{h/H}^2 = \frac{1}{2}\left[M_A^2 + m_Z^2 \mp \sqrt{(M_A^2 + m_Z^2)^2 - 4M_A^2 m_Z^2 \cos^2 2\beta}\right] \tag{5.169}$$

with the mixing angle α given by

$$\cos 2\alpha = -\cos 2\beta \frac{M_A^2 - m_Z^2}{M_H^2 - M_h^2}, \quad \sin 2\alpha = -\sin 2\beta \frac{M_A^2 + m_Z^2}{M_H^2 - M_h^2} , \tag{5.170}$$

or equivalently by

$$\alpha = \frac{1}{2} \arctan \left(\tan 2\beta \frac{M_A^2 + m_Z^2}{M_A^2 - m_Z^2} \right), \quad -\frac{\pi}{2} \leq \alpha \leq 0 . \tag{5.171}$$

Consequently the Higgs spectrum of the MSSM can be described by only two parameters at tree level ($\tan\beta$ and M_A for example). There are also strong constraints, namely : $M_{H^\pm} > m_W$, $M_H > \max(m_Z, M_A)$, and the one concerning the lightest Higgs boson

$$M_h \leq \min(m_Z, M_A) |\cos 2\beta| \leq m_Z . \tag{5.172}$$

This last upper bound is in contradiction with the recent observation of a 125 GeV SM Higgs boson. Nevertheless, the lightest Higgs boson can receive large quantum corrections most especially through top quark and squark loop effects. We will study this point in detail later in this same part.

5.2.3 Supersymmetric particle spectrum

The sfermion masses in the MSSM

The left and right-handed sfermions have a mass term coming from the soft supersymmetry breaking Lagrangian ($\mathcal{L}_{\text{sfermions}}$ in Eq. (5.142)). The same Lagrangian also introduces trilinear interactions ($\mathcal{L}_{\text{tril.}}$ in Eq. (5.144)) that mix left and right-handed sfermion states. In the interaction basis the sfermion mass matrix for a given sfermion generation $\tilde{f}$ ($\tilde{f}_R$,$\tilde{f}_L$) can be arranged in the form

$$\mathcal{M}^2_{\tilde{f}} = \begin{pmatrix} m_f^2 + m_{LL}^2 & m_f X_f \\ m_f X_f & m_f^2 + m_{RR}^2 \end{pmatrix} \tag{5.173}$$

with the various entries given by

$$\begin{aligned} m_{LL}^2 &= m_{\tilde{f}_L}^2 + (I_f^{3L} - Q_f s_W^2)\, m_Z^2\, c_{2\beta} \\ m_{RR}^2 &= m_{\tilde{f}_R}^2 + Q_f s_W^2\, m_Z^2\, c_{2\beta} \\ X_f &= A_f - \mu (\tan\beta)^{-2I_f^{3L}} \end{aligned} \tag{5.174}$$

I_f^{3L} being the associated third component of the isospin and Q_f the associated charge. The current eigenstates $\tilde{f}_L$ and $\tilde{f}_R$ are turned into the mass eigenstates $\tilde{f}_1$ and $\tilde{f}_2$ after diagonalization using a 2×2 rotation matrix of angle θ_f

$$R^{\tilde{f}} = \begin{pmatrix} \cos\theta_{\tilde{f}} & \sin\theta_{\tilde{f}} \\ -\sin\theta_{\tilde{f}} & \cos\theta_{\tilde{f}} \end{pmatrix} \tag{5.175}$$

The sfermion masses and the mixing angle are given by

$$m^2_{\tilde{f}_{1,2}} = m_f^2 + \frac{1}{2} \left[m_{LL}^2 + m_{RR}^2 \mp \sqrt{(m_{LL}^2 - m_{RR}^2)^2 + 4 m_f^2 X_f^2} \right] , \tag{5.176}$$

$$\sin 2\theta_{\tilde{f}} = \frac{2 m_f X_f}{m^2_{\tilde{f}_1} - m^2_{\tilde{f}_2}} , \quad \cos 2\theta_{\tilde{f}} = \frac{m_{LL}^2 - m_{RR}^2}{m^2_{\tilde{f}_1} - m^2_{\tilde{f}_2}} . \tag{5.177}$$

The fermion masses in the MSSM

Concerning the SM leptons and quarks the situation is exactly the one of the SM i.e their mass matrices have to be diagonalized in the flavor space

$$m_e^{ff'} = y_e^{ff'} v_u, \quad m_u^{ff'} = y_u^{ff'} v_u, \quad m_d^{ff'} = y_d^{ff'} v_d \tag{5.178}$$

Nevertheless, the up and down-type masses are now generated by two distinct v.e.v. : v_u and v_d.

We will now concentrate on the spectrum of the new MSSM fermions, namely the gauginos and higgsinos.

At tree-level the gluino mass receives a soft mass term from $\mathcal{L}_{\text{gauginos}}$ in Eq. (5.141)

$$m_{\tilde{g}} = M_3 \ . \tag{5.179}$$

Because of electroweak symmetry breaking winos and bino will mix with the higgsinos. Separating the neutral and charged states, we firstly focus on the neutral fields.

The mass matrix of the neutral states in the $(-i\tilde{B}, -i\tilde{W}_3, \tilde{h}_d^0, \tilde{h}_u^0)$ basis reads

$$\mathcal{M}_N = \begin{bmatrix} M_1 & 0 & -m_Z \sin\theta_w \cos\beta & m_Z \sin\theta_w \sin\beta \\ 0 & M_2 & m_Z \cos\theta_w \cos\beta & -m_Z \cos\theta_w \sin\beta \\ -m_Z \sin\theta_w \cos\beta & m_Z \cos\theta_w \cos\beta & 0 & -\mu \\ m_Z \sin\theta_w \sin\beta & -m_Z \cos\theta_w \sin\beta & -\mu & 0 \end{bmatrix} .$$

The previous matrix is real and symmetric, therefore it can be diagonalized by a unitarity matrix N

$$N^T \mathcal{M}_N N^{-1} = diag(m_{\chi_1^0}, m_{\chi_2^0}, m_{\chi_3^0}, m_{\chi_4^0}) \ . \tag{5.180}$$

The resulting mass eigenstates χ_i^0 are called the neutralinos. If χ_1^0 (usually taken as the lightest one) is the Lightest Supersymmetric Particle (LSP), it is also stable due to R-parity. It embodies a serious dark matter candidate.

The mass matrix of the charged states $\varphi^+ = (-i\tilde{W}^+, \tilde{h}_u^+)$ and $\varphi^- = (-i\tilde{W}^-, \tilde{h}_d^-)$ mix through the mass matrix $\varphi^- \mathcal{M}_\pm \varphi^+$ with

$$\mathcal{M}_\pm = \begin{bmatrix} M_2 & \sqrt{2} m_W \sin\beta \\ \sqrt{2} m_W \cos\beta & \mu \end{bmatrix} . \tag{5.181}$$

$\mathcal{M}_\pm$ is diagonalized by two unitarity matrices U and V,

$$U^* \mathcal{M}_C V^{-1} = diag(m_{\chi_1^\pm}, m_{\chi_2^\pm}) \tag{5.182}$$

where the eigenstates $\chi_1^\pm$ and $\chi_2^\pm$ are called the charginos and their mass read (introducing the shorthand notation $c_{2\beta} \equiv \cos 2\beta$)

$$m^2_{\chi^\pm_{1/2}} = \frac{1}{2}\left(M_2^2 + \mu^2 + 2m_W^2 \mp \left[(M_2^2 - \mu^2)^2 + 4m_W^2 (m_W^2 c_{2\beta}^2 + M_2^2 + \mu^2 + 2M_2 \mu s_{2\beta}) \right]^{\frac{1}{2}} \right)$$

We have derived the masses of the different particles of the MSSM. We now study their couplings with the Higgs bosons.

5.2.4 The couplings of the MSSM Higgs bosons

The Higgs couplings to vector bosons

The expressions of the couplings between the Higgs fields and the gauge bosons in the MSSM are obtained from the usual Higgs kinetic Lagrangian

$$\mathcal{L}_{\rm EW} = D_\mu H_u^\dagger D^\mu H_u + D_\mu H_d^\dagger D^\mu H_d \tag{5.183}$$

after making explicit the covariant derivative and performing the canonical rotation of the scalar and vector fields in order to recover the physical fields. We will only write here the trilinear couplings which will be useful for our analysis in the next sections. One can find the full list of these couplings including the one of the form $H_i H_j V_\mu V_\nu$ in Refs. [48, 181]. We introduce in the following trilinear couplings the abbreviations $g_Z = g/\cos\theta_w$ and $g_W = g$

$$\begin{aligned} W_\mu^+ W_\nu^+ h &: i g_W m_W \sin(\beta-\alpha) g_{\mu\nu} \quad , \quad W_\mu^+ W_\nu^- H : i g_W m_W \cos(\beta-\alpha) g_{\mu\nu} \\ Z_\mu Z_\nu h &: i g_Z m_Z \sin(\beta-\alpha) g_{\mu\nu} \quad , \quad Z_\mu Z_\nu H : i g_Z m_Z \cos(\beta-\alpha) g_{\mu\nu} \end{aligned} \tag{5.184}$$

$$\begin{aligned} W_\mu^\pm H^\pm h &: \mp i \frac{g_W}{2} \cos(\beta-\alpha)(p+p')_\mu \quad , \quad W_\mu^\pm H^\pm H : \pm i \frac{g_2}{2} \sin(\beta-\alpha)(p+p')_\mu \\ W_\mu^\pm H^\pm A &: \frac{g_W}{2}(p+p')_\mu \\ Z_\mu h A &: + \frac{g_Z}{2} \cos(\beta-\alpha)(p+p')_\mu \quad , \quad Z_\mu H A : - \frac{g_Z}{2} \sin(\beta-\alpha)(p+p')_\mu \\ Z_\mu H^+ H^- &: - \frac{g_Z}{2} \cos 2\theta_W (p+p')_\mu \quad , \quad \gamma_\mu H^+ H^- : -ie(p+p')_\mu \end{aligned} \tag{5.185}$$

Some of these couplings are expressed in terms of the two angles β and α, we can easily write them in function of the physical masses with the formula

$$\cos^2(\beta-\alpha) = \frac{M_h^2 (m_Z^2 - M_h^2)}{M_A^2 (M_H^2 - M_h^2)} \tag{5.186}$$

The Higgs couplings to fermions

The MSSM Higgs bosons couplings to fermions can be derived from the superpotential through

$$\mathcal{L}_{\rm Yukawa} = -\frac{1}{2} \sum_{ij} \left(\bar{\psi}_{iL} \frac{\partial^2 W}{\partial \Phi_i \partial \Phi_j} \psi_{jL} + \text{h.c.} \right) . \tag{5.187}$$

Plugging in the superpotential of Eq. (5.140) and using the chiral projector $P_{L/R} = \frac{1}{2}(1 \pm \gamma^5)$, we can re-write the Yukaka Lagrangian of a given fermion generation as

$$\mathcal{L}_{\rm Yukawa} = -\lambda_u \left(\bar{u} P_L u H_u^0 - \bar{u} P_L d H_u^+ \right) - \lambda_d \left(\bar{d} P_L d H_d^0 - \bar{d} P_L u H_d^- \right) + \text{h.c.} \tag{5.188}$$

After EWSB, the fermion masses are generated. They are linked to the fermion Yukawa interaction and to the corresponding Higgs vev as shown by the two expressions

$$\lambda_u = \frac{\sqrt{2} m_u}{v \sin\beta} \quad , \quad \lambda_d = \frac{\sqrt{2} m_d}{v \cos\beta} . \tag{5.189}$$

Finally, rotating the fields H_u and H_d in their physical state, one can get the following Yukawa Lagrangian

$$\begin{aligned}\mathcal{L}_{\rm Yukawa} &= -\frac{m_u}{v\sin\beta}\left[\bar{u}u(H\sin\alpha + h\cos\alpha) - i\bar{u}\gamma_5 u\, A\cos\beta\right] \\ &\quad -\frac{m_d}{v\cos\beta}\left[\bar{d}d(H\cos\alpha - h\sin\alpha) - i\bar{d}\gamma_5 d\, A\sin\beta\right] \\ &\quad +\frac{1}{v\sqrt{2}}V_{ud}\left[H^+\bar{u}\left(\frac{m_u}{\tan\beta}(1-\gamma_5) + m_d\tan\beta(1+\gamma_5)\right)d + h.c.\right] \end{aligned} \quad (5.190)$$

where, in the case of the quarks, V_{ud} is the CKM matrix element. The Higgs couplings to fermions are then given by

$$\begin{aligned} G_{huu} &= i\frac{m_u}{v}\frac{\cos\alpha}{\sin\beta}\ , \qquad G_{Huu} = i\frac{m_u}{v}\frac{\sin\alpha}{\sin\beta}\ , \quad G_{Auu} = \frac{m_u}{v}\cot\beta\,\gamma_5 \\ G_{hdd} &= -i\frac{m_d}{v}\frac{\sin\alpha}{\cos\beta}\ , \qquad G_{Hdd} = i\frac{m_d}{v}\frac{\cos\alpha}{\cos\beta}\ , \quad G_{Add} = \frac{m_d}{v}\tan\beta\gamma_5 \end{aligned}$$

$$\begin{aligned} G_{H^-u\bar{d}} &= -\frac{i}{\sqrt{2}v}V_{ud}[\frac{m_u}{\tan\beta}(1+\gamma_5) + m_d\tan\beta(1-\gamma_5)] \\ G_{H^+\bar{u}d} &= -\frac{i}{\sqrt{2}v}V^*_{ud}[\frac{m_u}{\tan\beta}(1-\gamma_5) + m_d\tan\beta(1+\gamma_5)] \end{aligned} \quad (5.191)$$

At this stage we can make several remarks which might be useful to proceed. The pseudoscalar boson, A, has the same $\tan\beta$ dependence as the charged Higgs bosons, $H^\pm$. Thus their couplings to up-type quark (basically the top quark) are suppressed at high $\tan\beta$ and are enhanced at low $\tan\beta$ (this might lead to an interesting phenomenological signature as we will see in the following). On the contrary, for their couplings to down-type quark (basically the b quark) their couplings are enhanced at high $\tan\beta$ and are suppressed at low $\tan\beta$. It will be very convenient for our next discussions to normalize the couplings of the MSSM neutral CP-even Higgs bosons to their SM one

$$\begin{aligned} g_{huu} &= \frac{\cos\alpha}{\sin\beta} = \sin(\beta-\alpha) + \cot\beta\cos(\beta-\alpha)\ , \\ g_{hdd} &= -\frac{\sin\alpha}{\cos\beta} = \sin(\beta-\alpha) - \tan\beta\cos(\beta-\alpha)\ , \\ g_{Huu} &= \frac{\sin\alpha}{\sin\beta} = \cos(\beta-\alpha) - \cot\beta\sin(\beta-\alpha)\ , \\ g_{Hdd} &= \frac{\cos\alpha}{\cos\beta} = \cos(\beta-\alpha) + \tan\beta\sin(\beta-\alpha)\ . \end{aligned} \quad (5.192)$$

The Higgs self-couplings

The couplings between three or four Higgs boson fields are obtained from the scalar potential by performing successive derivatives

$$\begin{aligned} \lambda_{ijk} &= \left.\frac{\partial^3 V}{\partial H_i\partial H_j\partial H_k}\right|_{\langle h_u^0\rangle = v_u/\sqrt{2}, \langle h_d^0\rangle = v_d/\sqrt{2}, \langle h^\pm_{u/d}\rangle = 0}\ , \\ \lambda_{ijkl} &= \left.\frac{\partial^4 V}{\partial H_i\partial H_j\partial H_k\partial H_l}\right|_{\langle h_u^0\rangle = v_u/\sqrt{2}, \langle h_d^0\rangle = v_d/\sqrt{2}, \langle h^\pm_{u/d}\rangle = 0}\ , \end{aligned} \quad (5.193)$$

and expressing the Higgs states in linear combinations of the physical states $h, H, A, H^\pm$. The neutral Higgs boson trilinear couplings can be written, in units of $\lambda_0 = -im_Z^2/v$, as

$$\begin{aligned}
\lambda_{hhh} &= 3\cos 2\alpha \sin(\beta+\alpha) \; , \\
\lambda_{Hhh} &= 2\sin 2\alpha \sin(\beta+\alpha) - \cos 2\alpha \cos(\beta+\alpha) \; , \\
\lambda_{HHH} &= 3\cos 2\alpha \cos(\beta+\alpha) \; , \\
\lambda_{HHh} &= -2\sin 2\alpha \cos(\beta+\alpha) - \cos 2\alpha \sin(\beta+\alpha) \; , \\
\lambda_{HAA} &= -\cos 2\beta \cos(\beta+\alpha) \; , \\
\lambda_{hAA} &= \cos 2\beta \sin(\beta+\alpha) \; .
\end{aligned} \tag{5.194}$$

The trilinear couplings involving the $H^\pm$ bosons, $\lambda_{HH^+H^-}$ and $\lambda_{hH^+H^-}$, are related to those involving the pseudoscalar Higgs boson with contributions proportional to the couplings of the neutral CP-even Higgs boson to electroweak bosons

$$\begin{aligned}
\lambda_{HH^+H^-} &= -\cos 2\beta \cos(\beta+\alpha) + 2c_w^2 \cos(\beta-\alpha) = \lambda_{HAA} + 2c_w^2 g_{HVV} \; , \\
\lambda_{hH^+H^-} &= \cos 2\beta \sin(\beta+\alpha) + 2c_w^2 \sin(\beta-\alpha) = \lambda_{hAA} + 2c_w^2 g_{hVV} \; .
\end{aligned} \tag{5.195}$$

The quartic couplings among the MSSM Higgs bosons are quite numerous and can be found in Ref. [182]. The quadrilinear couplings between h or H bosons, in units of $\lambda_0/v = -im_Z^2/v^2$, are

$$\lambda_{hhhh} = \lambda_{HHHH} = 3\cos^2 2\alpha \; . \tag{5.196}$$

The Higgs couplings to sfermions

The couplings between the MSSM Higgs bosons to superpartners of fermions come from three different contributions : from the F and D-terms in the superpotential and from the trilinear soft supersymmetry breaking terms ($\mathcal{L}_{tril.}$ in Eq. (5.144))

$$g_{\Phi\tilde{q}\tilde{q}} = \frac{g}{m_W} R^{\tilde{q}T} C_{\Phi\tilde{q}\tilde{q}'} R^{\tilde{q}} \tag{5.197}$$

with the 2×2 matrices $C_{\Phi\tilde{q}\tilde{q}'}$ which summarize in a compact way the couplings of the physical Higgs bosons to the squark interaction eigenstates and $R^{\tilde{q}}$ is the rotation matrix associated to the mass basis. These coupling matrices are given by

$$\begin{aligned}
C_{h\tilde{q}\tilde{q}} &= \begin{pmatrix} -\left(I_q^{3L} - Q_q s_W^2\right) m_Z^2 \sin(\beta+\alpha) + m_q^2 s_1^q & \frac{1}{2} m_q (A_q s_1^q + \mu s_2^q) \\ \frac{1}{2} m_q (A_q s_1^q + \mu s_2^q) & -Q_q s_W^2 m_Z^2 \sin(\beta+\alpha) + m_q^2 s_1^q \end{pmatrix} , \\
C_{H\tilde{q}\tilde{q}} &= \begin{pmatrix} \left(I_q^{3L} - Q_q s_W^2\right) m_Z^2 \cos(\beta+\alpha) + m_q^2 r_1^q & \frac{1}{2} m_q (A_q r_1^q + \mu r_2^q) \\ \frac{1}{2} m_q (A_q r_1^q + \mu r_2^q) & Q_q s_W^2 m_Z^2 \cos(\beta+\alpha) + m_q^2 r_1^q \end{pmatrix} , \\
C_{A\tilde{q}\tilde{q}} &= \begin{pmatrix} 0 & -\frac{1}{2} m_q \left[\mu + A_q (\tan\beta)^{-2I_3^q}\right] \\ \frac{1}{2} m_q \left[\mu + A_q (\tan\beta)^{-2I_3^q}\right] & 0 \end{pmatrix} , \\
C_{H^\pm t\tilde{b}} &= \frac{1}{\sqrt{2}} \begin{pmatrix} m_d^2 \tan\beta + m_u^2 \cot\beta - m_W^2 \sin 2\beta & m_d \left(A_d \tan\beta + \mu\right) \\ m_u \left(A_u \cot\beta + \mu\right) & m_u \, m_d (\tan\beta + \cot\beta) \end{pmatrix} ,
\end{aligned} \tag{5.198}$$

with the coefficients $r_{1/2}^{u/q}$ and $s_{1/2}^{u/q}$ defined by

$$s_1^u = -r_2^u = \frac{\cos\alpha}{\sin\beta} \; , \quad s_2^u = r_1^u = \frac{\sin\alpha}{\sin\beta} \; , \quad s_1^d = r_2^d = -\frac{\sin\alpha}{\cos\beta} \; , \quad s_2^d = -r_1^d = \frac{\cos\alpha}{\cos\beta} \tag{5.199}$$

In the case of the Higgs boson couplings to sleptons we have just to consider the down-type squark case (with $m_l = m_q$). At least in the case of the stop and sbottom squark these couplings can be large since they involve terms respectively proportional to m_t^2,$m_t A_t$ and $m_b \tan\beta$; this last term can be strongly enhanced for large values of $\tan\beta$. In the limit $M_A \gg m_Z$, the lightest CP-even Higgs boson couples to the stops through a simple expression given by (normalized by g/m_W)

$$\begin{aligned} g_{h\tilde{t}_1\tilde{t}_2} &= \cos 2\beta \sin 2\theta_t m_Z^2 \left[\frac{2}{3}s_W^2 - \frac{1}{4}\right] + \frac{1}{2}\cos 2\theta_t m_t X_t \ , \\ g_{h\tilde{t}_1\tilde{t}_1} &= \cos 2\beta m_Z^2 \left[\frac{1}{2}\cos^2\theta_t - \frac{2}{3}s_W^2 \cos 2\theta_t\right] + m_t^2 + \frac{1}{2}\sin 2\theta_t m_t X_t \ , \\ g_{h\tilde{t}_2\tilde{t}_2} &= \cos 2\beta m_Z^2 \left[\frac{1}{2}\sin^2\theta_t - \frac{2}{3}s_W^2 \cos 2\theta_t\right] + m_t^2 - \frac{1}{2}\sin 2\theta_t m_t X_t \ . \end{aligned} \quad (5.200)$$

For sufficiently large mixing, the coupling of the lighter h Higgs to the lighter stop is strongly enhanced and can be larger than its coupling to the top quark.

5.3 Radiative corrections in the Higgs sector of the MSSM

5.3.1 Upper bound on the lightest Higgs boson mass

As we have seen until now, the MSSM has an extended Higgs sector compared to the SM, which can be described with a few parameters at tree-level and in addition its spectrum is quite constrained. More specifically, we have demonstrated that the lightest neutral CP-even Higgs boson is expected to have a mass below the Z boson mass. We approach this upper bound $M_h \simeq m_Z$ when $M_A > m_Z$ and $|\cos 2\beta| \simeq 1$ which imply large values of $\tan\beta$ ($\beta \simeq \pi/2$). In the particular case where the pseudoscalar Higgs boson is heavy (which will be analyzed in details in the following), $M_A \gg m_Z$, the mixing angle α approaches the value $\alpha \simeq \beta - \pi/2$ which has a great impact because the reduced coupling of the lightest CP-even Higgs boson to fermions tends to one i.e h is SM-like : we call this regime the decoupling limit. This lightest MSSM Higgs boson with a mass near m_Z should have been discovered already at LEP2. However, as it has been already presented in the beginning of this part devoted to supersymmetry, quantum loop effects may push upward its mass well above its tree-level upper bound. These radiative corrections would then explain why LEP2 has not observed the lightest CP-even Higgs state. In fact the SM-like h state has a significant coupling with the top quark and also to its associated supersymmetric scalar, the stop. So we are expecting potentially large loop effects which should be included in the MSSM Higgs sector description. These quantum loop corrections are quite simple to evaluate in the limits $M_A \gg m_Z$, $\tan\beta \gg 1$ and we also assume that the stop quarks are degenerated in mass i.e $m_{\tilde{t}_1} = m_{\tilde{t}_2}$ and they do not mix i.e $X_t = A_t - \mu \,\mathrm{cotan}\,\beta \ll M_S$ where we define the supersymmetric scale $M_S = \sqrt{m_{\tilde{t}_1} m_{\tilde{t}_2}}/2$. If we also make the hypothesis that $M_h \ll m_t, m_{\tilde{t}_i}$ then we can neglect the external momentum of its self-energy and in conclusion we can make use of the loop diagrams that we have already computed in Fig. 18(d)-(g), adapting them to the stop and top loops. We just need to include the tadpole contributions to the mass at one-loop, represented in Fig. 19. These tadpole terms can be arranged in the following

expression

$$\delta M_h^2\big|_{\rm tadpoles} \;=\; -\frac{3\lambda_t^2}{4\pi^2}\left[m_{\tilde t}^2\ln\left(\frac{\Lambda}{m_{\tilde t}}\right) - m_t^2\ln\left(\frac{\Lambda}{m_t}\right)\;.\right] \tag{5.201}$$

Adding this new contribution to the one derived from Eq. (3.68), one gets the following radiative correction estimate at one-loop

$$\delta M_h^2 \;=\; \frac{3v^2}{2\pi^2}m_t^4\ln\frac{M_S^2}{m_t^2}\;. \tag{5.202}$$

Consequently radiative corrections grows quadratically with the top quark mass and logarithmically with the stop masses. So corrections can be extremely large and push upward the h mass from m_Z to $M_h^{\rm max}\simeq 140$ GeV. This is the reason why LEP2 did not discovered the h boson state.

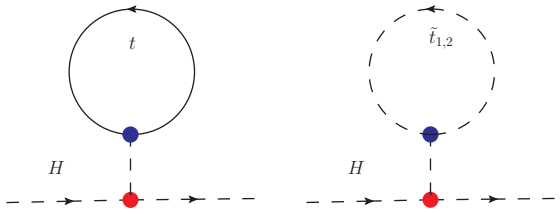

Figure 19: Tadpole contributions to the lightest Higgs boson mass at one–loop.

5.3.2 Radiative corrections on the MSSM Higgs masses

First, as an important remark, we should clarify the meaning of the physical Higgs mass when we incorporate radiative corrections. We defined the on-shell mass as the momentum squared which makes the corrected inverse propagator vanish i.e

$$q^2 - M_h^{2,tree} + \Sigma(q^2) = 0\;. \tag{5.203}$$

The correction, noted $\Sigma(q^2)$ here, corresponds to the loop self-energy improvement.

The main quantum loop effects involve the third generation of quarks and squarks through their Yukawa interaction. Thus, the parameters of interest are those which control the physical masses of the third generation squarks after mixing. We recall that for a given flavor of the left and right handed quark, q_R, q_L, there is an associated squark in the interaction basis, $\tilde q_L, \tilde q_R$. The physical mass eigenstates, $\tilde q_1, \tilde q_2$, are obtained by diagonalizing the mass matrix which mix $\tilde q_L$ and $\tilde q_R$ with each other. We basically get the matrix written in Eq. (5.174) where the parameters which trigger the mixing are, for the heavier quark generation,

$$X_{t/b} \equiv A_{t/b} - \mu\cot\beta \tag{5.204}$$

So, the main ingredients that will enter the radiative corrections are the mass terms m_f, m_{LL}, m_{RR} the trilinear terms A_t, A_b and the Higgsino mass term μ in addition to $\tan\beta$ which already enters at tree-level.

The calculations of the radiatively corrected Higgs masses in the MSSM have been important topics over several years. It exists three main methods to improve the theoretical prediction for the lighter MSSM boson h mass. One is to proceed by diagrammatic calculations, one other by renormalization group methods and the last one by effective potential methods.

Diagrammatic methods

The technique is to calculate the loop self energy diagrams. The first calculation including the one-loop $\mathcal{O}(\lambda_t^2 m_t^2)$ correction was done in Ref. [183–186]. Thus underlining the importance of loop effects on the tree-level upper bound, a huge theoretical effort has followed. The full one-loop calculations which include all the supersymmetric particle contributions, the b quark contribution and the contributions of the vector bosons have been realized in Refs. [187–191]. The logical next step was to compute the two-loop effects that now introduce the strong coupling. A partial two-loop results have been obtained in Refs. [192–194].

Renormalization group methods

This technique is that of Renormalization Group Evolution. When the supersymmetric scale, M_S, is well above the electroweak scale, we set the quartic Higgs coupling at the supersymmetric scale to the value

$$\lambda(M_S) = \frac{1}{32}\cos^2 2\beta \left(g'^2(M_S) + g^2(M_S)\right) \ . \tag{5.205}$$

The mass of h is canonically computed from its quartic coupling at the electroweak scale, which is obtained by running down $\lambda(M_S)$ through the SM RGEs. These techniques provide an efficient method for identifying the most important contributions to the radiatively corrected Higgs masses [184, 195–203].

Effective potential methods

The effective potential has been calculated at one-loop in Refs. [183, 185, 195, 204–208] and at two-loops in Refs. [209–213].

We give now an idea of this effective potential method at one-loop.

5.3.3 The one-loop effective potential approach

In this section we calculate the leading one-loop radiative corrections to the Higgs h in the framework of the effective potential. We will first consider the simpler situation where the stop masses are degenerate. Afterwards, we will include contributions from the mixing between the stops.

We start by writing the one-loop scalar potential at a generic scale Q

$$\begin{aligned} V^{(1)}(Q) &= V^{(0)}(Q) + \delta V^{(1)}(Q) \ , \\ \delta V^{(1)}(Q) &= \frac{1}{64\pi^2}\mathrm{sTr}\mathcal{M}^4(h)\left(\ln\frac{\mathcal{M}^2(h)}{Q^2} - \frac{3}{2}\right) \ , \end{aligned} \tag{5.206}$$

where we note here, $\mathcal{M}$, the mass matrix depending on the Higgs field.

Radiative corrections without stop mixing

In a first step, let us start by adding the one-loop stop correction when $m_{\tilde{t}_1} = m_{\tilde{t}_2} = m_{\tilde{t}}$. The mass of the top quark and the mass of the stops depends on the Higgs field through the relations

$$\begin{aligned} m_t &= \lambda_t^2 |h_u^0|^2 \, , \\ m_{\tilde{t}} &= \lambda_t^2 |h_u^0|^2 + \tilde{m}^2 \, . \end{aligned} \tag{5.207}$$

$\tilde{m}$ is the supersymmetric soft breaking mass term and we neglect the D-terms since they are multiplied by gauge electroweak couplings. Then, we only consider the propagation of the top quark and of the degenerated stops in the loop of Eq. 5.206. Paying attention to the correct multiplying factors we end up with

$$\delta V^{(1)}_{+t,\tilde{t}}(Q) = \frac{2}{16\pi^2}\left(-(\lambda_t^2|h_u^0|^2)^2\left[\ln\frac{\lambda_t^2|h_u^0|^2}{Q^2} - \frac{3}{2}\right] + (\lambda_t^2|h_u^0|^2 + \tilde{m}^2)^2\left[\ln\frac{(\lambda_t^2|h_u^0|^2+\tilde{m}^2)^2}{Q^2} - \frac{3}{2}\right]\right) . \tag{5.208}$$

Obviously in the case of exact supersymmetry radiative corrections vanish. Having now a different scalar potential, in order to compute the lighter Higgs boson mass one should perform exactly what we have done previously i.e minimize the scalar potential so that the electroweak symmetry occurs and compute the scalar mass. Here since there is no mixing between the stops only one of the two equations Eq. (5.153) is altered, the one corresponding to $\partial V/\partial h_u^0 = 0$. Furthermore we introduce in this extremum constraint a dependence on the generic scale Q which will be absorbed, after renormalization, by M_{H_u}. Afterwards, we can compute the second derivative of the one-loop improved scalar potential that gives the scalar mass squared matrix. Again, rotating and developing the Higgs doublet fields around their vev, one find logically modification only in the $(2,2)$ entry (corresponding to the H_u field). We get the following positive correction

$$\Delta\mathcal{M}_{22} = \frac{3\lambda_t^2 m_t^2}{4\pi^2}\ln\frac{m_{\tilde{t}}^2}{m_t^2} \tag{5.209}$$

Radiative corrections with stop mixing

We now introduce a non vanishing mixing between $\tilde{t}_R$ and $\tilde{t}_L$ by introducing a nonzero X_t. The stop mass eigenvalues now depend on both h_u^0 and h_d^0

$$m^2_{\tilde{t}_{1/2}} = \lambda_t^2|h_u^0|^2 + \frac{1}{2}\left(m^2_{\tilde{t}_L} + m^2_{\tilde{t}_R} \mp \sqrt{(m^2_{\tilde{t}_L} - m^2_{\tilde{t}_R})^2 + 4\lambda_t^2|A_t h_u^0 - \mu h_d^{0*}|^2}\right) . \tag{5.210}$$

The associated one-loop contributions to the effective potential is

$$\begin{aligned} \delta V^{(1)}_{+t,\tilde{t}_{1/2}}(Q) = \frac{3}{32\pi^2}\Bigg(&-2(\lambda_t^2|h_u^0|^2)^2\left[\ln\frac{\lambda_t^2|h_u^0|^2}{Q^2} - \frac{3}{2}\right] + m^4_{\tilde{t}_1}(h)\left[\ln\frac{m^2_{\tilde{t}_1}(h)}{Q^2} - \frac{3}{2}\right] \\ &+ m^4_{\tilde{t}_2}(h)\left[\ln\frac{m^2_{\tilde{t}_2}(h)}{Q^2} - \frac{3}{2}\right]\Bigg) . \end{aligned} \tag{5.211}$$

The two minimization conditions $\partial V/\partial h^0_{u/d} = 0$ are modified and the second derivative to the one-loop potential give the 2×2 correction mass matrix

$$\Delta\mathcal{M}_S^2 = \begin{pmatrix} \Delta\mathcal{M}^2_{11} & \Delta\mathcal{M}^2_{12} \\ \Delta\mathcal{M}^2_{12} & \Delta\mathcal{M}^2_{22} \end{pmatrix} \tag{5.212}$$

with

$$\begin{aligned}
\Delta\mathcal{M}^2_{11} &= \frac{3G_F m_t^4}{2\sqrt{2}\pi^2 \sin^2\beta}\left[\frac{\mu(X_t)}{m^2_{\tilde{t}_1}-m^2_{\tilde{t}_2}}\right]^2\left(2-\frac{m^2_{\tilde{t}_1}+m^2_{\tilde{t}_2}}{m^2_{\tilde{t}_2}-m^2_{\tilde{t}_1}}\ln\frac{m^2_{\tilde{t}_2}}{m^2_{\tilde{t}_1}}\right)\,,\\
\Delta\mathcal{M}^2_{12} &= \frac{3G_F m_t^4}{2\sqrt{2}\pi^2 \sin^2\beta}\frac{\mu X_t}{m^2_{\tilde{t}_2}-m^2_{\tilde{t}_1}}\ln\frac{m^2_{\tilde{t}_2}}{m^2_{\tilde{t}_1}}+\frac{A_t}{\mu}\Delta\mathcal{M}_{11}\,,\\
\Delta\mathcal{M}^2_{22} &= \frac{3G_F m_t^4}{\sqrt{2}\pi^2 \sin^2\beta}\left[\ln\frac{m^2_{\tilde{t}_1}m^2_{\tilde{t}_2}{}^2}{m_t}+\frac{A_t X_t}{m^2_{\tilde{t}_2}-m^2_{\tilde{t}_1}}\ln\frac{m^2_{\tilde{t}_2}}{m^2_{\tilde{t}_1}}\right]+\left(\frac{A_t}{\mu}\right)^2\Delta\mathcal{M}_{11}\,.
\end{aligned} \tag{5.213}$$

The masses of the neutral CP-even Higgs bosons will now depend on these loop corrections terms $\Delta\mathcal{M}_{ij}$.

Beyond the one-loop corrections

In the same way we can include the one loop bottom quark and sbottom contributions. Adding also the leading two-loop logarithmic corrections, corresponding to $\mathcal{O}(\lambda_t^4,\lambda_b^4)$, we obtain the compact expressions [201–203, 214]

$$\begin{aligned}
\Delta\mathcal{M}^2_{11} &\simeq -\bar{\mu}^2 x_t^2\frac{\lambda_t^4 v^2}{32\pi^2}s_\beta^2\left[1+c_{11}\ln\left(\frac{M_S^2}{m_t^2}\right)\right]-\bar{\mu}^2 a_b^2\frac{\lambda_b^4 v^2}{32\pi^2}s_\beta^2\left[1+c_{12}\ln\left(\frac{M_S^2}{m_t^2}\right)\right],\\
\Delta\mathcal{M}^2_{12} &\simeq -\bar{\mu}x_t\frac{\lambda_t^4 v^2}{32\pi^2}(6-x_t a_t)s_\beta^2\left[1+c_{31}\ln\left(\frac{M_S^2}{m_t^2}\right)\right]+\bar{\mu}^3 a_b\frac{\lambda_b^4 v^2}{32\pi^2}s_\beta^2\left[1+c_{32}\ln\left(\frac{M_S^2}{m_t^2}\right)\right],\\
\Delta\mathcal{M}^2_{22} &\simeq \frac{3\lambda_t^4 v^2}{8\pi^2}s_\beta^2\ln\left(\frac{M_S^2}{m_t^2}\right)\left[1+\frac{1}{2}c_{21}\ln\left(\frac{M_S^2}{m_t^2}\right)\right]\\
&\quad+\frac{\lambda_t^4 v^2}{32\pi^2}s_\beta^2 x_t a_t(12-x_t a_t)\left[1+c_{21}\ln\left(\frac{M_S^2}{m_t^2}\right)\right]-\bar{\mu}^4\frac{\lambda_b^4 v^2}{32\pi^2}s_\beta^2\left[1+c_{22}\ln\left(\frac{M_S^2}{m_t^2}\right)\right],
\end{aligned} \tag{5.214}$$

where $s_\beta\equiv\sin\beta$, $c_\beta\equiv\cos\beta$, and the coefficients c_{ij} are:

$$c_{ij}\equiv\frac{t_{ij}\lambda_t^2+b_{ij}\lambda_b^2-32g_3^2}{32\pi^2}\,, \tag{5.215}$$

$(t_{11},t_{12},t_{21},t_{22},t_{31},t_{32}) = (12,-4,6,-10,9,-7)$ and $(b_{11},b_{12},b_{21},b_{22},b_{31},b_{32}) = (-4,12,2,18,-1,15)$. Here $M_S^2=\frac{1}{2}(m^2_{\tilde{t}_1}+m^2_{\tilde{t}_2})$ is the average squared top squark mass. Eqs. (5.214) have been derived under the assumption that $|m^2_{\tilde{t}_1}-m^2_{\tilde{t}_2}|/(m^2_{\tilde{t}_1}+m^2_{\tilde{t}_2})\ll 1$. The $\Delta\mathcal{M}^2_{ij}$ depend also on the MSSM parameters A_t, A_b and μ that enter the off-diagonal top-squark and bottom-squark squared-mass matrices. We employ the following notation: $\bar{\mu}\equiv\mu/M_S$, $a_t\equiv A_t/M_S$, $a_b\equiv A_b/M_S$ and $x_t\equiv X_t/M_S$.

We finish here our description of the MSSM Higgs sector. We have all the needed ingredients in order to address the implications of the LHC Higgs searches for supersymmetric models.

6 Implications of a 125 GeV Higgs for supersymmetric models

6.1 Context setting

The ATLAS and CMS collaborations had released the preliminary results of their search for the Standard Model Higgs boson at the LHC on almost 5 fb^{-1} data per experiment with a center of mass energy of 7 TeV [215, 216]. While these results were not sufficient for the two experiments to make any conclusive statement, the reported excess of events over the SM background at a mass of ~ 125 GeV offered a tantalising indication that the first sign of the Higgs particle might be emerging. A Higgs particle with a mass of ≈ 125 GeV would be a triumph for the SM as the high–precision electroweak data are hinting since many years to a light Higgs boson, $M_H \lesssim 160$ GeV at the 95% confidence level [217, 218]. As it has been confirmed later, the ATLAS and CMS results have far reaching consequences for extensions of the SM and, in particular, for supersymmetric theories. As we have seen, the latter are widely considered to be the most attractive extensions as they naturally protect the Higgs mass against large radiative corrections and stabilize the hierarchy between the electroweak and Planck scales. Furthermore, they allow for gauge coupling unification and the lightest SUSY particle is a good dark matter candidate; see Refs. [181, 219] for a review.

In the minimal SUSY extension, the MSSM [181, 219], two Higgs doublet fields are required to break the electroweak symmetry, leading to the existence of five Higgs particles: two CP–even h and H, a CP–odd A and two charged $H^\pm$ particles [47, 48]. Two parameters are needed to describe the Higgs sector at the tree–level: one Higgs mass, which is generally taken to be that of the pseudoscalar boson M_A, and the ratio of vacuum expectation values of the two Higgs fields, $\tan\beta$, that is expected to lie in the range $1 \lesssim \tan\beta \lesssim 60$. At high M_A values, $M_A \gg M_Z$, one is in the so–called decoupling regime in which the neutral CP–even state h is light and has almost exactly the properties of the SM Higgs particle, i.e. its couplings to fermions and gauge bosons are the same, while the other CP–even state H and the charged Higgs boson $H^\pm$ are heavy and degenerate in mass with the pseudoscalar Higgs particle, $M_H \approx M_{H^\pm} \approx M_A$. In this regime, the Higgs sector of the MSSM thus looks almost exactly as the one of the SM with its unique Higgs particle.

There is, however, one major difference between the two cases: while in the SM the Higgs mass is essentially a free parameter (and should simply be smaller than about 1 TeV), the lightest CP–even Higgs particle in the MSSM is bounded from above and, depending on the SUSY parameters that enter the radiative corrections, it is restricted to values [47, 48, 220, 221]

$$M_h^{\rm max} \approx M_Z |\cos 2\beta| + \text{radiative corrections} \lesssim 110 - 135 \text{ GeV} \tag{6.216}$$

Hence, the requirement that the h boson mass coincides with the value of the Higgs particle "observed" at the LHC, i.e. $M_h \approx 125$ GeV, would place very strong constraints on the MSSM parameters through their contributions to the radiative corrections to the Higgs sector.

In this section, we discuss the consequences of such a value of M_h for the MSSM. We first consider the unconstrained or the phenomenological MSSM [222] in which

the relevant soft SUSY–breaking parameters are allowed to vary freely (but with some restrictions such as the absence of CP and flavour violation) and, then, constrained MSSM scenarios such as the minimal supergravity model, mSUGRA [223–226], gauge mediated, GMSB [227–231] and anomaly mediated, AMSB [232–234], supersymmetry breaking models. We also discuss the implications of such an M_h value for scenarios in which the supersymmetric spectrum is extremely heavy, the so–called split SUSY [235–237] or high–scale SUSY [238] models.

In the context of the phenomenological MSSM, we show that some scenarios which were used as benchmarks for LEP2 and Tevatron Higgs analyses and are still used at the LHC [239] are excluded if $M_h \approx 125$ GeV, while some other scenarios are severely restricted. In particular, only when the SUSY–breaking scale is very large and the mixing in the stop sector significant that one reaches this M_h value. We also show that some constrained models, such as the minimal versions of GMSB and AMSB, do not allow for a sufficiently large mass of the lighter Higgs boson and would be disfavored if the requirement $M_h \approx 125$ GeV is imposed. This requirement sets also strong constraints on the basic parameters of the mSUGRA scenario and only small areas of the parameter space would be still allowed; this is particularly true in mSUGRA versions in which one sets restrictions on the trilinear coupling. Finally, in the case of split or high–scale SUSY models, the resulting Higgs mass is in general much larger than $M_h \approx 125$ GeV and energy scales above approximately 10^5–10^8 GeV, depending on the value of $\tan\beta$, would also be disfavored.

6.2 Implications in the phenomenological MSSM

The value of the lightest CP–even Higgs boson mass $M_h^{\rm max}$ should in principle depend on all the soft SUSY–breaking parameters which enter the radiative corrections [220, 221]. In an unconstrained MSSM, there is a large number of such parameters but analyses can be performed in the so–called pMSSM [222], in which CP conservation, flavour diagonal sfermion mass and coupling matrices and universality of the first and second generations are imposed. The pMSSM involves 22 free parameters in addition to those of the SM: besides $\tan\beta$ and M_A, these are the higgsino mass parameter μ, the three gaugino mass parameters M_1, M_2 and M_3, the diagonal left– and right–handed sfermion mass parameters $m_{\tilde{f}_{L,R}}$ (5 for the third generation sfermions and 5 others for the first/second generation sfermions) and the trilinear sfermion couplings A_f (3 for the third generation and 3 others for the first/second generation sfermions). Fortunately, most of these parameters have only a marginal impact on the MSSM Higgs masses and, besides $\tan\beta$ and M_A, two of them play a major role: the SUSY breaking scale that is given in terms of the two top squark masses as $M_S = \sqrt{m_{\tilde{t}_1} m_{\tilde{t}_2}}$ and the mixing parameter in the stop sector, $X_t = A_t - \mu \cot\beta$.

The maximal value of the h mass, $M_h^{\rm max}$ is then obtained for the following choice of parameters:

i) a decoupling regime with a heavy pseudoscalar Higgs boson, $M_A \sim \mathcal{O}(\text{TeV})$;

ii) large values of the parameter $\tan\beta$, $\tan\beta \gtrsim 10$;

iii) heavy stops, i.e. large M_S and we choose $M_S = 3$ TeV as a maximal value[5];

iv) a stop trilinear coupling $X_t = \sqrt{6} M_S$, the so–called maximal mixing scenario [239].

An estimate of the upper bound can be obtained by adopting the maximal mixing scenario of Ref. [239], which is often used as a benchmark scenario in Higgs analyses. We choose however to be conservative, scaling the relevant soft SUSY–breaking parameters by a factor of three compared to Ref. [239] and using the upper limit $\tan\beta \sim 60$:

$$M_{h_{\rm bench}}^{\rm max} \; : \quad \begin{array}{c} \tan\beta = 60\,,\; M_S = M_A = 3 \text{ TeV}\,,\; A_t = A_b = \sqrt{6}\, M_S\,, \\ M_2 \simeq 2\, M_1 = |\mu| = \frac{1}{5} M_S\,,\; M_3 = 0.8\, M_S\,. \end{array} \tag{6.217}$$

For the following values of the top quark pole mass, the $\overline{\rm MS}$ bottom quark mass, the electroweak gauge boson masses as well as the electromagnetic and strong coupling constants defined at the scale M_Z, including their 1σ allowed range [218],

$$\begin{array}{c} m_t = 172.9 \pm 1,\; \bar{m}_b(\bar{m}_b) = 4.19 \pm 0.02,\; M_Z = 91.19 \pm 0.002,\; M_W = 80.42 \pm 0.003 \text{ [in GeV]} \\ \alpha(M_Z^2) = 1/127.916 \pm 0.015,\; \alpha_s(M_Z^2) = 0.1184 \pm 0.0014 \end{array} \tag{6.218}$$

we use the programs `Suspect` [240] and `Softsusy` [241] which calculate the Higgs and superparticle spectrum in the MSSM including the most up–to–date information (in particular, they implement in a similar way the full one–loop and the dominant two–loop corrections in the Higgs sector; see Ref. [242]). One obtains the maximal value of the lighter Higgs boson, $M_h^{\rm max} \simeq 134$ GeV for maximal mixing. Hence, if one assumes that the particle observed at the LHC is the lightest MSSM Higgs boson h, there is a significant portion of the pMSSM parameter space which could match the observed mass of $M_h \approx 125$ GeV in this scenario. However, in this case either $\tan\beta$ or the SUSY scale M_S should be much lower than in Eq. (7.228).

In contrast, in the scenarios of no–mixing $A_t \approx A_b \approx 0$ and typical mixing $A_t \approx A_b \approx M_S$ (with all other parameters left as in Eq. (7.228) above) that are also used as benchmarks [239], one obtains much smaller $M_h^{\rm max}$ values than compared to maximal mixing, $M_h^{\rm max} \simeq 121$ GeV and $M_h^{\rm max} \simeq 125$ for, respectively, no–mixing and typical mixing. Thus, if $M_h \approx 125$ GeV, the no–mixing scenario is entirely ruled out, while only a small fraction of the typical-mixing scenario parameter space, with high $\tan\beta$ and M_S values, would survive.

The mass bounds above are not yet fully optimised and $M_h^{\rm max}$ values that are larger by a few (1 or 2) GeV can be obtained by varying in a reasonable range the SUSY parameters entering the radiative corrections and add an estimated theoretical uncertainty[6] of about 1 GeV. To obtain a more precise determination of $M_h^{\rm max}$ in the pMSSM, we have again used the programs `Softsusy` and `Suspect` to perform a flat scan of the pMSSM parameter space by allowing its 22 input parameters to vary in an uncorrelated

[5] This value for M_S would lead to an "acceptable" fine–tuning and would correspond to squark masses of about 3 TeV, which is close to the maximal value at which these particles can be detected at the 14 TeV LHC.

[6] The theoretical uncertainties in the determination of M_h should be small as the three–loop corrections to M_h turn out to be rather tiny, being less than 1 GeV [243]. Note that our $M_h^{\rm max}$ values are slightly smaller than the ones obtained in Ref. [242] (despite of the higher M_S used here) because of the different top quark mass.

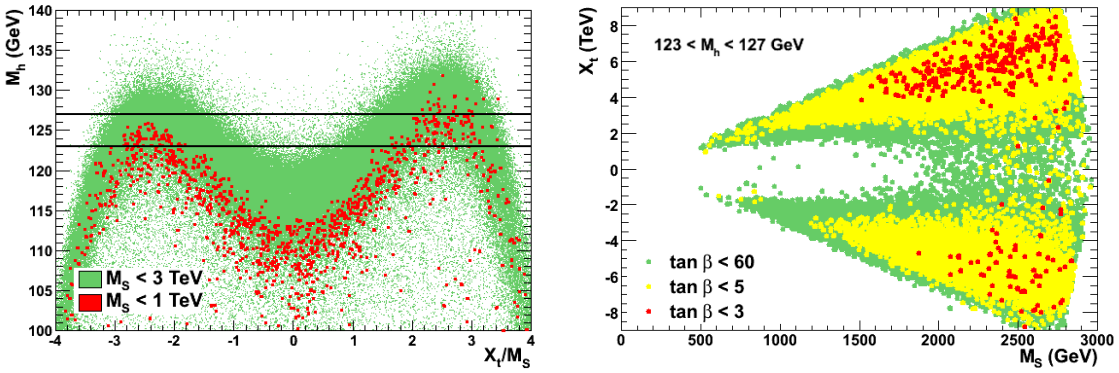

Figure 20: The maximal value of the h boson mass as a function of X_t/M_S in the pMSSM when all other soft SUSY–breaking parameters and $\tan\beta$ are scanned in the range Eq. (6.219) (left) and the contours for 123< M_h <127 GeV in the $[M_S, X_t]$ plane for some selected range of $\tan\beta$ values (right).

way in the following domains:

$$1 \leq \tan\beta \leq 60\,,\ 50\ \text{GeV} \leq M_A \leq 3\ \text{TeV}\,,\ -9\ \text{TeV} \leq A_f \leq 9\ \text{TeV}\,,$$
$$50\ \text{GeV} \leq m_{\tilde{f}_L}, m_{\tilde{f}_R}, M_3 \leq 3\ \text{TeV}\,,\ 50\ \text{GeV} \leq M_1, M_2, |\mu| \leq 1.5\ \text{TeV}. \quad (6.219)$$

We have discarded points in the parameter space that lead to a non–viable spectrum (such as charge and colour breaking minima which imposes the constraint $A_t/M_S \lesssim 3$) or to unrealistic Higgs masses (such as large $(m_{\tilde{g}}/m_{\tilde{t}_{1,2}})^2$ terms that spoil the radiative corrections to M_h [242]). We select the Higgs mass for which 99% of the scan points give a value smaller than it. The results are shown in Fig. 20 where, in the left–hand side, the obtained maximal value of the h boson mass $M_h^{\rm max}$ is displayed as a function of the ratio of parameters X_t/M_S. The resulting values are confronted to the mass range

$$123\ \text{GeV} \leq M_h \leq 127\ \text{GeV} \quad (6.220)$$

where the upper limit corresponds to the 95% confidence level bound reported by the CMS collaboration [215, 216], once the parametric uncertainties from the SM inputs given in Eq. (6.218) and the theoretical uncertainties in the determination of M_h are included. Hence, only the scenarios with large X_t/M_S values and, in particular, those close to the maximal mixing scenario $A_t/M_S \approx \sqrt{6}$ survive (see also Refs. [244, 245]). The no–mixing scenario is ruled out for $M_S \lesssim 3$ TeV, while the typical mixing scenario needs large M_S and moderate to large $\tan\beta$ values. We obtain $M_h^{\rm max}$=136, 123 and 126 GeV in, the maximal, zero and typical mixing scenarios, respectively[7].

The right–hand side of Fig. 20 shows the contours in the $[M_S, X_t]$ plane where we obtain the mass range 123 GeV $< M_h <$ 127 GeV from our pMSSM scan with $X_t/M_S \lesssim 3$; the regions in which $\tan\beta \lesssim 3, 5$ and 60 are highlighted. One sees again that a large part of the parameter space is excluded if the Higgs mass constraint is imposed[8].

[7]We have checked that the program `FeynHiggs` [246] gives comparable values for M_h within ≈ 2 GeV which we consider to be our uncertainty as in Eq. (6.220).

[8]Note that the $M_h^{\rm max}$ values given above are obtained with a heavy superparticle spectrum, for which the constraints from flavour physics and sparticle searches are evaded, and in the decoupling limit in

6.3 Implications for constrained MSSM scenarios

In constrained MSSM scenarios the various soft SUSY–breaking parameters obey a number of universal boundary conditions at a high energy scale such as the GUT scale, thus reducing the number of basic input parameters to a handful. These inputs are evolved via the MSSM renormalisation group equations down to the low energy scale M_S where the conditions of proper electroweak symmetry breaking (EWSB) are imposed. The Higgs and superparticle spectrum is calculated, including the important radiative corrections. Three classes of such models have been introduced previously:

– The minimal supergravity, mSUGRA, model [223–226], in which SUSY–breaking is assumed to occur in a hidden sector which communicates with the visible sector only via flavour-blind gravitational interactions, leading to universal soft breaking terms. Besides the scale $M_{\rm GUT}$ which is derived from the unification of the three gauge coupling constants, mSUGRA has only four free parameters plus the sign of μ: $\tan\beta$ defined at the EWSB scale and $m_0, m_{1/2}, A_0$ which are respectively, the common soft terms of all scalar masses, gaugino masses and trilinear scalar interactions, all defined at $M_{\rm GUT}$.

– The gauge mediated SUSY–breaking, GMSB, model [227–231] in which SUSY–breaking is communicated to the visible sector via gauge interactions. The basic parameters of the minimal model are, besides $\tan\beta$ and sign(μ), the messenger field mass scale $M_{\rm mess}$, the number of SU(5) representations of the messenger fields $N_{\rm mess}$ and the SUSY–breaking scale in the visible sector Λ. To that, one adds the mass of the LSP gravitino which does not play any role here.

– The anomaly mediated SUSY–breaking, AMSB, model [232–234] in which SUSY–breaking is communicated to the visible sector via a super-Weyl anomaly. In the minimal AMSB version, there are three basic parameters in addition to sign(μ): $\tan\beta$, a universal parameter m_0 that contributes to the scalar masses at the GUT scale and the gravitino mass $m_{3/2}$.

In the case of the mSUGRA scenario, we will in fact study four special cases:

– The no-scale scenario with the requirement $m_0 \approx A_0 \approx 0$ [248–251]. This model leads to a viable spectrum compatible with all present experimental constraints and with light staus for moderate $m_{1/2}$ and sufficiently high $\tan\beta$ values; the mass of the gravitino (the lightest SUSY particle) is a free parameter and can be adjusted to provide the right amount of dark matter.

– A model with $m_0 \approx 0$ and $A_0 \approx -\frac{1}{4}m_{1/2}$ which, approximately, corresponds to the constrained next-to–MSSM (cNMSSM) [252–254] in which a singlet Higgs superfield is added to the two doublet superfields of the MSSM, whose components however mostly decouple from the rest of the spectrum. In this model, the requirement of a good singlino

which the h production cross sections and the decay branching ratios are those of the SM Higgs boson. However, we also searched for points in the parameter space in which the boson with mass $\simeq 125$ GeV is the heavier CP–even H^0 boson which corresponds to values of M_A of order 100 GeV. Among the $\approx 10^6$ valid MSSM points of the scan, only $\approx 1.5 \times 10^{-4}$ correspond to this scenario. However, if we impose that the H^0 cross sections times branching ratios are compatible with the SM values within a factor of 2 and include the constraints from MSSM Higgs searches in the $\tau^+\tau^-$ channel, only $\approx 4 \times 10^{-5}$ of the points survive. These are all excluded once the $b \to s\gamma$ and $B_s \to \mu^+\mu^-$ constraints are imposed. A detailed study of the pMSSM Higgs sector including the dark matter and flavour constraints as well as LHC Higgs and SUSY search limits is presented in Refs. [245, 247].

dark matter candidate imposes $\tan\beta \gg 1$ and the only relevant free parameter is thus $m_{1/2}$ [252–254].

– A model with $A_0 \approx -m_0$ which corresponds to a very constrained MSSM (VCMSSM) similar to the one discussed in Ref. [255] for input values of the B_0 parameter close to zero.

– The non–universal Higgs mass model (NUHM) in which the universal soft SUSY–breaking scalar mass terms are different for the sfermions and for the two Higgs doublet fields [256–259]. We will work in the general case in which, besides the four mSUGRA basic continuous inputs, there are two additional parameters[9] which can be taken to be M_A and μ.

In contrast to the pMSSM, the various parameters which enter the radiative corrections to the MSSM Higgs sector are not all independent in constrained scenarios as a consequence of the relations between SUSY breaking parameters that are set at the high–energy scale and the requirement that electroweak symmetry breaking is triggered radiatively for each set of input parameters which leads to additional constraints. Hence, it is not possible to freely tune the relevant weak–scale parameters to obtain the maximal value of M_h given previously. In order to obtain a reliable determination of $M_h^{\rm max}$ in a given constrained SUSY scenario, it is necessary to scan through the allowed range of values for all relevant SUSY parameters.

Following the analysis performed in Ref. [242], we adopt the ranges for the input parameters of the considered mSUGRA, GMSB and AMSB scenarios:

$$\begin{array}{rccc}
\text{mSUGRA:} & 50\ \text{GeV} \leq m_0 \leq 3\ \text{TeV}, & 50\ \text{GeV} \leq m_{1/2} \leq 3\ \text{TeV}, & |A_0| \leq 9\ \text{TeV}; \\
\text{GMSB:} & 10\ \text{TeV} \leq \Lambda \leq 1000\ \text{TeV}, & 1 \leq M_{\rm mess}/\Lambda \leq 10^{11}, & N_{\rm mess} = 1; \\
\text{AMSB:} & 1\ \text{TeV} \leq m_{3/2} \leq 100\ \text{TeV}, & 50\ \text{GeV} \leq m_0 \leq 3\ \text{TeV}. &
\end{array}$$

Moreover, in the three cases we allow for both signs of μ, require $1 \leq \tan\beta \leq 60$ and, to avoid the need for excessive fine–tuning in the EWSB conditions, impose an additional bound on the weak–scale parameters, i.e. $M_S = M_{\rm EWSB} = \sqrt{m_{\tilde{t}_1} m_{\tilde{t}_2}} < 3$ TeV.

Using the programs `Softsusy` and `Suspect`, we have performed a full scan of the GMSB, AMSB and mSUGRA scenarios, including the four options "no-scale", "cNMSSM", "VCMSSM" and "NUHM" in the later case. Using the SM inputs of Eq. (6.218) and varying the basic SUSY parameters of the various models in the ranges described above, we have determined the maximal M_h value in each scenario. The results for $M_h^{\rm max}$ are shown in Fig. 21 as a function of $\tan\beta$, the input parameter that is common to all models. The highest M_h values, defined as that which have 99% of the scan points below it, for any $\tan\beta$ value, are summarised in Table 14; one needs to add ≈ 1 GeV to take into account the uncertainties in the SM inputs Eq. (6.218).

In all cases, the maximal M_h value is obtained for $\tan\beta$ around 20. We observe that in the adopted parameter space of the models and with the central values of the SM inputs, the upper h mass value (rounded to the upper half GeV) is $M_h^{\rm max} = 121$ GeV in AMSB, i.e. much less that 125 GeV, while in the GMSB scenario one has $M_h^{\rm max} =$

[9] This scenario corresponds to the NUHM2 discussed e.g. in Ref. [255]; the model NUHM1 also discussed in Refs. [255–259] and which has only one additional parameter is simply a special case of our NUHM scenario.

model	AMSB	GMSB	mSUGRA	no-scale	cNMSSM	VCMSSM	NUHM
$M_h^{\max}$	121.0	121.5	128.0	123.0	123.5	124.5	128.5

Table 14: Maximal h^0 boson mass (in GeV) in the various constrained MSSM scenarios when scanning over all the input parameters in the ranges described in the text.

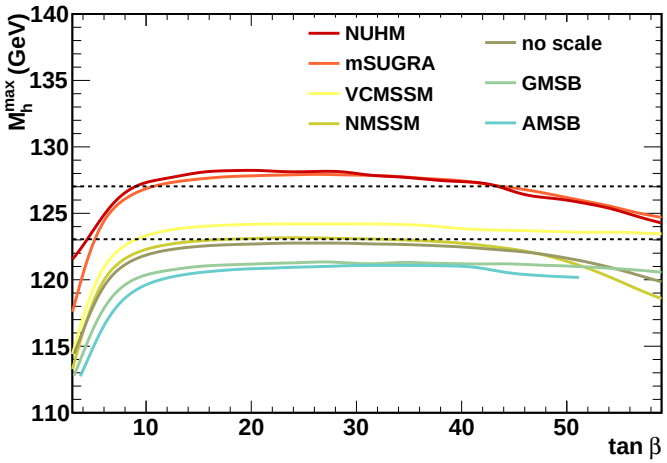

Figure 21: The maximal value of the h mass defined as the value for which 99% of the scan points have a mass smaller than it, shown as a function of $\tan\beta$ for the various constrained MSSM models.

121.5 GeV. Thus, clearly, the two scenarios are disfavoured if the lightest CP–even Higgs particle has indeed a mass in the range $123 < M_h < 127$ GeV. In the case of mSUGRA, we obtain a maximal value $M_h^{\max} = 128$ GeV and, thus, some parameter space of the model would still survive the M_h constraint.

The upper bound on M_h in these scenarios can be qualitatively understood by considering in each model the allowed values of the trilinear coupling A_t, which essentially determines the stop mixing parameter X_t and thus the value of M_h for a given scale M_S. In GMSB, one has $A_t \approx 0$ at relatively low scales and its magnitude does not significantly increase in the evolution down to the scale M_S; this implies that we are almost in the no–mixing scenario which gives a low value of M_h as can be seen from Fig. 20. In AMSB, one has a non-zero A_t that is fully predicted at any renormalisation scale in terms of the Yukawa and gauge couplings; however, the ratio A_t/M_S with M_S determined from the overall SUSY breaking scale $m_{3/2}$ turns out to be rather small, implying again that we are close to the no–mixing scenario. Finally, in the mSUGRA model, since we have allowed A_t to vary in a wide range as $|A_0| \leq 9$ TeV, one can get a large A_t/M_S ratio which leads to a heavier Higgs particle. However, one cannot easily reach A_t values such that $X_t/M_S \approx \sqrt{6}$ so that we are not in the maximal–mixing scenario and the higher upper bound on M_h in the pMSSM is not reached.

In turn, in two particular cases of mSUGRA that we have discussed in addition, the "no–scale" and the "approximate cNMSSM" scenarios, the upper bound on M_h is much lower than in the more general mSUGRA case and, in fact, barely reaches the value $M_h \approx 123$ GeV. The main reason is that these scenarios involve small values of A_0 at the GUT scale, $A_0 \approx 0$ for no–scale and $A_0 \approx -\frac{1}{4}m_{1/2}$ for the cNMSSM. One then obtains A_t values at the weak scale that are too low to generate a significant stop

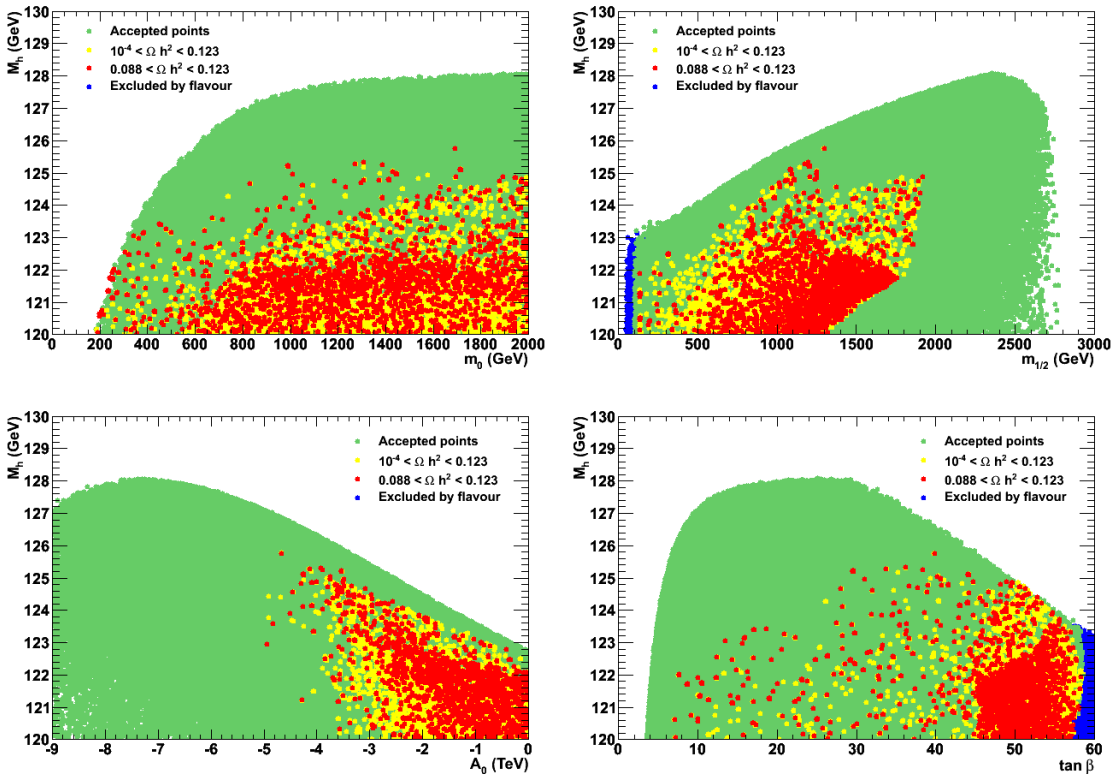

Figure 22: The value of M_h as a function of one mSUGRA continuous parameter when a scan is performed on the other parameters. The constraints from Higgs and SUSY searches at the LHC are included and the impact of flavour ($b \to s\gamma, B_s \to \mu^+\mu^-$, $B \to \tau\nu$) and DM constraints are shown.

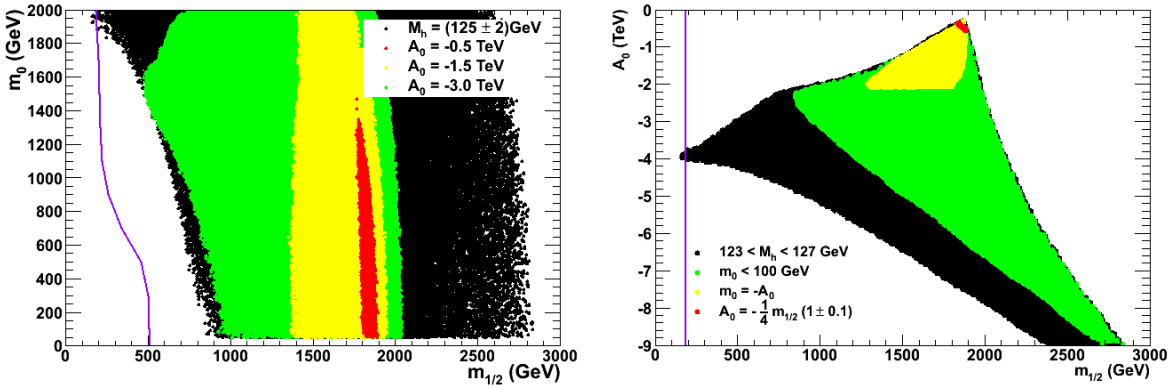

Figure 23: Contours in which $123 < M_h < 127$ GeV, resulting of a full scan of the mSUGRA parameter but for particular choices of the inputs A_0 (left) and m_0 (right). The lower bound from LHC searches of SUSY strongly interacting particles in the fully hadronic channel with 1 fb^{-1} data [260] is shown by a continuous line.

mixing and, hence, one is again close to the no–mixing scenario. Thus, only a very small fraction of the parameter space of these two sub–classes of the mSUGRA model survive (in fact, those leading to the $M_h^{\rm max}$ value) if we impose $123 < M_h < 127$ GeV. These models hence should have a very heavy spectrum as a value $M_S \gtrsim 3$ TeV is required to increase $M_h^{\rm max}$. In the VCMSSM, $M_h \simeq 124.5$ GeV can be reached as $|A_0|$ can be large for large m_0, $A_0 \approx -m_0$, allowing at least for typical mixing.

Finally, since the NUHM is more general than mSUGRA as we have two more free parameters, the $[\tan\beta, M_h]$ area shown in Fig. 21 is larger than in the mSUGRA case. However, since we are in the decoupling regime and the value of M_A does not matter much (as long as it is larger than a few hundred GeV) and the key weak–scale parameters entering the determination of M_h, i.e. $\tan\beta, M_S$ and A_t are approximately the same in both models, one obtains a bound $M_h^{\rm max}$ that is only slightly higher in NUHM compared to mSUGRA. Thus, the same discussion above on the mSUGRA scenario, holds also true in the NUHM case.

In the case of the "general" mSUGRA model, we show in Figs. 22 and 23 some contours in the parameter space which highlight some of the points discussed above. Following Refs. [261–263] where the relevant details can be found, constraints[10] from the LHC in Higgs [247] and superparticle searches [260] and the measurement of $B_s \to \mu^+\mu^-$ as well as the requirement of a correct cosmological density as required by WMAP have been implemented. We use the program `SuperIso Relic` [264, 265] for the calculation of dark matter relic density and flavour constraints.

6.4 Split and high–scale SUSY models

In the preceding discussion, we have always assumed that the SUSY–breaking scale is relatively low, $M_S \lesssim 3$ TeV, which implies that some of the supersymmetric and heavier Higgs particles could be observed at the LHC or at some other TeV collider. However, as already mentioned, this choice is mainly dictated by fine–tuning considerations which are a rather subjective matter as there is no compelling criterion to quantify the acceptable amount of tuning. One could well have a very large value of M_S which implies that, except for the lightest h boson, no other scalar particle is accessible at the LHC or at any foreseen collider.

This argument has been advocated to construct the so–called split SUSY scenario [235–237] in which the soft SUSY–breaking mass terms for all the scalars of the theory, except for one Higgs doublet, are extremely large, i.e. their common value M_S is such that $M_S \gg 1$ TeV (such a situation occurs e.g. in some string motivated models, see Refs. [266–268]). Instead, the mass parameters for the spin–$\frac{1}{2}$ particles, the gauginos and the higgsinos, are left in the vicinity of the EWSB scale, allowing for a solution to the dark matter problem and a successful gauge coupling unification, the two other SUSY virtues. The split SUSY models are much more predictive than the usual pMSSM as only a handful parameters are needed to describe the low energy theory. Besides the common value M_S of the soft SUSY-breaking sfermion and one Higgs mass parameters, the basic inputs are essentially the three gaugino masses M_1, M_2, M_3 (which can be unified to a common value at $M_{\rm GUT}$ as in mSUGRA), the higgsino parameter μ and $\tan\beta$. The trilinear couplings A_f, which are expected to have values close to the EWSB scale, and thus much smaller than M_S, will in general play a negligible role.

Concerning the Higgs sector, the main feature of split SUSY is that at the high scale M_S, the boundary condition on the quartic Higgs coupling of the theory is determined

[10] All the points in Fig. 4 correspond to the decoupling regime of the MSSM Higgs sector and, hence, to an h boson with SM cross sections and branching ratios. Furthermore, as the resulting SUSY spectrum for $M_h = 125 \pm 2$ GeV is rather heavy in constrained scenarios, one obtains very small contributions to $(g-2)_\mu$.

by SUSY:

$$\lambda(M_S) = \frac{1}{4}\left[g^2(M_S) + g'^2(M_S)\right]\, \cos^2 2\beta \; . \tag{6.221}$$

where g and g' are the SU(2) and U(1) gauge couplings. Here, $\tan\beta$ is not a parameter of the low-energy effective theory: it enters only the boundary condition above and cannot be interpreted as the ratio of two Higgs vacuum expectation values. In this case, it should not be assumed to be larger than unity as usual and will indeed adopt the choice $1/60 \leq \tan\beta \leq 60$.

If the scalars are very heavy, they will lead to radiative corrections in the Higgs sector that are significantly enhanced by large logarithms, $\log(M_{\rm EWSB}/M_S)$, where $M_{\rm EWSB}$ is the scale set by the gaugino and higgsino masses. In order to have reliable predictions, one has to properly decouple the heavy states from the low-energy theory and resum the large logarithmic corrections; in addition, the radiative corrections due to the gauginos and the higgsinos have to be implemented. Following the early work of Refs. [235–237], a comprehensive study of the split SUSY spectrum has been performed in Ref. [269]; see also Ref. [270] that appeared recently. All the features of the model have been implemented in the Fortran code `SuSpect` upon which the numerical analysis presented here is based.

One can adopt an even more radical attitude than in the split SUSY case and assume that the gauginos and higgsinos are also very heavy, with a mass close to the scale M_S; this is the case in the so–called high–scale SUSY model [238]. Here, one abandons not only the SUSY solution to the fine-tuning problem but also the solution to the dark matter problem by means of the LSP and the successful unification of the gauge coupling constants. However, there will still be a trace of SUSY at low energy: the matching of the SUSY and the low–energy theories is indeed encoded in the Higgs quartic coupling λ given by Eq. (6.221). Hence, even if broken at very high scales, SUSY would still lead to a "light" Higgs boson whose mass will contain information on M_S and $\tan\beta$.

The treatment of the Higgs sector of the high–scale SUSY scenario is similar to that of split SUSY: one simply needs to decouple the gauginos and higgsinos from the low energy spectrum (in particular remove their contributions to the renormalisation group evolution of the gauge and Yukawa couplings and to the radiative corrections to the h boson mass) and set their masses to M_S. We have adapted the version of the program `Suspect` which handles the split SUSY case to also cover the case where $M_1 \approx M_2 \approx M_3 \approx |\mu| \approx M_S$. Using this program, we have performed a scan in the $[\tan\beta, M_S]$ plane to determine the value of M_h in the split SUSY and high–scale SUSY scenarios. The values given in Eq. (6.218) for the SM input parameters have been adopted and, in the case of split SUSY, we have chosen $M_{\rm EWSB} \approx \sqrt{|M_2\mu|} \approx 246$ GeV for the low scale. The results are shown in Fig. 24. In this figure M_h is displayed as a function of M_S for selected values of $\tan\beta$ in split and heavy–scale SUSY.

As expected, the maximal M_h values are obtained at high $\tan\beta$ and M_S values and, at the scale $M_S \approx 10^{16}$ GeV at which the couplings g and g' approximately unify in the split SUSY scenario, one obtains $M_h \approx 160$ GeV for the higher $\tan\beta = 50$ value[11]. We

[11] Our result is different by a few GeV from that given in Ref. [270] as the gaugino/higgsino two loop RGEs were used in that reference while we include only the one–loop RGEs, and different choices for scales have been adopted. This points to sizable theoretical uncertainties that we are presently analysing.

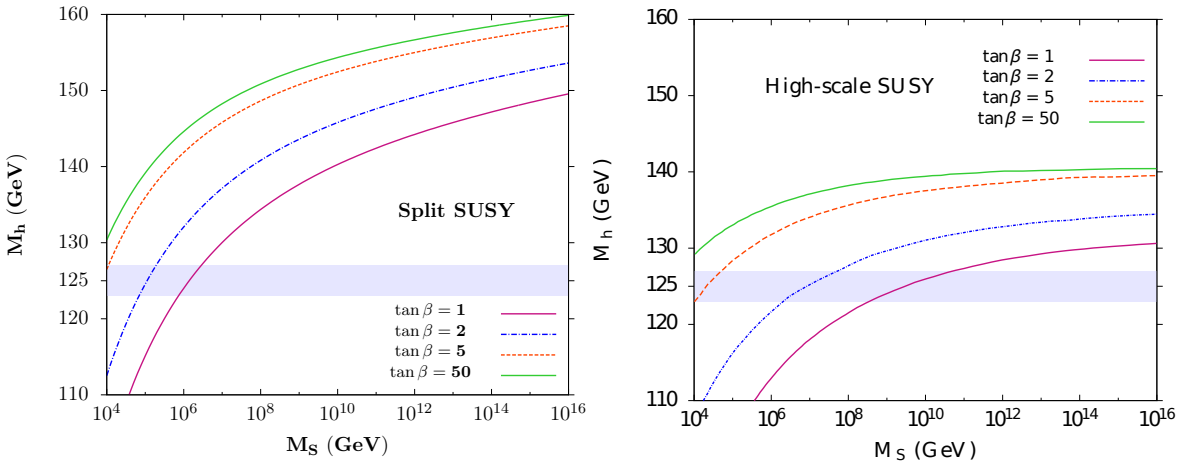

Figure 24: The value of M_h as a function of M_S for several values of $\tan\beta = 1, 2, 5, 50$ in the split SUSY (left) and high–scale SUSY (right) scenarios.

do not include the error bands in the SM inputs which would lead to an uncertainty of about 2 GeV on M_h, mainly due to the 1 GeV uncertainty on the top quark mass. In addition, we have assumed the zero–mixing scenario as the parameter A_t is expected to be much smaller than M_S; this approximation might not be valid for M_S values below 10 TeV and a maximal mixing $A_t/M_S = \sqrt{6}$ would increase the Higgs mass value by up to 10 GeV at $M_S = \mathcal{O}(1$ TeV) as was discussed earlier for the pMSSM. In the high–scale SUSY scenario, we obtain a value $M_h \approx 142$ GeV (with again an uncertainty of approximately 2 GeV from the top mass) for high $\tan\beta$ values and at the unification scale $M_S \approx 10^{14}$ GeV as in Refs. [238, 270]. Much smaller M_h values, in the 120 GeV range, can be obtained for lower scales and $\tan\beta$.

Hence, the requirement that the Higgs boson mass is in the range $123 < M_h < 127$ GeV imposes strong constraints on the parameters of these two models. For this Higgs mass range, very large scales are needed for $\tan\beta \approx 1$ in the split (high–scale) SUSY scenario, while scales not too far from $M_S \approx 10^4$ GeV are required at high $\tan\beta$. Thus, even in these extreme scenarios, SUSY should manifest itself at scales much below $M_{\rm GUT}$ if $M_h \approx 125$ GeV.

6.5 Status of supersymmetric models after the 125 GeV Higgs discovery

In conclusion, we have shown that in the phenomenological MSSM, strong restrictions can be set on the mixing in the top sector and, for instance, the no–mixing scenario is excluded unless the supersymmetry breaking scale is extremely large, $M_S \gg 1$ TeV, while the maximal mixing scenario is disfavored for large M_S and $\tan\beta$ values.

In constrained MSSM scenarios, the impact is even stronger. Several scenarios, such as minimal AMSB and GMSB are disfavored as they lead to a too light h particle. In the mSUGRA case, including the possibility that the Higgs mass parameters are non–universal, the allowed part of the parameter space should have large stop masses and A_0 values. In more constrained versions of this model such as the "no–scale" and approximate "cNMSSM" scenarios, only a very small portion of the parameter space is allowed by the Higgs mass bound.

Finally, significant areas of the parameter space of models with large M_S values leading to very heavy supersymmetric particles, such as split SUSY or high–scale SUSY, can also be excluded as, in turn, they tend to predict a too heavy Higgs particle with $M_h \gtrsim 125$ GeV.

One of the main implications of the LHC discovery of a Higgs boson with a mass $M_h \approx 125$ GeV is that the scale of supersymmetry–breaking in the MSSM might be rather high, $M_S \gg M_Z$. In the next section, we consider the high M_S regime and study the spectrum of the extended Higgs sector of the MSSM, including the LHC constraints on the mass and the rates of the observed light h state. In particular, we show that in a simplified model that approximates the important radiative corrections, the unknown scale M_S (and some other leading SUSY parameters) can be traded against the measured value of M_h. One would be then essentially left with only two free parameters to describe the Higgs sector, $\tan\beta$ and the pseudoscalar Higgs mass M_A, even at higher orders. The main phenomenological consequence of these high M_S values is to reopen the low $\tan\beta$ region, $\tan\beta \lesssim 3$–5, which was for a long time buried under the LEP constraint on the lightest h mass when a low SUSY scale was assumed. We show that, in this case, the heavier MSSM neutral H/A and charged $H^\pm$ states can be searched for in a variety of interesting final states such as decays into gauge and lighter Higgs bosons (in pairs on in mixed states) and decays into heavy top quarks. Examples of sensitivity on the $[\tan\beta, M_A]$ parameter space at the LHC in these channels will also be discussed.

7 The MSSM Higgs sector at a high M_{SUSY}: reopening the low $\tan\beta$ regime and heavy Higgs searches

7.1 Motivations

The Higgs observation at the LHC with a mass of approximately 125-126 GeV first gave support to the MSSM in which the lightest CP–even h boson was predicted to have a mass less than ≈ 130 GeV [220, 242, 271]. An annoying problem is that the measured mass value is too close to the predicted upper limit on M_h in the MSSM, suggesting that the SUSY scale is rather high, $M_S \gtrsim 1$ TeV; as we have just seen it in our previous discussion. The fact that M_S is large is backed up by direct SUSY particle searches, which set limits of the order of 1 TeV for the strongly interacting superparticles [272]. In addition, with the precision measurements of its couplings to fermions and gauge bosons, the Higgs state looked more and more SM–like, as no significant deviations from the SM expectation is presently observed [272]. Although this had to be expected since, as is the case in many extended Higgs sectors, there is a decoupling limit [273] in which all the heavier Higgs particles decouple from the SM spectrum and one is left only with the lightest h state which has almost the SM properties, this is again unfortunate. Tests of the properties of the observed Higgs state have to be pursued with more accuracy in order to pin down small deviations from the SM prediction.

An equally important way to probe the MSSM is to search for the direct manifestation of the heavier H, A and $H^\pm$ states. These searches are presently conducted by the ATLAS and CMS collaborations in the regime where $\tan\beta$, the ratio of the vacuum expectations values of the two Higgs fields, is very large, $\tan\beta \equiv v_2/v_1 \gtrsim 5$–$10$, which significantly enhances the Higgs production rates at the LHC. The regime with low $\tan\beta$, $\tan\beta \lesssim 3$–5, is ignored, the main reason being that if the SUSY scale should not exceed $M_S \approx 3$ TeV to have a still acceptable fine–tuning in the model [274], the h mass is too low and does not match the observed value. More precisely, this $\tan\beta$ region was excluded by the negative Higgs searches that were performed at the ancestor of the LHC, the LEP collider [275].

In this section, we reopen this low $\tan\beta$ region by simply relaxing the usual assumption that the SUSY scale should be in the vicinity of 1 TeV. In fact, many scenarios with a very large scale M_S have been considered in the recent years, the most popular ones being split–SUSY [235–237] and high–scale SUSY [238] which have been detailed in the previous section. In these constructions, the SUSY solution to the hierarchy problem is abandoned and the masses of all the scalars of the theory (and eventually also those of the spin–$\frac{1}{2}$ superparticles in high–scale SUSY) are set to very high values, $M_S \gg M_Z$. Hence, all the sfermions and Higgs bosons are very heavy, except for a light SM–like Higgs boson whose mass can be as low as $M_h \approx 120$ GeV even if $\tan\beta$ is very close to unity. In fact, for this purpose, the scale M_S needs not to be extremely high, for instance close to the unification scale as in the original scenarii of Refs. [235–238], and values of M_S of order 10 to 100 TeV would be sufficient.

In addition, one may assume that only the sfermions are very heavy and not the Higgs particles, as it would be the case in non–universal Higgs models where the soft–SUSY breaking mass parameters for the sfermion and the two Higgs doublet fields are disconnected [255–259]. One would have then a scenario in which the entire MSSM

Higgs sector is kept at the electroweak scale, while the sfermions are pushed to the high scale. Such scenarios are also being considered [276–278] and they might occur in many theoretical constructions.

A first important aspect that we will address now is the treatment of the radiative corrections in the Higgs sector and the derivation of the superparticle and Higgs spectrum in these high scale scenarios. It is well known that for M_S values in the multi–TeV range, the MSSM spectrum cannot be obtained in a reliable way using the usual RGE codes that incorporate the higher order effects [240, 241, 279, 280]: one has first to decouple properly the heavy particles and to resum the large logarithmic contributions. Such a program has been performed in the case where $M_A \approx M_S \gg M_Z$ and the results have been implemented in one of the RGE codes [269]. In the absence of such a tool for $M_S \gg M_A \approx M_Z$ (that is under development [281]), we will adopt the simple approach where the radiative corrections in the Higgs sector are approximated by the dominant contribution in the top and stop sector, which involves the logarithm of the scale M_S and the stop mixing parameter [183, 185, 186]. We will show that, in this approach, the situation simplifies to the extent that one can simply trade the dominant radiative correction against the actual value of the mass of the lighter h boson that has been measured at the LHC to be $M_h \approx 126$ GeV. An approach that is similar in spirit has also been advocated in Ref. [282, 283].

One would then deal with a very simple post–h discovery model in which, to a very good approximation, there are only two input parameters in the Higgs sector, M_A and $\tan\beta$ which can take any value (in particular low values $\tan\beta \approx 1$ and $M_A \approx 100$ GeV unless they are excluded by the measurements of the h properties at the LHC) with the mass M_h fixed to its measured value. If one is mainly concerned with the MSSM Higgs sector, this allows to perform rather model–independent studies of this sector.

We should note that while the working approximation for the radiative corrections to Higgs sector is important for the determination of the correct value of M_S (and eventually some other supersymmetric parameters such as the mixing in the stop sector), it has little impact on Higgs phenomenology, i.e. on the MSSM Higgs masses and couplings.

The reopening of the low $\tan\beta$ region allows then to consider a plethora of very interesting Higgs channels to be investigated at the LHC: heavier CP–even H decays into massive gauge bosons $H \to WW, ZZ$ and Higgs bosons $H \to hh$, CP–odd Higgs decays into a vector and a Higgs boson, $A \to hZ$, CP–even and CP–odd Higgs decays into top quarks, $H/A \to t\bar{t}$, and even charged Higgs decay $H^\pm \to Wh$. Many search channels discussed in the context of a heavy SM Higgs boson or for resonances in some non–SUSY beyond the SM (new gauge bosons or Kaluza–Klein excitations) can be used to search for these final states. A detailed discussion of the Higgs cross sections times decay rates in these process is made in this section and an estimate of the sensitivity that could be achieved at the present $\sqrt{s} = 8$ TeV run with the full data set is given. These processes allow to cover a large part of the parameter space of the MSSM Higgs sector in a model–independent way, i.e. without using the information on the scale M_S and more generally on the SUSY particle spectrum that appear in the radiative corrections.

The rest of this part is organised as follows. In the next section, we discuss the radiative corrections in the Higgs sector when M_h is used as input and their impact on the Higgs masses and couplings. Afterwards, we summarize the various processes for Higgs production and decay in the high and low $\tan\beta$ regions and then, their implications

for the MSSM parameter space. We will also discuss the important new heavy Higgs channels that can be probed at the LHC at low $\tan\beta$.

7.2 The Higgs sector of the MSSM in the various $\tan\beta$ regimes

In this section, we review the theoretical aspects of the MSSM Higgs sector with some emphasis on the properties of the Higgs particles in the low $\tan\beta$ regime, $1 \lesssim \tan\beta \lesssim 3$, which contrary to the high $\tan\beta$ regime, has not received much attention in the literature.

7.2.1 The radiatively corrected Higgs masses

Let us begin by recalling a few basics facts about the MSSM and its extended Higgs sector. In the MSSM, two chiral superfields with respective hypercharges -1 and $+1$ are needed for the cancellation of chiral anomalies and their scalar components, the two doublet fields H_1 and H_2, give separately masses to the isospin $-\frac{1}{2}$ and $+\frac{1}{2}$ fermions in a SUSY invariant way. After spontaneous symmetry breaking, the two doublet fields lead to five Higgs particles: two CP–even h, H bosons, a pseudoscalar A boson and two charged $H^\pm$ bosons [48, 182].

The Higgs sector should be in principle described by the four Higgs boson masses and by two mixing angle α and β, with α being the angle which diagonalises the mass matrix of the two CP–even neutral h and H states while β is given in terms of the ratio of vacuum expectation values of the two Higgs fields H_1 and H_2, $\tan\beta = v_2/v_1$. However, by virtue of SUSY, only two parameters are needed to describe the system at tree–level. It is common practice to chose the two basic inputs to be the pseudoscalar mass M_A, expected to lie in the range between M_Z and the SUSY breaking scale M_S, and the ratio $\tan\beta$, which is expected to take values in the range [284]

$$1 \lesssim \tan\beta \lesssim \bar{m}_t/\bar{m}_b \approx 60 \tag{7.222}$$

with $\bar{m}_t$ and $\bar{m}_b$ the running top and bottom quark masses in the $\overline{\rm MS}$ renormalisation scheme evaluated at a scale close to the SUSY scale M_S.

At tree–level, the CP–even h boson mass is then bound to be lighter than the Z boson, $M_h \leq \min(M_Z, M_A)|\cos 2\beta| \leq M_Z$, while the heavier H and $H^\pm$ boson have masses that are comparable to that of the A state if $M_A \gtrsim M_Z$. Likewise, the mixing angle α can be written in compact form in terms of M_A and $\tan\beta$. If the mass M_A is large compared to the Z boson mass, the so called decoupling limit [273] that we will discuss in some detail here, the lighter h state reaches its maximal mass value, $M_h \approx M_Z|\cos 2\beta|$, the heavier CP–even and CP–odd and the charged Higgs states become almost degenerate in mass, $M_H \approx M_A \approx M_{H^\pm}$, while the mixing angle α becomes close to $\alpha \approx \frac{\pi}{2} - \beta$.

As is well known this simple pattern is spoiled when one includes the radiative corrections which have been shown to be extremely important [183, 185, 186, 190, 193, 194, 201, 203, 212, 213, 220, 242, 243, 271, 285]. Once these corrections are included, the Higgs masses (and their couplings) will, in principle, depend on all the MSSM parameters. In the phenomenological MSSM (pMSSM) [222], defined by the assumptions

that all the soft–SUSY breaking parameters are real with the matrices that eventually describe them being diagonal (and thus, there is no new source of CP or flavor violation) and by the requirement of universal parameters for the first and second generation sfermions, the Higgs sector will depend on, besides M_A and $\tan\beta$, 20 additional parameters: the higgsino mass parameter μ; the bino, wino and gluino mass parameters M_1, M_2, M_3; the first/second and third generation left– and right–handed sfermion mass parameters $m_{\tilde{q}}, m_{\tilde{u}_R}, m_{\tilde{d}_R}, m_{\tilde{l}}, m_{\tilde{e}_R}$ and $m_{\tilde{Q}}, m_{\tilde{t}_R}, m_{\tilde{b}_R}, m_{\tilde{L}}, m_{\tilde{\tau}_R}$; and finally the (common) first/second and third generation trilinear A_u, A_d, A_e and A_t, A_b, A_τ couplings[12].

Fortunately, only a small subset of these parameters has a significant impact on the radiative corrections to the Higgs sector. At the one loop level, the by far dominant correction to the Higgs masses is originating from top and stop loops and grows like the fourth power of the top quark mass, logarithmically with the stop masses and quadratically with the stop trilinear coupling. The leading component of this correction reads[13] [183, 185, 186]

$$\epsilon = \frac{3\,\bar{m}_t^4}{2\pi^2 v^2 \sin^2\beta}\left[\log\frac{M_S^2}{\bar{m}_t^2} + \frac{X_t^2}{M_S^2}\left(1 - \frac{X_t^2}{12\,M_S^2}\right)\right] \tag{7.223}$$

where $\bar{m}_t$ is again the running $\overline{\rm MS}$ top quark mass to account for the leading two–loop QCD and electroweak corrections in a renormalisation group (RG) improvement (some higher order effects can also be included) [201,203]. We have defined the SUSY–breaking scale M_S to be the geometric average of the two stop masses $M_S = \sqrt{m_{\tilde{t}_1} m_{\tilde{t}_2}}$; this scale is generally kept in the vicinity of the TeV scale to minimize the amount of fine tuning. We have also introduced the stop mixing parameter $X_t = A_t - \mu\cot\beta$, that we define here in the $\overline{\rm DR}$ scheme, which plays an important role and maximizes the radiative correction when

$$X_t = \sqrt{6}\,M_S \;:\; \text{maximal mixing scenario} \tag{7.224}$$

while the radiative corrections is smallest for a vanishing X_t value, i.e. in the no mixing scenario $X_t = 0$. An intermediate scenario is when X_t is of the same order as the SUSY scale, $X_t = M_S$, the typical mixing scenario. These scenarios have been often used in the past as benchmarks for MSSM Higgs studies [288] and have been updated recently [289].

The ϵ approximation above allows to write the masses of CP–even Higgs bosons in a particularly simple form

$$M_{h,H}^2 = \frac{1}{2}(M_A^2 + M_Z^2 + \epsilon)\left[1 \mp \sqrt{1 - 4\frac{M_Z^2 M_A^2 \cos^2 2\beta + \epsilon(M_A^2\sin^2\beta + M_Z^2\cos^2\beta)}{(M_A^2 + M_Z^2 + \epsilon)^2}}\right] \tag{7.225}$$

In this approximation, the charged Higgs mass does not receive radiative corrections, the leading contributions being of $\mathcal{O}(\alpha m_t^2)$ and one can still write the tree-level relation $M_{H^\pm} = \sqrt{M_A^2 + M_W^2}$. For large values of the pseudoscalar Higgs boson mass, the CP–even Higgs masses can be expanded in powers of M_Z^2/M_A^2 to obtain at first order

$$\begin{aligned} M_h^2 &\overset{M_A \gg M_Z}{\to} (M_Z^2\cos^2 2\beta + \epsilon\sin^2\beta)\left[1 + \frac{\epsilon M_Z^2\cos^2\beta}{M_A^2(M_Z^2 + \epsilon\sin^2\beta)} - \frac{M_Z^2\sin^2\beta + \epsilon\cos^2\beta}{M_A^2}\right] \\ M_H^2 &\overset{M_A \gg M_Z}{\to} M_A^2\left[1 + \frac{M_Z^2\sin^2 2\beta + \epsilon\cos^2\beta}{M_A^2}\right] \end{aligned} \tag{7.226}$$

[12] The first/second generation couplings have no impact in general and can be ignored in practice, reducing the effective number of free inputs of the pMSSM, from 22 to 19 parameters.

[13] Note the typographical error for this equation in Ref. [48] which translated to Refs. [191, 286, 287].

and indeed, in exact decoupling $M_A/M_Z \to \infty$, one would have $M_H = M_A = M_{H^+}$ for the heavier Higgs states and, for the lighter h boson, the well known relation

$$M_h \equiv M_h^{\rm max} = \sqrt{M_Z^2 \cos^2 2\beta + \epsilon \sin^2\beta} \tag{7.227}$$

In view of the large value $M_h \approx 126$ GeV of the observed Higgs state at the LHC, it is clear that some optimization of the various terms that enter the mass formula Eq. (7.227) with the radiative correction Eq. (7.223) is required. As was discussed in many instances including Refs. [191,286,287], one needs: *i*) to be close to the decoupling limit $M_A \gg M_Z$ and to have significant $\tan\beta$ values that lead to $|\cos 2\beta| \to 1$ to maximize the tree–level mass and, *ii*) to be in the maximal mixing scenario $X_t = \sqrt{6} M_S$ with the largest possible value of the SUSY–breaking scale M_S to maximize the radiative corrections. As the other SUSY–breaking parameters do not affect significantly the $M_h^{\rm max}$ value, one can fix them to some value. For instance, one can make the choice [289]

$$M_{h\,{\rm bench}}^{\rm max}: \quad \begin{array}{c} M_2 \simeq 2M_1 = |\mu| = \frac{1}{5} M_S,\; M_3 = m_{\tilde{q}_i} = \frac{1}{3} m_{\tilde{\ell}_i} = 1.5 M_S,\; A_i = 0, \\ m_{\tilde{b}_R} = \frac{1}{3} m_{\tilde{\tau}_i} = M_S\,,\; A_b = A_\tau = A_t \end{array} \tag{7.228}$$

where $m_{\tilde{q}_i}$ and $m_{\tilde{\ell}_i}$ are the common first/second sfermion SUSY–breaking masses and A_i their trilinear couplings. Alternatively, one can perform a scan of these parameters in a reasonable range which should change the resulting value of $M_h^{\rm max}$ in the $\overline{\rm DR}$ scheme only by a few GeV in general.

In the case of a not too large SUSY scale, $M_S \lesssim 3$ TeV, the numerical analyses of the MSSM Higgs sector can be performed with RGE programs [240, 241, 279, 280] such as `Suspect` which include the most relevant higher order radiative corrections in the calculation of the Higgs and superparticle masses (and their couplings). In particular, for the Higgs sector, the full set of one–loop radiative corrections which include also the sbottom and stau loop corrections that are important at high $\tan\beta$ values [190] and the dominant two–loop QCD and electroweak corrections [212, 213, 285] are incorporated in the $\overline{\rm DR}$ scheme; the dominant three–loop corrections are also known [243] but they are quite small and they can be neglected.

One should compare the results with those obtained with the program `FeynHiggs` [246] which incorporates the radiative corrections at the same level of accuracy but in the on–shell renormalisation scheme [193, 194]. In most cases, one obtains comparable results but in some scenarios, the difference in the values of M_h can be as large as 3 GeV. We will thus assume, as in Ref. [289], that there is a $\Delta M_h \approx 3$ GeV uncertainty on the determination of the h mass in the MSSM and that the value $M_h = 126$ GeV of the particle observed at the LHC corresponds to a calculated mass within the pMSSM of

$$123 \text{ GeV} \leq M_h \leq 129 \text{ GeV} \tag{7.229}$$

This uncertainty includes the parametric uncertainties of the SM inputs, in particular the $\overline{\rm MS}$ b–quark mass and the top quark pole mass $\overline{m}_b(m_b) = 4.7$ GeV and $m_t^{\rm pole} = 173.2 \pm 1$ GeV [290]. In the latter case, it is assumed that the top quark mass measured at the Tevatron, with the uncertainty of 1 GeV, is indeed the pole mass. If the top mass is instead extracted from the top pair production cross section, which provides a theoretically less ambiguous determination of $m_t^{\rm pole}$, the uncertainty would be of order 3 GeV [291]. Including also the experimental error in the M_h measurement by ATLAS

and CMS, $M_h = 125.7 \pm 0.4$ GeV, the possible calculated mass value of the h boson in the MSSM can be extended to the much wider and admittedly rather conservative range 120 GeV $\leq M_h \leq$ 132 GeV.

7.2.2 The low $\tan\beta$ regime

The previous discussion assumed a not too high SUSY–breaking scale, $M_S \lesssim 3$ TeV, in order not to have a too large fine-tuning in the model. However, in many scenarios, values of M_S in the 10 TeV range and even beyond have been considered, with a most popular one being the split–SUSY scenario [235–237, 270]. Indeed, as the criterion to quantify the acceptable amount of tuning is rather subjective, one could well have a very large value of M_S which implies that no sfermion is accessible at the LHC or at any foreseen collider, with the immediate advantage of solving the flavor and CP problems in the MSSM by simply decoupling these states. The mass parameters for the spin–$\frac{1}{2}$ particles, the gauginos and the higgsinos, can be kept close to the electroweak scale, allowing for a solution to the dark matter problem and a successful gauge coupling unification, the two other SUSY virtues. The SUSY solutions to these two remaining problems are abandoned if one takes the very extreme attitude of assuming that the gauginos and higgsinos are also very heavy, with a mass close to the scale M_S, as is the case of the so–called high–scale SUSY models [238, 270].

In all these these SUSY scenarios, there is still a light particle, the h boson, which can have a mass close to 126 GeV for a given choice of parameters such as M_S and $\tan\beta$; see for instance Refs. [191, 270]. The other Higgs particles are much heavier as the pseudoscalar Higgs mass is very often related to the mass scale of the scalar fermions of the theory, $M_A \approx M_S$. However, this needs not to be the case in general, in particular for M_S values not orders of magnitude larger than 1 TeV. Even, in constrained minimal Supergravity–like scenarios, one can assume that the soft SUSY–breaking scalar mass terms are different for the sfermions and for the two Higgs doublets, the so–called non–universal Higgs mass models [255–259] in which the mass M_A is decoupled from M_S. Scenarios with very large values of M_S and values of M_A close to the weak scale have been advocated in the literature [276–278], while models in which one of the soft SUSY–breaking Higgs mass parameters, in general M_{H_1}, is at the weak scale while M_S is large are popular; examples are the focus point scenario [292–294] and the possibility also occurs in M/string theory inspired scenarios [267, 295–297].

Hence, if one is primarily concerned with the MSSM Higgs sector, one may be rather conservative and assume any value for the pseudoscalar Higgs mass M_A irrespective of the SUSY scale M_S. This is the quite "model–independent" approach that we advocate and will follow in this part: we take M_A as a free parameter of the pMSSM, with values ranging from slightly above 100 GeV up to order M_S, but make no restriction on the SUSY scale which can be set to any value.

Nevertheless, in scenarios with $M_S \gg 1$ TeV, the Higgs and SUSY mass spectrum cannot be calculated reliably using standard RGE programs as one has to properly decouple the heavy states from the low-energy theory and resum the large logarithmic corrections. A comprehensive study of the split SUSY spectrum has been performed in Ref. [269] and the various features implemented in an adapted version of the code `SuSpect`. However, this version does not include the possibility $M_S \gg M_A \gtrsim M_Z$ that is

of interest for us here. A comprehensive and accurate description of the high M_S scenario in the MSSM in the light of the h discovery, including the possibility of a Higgs sector at the weak scale, is under way [281]. In the meantime, we will use the ϵ approximation of Eq. (7.223) to describe the radiative corrections in our high M_S scenario which should be a good approximation for our purpose. In particular, for $M_A \gg M_Z$, we have verified that our results are in a relatively good agreement with those derived in the more refined approach of Ref. [269].

Let us now discuss the magnitude of the SUSY scale that is needed to make small $\tan\beta$ values viable. We make use of the program `Suspect` in which the possibility $M_S \gg 1$ TeV is implemented [269] and which includes the full set of radiative corrections (here we assume the maximal mixing $X_t = \sqrt{6}M_S$ scenario and we take 1 TeV for the gaugino and higgsino masses). In Fig. 25, displayed are the contours in the plane $[\tan\beta, M_S]$ for fixed mass values $M_h = 120, 123, 126, 129$ and 132 GeV of the observed Higgs state (these include the 3 GeV theoretical uncertainty and also a 3 GeV uncertainty on the top quark mass).

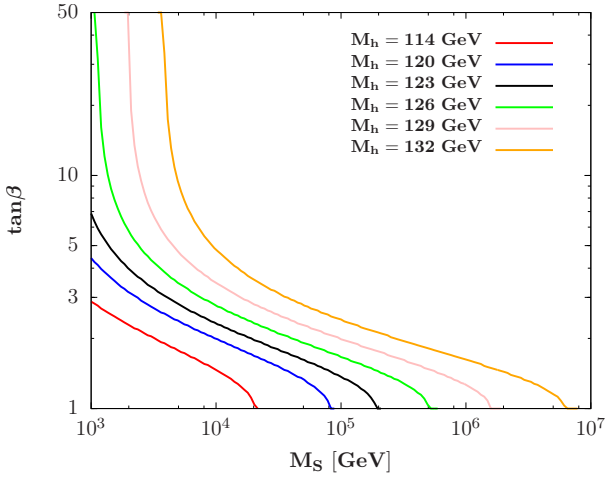

Figure 25: Contours for fixed values $M_h = 120, 123, 126, 129$ and 132 GeV in the $[\tan\beta, M_S]$ plane in the decoupling limit $M_A \gg M_Z$; the "LEP2 contour" for $M_h = 114$ GeV is also shown.

From the figure, one concludes that values of $\tan\beta$ close to unity are possible and allow for an acceptable M_h value provided the scale M_S is large enough. For instance, while one can accommodate a scale $M_S \approx 1$ TeV with $\tan\beta \approx 5$, a large scale $M_S \approx 20$ TeV is required to reach $\tan\beta \approx 2$; to reach the limit $\tan\beta = 1$, an order of magnitude increase of M_S will be needed. Outside the decoupling regime, the obtained M_S for a given M_h value will be of course larger. For completeness, we also show the contour for the mass value $M_h = 114$ GeV, the 95% confidence level limit obtained at LEP2 on a SM–like Higgs boson; it illustrates the fact that values down to $\tan\beta \approx 1$ are still allowed by this bound provided that $M_S \gtrsim 10$ TeV. The implications of this feature will be discussed later.

In the rest of this section, we will thus consider situations with the MSSM Higgs sector at the weak scale and the only requirement that we impose is that it should be compatible with the LHC data and, in particular, with the mass and production rates of the Higgs boson that has been observed. The requirement that $M_h \approx 126$ GeV, within the theoretical and experimental uncertainties, will be turned into a requirement on the

parameters that enter the radiative corrections and, hence, on the scale M_S and the mixing parameter X_t, for given values of the two basics inputs M_A and $\tan\beta$.

7.2.3 The Higgs couplings and the approach to the decoupling limit

Let us now turn to the important issue of the Higgs couplings to fermions and gauge bosons. These couplings strongly depend on $\tan\beta$ as well as on the angle α (and hence on M_A); normalized to the SM Higgs couplings, they are given in Table 15. The A boson has no tree level couplings to gauge bosons as a result of CP–invariance, and its couplings to down–type and up–type fermions are, respectively, proportional and inversely proportional to $\tan\beta$. This is also the case for the couplings of the charged Higgs boson to fermions, which are admixtures of $\bar{m}_b \tan\beta$ and $\bar{m}_t \cot\beta$ terms and depend only on $\tan\beta$. For the CP–even Higgs bosons h and H, the couplings to fermions are ratios of sines and cosines of the angles α and β; the couplings to down (up) type are enhanced (suppressed) compared to the SM Higgs couplings for $\tan\beta > 1$. The two states share the SM Higgs couplings to vector bosons as they are suppressed by $\sin(\beta-\alpha)$ and $\cos(\beta-\alpha)$, respectively for h and H. We note that there are also couplings between a gauge and two Higgs bosons which in the case of the CP–even states are complementary to those to two gauge bosons $g_{hAZ} \propto g_{hH^+W^-} \propto g_{HVV}$ and vice versa for $h \leftrightarrow H$; the coupling $g_{AH^+W^-}$ has full strength.

Φ	$g_{\Phi\bar{u}u}$	$g_{\Phi\bar{d}d}$	$g_{\Phi VV}$	$g_{\Phi AZ}/g_{\Phi H^+W^-}$
h	$\cos\alpha/\sin\beta$	$-\sin\alpha/\cos\beta$	$\sin(\beta-\alpha)$	$\propto \cos(\beta-\alpha)$
H	$\sin\alpha/\sin\beta$	$\cos\alpha/\cos\beta$	$\cos(\beta-\alpha)$	$\propto \sin(\beta-\alpha)$
A	$\cot\beta$	$\tan\beta$	0	$\propto 0/1$

Table 15: The couplings of the neutral MSSM Higgs bosons, collectively denoted by Φ, to fermions and gauge bosons when normalized to the SM Higgs boson couplings.

These couplings are renormalized essentially by the same radiative corrections that affect the CP–even neutral Higgs masses. In the ϵ approximation discussed above, the one–loop radiatively corrected mixing angle $\bar{\alpha}$ will indeed read

$$\tan 2\bar{\alpha} = \tan 2\beta \, \frac{M_A^2 + M_Z^2}{M_A^2 - M_Z^2 + \epsilon/\cos 2\beta} \tag{7.230}$$

This leads to corrected reduced h, H couplings to gauge bosons that are simply $g_{hVV} = \sin(\beta-\bar{\alpha})$ and $g_{HVV} = \cos(\beta-\bar{\alpha})$ and similarly for the couplings to fermions.

The decoupling limit is controlled by the VV coupling of the heavier CP–even Higgs boson, $g_{HVV} = \cos(\beta-\bar{\alpha})$, which vanishes in this case, while the hVV coupling $g^2_{hVV} = 1 - g^2_{HVV} = \sin^2(\beta-\bar{\alpha})$ becomes SM–like. Performing again an expansion in terms of the pseudoscalar Higgs mass, one obtains in the approach to the decoupling limit[14]

$$g_{HVV} \overset{M_A \gg M_Z}{\longrightarrow} \chi \equiv \frac{1}{2}\frac{M_Z^2}{M_A^2} \sin 4\beta - \frac{1}{2}\frac{\epsilon}{M_A^2} \sin 2\beta \quad \to 0 \tag{7.231}$$

[14]We thank Nazila Mahmoudi for discussions and help concerning these limits.

where, in the intermediate step, the first term is due to the tree–level contribution and the second one to the one–loop contribution ϵ. Concentrating first on the tree–level part, one realises that for large values of $\tan\beta$ and also for values very close to unity, the decoupling limit is reached more quickly. Indeed the expansion parameter involves also the factor $\sin 4\beta$ which becomes in these two limiting cases

$$\sin 4\beta = \frac{4\tan\beta(1-\tan^2\beta)}{(1+\tan^2\beta)^2} \to \begin{cases} -4/\tan\beta & \text{for } \tan\beta \gg 1 \\ 1-\tan^2\beta & \text{for } \tan\beta \sim 1 \end{cases} \to 0 \qquad (7.232)$$

Hence, in both the $\tan\beta \gg 1$ and $\tan\beta \sim 1$ cases, the g_{HVV} coupling that controls the decoupling limit $M_Z^2/M_A^2 \to 0$, is doubly suppressed. The radiatively generated component, if one recalls that the one–loop correction in Eq. (7.223) involves a $1/\sin^2\beta$ term which makes it behave as $-\epsilon/M_A^2 \times \cot\beta$, also vanishes at high $\tan\beta$ values. This leads to the well known fact that the decoupling limit $g_{HVV} \to 0$ is reached very quickly in this case, in fact as soon as $M_A \gtrsim M_h^{\rm max}$. Instead, for $\tan\beta \approx 1$, this radiatively generated component is maximal. However, when both components are included, the departure from the decoupling limit in the coupling g_{HVV} for a fixed M_A value occurs when $\sin 4\beta \approx -1$, which corresponds to $\beta = 3\pi/8$ and hence to the value $\tan\beta \approx 2.4$.

Similarly to the HVV case, one can write the couplings of the CP–even Higgs states to isospin $\frac{1}{2}$ and $-\frac{1}{2}$ fermions in the approach to the decoupling limit $M_Z^2/M_A^2 \ll 1$ as

$$\begin{aligned} g_{huu} &\xrightarrow{M_A \gg M_Z} 1 + \chi\ \cot\beta &&\to 1 \\ g_{hdd} &\xrightarrow{M_A \gg M_Z} 1 - \chi\ \tan\beta &&\to 1 \\ g_{Huu} &\xrightarrow{M_A \gg M_Z} -\cot\beta + \chi &&\to -\cot\beta \\ g_{Hdd} &\xrightarrow{M_A \gg M_Z} +\tan\beta + \chi &&\to +\tan\beta \end{aligned}$$

with the expansion parameter $\chi \propto 1/M_A^2$ is the same as the one given in Eq. (7.231). In the $M_A \gg M_Z$ regime, the couplings of the h boson approach those of the SM Higgs boson, $g_{huu} \approx g_{hdd} \approx 1$, while the couplings of the H boson reduce, up to a sign, to those of the pseudoscalar Higgs boson, $g_{Huu} \approx g_{Auu} = \cot\beta$ and $g_{Hdd} \approx g_{Add} = \tan\beta$. Again, as a result of the presence of the same combination of $M_Z^2 \sin 4\beta$ and $\epsilon \sin 2\beta$ factors in the expansion term χ of all couplings, the limiting values are reached more quickly at large values of $\tan\beta$ but the departure from these values is slower at low $\tan\beta$.

In Fig. 26, we display the square of the H couplings to gauge bosons and fermions as a function of $\tan\beta$ for $M_A = 300$ GeV. Again the maximal mixing scenario is assumed and M_S is chosen in such way that for any $\tan\beta$ value, one has $M_h = 126$ GeV. At such A masses, the couplings of the lighter h boson to all particles deviate little from unity even for small $\tan\beta$ values and in this case too one can consider that we are already in the decoupling regime. Nevertheless, the coupling of the heavier H boson to VV states is still non–zero, in particular at low $\tan\beta$. The H coupling to $t\bar{t}$ pairs states (as well as the A coupling) is significant at low $\tan\beta$ values, $g_{Htt}^2 \gtrsim 0.1$ for $\tan\beta \lesssim 3$. It even becomes larger (and the Hbb coupling smaller) than unity for $\tan\beta \lesssim 1.2$.

This demonstrates that the heavier $H/A/H^\pm$ bosons can have sizable couplings to top quarks (and to massive gauge bosons for H outside the decoupling regime) if $\tan\beta$ values as low as ~ 3 are allowed. In fact, the $H/A/H^\pm$ couplings to top quarks $\propto \cot\beta$ are larger that the couplings to bottom quarks $\propto \tan\beta$ for values $\tan\beta \approx \sqrt{\bar{m}_t/\bar{m}_b} \lesssim 7$ and this value should be considered as the boundary between the high and low $\tan\beta$

regimes. With more refinement, one can consider three $\tan\beta$ regimes: the high regime with $\tan\beta \gtrsim 10$, the intermediate regime with $5 \lesssim \tan\beta \lesssim 10$ and the low regime with $\tan\beta \lesssim 5$.

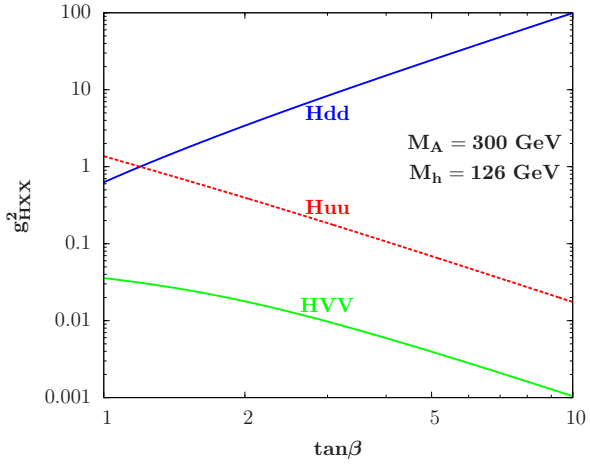

Figure 26: The squared couplings of the heavier CP–even H state to gauge bosons and fermions as a function of $\tan\beta$ for $M_A = 300$ GeV. The SUSY scale is chosen so that $M_h = 126$ GeV.

There are two important remarks which should be made before closing this section. The first one is that besides the ϵ correction, there are additional one–loop vertex corrections which modify the tree–level Higgs–fermion couplings [298, 299]. In the case of b–quarks in the high (and eventually intermediate) $\tan\beta$ regime, they can be very large in the b–quark case as they grow as $\bar{m}_b \tan\beta$. The dominant component comes from the SUSY–QCD corrections with sbottom–gluino loops that can be approximated by

$$\Delta_b \simeq \frac{2\alpha_s}{3\pi}\mu m_{\tilde{g}} \tan\beta / \max(m^2_{\tilde{g}}, m^2_{\tilde{b}_1}, m^2_{\tilde{b}_2}) \tag{7.233}$$

In the decoupling limit $M_A \gg M_Z$, the reduced $b\bar{b}$ couplings of the H, A states read

$$g_{Hbb} \approx g_{Abb} \approx \tan\beta \left[1 - \frac{\Delta_b}{1+\Delta_b}\right] \tag{7.234}$$

In the case of the lighter h boson, the hbb couplings stay SM–like in this limit in principle, but slightly outside the decoupling limit, there is a combination of SUSY parameters which realises the so–called "vanishing coupling" regime [288] in which $\bar{\alpha} \to 0$ and hence $g_{hbb} \ll 1$.

The second remark concerns the trilinear Hhh coupling which will be needed in our analysis. In units of M_Z^2/v, this coupling is given at tree–level by [182]

$$\lambda_{Hhh} \approx 2\sin 2\alpha \sin(\beta+\alpha) - \cos 2\alpha \cos(\beta+\alpha) \tag{7.235}$$

Again, to include the radiative corrections in the ϵ approximation, one needs to perform the change $\alpha \to \bar{\alpha}$; however, in this case, there are also direct vertex corrections but they can be still described by the ϵ parameter. One obtains in this approach [38, 42]

$$\lambda_{Hhh} \overset{M_A \gg M_Z}{\longrightarrow} -\frac{3}{M_Z^2}\left[\sqrt{(M_h^2 - \epsilon\sin^2\beta)(M_Z^2 - M_h^2 + \epsilon\sin^2\beta)} + \epsilon \sin\beta\cos\beta\right] \tag{7.236}$$

At high–$\tan\beta$, the trilinear coupling vanishes $\lambda_{Hhh} \to 0$ while for small and intermediate $\tan\beta$ values it stays quite substantial as a result of the large ϵ corrections.

7.3 Higgs decays and production at the LHC

7.3.1 The high and intermediate $\tan\beta$ regimes

The production and decay pattern of the MSSM Higgs bosons crucially depend on $\tan\beta$. In the LHC run up to now, i.e. with center of mass energies up to $\sqrt{s} = 8$ TeV, only relatively large $\tan\beta$ values, $\tan\beta \gtrsim 5$–10 which correspond to the high and intermediate regimes, are probed in the search of the neutral H/A and the charged $H^\pm$ bosons. In the high $\tan\beta$ regime, the couplings of these non–SM like Higgs bosons to b quarks and to τ leptons are so strongly enhanced, and the couplings to top quarks and massive gauge bosons so suppressed, that the pattern becomes rather simple.

A first simplifying feature is that the decoupling regime in which the lighter h boson attains its maximal mass $M_h^{\rm max}$ value for a given SUSY parameter set[15] and has SM–couplings already at $M_A \gtrsim M_h^{\rm max}$ for $\tan\beta \gtrsim 10$. In this case, the heavier CP–even H boson has approximately the same mass as the A boson and its interactions are similar. Hence, the spectrum will consist of a SM–like Higgs $h \equiv H_{\rm SM}$ and two pseudoscalar (like) Higgs particles, $\Phi = H/A$. The $H^\pm$ boson will also be approximately degenerate in mass with the Φ states and the intensity of its couplings to fermions will be similar.

An immediate consequence will be that the h boson will precisely decay into the variety of final states and will be produced in the various channels that are present in the SM. These decay and production processes have been studied in detail at various places, see Ref. [47] for a detailed review and Refs. [103,106] for updates. We will discuss the implications of these channels for the properties of the state observed at the LHC in the next section.

In the case of the heavier neutral $\Phi = H/A$ bosons, the decay pattern is very simple: the $t\bar{t}$ channel and all other decay modes are suppressed to a level where their branching ratios are negligible and the Φ states decay almost exclusively into $\tau^+\tau^-$ and $b\bar{b}$ pairs, with branching ratios of ${\rm BR}(\Phi \to \tau^+\tau^-) \approx m_\tau^2/[3\overline{m}_b^2(M_\Phi) + m_\tau^2] \approx 10\%$ and ${\rm BR}(\Phi \to b\bar{b}) \approx 90\%$. The charged Higgs particles decay into $H^\pm \to \tau\nu_\tau$ final states with a branching fraction of almost 100% for $H^\pm$ masses below the tb threshold, $M_{H^\pm} \lesssim m_t - m_b$, and a branching ratio of only $\approx 10\%$ for masses above this threshold. The by far dominant channel in the latter case is $H^\pm \to tb$ which occurs with a $\approx 90\%$ probability for the same reason as above.

Concerning Higgs production in the high $\tan\beta$ regime, the enhancement of the b–quark couplings makes that only processes involving this quark are important for the $\Phi = H/A$ states. In the dominant gluon fusion production channel, $gg \to \Phi$, one should take into account the b–quark loop which provides the largest contribution (in contrast to the SM where the top quark contribution largely dominates) and in associated Higgs

[15] The present discussion holds in the case where the h boson is the SM–like state which implies $M_A \gtrsim M_h^{\rm max}$. At low M_A values, the role of the CP–even h and H states are reversed: it is H which is the SM–like particle $H \equiv H_{\rm SM}$ and h would correspond to the pseudoscalar–like Higgs particle. However, the possibility that the H state is the observed particle at the LHC is ruled out by present data [287]. A special case would be $M_A \approx M_h^{\rm max}$, which is called the intense coupling regime in Ref. [300,301] and which leads to mass degenerate h, H, A states with comparable couplings to fermions; as the h and H states are close in mass, one has the same phenomenology as in the decoupling limit where H has the same properties as A [106]. Again, this scenario is strongly disfavored by present data [287].

production with heavy quarks, $b\bar{b}$ final states and hence the processes $gg/q\bar{q} \to b\bar{b} + \Phi$, must be considered. The latter processes are equivalent to the $b\bar{b} \to \Phi$ channels when no–additional b–quark in the final state is present, if one considers the b–quark as a massless parton and uses heavy quark distribution functions in a five active flavor scheme [302].

Hence, except for the $gg \to \Phi$ and $b\bar{b} \to \Phi$ fusion processes, all the other production channels are irrelevant in the high $\tan\beta$ regime, in particular the vector boson fusion and the Higgs–strahlung channels, that are absent for A and strongly suppressed for H. In both cases, as $M_\Phi \gg m_b$, chiral symmetry holds and the cross sections are approximately the same for the CP–even H and CP–odd A bosons. The cross section for $gg \to \Phi$ is known up to next–to–leading order in QCD [72] and can be calculated using the program `HIGLU` [117, 303]. The $bb \to \Phi$ rate is instead known up to NNLO in QCD [304–306] and its evaluation can be made using the programs `bb@nnlo` or `SUSHI` [307]. Note that for associated H/A production with two tagged b–quarks in the final states that can be used, one should instead consider the process $gg/q\bar{q} \to bb + \Phi$ which is known up to NLO QCD [308,309]; they leading order cross section can be obtained using the program `QQH` [117].

The most powerful search channel for the heavier MSSM Higgs particles at the LHC is by far the process

$$pp \to gg + b\bar{b} \to \Phi \to \tau^+\tau^- \tag{7.237}$$

The precise values of the cross section times branching fraction for this process at the LHC have been recently updated in Refs. [103, 106] and an assessment of the associated theoretical uncertainties has been made. It turns out that these uncertainties are not that small. They consist mainly of the scale uncertainties due to the missing higher orders in perturbation theory and of the combined uncertainty from the parton distribution functions and the strong coupling constant α_s. When combined, they lead to a total theoretical uncertainty of 20–30% in both the $gg \to \Phi$ and $b\bar{b} \to \Phi$ channels[16]. We will assume here for the combined $gg + b\bar{b} \to \Phi$ channel a theoretical uncertainty of

$$\Delta^{\rm TH}\sigma(pp \to \Phi) \times {\rm BR}(\Phi \to \tau\tau) = \pm 25\% \tag{7.238}$$

in the entire M_Φ range probed at the LHC and for both $\sqrt{s} = 8$ and 14 TeV.

Besides the QCD uncertainty, three other features could alter the rate $\sigma(pp \to \Phi \to \tau\tau)$ in the MSSM and they are related to the impact of the SUSY particle contributions. We briefly summarise them below and some discussions are also given in Refs. [287,310].

While the CP–odd A state does not couple to identical squarks as a result of CP–invariance, there is a $H\tilde{q}_i\tilde{q}_i$ coupling in the case of the H state which allows squarks, and mainly top and bottom squarks, to contribute to the $gg \to H$ amplitude at leading order (there are NLO contributions [311–314] for both the Hgg and Agg amplitudes via gluino exchange but they should be smaller). However, as squarks do not couple to the Higgs bosons proportionally to their masses, these contributions are damped by powers of $\tilde{m}_Q^2$ for $M_H \lesssim 2m_Q^2$ and, at high $\tan\beta$. the b–loop contribution stays largely dominant.

[16] It was advocated in Ref. [106] that there are two additional sources of uncertainties related to the b–quark mass which should be considered: the one in the $gg \to \Phi$ process due to the choice of the renormalization scheme for m_b and the parametric uncertainty. These could significantly increase the total uncertainty. We will however, ignore this complication and retain the "official" estimate of the error given in Ref. [103].

These SUSY contributions are thus expected to be small and can be neglected in most cases.

A more important effect of the SUSY sector is due to the one–loop vertex correction to the $\Phi b\bar{b}$ couplings, Δ_b of eqs. (8.3–7.234), which can be large in the high $\tan\beta$ regime as discussed previously. However, in the case of the full process $pp \to \Phi \to \tau^+\tau^-$, this correction appears in both the cross section, $\sigma(\Phi) \propto (1+\Delta_b)^{-2}$, and in the branching fraction, $\text{BR}(\tau\tau) = \Gamma(\Phi \to \tau\tau)/[(1+\Delta_b)^{-2}\Gamma(\Phi \to b\bar{b}) + \Gamma(\Phi \to \tau\tau)]$, which involves the Δ_b correction above in the denominator. Hence, in the cross section times branching ratio, the Δ_b corrections largely cancels out and for $\text{BR}(\tau\tau) \approx 10\%$, one obtains

$$\sigma(gg + b\bar{b} \to \Phi) \times \text{BR}(\Phi \to \tau\tau) \approx \sigma \times \text{BR} \times (1 - \frac{1}{5}\Delta_b) \tag{7.239}$$

Hence, one needs a very large Δ_b term (which, one should recall, is a radiative correction and should be small, for a recent discussion, see for instance Ref. [315]), of order unity or more, in order to alter significantly the $pp \to \Phi \to \tau\tau$ rate[17].

Finally, there is the possibility that there are light SUSY particles with masses $\widetilde{m} \lesssim \frac{1}{2}M_\Phi$ which lead to the opening of SUSY decay channels for the H/A states that might reduce the $\Phi \to \tau\tau$ branching fraction. For $M_\Phi \lesssim 1$ TeV, the only possibilities for these superparticles seem to be light neutralinos and charginos (χ) and light sleptons ($\widetilde{\ell}$). These decays have been reviewed in Ref. [48] and they have been found to be in general disfavored in the high $\tan\beta$ regime as the $\Phi \to b\bar{b} + \tau\tau$ decays are so strongly enhanced that they leave little room for other possibilities. Only in a few special situations that these SUSY decays can be significant. For the decays $\Phi \to \chi\chi$, it is the case when *i*) all $\chi = \chi^\pm_{1,2}$ and $\chi^0_{1\text{–}4}$ channels are kinematically open or *ii*) if only a subset of χ particles is light, they should be mixtures of gauginos and higgsinos to maximize the $\Phi\chi\chi$ couplings. Both scenarios should be challenged by the present LHC constraints[18]. In the case of sleptons, only the decays into light $\tilde{\tau}$ states could be important; while the decay $A \to \tilde{\tau}_1\tilde{\tau}_1$ is forbidden by CP–invariance, the decays $H \to \tilde{\tau}_1\tilde{\tau}_1$ and $H/A \to \tilde{\tau}_1\tilde{\tau}_2$ can have substantial rates at high $\tan\beta$ when the $\Phi\tilde{\tau}\tilde{\tau}$ coupling is enhanced. However, again, at these large $\tan\beta$ values, the $\Phi \to b\bar{b}$ and $\Phi \to \tau\tau$ decays are extremely enhanced and leave little room for competition.

Thus, only in the unlikely cases where the decay $H \to \tilde{\tau}_1\tilde{\tau}_1$ has a branching rate of the order of 50%, the squark loop contribution to the $gg \to H$ process is of the order 50%, or the Δ_b SUSY correction is larger than 100%, that one can change the $pp \to \Phi \to \tau\tau$ rate by $\approx 25\%$, which is the level of the QCD uncertainty. One thus expects $\sigma(pp \to \Phi) \times \text{BR}(\Phi \to \tau\tau)$ to be extremely robust and to depend almost exclusively on M_A and $\tan\beta$.

Two more processes are considered for the heavier MSSM neutral Higgs bosons at

[17] In any case, if one insists to take this Δ_b correction into account in the constraint on the $[\tan\beta, M_A]$ plane that is obtained from the $pp \to \Phi \to \tau\tau$ rate, one could simply replace $\tan\beta$ by $\tan\beta/(1+\Delta_b/10)$. A contribution $\Delta_b \approx 1$ will change the limit on $\tan\beta$ by only 10%, i.e. less than the QCD uncertainty.

[18] The searches of charginos and neutralinos in the same-sign lepton and tri-lepton topologies at the LHC are now probing significant portions of the gaugino–higgsino parameter space and they exclude more and more the possibility of light χ states [316–319]. This is particularly true for mixed gaugino–higgsino states in which the $\Phi\chi\chi$ couplings are maximised: the lead to a large gap between the lightest and the next-to-lightest χ masses and hence a large amount of missing energy that make the searches more effective.

high $\tan\beta$. The first one is $pp \to \Phi \to \mu^+\mu^-$ for which the rate is simply $\sigma(pp \to \Phi \to \tau\tau)$ rescaled by $\text{BR}(\Phi \to \mu\mu)/\text{BR}(\Phi \to \tau\tau) = m_\mu^2/m_\tau^2 \approx 4 \times 10^{-3}$. The rate is much smaller than in the $\tau\tau$ case and is not compensated by the much cleaner $\mu\mu$ final state and the better resolution on the invariant mass. Searches in this channel have been performed in the SM Higgs case [320, 321] and the sensitivity is very low. In addition, there is the process in which the H/A bosons are produced in association with two b–quark jets and decay into $b\bar{b}$ final states and searches in this channel have been performed by the CMS collaboration with the 7 TeV data [322]. However, the sensitivity is far lower than in the $\tau^+\tau^-$ channel.

Thus, the $pp \to \Phi \to \tau^+\tau^-$ search for the neutral Higgs bosons provides the most stringent limits on the MSSM parameter space at large $\tan\beta$ and all other channels are weaker in comparison and provide only cross checks. We will thus concentrate on this process in the rest of our discussion of the high $\tan\beta$ regime.

A final remark needs to be made on the charged Higgs boson. The dominant $H^\pm$ search channel at present energies is in $H^\pm \to \tau\nu$ final states with the $H^\pm$ bosons produced in top quark decays for masses not too close to $M_{H^\pm} = m_t - m_b \approx 170$ GeV

$$pp \to t\bar{t} \;\text{ with }\; t \to H^+ b \to \tau\nu\, b \tag{7.240}$$

This is particularly true at high $\tan\beta$ values when the $t \to H^+ b$ branching ratio which grows with $\bar{m}_b^2 \tan^2\beta$, is significant. For higher $H^\pm$ masses, one should rely on the three–body production process $pp \to tbH^\pm \to tb\tau\nu$ which leads to a cross section that is also proportional to $\tan^2\beta$, but the rates are presently too small. Hence, processes beyond $t \to bH^+$ can be considered only at the upgraded LHC.

7.3.2 The low $\tan\beta$ regime

The phenomenology of the heavy MSSM $A, H, H^\pm$ bosons is richer at low $\tan\beta$ and leads to a production and decay pattern that is slightly more involved than in the high $\tan\beta$ regime. Starting with the production cross sections, we display in Fig. 27 the rates for the relevant $H/A/H^\pm$ production processes at the LHC with center of mass energies of $\sqrt{s} = 8$ TeV and $\sqrt{s} = 14$ GeV assuming $\tan\beta = 2.5$. The programs `HIGLU` [303], `SUSHI` [307] and those of Ref. [117] have been modified in such a way that the radiative corrections in the Higgs sector are calculated according to what has been seen previously and lead to a fixed $M_h = 126$ GeV value. The MSTW set of parton distribution functions (PDFs) [133] has been adopted. For smaller $\tan\beta$ values, the cross sections for the various processes, except for $pp \to H/A + b\bar{b}$, are even larger as the H/A couplings to top quarks and the HVV coupling outside the decoupling limit are less suppressed.

Because of CP invariance which forbids AVV couplings, the pseudoscalar state A cannot be produced in the Higgs-strahlung and vector boson fusion processes. For $M_A \gtrsim 300$ GeV, the rate for the associated $pp \to t\bar{t}A$ process is rather small, as is also the case of the $pp \to b\bar{b}A$ cross section which is not sufficiently enhanced by the $Abb \propto \tan\beta$ coupling. Hence, only the $gg \to A$ fusion process with the dominant t–quark and sub-dominant b–quark loop contributions included provides large rates at low $\tan\beta$.

The situation is approximately the same for the CP–even H boson: only the $gg \to H$ process provides significant production rates at relatively high values of M_H, $M_H \gtrsim 300$ GeV, and low $\tan\beta$, $\tan\beta \lesssim 5$. As in the case of A, the cross section for $pp \to t\bar{t}H$ is suppressed compared to the SM case while the rate for $pp \to b\bar{b}H$ is not enough enhanced. However, in this case, the vector boson fusion $pp \to Hqq$ and Higgs-strahlung processes $q\bar{q} \to HW/HZ$ are also at work and have production rates that are not too suppressed compared to the SM at sufficiently low M_H values, $M_H \lesssim 200$–300 GeV and $\tan\beta \approx 1$.

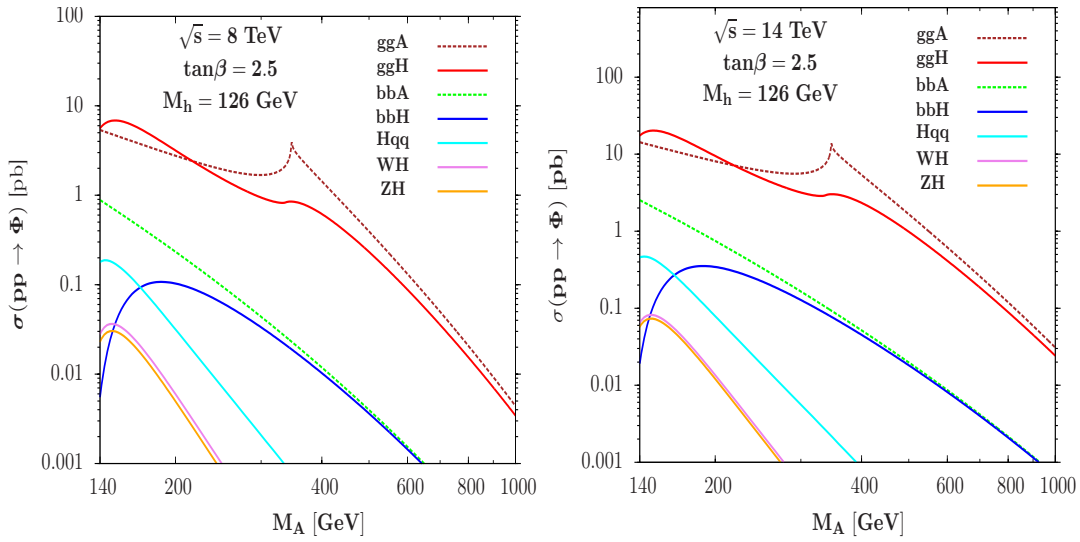

Figure 27: The production cross sections of the MSSM heavier Higgs bosons at the LHC with $\sqrt{s} = 8$ TeV (left) and $\sqrt{s} = 14$ TeV (right) for $\tan\beta = 2.5$. Only the main channels are presented. The higher order corrections are included (see text) and the MSTW PDFs have been adopted.

Hence, for $M_A \gtrsim 300$ GeV, the only relevant production process is $gg \to \Phi$ with the dominant contribution provided by the heavy top quark loop. In this case, one can include not only the large NLO QCD corrections [67, 68, 323], which are known in the exact case [72], but also the NNLO QCD corrections [74–76, 122, 324] calculated in a effective approach with $m_t \gg M_\Phi$ which should work in practice for $M_\Phi \lesssim 300$ GeV but can be extended to higher masses.

For the charged Higgs boson, the dominant production channel in the low $\tan\beta$ regime is again top quark decays, $t \to H^+b$, for $M_{H^\pm} \lesssim 170$ GeV. Indeed, for $\tan\beta \lesssim 5$, the $m_t/\tan\beta$ component of the $H^\pm tb$ coupling becomes rather large, leading to a significant $t \to H^+b$ branching ratio. For higher $H^\pm$ masses, the main process to be considered is $gg/q\bar{q} \to H^\pm tb$ [325–329]. As in the case of $pp \to b\bar{b}\Phi$, one can take the b–quark as a parton and consider the equivalent but simpler $2 \to 2$ channel $gb \to H^\pm t$. One obtains an accurate description of the cross section if the renormalisation and factorisation scales are chosen to be low, $\mu_R = \mu_F \approx \frac{1}{6}(M_{H^\pm} + m_t)$ in order to account for the large NLO QCD corrections [330]; the scales uncertainties are large though, being of order 20% [103]. Additional sources of $H^\pm$ states for $M_{H^\pm} \lesssim 250$ GeV are provided by pair and associated production with neutral Higgs bosons in $q\bar{q}$ annihilation as well as H^+H^- pair and associated $H^\pm W^\mp$ production in gg and/or $b\bar{b}$ fusion but the rates are very small [331].

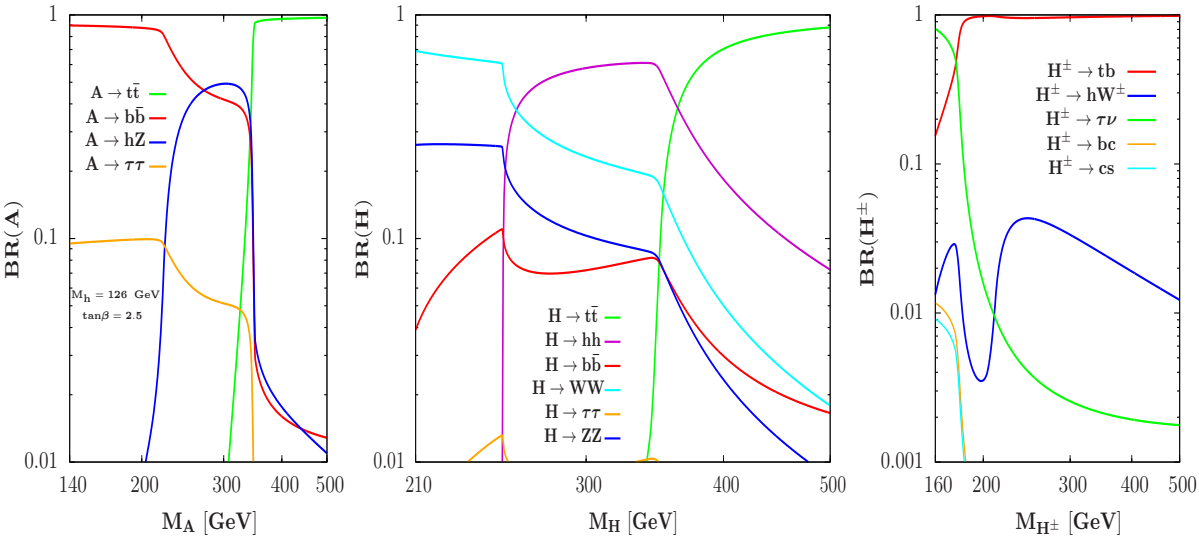

Figure 28: The decay branching ratios of the heavier MSSM Higgs bosons A (left), H (center) and $H^\pm$ (right) as a function of their masses for $\tan\beta = 2.5$. The program HDECAY [115, 116] has been used with modifications so that the radiative corrections lead to $M_h = 126$ GeV.

Let us turn to the decay pattern of the heavier MSSM Higgs particles which can be rather involved in the low $\tan\beta$ regime. In this case, as the couplings of the H/A bosons to b–quarks are not very strongly enhanced and the couplings to top quarks (and gauge bosons in the case of the H state) not too suppressed, many interesting channels appear. The branching fractions for the $H/A/H^\pm$ decays are shown in Fig. 28 as functions of their masses at $\tan\beta = 2.5$. They have been obtained using the program HDECAY [115, 116] assuming large M_S values that lead to a fixed $M_h = 126$ GeV value. The pattern does not significantly depend on other SUSY parameters, provided that Higgs decays into supersymmetric particles are kinematically closed as it will be implicitly assumed in the following[19], where the main features of the decays are summarised in a few points.

– Sufficiently above the $t\bar{t}$ threshold for the neutral and the tb threshold for the charged Higgs bosons, the decay channels $H/A \to t\bar{t}$ and $H^+ \to t\bar{b}$ become by far dominant for $\tan\beta \lesssim 3$ and do not leave space for any other decay mode. Note that these decays have also significant branching fractions below the respective kinematical thresholds [332–334]. It is especially true for the charged Higgs state for which BR($H^+ \to t\bar{b}$) $\gtrsim 1\%$ for $M_{H^\pm} \approx 130$ GeV.

– Below the $t\bar{t}$ threshold, the H boson can still decay into gauge bosons $H \to WW$ and ZZ with rather substantial rates as the HVV couplings are not completely suppressed.

– In the window $2M_h \lesssim M_H \lesssim 2m_t$, the dominant decay mode for $\tan\beta \lesssim 3$ turns out to be the very interesting channel $H \to hh$ channel. As discussed earlier, the Hhh self–couplings given in Eq. (7.236) is significant at low $\tan\beta$ values.

– If allowed kinematically, i.e. for $M_A \gtrsim M_h + M_Z$ GeV, the CP–odd Higgs boson

[19] In fact, even in this low $\tan\beta$ case, the $t\bar{t}$ decays for sufficiently large masses are so dominant that they do not lead to any significant quantitative change if SUSY particles are light. In addition, being not enhanced by $\tan\beta$, the Δ_b correction has no impact in this low $\tan\beta$ regime.

can also decay into hZ final states with a significant rate below the $t\bar{t}$ threshold as the AZh coupling (that is the same as the HVV coupling) is substantial. Nevertheless, the $A \to \tau\tau$ channel is still important as it has a branching fraction above $\approx 5\%$ up to $M_A \approx 2m_t$.

– In the case of the charged Higgs state, there is also the channel $H^+ \to Wh$ which is important similarly to the $A \to hZ$ case. Note that for $M_{H^\pm} \lesssim 170$ GeV, the decay $H^+ \to c\bar{s}$ that is usually considered only in two–Higgs doublet models and the very interesting flavor changing mode $H^+ \to c\bar{b}$ have rates that are at the percent level. All these exotic channels have larger branching ratios, above $\approx 10\%$, for $\tan\beta$ values close to unity.

7.3.3 The case of the h boson

Assuming the lighter h boson to be the 126 GeV Higgs observed at the LHC, we now briefly mention its production and decay rates.

In the left–hand side of Fig. 29, we display the cross sections for the relevant Higgs production channels at the LHC with $\sqrt{s} = 8$ TeV as a function of M_A at $\tan\beta = 2.5$. Again, the radiative corrections in the ϵ approach are such that M_h is fixed to 126 GeV. Shown are the rates for the gluon fusion $gg \to h$, vector boson fusion $qq \to hqq$, Higgs–strahlung $q\bar{q} \to hW, hZ$ as well as associated $pp \to t\bar{t}h$ processes. The relevant higher order QCD corrections are implemented and the MSTW set of PDFs has been adopted. The rates can be very different whether one is in the decoupling limit $M_A \approx 1$ TeV where the h couplings are SM–like or at low M_A values when the h couplings are modified.

The variation of the branching ratios compared to their SM values, which correspond to their MSSM values in the decoupling limit, are displayed as a function of M_A for $\tan\beta = 2.5$ in the right-hand side of the figure. Sown are the branching fractions for the decays that are currently used to search for the SM Higgs boson, i.e. the channels $h \to bb, \tau\tau, ZZ, WW, \gamma\gamma$. Again, large differences compared to the SM can occur at low to moderate M_A values.

The data collected so far by the ATLAS and CMS collaborations on the observed 126 GeV Higgs particle should thus put strong constraints on the parameters $\tan\beta$ and M_A.

7.4 Present constraints on the MSSM parameter space

7.4.1 Constraints from the h boson mass and rates

We start this section by discussing the impact of the large amount of ATLAS and CMS data for the observed Higgs state at the LHC on the MSSM parameter space. We will assume for definiteness that the h boson is indeed the observed particle as the possibility that it is the H state instead is ruled out by the LHC data [287].

A first constraint comes from the measured mass of the observed state, $M_h \approx 126$ GeV. As discussed previously and in several other instances such as Ref. [191], in the

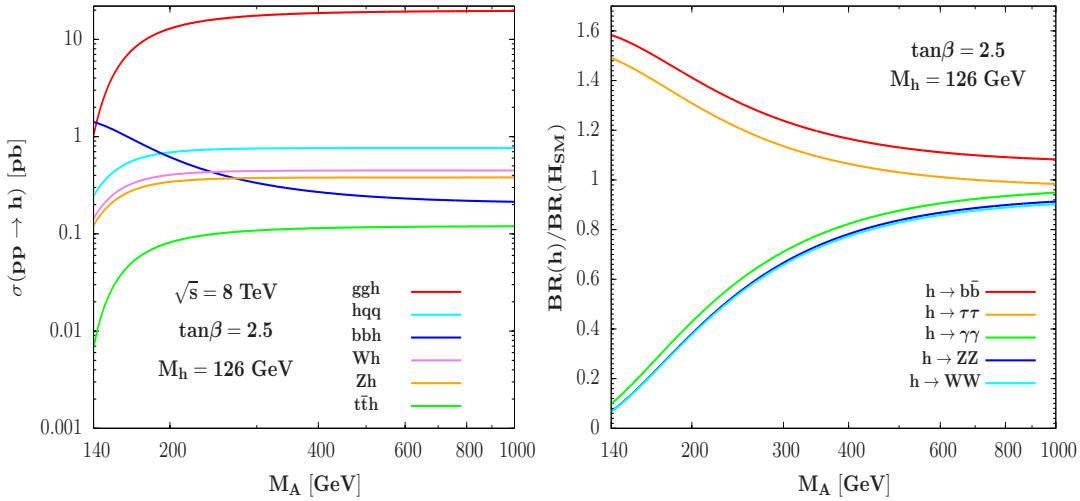

Figure 29: The production cross sections of the lighter h boson at the LHC with $\sqrt{s} = 8$ TeV (left) and the variation of its decay branching fractions compared to the SM values (right) for $\tan\beta = 2.5$. Again, the radiative corrections in the Higgs sector are such that $M_h = 126$ GeV.

phenomenological MSSM, this large M_h value indicates that the radiative corrections in the Higgs sector are maximised. If the scale M_S is close to 1 TeV as dictated by naturalness arguments, this implies that one is in the decoupling regime (and hence, dealing with a SM–like Higgs particle) with intermediate to high–$\tan\beta$ values and maximal stop mixing. If the SUSY scale is pushed to $M_S \approx 3$ TeV, the highest acceptable value from fine-tuning adopted in many analyses such that of Refs. [286, 287], a smaller mixing in the Higgs sector and values of M_A of order of a few hundred GeV can be made possible. However, $\tan\beta$ values in the low regime, $\tan\beta \lesssim 3$–5 cannot be accommodated as they lead to $M_h \lesssim 123$ GeV and even to $M_h \lesssim 120$ GeV, which is the lowest value that can be reached when including the theoretical and the top-quark mass uncertainties in the calculation of M_h.

To obtain an acceptable value of M_h in the low $\tan\beta$ regime, one needs to push M_S to the 10 TeV domain or higher. In the approach that we are advocating here, in which the radiative corrections in the MSSM Higgs sector are implemented in the rather simple (but not completely inaccurate) approximation where only the leading RGE improved one–loop correction of Eq. (7.223) is taken into account, one can trade the (unknown) values of M_S and the mixing parameter X_t with the (known) value of the Higgs mass M_h. In other words, for each set of $\tan\beta$ and M_A inputs, one selects the ϵ radiative correction that leads to the correct mass $M_h = 126$ GeV. The LHC constraint on the mass of the observed Higgs state is then automatically satisfied. We emphasize again that for the large SUSY scales that are needed for the low $\tan\beta$ regime, $\tan\beta \lesssim 3$, the MSSM spectrum cannot be calculated in a reliable way using the usual versions of the RGE programs such as `Suspect`.

A second constraint comes from the measurement of the production and decay rates of the observed Higgs particle. The ATLAS and CMS collaborations have provided the signal strength modifiers μ_{XX}, that are identified with the Higgs cross section times decay branching ratio normalized to the SM expectation in a given $H \to XX$ search channel. For the various searches that have been conducted, $h \to ZZ, WW, \gamma\gamma, \tau\tau$ and

$b\bar{b}$ with the entire set of data collected in the runs at $\sqrt{s} = 7$ TeV and 8 TeV, i.e. ≈ 5 fb^{-1} and ≈ 20 fb^{-1} (with the exception of $h \to b\bar{b}$ which has been analyzed only with 17 fb^{-1} of the 7+8 TeV data) [335–345]. These various channels that have been measured are used to constrain the couplings of the h state and, hence, the $[\tan\beta, M_A]$ parameter space.

Rather than performing a complete fit of the ATLAS and CMS light Higgs data including all the signal strengths, we will simply use the most precise and cleanest observable in this context: the signal strength μ_{ZZ} in the search channel $h \to ZZ$. As recently discussed in Refs. [346, 346] (to which we refer for the details), this channel is fully inclusive and does not involve the additional large theoretical uncertainties that occur when breaking the cross section of the dominant production process $gg \to h$ into jet categories[20]. In addition, contrary to the global signal strength $\mu_{\rm tot}$, it does not involve the channel $h \to \gamma\gamma$ which, at least in the ATLAS case, deviates from the SM prediction and might indicate the presence of new contributions (such as those of light charginos?) in the $h\gamma\gamma$ loop. The combination of the ATLAS and CMS data in the ZZ channel gives, $\mu_{ZZ} = 1.10 \pm 0.22 \pm 0.20$ where the first uncertainty is experimental and the second one theoretical. Following Ref. [106], we assume a total theoretical uncertainty of $\Delta^{\rm th} = \pm 20\%$ and, since it should be considered as a bias, we add it linearly to the experimental error. This gives a lower limit on the $h \to ZZ$ signal strength of $\mu_{ZZ} \gtrsim 0.62$ at 68%CL and $\mu_{ZZ} \gtrsim 0.4$ at 95%CL.

In the MSSM case, the signal strength will be given by $\mu_{ZZ} = \sigma(h) \times {\rm BR}(h \to ZZ) / \sigma(H_{\rm SM}) \times {\rm BR}(H_{\rm SM} \to ZZ)$ and will be thus proportional to combinations of reduced h coupling squared to fermions and gauge bosons, $g^2_{htt} \times g^2_{hVV}/g^2_{hbb}$... The fact that μ_{ZZ} can be as low at 0.4 at 95%CL means that we can be substantially far from the decoupling limit, $g^2_{HVV} \approx 0.1$, with not too heavy $H/A/H^\pm$ states even at low $\tan\beta$.

In Fig. 30, we have scanned the $[\tan\beta, M_A]$ parameter space and delineated the areas in which the 68%CL and 95%CL constraints on μ_{ZZ} are fulfilled. We observe that indeed, the entire range with $M_A \lesssim 200$ GeV for most value of $\tan\beta$ is excluded at the 95%CL. With increasing $\tan\beta$, the excluded M_A values are lower and one recovers the well known fact that the decoupling limit is reached more quickly at higher $\tan\beta$ values. In most cases, we will use this indirect limit of $M_A \lesssim 200$ GeV prior to any other constraint (except for illustrations in the $H^\pm$ case where the low mass range will be kept).

7.4.2 Constraints from the heavier Higgs searches at high $\tan\beta$

As discussed previously, the most efficient channel to search for the heavier MSSM Higgs bosons is by far H/A production in gg and $b\bar{b}$ fusion with the Higgs bosons decaying into τ lepton pairs, $pp \to \Phi \to \tau^+\tau^-$. Searches for this process have been performed by the ATLAS collaboration with ≈ 5 fb^{-1} data at the 7 TeV run [343, 344] and by the CMS collaboration with $\approx 5 + 12$ fb^{-1} data at the 7 TeV and 8 TeV runs [345]. Upper limits on the production times decay rates of these processes (which, unfortunately, have not

[20] For instance, the signal strengths in the $\tau\tau$ and WW channels are obtained by considering the $gg \to H + 0j, 1j$ and/or the vector boson fusion categories. The signal strength μ_{WW} provides the same information as μ_{ZZ}, while the measurement of the signal strengths in the $h \to b\bar{b}$ and $h \to \tau^+\tau^-$ channels are not yet very accurate. Hence, using only the $h \to ZZ$ channel should be a good approximation.

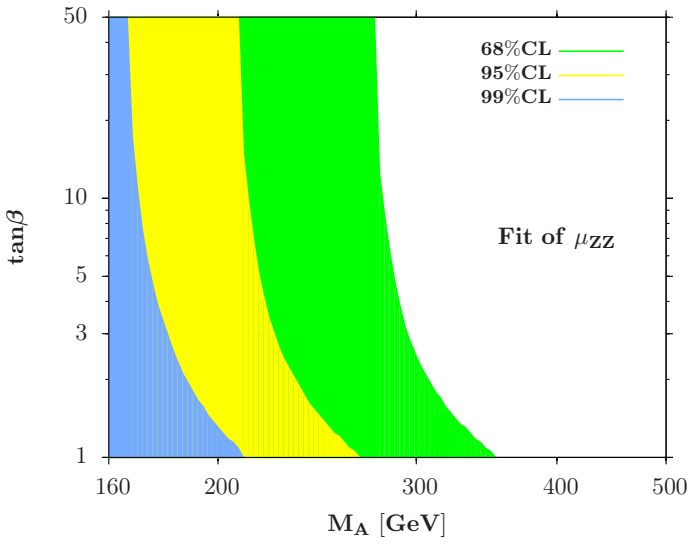

Figure 30: The $[\tan\beta, M_A]$ parameter space of the MSSM in which the signal strength in the $h \to ZZ$ search channel is not compatible with the LHC data on the rates of the observed h boson at the 68%CL (green), 95%CL (yellow) and 99%CL (blue).

given by the collaborations) have been set and they can be turned into constraints on the MSSM parameter space which, in the Higgs sector, corresponds to the $[\tan\beta, M_A]$ plane.

In Fig. 31, we display the sensitivity of the CMS $\Phi \to \tau\tau$ analysis in the $[\tan\beta, M_A]$ plane. The excluded region, obtained from the observed limit at the 95%CL is drawn in light blue. The solid line represents the median expected limit which turns out to be weaker than the observed limit. As can be seen, this constraint is extremely restrictive and for values $M_A \lesssim 250$ GeV, it excludes almost the entire intermediate and high $\tan\beta$ regimes, $\tan\beta \gtrsim 5$. The constraint is of course less effective for a heavier pseudoscalar Higgs boson, but even for $M_A = 400$ GeV the high $\tan\beta \gtrsim 10$ region is excluded and one is even sensitive to large values $M_A \approx 700$ GeV for $\tan\beta \gtrsim 50$.

There are, however, some caveats to this exclusion limit as discussed previously. The first one is that there is a theoretical uncertainty that affects the Higgs production cross section times decay branching ratios which is of the order of $\pm 25\%$ when the $gg \to \Phi$ and $b\bar{b} \to \Phi$ cross sections are combined. If this theoretical uncertainty is included when setting the limit in the $[\tan\beta, M_A]$ plane, as shown by the dashed contours around the expected limit in Fig. 31, the constraint will be slightly weaker as one then needs to consider the lower value of the $\sigma(pp \to \Phi) \times \text{BR}(\Phi \to \tau^+\tau^-)$ rate predicted by theory.

The second caveat is that the CMS (and ATLAS) constraint has been given in a specific benchmark scenario, the maximal mixing scenario with the choice $X_t/M_S = \sqrt{6}$ and the value of the SUSY scale set to $M_S = 1$ TeV; the other parameters such as the gaugino and higgsino masses and the first/second generation fermion parameters that have little impact can be chosen as in Eq. (7.228). However, as was previously argued, the $pp \to \Phi \to \tau\tau$ cross section times decay branching fraction is very robust and, hence, the exclusion limit is almost model independent. It is altered only very mildly by the radiative corrections in the MSSM Higgs sector, in particular by the choice of the parameters M_S and X_t (this is especially true if these parameters are to be traded against the measured values of M_h).

In fact, the exclusion limit in Fig. 31 can be obtained in any MSSM sce-

nario with the only assumption being that SUSY particles are too heavy to affect $\sigma(pp \to \Phi) \times \mathrm{BR}(\Phi \to \tau\tau)$ by more than 25%, which is the estimated theoretical uncertainty. Even in the case of light SUSY particles, it is very hard to make that stop/sbottom squarks contribute significantly to the $gg \to H$ production processes, or to have a significant Δ_b correction to the Φbb coupling which largely cancels out as indicated by Eq. (8.3), or to have a substantial change of the $\Phi \to \tau\tau$ fraction due to light SUSY particles that appear in the decays.

Thus, the limit for the $pp \to \tau^+\tau^-$ searches is robust with respect to the SUSY parameters and is valid in far more situations and scenarios than the "MSSM $M_h^{\rm max}$ scenario" that is usually quoted by the experimental collaborations. We thus suggest to remove this assumption on the benchmark scenario (in particular it adopts the choice $M_S = 1$ TeV which does not allow low $\tan\beta$ values and which starts to be challenged by direct SUSY searches), as the only relevant assumption, if any, should be that we do not consider cases in which the SUSY particles are too light to alter the Higgs production and decay rates. This is a very reasonable attitude if we are interested mainly in the Higgs sector.

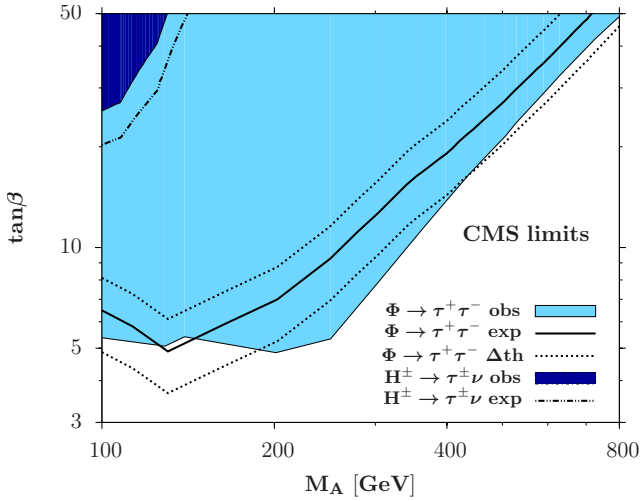

Figure 31: The $[\tan\beta, M_A]$ plane in the MSSM in which the $pp \to H/A \to \tau^+\tau^-$ (light blue) and $t \to bH^+ \to b\tau\nu$ (dark blue) search constraints using the CMS data are included (observed limits). The solid contour for the $pp \to \tau\tau$ mode is for the median expected limit and the two dashed ones are when the QCD uncertainties on the rates are included.

Another constraint on the MSSM Higgs sector[21] is the one from charged Higgs searches in the $H^- \to \tau\nu$ final states with the $H^\pm$ bosons produced in top quark decays, $t \to H^+b \to \tau\nu b$. Up to now, the ATLAS and CMS collaborations have released results only with the ≈ 5 fb^{-1} collected at $\sqrt{s} = 7$ TeV [347–349]. We have also delineated in Fig. 31 the impact on the $[\tan\beta, MA]$ parameter space of the CMS 95%CL observed limits in this channel.

As can be observed, the constraint is effective only for values $M_A \lesssim 150$ GeV which correspond to a light H^+ state that could be produced in top quark decays. The search is sensitive to the very high $\tan\beta$ region which is completely excluded by the $\tau\tau$ search,

[21] A search has also been performed by the CMS collaboration based on the 7 TeV data in the channel $pp \to \Phi b\bar{b} \to bbbb$ [322]. This search is much less sensitive than the $\tau\tau$ search even if one extrapolates the expected limits to the same amount of data. We will thus ignore it in our study.

that is performed with much more data though. However, even if the comparison is made for the same amount of data, the $pp \to \Phi \to \tau\tau$ search is by far more sensitive.

Note that contrary to the $pp \to \tau^+\tau^-$ case, the limits at high $\tan\beta$ from the process $pp \to t\bar{t}$ with $t \to bH^+ \to b\tau\nu$ might be more model dependent. Indeed, while SUSY decays might not be important as the small $M_{H^\pm}$ value leaves little room for light sparticles (and the high $\tan\beta$ values would suppress these decays anyway), the effect of the Δ_b corrections might be larger as there is no cancellation between production and decay rates. Nevertheless, the $H^\pm$ limit is effective only for $M_A \lesssim 150$ GeV values excluded by the h data. We keep this $H^\pm$ constraint though, as it is also valid in two-Higgs doublet models.

7.4.3 Extrapolation to the low $\tan\beta$ region and the full 7+8 data

A very important remark is that in our version of the constraints in the $[\tan\beta, M_A]$ plane of Fig. 31, we have removed the region excluded by the bound on the h mass, $M_h \gtrsim 114$ GeV from negative Higgs searches at LEP2, which is also usually displayed by the experimental collaborations. In the usual benchmark scenario, this constraint excludes the entire low $\tan\beta$ regime, $\tan\beta \lesssim 3$, and at low $M_A \approx 100$ GeV, $\tan\beta$ values up to $\tan\beta \approx 10$.

A first reason for removing the "LEP exclusion" region is that it is now superseded by the "observation" constraint 123 GeV $\lesssim M_h \lesssim$ 129 GeV (once the theoretical and experimental uncertainties are included) which is by far stronger. In fact, as was discussed in Ref. [286], if the benchmark scenario with $M_S = 1$ TeV and maximal stop mixing is to be adopted, the entire range $\tan\beta \lesssim 5$ and $\tan\beta \gtrsim 20$ for any M_A value would be excluded simply by requiring that 123 GeV $\lesssim M_h \lesssim$ 129 GeV (and the excluded regions would be completely different for other M_S and X_t values as also shown in Ref. [286]).

A second reason is that the LEP2 M_h constraint and even the constraint $M_h \gtrsim 123$ GeV can be simply evaded for any value of $\tan\beta$ or M_A by assuming large enough M_S values as discussed previously. This will then open the very interesting low $\tan\beta$ region which can be probed in a model independent way by Higgs search channels involving the $H, A, H^\pm$ bosons, including the $t \to bH^+ \to b\tau\nu$ channel discussed previously.

Indeed, the branching fraction for the decay $t \to bH^+$ is also significant at low $\tan\beta$ values, when the component of the coupling g_{tbH^+} that is proportional to $\bar{m}_t/\tan\beta$ becomes dominant. On the other hand, the branching fraction for the decay $H^\pm \to \tau\nu$ stays close to 100%. Hence, the rates for $pp \to t\bar{t}$ with $t \to bH^+ \to b\tau\nu$ are comparable for $\tan\beta \approx 3$ and $\tan\beta \approx 30$ and the processes can also probe the low $\tan\beta$ region. This is exemplified in Fig. 32 where the $t \to bH^+$ CMS median expected and observed limits obtained with the 7 TeV data are extrapolated to the low $\tan\beta$ region. As can be seen, the region $\tan\beta \lesssim 2$ is excluded for $M_A \lesssim 140$ GeV (this region can also be probed in the $H^+ \to c\bar{s}$ mode).

In fact, as is shown in the lower part of Fig. 32, even the channel $pp \to \Phi \to \tau\tau$ is useful at low $\tan\beta$. Indeed, for $\tan\beta$ values close to unity, while the $b\bar{b} \to \Phi$ process becomes irrelevant, the cross sections for the $gg \to \Phi$ process becomes very large, the reason being that for $\tan\beta \approx 1$ the couplings $g_{\Phi tt} \propto \bar{m}_t/\tan\beta$ are significant and the

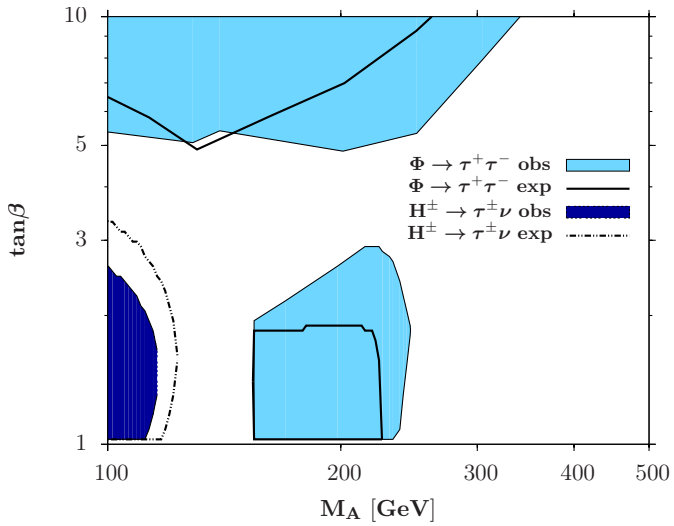

Figure 32: The $[\tan\beta, M_A]$ plane in the MSSM in which the $pp \to H/A \to \tau^+\tau^-$ (light blue) and $t \to bH^+ \to b\tau\nu$ (dark blue) observed limits using the CMS data are extrapolated to low $\tan\beta$. The solid contours in the $\tau\tau$ and $\tau\nu$ cases are for the expected limits.

dominant top quark loop contribution becomes less suppressed compared to the SM. On the other hand, at least in the case of the pseudoscalar A, the branching ratio for the $\tau^+\tau^-$ decay stays significant for M_A values up to the $t\bar{t}$ threshold as shown in Fig. 28. Hence, the production times decay rate for $gg \to A \to \tau\tau$ stays large and the CMS search limit is effective and excludes $\tan\beta$ values close to 1, for pseudoscalar masses up to $M_A \approx 350$ GeV.

One would get a better feeling of the power of these constraints at low $\tan\beta$ values (and in the charged Higgs case also at high $\tan\beta$), if the present limits in the $pp \to \tau\tau$ and $t \to bH^+ \to b\tau\nu$ channels are extrapolated to the full set of data collected in the 2011 and 2012 LHC runs. This is shown in Fig. 33 where the median expected CMS limits in the two search channels are extrapolated to an integrated luminosity of 25 fb^{-1}, assuming that the limits simply scale like the square–root of the number of events.

The gain in sensitivity is very significant in the $H^\pm$ case as the gap between the present CMS limit with the ≈ 5 fb^{-1} of the 7 TeV data and the expected limit with the additional ≈ 20 fb^{-1} data at 8 TeV is large (there is an additional increase of the $pp \to t\bar{t}$ production cross section from $\sqrt{s} = 7$ TeV to 8 TeV). In the case of the $pp \to \tau\tau$ channel, the increase of sensitivity is much more modest, not only because the gap from the 17 fb^{-1} data used in the latest CMS analysis and the full 25 fb^{-1} data collected up to now is not large but, also, because presently the observed limit is much stronger than the expected limit.

Hence, these interesting low $\tan\beta$ areas that were thought to be buried under the LEP2 exclusion bound on M_h are now open territory for heavy MSSM Higgs hunting. This can be done not only in the two channels $pp \to \tau^+\tau^-$ and $t \to bH^+ \to b\tau\nu$ above (and which were anyway used at high $\tan\beta$) but also in a plethora of channels that have not been discussed before (or at least abandoned after the LEP2 results) and to which we turn now.

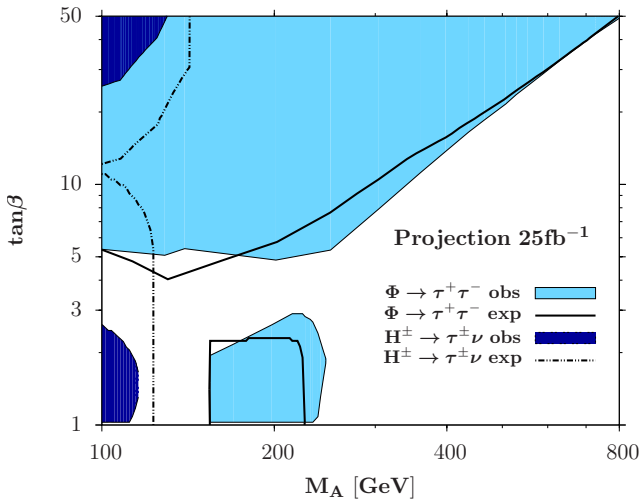

Figure 33: The $[\tan\beta, M_A]$ plane in the MSSM in which the $pp \to H/A \to \tau^+\tau^-$ and $t \to bH^+ \to b\tau\nu$ CMS expected limits are extrapolated to the full 7+8 TeV data with ≈ 25 fb^{-1}. The present observed limits are still shown in blue.

7.5 Heavy Higgs searches channels at low $\tan\beta$

We come now to the main phenomenological issue of this part: the probe at the LHC of the low $\tan\beta$ region for a not too heavy pseudoscalar A state[22]. We stress again that this region can be resurrected simply by allowing a large SUSY scale M_S which removes the LEP2 $M_h \gtrsim 114$ GeV constraint (and now the LHC mass constraint $M_h \approx 126$ GeV). We show that several channels discussed in the case of a high mass SM Higgs or in scenarios beyond the SM can be used for the search of the MSSM H, A and $H^\pm$ bosons.

7.5.1 The main search channels for the neutral H/A states

The $\mathbf{H \to WW, ZZ}$ channels

These are possible only for the heavier H boson (because of CP invariance there are no VV couplings for A) with masses below the $t\bar{t}$ threshold where the branching ratios for the decays $H \to WW$ and $H \to ZZ$ are significant; see Fig. 28. The $H \to WW$ process is particularly useful in the region $160 \lesssim M_H \lesssim 180$ GeV where the branching ratio is close to 100%. In both cases, the $gg \to H$ production process can be used but, eventually, vector boson fusion can also be relevant at the lowest $\tan\beta$ and M_H possible values.

The search modes that are most useful at relatively low M_H values, should be the $pp \to H \to ZZ \to 4\ell^\pm$ and $pp \to H \to WW \to 2\ell 2\nu$ channels that have been used to observe the SM–like light h boson (as the mass resolution of the $H \to WW$ channel is rather poor, one has to subtract the observed signal events in the low mass range, $M_H \lesssim 160$ GeV) and to exclude a SM–like Higgs particle with a mass up to 800 GeV [338, 340]. When the two processes are combined, the sensitivity is an order of

[22] This issue has been discussed in the past and a summary can be found in Section 3.3.2 of Ref. [48]. It has been also addressed recently in Ref. [310] (where, in particular, a feasibility study of the $H \to hh$ and $A \to hZ$ modes at $\sqrt{s} = 14$ TeV is made). Recents analyses of heavier MSSM Higgsses at intermediate and high $\tan\beta$ can be found in Refs. [282, 283, 350–352].

magnitude larger than for the SM Higgs for masses below 400 GeV and one can thus afford a substantial reduction of the couplings g_{Htt} and g_{HVV} which should allow to probe $\tan\beta$ values significantly higher than unity[23]. At high H masses, $M_H \gtrsim 300$ GeV, one could also add the $pp \to H \to ZZ \to 2\ell 2q, 2\nu 2q, 2\ell 2\nu$ and $pp \to H \to WW \to \ell\nu 2q$ channels to increase the statistics, as done in a recent study by the CMS collaboration [354].

There is one difference with the SM Higgs case though. While in the SM, the Higgs particle has a large total width at high masses as a result of the decays into longitudinal W/Z bosons which make it grow as $M^3_{H_{\rm SM}}$, the MSSM H boson remain narrow as the coupling g_{HVV} is suppressed. In fact, all MSSM Higgs particles will have a total width that is smaller than ≈ 3 GeV for $\tan\beta \approx 3$ and masses below 500 GeV. The smaller total width in the MSSM can be rather helpful at relatively high H masses as, for instance, it allows to suppress the continuum ZZ background by selecting smaller bins for the invariant mass of the ZZ system in the signal events. Issues like the interference of the signal and the $gg \to VV$ backgrounds will also be less important than in the SM.

The $\mathbf{H/A \to t\bar{t}}$ channels

This search channel has not been considered in the case of the SM Higgs boson for two reasons [47]. The first one is that for $M_{H_{\rm SM}} \gtrsim 350$ GeV, the $H_{\rm SM} \to WW, ZZ$ channels are still relevant and largely dominate over the $H_{\rm SM} \to t\bar{t}$ decay channel which has a branching fraction that is less than 20% in the entire Higgs mass range (the reason being again that the partial widths for $H_{\rm SM} \to VV$ grow as $M^3_{H_{\rm SM}}$ while for $H_{\rm SM} \to t\bar{t}$ it grows only like $M_{H_{\rm SM}}$). The other reason is that the continuum $t\bar{t}$ background was thought to be overwhelmingly large as it had to be evaluated in a large mass window because of the large Higgs total width (in addition, the events from $H_{\rm SM} \to t\bar{t}$ produce a dip–peak structure in the $gg \to t\bar{t}$ invariant mass spectrum that was unobservable for a large total width).

The situation in the MSSM is very different. First, as mentioned previously, the total width for heavy H and A states are much smaller, less than $\lesssim 20$ GeV for any $\tan\beta \gtrsim 1$ value for $M_{H,A} \lesssim 500$ GeV and grow (almost) linearly with the Higgs masses beyond this value. One can thus integrate the $t\bar{t}$ continuum background in a smaller invariant mass bin and significantly enhance the signal to background ratio. A second feature is that contrary to the SM case, the branching ratios for the $H/A \to t\bar{t}$ decays are almost 100% for $\tan\beta \lesssim 3$ as soon as the channels are kinematically open (this is particularly true for A where even below the threshold, the three–body decay $A \to tt^* \to tbW$ is important).

The only disadvantage compared to the SM is that the production cross section could be smaller. In the MSSM, the only relevant process in the low $\tan\beta$ regime for $M_\Phi \gtrsim 350$ GeV is $gg \to \Phi$ with the dominant (almost only) contribution being due to the top quark loop. The latter is suppressed by the square of the coupling $g_{\Phi tt} \propto 1/\tan\beta$ if $\tan\beta$ is not close to unity. However, in the MSSM, one has to add the cross sections of

[23] The ATLAS collaboration has recently analyzed heavy H production in a two–Higgs doublet model in the channel $H \to WW \to e\nu\mu\nu$ with 13 fb^{-1} data collected at $\sqrt{s} = 8$ TeV [353]. Unfortunately, this analysis cannot readily be used as the limit on the cross section times branching fraction has not been explicitly given and the results are displayed in terms of $\cos(\alpha)$ (and not $\cos(\beta-\alpha)$ which would have corresponded to the HWW coupling) which does not allow an easy interpretation in the MSSM.

both the H and A states. In addition, the loop form factors in the pseudoscalar A and scalar $H/H_{\rm SM}$ cases are different and, as can been seen from Fig. 27, the $gg \to \Phi$ cross section is larger in the pseudoscalar Higgs case when the same top Yukawa coupling is assumed.

In toto, the situation for $H/A \to t\bar{t}$ will certainly be more favorable for the MSSM at low $\tan\beta$ than in the SM. While there was no search for the SM Higgs in this channel, the ATLAS [355] and CMS [356] collaborations have looked for heavy resonances (such as new Z' gauge bosons in extended gauge models or Kaluza–Klein excitations in scenarios with extra space–time dimensions) that decay into $t\bar{t}$ pairs with the data collected at the 7 TeV run. The lepton+jets final state has been studied in the topology where the top quarks are highly boosted which allows a good discrimination from the continuum $t\bar{t}$ background [357] (the ATLAS and CMS collaborations searches assume resonance masses $M_{tt} \gtrsim 700$ GeV to benefit from this topology). Limits on the cross sections times branching ratios have been set, corresponding to roughly $\sigma_{tt} \approx 0.7$ pb for a resonance with a mass of 1 TeV and a narrow width, $\Gamma_{tt} \approx 10^{-2} M_{tt}$ (which is more or less the case of the MSSM H/A states at $\tan\beta \approx 3$). A lower (higher) cross section is needed at larger (smaller) resonance mass when the top quarks are (not) sufficiently boosted and, at $M_{tt} \approx 500$ GeV, one needs $\sigma_{tt} \approx 3$ pb which approximately corresponds to an increase with $1/M_{tt}^2$.

The A → Zh channel

As discussed earlier, the $gg \to A$ production cross section is very large at low $\tan\beta$ values: it is higher than for the SM Higgs boson at $\tan\beta = 1$ (as the form factor for the ggA amplitude is larger than in the scalar Higgs case) and is suppressed only by a factor $g^2_{Att} \propto 1/\tan^2\beta$. On the other hand, in the range $M_h + M_Z \lesssim M_A \lesssim 2m_t$, the branching ratio for the decay $A \to hZ$ is large for $\tan\beta \approx 3$ and largely dominant for $\tan\beta \approx 1$. In the mass window $M_A = 210$–350 GeV, the production times decay rate for the process $gg \to A \to hZ$ should be thus very high in the low $\tan\beta$ region.

The hZ final state has been searched for in the SM in the Higgs–strahlung process, $q\bar{q} \to Z^* \to Zh$ with the Z boson decaying into leptons or neutrinos, $Z \to \ell^+\ell^-, \nu\bar{\nu}$ and the h boson decaying into $b\bar{b}$ final states [341, 342]. The significance of the signal is strongly increased by looking at boosted jets when the Higgs has a large transverse momentum [113]. In the CMS analysis with 17 fb^{-1} of the 2011 and 2012 data [342], a signal strength $\mu_{bb} \approx 1.5$ has been found in the $Z \to \nu\bar{\nu}$ and $Z \to \ell^+\ell^-$ channels with a large error bar. Very roughly, one can assume that the additional events from the $A \to Zh$ channel should be observed if they exceed this sensitivity when extrapolated to include the full 2012 data.

One should note that the information from the $pp \to Zh$ search in the SM provides only a lower limit for the sensitivity as in the present case one can benefit from the fact that the invariant mass of the four fermion final state (without neutrinos) which should peak at the value M_A will further suppress the continuum background, in particular the $Z + b\bar{b}$ events. However, as h is originating from the decay of the state A which should not be very heavy, it has not enough transverse momentum to strengthen the boosted jet techniques that allow to isolate the $h \to b\bar{b}$ signal from the QCD background.

The H → hh channel

The channel $pp \to H \to hh$ is similar to $A \to hZ$: it has very large production rates in the low $\tan\beta$ regime in the mass range 250 GeV $\lesssim M_H \lesssim$ 350 GeV when the decay channels $H \to hh$ is kinematically open and the $H \to t\bar{t}$ mode is closed; the $gg \to H$ cross section should be substantial in this area of the parameter space.

If the dominant $h \to b\bar{b}$ decay is considered, the signal topology has some similarities with that of the process $gg \to b\bar{b} + A/H$ which was discussed here as being one of the main MSSM Higgs processes at high $\tan\beta$ and searched for by the CMS collaboration with the 7 TeV data [322]. However, the kinematical behavior is very different and in the signal events, one can use further constraints, $M_{bb} \approx M_h$ and $M_{bbbb} \approx M_H$ (see Ref. [310] where a characterization of this channel has been made). In fact, the $H \to hh$ channel has more similarities with double production of the SM–like Higgs boson, $gg \to hh$, which is considered for the measurement of the Higgs self–coupling a the 14 TeV LHC with a high luminosity. This process has been revisited recently [111,358,359] and it has been shown that the final state channels $b\bar{b}\tau\tau$ and $b\bar{b}\gamma\gamma$ would be viable at $\sqrt{s} = 14$ TeV and $\mathcal{L} \gtrsim 300$ fb^{-1}. Because the $h \to \gamma\gamma$ decay is too rare, only the first process could be considered at $\sqrt{s} = 8$ TeV with 25 fb^{-1} data. Note that here again, one could use the reconstructed H mass constraint, $M_H = M_{hh}$, to further suppress the continuum background.

7.5.2 Expectations for the LHC at 8 TeV

It is obvious that a truly reliable estimate of the sensitivity on the heavy neutral MSSM Higgs bosons in the various channels discussed before can only come from the ATLAS and CMS collaborations. We will nevertheless attempt in this section to provide a very rough estimate of the achievable sensitivities using present searches conducted for a heavy SM Higgs and in beyond the SM scenarios. The very interesting results that could be obtained would hopefully convince the experimental collaborations to conduct analyses in this area.

Following the previous discussions, our working assumptions to derive the possible sensitivities in the various considered search channels are as follows:

– $H \to WW, ZZ$: we will use the recently published CMS analysis of Ref. [354] that has been performed with the ≈ 10 fb^{-1} data collected in the 7+8 TeV runs and in which all possible channels $H \to ZZ \to 4\ell, 2\ell 2\nu, 2\ell jj, 2\nu jj$ and $H \to WW \to 2\ell 2\nu, \ell\nu jj$ have been included and combined. In the entire range $M_H = 160$–350 GeV, where the SM Higgs boson almost exclusively decays into WW or ZZ states, we will assume the cross section times decay branching ratio upper limit that has been given in this CMS study,

– $H/A \to t\bar{t}$: we will make use of the ATLAS [355] and CMS [356] searches at $\sqrt{s} = 7$ TeV for new Z' or Kaluza–Klein gauge bosons that decay into $t\bar{t}$ pairs in the lepton+jets final state topology. Considering a small total width for the resonance, limits on the cross sections times branching ratio of $\approx 6,3$ and 0.75 pb for a resonance mass of, respectively, 350, 500 and 1000 GeV are assumed. This is equivalent to a sensitivity that varies with $1/M_{tt}^2$ that we will optimistically assume to also cover the low mass resonance range.

– $A \to hZ$: we will use the sensitivity given by ATLAS [341] and CMS [342] in their

search for the SM Higgs–like strahlung process $pp \to hZ$ with $h \to b\bar{b}$ and $Z \to \ell\ell, \nu\bar{\nu}$, $\sigma/\sigma^{\rm SM} = 2.8$ with 17 fb^{-1} data at $\sqrt{s} = 7+8$ TeV (we will include the error bar). This should be sufficient as, in addition, we would have on top the constraint from the reconstructed mass in the $\ell\ell b\bar{b}$ channel which is not used in our analysis.

– $H \to hh$: we will use the analysis of the process $gg \to hh$ in the SM performed in Ref. [111, 358] for the 14 TeV LHC that we also scale down to the current energy and luminosity. The final state $bb\tau\tau$ final state will be considered, with the assumption that the cross section times branching ratio should be larger than $\sigma \times {\rm BR} \sim 50$ fb for illustration.

The results are shown in Fig. 34 with an extrapolation to the full 25 fb^{-1} data of the 7+8 TeV LHC run. Again, we assumed that the sensitivity scales simply as the square root of the number of events. The sensitivities from the usual $H/A \to \tau^+\tau^-$ channel is also shown. The green and red areas correspond to the domains where the $H \to VV$ and $H/A \to t\bar{t}$ channels become constraining with the assumptions above. The sensitivities in the $H \to hh$ and $A \to hZ$ modes are given by, respectively, the yellow and brown areas that peak in the mass range $MA = 250$–350 GeV visible at very low $\tan\beta$ values. We refrain from extrapolating to the LHC with 14 TeV c.m. energy.

The outcome is impressive. These channels, in particular the $H \to VV$ and $H/A \to t\bar{t}$ processes, are very constraining as they cover the entire low $\tan\beta$ area that was previously thought to be excluded by the LEP2 bound up to $M_A \approx 500$ GeV. Even $A \to hZ$ and $H \to hh$ are visible in small portions of the parameter space at the upgraded LHC.

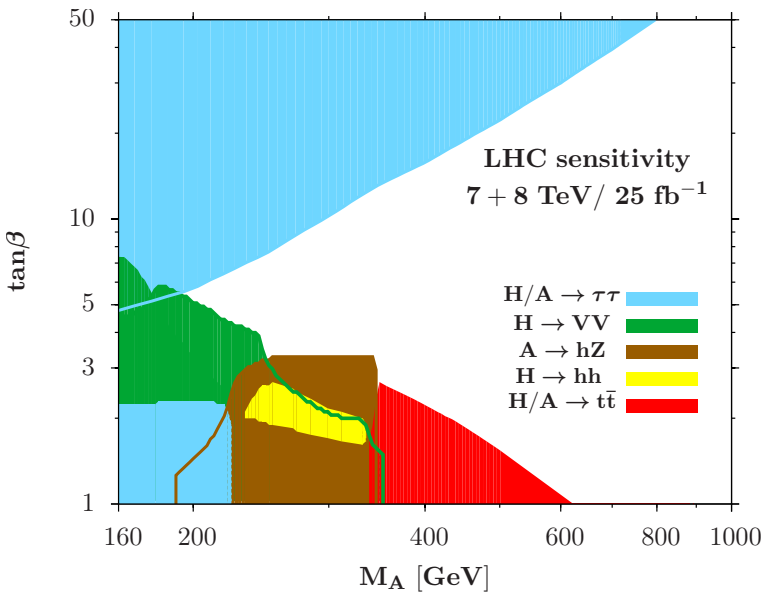

Figure 34: The estimated sensitivities in the various search channels for the heavier MSSM Higgs bosons in the $[\tan\beta, M_A]$ plane: $H/A \to \tau^+\tau^-$ (light blue), $H \to WW + ZZ$ (green), $H/A \to t\bar{t}$ (red), $A \to hZ$ (brown) and $H \to hh$ (yellow). The projection is made for the LHC with 7+8 TeV and the full 25 fb^{-1} of data collected so far. The radiative corrections are such that the lightest h mass is $M_h = 126$ GeV.

7.5.3 Remarks on the charged Higgs boson

We close this discussions with a few remarks on the charged Higgs boson case. First of all, the production rates are very large only for $M_{H^\pm} \lesssim 170$ GeV when the $H^\pm$ state can be produced in top decays. In this case, the decay channel $H^\pm \to \tau\nu$ is always substantial and leads to the constraints that have been discussed earlier and which are less effective than those coming from $H/A \to \tau\tau$ searches at high $\tan\beta$. In the low $\tan\beta$ region, two other channels can be considered: $H^+ \to c\bar{s}$ that has been studied by the ATLAS collaboration in a two–Higgs doublet model with the 7 TeV data [360, 361] and $H^+ \to c\bar{b}$. The branching ratio for the latter channel is significant for $\tan\beta \lesssim 3$ and has been obtained by assuming the same CKM angles as in the SM, in particular $V_{cb} \approx 0.04$ [290]. This channel, if observed would thus allow to check some of the CKM matrix elements in the charged Higgs sector.

Finally, the processes $t \to H^+ b$ at low mass and $pp \to btH^\pm$ at high mass with $H^\pm \to Wh$ can have large rates at sufficiently low $\tan\beta$. The cross section times branching fraction is displayed in Fig. 35 in the $[\tan\beta, M_A]$ plane for a 14 TeV c.m. energy. Shown are the contours with $\sigma \times \text{BR} = 1, 5$ and 10 fb which, for a luminosity of 300 fb^{-1} would correspond to a small number of events. We will not perform an analysis for this particular final state. We simply note that the final state topology, $pp \to tbH^\pm \to tbWh$ resembles that of the $pp \to t\bar{t}h$ process that is considered as a means to measure the $ht\bar{t}$ Yukawa coupling and which is considered to be viable at 14 TeV with a high luminosity.

Hence, even for the charged Higgs bosons, there are interesting search channels which can be considered if the low $\tan\beta$ region is reopened.

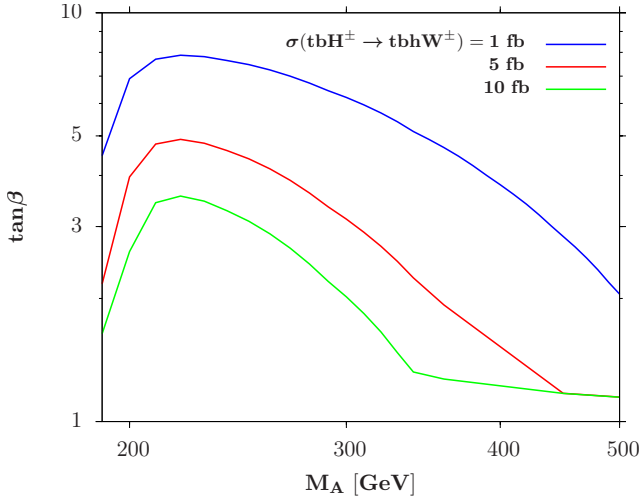

Figure 35: The production cross sections times decay branching ratio at the LHC with $\sqrt{s} = 14$ TeV for the process $pp \to t\bar{b}H^- + \bar{t}bH^+$ with $H^\pm \to hW^\pm$ in the $[\tan\beta, M_A]$ plane. The contours are for some (rough estimates of) limiting values of $\sigma \times$ BR.

7.6 Conclusions about heavy Higgs searches in the low $\tan\beta$ region

After the observation of the 126 GeV SM–like Higgs boson by the ATLAS and CMS collaborations, the next challenge at the LHC should be to search for new phenomena

beyond the SM. This can be done not only by refining the precision determination of the properties of the observed Higgs particle to pin down small deviations of its couplings from the SM expectations, but also by looking for the direct production of new states.

In this part, we have considered the production of the heavier H, A and $H^\pm$ bosons of the MSSM at the LHC, focusing on the low $\tan\beta$ regime, $\tan\beta \lesssim 3$–5. We have first shown that this area of the MSSM parameter space, which was long thought to be excluded, is still viable provided that the SUSY scale is assumed to be very high, $M_S \gtrsim 10$ TeV. For such M_S values, the usual tools that allow to determine the masses and couplings of the Higgs and SUSY particles in the MSSM, including the higher order corrections, become inadequate. We have used a simple but not too inaccurate approximation to describe the radiative corrections to the Higgs sector, in which the unknown scale M_S and stop mixing parameter X_t are traded against the measured h boson mass, $M_h \approx 126$ GeV. One would then have, to a good approximation, only two basic input parameters in the MSSM Higgs sector even at higher orders: $\tan\beta$ and M_A, which can take small values, $\tan\beta \approx 1$ and $M_A = \mathcal{O}(200)$ GeV, provided that M_S is chosen to be sufficiently large.

In the low $\tan\beta$ region, there is a plethora of new search channels for the heavy MSSM Higgs bosons that can be analyzed at the LHC. The neutral H/A states can be still be produced in the gluon fusion mechanism with large rates, and they will decay into a variety of interesting final states such as $H \to WW, ZZ$, $H \to hh$, $H/A \to t\bar{t}$, $A \to hZ$. Interesting decays can also occur in the case of the charged Higgs bosons, e.g. $H^+ \to hW, c\bar{s}, c\bar{b}$. These modes come in addition to the two channels $H/A \to \tau^+\tau^-$ and $t \to bH^+ \to b\tau\nu$ which are currently being studied by ATLAS and CMS and which are very powerful in constraining the parameter space at high $\tan\beta$ values and, as is shown here, also at low $\tan\beta$ values.

We have shown that already with the current LHC data at $\sqrt{s} = 7{+}8$ TeV, the area with small $\tan\beta$ and M_A values can be probed by simply extrapolating to the MSSM Higgs sector the available analyses in the search of the SM Higgs boson at high masses in the WW and ZZ channels and the limits obtained in the $t\bar{t}$ channels in the search for high–mass new gauge bosons from extended gauge or extra–dimensional theories. The sensitivity in these channels will be significantly enhanced at the 14 TeV LHC run once 300 fb^{-1} data will be collected. In the absence of any signal at this energy, the $[\tan\beta, M_A]$ plane can be entirely closed for any $\tan\beta$ value and a pseudoscalar mass below $M_A \approx 500$ GeV. Additional and complementary searches can also be done in the charged Higgs case in channels that have not been studied so far such as $H^+ \to Wh$ but we did not analyze this issue in detail.

Hence, all channels that have been considered for the SM Higgs boson in the high mass range, plus some processes that have been considered for other new physics searches, can be recycled for the search of the heavier MSSM Higgs bosons in the low $\tan\beta$ regime. For instance, many of these MSSM Higgs processes could benefit from the current searches of multi–lepton events with missing energy in SUSY theories. As in all channels we have W, Z and additional h bosons in the final states, multileptons and missing energy are present in most of the topologies. One could then use the direct searches for SUSY particles such as charginos and neutralinos to probe also the MSSM heavier Higgs states.

All this promises a very nice and exciting program for Higgs searches at the LHC

in both the present and future runs. One could then cover the entire MSSM parameter space: from above (at high $\tan\beta$) by improving the $H/A \to \tau\tau$ searches but also from below (at low $\tan\beta$) by using the $WW, ZZ, tt, ..$ searches. The coverage of the $[\tan\beta, M_A]$ plane will be done in a model independent way, with no assumption on M_S and possibly on any other SUSY parameter[24]. The indirect information from the lighter Higgs mass will be included as well as the information from the Higgs couplings, as the sensitivity regions cover also that which are excluded from the measurement of the h properties at the LHC.

One can of course use these channels in other extensions of the SM. An example would be SUSY extensions beyond the MSSM where M_h can be made large enough without having large M_S values; this is the case of the NMSSM where the maximal M_h value can be obtained at $\tan\beta \approx 2$ [254, 362–364]. Another example would be a non–SUSY two–Higgs doublet model where there is more freedom in the parameters space and all channels analyzed here and even some more could be relevant; discussions along these lines have already started [352, 353, 365–369]. The numerous search channels discussed in this section might allow to probe in a more comprehensive manner the extended parameter space of these models.

In the next section, we will introduce and discuss into detail a new version of the MSSM i.e the post Higgs MSSM model [370, 371].

[24]This approach is orthogonal to that of Ref. [289] in which specific benchmark scenarios with fixed SUSY parameters (which might need to be updated soon) are proposed. We note that for all the proposed benchmarks scenarios [289], the SUSY scale is fixed to $M_S = 1$ or 1.5 TeV which excludes the low (and possibly intermediate) $\tan\beta$ regime and, hence, the possibility of discussing the processes analysed here.

8 The post Higgs MSSM scenario

We analyze here the MSSM that we have after the discovery of the Higgs boson at the LHC, the hMSSM (habemus MSSM?), i.e. a model in which the lighter h boson has a mass of approximately 125 GeV which, together with the non-observation of superparticles at the LHC, indicates that the SUSY–breaking scale M_S is rather high, $M_S \gtrsim 1$ TeV. We first demonstrate that the value $M_h \approx 125$ GeV fixes the dominant radiative corrections that enter the MSSM Higgs boson masses, leading to a Higgs sector that can be described, to a good approximation, by only two free parameters. In a second step, we consider the direct supersymmetric radiative corrections and show that, to a good approximation, the phenomenology of the lighter Higgs state can be described by its mass and three couplings: those to massive gauge bosons and to top and bottom quarks. We perform a fit of these couplings using the latest LHC data on the production and decay rates of the light h boson and combine it with the limits from the negative search of the heavier H, A and $H^\pm$ states, taking into account the current uncertainties.

8.1 Introduction

In the MSSM at tree level, the masses of Higgs particles and their mixings are described by only two parameters usually chosen to be the ratio of the vacuum expectations values of the two doublet fields $\tan\beta = v_d/v_u$ and the mass M_A of the pseudoscalar Higgs boson. However, as is well known, the radiative corrections play a very important role as their dominant component grows like the fourth power of the top quark mass, logarithmically with the supersymmetry breaking scale M_S and quadratically with the stop mixing parameter A_t; see e.g. Refs. [183, 185, 186, 186, 201, 203, 271].

The impact of the Higgs discovery is two–fold. On the one hand, it gives support to the MSSM in which the lightest Higgs boson is predicted to have a mass below ≈ 130 GeV when the radiative corrections are included [183,185,186,186,201,203,271]. On the other hand, the fact that the measured value $M_h \approx 125$ GeV is close to this upper mass limit implies that the SUSY–breaking scale M_S might be rather high. This is backed up by the presently strong limits on supersymmetric particle masses from direct searches that indicate that the SUSY partners of the strongly interacting particles, the squarks and gluinos, are heavier than ≈ 1 TeV [316–319]. Hence, the MSSM that we currently have, and that we call hMSSM (habemus MSSM?) in the subsequent discussion, appears to have $M_h \approx 125$ GeV and $M_S \gtrsim 1$ TeV.

It was pointed out in Refs. [282, 283, 372] that when the information $M_h = 125$ GeV is taken into account, the MSSM Higgs sector with solely the dominant radiative correction to the Higgs boson masses included, can be again described with only the two free parameters $\tan\beta$ and M_A as it was the case at tree–level. In other words, the dominant radiative corrections that involve the SUSY parameters are fixed by the value of M_h. In this section, we show that to a good approximation, this remains true even when the full set of radiative corrections to the Higgs masses at the two–loop level is included. This is demonstrated in particular by performing a full scan on the MSSM parameters that have an impact on the Higgs sector such as for instance $\tan\beta$ and the stop and sbottom mass and mixing parameters. The subleading radiative corrections are shown to have little impact on the mass and mixing of the heavier Higgs bosons

when these SUSY parameters are varied in a reasonable range.

Nevertheless, there are also possibly large direct SUSY radiative corrections that modify the Higgs boson couplings and which might alter this simple picture. Among such corrections are, for instance, the stop contribution [373–376] to the dominant Higgs production mechanism at the LHC, the gluon fusion process $gg \to h$, and to the important decay into two photons $h \to \gamma\gamma$, and the additional one–loop vertex corrections to the h couplings to b–quarks that grow with $\tan\beta$ [298]. In the most general case, besides M_h, seven couplings need to be considered to fully describe the properties of the observed h boson: those to gluons, photons, massive gauge bosons, t, b, c quarks and τ leptons. However, we show that given the accuracy that is foreseen at the LHC, a good approximation is to consider the three effective couplings to t, b quarks and to $V = W/Z$ bosons, c_t, c_b and c_V, as it was suggested in Ref. [377]. Following the approach of Ref. [346,378,379] for the inclusion of the current theoretical and experimental uncertainties, we perform a fit of these three couplings using the latest LHC data on the production and decay rates of the lighter h boson and the limits from the negative search of the heavier H, A and $H^\pm$ MSSM states.

The best fit points to low values of $\tan\beta$ and to M_A values of the order of 500 GeV, leading to a spectrum in the Higgs sector that can be fully explored at the 14 TeV LHC.

8.2 Post Higgs discovery parametrization of radiative corrections

In the MSSM, the tree–level masses of the CP–even h and H bosons depend on M_A, $\tan\beta$ and the Z boson mass. However, many parameters of the MSSM such as the SUSY scale, taken to be the geometric average of the stop masses $M_S = \sqrt{m_{\tilde{t}_1} m_{\tilde{t}_2}}$, the stop/sbottom trilinear couplings $A_{t/b}$ or the higgsino mass μ enter M_h and M_H through radiative corrections. In the basis (H_d, H_u), we recall that the CP–even Higgs mass matrix can be written as:

$$M_S^2 = M_Z^2 \begin{pmatrix} c_\beta^2 & -s_\beta c_\beta \\ -s_\beta c_\beta & s_\beta^2 \end{pmatrix} + M_A^2 \begin{pmatrix} s_\beta^2 & -s_\beta c_\beta \\ -s_\beta c_\beta & c_\beta^2 \end{pmatrix} + \begin{pmatrix} \Delta\mathcal{M}_{11}^2 & \Delta\mathcal{M}_{12}^2 \\ \Delta\mathcal{M}_{12}^2 & \Delta\mathcal{M}_{22}^2 \end{pmatrix} \quad (8.241)$$

where we introduced the radiative corrections by a 2×2 general matrix $\Delta\mathcal{M}_{ij}^2$. One can then easily derive the neutral CP even Higgs boson masses and the mixing angle α that diagonalizes the h, H states[25], $H = \cos\alpha H_d^0 + \sin\alpha H_u^0$ and $h = -\sin\alpha H_d^0 + \cos\alpha H_u^0$

$$M_{h/H}^2 = \frac{1}{2}\big(M_A^2 + M_Z^2 + \Delta\mathcal{M}_{11}^2 + \Delta\mathcal{M}_{22}^2 \mp \sqrt{M_A^4 + M_Z^4 - 2M_A^2 M_Z^2 c_{4\beta} + C}\big) \quad (8.242)$$

$$\tan\alpha = \frac{2\Delta\mathcal{M}_{12}^2 - (M_A^2 + M_Z^2)s_\beta}{\Delta\mathcal{M}_{11}^2 - \Delta\mathcal{M}_{22}^2 + (M_Z^2 - M_A^2)c_{2\beta} + \sqrt{M_A^4 + M_Z^4 - 2M_A^2 M_Z^2 c_{4\beta} + C}} \quad (8.243)$$

$$C = 4\Delta\mathcal{M}_{12}^4 + (\Delta\mathcal{M}_{11}^2 - \Delta\mathcal{M}_{22}^2)^2 - 2(M_A^2 - M_Z^2)(\Delta\mathcal{M}_{11}^2 - \Delta M_{22}^2)c_{2\beta} - 4(M_A^2 + M_Z^2)\Delta\mathcal{M}_{12}^2 s_{2\beta}$$

In previous analyses [282,283,372], we have assumed that in the 2×2 matrix for the radiative corrections, only the $\Delta\mathcal{M}_{22}^2$ entry which involves the by far dominant stop–top

[25] A different definition for the mixing angle α, namely $\alpha \to \frac{\pi}{2} - \alpha$, has been adopted in Refs. [282, 283, 377].

sector correction, is relevant, $\Delta\mathcal{M}_{22}^2 \gg \Delta\mathcal{M}_{11}^2, \Delta\mathcal{M}_{12}^2$. This occurs, for instance, in the so–called ϵ approximation [183,185,186,186] and its refinements [201,203] that are given in Eq. (5.214). In this case, one can simply trade $\Delta\mathcal{M}_{22}^2$ for the by now known M_h using

$$\Delta\mathcal{M}_{22}^2 = \frac{M_h^2(M_A^2 + M_Z^2 - M_h^2) - M_A^2 M_Z^2 c_{2\beta}^2}{M_Z^2 c_\beta^2 + M_A^2 s_\beta^2 - M_h^2} \tag{8.244}$$

In this case, one can simply write M_H and α in terms of $M_A, \tan\beta$ and M_h:

$$\text{hMSSM}: \quad \begin{aligned} M_H^2 &= \frac{(M_A^2+M_Z^2-M_h^2)(M_Z^2 c_\beta^2+M_A^2 s_\beta^2)-M_A^2 M_Z^2 c_{2\beta}^2}{M_Z^2 c_\beta^2+M_A^2 s_\beta^2-M_h^2} \\ \alpha &= -\arctan\left(\frac{(M_Z^2+M_A^2)c_\beta s_\beta}{M_Z^2 c_\beta^2+M_A^2 s_\beta^2-M_h^2}\right) \end{aligned} \tag{8.245}$$

In this section, we will check the validity of the $\Delta\mathcal{M}_{11}^2 = \Delta\mathcal{M}_{12}^2 = 0$ approximation. To do so, we first consider the radiative corrections when the subleading contributions proportional to μ, A_t or A_b are included in the form of Eqs. 5.214, that is expected to be a good approximation [271,285], and in which one has $\Delta\mathcal{M}_{11}^2 \neq \Delta\mathcal{M}_{12}^2 \neq 0$.

As a first step we only consider the stop-top sector corrections which enter the $\Delta\mathcal{M}_{ij}^2$ terms and confront in Fig. 36, the values of $\Delta\mathcal{M}_{11}^2$, $\Delta\mathcal{M}_{12}^2$ to $\Delta\mathcal{M}_{22}^2$ for three different scenarios with $M_A = 300$ GeV (i.e. before the onset of the decoupling regime $M_A \gg M_Z$): $M_S = 3$ TeV and $\tan\beta = 2.5$, $M_S = 1.5$ TeV and $\tan\beta = 5$, $M_S = 1$ TeV and $\tan\beta = 30$. The parameter A_t is adjusted in order to accommodate a light Higgs boson with a mass $M_h = 126 \pm 3$ GeV, including an expected theoretical and experimental uncertainty of 3 GeV [191,289,380]. One observes that for reasonable μ values, one obtains naturally $\Delta\mathcal{M}_{11}^2, \Delta\mathcal{M}_{12}^2 \ll \Delta\mathcal{M}_{22}^2$.

We have verified that the situation is not very different if the corrections in the sbottom sector are also included: assuming $A_b = A_t$, we also obtain the hierarchy $\Delta\mathcal{M}_{11}^2, \Delta\mathcal{M}_{12}^2 \ll \Delta\mathcal{M}_{22}^2$ for $\mu \lesssim 3$ TeV even for $\tan\beta = 30$ where contributions $\propto \mu\tan\beta$ become important.

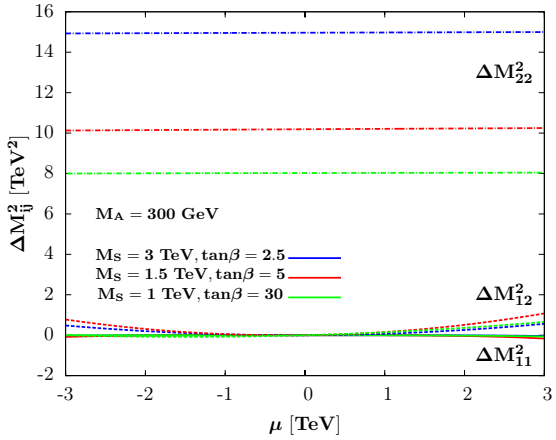

Figure 36: The entries $\Delta\mathcal{M}_{11}^2$ (solid), $\Delta\mathcal{M}_{12}^2$ (dashed), and $\Delta\mathcal{M}_{22}^2$ (dotted-dashed lines) of the radiative corrections matrix as functions of μ with a fixed $M_A = 300$ GeV for three different $(M_S, \tan\beta)$ sets and A_t such that it accommodates the mass range $M_h = 123$–129 GeV.

Taking into account only the dominant top–stop radiative corrections in the approximations of Eqs. 5.214, Fig. 37 displays the mass of the heavy CP–even Higgs state (left) and the mixing angle α (right) as a function of μ when $\Delta\mathcal{M}_{11}^2$ and $\Delta\mathcal{M}_{12}^2$ are

set to zero (dashed lines) and when they are included (solid lines). We have assumed the same $(M_S, \tan\beta)$ sets as above and for each value of μ, we calculate "approximate" and 'exact" M_H and α values assuming $M_h = 126 \pm 3$ GeV. Even for large values of the parameter μ (but $\mu \lesssim 3$ TeV), the relative variation for M_H never exceeds the 0.5% level while the variation of the angle α is bounded by $\Delta\alpha \lesssim 0.015$. Hence, in this scenario for the radiative corrections, the approximation of determining the parameters M_H and α from $\tan\beta, M_A$ and the value of M_h is extremely good. We have again verified that it stays the case when the corrections in the sbottom sector, with $A_b = A_t$, are included.

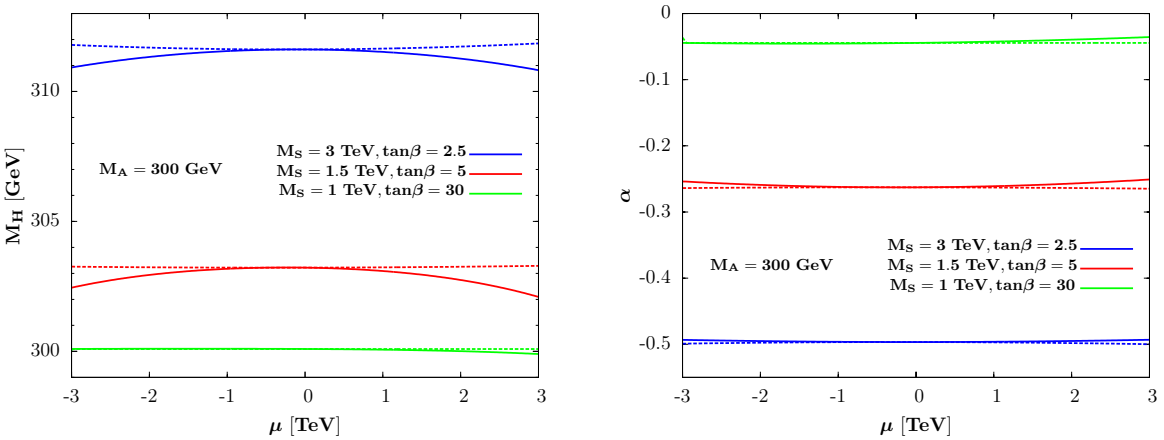

Figure 37: The mass of the heavier CP–even H boson (left) and the mixing angle α (right) as a function of μ with (solid lines) and without (dashed) the off–diagonal components components for $M_A = 300$ GeV and three $(M_S, \tan\beta)$ sets. A_t is such that $M_h = 123$–129 GeV and $A_b = 0$.

We should note that for higher M_A values, $M_A \gtrsim 300$ GeV, the approximation is even better as we are closer to the decoupling limit in which one has $M_H = M_A$ and $\alpha = \frac{\pi}{2} - \beta$. Lower values, $M_A \lesssim 300$ GeV, are disfavored by the observed h rates [283, 372] as seen later.

In order to check more thoroughly the impact of the subleading corrections $\Delta\mathcal{M}^2_{11}$, $\Delta\mathcal{M}^2_{12}$, we perform a scan of the MSSM parameter space using the program `SuSpect` [240, 242] in which the full two–loop radiative corrections to the Higgs sector are implemented. For a chosen $(\tan\beta, M_A)$ input set, the soft–SUSY parameters that play an important role in the Higgs sector are varied in the following ranges: $|\mu| \leq 3$ TeV, $|A_t, A_b| \leq 3M_S$, 1 TeV$\leq M_3 \leq 3$ TeV and 0.5 TeV$\leq M_S \leq 3$ TeV (≈ 3 TeV is the scale up to which programs such as `SuSpect` are expected to be reliable). We assume the usual relation between the weak scale gaugino masses $6M_1 = 3M_2 = M_3$ and set $A_u, A_d, A_\tau = 0$ (these last parameters have little impact).

We have computed the MSSM Higgs sector parameters all across the parameter space selecting the points which satisfy the constraint $123 \leq M_h \leq 129$ GeV. For each of the points, we have compared the Higgs parameters to those obtained in the simplified MSSM approximation, $\Delta\mathcal{M}^2_{11} = \Delta\mathcal{M}^2_{12} = 0$, with the lightest Higgs boson mass as input. We also required M_h to lie in the range 123–129 GeV, but allowed it to be different from the one obtained in the "exact" case $\Delta\mathcal{M}^2_{11}, \Delta\mathcal{M}^2_{12} \neq 0$.

For the mass M_H and the angle α, we display in Fig. 38 the difference between the values obtained when the two possibilities $\Delta\mathcal{M}^2_{11} = \Delta\mathcal{M}^2_{12} = 0$ and $\Delta\mathcal{M}^2_{11}, \Delta\mathcal{M}^2_{12} \neq 0$ are considered. This is shown in the plane $[M_S, X_t]$ with $X_t = A_t - \mu\cot\beta$ when all other parameters are scanned as above. Again, we have fixed the pseudoscalar Higgs

mass to $M_A = 300$ GeV and used the two representative values $\tan\beta = 5$ and 30. We have adopted the conservative approach of plotting only points which maximize these differences.

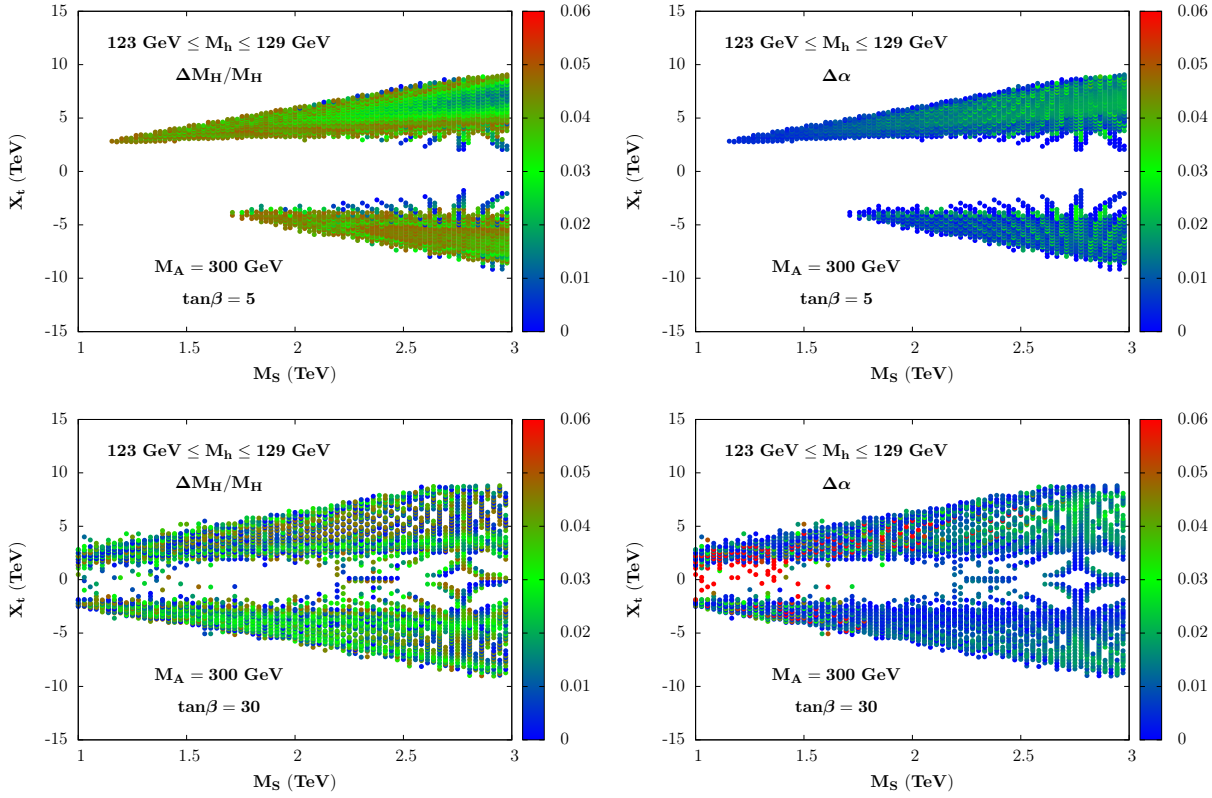

Figure 38: The variation of the mass M_H (left) and the mixing angle α (right), are shown as separate vertical colored scales, in the plane $[M_S, X_t]$ when the full two loop corrections are included with and without the subleading matrix elements $\Delta\mathcal{M}^2_{11}$ and $\Delta\mathcal{M}^2_{12}$. We take $M_A = 300$ GeV, $\tan\beta = 5$ (top) and 30 (bottom) and the other parameters are varied as described in the text.

In all cases, the difference between the two M_H values is very small (in fact, much smaller than the total decay width Γ_H), less than a few percent, while for α the difference does not exceed ≈ 0.025 for low values of $\tan\beta$ but at high $\tan\beta$ values, one can reach the level of ≈ 0.05 in some rare situations (large values of μ, which enhance the $\mu\tan\beta$ contributions). Nevertheless, at high enough $\tan\beta$, we are far in the decoupling regime already for $M_A \gtrsim 200$ GeV and such a difference does not significantly affect the couplings of the h and H bosons which, phenomenologically, are the main ingredients.

Hence, even when including the full set of radiative corrections up to two loops, it is a good approximation to use Eqs. (8.245) to derive the parameters M_H and α in terms of the inputs $\tan\beta, M_A$ and the measured value of M_h. In the case of the charged Higgs boson mass, the radiative corrections are much smaller for large enough M_A and one has, at the few percent level (which is again smaller than the total $H^\pm$ decay width), $M_{H^\pm} \simeq \sqrt{M_A^2 + M_W^2}$ except in very rare situations[26] [381].

[26]The physics of the charged boson, i.e the production and decay rates, can be accurately described by $\tan\beta, M_{H^\pm}$ (and eventually α if the subleading processes involving the h state are also considered).

8.3 Determination of the h boson couplings in a generic MSSM

A second important issue is the MSSM Higgs couplings. In principle and as discussed earlier, knowing two parameters such as the pair of inputs $[\tan\beta, M_A]$ and fixing the value of M_h to its measured value, the couplings of the Higgs bosons, in particular h, to fermions and gauge bosons can be derived, including the generally dominant radiative corrections that enter in the MSSM Higgs masses. Indeed, in terms of the angles β and α, one has for the reduced couplings (i.e. normalized to their SM values) of the lighter h state to third generation t, b fermions and gauge bosons $V = W/Z$,

$$c_V^0 = \sin(\beta-\alpha)\ , \quad c_t^0 = \frac{\cos\alpha}{\sin\beta}\ , \quad c_b^0 = -\frac{\sin\alpha}{\cos\beta} \tag{8.246}$$

However, outside the regime in which the pseudoscalar A boson and some supersymmetric particles are very heavy, there are also direct radiative corrections to the Higgs couplings not contained in the mass matrix of Eq. (8.241). These can alter this simple picture.

First, in the case of b–quarks, additional one–loop vertex corrections modify the tree–level $hb\bar{b}$ coupling: they grow as $m_b\mu\tan\beta$ and are thus very large at high $\tan\beta$. The dominant component comes from the SUSY–QCD corrections with sbottom–gluino loops that can be approximated by $\Delta_b \simeq 2\alpha_s/(3\pi)\times\mu m_{\tilde{g}}\tan\beta/\max(m_{\tilde{g}}^2, m_{\tilde{b}_1}^2, m_{\tilde{b}_2}^2)$ [298].

Outside the decoupling regime, the $hb\bar{b}$ coupling receives the possibly large correction

$$c_b \approx c_b^0 \times [1-\Delta_b/(1+\Delta_b)\times(1+\cot\alpha\cot\beta)] \ \text{ with } \ \tan\alpha \overset{M_A\gg M_Z}{\to} -1/\tan\beta \tag{8.247}$$

which would significantly alter the partial width of the decay $h\to b\bar{b}$ that is, in principle, by far the dominant one and, hence, affect the branching fractions of all other decay modes.

In addition, the $ht\bar{t}$ coupling is derived indirectly from the $gg\to h$ production cross section and the $h\to\gamma\gamma$ decay branching ratio, two processes that are generated via triangular loops. In the MSSM, these loops involve not only the top quark (and the W boson in the decay $h\to\gamma\gamma$) but also contributions from supersymmetric particles, if they are not too heavy. In the case of the $gg\to h$ process, only the contributions of stops is generally important. Including the later and working in the limit $M_h \ll m_t, m_{\tilde{t}_1}, m_{\tilde{t}_2}$, the hgg amplitude can be (very well) approximated by the expression [373–375]

$$c_t \approx c_t^0 \times \left[1 + \frac{m_t^2}{4m_{\tilde{t}_1}^2 m_{\tilde{t}_2}^2}(m_{\tilde{t}_1}^2 + m_{\tilde{t}_2}^2 - (A_t-\mu\cot\alpha)(A_t+\mu\tan\alpha)\ )\right] \tag{8.248}$$

which shows that indeed, $\tilde{t}$ contributions can be very large for sufficiently light stops and in the presence of large stop mixing. In the $h\to\gamma\gamma$ decay rate, because the $t, \tilde{t}$ electric charges are the same, the $ht\bar{t}$ coupling is shifted by the same amount as above [376].

If one ignores the usually small $\tilde{b}$ contributions in the $gg\to h$ production and $h\to\gamma\gamma$ decay processes (in the latter case, it is suppressed by powers of the b electric charge $e_b^2/e_t^2 = \frac{1}{4}$ in addition) as well as the contributions of other SUSY particles such as charginos and stau's in the $h\to\gamma\gamma$ decay rate[27], the leading corrections to the $ht\bar{t}$

[27] The chargino contribution cannot exceed the 10% level even for very favorable gaugino-higgsino parameters [376], while the $\tilde{\tau}$ contributions are important only for extreme values of $\tan\beta$ and μ [382, 383].

vertex can be simply accounted for by using the effective coupling given in Eq. (8.248); see e.g. Ref. [283].

Note that in the case of associated production of the h boson with top quarks, $gg/q\bar{q} \to ht\bar{t}$, it is the parameter c_t^0 which should be considered for the direct $ht\bar{t}$ coupling. However, for the time being (and presumably for a long time), the constraints on the h properties from this process are very weak as the cross section has very large uncertainties.

One also should note that the couplings of the h boson to τ leptons and charm quarks do not receive the direct corrections of respectively Eqs. (8.247) and (8.248) and one should still have $c_c = c_t^0$ and $c_\tau = c_b^0$. However, using $c_{t,b}$ or $c_{t,b}^0$ in this case has almost no impact in practice as these couplings appear only in the branching ratios for the decays $h \to c\bar{c}$ and $\tau^+\tau^-$ which are small, below 5%, and the direct corrections cannot be very large (these are radiative corrections after all). One can thus, in a first approximation, ignore them and assume that $c_c = c_t$ and $c_\tau = c_b$. Note that $\text{BR}(h \to c\bar{c})$ cannot be measured at the LHC while the $h \to \tau^+\tau^-$ rate is presently measured only at the level of 40% or so.

Another caveat is that possible invisible decays (which at present are probed directly only for rates that are at the 50% to 100% level [384]), can also affect the properties of the observed h particle. However, a large invisible rate implies that the neutralinos that are considered as the lightest SUSY particles, are relatively light and couple significantly to the h boson, a situation that is rather unlikely (if the LSP is very light, $2m_{\chi_1^0} \lesssim M_h$, it should be mostly bino–like and, hence, has very suppressed couplings to the Higgs bosons that prefer to couple to mixtures of higgsinos and gauginos; see for instance Refs. [376, 385–387]). Notice that we will study the Higgs invisible decays into more detail in the next part of this thesis.

In the case of large direct corrections, the Higgs couplings cannot be described only by the parameters β and α as in Eq. (8.246). One should consider at least three independent h couplings, namely $c_c = c_t$, $c_\tau = c_b$ and $c_V = c_V^0$ as advocated in Ref. [377]. This is equivalent to exclude the $h \to \tau\tau$ data from the global fit which, in practice, has no significant impact as the experimental error on the signal strength in this channel is presently large. Note that a future determination of the theoretically clean ratio of the $b\bar{b}$ and $\tau^+\tau^-$ signals in $pp \to hV$ gives a direct access to the Δ_b correction outside the decoupling regime [346, 378, 379].

To study the h state at the LHC, we thus define the following effective Lagrangian,

$$\begin{aligned} \mathcal{L}_h \;&=\; c_V\; g_{hWW}\; h\; W_\mu^+ W^{-\mu} +\; c_V\; g_{hZZ}\; h\; Z_\mu^0 Z^{0\mu} \\ &-\; c_t\; y_t\; h\bar{t}_L t_R - c_t\; y_c\; h\bar{c}_L c_R - c_b\; y_b\; h\bar{b}_L b_R - c_b\; y_\tau\; h\bar{\tau}_L \tau_R \;+\; \text{h.c.} \end{aligned} \tag{8.249}$$

where $y_{t,c,b,\tau} = m_{t,c,b,\tau}/v$ are the SM Yukawa coupling constants in the mass eigenbasis (L/R indicates the fermion chirality and we consider only the heavy fermions that have substantial couplings to the Higgs boson), $g_{hWW} = 2M_W^2/v$ and $g_{hZZ} = M_Z^2/v$ are the electroweak gauge boson couplings and v is the Higgs vacuum expectation value.

We present the results for the fits of the Higgs signal strengths in the various channels

$$\mu_X \simeq \sigma(pp \to h) \times \text{BR}(h \to XX)/\sigma(pp \to h)_{\text{SM}} \times \text{BR}(h \to XX)_{\text{SM}} \tag{8.250}$$

closely following the procedure of Ref. [346, 378, 379] but in the case of the phenomenological MSSM. All the Higgs production/decay channels are considered and the data

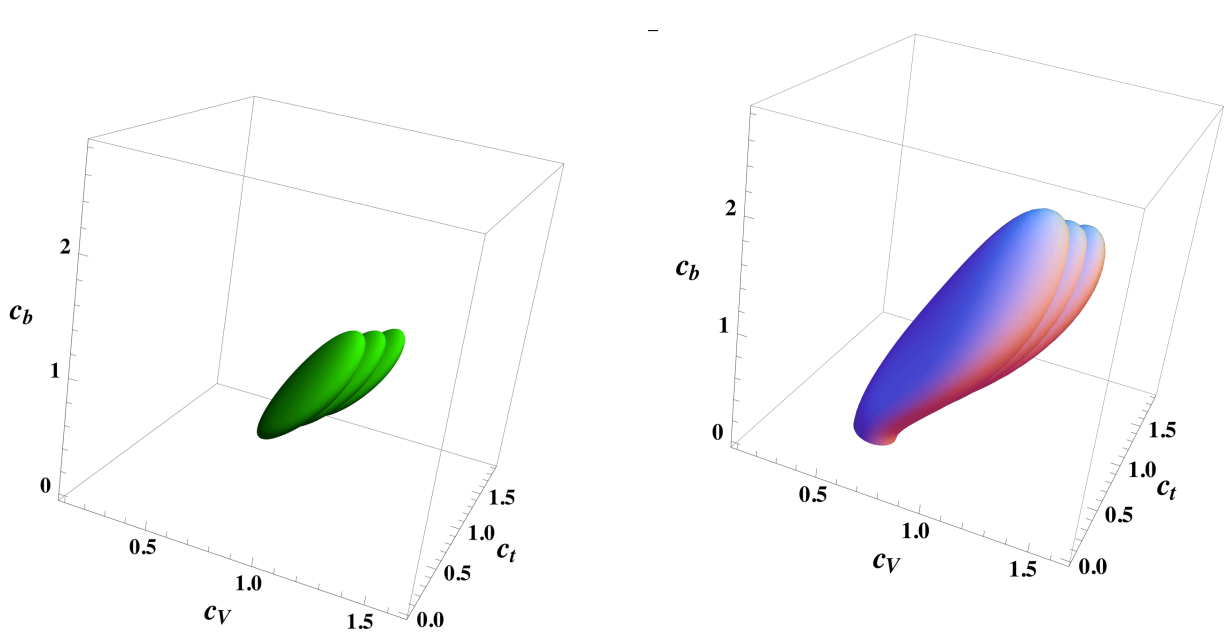

Figure 39: Best-fit regions at 68%CL (green, left) and 99%CL (light gray, right) for the Higgs signal strengths in the three–dimensional space $[c_t, c_b, c_V]$. The three overlapped regions are associated to central and two extreme choices of the theoretical prediction for the Higgs rates.

used are the latest ones using the full ≈ 25 fb^{-1} statistics for the $\gamma\gamma, ZZ, WW$ channels as well as the $h \to b\bar{b}$ and $\tau\tau$ modes for CMS, but only ≈ 17 fb^{-1} data for the ATLAS fermionic channels.

We have performed the appropriate three-parameter fit in the three-dimensional space[28] $[c_t, c_b, c_V]$, assuming $c_c = c_t$ and $c_\tau = c_b$ as discussed above and of course the custodial symmetry relation $c_V = c_W = c_Z$ which holds in supersymmetric models. The results of this fit are presented in Fig. 39 for $c_t, c_b, c_V \geq 0$, as motivated by the supersymmetric structure of the Higgs couplings (there is also an exact reflection symmetry under, $c \to -c$ or equivalently $\beta \to \beta + \pi$, leaving the squared amplitudes of the Higgs rates unaffected). Again following Refs. [346, 378, 379], we have treated the theoretical uncertainty as a bias and not as if it were associated to a statistical distribution and have performed the fit for values of the signal strength $\mu_i|_{\rm exp}[1 \pm \Delta\mu_i/\mu_i|_{\rm th}]$ with the theoretical uncertainty $\Delta\mu_i/\mu_i|_{\rm th}$ conservatively assumed to be 20% for both the gluon and vector boson fusion mechanisms (because of contamination) and $\approx 5\%$ for h production in association with $V = W/Z$ [103, 106].

The best-fit value for the couplings, when the ATLAS and CMS data are combined, is $c_t = 0.89$, $c_b = 1.01$ and $c_V = 1.02$ with $\chi^2 = 64.8$ ($\chi^2 = 66.7$ in the SM).

In turn, in scenarios where the direct corrections in Eqs. (8.247)-(8.248) are not quantitatively significant (i.e. considering either not too large values of $\mu \tan\beta$ or high stop/sbottom masses), one can use the MSSM relations of Eq. (8.246) to reduce the number of effective parameters down to two. For instance, using $c_t = \cos\alpha/\sin\beta$ and $c_V = \sin(\beta - \alpha)$, one can derive the following relation, $c_b \equiv -\sin\alpha/\cos\beta = (1 - c_V c_t)/(c_V - c_t)$. This allows to perform the two-parameter fit in the plane $[c_V, c_t]$. Similarly, one can study the planes $[c_V, c_b]$ and $[c_t, c_b]$. The two-dimensional fits in these three planes are displayed in Fig. 40. As in the MSSM one has $\alpha \in [-\pi/2, 0]$ and

[28] Higgs coupling fits have been performed most often in the $[c_V, c_f]$ parameter space with $c_f = c_t = c_b \ldots$. Fits of the LHC data in SUSY scenarios including also the NMSSM can be found in Refs. [286, 287, 388–393] for instance.

$\tan\beta \in [1, \sim 50]$, one obtains the following variation ranges: $c_V \in [0,1]$, $c_t \in [0, \sqrt{2}]$ and $c_b > 0$.

We also show on these figures the potential constraints obtained from fitting ratios of the Higgs signal strengths (essentially the two ratios $R_{\gamma\gamma} = \mu_{\gamma\gamma}/\mu_{ZZ}$ and $R_{\tau\tau} = \mu_{\tau\tau}/\mu_{WW}$) that are not or much less affected by the QCD uncertainties at the production level [346, 378, 379]. In this two–dimensional case, the best-fit points are located at ($c_t = 0.88$, $c_V = 1.0$), ($c_b = 0.97$, $c_V = 1.0$) and ($c_t = 0.88$, $c_b = 0.97$). Note that although for the best–fit point one has $c_b \lesssim 1$, actually $c_b \gtrsim 1$ in most of the 1σ region.

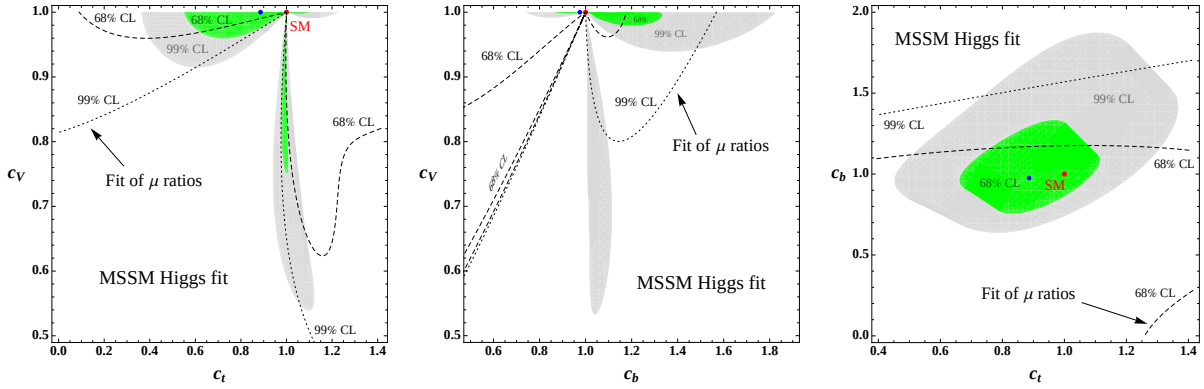

Figure 40: Best-fit regions at 68%CL (green) and 99%CL (light gray) for the Higgs signal strengths in the planes $[c_t, c_V]$ (left), $[c_b, c_V]$ (center) and $[c_t, c_b]$ (right). The theoretical uncertainty on the Higgs signal strengths is taken into account as a bias. The best-fit contours at 68%CL (dashed) and 99%CL (dotted) from the fit of signal strength ratios are superimposed as well. The SM points are indicated in red and the best-fit points in blue.

Alternatively, using the expressions of Eq. (8.246), one can also realize a two-parameter fit in the $[\tan\beta, \alpha]$ plane[29]. However, using the expressions of Eq. (8.245) for the mixing angle α and fixing M_h to the measured value $M_h \approx 125$ GeV, one can perform a fit in the plane $[\tan\beta, M_A]$. This is shown in the left–hand side of Fig. 41 where the 68%CL, 95%CL and 99%CL contours from the signal strengths only are displayed when, again, the theoretical uncertainty is considered as a bias. We also display the best-fit contours for the signal strength ratios at the 68%CL and 95%CL. The best-fit point for the signal strengths when the theoretical uncertainty is set to zero, is obtained for the values $\tan\beta = 1$ and $M_A = 557$ GeV, which implies for the other parameters, when the radiative corrections entering the Higgs masses and the angle α are derived using the information $M_h = 125$ GeV : $M_H = 580$ GeV, $M_{H^\pm} = 563$ GeV and $\alpha = -0.837$ rad. Regarding this best-fit point, one should note that the χ^2 value is relatively stable all over the 1σ region shown in Fig. 41.

It is interesting to superimpose on these indirect limits in the $[\tan\beta, M_A]$ plane, the direct constraints on the heavy $H/A/H^\pm$ boson searches performed by the ATLAS and CMS collaborations as shown in the right–hand side of Fig. 41. As discussed in Ref. [372] (see also Ref. [310]), besides the limits from the $A/H \to \tau^+\tau^-$ and to a lesser extent $t \to bH^+ \to b\tau\nu$ searches which exclude high $\tan\beta$ values and which can be extended

[29] This corresponds in fact to the case of a two–Higgs doublet model in which the direct corrections are expected to be small in contrast to the SUSY case: one can then parametrise the couplings of the h boson, that are given by Eq. (8.246), by still two parameters α and β but with the angle α being a free input.

to very low $\tan\beta$ as well, there are also limits from adapting to the MSSM the high mass SM Higgs searches in the channels[30] $H \to WW$ and ZZ as well as the searches for heavy resonances decaying into $t\bar{t}$ final states that exclude low values of $\tan\beta$ and M_A. For values $250 \lesssim M_A \lesssim 350$ GeV, only the intermediate $\tan\beta \approx 2$–10 range is still allowed.

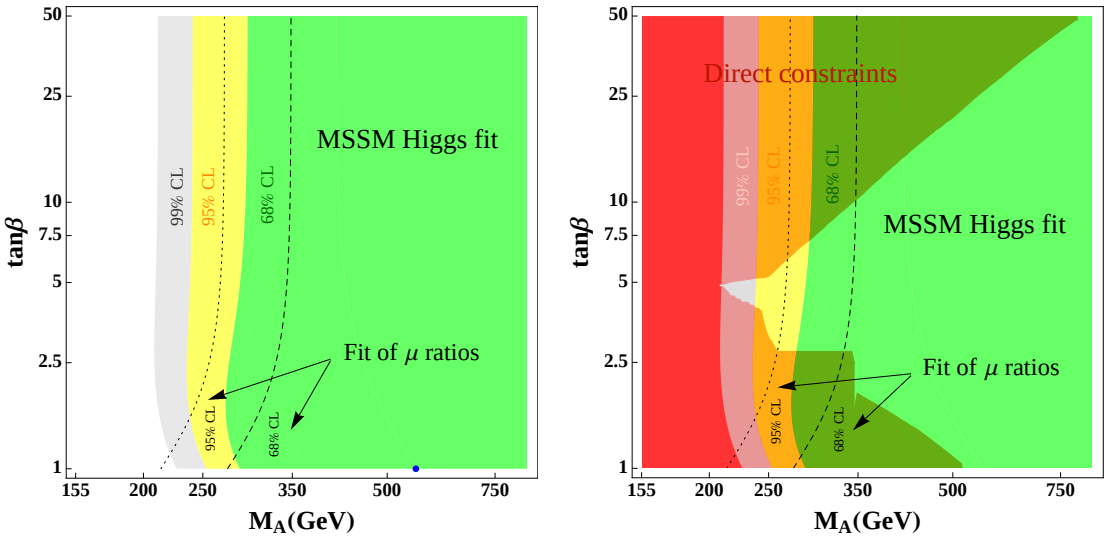

Figure 41: Left: best-fit regions at 68%CL (green), 95%CL (yellow) and 99%CL (light gray) for the Higgs signal strengths in the plane $[\tan\beta, M_A]$; the best–fit point is shown in blue and the theoretical uncertainty is taken into account as a bias as in the previous figures. The best-fit contours at 1σ (dashed) and 2σ (dotted) for the signal strength ratios are also shown. Right: we superimpose on these constraints the excluded regions (in red, and as a shadow when superimposed on the best-fit regions) from the direct searches of the heavier Higgs bosons at the LHC following the analysis of Ref. [372].

8.4 Conclusion concerning the hMSSM

We have discussed the hMSSM, i.e. the MSSM that we seem to have after the discovery of the Higgs boson at the LHC that we identify with the lighter h state. The mass $M_h \approx 125$ GeV and the non–observation of SUSY particles, seems to indicate that the soft–SUSY breaking scale might be large, $M_S \gtrsim 1$ TeV. We have shown, using both approximate analytical formulae and a scan of the MSSM parameters, that the MSSM Higgs sector can be described to a good approximation by only the two parameters $\tan\beta$ and M_A if the information $M_h = 125$ GeV is used. One could then ignore the radiative corrections to the Higgs masses and their complicated dependence on the MSSM parameters and use a simple formula to derive the other parameters of the Higgs sector, α, M_H and $M_{H^\pm}$.

In a second step, we have shown that to describe accurately the h properties when the direct radiative corrections are also important, the three couplings c_t, c_b and c_V are

[30] At low $\tan\beta$, channels such as $A \to hZ$ and $H \to hh$ need also to be considered [372]. In the latter case, special care is needed in the treatment of the trilinear Hhh coupling as will be discussed in Ref. [394].

needed besides the h mass. We have performed a fit of these couplings using the latest LHC data and taking into account properly the theoretical uncertainties. In the limit of heavy sparticles (i.e. with small direct corrections), the best fit point turns out to be at low $\tan\beta$, $\tan\beta \approx 1$, and with a not too high CP–odd Higgs mass, $M_A \approx 560$ GeV.

The phenomenology of this particular point is quite interesting. First, the heavier Higgs particles will be accessible in the next LHC run at least in the channels $A, H \to t\bar{t}$ and presumably also in the modes $H \to WW, ZZ$ as the rates are rather large for $\tan\beta \approx 1$. This is shown in Fig. 42 where the cross sections times decay branching ratios for A and H are displayed as a function of $\tan\beta$ for the choice $M_A = 557$ GeV for $\sqrt{s} = 14$ TeV. Further more, the correct relic abundance of the LSP neutralino can be easily obtained through $\chi_1^0\chi_1^0 \to A \to t\bar{t}$ annihilation by allowing the parameters μ and M_1 to be comparable and have an LSP mass close to the A–pole, $m_{\chi_1^0} \approx \frac{1}{2}M_A$.

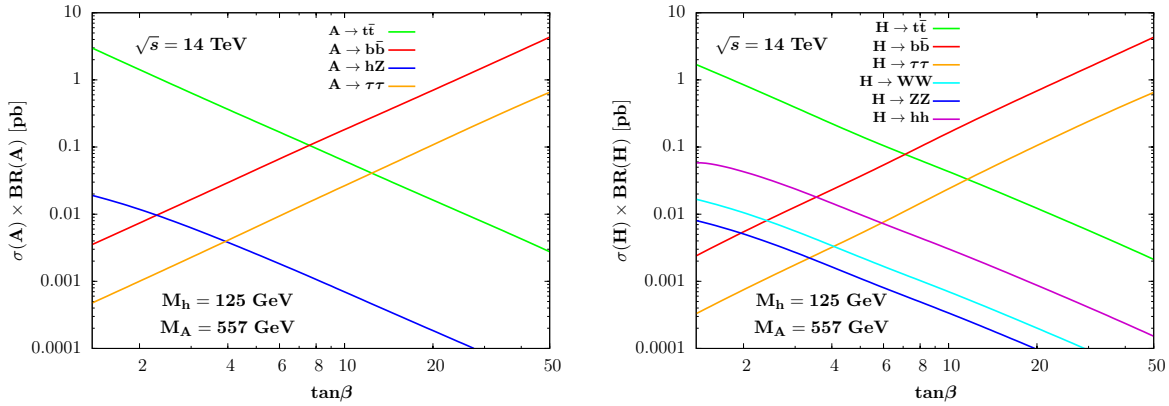

Figure 42: The cross section times branching fractions for the A (left) and H (right) MSSM Higgs bosons at the LHC with $\sqrt{s} = 14$ TeV as a function of $\tan\beta$ for the best–fit mass $M_A = 557$ GeV and with $M_h = 125$ GeV. For the production, we have taken into account only the gluon and bottom quark fusion processes and followed the analysis given in Ref. [372].

We will now turn to the third chapter of this thesis that focusses on dark mater.

Part III

The dark matter problem

Summary

9 The early universe

In 1933, Zwicky analyzed the motion of the galaxies inside the Coma cluster and obtained the first evidence in favor of the existence of a new form of matter. This exotic matter would not emit luminous radiation and for this reason it has been called dark matter. Afterwards, several observations have confirmed the presence of dark matter in our universe. In this section, we will first introduce the main astrophysical and cosmological evidences for dark matter. Secondly, we will talk about the thermal history of the universe and we will define some tools in order to quantify the dark matter abundance. We will finish by mentioning the astrophysical technics used to look for the dark matter.

9.1 Dark matter evidences

9.1.1 Astrophysical evidences

Galactic rotation curves

Inside galaxies the stars orbit around the center. Their velocity distribution, $v(r)$, can be reconstructed as a function of the distance to the galactic center r. In the framework of the Newtonian mechanics, if one knows the mass distribution ρ, one could predict the gravitational potential Φ and then the velocity distribution via the following equations

$$\begin{aligned} \Delta\Phi(r) &= 4\pi G_N \rho(r) \,, \\ v^2(r) &= r\frac{\partial}{\partial r}\Phi(r) \,. \end{aligned} \tag{9.251}$$

However, this mass distribution is not directly observable, but it seems reasonable to make the hypothesis that the mass distribution is related to the luminosity distribution, $\rho_{\rm lum}(r) \propto I(r)$. We then obtain the velocity distribution corresponding to the observed luminous matter, that we call $v_{\rm lum}$. A problem arises when one tries to compare the luminous matter velocity distribution $v_{\rm lum}(r)$ with the stars velocity distribution $v(r)$. Introducing $M(r)$, the mass inside the sphere of radius r, we can rewrite the luminous velocity distribution as

$$v_{\rm lum}(r) = \sqrt{\frac{G_N M(r)}{r}} \,. \tag{9.252}$$

So beyond the visible matter, when $M(r)$ does not depend on r anymore, one would expect $v_{\rm lum} \propto 1/\sqrt{r}$. Looking at Fig.43, the flatness at large radius of the line (fitting the experimental data) means that the stars rotate much faster than expected at large r. This apparent disagreement can be explained if one assumes the existence of a halo of non visible matter, that we will call dark matter (DM), with a mass profile $M(r) \propto r$ (or a density profile $\rho \propto 1/r^2$).

Gravitational lensing

In General Relativity (GR), matter induces a curvature of space-time. The light waves are then deflected by this modification. This phenomena is known as gravitational lensing. Since the deflection angle is proportional to the mass of the astrophysical object which curves the space-time, this is a good method to estimate the matter distribution of such objects that one can compare to their dust and gas distribution. A compelling

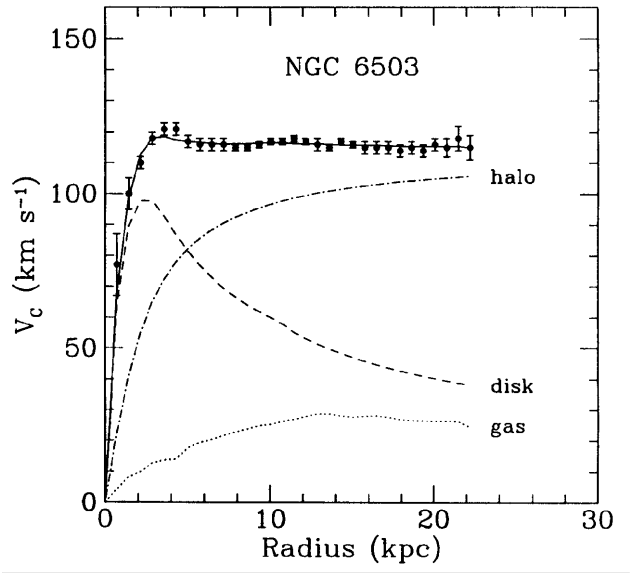

Figure 43: Rotation curve of the galaxy NGC 6503. Lines correspond to the contribution of the interstellar gas, or the disk of visible matter or the halo of dark matter. Taken from [395]

.

evidence of dark matter came with the weak lensing observations of the Bullet galaxy cluster 1E 0657-56 [396] by the Hubble Space Telescope. This bullet cluster is made of two colliding smaller clusters. Weak lensing effects allow to draw the mass distribution (in green contours in Fig.44). Visible matter distribution can be estimated by X-rays (colored area in Fig.44). By looking at the Fig.44, one can see a clear separation between the two matter distributions. The visible matter is slowed down due to the collision while

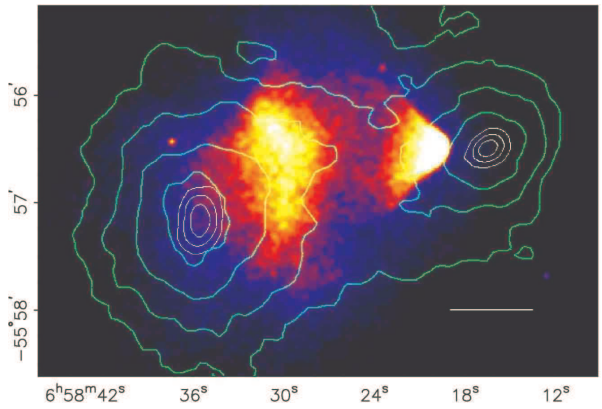

Figure 44: Weak lensing distribution of the Bullet cluster (green contours) and X-rays matter distribution (colored area) .Taken from [396].

the would be dark matter is not (weak interacting behaviour).

9.1.2 Cosmological evidences

The Friedmann law

In General Relativity, the Einstein equation establishes the relation between curvature of the space-time and the matter properties at a given point by

$$G_{\mu\nu} = R_{\mu\nu} - \frac{1}{2}Rg_{\mu\nu} = 8\pi G_N T_{\mu\nu} \ , \tag{9.253}$$

where $R_{\mu\nu}$ is the Ricci tensor, $R \equiv R^{\mu}{}_{\mu}$ the Ricci scalar, $g_{\mu\nu}$ the time-space metric and $T_{\mu\nu}$ the energy-momentum tensor. The Friedmann-Lemaître-Robertson-Walker (FLRW) metric is the most general solution of the Einstein's GR equations under the assumption that the universe is homogeneous and isotropic. This postulate means it exists a definition of time for which all directions are equivalent. Inside this metric the space-time distance reads

$$ds^2 = dt^2 - a^2(t)\left[\frac{dr^2}{1-kr^2} + r^2(d\theta^2 + \sin^2\theta d\phi^2)\right] \tag{9.254}$$

where (r, θ, ϕ) are the spherical coordinates and k the comoving spatial curvature parameter (when $k = -1/0/1$ the space-time is open/flat/closed) and $a(t)$ is the universe scale factor. The most general energy-momentum tensor in such an homogeneous and isotropic universe has to be

$$T^{\mu}{}_{\nu} = \begin{pmatrix} \rho & 0 & 0 & 0 \\ 0 & -p & 0 & 0 \\ 0 & 0 & -p & 0 \\ 0 & 0 & 0 & -p \end{pmatrix} \tag{9.255}$$

with ρ the energy density and p the pressure of the cosmological fluid. The first Einstein equation is then

$$H^2 = \left(\frac{\dot{a}}{a}\right)^2 = \frac{8\pi G_N}{3}\rho - \frac{k}{a^2} \tag{9.256}$$

where H is called the Hubble parameter and the dot means time derivative. This last equation is the famous Friedman law and gives the expansion rate of the universe. The Einstein's GR equation also implies Bianchi identities and especially the first one ($T^{\nu}_{0;\nu}$) which is the equation of energy conservation. In the FLRW model it reads

$$\dot{\rho} = -3\frac{\dot{a}}{a}(\rho + p) \ . \tag{9.257}$$

At this stage one can distinguish two important situations:

- Matter is ultra-relativistic (radiation domination)
  In that case the particle velocity generates pressure and we know from statistical thermodynamics that an ultra relativistic gas has an equation of state $p = \rho/3$.

$$\dot{\rho} = -4\frac{\dot{a}}{a}\rho \quad \Rightarrow \quad \rho \propto a^{-4} \ . \tag{9.258}$$

- Matter is non-relativistic (matter domination)
  In that situation the negligible kinetic energy implies $p = 0$, then

$$\dot{\rho} = -3\frac{\dot{a}}{a}\rho \quad \Rightarrow \quad \rho \propto a^{-3} \, . \tag{9.259}$$

  A non-relativistic fluid dilutes slower than an ultra-relativistic one.

Einstein also noticed that a simple geometric term could be added to its equation without violating any principle

$$G_{\mu\nu} + \Lambda g_{\mu\nu} = 8\pi G_N T_{\mu\nu} \tag{9.260}$$

This constant Λ is equivalent to an homogeneous fluid with the energy-momentum tensor

$$T^{\mu}{}_{\nu} = \frac{\Lambda}{8\pi G_N} = \begin{pmatrix} \frac{\Lambda}{8\pi G_N} & 0 & 0 & 0 \\ 0 & \frac{\Lambda}{8\pi G_N} & 0 & 0 \\ 0 & 0 & \frac{\Lambda}{8\pi G_N} & 0 \\ 0 & 0 & 0 & \frac{\Lambda}{8\pi G_N} \end{pmatrix} . \tag{9.261}$$

This fluid respects the equation of state $\rho = -p = \frac{\Lambda}{8\pi G_N}$, note the unusual sign. This new term in the Einstein equation is interpreted as a vacuum energy or a fluid which accelerate the expansion of the universe, it is the so-called Dark-Energy.

We can now rewrite the Friedmann law including all the different contributions to the homogeneous cosmological fluid

$$H^2 = \frac{8\pi G_N}{3}(\rho_R + \rho_M) - \frac{k}{a^2} + \frac{\Lambda}{3} \tag{9.262}$$

with $\rho_{R/M}$ the radiation/matter density.

If we take the Friedman equation, evaluated today, and divide it by H_0^2 (the subscript 0 means "evaluated today"), we obtain the matter budget equation

$$\Omega_R + \Omega_M - \Omega_k + \Omega_\Lambda = 1 \, , \tag{9.263}$$

where we define

$$\begin{aligned} \Omega_R &= \frac{8\pi G_N}{3H_0^2}\rho_{R_0} \, , \\ \Omega_M &= \frac{8\pi G_N}{3H_0^2}\rho_{M_0} \, , \\ \Omega_k &= \frac{k}{3a_0^2 H_0^2} \, , \\ \Omega_\Lambda &= \frac{\Lambda}{3H_0^2} \, . \end{aligned} \tag{9.264}$$

Assuming a flat universe ($k = 0$) as it seems experimentally the case, we get

$$\Omega_R + \Omega_M + \Omega_\Lambda = 1 \tag{9.265}$$

In conclusion, the evolution of the universe can be described in terms of the four cosmological parameters $\Omega_{R/M/\Lambda}, H_0$. The Friedmann equation would then allow us to extrapolate the scale factor $a(t)$ at any time. We can understand now why the main purposes of observational cosmology is to measure these four parameters.

The Cosmic Microwave Background

We have seen previously that it exists astrophysical evidences for dark matter. However, we cannot extract from it an estimation of the total amount of dark matter. This quantity can be measured by looking at the anisotropies of the Cosmic Microwave Background (CMB). The detected quantities are photons which have decoupled from the matter in the primordial universe, the so-called matter-radiation decoupling. The existence of the CMB was predicted by Gamow and Teller in 1948 and was experimentally discovered only in 1965 by Penzias and Wilson. The first observations of the CMB spectrum has been done by the Cosmic Background mission (COBE) in 1989. In 2001, COBE was followed by the Wilkinson Microwave Anisotropy Probe (WMAP). In 2009, the Planck spacecraft was launched and it delivered its data in March 2013. Their interpretation allow to measure the cosmological parameters with the highest precision. The temperature spectrum of the CMB follows extremely precisely a black body law with an average temperature of 2.725 K. This radiation is homogeneous and isotropic, however, there are small fluctuations ($\delta T/T \approx 0.01‰$). An analysis of these CMB anisotropies puts strong constraints on the cosmological parameters. In the case of the ΛCDM model considering the latest Planck results [397] (we quote here the 68% confidence limits combining the Planck+WP+highL likelihood with the Planck lensing and BAO likelihoods) the curvature of the universe is to a good approximation equal to zero, $\Omega_{k0}h^2 = -0.0005^{+0.0065}_{-0.0066}$, with $h^2 = 0.6780 \pm 0.0077$. The universe is mainly filled by dark energy which drives the acceleration of its expansion, $\Omega_\Lambda h^2 = 0.692 \pm 0.010$. The baryonic matter represents only a small fraction of the matter budget, $\Omega_b h^2 = 0.02214 \pm 0.00024$, since most of the matter is unknown, i.e accounts for dark matter: $\Omega_{DM}h^2 = 0.1187 \pm 0.0017$.

9.2 Thermal history of the universe and thermal relics

9.2.1 From a cold big bang to the hot big bang scenario

The pioneers who have considered the far past of the universe (near the initial singularity), have firstly assumed that the expansion of the universe was dominated by pressureless matter (component of galaxies) since the beginning. This assumption corresponds to the Cold Big Bang scenario, since under this hypothesis matter was really dense in the early universe ($\rho_M(t) \propto a(t)^{-3}$). At that time, matter consisted of a gas of electrons and nucleons. As soon as the density fell down to a critical value nuclei were formed through nuclear reactions, this corresponds to the nucleosynthesis. In the Cold Big Bang framework, nucleosynthesis is not satisfactory because heavier elements are much more produced compared to hydrogen. This is in contradiction with astrophysical observations which tell us that clouds of gas and stars contain a lot of hydrogen. In order to reconcile nucleosynthesis with experiments, one has to modify the kinematics of the nuclear reactions. This can be done by modifying the expansion rate of the universe by supposing that during the nucleosynthesis, radiation density of the photons was dominating ($\rho_R(t) \propto a(t)^{-4}$). This scenario where radiation density dominates at early time before the matter density domination era is called the Hot Big Bang scenario. Before nucleosynthesis occurred, the photons were interacting with an extremely small mean-free-path, then having a Brownian motion in a particle gas. The photons were then maintained in thermal equilibrium with the background gas and formed a black-body which has a well defined spectrum associated to a precise temperature

(Planck law). After nucleosynthesis, matter was a gas of electrons and nuclei. When the density decreases, since they interact electromagnetically, they combined into atoms, this transition is called recombination. Afterwards, photons did not interact anymore with charged particles, the gas being filled of neutral atoms, then their mean-free-path severely increased and basically photons travelled freely from the recombination epoch until now. Thus the photon black-body spectrum stays the same $\langle E\rangle \approx T \approx 1/\langle\lambda\rangle$ but as the photon wavelength $\lambda(t) \propto a(t)$ then the black-body spectrum is shifted towards smaller temperatures. The first measurement of this homogeneous radiation (CMB) that was performed by Penzias and Wilson (that we have talked before) was a very strong evidence for the Hot Big Bang scenario.

9.2.2 Quantum thermodynamics

Even if the whole universe can be described by its gravitational forces, one may need to study its particle content at high temperature. Thermodynamics is then needed. In the FLRW universe, the homogeneity and isotropy assumptions enforce that the phase-space distribution function of a given species A inside the cosmological fluid can be written only as a function of the momentum modulus and time $f_A(p,t)$. For such species, the general expressions of the number density (n_A), energy density (ρ_A) and pressure (p_A) are the following

$$\begin{aligned} n_A(t) &= \frac{g_A}{(2\pi)^3}\int d^3p f_A(p,t)\ , \\ \rho_A(t) &= \frac{g_A}{(2\pi)^3}\int d^3p E_A f_A(p,t)\ , \\ p_A(t) &= \frac{g_A}{(2\pi)^3}\int d^3p \frac{p^2}{3E_A} f_A(p,t)\ , \end{aligned} \tag{9.266}$$

where g_A is the number of quantum degrees of freedom and $E_A = \sqrt{p^2+m_A^2}$ the energy of the particle. Each species interact, or not, then these previous densities evolve, or not. Their interactions can be represented by a set of reactions $A+B \leftrightarrow C+D$, with the particular case of elastic scattering $A+B \to A+B$. Generically the evolution of each species is obtained by resolving the Boltzmann equation of the form $df_A/dt = \mathcal{F}(f_A, f_B, f_C, f_D)$. We will focus on this important point after discussing the possible equilibriums namely thermal and chemical equilibriums.

9.2.3 Equilibriums

Thermal equilibrium

Because of the correlation between temperature and average kinetic energy, the thermal equilibrium is associated to the kinetic equilibrium. Two species A and B which have frequent interactions ($A+B \to A+B$) , thus randomly exchanging momentum, reach a kinetic/thermal equilibrium. So we can define a temperature in the thermodynamical sense $T \equiv \partial U/\partial S|_X$ as being the variation of the internal energy relatively to the entropy, when all others macroscopic observables are kept the same. The thermal distribution for a given species A reads

$$f_A = \frac{1}{e^{\frac{E_A-\mu_A}{T}} \pm 1} \tag{9.267}$$

where μ_A is the chemical potential of the species which contains the effect of the balance between all the inelastic reactions involved in the fluid. The case $(+1)$ is for fermions which obey at quantum level the Fermi-Dirac statistics and (-1) is for bosons which obey the Bose-Einstein statistics. In the classical limit, where particles are non-relativistic, the quantum behavior is negligible and one recover the Maxwell-Boltzmann approximation $f_A \approx e^{-(E_A-\mu_A)/T}$. Two extremal cases will be useful in our following studies, the relativistic and non-relativistic particle limits.

- In the limit of high temperature where the mass is negligible, $T \gg m_A$, particles are ultra-relativistic and one can compute both the number and energy density and the pressure with the simplified formulas (we assume $\mu_A \ll T$ and $m_A = 0$)

$$\begin{aligned} n_A &= \frac{\xi(3)}{\pi^2} g_A T^3 \times \left\{ \begin{array}{cc} 1 & \text{(for boson)} \\ 3/4 & \text{(for fermion)} \end{array} \right. , \\ \rho_A &= \frac{\pi^2}{30} g_A T^4 \times \left\{ \begin{array}{cc} 1 & \text{(for boson)} \\ 7/8 & \text{(for fermion)} \end{array} \right. , \\ p_A &= \frac{1}{3}\rho_A \, , \end{aligned} \tag{9.268}$$

  where $\xi(x)$ is the Riemann zeta function ($\xi(3) \approx 1.202$).

- In the limit of low temperature where the mass is not anymore negligible, $T \ll m_A$, particles are non-relativistic and one can compute the number, energy density and the pressure with the formulas (for both fermions and bosons)

$$\begin{aligned} n_A &= g_A \left(\frac{m_A T}{2\pi} \right)^{3/2} e^{-\frac{(m_A-\mu_A)}{T}} \, , \\ \rho_A &= m_A n_A \, , \\ p_A &= T n_A \, . \end{aligned} \tag{9.269}$$

In the realistic case where $\mu_A \ll T$, the number density of non-relativistic particles is exponentially suppressed regarding the relativistic case. Then, in a thermal plasma the number density mostly come from relativistic particles.

Thermal decoupling

During thermal equilibrium the interaction between particles A and B is represented through a thermally averaged cross-section velocity product $\langle \sigma v \rangle$. The scattering rate of A over B is $\Gamma_{A/B} = n_{B/A} \langle \sigma v \rangle$. These particles are in the thermal equilibrium when their interaction rate is sufficiently large. Quantitatively $\Gamma_{A/B}$ has to be bigger than the Hubble constant H which is the expansion factor of the universe. When $\Gamma_{A/B} < H$, the universe expansion has sufficiently diluted the particles so that the probability that A and B interact within a time comparables to the age of the universe is negligible. So these stable and non-interacting particles are decoupled and their distribution is frozen (being the same to the one of their last scattering). They are just following the universe expansion.

Chemical equilibrium

If it exists an inelastic scattering reaction of the type $A + B \leftrightarrow C + D$ then in any

comoving volume the number of particles of a given species, $n_A a^3$, is not conserved: conservation laws do not apply for number density but for quantum numbers, for example the electric charge number. These quantum numbers are the equivalent, at quantum level, of the chemical potentials which are thermodynamic quantities defined when there are conserved charges in the system. Classically, the chemical potential is the variation of the internal energy that one needs to extract/introduce a particle (all other things being equal) i.e $\mu \equiv \partial U/\partial N|_X$. Consequently, when the reaction is frequent enough the relative number density of particles is not aleatory and must follow the chemical equilibrium condition

$$\mu_A + \mu_B = \mu_C + \mu_D \tag{9.270}$$

Usually, each conserved quantum number is associated with a non-vanishing chemical potential. For instance, the photon which does not carry any conserved charge has $\mu_\gamma = 0$. This implies for example $\mu_e = -\mu_{\bar{e}}$ looking at the reaction $e^+ + e^- \to 2\gamma$. An important consequence of chemical equilibrium is that a vanishing asymmetry $n_A - n_{\bar{A}}$ implies a vanishing chemical potential $\mu_A = 0$. As an example, for leptons, the fact that it exists a conserved charge, $\mu_L \neq 0$ means that an asymmetry is present.

Chemical decoupling

When the reaction which defines the chemical equilibrium is not sufficiently frequent, the concerned particles chemically decouple. We should note that these particles can still be in thermal equilibrium. In that situation the evolution of their number density is given by a simplified Boltzmann equation which will be studied in details in the following subsection.

9.2.4 Entropy conservation in the thermal bath

For a system in thermal equilibrium (with small chemical potentials) of internal energy $U = \rho V$, V being the comoving volume ($\propto a^3$), the second Law of thermodynamics reads

$$dU = \rho dV + V d\rho = TdS - PdV \ . \tag{9.271}$$

Remembering the energy conservation equation (Eq.9.257) and writing it in terms of the covolume, we get

$$\frac{\partial \rho}{dt} = -\frac{1}{V}\frac{dV}{dt}(\rho + P) \ . \tag{9.272}$$

Combining these two last equations, one obtains

$$\frac{dS}{dt} = 0 \ . \tag{9.273}$$

Considering now the density of entropy defined by $s \equiv S/V$, we can rewrite the Eq.9.271 as

$$(Ts - \rho - P)\frac{dV}{V} = d\rho - Tds \ . \tag{9.274}$$

Since the energy and entropy density depend only on the temperature in thermal equilibrium then we get the important result

$$s = \frac{\rho + P}{T} \ . \tag{9.275}$$

The entropy density of the cosmological fluid is then dominated by the relativistic components. For a relativistic species the entropy density reads

$$s_A = \frac{4\pi^2}{45}\frac{g_A}{2}T^3 \times \begin{cases} 1 & \text{(for boson)} \\ 7/8 & \text{(for fermion)} \end{cases} . \tag{9.276}$$

For the whole plasma, it is convenient to write the entropy density as if it was due to photons only. The degeneracy factor g_γ is then replaced by an effective one which includes all the different particles existing at a given temperature

$$\begin{aligned} s_{plasma}(T) &= \frac{4\pi^2}{45}h_*(T)T_\gamma^3 , \\ h_*(T) &= \sum_{b=\text{rel. bos.}} \frac{g_b}{2}\left(\frac{T}{T_\gamma}\right)^3 + \frac{7}{8}\sum_{f=\text{rel. fer.}} \frac{g_f}{2}\left(\frac{T}{T_\gamma}\right)^3 . \end{aligned} \tag{9.277}$$

For next sections it will be also convenient to introduce a similar expression for the energy density of the plasma

$$\begin{aligned} \rho_{plasma}(T) &= \frac{\pi^2}{15}g_*(T)T_\gamma^4 , \\ g_*(T) &= \sum_{b=\text{rel. bos.}} \frac{g_b}{2}\left(\frac{T}{T_\gamma}\right)^4 + \frac{7}{8}\sum_{f=\text{rel. fer.}} \frac{g_f}{2}\left(\frac{T}{T_\gamma}\right)^4 . \end{aligned} \tag{9.278}$$

The entropy density conservation implies $h_* T_\gamma^3 a^3 = \text{constant}$. So as long h_* remains constant, $T_\gamma \propto 1/a$. Nevertheless, as soon as one particle species becomes non-relativistic, h_* diminishes so T_γ varies as $T_\gamma \propto 1/h_*^{1/3} 1/a$.

9.2.5 Dark matter abundance and thermal relic

The well-tempered dark matter

What about dark matter in the thermal history of the universe? Dark matter, as we have seen is non-baryonic, is characterized by its kinetic energy at the instant where it decouples from the thermal bath.

We talk about Hot Dark Matter (HDM) when after decoupling the DM is still relativistic ("hot"). Neutrinos which could be thought as the natural SM candidate for DM is one example. At high temperature neutrinos are in thermal and chemical equilibrium with the plasma through weak interactions ($\bar{\nu}e^- \leftrightarrow \bar{\nu}e^-$, $\nu\bar{\nu} \leftrightarrow e^-e^+$ ...). The collision rate of neutrinos with the primordial plasma is of the order

$$\Gamma_c \approx n_\nu \langle \sigma v \rangle \approx G_F^2 T^5 . \tag{9.279}$$

On the other hand at the radiation-dominated era the expansion was driven by the energy density ($H^2 = \frac{8\pi G_N}{3}\rho$). Thus, if we consider the main contribution which comes from photons,

$$H = \sqrt{\frac{4\pi^3}{45}}\sqrt{g_*(T)}\frac{T^2}{M_P} \approx \frac{T^2}{M_P} , \tag{9.280}$$

the neutrinos decouple from the thermal bath when $\Gamma_c = H$, that defines the decoupling temperature T_d

$$T_d \approx \left(G_F^2 M_P\right)^{-1/3} \approx 1\text{MeV} \tag{9.281}$$

So when the thermal bath was at this temperature of 1 MeV, the neutrinos were relativistic and this is in disagreement with the generic size of the gravitational structures. HDM is in strong disagreement with astrophysical observations.

We talk about Cold Dark Matter (CDM) when the DM is non-relativistic at the decoupling period. It is favoured by observations and most of the DM candidates of BSM models fall into this category. The most famous example are neutralinos from supersymmetric models and heavy sterile neutrinos.

Otherwise we talk about Warm Dark Matter (WDM) which is an intermediate situation. It concerns dark matter particles which interact more weakly than neutrinos, are less abundant, and have a mass of a few keV (the "warm" denomination comes from the fact that the dark matter candidate has lower thermal velocities than massive neutrinos). The sterile neutrinos and the gravitinos are the most famous WDM candidates [398].

In our next discussion, we will focus on thermally produced CDM, i.e DM candidate that is non-relativistic during the decoupling epoch. One can compare the number density of non-relativistic DM compared to the case where it would have been relativistic

$$\frac{n_{DM}^{NR}}{n_{DM}^{R}} \propto e^{\frac{\mu_{DM}}{T}} \left(\frac{m_{DM}}{T}\right)^{3/2} e^{-\frac{m_{DM}}{T}} \tag{9.282}$$

So in the realistic case where μ_{DM} is not huge, the non-relativistic species in thermal equilibrium are exponentially suppressed (Boltzmann suppressed) with respect to that of relativistic one. This would explain why the DM population in the primordial time is significantly reduced.

Generically, when a particle species decouples from the chemical equilibrium the particle production/annihilation must be followed by the Boltzmann equation.

The Boltzmann equation

The Einstein energy conservation equation describes how the energy density evolves with time and how it reflects the effects of the metric. For a matter domination era ($\rho \propto n$ with n the number density) we have

$$\dot{\rho} = -3\frac{\dot{a}}{a}\rho \Rightarrow a^{-3}\frac{d}{dt}(\rho a^3) = 0 \Rightarrow a^{-3}\frac{d}{dt}(n a^3) = 0\ . \tag{9.283}$$

The Boltzmann equation generalizes this last conservation equation by including the interactions of the considered particle species with the thermal bath. Let us study the Boltzmann equation on a generic process $1 + 2 \leftrightarrow 3 + 4$. The number density of the species 1 satisfies

$$\begin{aligned}\frac{1}{a^3}\frac{d(n_1 a^3)}{dt} = \dot{n}_1 + 3Hn_1 \ &= \int \prod_{i=1}^{4} \frac{d^3p_i}{(2\pi)^2 2E_i}(2\pi)^4\delta^{(4)}(p_1+p_2-p_3-p_4)\,|\mathcal{M}|^2 \\ &\quad \times [f_3 f_4(1\pm f_1)(1\pm f_2) - f_1 f_2(1\pm f_3)(1\pm f_4)]\end{aligned} \tag{9.284}$$

where $H \equiv \dot{a}/a$, f_i is the phase space density distribution of species i; $(+)$ applies to bosons and $(-)$ applies to fermions. We have assumed CP invariance meaning $\mathcal{M} = \mathcal{M}_{1+2\to3+4} = \mathcal{M}_{3+4\to1+2}$. A second well justified simplification is the usage of the Maxwell-Boltzmann statistics for all species instead of the Bose-Einstein one for bosons

and the Fermi-Dirac one for fermions. Thus $1 \pm f_i \approx 1$ and $f_i(E_i) \approx e^{-(E_i-\mu_i)/T}$ for all species in kinetic equilibrium. We also introduce the equilibrium number density through the relation $n_i = e^{\mu_i/T} n_i^{eq}$. We recall the definition of the thermally averaged cross section in the Maxwell-Boltzmann approximation

$$\langle \sigma v \rangle = \frac{1}{n_1^{eq} n_2^{eq}} \int \prod_{i=1}^{4} \frac{d^3 p_i}{(2\pi)^2 2E_i} (2\pi)^4 \delta^{(4)}(p_1 + p_2 - p_3 - p_4) \, |\mathcal{M}|^2 \, e^{-\frac{E_1+E_2}{T}} \quad (9.285)$$

We end-up with the simplified Boltzmann equation

$$\dot{n}_1 + 3Hn_1 = n_1^{eq} n_2^{eq} \langle \sigma v \rangle \left[\frac{n_3 n_4}{n_3^{eq} n_4^{eq}} - \frac{n_1 n_2}{n_1^{eq} n_2^{eq}} \right] . \quad (9.286)$$

We now focus on a particle species that has lost its chemical equilibrium so that one needs to solve its Boltzmann equation in order to compute its relic density.

Cold dark matter Freeze-out

We consider a generic scenario where the DM (noted χ) particles annihilate into two light particles (noted a) through $\chi\bar{\chi} \to a\bar{a}$. Assuming that a and $\bar{a}$ are in kinetic and chemical equilibrium leads to $n_a n_{\bar{a}} = n_a^{eq} n_{\bar{a}}^{eq}$. On the contrary χ and $\bar{\chi}$ are chemically decoupled but still preserve their kinetic equilibrium. With the hypothesis $n_\chi = n_{\bar{\chi}}$ we obtain an extremely simple Boltzmann equation

$$\dot{n}_\chi + 3Hn_\chi = \langle \sigma v \rangle \left[n_\chi^{eq2} - n_\chi^2 \right] . \quad (9.287)$$

To get ride of the Hubble parameter we use the comobile density $Y_\chi = n_\chi / s$. The entropy conservation in a comoving volume gives $s\dot{Y}_\chi = \dot{n}_\chi + 3Hn_\chi$, which transforms the Boltzmann equation in

$$\dot{Y}_\chi = s \langle \sigma v \rangle \left[Y_\chi^{eq2} - Y_\chi^2 \right] , \quad (9.288)$$

which can be written in function of $x = m_\chi / T$ as

$$\begin{aligned} \frac{dY_\chi}{dx} &= \frac{\lambda}{x^2} \left[Y_\chi^{eq2} - Y_\chi^2 \right] , \quad (9.289) \\ \lambda &= \frac{2\pi^2}{45} h_* m_\chi^3 \frac{\langle \sigma v \rangle}{H(x=1)} . \end{aligned}$$

The typical behavior of the solution can be seen in Fig.45. At a typical value, x_{FO}, the DM yields departure from equilibrium. In many models $x_{FO} \approx \mathcal{O}(20)$ and the current yield is estimated as $Y_\chi^0 \approx x_{FO}/\lambda$. Then, when the temperature becomes negligible compared to the DM mass its yield decreases because only the DM annihilation process is occurring. Nevertheless, when DM interactions with the thermal bath are slower than the universe expansion rate, the DM decouples from the thermal bath, we call this the DM freeze-out. Since this moment to now, its yield remains nearly constant and the only reminiscence that we get from it, is a relic density which reads

$$\Omega_\chi h^2 = \frac{2\rho}{\rho_c} \approx \frac{2 m_\chi Y_\chi^0}{3.6 \times 10^{-9} \text{GeV}} . \quad (9.290)$$

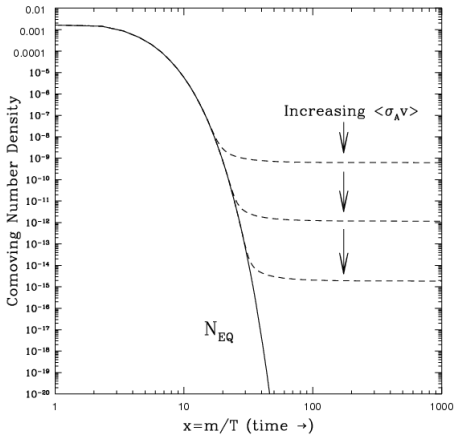

Figure 45: Dark matter comoving number density evolutions as a function of its mass over the temperature. Taken from [399].

An important remark is that the more DM annihilation cross-section is important, the less nowadays DM relic density is big. A Weakly Interacting Massive Particle (WIMP) with a mass at the weak scale could get the expected (from cosmological observations) relic density, this is the famous WIMP miracle.

We now switch to the astrophysical searches for dark matter. We will mostly describe direct detection searches because we will use their bounds on different phenomenological models in the next sections.

9.3 Astrophysical dark matter detection

9.3.1 Direct detection

Since dark matter interacts very weakly with baryonic matter, it could be around us but we just do not "see" it. Direct Detection methods try to observe recoil of nuclei due to interaction with WIMP particles. Even if the interaction rate is extremely small, sufficiently massive detector during long exposure time should distinguish some DM signal from the background. The scattering between DM and ordinary matter might be of two different types. In the case of elastic scattering the WIMP only gives a recoil energy to the nuclei which is of order of tens of keV. In case of inelastic scattering, that is less frequent than the elastic one, the WIMP excites the electronic orbitals of the atom and eventually ionizes it. So one can also measure nuclei recoil but it is now associated with a desexcitation of the atom via the emission of a photon. Several methods can be used in order to measure the energy recoil of a nuclei, amongst them we can cite the observation of phonons, scintillation and ionization. One can estimate the number of collisions per unit of time, N, measured by the experiments as

$$N \approx n_\chi n_N \sigma_{\chi-N} \langle v_\chi \rangle \tag{9.291}$$

where $n_{\chi/N}$ are the local densities of dark matter/nuclei, $\sigma_{\chi-n}$ is the cross-section between WIMP and nucleus and $\langle v_\chi \rangle$ is the average velocity of the WIMPs. The

WIMP-nucleus cross-section is composed of different contributions, one part is spin-independent (comes from scalar-scalar and vector-vector couplings) and the other part is spin-dependent (comes from axial couplings). Generally, the spin-dependent contribution is smaller and especially for nuclei with a vanishing total nuclear spin i.e an even number of protons and neutrons. However, WIMPs hit protons and neutrons of the nucleus (and more precisely quarks). One can relate the WIMP-nucleus cross-section to the WIMP-proton cross-section by the following relation

$$\sigma_{\chi-N} = \left(\frac{\mu_N A}{\mu_p}\right)^2 \sigma_{\chi-p} \tag{9.292}$$

where $\mu_{N/p} \equiv \frac{m_{N/p} m_\chi}{m_{N/p}+m_\chi}$ is the reduced mass of the system Nucleus/proton-WIMP, the atomic number A being the number of nucleons. After some work, the events rate (per unit of time and detector mass) can be expressed as

$$\frac{dN}{dE_r} = \frac{\sigma_{\chi-N} n_\chi}{2\mu_N^2} F(E_r)^2 \int_{v_{\min}(E_r)}^{\infty} \frac{f(v_\chi)}{v_\chi} d^3 v_\chi \tag{9.293}$$

where F is the nuclei form factor, f the WIMPs velocity distribution and $v_{\min}(E_r) \equiv \sqrt{\frac{m_N E_r}{2\mu_N}}$ is the minimum velocity to transfer the amount of energy E_r to the nuclei. Assuming that the WIMP velocities follow a Maxwell-Boltzmann distribution we simply obtain

$$\frac{dN}{dE_r} = \frac{\sigma_{\chi-N} n_\chi}{\mu_N^2 \sqrt{\pi}} F(E_r)^2 e^{-\frac{m_N E_r}{2\mu_N v_0^2}} \tag{9.294}$$

where $v_0 \approx 220$km/s is the velocity of the sun relative to the galactic center. We see that the majority of events appear at low energy of recoil due to the Boltzmann suppression. Lowering the threshold energy of the experiment is consequently of most importance in order to detect light dark matter particles. As an example, for a 100 GeV WIMP hitting the Xenon100 detector experiment (100 kg of Xenon(A=131)) with a rate of 1 pb, one expects 5 events per day.

9.3.2 Indirect detection

The indirect detection of dark matter consists in observing the disintegration products of the dark matter through annihilation or co-annihilation. These decay products could reach the Earth through cosmic rays. Then looking at the galactic center, where the dark matter density is very important, indirect detection experiments try to distinguish known signatures of astrophysical sources from potential DM signal.

In the next section we will study a minimal extension of the Standard Model in order to accommodate dark matter, this is the so called Higgs-portal model.

10 Higgs–portal dark matter

We study the implications of the LHC Higgs searches i.e a 125 GeV SM like scalar for Higgs-portal models of dark matter in a rather model independent way. Their impact on the cosmological relic density and on the direct detection rates are studied in the context of generic scalar, vector and fermionic thermal dark matter particles. Possible observation of these particles at the planned upgrade of the XENON experiment as well as in collider searches will be discussed in our following discussions.

10.1 Implications of LHC searches for Higgs–portal dark matter

10.1.1 Goals setting

In this subsection, we study the implications of these LHC results for Higgs-portal models of dark matter. The Higgs sector of the SM enjoys a special status since it allows for a direct coupling to the hidden sector that is renormalizable. Hence, determination of the properties of the Higgs boson would allow us to gain information about the hidden world. The latter is particularly important in the context of dark matter since hidden sector particles can be stable and couple very weakly to the SM sector, thereby offering a viable dark matter candidate [400]. In principle, the Higgs boson could decay into light DM particles which escape detection [401]. However, given the fact that the ATLAS and CMS signal is close to what one expects for a Standard Model–like Higgs particle, there is little room for invisible decays. In what follows, we will assume that 10% [31] is the upper bound on the invisible Higgs decay branching ratio, although values up to 20% will not change our conclusions.

We adopt a model independent approach and study generic scenarios in which the Higgs-portal DM is a scalar, a vector or a Majorana fermion. We first discuss the available constraints on the thermal DM from WMAP and current direct detection experiments, and show that the fermionic DM case is excluded while in the scalar and vector cases, one needs DM particles that are heavier than about 60 GeV. We then derive the direct DM detection rates to be probed by the XENON100–upgrade and XENON1T experiments. Finally, we discuss the possibility of observing directly or indirectly these DM particles in collider experiments and, in particular, we determine the rate for the pair production of scalar particles at the LHC and a high-energy e^+e^- collider.

10.1.2 The models

Following the model independent approach of Ref. [403], we consider the three possibilities that dark matter consists of real scalars S, vectors V or Majorana fermions χ which interact with the SM fields only through the Higgs-portal. The stability of the DM particle is ensured by a Z_2 parity, whose origin is model–dependent. For example, in the vector case it stems from a natural parity symmetry of abelian gauge sectors with

[31] More accurate upper limits can be find in Refs. [390, 402]

minimal field content [404]. The relevant terms in the Lagrangians are

$$\begin{aligned}
\Delta\mathcal{L}_S &= -\frac{1}{2}m_S^2 S^2 - \frac{1}{4}\lambda_S S^4 - \frac{1}{4}\lambda_{hSS} H^\dagger H S^2 \,, \\
\Delta\mathcal{L}_V &= \frac{1}{2}m_V^2 V_\mu V^\mu + \frac{1}{4}\lambda_V (V_\mu V^\mu)^2 + \frac{1}{4}\lambda_{hVV} H^\dagger H V_\mu V^\mu, \\
\Delta\mathcal{L}_f &= -\frac{1}{2}m_f \bar{\chi}\chi - \frac{1}{4}\frac{\lambda_{hff}}{\Lambda} H^\dagger H \bar{\chi}\chi \,.
\end{aligned} \tag{10.295}$$

Although in the fermionic case above the Higgs–DM coupling is not renormalizable, we still include it for completeness. The self–interaction terms S^4 in the scalar case and the $(V_\mu V^\mu)^2$ term in the vector case are not essential for our discussion and we will ignore them. After electroweak symmetry breaking, the neutral component of the doublet field H is shifted to $H^0 \to v + h/\sqrt{2}$ with $v = 174$ GeV and the physical masses of the DM particles will be given by

$$\begin{aligned}
M_S^2 &= m_S^2 + \frac{1}{2}\lambda_{hSS} v^2 \,, \\
M_V^2 &= m_V^2 + \frac{1}{2}\lambda_{hVV} v^2 \,, \\
M_f &= m_f + \frac{1}{2}\frac{\lambda_{hff}}{\Lambda} v^2 \,.
\end{aligned} \tag{10.296}$$

In what follows, we summarize the most important formulas relevant to our study. Related ideas and analyses can be found in [405–429] and more recent studies of Higgs-portal scenarios have appeared in [430–436].

The relic abundance of the DM particles is obtained through the s–channel annihilation via the exchange of the Higgs boson. For instance, the annihilation cross section into light fermions of mass $m_{\rm ferm}$ is given by

$$\begin{aligned}
\langle \sigma^S_{\rm ferm} v_r \rangle &= \frac{\lambda_{hSS}^2 m_{\rm ferm}^2}{16\pi} \, \frac{1}{(4M_S^2 - m_h^2)^2} \,, \\
\langle \sigma^V_{\rm ferm} v_r \rangle &= \frac{\lambda_{hVV}^2 m_{\rm ferm}^2}{48\pi} \, \frac{1}{(4M_V^2 - m_h^2)^2} \,, \\
\langle \sigma^f_{\rm ferm} v_r \rangle &= \frac{\lambda_{hff}^2 m_{\rm ferm}^2}{32\pi} \, \frac{M_f^2}{\Lambda^2} \, \frac{v_r^2}{(4M_f^2 - m_h^2)^2} \,,
\end{aligned} \tag{10.297}$$

where v_r is the DM relative velocity. (The cross section for Majorana fermion annihilation was computed in [437] in a similar framework.) We should note that in our numerical analysis, we take into account the full set of relevant diagrams and channels, and we have adapted the program micrOMEGAs [438–440] to calculate the relic DM density.

The properties of the dark matter particles can be studied in direct detection experiments. The DM interacts elastically with nuclei through the Higgs boson exchange. The resulting nuclear recoil is then interpreted in terms of the DM mass and DM–nucleon

cross section. The spin–independent DM–nucleon interaction can be expressed as [403]

$$\sigma^{SI}_{S-N} = \frac{\lambda^2_{hSS}}{16\pi m_h^4}\frac{m_N^4 f_N^2}{(M_S+m_N)^2} ,$$
$$\sigma^{SI}_{V-N} = \frac{\lambda^2_{hVV}}{16\pi m_h^4}\frac{m_N^4 f_N^2}{(M_V+m_N)^2} ,$$
$$\sigma^{SI}_{f-N} = \frac{\lambda^2_{hff}}{4\pi\Lambda^2 m_h^4}\frac{m_N^4 M_f^2 f_N^2}{(M_f+m_N)^2} , \qquad (10.298)$$

where m_N is the nucleon mass and f_N parameterizes the Higgs–nucleon coupling. The latter subsumes contributions of the light quarks (f_L) and heavy quarks (f_H), $f_N = \sum f_L + 3 \times \frac{2}{27} f_H$. There exist different estimations of this factor and in what follows we will use the lattice result $f_N = 0.326$ [441] as well as the MILC results [442] which provide the minimal value $f_N = 0.260$ and the maximal value $f_N = 0.629$. We note that the most recent lattice evaluation of the strangeness content of the nucleon [443] favors f_N values closer to the lower end of the above range. In our numerical analysis, we have taken into account these lattice results, which appear more reliable than those extracted from the pion–nucleon cross section.

If the DM particles are light enough, $M_{\rm DM} \leq \frac{1}{2} m_h$, they will appear as invisible decay products of the Higgs boson. For the various cases, the Higgs partial decay widths into invisible DM particles are given by

$$\Gamma^{\rm inv}_{h\to SS} = \frac{\lambda^2_{hSS} v^2 \beta_S}{64\pi m_h} ,$$
$$\Gamma^{\rm inv}_{h\to VV} = \frac{\lambda^2_{hVV} v^2 m_h^3 \beta_V}{256\pi M_V^4}\left(1 - 4\frac{M_V^2}{m_h^2} + 12\frac{M_V^4}{m_h^4}\right) ,$$
$$\Gamma^{\rm inv}_{h\to \chi\chi} = \frac{\lambda^2_{hff} v^2 m_h \beta_f^3}{32\pi\Lambda^2} , \qquad (10.299)$$

where $\beta_X = \sqrt{1-4M_X^2/m_h^2}$. We have adapted the program HDECAY [115] which calculates all Higgs decay widths and branching ratios to include invisible decays.

10.1.3 Astrophysical consequences

The first aim of our study is to derive constraints on the various DM particles from the WMAP satellite [444,445] and from the current direct detection experiment XENON100 [446,447], and to make predictions for future upgrades of the latter experiment, assuming that the Higgs boson has a mass $m_h = 125$ GeV and is approximately SM–like such that its invisible decay branching ratio is smaller than 10%; we have checked that increasing this fraction to 20% does not change our conclusions.

In Fig. 46, we delineate the viable parameter space for the Higgs-portal scalar DM particle. The area between the two solid (red) curves satisfies the WMAP constraint $\Omega_{DM}h^2 = 0.111 \pm 0.012$ (WMAP 5-year Mean and its 2-σ intervals [445]) [32], with the dip corresponding to resonant DM annihilation mediated by the Higgs exchange. We display three versions of the XENON100 direct DM detection bound corresponding to

[32] Notice that the recent constraint coming from Planck [397] does not significantly change our results.

the three values of f_N discussed above. The dash–dotted (brown) curve around the Higgs pole region represents $\mathrm{BR}^{\mathrm{inv}} = 10\%$ such that the area to the left of this line is excluded by our constraint $\mathrm{BR}^{\mathrm{inv}} < 10\%$. The prospects for the upgrade of XENON100 (with a projected sensitivity corresponding to 60,000 kg-d, 5-30 keV and 45% efficiency) and XENON1T are shown by the dotted lines.

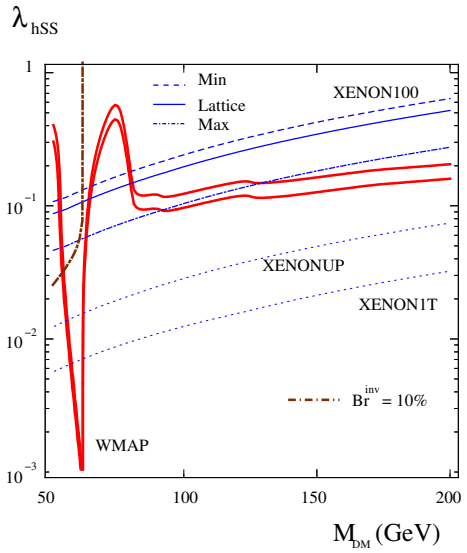

Figure 46: Scalar Higgs-portal parameter space allowed by WMAP (between the solid red curves), XENON100 and $\mathrm{BR}^{\mathrm{inv}} = 10\%$ for $m_h = 125$ GeV. Shown also are the prospects for XENON upgrades.

We find that light dark matter, $M_{\mathrm{DM}} \lesssim 60$ GeV, violates the bound on the invisible Higgs decay branching ratio and thus is excluded. This applies in particular to the case of scalar DM with a mass of 5–10 GeV considered, for instance, in Ref. [427]. On the other hand, heavier dark matter, particularly for $M_{\mathrm{DM}} \gtrsim 80$ GeV, is allowed by both $\mathrm{BR}^{\mathrm{inv}}$ and XENON100. We note that almost the entire available parameter space will be probed by the XENON100 upgrade. The exception is a small resonant region around 62 GeV, where the Higgs–DM coupling is extremely small.

In the case of vector Higgs-portal DM, the results are shown in Fig. 47 and are quite similar to the scalar case. WMAP requires the Higgs–DM coupling to be almost twice as large as that in the scalar case. This is because only opposite polarization states can annihilate through the Higgs channel, which reduces the annihilation cross section by a factor of 3. The resulting direct detection rates are therefore somewhat higher in the vector case. Note that for DM masses below $m_h/2$, only very small values $\lambda_{hVV} < \mathcal{O}(10^{-2})$ are allowed if $\mathrm{BR}^{\mathrm{inv}} < 10\%$.

Similarly, the fermion Higgs-portal results are shown in Fig. 48. We find no parameter regions satisfying the constraints, most notably the XENON100 bound, and this scenario is thus ruled out for $\lambda_{hff}/\Lambda \gtrsim 10^{-3}$.

This can also be seen from Fig. 49, which displays predictions for the spin–independent DM–nucleon cross section σ_{SI} (based on the lattice f_N) subject to the WMAP and $\mathrm{BR}^{\mathrm{inv}} < 10\%$ bounds. The upper band corresponds to the fermion Higgs-portal DM and is excluded by XENON100. On the other hand, scalar and vector DM are both allowed for a wide range of masses. The dark matter results from 225 live days of XENON100 data [448] exclude the vectorial DM mass region above $\frac{1}{2}m_h$ up to

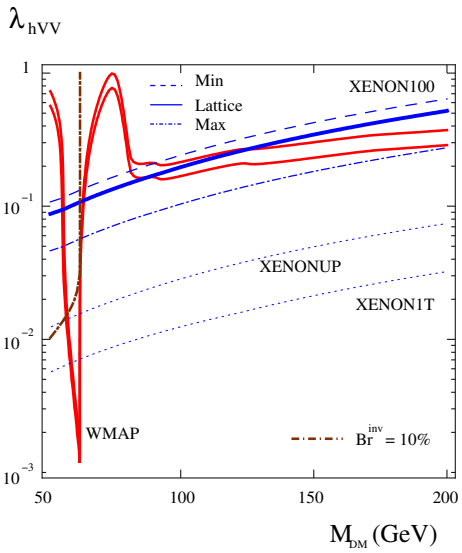

Figure 47: Same as Fig. 1 for vector DM particles.

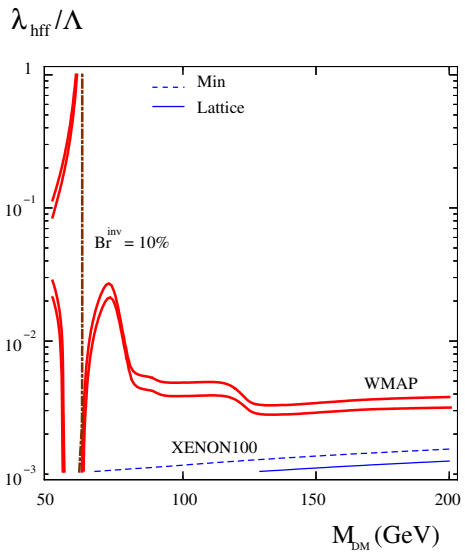

Figure 48: Same as in Fig.1 for fermion DM; λ_{hff}/Λ is in GeV^{-1}.

$\approx$ 200 GeV. Apart from a very small region around $\frac{1}{2}m_h$, this parameter space will be probed by XENON100–upgrade and XENON1T. The typical value for the scalar $\sigma_{\rm SI}$ is a few times 10^{-9} pb, whereas $\sigma_{\rm SI}$ for vectors is larger by a factor of 3 which accounts for the number of degrees of freedom. However, since the XENON100 limit has been superseded by the LUX results [449] the allowed regions for the scalar, vector and fermion candidates have been slightly reduced (for a recent discussion see Ref. [450]).

10.1.4 Dark matter production at colliders

The next issue to discuss is how to observe directly the Higgs-portal DM particles at high energy colliders. There are essentially two ways, depending on the Higgs versus DM particle masses. If the DM particles are light enough for the invisible Higgs decay to occur, $M_{\rm DM} \lesssim \frac{1}{2}m_h$, we have seen that the astrophysical constraints are weak in that region but the Higgs cross sections times the branching ratios for the visible decays will

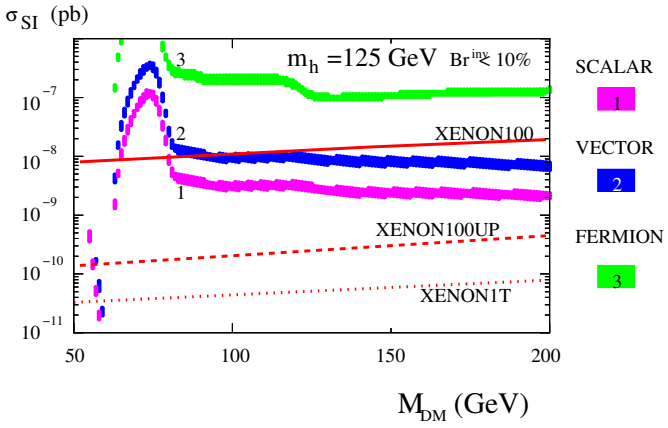

Figure 49: Spin independent DM–nucleon cross section versus DM mass. The upper band (3) corresponds to fermion DM, the middle one (2) to vector DM and the lower one (1) to scalar DM. The solid, dashed and dotted lines represent XENON100, XENON100 upgrade and XENON1T sensitivities, respectively.

be altered, providing indirect evidence for the invisible decay channel. In the case of the LHC, a detailed analysis of this issue has been performed in Refs. [425,426] for instance and we have little to add to it. Nevertheless, if the invisible Higgs branching ratio is smaller than $\approx 10\%$, its observation would be extremely difficult in view of the large QCD uncertainties that affect the Higgs production cross sections, in particular in the main production channel, the gluon fusion mechanism $gg \to h$ [103, 106]. In fact, the chances of observing indirectly the invisible Higgs decays are much better at a future e^+e^- collider. Indeed, it has been shown that, at $\sqrt{s} \approx 500$ GeV collider with 100 fb^{-1} data, the Higgs production cross sections times the visible decay branching fractions can be determined at the percent level [48, 451, 452].

The DM particles could be observed directly by studying associated Higgs production with a vector boson and Higgs production in vector boson fusion with the Higgs particle decaying invisibly. At the LHC, parton level analyses have shown that, although extremely difficult, this channel can be probed at the 14 TeV upgrade with a sufficiently large amount of data [453, 454] if the fraction of invisible decays is significant. A more sophisticated ATLAS analysis has shown that only for branching ratios above 30% that a signal can be observed at $\sqrt{s} = 14$ TeV and 10 fb^{-1} data in the mass range $m_h = 100$–250 GeV [455, 456]. Again, at a 500 GeV e^+e^- collider, invisible decays at the level of a few percent can be observed in the process $e^+e^- \to hZ$ by simply analyzing the recoil of the leptonically decaying Z boson [48, 451, 452].

If the DM particles are heavy, $M_{\rm DM} \gtrsim \frac{1}{2} m_h$, the situation becomes much more difficult and the only possibility to observe them would be via their pair production in the continuum through the s–channel exchange of the Higgs boson. At the LHC, taking the example of the scalar DM particle S, three main processes can be used: a) double production with Higgs–strahlung from either a W or a Z boson, $q\bar{q} \to V^* \to VSS$ with $V = W$ or Z, b) the WW/ZZ fusion processes which lead to two jets and missing energy $qq \to V^*V^*qq \to SSqq$ and c) the gluon–gluon fusion mechanism which is mainly mediated by loops of the heavy top quark that couples strongly to the Higgs boson, $gg \to h^* \to SS$.

The third process, $gg \to SS$, leads to only invisible particles in the final state, unless

some additional jets from higher order contributions are present and reduce the cross section [67, 68, 72] and we will ignore it here. For the two first processes, following Refs. [38,42,44] in which double Higgs production in the SM and its minimal supersymmetric extension has been analyzed, we have calculated the production cross sections. The exact matrix elements have been used in the $q\bar{q} \to ZSS, WSS$ processes while in vector boson fusion, we have used the longitudinal vector boson approximations and specialized to the $W_L W_L + Z_L Z_L \to SS$ case which is expected to provide larger rates at the highest energy available at the LHC i.e. $\sqrt{s}=14$ TeV (the result obtained in this way is expected to approximate the exact result within about a factor of two for low scalar masses and very high energies); we give now the analytical expressions.

The differential cross section for the pair production of two scalar particles in association with a Z boson, $e^+e^- \to ZSS$, after the angular dependence is integrated out, can be cast into the form ($v = 174$ GeV):

$$\frac{\mathrm{d}\sigma(e^+e^- \to ZSS)}{\mathrm{d}x_1 \mathrm{d}x_2} = \frac{G_F^3 M_Z^2 v^4}{384\sqrt{2}\pi^3 s} \frac{(\hat{a}_e^2 + \hat{v}_e^2)}{(1-\mu_Z)^2} \lambda_{hSS}^2 \mathcal{Z} \ , \tag{10.300}$$

where the electron–Z couplings are defined as $\hat{a}_e = -1$ and $\hat{v}_e = -1 + 4\sin^2\theta_W$, $x_{1,2} = 2E_{1,2}/\sqrt{s}$ are the scaled energies of the two scalar particles, $x_3 = 2 - x_1 - x_2$ is the scaled energy of the Z boson; the scaled masses are denoted by $\mu_i = M_i^2/s$. In terms of these variables, the coefficient $\mathcal{Z}$ may be written as

$$\mathcal{Z} = \frac{1}{4} \frac{\mu_Z(x_3^2 + 8\mu_Z)}{(1 - x_3 + \mu_Z - \mu_h)^2} \ . \tag{10.301}$$

The differential cross section has to be integrated over the allowed range of the x_1, x_2 variables; the boundary condition is

$$\left| \frac{2(1 - x_1 - x_2 + 2\mu_S - \mu_Z) + x_1 x_2}{\sqrt{x_1^2 - 4\mu_S}\sqrt{x_2^2 - 4\mu_S}} \right| \leq 1 \ . \tag{10.302}$$

For the cross section at hadron colliders, i.e. for the process $q\bar{q} \to ZSS$ one has to divide the amplitude squared given above by a factor 3 to take into account color sum/averaging, replace e by q (with $a_q = 2I_q^3, v_q = 2I_q^3 - 4e_q \sin^2\theta_W$ with I_q^3 and e_q for isospin and electric charge) and the center of mass energy s by the partonic one $\hat{s}$; one has then to fold the obtained partonic cross section with the quark/antiquark luminosities. The extension to the $q\bar{q} \to WSS$ case (with $a_q = v_q = \sqrt{2}$) is straightforward.

For the vector boson fusion processes, one calculates the cross sections for the $2 \to 2$ processes $V_L V_L \to SS$ in the equivalent longitudinal vector boson approximation and then fold with the V_L spectra to obtain the cross section of the entire processes $e^+e^- \to SS\ell\ell$ and $qq \to qqSS$; see Refs. [38, 42, 44] for details. Taking into account only the dominant longitudinal vector boson contribution, denoting by $\beta_{V,S}$ the V, S velocities in the center of mass frame, $\hat{s}^{1/2}$ the invariant energy of the VV pair, the corresponding cross section of the subprocess $V_L V_L \to SS$ reads

$$\hat{\sigma}_{V_L V_L} = \frac{G_F^2 M_V^4 v^4}{4\pi\hat{s}} \lambda_{hSS}^2 \frac{\beta_S}{\beta_W} \left[\frac{1 + \beta_W^2}{1 - \beta_W^2} \frac{1}{(\hat{s} - M_h^2)} \right]^2 \ . \tag{10.303}$$

The result obtained after folding with the vector boson spectra is expected to approximate the exact result within about a factor of two for low scalar masses and very high energies.

As can be seen from Fig. 61 where the cross sections are shown as a function of $M_{\rm DM}$ for $\lambda_{hSS} = 1$, the rates at $\sqrt{s} = 14$ TeV are at the level of 10 fb in the $WW + ZZ \to SS$ process for $M_h \lesssim 120$ GeV and one order of magnitude smaller for associated production with W and Z bosons. Thus, for both processes, even before selection cuts are applied to suppress the backgrounds, the rates are small for DM masses of order 100 GeV and will require extremely high luminosities to be observed.

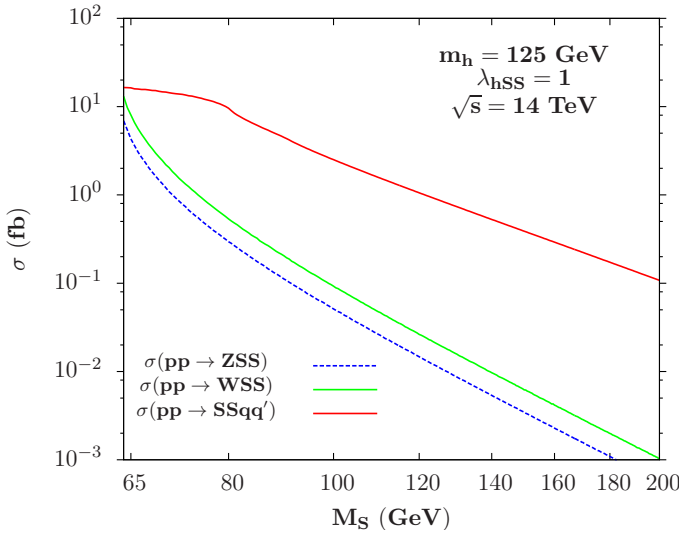

Figure 50: Scalar DM pair production cross sections at the LHC with $\sqrt{s} = 14$ TeV as a function of their mass for $\lambda_{hSS} = 1$ in the processes $pp \to ZSS, WSS$ and $pp \to W^*W^* + Z^*Z^* \to SSqq$.

Again, the chances of observing DM pair production in the continuum might be higher in the cleaner environment of e^+e^- collisions. The two most important production processes in this context, taking again the example of a scalar DM particle, are $e^+e^- \to ZSS$ that dominates at relatively low energies and $e^+e^- \to Z^*Z^*e^+e^- \to e^+e^-SS$ which becomes important at high energies. The rate for WW fusion is one order of magnitude larger but it leads to a fully invisible signal, $e^+e^- \to W^*W^*\nu\bar{\nu} \to \nu\bar{\nu}SS$. Following again Refs. [38,42,44], we have evaluated the cross sections for $e^+e^- \to ZSS$ at $\sqrt{s} = 500$ GeV (the energy range relevant for the ILC) and for $Z_LZ_L \to SS$ at $\sqrt{s} = 3$ TeV (relevant for the CERN CLIC) and the results are shown in Fig.51 as a function of the mass M_S for $\lambda_{hSS} = 1$. One observes that the maximal rate that one can obtain is about 10 fb near the Higgs pole in ZSS production and which drops quickly with increasing M_S. The process $ZZ \to SS$ becomes dominant for $M_S \gtrsim 100$ GeV, but the rates are extremely low, below ≈ 0.1 fb.

For more details concerning dark matter pair production at hadron and lepton colliders much more details can be find in the appendix A.

10.1.5 Status of Higgs–portal dark matter

We have analyzed the implications of the recent LHC Higgs results for generic Higgs-portal models of scalar, vector and fermionic dark matter particles. Requiring the branching ratio for invisible Higgs decay to be less than 10%, we find that the DM–

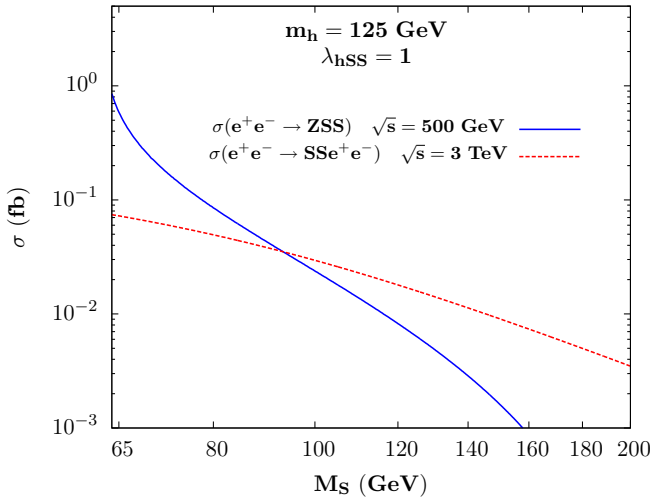

Figure 51: Scalar DM pair production cross sections at e^+e^- colliders as a function of the DM mass for $\lambda_{hSS} = 1$ in the processes $e^+e^- \to ZSS$ at $\sqrt{s} = 500$ GeV and $ZZ \to SS$ at $\sqrt{s} = 3$ TeV.

nucleon cross section for electroweak–size DM masses is predicted to be in the range $10^{-9} - 10^{-8}$ pb in almost all of the parameter space. Thus, the entire class of Higgs-portal DM models will be probed by the XENON100–upgrade and XENON1T direct detection experiments, which will also be able to discriminate between the vector and scalar cases. The fermion DM is essentially ruled out by the current data, most notably by XENON100. Furthermore, we find that light Higgs-portal DM $M_{\rm DM} \lesssim 60$ GeV is excluded independently of its nature since it predicts a large invisible Higgs decay branching ratio, which should be incompatible with the production of an SM–like Higgs boson at the LHC. Finally, it will be difficult to observe the DM effects by studying Higgs physics at the LHC. Such studies can be best performed in Higgs decays at the planned e^+e^- colliders. However, the DM particles have pair production cross sections that are too low to be observed at the LHC and eventually also at future e^+e^- colliders unless very high luminosities are made available.

We now consider the process in which a Higgs particle is produced in association with jets and show that monojet searches at the LHC already provide interesting constraints on the invisible decays of a 125 GeV Higgs boson. We also compare these direct constraints on the invisible rate with indirect ones based on measuring the Higgs rates in visible channels. In the context of Higgs portal models of dark matter, we then discuss how the LHC limits on the invisible Higgs branching fraction impose strong constraints on the dark matter scattering cross section on nucleons probed in direct detection experiments.

10.2 Direct detection of Higgs-portal dark matter at the LHC

The existence of a boson with a mass around $M_H = 125$ GeV is now firmly established [457, 458]. The observed properties of the new particle are consistent with those of the Standard Model Higgs boson [390, 402]. Nevertheless, it is conceivable that the Higgs particle may have other decay channels that are not predicted by the SM. Determining or constraining non-standard Higgs boson decays will provide a vital input to model building beyond the SM.

10.2.1 Motivations

A very interesting possibility that is often discussed is a Higgs boson decaying into stable particles that do not interact with the detector. Common examples where Higgs particles can have invisible decay modes include decays into the lightest supersymmetric particle [47,48] or decays into heavy neutrinos in the SM extended by a fourth generation of fermions [459, 460]. In a wider context, the Higgs boson could be coupled to the particle that constitutes all or part of the dark matter in the universe. In these so-called Higgs portal models [400,405–408,427,430–433,461] that we have studied in the previous subsection, the Higgs boson is the key mediator in the process of dark matter annihilation and scattering, providing an intimate link between Higgs hunting in collider experiments and the direct search for dark matter particles in their elastic scattering on nucleons. In fact, the present LHC Higgs search results, combined with the constraints on the direct detection cross section from the XENON experiment [446], severely constrain the Higgs couplings to dark matter particles and have strong consequences on invisible Higgs decay modes for scalar, fermionic or vectorial dark matter candidates [462].

At the LHC, the main channel for producing a relatively light SM–like Higgs boson is the gluon–gluon fusion (ggF) mechanism. At leading order (LO), the process proceeds through a heavy top quark loop, leading to a single Higgs boson in the final state, $gg \to H$ [463]. At next-to-leading order (NLO) in perturbative QCD, an additional jet can be emitted by the initial gluons or the internal heavy quarks, leading to $gg \to Hg$ final states [67, 68, 72, 464] (additional contributions are also provided by the $gq \to Hq$ process). As the QCD corrections turn out to be quite large, the rate for $H+1$ jet is not much smaller than the rate for $H+0$ jet. The next-to-next-to-leading order (NNLO) QCD corrections [74–76, 122, 324, 465], besides significantly increasing the $H+0$ and $H+1$ jet rates, lead to $H+2$ jet events. The latter event topology also occurs at LO in two other Higgs production mechanisms: vector boson fusion (VBF) $qq \to Hqq$ and Higgs–strahlung (VH) $q\bar{q} \to HW/HZ \to Hq\bar{q}$ which have rather distinct kinematical features compared to the gluon fusion process; for a review, see Refs. [47, 48]

Hence, if the Higgs boson is coupled to invisible particles, it may recoil against hard QCD radiation, leading to monojet events at the LHC. The potential of monojets searches to constrain the invisible decay width of a light Higgs boson has been pointed out before [466, 467]. In this subsection we update and extend these analyses. We place constraints on the Higgs invisible rate defined as

$$R_{\rm inv}^{\rm pp} \;=\; \frac{\sigma(pp \to H) \times {\rm BR}(H \to {\rm inv.})}{\sigma(pp \to H)_{SM}}. \qquad (10.304)$$

We will argue that the existing monojet searches at the LHC [468, 469] yield the con-

straint $R_{\rm inv}^{\rm pp} \lesssim 1$. The constraint is much better than expected. Indeed, early studies [453–455, 470–472], focusing mainly on the VBF production channel, concluded that observation of invisible Higgs decays was only possible at the highest LHC energy, $\sqrt{s} = 14$ TeV, and with more than 10 fb^{-1} data. Bounds on invisible Higgs based on the 1 fb^{-1} monojet search in ATLAS [473] were studied in Refs. [466, 467], where a weaker limit of $R_{\rm inv}^{\rm pp} \lesssim 4$ was obtained for $M_h \sim 125$ GeV.

On one hand, the constraint at the level $R_{\rm inv}^{\rm pp} \sim 1$ means that the monojet searches cannot yet significantly constrain the invisible Higgs branching fraction if the production rate of the 125 GeV Higgs boson is close to the SM one. In fact, in that case much stronger constraints follow from global analyses of the visible Higgs decay channels, which disfavor BR($H \to$ inv.) > 0.2 at 95% confidence level (CL) for SM-like couplings [388, 390]. However, in models beyond the SM, the Higgs production rate may well be enhanced, and in that case the monojet constraints discussed here may become relevant. In this sense, our results are complementary to the indirect constraints on the invisible branching fraction obtained by measuring visible Higgs decays.

In the next step, we discuss the connection between the Higgs invisible branching fraction and the direct dark matter detection cross section. We work in the context of Higgs portal models and consider the cases of scalar, fermionic and vectorial dark matter particles (that we generically denote by χ) coupled to the Higgs boson. To keep our discussion more general, the Higgs–$\chi\chi$ couplings are not fixed by the requirement of obtaining the correct relic density from thermal history[33]. In each case, the LHC constraint BR($H \to$ inv.) can be translated into a constraint on the Higgs boson couplings to the dark matter particles. We will show that these constraints are competitive with those derived from the XENON bounds on the dark matter scattering cross section on nucleons[34]. We discuss how future results from invisible Higgs searches at the LHC and from direct detection experiments will be complementary in exploring the parameter space of Higgs portal models.

In the next section, we present our analysis of invisible Higgs production at the LHC. We estimate the sensitivity to the invisible Higgs rate of the CMS monojet search using 4.7 fb^{-1} of data at $\sqrt{s} = 7$ TeV [469]. We also study the constraints from the recent ATLAS monojet search using 10 fb^{-1} of data at $\sqrt{s} = 8$ TeV [468]. In the following section we discuss the interplay of the monojet constraints on the invisible Higgs decays and the indirect constraints from the global analysis of the LHC Higgs data. We show that a portion of the theory space with a large Higgs invisible branching fraction favored by global fits is excluded by the monojet constraints. We then move on to discuss the implications for Higgs portal dark matter models and the complementarity between dark matter direct detection at the LHC and in XENON. In the last section we present short conclusions.

[33] Instead, we assume that one of the multiple possible processes (e.g. co-annihilation, non-thermal production, s–channel poles of particles from another sector) could arrange that the dark matter relic abundance is consistent with cosmological observations.

[34] We note that the process $gg \to H \to \chi\chi$ for dark matter χ production at the LHC is an important component of the (crossed) process for dark matter scattering on nucleons, $g\chi \to g\chi$ [474].

10.2.2 Monojet constraints on the invisible width

In this section we estimate the sensitivity of current monojet searches at the LHC to a Higgs particles that decays invisibly. We rely on the searches for monojets performed by CMS using 4.7 fb^{-1} of data at 7 TeV center of mass energy [469]. The basic selection requirements used by CMS are as follows:

- at least 1 jet with $p_T^j > 110$ GeV and $|\eta^j| < 2.4$;
- at most 2 jets with $p_T^j > 30$ GeV;
- no isolated leptons;

A second jet with p_T^j above 30 GeV is allowed provided it is not back-to-back with the leading one, $\Delta\phi(j_1, j_2) < 2.5$. Incidentally, this is advantageous from the point of view of invisible Higgs searches, as Higgs production at the LHC is often accompanied by more than one jet; vetoing the second jet would reduce the signal acceptance by a factor of ~ 2. The CMS collaboration quotes the observed event yields and expected SM background for 4 different cuts on the missing transverse momentum: $p_T^{\rm miss} > 250, 300, 350, 400$ GeV. These events are largely dominated by the SM backgrounds, namely Z+jets, where the Z boson decays invisibly, and W+jets, where the W boson decays leptonically and the charged lepton is not reconstructed. In particular, with 4.7 fb^{-1} data, the CMS collaboration estimates the background to be 7842 ± 367 events for $p_T^{\rm miss} > 250$ GeV.

A Higgs boson produced with a significant transverse momentum and decaying to invisible particles may also contribute to the final state targeted by monojet searches. In Fig. 52, we show the fraction of Higgs events produced at the parton level in the ggF and VBF processes with $p_T^{\rm Higgs}$ above a given threshold, assuming $M_H = 125$ GeV. One observes that about 0.5% of ggF events are produced with $p_T^{\rm Higgs} > 250$ GeV, while for the VBF production processes that fraction is larger by a factor of ~ 3. In 4.7 fb^{-1} data at $\sqrt{s} = 7$ TeV this corresponds to about 500 events, assuming the SM production cross sections. This suggests that if an invisible Higgs boson is produced with rates that are comparable or larger than that of the SM Higgs boson, the monojet searches may already provide meaningful constraints.

In order to estimate the sensitivity of the CMS monojet search to the invisible Higgs signal, we generated the $pp \to H$+jets $\to$ invisible+jets process. We used the program `POWHEG` [475, 476] for the ggF and VBF channels at the parton level, and `Madgraph 5` [145] for the VH channels. Showering and hadronization was performed using `Pythia 6` [144] and `Delphes 1.9` [147] was employed to simulate the CMS detector response. We imposed the analysis cuts listed above on the simulated events so as to find the signal efficiency. As a cross-check, we passed $(Z \to \nu\nu)$ + jets background events through the same simulation chain, obtaining efficiencies consistent within 15% with the data–driven estimates of that background provided by CMS.

The signal event yield depends on the cross section in each Higgs production channel and on the Higgs branching fraction into invisible final states. Thus, strictly speaking, the quantities that are being constrained by the CMS search are[35] $R_{\rm inv}^{\rm gg}$ and $R_{\rm inv}^{\rm V}$ defined

[35] Assuming custodial symmetry, $R_{\rm inv}^{\rm VH} = R_{\rm inv}^{\rm VBF} \equiv R_{\rm inv}^{\rm V}$.

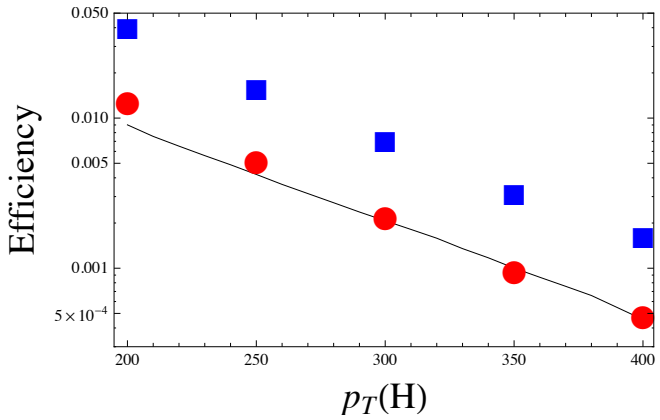

Figure 52: The fraction of events with Higgs transverse momentum above a given threshold for the ggF (red circles) and VBF (blue squares) production modes. The distributions were obtained at NLO using the program `POWHEG` [475]. In the case of ggF, the simulations included the finite quark mass effects [476], and we find good agreement with the NNLO distribution obtained using the program `HRes` [465] (black line).

as

$$\begin{aligned} R_{\rm inv}^{\rm gg} &= \frac{\sigma(gg\to H)\times {\rm BR}(H\to {\rm inv})}{\sigma(gg\to H)_{SM}}, \\ R_{\rm inv}^{\rm V} &= \frac{[\sigma(qq\to Hqq)+\sigma(q\bar{q}\to VH)]\times {\rm BR}(H\to {\rm inv})}{\sigma(qq\to Hqq)_{SM}+\sigma(q\bar{q}\to VH)_{SM}} \end{aligned} \tag{10.305}$$

Currently available data do not allow us to independently constrain $R_{\rm inv}^{\rm gg}$ and $R_{\rm inv}^{\rm V}$. Thus, for the sake of setting limits, we assume that the proportions of ggF, VBF and VH rates are the same as in the SM, and we take the inclusive cross sections to be $\sigma(gg\to H)_{\rm SM}=15.3$ pb, $\sigma(qq\to Hqq)_{\rm SM}=1.2$ pb and $\sigma(q\bar{q}\to HV)_{\rm SM}=0.9$ pb [103, 106]. With this assumption, after the analysis cuts the signal receives about 30% contribution from the VBF and VH production modes, and the rest from ggF; thus CMS constrains the combination $R_{\rm inv}^{\rm pp}\approx\frac{2}{3}R_{\rm inv}^{\rm gg}+\frac{1}{3}R_{\rm inv}^{\rm V}$.

Our results are presented in Table 16. We display the predicted event yields $N_{\rm inv}^{\rm gg}$, $N_{\rm inv}^{\rm V}$ in, respectively, the ggF and VBF+VH channels for the four CMS $p_T^{\rm miss}$ cuts.[36] For convenience, we also reproduce the expected $\Delta N_{95\%}^{i,\rm exp}$ and observed $\Delta N_{95\%}^{\rm obs}$ 95% CL limits on the number of extra non-SM events quoted by CMS in Ref. [469] for each cut. Comparing $N_{\rm inv}^{\rm gg}+N_{\rm inv}^{\rm V}$ with $\Delta N_{95\%}$ it is straightforward to obtain 95% CL expected and observed limits on $R_{\rm inv}^{\rm pp}$ corresponding to each cut reported in Table 16. We find the best expected limit $R_{\rm inv}^{\rm pp}\le 2.1$ for the $p_T^{\rm miss}\ge 250$ GeV cut. The observed limit is better than the expected one thanks to an $\mathcal{O}(1\sigma)$ downward fluctuation of the SM background, and we find $R_{\rm inv}^{\rm pp}\le 1.6$ at 95% CL for that cut. A stronger limit on $R_{\rm inv}^{\rm pp}$ can be derived by binning the number of events given in Table 16 into exclusive bins, and then combining exclusion limits from all four $p_T^{\rm miss}$ bins. Assuming Gaussian errors, one can recast the limits on the number of non-SM events as $\Delta N^i=\Delta N_0^i\pm\Delta N_{1\sigma}^i$, with $\Delta N_0^i=\Delta N_{95\%}^{i,\rm obs}-\Delta N_{95\%}^{i,\rm exp}$, $\Delta N_{1\sigma}^i=\Delta N_{95\%}^{i,\rm exp}/1.96$, where $i=1\ldots4$ indexes the $p_T^{\rm miss}$ bins. Invisible Higgs decays would produce an excess of events $\delta N^i(R_{\rm inv}^{\rm pp})$ in all the bins.

[36] Note that we did not consider the theoretical uncertainties on the cross sections [103,106] and the efficiencies of the p_T cuts which, although significant, are currently smaller than the experimental ones.

Assuming in addition small correlations between the errors in various bins, we can thus construct a global χ^2 function, $\chi^2 = \sum_i [\Delta N_0^i - \delta N^i(R_{\rm inv}^{\rm pp})]^2/[\Delta N_{1\sigma}^i]^2$ so as to constrain $R_{\rm inv}^{\rm pp}$. Using this procedure we obtain

$$R_{\rm inv}^{\rm pp} \leq 1.10 \quad \text{at } 95\% \text{ CL.} \tag{10.306}$$

Following the same procedure, we can also constrain separately $R_{\rm inv}^{\rm gg}$ and $R_{\rm inv}^{\rm V}$, assuming only the ggF or only the VBF+VH Higgs production mode is present. We find $R_{\rm inv}^{\rm gg} \leq 2.0$ (when VBF and VH are absent) or $R_{\rm inv}^{\rm V} \leq 4.0$ (when ggF is absent) at 95% CL.

$p_T^{\rm miss}$[GeV]	$N_{\rm inv}^{\rm gg}$	$N_{\rm inv}^{\rm V}$	$\Delta N_{95\%}^{\rm exp}$	$\Delta N_{95\%}^{\rm obs}$	exp. $R_{\rm inv}^{\rm pp}$	obs. $R_{\rm inv}^{\rm pp}$
250	250	110	779	600	2.1	1.6
300	110	50	325	368	2.1	2.3
350	46	25	200	158	2.8	2.2
400	22	13	118	95	3.4	2.7

Table 16: Limits on the on the invisible Higgs rate $R_{\rm inv}^{\rm pp}$. The event yields are given for each reported $p_T^{\rm miss}$ cut of the CMS monojet search, separately for the ggF and VBF+VH production modes, assuming the SM Higgs production cross sections in these channels and BR($H \to$ inv) = 100%. We also give the expected and observed 95% CL limits on the number of non-SM events reported by CMS [469], which allow us to derive 95%CL expected and observed limits on $R_{\rm inv}^{\rm pp}$.

We also study the impact of the ATLAS monojet search [468] with 10 fb^{-1} at $\sqrt{s} =$ 8 TeV. ATLAS defines 4 search categories: SR1, SR2, SR3, SR4 with similar cuts on the visible jets as discussed above for the CMS case, and with the missing energy cut $p_T^{\rm miss} > 120, 220, 350, 500$ GeV, respectively. In Table 17 we give the 95% CL limits on the invisible rate deduced from the number monojet events reported by ATLAS for each of these categories. We find the best expected limit $R_{\rm inv}^{\rm pp} \leq 1.7$ using the $p_T^{\rm miss} \geq 220$ GeV cut, while the best observed limit is $R_{\rm inv}^{\rm pp} \leq 1.4$ using the $p_T^{\rm miss} \geq 500$ GeV. Unlike in the CMS case, combining ATLAS exclusion limits from different $p_T^{\rm miss}$ bins does not improve the limit of $R_{\rm inv}^{\rm pp}$.

$p_T^{\rm miss}$[GeV]	$N_{\rm inv}^{\rm gg}$	$N_{\rm inv}^{\rm V}$	$\Delta N_{\rm Bkg}$	exp. $R_{\rm inv}^{\rm pp}$	obs. $R_{\rm inv}^{\rm pp}$
120	5694	1543	12820	3.5	4.4
220	904	286	1030	1.7	1.6
350	110	45	171	2.2	3.3
500	15	9	73	6.0	1.4

Table 17: Predicted event yields $N_{\rm inv}$ (assuming BR($H \to$ inv) = 100%), the 1σ background uncertainty $\Delta N_{\rm Bkg}$, and the expected and observed 95% CL limits on the invisible Higgs rate $R_{\rm inv}^{\rm pp}$ for each reported missing energy cut in the 8 TeV 10 fb $^{-1}$ ATLAS monojet search [468]. The event yields are given separately for the ggF and VBF+VH production modes, assuming the SM Higgs production cross sections in these channels.

10.2.3 Monojet vs. indirect constraints on invisible decays

In this section we discuss the interplay between the monojet constraints on the invisible Higgs decays and the indirect constraints from the global analysis of the LHC Higgs data [272, 477]. Assuming the Higgs is produced with the SM cross section, the monojet constraints on the invisible branching fraction are not yet relevant. However, in models beyond the SM the Higgs production rate can be significantly enhanced, especially in the gluon fusion channel. One well known example is the case of the SM extended by the 4th generation of chiral fermions where the $gg \to H$ cross section is enhanced by an order of magnitude. In that class of models a large invisible width may easily arise due to Higgs decays to the 4th generation neutrinos, in which case the monojet constraints discussed here become very important. More generally, the ggF rate can be enhanced whenever there exist additional colored scalars or fermions whose mass originates (entirely or in part) from electroweak symmetry breaking. In a model-independent way, we can describe their effect on the ggF rate via the effective Higgs coupling to gluons:

$$\Delta\mathcal{L} = \frac{c_{gg}}{4} H G^a_{\mu\nu} G^{\mu\nu,a}, \tag{10.307}$$

where c_{gg} can take arbitrary real values depending on the number of additional colored species, their masses, their spins, and their couplings to the Higgs. Furthermore, given the small Higgs width in the SM, $\Gamma_{H,SM} \sim 10^{-5} m_H$, a significant invisible width $\Gamma_{H,\text{inv}} \sim \Gamma_{H,SM}$ may easily arise even from small couplings of the Higgs to new physics, for example to massive neutrinos or to dark matter in Higgs portal models. We parametrize these possible couplings simply via the invisible branching fraction Br_{inv}, which is allowed to take any value between 0 and 1. In Fig. 53 we plot the best fit region to the LHC Higgs data in the Br_{inv}-c_{gg} parameter space. For the SM value $c_{gg} = 0$ an invisible branching fraction larger than $\sim 20\%$ is disfavored at 95% CL. When $c_{gg} > 0$, the global fit admits a larger invisible branching fraction, even up to $\text{Br}_{\text{inv}} \sim 50\%$. Nevertheless, the monojet constraints on the Higgs invisible width derived in this subsection are weaker then the indirect constraints from the global fits, when the latest Higgs data are taken into account [388, 390].

10.2.4 Invisible branching fraction and direct detection

If the invisible particle into which the Higgs boson decays is a constituent of dark matter in the universe, the Higgs coupling to dark matter can be probed not only at the LHC but also in direct detection experiments. In this section, we discuss the complementarity of these two direct detection methods. We consider the generic Higgs-portal scenarios, that have been presented above, in which the dark matter particle is a real scalar, a real vector, or a Majorana fermion, $\chi = S, V, f$ [404, 423, 462, 479, 480]. We recall that the relevant terms in the effective Lagrangian in each of these cases are

$$\begin{aligned}
\Delta\mathcal{L}_S &= -\frac{1}{2} m_S^2 S^2 - \frac{1}{4}\lambda_S S^4 - \frac{1}{4}\lambda_{hSS} H^\dagger H S^2 \,, \\
\Delta\mathcal{L}_V &= \frac{1}{2} m_V^2 V_\mu V^\mu + \frac{1}{4}\lambda_V (V_\mu V^\mu)^2 + \frac{1}{4}\lambda_{hVV} H^\dagger H V_\mu V^\mu, \\
\Delta\mathcal{L}_f &= -\frac{1}{2} m_f f f - \frac{1}{4}\frac{\lambda_{hff}}{\Lambda} H^\dagger H f f + \text{h.c.} \,.
\end{aligned} \tag{10.308}$$

The partial Higgs decay width into dark matter $\Gamma(H \to \chi\chi)$ and the spin–independent χ–proton elastic cross section $\sigma^{\text{SI}}_{\chi p}$ can be easily calculated in terms of the parameters

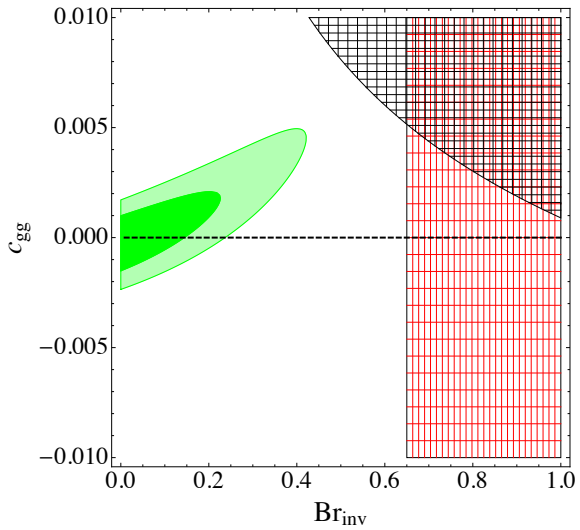

Figure 53: 68% CL (light green) and 95% CL (dark green) best fit regions to the combined LHC Higgs data. The black meshed region is excluded by the monojet constraints derived in this part, while the red meshed region is excluded by the recent ATLAS $Z + (H \to \mathrm{MET})$ search [478].

of the Lagrangian, and we refer to Ref. [462] for complete expressions. For the present purpose, it is important that both $\Gamma(H \to \chi\chi)$ and $\sigma^{\mathrm{SI}}_{\chi p}$ are proportional to $\lambda^2_{H\chi\chi}$; therefore, the ratio $r_\chi = \Gamma(H \to \chi\chi)/\sigma^{\mathrm{SI}}_{\chi p}$ depends only on the dark matter mass M_χ and known masses and couplings (throughout, we assume the Higgs mass be $M_H = 125$ GeV). This allows us to relate the invisible Higgs branching fraction to the direct detection cross section:

$$\mathrm{BR}^{\mathrm{inv}}_\chi \equiv \frac{\Gamma(H \to \chi\chi)}{\Gamma^{\mathrm{SM}}_H + \Gamma(H \to \chi\chi)} = \frac{\sigma^{\mathrm{SI}}_{\chi p}}{\Gamma^{\mathrm{SM}}_H / r_\chi + \sigma^{\mathrm{SI}}_{\chi p}} \tag{10.309}$$

with Γ^{SM}_H the total decay width into all particles in the SM. For a given M_χ, the above formula connects the invisible branching fraction probed at the LHC to the dark matter-nucleon scattering cross section probed by XENON100. For $m_p \ll M_\chi \ll \frac{1}{2}M_H$, and assuming the visible decay width equals to the SM total width $\Gamma^{\mathrm{SM}}_H = 4.0$ MeV [115], one can write down the approximate relations in the three cases that we are considering,

$$\begin{aligned}
\mathrm{BR}^{\mathrm{inv}}_S &\simeq \frac{\left(\frac{\sigma^{\mathrm{SI}}_{Sp}}{10^{-9}\mathrm{pb}}\right)}{400\left(\frac{10\ \mathrm{GeV}}{M_S}\right)^2 + \left(\frac{\sigma^{\mathrm{SI}}_{Sp}}{10^{-9}\mathrm{pb}}\right)} \\
\mathrm{BR}^{\mathrm{inv}}_V &\simeq \frac{\left(\frac{\sigma^{\mathrm{SI}}_{Vp}}{10^{-9}\mathrm{pb}}\right)}{4\times 10^{-2}\left(\frac{M_V}{10\ \mathrm{GeV}}\right)^2 + \left(\frac{\sigma^{\mathrm{SI}}_{Vp}}{10^{-9}\mathrm{pb}}\right)} \\
\mathrm{BR}^{\mathrm{inv}}_f &\simeq \frac{\left(\frac{\sigma^{\mathrm{SI}}_{fp}}{10^{-9}\mathrm{pb}}\right)}{3.47 + \left(\frac{\sigma^{\mathrm{SI}}_{fp}}{10^{-9}\mathrm{pb}}\right)}
\end{aligned} \tag{10.310}$$

Thus, for a given mass of dark matter, an upper bound on the Higgs invisible branching fraction implies an upper bound on the dark matter scattering cross section on nucleons.

In Fig. 54 we show the maximum allowed values of the scattering cross section, assuming the 20% bound on $\mathrm{BR}_\chi^{\mathrm{inv}}$, as follows from indirect constraints on the invisible width discussed in the previous section. Clearly, the relation between the invisible branching fraction and the direct detection cross section strongly depends on the spinorial nature of the dark matter particle, in particular, the strongest (weakest) bound is derived in the vectorial (scalar) case.

In all cases, the derived bounds on $\sigma_{\chi p}^{\mathrm{SI}}$ are stronger than the direct one from XENON100 in the entire range where $M_\chi \ll \frac{1}{2}M_H$. In other words, the LHC is currently the most sensitive dark matter detection apparatus, at least in the context of simple Higgs-portal models (even more so if χ is a pseudoscalar, as in [481]). This conclusion does not rely on the assumption that the present abundance of χ is a thermal relic fulfilling the WMAP constraint of $\Omega_{DM} = 0.226$ [482], and would only be stronger if χ constitutes only a fraction of dark matter in the universe. We also compared the bounds to the projected future sensitivity of the XENON100 experiment (corresponding to 60,000 kg-d, 5-30 keV and 45% efficiency).

Of course, for $M_\chi > \frac{1}{2}M_H$, the Higgs boson cannot decay into dark matter[37], in which case the LHC cannot compete with the XENON bounds.

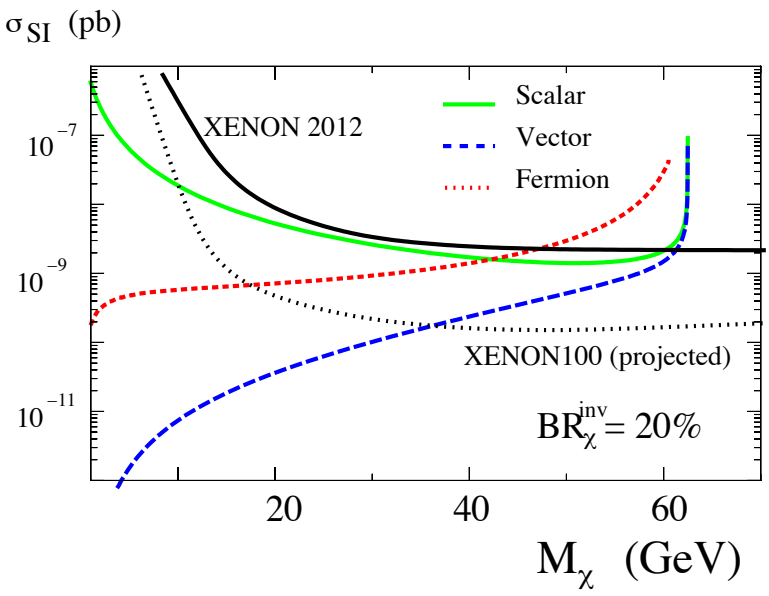

Figure 54: Bounds on the spin-independent direct detection cross section $\sigma_{\chi p}^{\mathrm{SI}}$ in Higgs portal models derived for $M_H = 125$ GeV and the invisible branching fraction of 20 % (colored lines). The curves take into account the full M_χ dependence, without using the approximation in Eq. 10.310. For comparison, we plot the current and future direct bounds from the XENON experiment (black lines).

10.2.5 Conclusions about the invisible Higgs

We have shown that monojet searches at the LHC already provide interesting limits on invisible Higgs decays, constraining the invisible rate to be less than the total SM Higgs production rate at the 95% CL. This provides an important constrain on the models where the Higgs production cross section is enhanced and the invisible branching fraction is significant. Monojets searches are sensitive mostly to the gluon–gluon fusion

[37] In this case, one should consider the pair production of dark matter particles through virtual Higgs boson exchange, $pp \to H^* X \to \chi\chi X$. The rates are expected to be rather small [462].

production mode and, thus, they can also probe invisible Higgs decays in models where the Higgs coupling to the electroweak gauge bosons is suppressed. The limits could be significantly improved when more data at higher center of mass energies are collected, provided systematic errors on the Standard Model contribution to the monojet background can be reduced.

We also analyzed in a model–independent way the interplay between the invisible Higgs branching fraction and the dark matter scattering cross section on nucleons, in the context of effective Higgs portal models. The limit $\mathrm{BR}_{\mathrm{inv}} < 0.2$, suggested by the combination of Higgs data in the visible channels, implies a limit on the direct detection cross section that is stronger than the current bounds from XENON100, for scalar, fermionic, and vectorial dark matter alike. Hence, in the context of Higgs-portal models, the LHC is currently the most sensitive dark matter detection apparatus.

We now switch from the Higgs–portal model to another alternative accounting for dark matter. If the hidden sector contains more than one U(1) groups, additional dim-4 couplings (beyond the kinetic mixing) between the massive U(1) fields and the hypercharge generally appear. These are of the form similar to the Chern–Simons interactions. We study now the phenomenology of such couplings including constraints from laboratory experiments and implications for dark matter. The hidden vector fields can play the role of dark matter whose characteristic signature would be monochromatic gamma ray emission from the galactic center. We show that this possibility is consistent with the LHC and other laboratory constraints, as well as astrophysical bounds.

11 The hypercharge portal into the dark sector

11.1 Introduction

The existence of new physics structures beyond those of the Standard Model is motivated, among other facts, by the puzzles of dark matter and inflation. The minimal way to address these problems is to add a "hidden" sector containing the required SM–singlet fields. The existence of the hidden sector can also be motivated from the top–down viewpoint, in particular, by realistic string models [483,484]. Such a sector can couple to the SM fields through products of gauge–singlet operators, including those of dimension 2 and 3. In this section, we study in detail the corresponding couplings to the hypercharge field.

Let us define the "hidden sector" as a set of fields which carry no SM gauge quantum numbers. Thus a "portal" [408] would be an operator that couples the SM fields to such SM singlets. Let us consider the minimal case: suppose that the relevant low energy degrees of freedom in the dark sector are those of a Weyl fermion χ, or a massive vector V_μ, or a real scalar S (one field at a time). Then the lowest, up to *dim*–4, dimension operators that couple the SM to the hidden sector are given by

$$\begin{aligned} O_1 &= \Psi_L H \chi + \text{h.c.} \,, \\ O_2 &= F^Y_{\mu\nu} \, F^{V\,\mu\nu} \,, \\ O_3 &= \overline{\Psi}_i \gamma_\mu (1 + \alpha_{ij}\gamma_5) \Psi_j \, V^\mu + \text{h.c.} \,, \\ O_4 &= H^\dagger H \, V_\mu V^\mu + \beta \, H^\dagger i D_\mu H \, V^\mu + \text{h.c.} \,, \\ O_5 &= H^\dagger H \, S^2 + \mu_S \, H^\dagger H \, S \,. \end{aligned} \tag{11.311}$$

Here Ψ_L is a lepton doublet; $F^Y_{\mu\nu}$ and $F^V_{\mu\nu}$ are the field strength tensors for hypercharge and V_μ respectively; Ψ_i is an SM fermion with the generation index i; D_μ is the covariant derivative with respect to the SM gauge symmetries, and $\alpha_{ij}, \beta, \mu_S$ are constants. Note that a particular version of operator O_3 is induced by O_2 after diagonalization of the vector kinetic terms.

An attractive feature of such an extension of the Standard Model is that it can offer viable dark matter candidates as well as provide a link to the inflaton sector. In particular, a sufficiently light "right–handed neutrino" χ is long–lived and could constitute warm dark matter [485]. Also, a massive vector V_μ (or a scalar S [400]) can inherit a Z_2 symmetry from hidden sector gauge interactions, which would eliminate terms linear in V_μ and make it a stable cold dark matter candidate [404]. Finally, the Higgs coupling $H^\dagger H \; S^2$ to the inflaton S would be instrumental in reconciling metastability of the electroweak vacuum with inflation [486].

In this section, we explore a more general dimensional-four-hypercharge coupling to the hidden sector, when the latter contains multiple U(1)'s. In this case, a Chern–Simons–type coupling becomes possible [487–491]. If such a coupling is the only SM portal into the hidden sector, the lightest U(1) vector field can play the role of dark matter. The trademark signature of this scenario is the presence of monochromatic gamma–ray lines in the photon spectrum inside the galactic center. We analyze general experimental constraints on the Chern–Simons–type coupling as well as the constraints applicable when the vector field constitutes dark matter.

11.2 Hypercharge couplings to the dark-sector

Let us suppose that the dark-sector contains two massive U(1) gauge fields C_μ and D_μ. Before electroweak symmetry breaking, the most general dim-4 interactions of these fields with the hypercharge boson B_μ are described by the Lagrangian

$$\begin{aligned}\mathcal{L} &= -\frac{1}{4}B_{\mu\nu}B^{\mu\nu} - \frac{1}{4}C_{\mu\nu}C^{\mu\nu} - \frac{1}{4}D_{\mu\nu}D^{\mu\nu} - \frac{\delta_1}{2}B_{\mu\nu}C^{\mu\nu} - \frac{\delta_2}{2}B_{\mu\nu}D^{\mu\nu} - \frac{\delta_3}{2}C_{\mu\nu}D^{\mu\nu} \\ &+ \frac{M_C^2}{2}C_\mu C^\mu + \frac{M_D^2}{2}D_\mu D^\mu + \delta M^2 C_\mu D^\mu + \kappa\,\epsilon_{\mu\nu\rho\sigma}B^{\mu\nu}C^\rho D^\sigma\ . \end{aligned} \tag{11.312}$$

Here we have assumed CP symmetry such that terms of the type $B^{\mu\nu}C_\mu D_\nu$ are not allowed (see [492, 493] for a study of the latter). The kinetic and mass mixing can be eliminated by field redefinition [493], which to first order in the mixing parameters δ_i and δM^2 reads

$$\begin{aligned} B_\mu &\to B_\mu + \delta_1\, C_\mu + \delta_2\, D_\mu\ , \\ C_\mu &\to C_\mu + \frac{\delta_3\, M_D^2 - \delta M^2}{M_D^2 - M_C^2}\, D_\mu\ , \\ D_\mu &\to D_\mu - \frac{\delta_3\, M_C^2 - \delta M^2}{M_D^2 - M_C^2}\, C_\mu\ . \end{aligned} \tag{11.313}$$

In terms of the new fields, the Lagrangian reads

$$\mathcal{L} = -\frac{1}{4}B_{\mu\nu}B^{\mu\nu} - \frac{1}{4}C_{\mu\nu}C^{\mu\nu} - \frac{1}{4}D_{\mu\nu}D^{\mu\nu} + \frac{M_C^2}{2}C_\mu C^\mu + \frac{M_D^2}{2}D_\mu D^\mu + \kappa\,\epsilon_{\mu\nu\rho\sigma}B^{\mu\nu}C^\rho D^\sigma, \tag{11.314}$$

which will be the starting point for our phenomenological analysis. We note that, due to the kinetic mixing $\delta_{1,2}$, C_μ and D_μ have small couplings to the Standard Model matter. Since we are mainly interested in the effect of the Chern–Simons–type term $\epsilon_{\mu\nu\rho\sigma}B^{\mu\nu}C^\rho D^\sigma$, we will set $\delta_{1,2}$ to be very small or zero in most of our analysis.

The term $\epsilon_{\mu\nu\rho\sigma}B^{\mu\nu}C^\rho D^\sigma$ has dimension 4. However, it vanishes in the limit of zero vector boson masses by gauge invariance, both for the Higgs and Stückelberg mechanisms. This means that it comes effectively from a higher dimensional operator with κ proportional to $M_C M_D/\Lambda^2$, where Λ is the cutoff scale or the mass scale of heavy particles we have integrated out. On one hand, this operator does not decouple as $\Lambda \to \infty$ since both $M_{C,D}$ and Λ are given by the "hidden" Higgs v.e.v times the appropriate couplings; on the other hand, $\epsilon_{\mu\nu\rho\sigma}B^{\mu\nu}C^\rho D^\sigma$ is phenomenologically relevant only if $M_{C,D}$ are not far above the weak scale. Thus, this term represents a meaningful approximation in a particular energy window, which we will quantify later. (A similar situation occurs in the vector Higgs portal models, where the interaction $H^\dagger H V_\mu V^\mu$ has naive dimension 4, but originates from a dim-6 operator [404].) From the phenomenological perspective, it is important that $\epsilon_{\mu\nu\rho\sigma}B^{\mu\nu}C^\rho D^\sigma$ is the leading operator at low energies, i.e relevant to non–relativistic annihilation of dark matter composed of C_μ or D_μ, and thus we will restrict our attention to this coupling only.

A coupling of this sort appears in various models upon integrating out heavy fields charged under both U(1)'s and hypercharge. Explicit anomaly–free examples can be found in [490] and [489]. In these cases, the Chern–Simons term arises upon integrating out heavy, vector–like with respect to the SM, fermions. Both the vectors and the

fermions get their masses from the Higgs mechanism, while the latter can be made heavy by choosing large Yukawa couplings compared to the gauge couplings. In this limit, Eq. (11.314) gives the corresponding low energy action.[38]

Finally, we note that increasing the number of hidden U(1)'s does not bring in hypercharge–portal interactions with a new structure, so our considerations apply quite generally.

11.3 Phenomenological constraints

In this section we derive constraints on the coupling constant κ from various laboratory experiments as well as unitarity considerations. The relevant interaction to leading order is given by

$$\Delta\mathcal{L} = \kappa\ \cos\theta_W\ \epsilon_{\mu\nu\rho\sigma}F^{\mu\nu}C^\rho D^\sigma - \kappa\ \sin\theta_W\ \epsilon_{\mu\nu\rho\sigma}Z^{\mu\nu}C^\rho D^\sigma\ , \tag{11.315}$$

where $F^{\mu\nu}$ and $Z^{\mu\nu}$ are the photon and Z-boson field strengths, respectively.

In what follows, we set the kinetic mixing to be negligibly small such that the lighter of the C and D fields is not detected and thus appears as missing energy and momentum. There are then two possibilities: the heavier state decays into the lighter state plus γ either outside or inside the detector. Let us consider first the case where the mass splitting and κ are relatively small such that both C and D are "invisible".

Unitarity

The coupling $\epsilon_{\mu\nu\rho\sigma}B^{\mu\nu}C^\rho D^\sigma$ involves longitudinal components of the massive vectors. Therefore, some scattering amplitudes will grow indefinitely with energy, which imposes a cutoff on our effective theory. For a fixed cutoff, this translates into a bound on κ.

Consider the scattering process

$$C_\mu\ C_\nu \to D_\rho\ D_\sigma \tag{11.316}$$

at high energies, $E \gg M_{C,D}$. The vertex can contain longitudinal components of at most one vector since $\epsilon_{\mu\nu\rho\sigma}(p_1+p_2)^\mu p_1^\nu p_2^\rho = 0$. Then one finds that the amplitude grows quadratically with energy,

$$\mathcal{A} \sim \kappa^2\ \frac{E^2}{M_{C,D}^2}\ , \tag{11.317}$$

with the subscripts C and D applying to the processes involving longitudinal components of C_μ and D_μ, respectively. On the other hand, the amplitude cannot exceed roughly 8π. Neglecting the factors of order one, the resulting constraint is

$$\frac{\kappa}{M} < \frac{\sqrt{8\pi}}{\Lambda}\ , \tag{11.318}$$

[38] We note that certain "genuine" gauge invariant dim-6 operators such as $\frac{1}{\Lambda^2}\epsilon^{\mu\nu\rho\sigma}B_{\mu\nu}C^\tau{}_\rho D_{\tau\sigma}$ reduce to the Chern-Simons term on–shell in the non–relativistic limit ($C_{\mu\nu} \to C_{0i} = iM_C C_i$; $C_0 = 0$ and similarly for $D_{\mu\nu}$). Such operators should generally be taken into account when deriving the low energy action in explicit microscopic models.

where $M = \min\{M_C, M_D\}$ and Λ is the cutoff scale. As explained in the previous paragraph, Λ is associated with the mass scale of the new states charged under $\mathrm{U}(1)_\mathrm{Y}$. Since constraints on such states are rather stringent, it is reasonable to take $\Lambda \sim 1$ TeV. This implies that light vector bosons can couple only very weakly, e.g. $\kappa < 10^{-5}$ for $M \sim 1$ MeV.

It is important to note that the unitarity bound applies irrespective of whether C and D are stable or not. Thus it applies to the case $M_D \gg M_C$ or vice versa and also in the presence of the kinetic mixing.

Invisible Υ decay

Suppose that D is the heavier state and the decay $D \to C + \gamma$ is not fast enough to occur inside the detector. Then production of C and D would appear as missing energy. In particular, light C, D can be produced in the invisible Υ meson ($b\bar{b}$) decay

$$\Upsilon \to \mathrm{inv} \quad , \tag{11.319}$$

which is a powerful probe of new physics since its branching ratio in the Standard Model is small, about 10^{-5} [494]. In our case, this decay is dominated by the s–channel annihilation through the photon, while the Z–contribution is suppressed by m_Υ^4/m_Z^4. We find

$$\begin{aligned}\Gamma(\Upsilon \to CD) &= 2\alpha\kappa^2 \cos^2\theta_W \, Q_d^2 \, \frac{f_\Upsilon^2}{m_\Upsilon} \sqrt{1 - 2\frac{M_C^2 + M_D^2}{m_\Upsilon^2} + \frac{(M_C^2 - M_D^2)^2}{m_\Upsilon^4}} \\ &\times \left[1 + \frac{m_\Upsilon^2}{12}\left(\frac{1}{M_C^2} + \frac{1}{M_D^2}\right)\left(1 - 2\frac{M_C^2 + M_D^2}{m_\Upsilon^2} + \frac{(M_C^2 - M_D^2)^2}{m_\Upsilon^4}\right)\right] \end{aligned} \tag{11.320}$$

where α is the fine structure constant, Q_d is the down quark charge and f_Υ is the Υ decay constant, $\langle 0|\bar{b}\gamma^\mu b|\Upsilon\rangle = f_\Upsilon m_\Upsilon \epsilon^\mu$ with ϵ^μ being the Υ polarization vector. In the limit $M_{C,D}^2 \ll m_\Upsilon^2$ and $M_C \simeq M_D = M$, the decay rate becomes

$$\Gamma(\Upsilon \to CD) \simeq \frac{1}{3}\alpha\kappa^2 \cos^2\theta_W \, Q_d^2 \, \frac{f_\Upsilon^2 m_\Upsilon}{M^2} \, . \tag{11.321}$$

Taking $m_\Upsilon(1S) = 9.5$ GeV, $\Gamma_\Upsilon(1S) = 5.4 \times 10^{-5}$ GeV, $f_\Upsilon = 0.7$ GeV and using the BaBar limit $\mathrm{BR}(\Upsilon \to \mathrm{inv}) < 3 \times 10^{-4}$ at 90% CL [495], we find

$$\frac{\kappa}{M} < 4 \times 10^{-3} \ \mathrm{GeV}^{-1} \, . \tag{11.322}$$

This bound applies to vector boson masses up to a few GeV and disappears above $m_\Upsilon/2$. An analogous bound from $J/\Psi \to \mathrm{inv}$ is weaker.

We note that the $\Gamma \propto 1/M^2$ dependence is characteristic to production of the longitudinal components of massive vector bosons. The corresponding polarization vector grows with energy as E/M, i.e at $M \ll m_\Upsilon$, the decay is dominated by the Goldstone boson production, whose couplings grow with energy. Then, stronger constraints on κ are expected from the decay of heavier states.

The corresponding bound from the radiative Υ decay $\Upsilon \to \gamma + \mathrm{inv}$ is much weaker. By C–parity, such a decay can only be mediated by the Z boson, which brings in the m_Υ^4/m_Z^4 suppression factor. The resulting constraint is negligible.

Invisible Z decay

The invisible width of the Z boson $\Gamma^Z_{\rm inv}$ is strongly constrained by the LEP measurements [496]. The process $Z \to CD$ contributes to $\Gamma^Z_{\rm inv}$ for vector boson masses up to about 45 GeV, thereby leading to a bound on κ. We find

$$\begin{aligned}\Gamma(Z \to CD) &= \frac{1}{2\pi}\,\kappa^2 \sin^2\theta_W\, m_Z\, \sqrt{1-2\frac{M_C^2+M_D^2}{m_Z^2}+\frac{(M_C^2-M_D^2)^2}{m_Z^4}} \\ &\times \left[1+\frac{m_Z^2}{12}\,\left(\frac{1}{M_C^2}+\frac{1}{M_D^2}\right)\left(1-2\frac{M_C^2+M_D^2}{m_Z^2}+\frac{(M_C^2-M_D^2)^2}{m_Z^4}\right)\right] \end{aligned} \tag{11.323}$$

In the limit $M^2_{C,D} \ll m_Z^2$ and $M_C \simeq M_D = M$, it becomes

$$\Gamma(Z \to CD) \simeq \frac{\kappa^2 \sin^2\theta_W}{12\pi}\,\frac{m_Z^3}{M^2}\,. \tag{11.324}$$

Taking the bound on the BSM contribution to $\Gamma^Z_{\rm inv}$ to be roughly 3 MeV (twice the experimental error–bar of $\Gamma^Z_{\rm inv}$ [496]), we have

$$\frac{\kappa}{M} < 8\times 10^{-4}\ {\rm GeV}^{-1}\,. \tag{11.325}$$

In the given kinematic range, this constraint is even stronger than the unitarity bound for $\Lambda = 1$ TeV and comparable to the latter with a multi–TeV cutoff. As explained above, such sensitivity of $Z \to$ inv to κ is due to the E/M enhancement of the longitudinal vector boson production.

$B \to K +$ inv **and** $K \to \pi +$ inv

Flavor changing transitions with missing energy are also a sensitive probe of matter couplings to "invisible" states (see e.g. [497]). The decay $B \to K + C\ D$ proceeds via the SM flavor violating $\bar b s Z$ and $\bar b s \gamma$ vertices with subsequent conversion of Z, γ into C and D. Numerically, the process is dominated by the Z contribution with the flavor changing vertex [498, 499]

$$\mathcal{L}_{\bar b s Z} = \lambda_{\bar b s Z}\ \bar b_L \gamma_\mu s_L\ Z^\mu\,, \tag{11.326}$$

with

$$\lambda_{\bar b s Z} = \frac{g^3}{16\pi^2\cos\theta_W}\,V_{tb}^* V_{ts}\ f\left(\frac{m_t^2}{m_W^2}\right)\,, \tag{11.327}$$

where V_{ij} are the CKM matrix elements and $f(x)$ is the Inami–Lim function [498],

$$f(x) = \frac{x}{4}\,\left(\frac{x-6}{x-1}+\frac{3x+2}{(x-1)^2}\,\ln x\right)\,. \tag{11.328}$$

We find

$$\Gamma(B \to K + C\ D) = \frac{\kappa^2 \lambda^2_{\bar b s Z}\sin^2\theta_W}{2^7\pi^3 m_B^3 m_Z^4}\int_{(M_C+M_D)^2}^{(m_B-m_K)^2}\frac{ds}{s}\ f_+^2(s) \tag{11.329}$$

$$\times\ \sqrt{(s-M_C^2-M_D^2)^2-4M_C^2M_D^2}\,\left((s+m_B^2-m_K^2)^2-4m_B^2 s\right)^{3/2}$$

$$\times\ \left[1+\frac{1}{12s}\left(\frac{1}{M_C^2}+\frac{1}{M_D^2}\right)\left((s-M_C^2-M_D^2)^2-4M_C^2M_D^2\right)\right]\,,$$

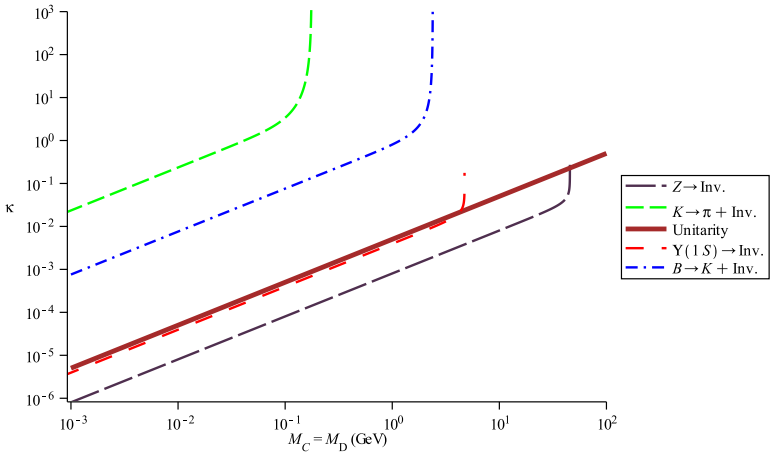

Figure 55: Bounds on κ. The unitarity bound assumes $\Lambda = 1$ TeV.

where the form factor $f_+(s)$ is defined by $\langle K(p_K)|\bar{b}\gamma^\mu s|B(p_B)\rangle = (p_K+p_B)^\mu f_+(s)+(p_B-p_K)^\mu f_-(s)$ with $s=(p_B-p_K)^2$. The decay rate is dominated by the contribution from large invariant masses of the C, D pair due to the longitudinal vector boson production. This justifies the subleading character of the photon contribution: the corresponding dipole operator can be significant at low invariant masses due to the $1/s$ pole, as in the $B \to K l^+ l^-$ processes (see e.g. [500] for a recent summary). The relative size of various $\Delta F = 1$ operators can be found in [498, 499], and we find that the photon contribution is unimportant.

The relevant experimental limit has been obtained by BaBar: $\mathrm{BR}(B^+ \to K^+ \nu\bar{\nu}) < 1.3 \times 10^{-5}$ at 90% CL [501]. Then taking $f_+(0) = 0.3$ and using its s–dependence from [500], we find

$$\frac{\kappa}{M} < 1 \text{ GeV}^{-1} , \tag{11.330}$$

for $M_C \simeq M_D = M$ up to roughly 2 GeV. The above considerations equally apply to the process $K \to \pi + \text{inv}$, up to trivial substitutions. We find that the resulting bound is weak, $\kappa/M < 30$ GeV^{-1}. This stems from the $m^7_{\text{meson}}/(M^2 m_Z^4)$ behavior of the rate, which favors heavier mesons.

Finally, the Chern–Simons coupling does not contribute to $B \to CD$ due to the ϵ–tensor contraction, so there is no bound from the $B \to$ inv decay. Also, κ contributes to $(g-2)_\mu$ only at the two loop level such that the resulting bound is insignificant.

The summary of the bounds is shown in Fig. 55. We see that the most stringent limits are set by the Z invisible width and unitarity considerations. The latter has the advantage of not being limited by kinematics and places a tight bound on κ for vector masses up to about 100 GeV.

Bounds on decaying vector bosons $D \to C + \gamma$

When the vector boson mass difference is not too small, the heavier particle, say D, will decay inside the detector. In this case, the constraints on κ get somewhat modified.

The decay width Γ_D is given by

$$\Gamma(D \to C + \gamma) = \frac{\kappa^2 \cos^2\theta_W}{24\pi} \, \frac{(M_D^2 - M_C^2)^3}{M_D^3} \, \left(\frac{1}{M_C^2} + \frac{1}{M_D^2}\right) , \tag{11.331}$$

assuming that the Z–emission is kinematically forbidden. Given the velocity v_D and lifetime τ_D, D decays inside the detector if $v_D \tau_D = |\mathbf{p}_D|/(M_D \Gamma_D)$ is less than the detector size l_0, which we take to be ~ 3 m. In this case, κ is constrained by radiative decays with missing energy.

Consider the radiative decay $\Upsilon(1S) \to \gamma + \text{inv}$. Its branching ratio is constrained by BaBar: $\text{BR}(\Upsilon(1S) \to \gamma + \text{inv}) < 6 \times 10^{-6}$ for a 3–body final state and M_C up to about 3 GeV [502]. Since $\text{BR}(D \to C + \gamma) \sim 100\%$, this requires approximately

$$\frac{\kappa}{M} < 6 \times 10^{-4} \text{ GeV}^{-1} , \tag{11.332}$$

which is the strongest bound on κ in the kinematic range $M \lesssim 3$ GeV. This bound applies for

$$\Delta M \gtrsim \left(\frac{3\pi m_\Upsilon M}{4\kappa^2 \cos^2\theta_W \, l_0}\right)^{1/3} , \tag{11.333}$$

where we have made the approximation $M_D - M_C = \Delta M \ll M \ll m_\Upsilon$. For example, taking the maximal allowed κ consistent with (11.332) at $M = 1$ GeV, the decay occurs within the detector for $\Delta M > 2$ MeV. (However, since the experimental cut on the photon energy is 150 MeV, ΔM close to this bound would not lead to a detectable signal.)

On the other hand, the bound on κ from the invisible Z width does not change even for decaying D. The reason is that the invisible width is defined by subtracting the visible decay width into fermions $\Gamma(Z \to \bar{f} f)$ from the total width Γ_Z measured via the energy dependence of the hadronic cross section [496]. Thus, $Z \to \gamma + \text{inv}$ qualifies as "invisible" decay and we still have

$$\frac{\kappa}{M} < 8 \times 10^{-4} \text{ GeV}^{-1} , \tag{11.334}$$

as long as the decay is kinematically allowed.

Finally, the unitarity bound

$$\frac{\kappa}{M} < \frac{\sqrt{8\pi}}{\Lambda} \tag{11.335}$$

remains intact as well. Another constraint in the higher mass range $m_Z/2 \lesssim M \lesssim 100$ GeV is imposed by the LEP monophoton searches $e^+e^- \to \gamma + \text{inv}$ [503]. We find, however, that it is somewhat weaker than the unitarity bound for $\Lambda = 1$ TeV (the same applies to $e^+e^- \to \text{inv}$).

Thus, the strongest constraints in Fig. 55 apply also to the case of decaying vector bosons, while the Υ bound becomes competitive and even the tightest one at lower masses. For $M \gtrsim 100$ GeV, some of the relevant LHC constraints will be discussed in the following.

Let us conclude by remarking on the astrophysical constraints. These apply to very light, up to $\mathcal{O}(\text{MeV})$, particles. In particular, the rate of energy loss in horizontal–branch stars sets stringent bounds on light particle emission in Compton–like scattering

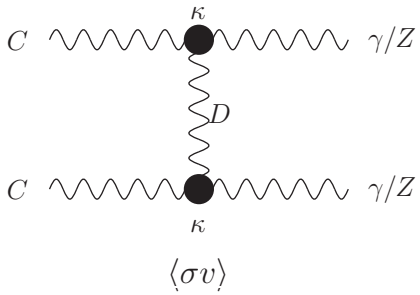

Figure 56: Dark matter annihilation into photons and Z–bosons.

$\gamma + e \to e + C + D$. We find that this cross section in the non–relativistic limit scales approximately as $\alpha^2\kappa^2/(6\pi m_e^2)\ (T/M)^2$, with $T \sim$ keV being the core temperature. Comparison to the axion models [504] leads then to the bound $\kappa/M < 10^{-7}$ GeV^{-1} for $M \ll$ keV, which is much stronger than the laboratory constraints in this mass range. Analogous supernova cooling considerations extend the range to $\mathcal{O}$(MeV). A dedicated study of astrophysical constraints will be presented elsewhere.

11.4 Vector dark matter and the Chern–Simons coupling

In this section, we consider a special case of the Lagrangian (11.312) with

$$\delta_{1,2} = 0\ , \tag{11.336}$$

that is, the new gauge bosons do not mix with the hypercharge. This can be enforced by the Z_2 symmetry

$$C_\mu \to -C_\mu \quad , \quad D_\mu \to -D_\mu\ . \tag{11.337}$$

It is straightforward to construct microscopic models which lead to an effective theory endowed with this symmetry at one loop. However, to make the Z_2 persist at higher loop levels is much more challenging and beyond the scope of our study.

The relevant Lagrangian in terms of the propagation eigenstates is again given by (11.314), except now C and D do not couple to ordinary matter. The Z_2 symmetry forbids their kinetic mixing with the photon and the Z. This makes the lighter state, C, stable and a good dark matter candidate. In what follows, we consider M_C of order the electroweak scale such that dark matter is of WIMP type.

Our vector dark matter interacts with the SM only via the Chern–Simons type terms (11.315). These allow for DM annihilation into photons and Z bosons (Fig. 56 and its cross–version). The corresponding cross sections for $M_C \simeq M_D = M$ in the

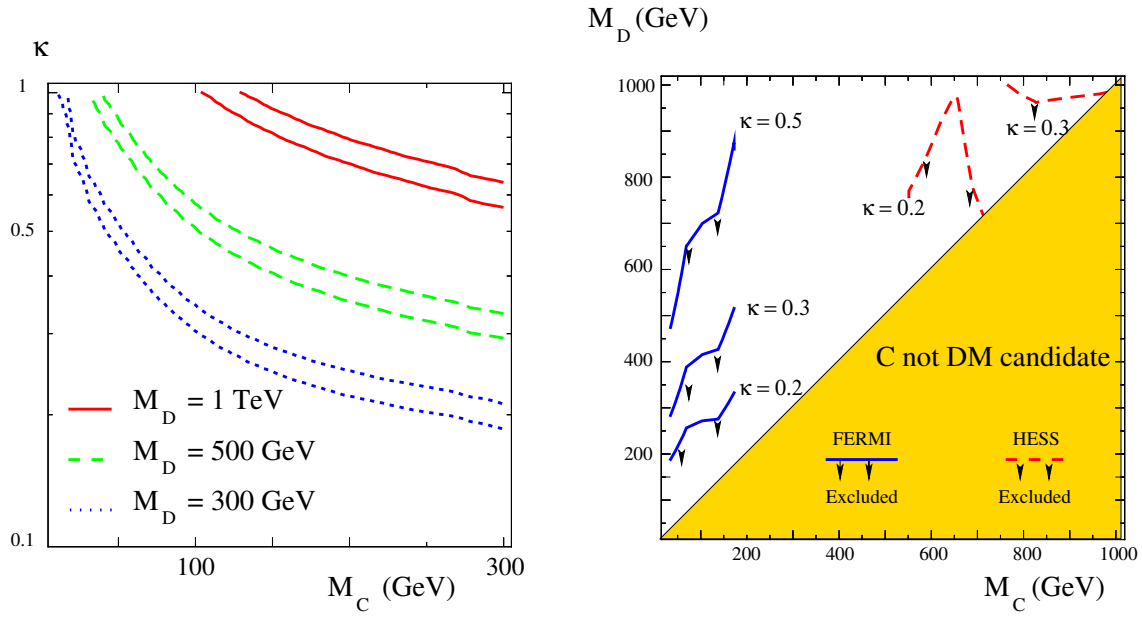

Figure 57: Left: the areas between the lines represent values of κ consistent with the WMAP/PLANCK constraint as a function of M_C for different values of M_D : 300 GeV (dotted blue), 500 GeV (dashed green), and 1 TeV (solid red). Right: constraints from the FERMI and HESS searches for monochromatic gamma–ray lines in the plane (M_C,M_D). (The area below the curve for a given κ is excluded.)

non–relativistic limit are given by[39]

$$\langle\sigma v\rangle(CC\to\gamma\gamma)\simeq\frac{29\kappa^4\cos^4\theta_W}{36\pi M^2}\,, \tag{11.338}$$

$$\langle\sigma v\rangle(CC\to\gamma Z)\simeq\frac{\kappa^4\sin^2\theta_W\,\cos^2\theta_W}{18\pi M^2}\left(1-\frac{M_Z^2}{4M^2}\right)\left[29-\frac{5M_Z^2}{2M^2}+\frac{5M_Z^4}{16M^4}\right]\Theta(2M-M_Z)\,,$$

$$\langle\sigma v\rangle(CC\to ZZ)\simeq\frac{\kappa^4\sin^4\theta_W}{36\pi M^2}\sqrt{1-\frac{M_Z^2}{M^2}}\left(1-\frac{M_Z^2}{2M^2}\right)^{-2}\left[29-34\frac{M_Z^2}{M^2}+14\frac{M_Z^4}{M^4}\right]\Theta(M-M_Z),$$

where Θ is the Heaviside distribution. These processes both regulate dark matter abundance and lead to potentially observable gamma–ray signatures, which we study in detail below.

The distinctive feature of the model is the presence of monochromatic gamma–ray lines in the spectrum of photons coming from the Galactic Center (see e.g. [505]). In particular, for heavy dark matter ($M^2\gg M_Z^2$), the final states $\gamma\gamma$, γZ and ZZ are produced in the proportion $\cos^4\theta_W$, $2\sin^2\theta_W\cos^2\theta_W$ and $\sin^4\theta_W$, respectively. This implies that continuous gamma–ray emission is subdominant and constitutes about a third of the annihilation cross section, while the monochromatic gamma–ray emission dominates.

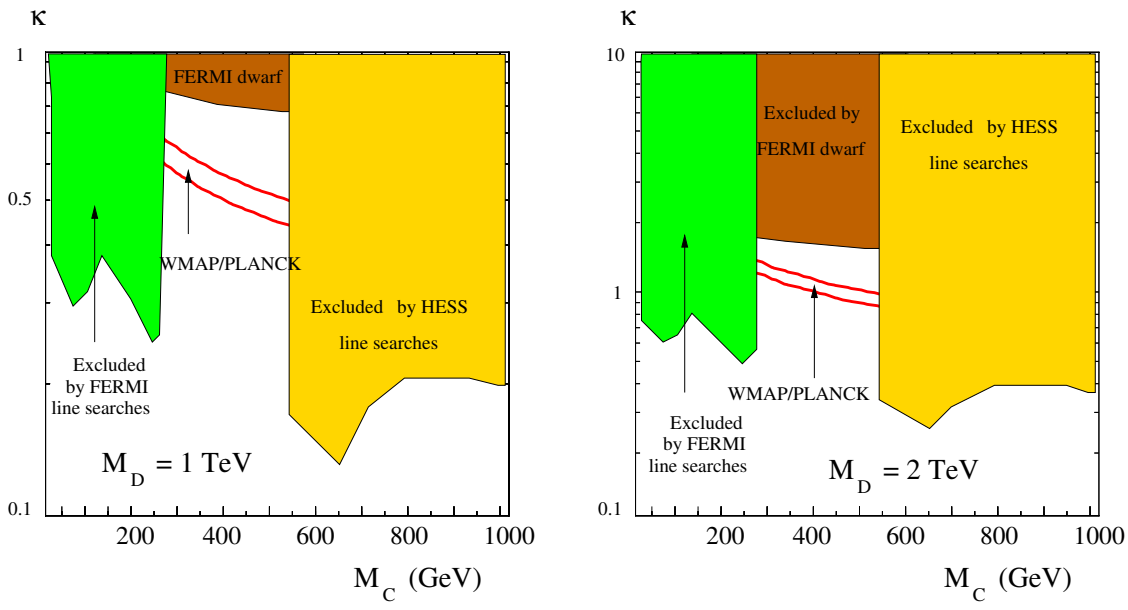

Figure 58: FERMI and HESS constraints on gamma–ray monochromatic lines and continuum in the plane $(M_C,\, \kappa)$ for $M_D = 1$ TeV [left] and 2 TeV [right]. The area between the red lines is consistent with thermal DM relic abundance.

WMAP/PLANCK constraints

Assuming that dark matter is thermally produced, its abundance should be consistent with the WIMP freeze–out paradigm. As explained above, the only DM annihilation channel is $CC \to VV$ with $V = \gamma, Z$. The corresponding cross section must be in a rather narrow window to fit observations. The left panel of Fig. 57 shows parameter space consistent with the WMAP/PLANCK measurements [506, 507] of the DM relic abundance for different values of κ, M_C and M_D. For generality, we allow for vastly different M_C and M_D in our numerical analysis. In the case $M_C^2 \ll M_D^2$, the scaling behaviour $\langle \sigma v \rangle \sim \kappa^4/M^2$ of Eq. (11.338) is replaced by

$$\langle \sigma v \rangle \sim \kappa^4 \, \frac{M_C^2}{M_D^4} \,, \tag{11.339}$$

which stems from the momentum factors at the vertices. Thus, the annihilation cross section grows with the dark matter mass and, in turn, the WMAP/PLANCK–allowed κ's decrease with increasing M_C. The former take on rather natural values of order one for M_D between 100 GeV and several TeV. The main annihilation channel is $CC \to \gamma\gamma$, which for $M_C \simeq M_D \simeq 200$ GeV constitutes about 60% of the total cross section. The channels $CC \to \gamma Z$ and $CC \to ZZ$ contribute 35% and 5%, respectively. The allowed parameter space is subject to the FERMI and HESS constraints on the gamma–ray emission, which we study in the next subsection.

Indirect DM detection constraints

Dark matter can be detected indirectly by observing products of its annihilation in regions with enhanced dark matter density. The main feature of the Chern–Simons–type dark matter is that the dominant annihilation channel leads to a di–photon final state. These photons are monochromatic due to the low DM velocity nowadays ($v_C \simeq 300$ kms^{-1}), which is a "smoking–gun" signature of our model. The proportion of the di–photon final state increases somewhat compared to that in the Early Universe due to the (slight) reduction of the center–of–mass energy of the colliding DM particles. In particular, for $M_C \simeq M_D \simeq 200$ GeV, the channels $CC \to \gamma\gamma$, $CC \to \gamma Z$ and $CC \to ZZ$ constitute approximately 63%, 33%, 4% of the total cross section. One therefore expects an intense monochromatic gamma–ray line at $E_\gamma = M_C$ and a weaker line at $E_\gamma = M_C - M_Z^2/(4M_C)$. Such lines would provide convincing evidence for DM annihilation since astrophysical processes are very unlikely to generate such a photon spectrum.

Recently, FERMI [508–510] and HESS [511] collaborations have released their analyses of the monochromatic line searches around the Galactic Center. Due to its limited energy sensitivity, the FERMI satellite sets a bound on the di–photon annihilation cross section $\langle\sigma v\rangle_{\gamma\gamma}$ in the DM mass range 1 GeV $\lesssim M_C \lesssim$ 300 GeV. HESS, on the other hand, is restrained by its threshold limitations and provides bounds in the DM mass range 500 GeV $\lesssim M_C \lesssim$ 20 TeV.[40] Combining the two analyses allows us to eliminate large portions of parameter space as shown in Fig. 57 [right] and Fig. 58. We note that increasing the mediator mass M_D has the same effect as decreasing the coupling κ. The important conclusion is that FERMI and HESS exclude the possibility of thermal DM relic abundance in the relevant mass ranges. Indeed, their bounds are of order $\langle\sigma v\rangle_{\gamma\gamma} \lesssim 10^{-27}$cm^{3}s^{-1}, whereas thermal dark matter requires $\langle\sigma v\rangle \simeq 10^{-26}$cm^{3}s^{-1}.

To fill the gap between 300 and 500 GeV where the monochromatic signal is not constrained, one can use the diffuse gamma–ray flux. Indeed, even though the FERMI energy cuf–off is at 300 GeV, annihilation of heavy particles produces a continuum photon spectrum which can be detected by FERMI. In our case, the continuum comes from the ZZ and $Z\gamma$ final states with subsequent Z–decay. Since such final states contribute about 40% to the total cross section, the resulting constraint is not very strong. There exist several analyses of bounds on dark matter annihilation in the galactic halo [512], galactic center [513] and dwarf galaxies [514]. The latter provides the strongest FERMI constraint at the moment, while that from HESS is very weak, and we use it to restrict our parameter space (Fig. 58). The conclusion is that thermal dark matter in the 300–500 GeV mass range remains viable and can soon be tested by HESS/FERMI.

On the tentative 135 GeV gamma–ray line

When analyzing FERMI data, several groups found some indications of a monochromatic (135 GeV) gamma–ray line from the galactic center [515–517]. The significance of the "signal" appears to be around 3.3 sigma taking into account the look–elsewhere

[39] For simplicity, we have assumed a single mass scale for the vectors with D being somewhat heavier such that it decays into C and a photon. Further details are unimportant for our purposes.

[40] HESS reports its results for the Einasto DM distribution profile, while FERMI has extended its study to other profiles as well. To be conservative, we use the FERMI limits for the isothermal profile.

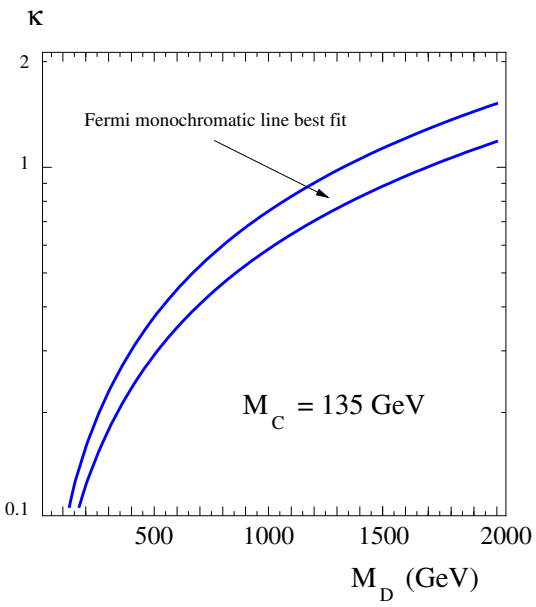

Figure 59: Parameter space (between the lines) satisfying $\langle\sigma v\rangle_{\gamma\gamma} = (1.27 \pm 0.32^{+0.18}_{-0.28}) \times 10^{-27}$ cm^{3}s^{-1} and fitting the tentative FERMI gamma–ray line at 135 GeV.

effect, although this has not been confirmed by the FERMI collaboration. A somewhat optimistic interpretation of the line is that it could be due to DM annihilation at the galactic center (see [518–521] for recent discussions), with the cross section $\langle\sigma v\rangle_{\gamma\gamma} = (1.27 \pm 0.32^{+0.18}_{-0.28}) \times 10^{-27}$ cm^{3}s^{-1} for an Einasto–like profile [515, 516].

In this section, we will be impartial as to whether the line is really present in the data or not. Instead, we use the analysis of [515, 516] as an example to show that the hypercharge portal can easily accommodate a monochromatic signal from the sky. Our result is shown in Fig. 59. Having fixed $M_C = 135$ GeV, we observe that the gamma–ray line can be accommodated for any mediator mass M_D. As explained above, the continuum constraint is inefficient here since it applies to subdominant final states. On the other hand, the required annihilation cross section is too small for DM to be a thermal relic.

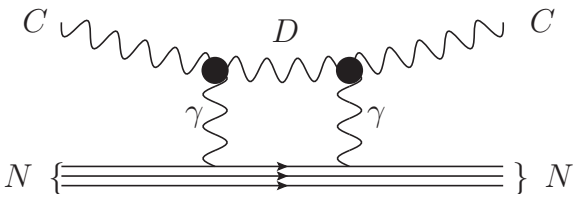

Figure 60: Dark matter scattering off a nucleon.

Direct detection constraints

An important constraint on properties of dark matter is set by direct detection experiments which utilize possible DM interactions with nuclei. In our case, dark matter scattering off nuclei is described by the 1–loop diagram of Fig. 60 together with its cross–version, and similar diagrams with Z–bosons in the loop. Setting for simplicity

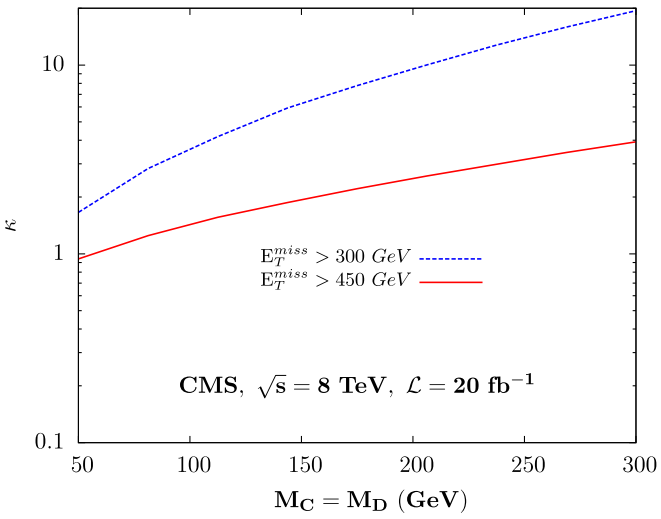

Figure 61: Limit on κ from monojet searches at CMS for $\sqrt{s}$ =8 TeV and 20 fb^{-1} integrated luminosity.

$M_C \simeq M_D = M$, we find that in the non–relativistic limit this process is described by the operators

$$O_{SI} \sim \frac{\alpha\kappa^2}{4\pi}\frac{m_N}{M^2}\,\overline{\Psi}\Psi\; C^\mu C_\mu\ ,$$
$$O_{SD} \sim \frac{\alpha\kappa^2}{4\pi}\frac{1}{M^2}\,\epsilon_{\mu\nu\rho\sigma}\overline{\Psi}\gamma^\mu\gamma^5\Psi\; C^\nu i\partial^\rho C^\sigma\ , \qquad (11.340)$$

where m_N is a hadronic scale of the order of the nucleon mass and Ψ is the nucleon spinor. O_{SI} and O_{SD} are responsible for spin–independent and spin–dependent scattering, respectively. The former is suppressed both by the loop factor and the nucleon mass, while the latter is suppressed by the loop factor only. The resulting cross sections are quite small, $\sigma_{SI} \sim \kappa^4/M^2\ (\alpha/4\pi)^2(m_N/M)^4 \sim 10^{-46}\text{cm}^2$ for $\kappa \sim 1$ and $M \sim 100$ GeV, whereas the spin–dependent cross–section is of the order of $\sigma_{SD} \sim \kappa^4/M^2\ (\alpha/4\pi)^2(m_N/M)^2 \sim 10^{-42}\text{cm}^2$ for the same parameters. The current XENON100 bounds are $\sigma_{SI} \lesssim \mathcal{O}(10^{-45})\text{cm}^2$ [448] and $\sigma_{SD} \lesssim \mathcal{O}(10^{-40})\text{cm}^2$ [522] for the DM mass around 100 GeV (which maximizes the XENON100 sensitivity). We thus conclude that no significant bounds on κ can be obtained from direct detection experiments. Furthermore, since the gamma–ray constraints require $\kappa < \mathcal{O}(10^{-1})$ in this mass range, the prospects for direct DM detection are rather bleak, orders of magnitude beyond the first results of LUX [449] and the projected sensitivity of XENON1T [523].

LHC monojet constraints

The vector states C and D can be produced at the LHC. If their mass difference is not sufficiently large, the photon coming from D–decay would not pass the experimental cut on the photon energy ($p_T > 150$ GeV). In this case, production of C and D would appear as missing energy. The latter can be detected in conjunction with a jet coming from initial–state radiation, which sets a bound on DM production (see also [384]).

In this subsection, we estimate the sensitivity of current monojet searches at the LHC to dark matter production through its coupling to Z and γ. Our constraints are based

on the search for monojets performed by the CMS collaboration which makes use of 19.5 fb^{-1} of data at 8 TeV center of mass energy [524]. The basic selection requirements used by the CMS experiment for monojet events are as follows:

- at least 1 jet with $p_T^j > 110$ GeV and $|\eta^j| < 2.4$;
- at most 2 jets with $p_T^j > 30$ GeV;
- no isolated leptons.

The CMS collaboration quotes the event yields for 7 different cuts on the missing transverse momentum $p_T^{\rm miss}$ between 250 and 550 GeV. These are largely dominated by the SM backgrounds, namely Z+jets, where the Z boson decays invisibly, and W+jets, where the W boson decays leptonically and the charged lepton is not reconstructed. In particular, with 19.5 fb^{-1} data, the CMS collaboration estimates the background to be $18506 \pm 690 (1931 \pm 131)$ events for $p_T^{\rm miss} > 300$ (450) GeV.

A virtual Z–boson or a photon produced with a significant transverse momentum and coupled to invisible states can also lead to the topology that is targeted by the monojet searches. In order to estimate the sensitivity of the CMS monojet search to the "$Z/\gamma \to$ invisible" signal, we generate the $pp \to Z/\gamma$+jets $\to$ CD+jets process at the parton level with `Madgraph 5` [145]. Showering and hadronization is performed using `Pythia 6` [144], while `Delphes 1.9` [147] is employed to simulate the ATLAS and CMS detector response. We have imposed the analysis cuts listed above on the simulated events to find the signal efficiency. As a cross-check, we have passed $(Z \to \nu\nu)$ + jets background events through the same simulation chain, obtaining efficiencies consistent with the data–driven estimates of that background provided by CMS.

We use the total event cross section to put constraints on the dark matter coupling to the Z/γ gauge bosons. We compute the observed 95%CL exclusion limits on the dark matter–SM coupling κ for given masses M_C, M_D by requiring (see, e.g. [525])

$$\chi^2 = \frac{(N_{obs} - N_{SM} - N_{DM}(M_C, M_D, \kappa))^2}{N_{SM} + N_{DM}(M_C, M_D, \kappa) + \sigma_{SM}^2} = 3.84 \, . \tag{11.341}$$

Here N_{obs} is the number of observed events, N_{SM} the number of expected events, N_{DM} the number of expected signal events and σ_{SM} being the uncertainty in the predicted number of backgrounds events. The expected strongest bounds should come from the analysis with the hardest $p_T^{\rm miss} > 550$ GeV cuts, but the strongest observed bound come from the $p_T^{\rm miss} > 450$ GeV cuts due to an important downward fluctuations in the data. Fig. 61 shows the resulting limits on κ for two different sets of cuts, $p_T^{\rm miss} > 300$ GeV and $p_T^{\rm miss} > 450$ GeV, with the latter providing the best limit. We see that the current monojet bounds are relatively weak, $\kappa < \mathcal{O}(1)$ for $M_C \sim M_D \sim 100$ GeV, and not competetive with the constraints from the monochromatic gamma–ray searches.

LHC monophoton constraints

Another characteristic collider signature of vector DM production is monophoton emission plus missing energy. In this case, C and D are produced on–shell through the photon or Z, while their mass difference must be sufficiently large such that D decays

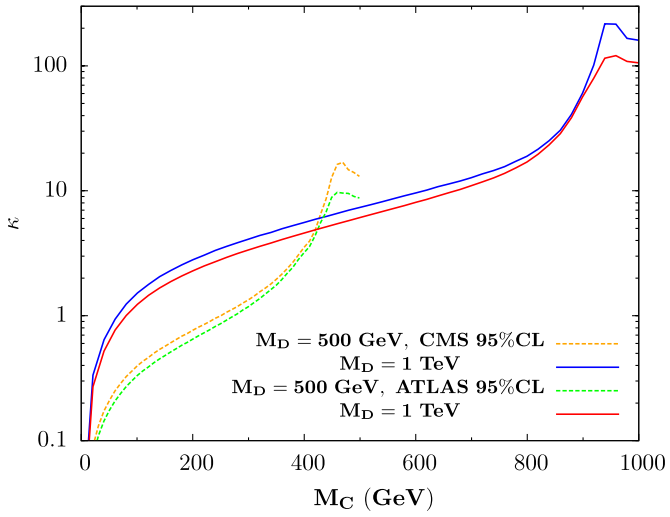

Figure 62: Limits on κ from monophoton searches at CMS (5 fb^{-1} at $\sqrt{s}$ =7 TeV) and ATLAS (4.6 fb^{-1} at $\sqrt{s}$ =7 TeV).

inside the detector and the photon energy is above the threshold. We rely on the search for a single photon performed by the CMS collaboration which makes use of 5 fb^{-1} of data at 7 TeV center of mass energy [526] and the one performed by the ATLAS collaboration which makes use of 4.6 fb^{-1} of data at 7 TeV center of mass energy [527]. The basic selection requirements used by the CMS experiment for monophoton events are as follows:

- 1 photon with $p_T^\gamma > 145$ GeV and $|\eta^\gamma| < 1.44$;
- $p_T^{\rm miss} > 130$ GeV;
- no jet with $p_T^j > 20$ GeV that is $\Delta R > 0.04$ away from the photon candidate;
- no jet with $p_T^j > 40$ GeV and $|\eta^j| < 3.0$ within $\Delta R < 0.5$ of the axis of the photon;

Analogous requirements used by ATLAS are:

- 1 photon with $p_T^\gamma > 150$ GeV and $|\eta^\gamma| < 2.37$;
- $p_T^{\rm miss} > 150$ GeV;
- no more than 1 jet with $p_T^j > 30$ GeV and $|\eta^j| < 4.5$;
- $\Delta\Phi(\gamma, p_T^\gamma) > 0.4$, $\Delta R(\gamma, jet) > 0.4$ and $\Delta\Phi(jet, p_T^{\rm miss}) > 0.4$;

The event yields obtained by ATLAS and CMS are largely dominated by the SM backgrounds, namely Z+γ, where the Z boson decays invisibly, and W+γ, where the W boson decays leptonically and the charged lepton is not reconstructed. Since ATLAS accepts events with one jet, W/Z+jets is also an important background for the ATLAS analysis. With 4.6 fb^{-1} data, the ATLAS collaboration estimates the background to be $137 \pm 18(stat.) \pm 9(syst.)$ events and observed 116 events. The analogous numbers for CMS with 5 fb^{-1} are 75.1 ± 9.4 and 73 events, respectively.

In order to estimate the sensitivity of the ATLAS and CMS single photon search to DM production, we have generated the $pp \to Z/\gamma \to CD \to CC + \gamma$ process. We have used the program `Madgraph 5` [145] for the channels at the parton level. Showering and hadronisation was performed using `Pythia 6` [144] and `Delphes 1.9` [147] was employed to simulate the CMS detector response. We have imposed the analysis cuts listed above on the simulated events to find the signal efficiency and used the total event cross–section to constrain the DM coupling to γ and Z. The observed 95%CL exclusion limits on κ for given M_C, M_D are obtained by requiring

$$\chi^2 = \frac{(N_{obs} - N_{SM} - N_{DM}(M_C, M_D, \kappa))^2}{N_{SM} + N_{DM}(M_C, M_D, \kappa) + \sigma_{SM}^2} = 3.84 \,. \tag{11.342}$$

The resulting limits on κ for two choices of $M_D = 500$ GeV and $M_D = 1$ TeV are shown in Fig. 62. In the latter case, the bounds are relatively weak, $\kappa < 1$ for $M_C > 100$ GeV, and do not constrain the parameter space consistent with WMAP/PLANCK, FERMI and HESS (Fig. 58). For $M_D = 500$ GeV, the monophoton constraint is more important, although it does not yet probe interesting regions of parameter space (Fig. 57). In particular, it does not rule out the DM interpretation of the 135 GeV gamma–ray line (Fig. 59). Indeed, for $M_C = 135$ GeV, the LHC bound is about $\kappa < 0.5$, whereas the gamma–ray line requires $\kappa \sim 0.3$.

We thus find that the monophoton constraint is not yet competitive with the astrophysical/cosmological ones. We have also checked that no useful constraint is imposed by searches for mono–Z emission ($D \to Z + C$), mostly due to its smaller production cross section.

Summary of constraints

For the dark matter mass above 100 GeV, the most relevant laboratory constraints are imposed by the LHC searches for monojets and monophotons. The former are applicable for quasi–degenerate C and D, while the latter apply if there is a substantial mass difference between them. The monophoton constraint is rather tight for light DM, e.g. $\kappa <$ few$\times 10^{-1}$ for $M_C \sim 100$ GeV and $M_D \sim 500$ GeV. This is stronger than the unitarity bound (11.318), which only applies for $\Lambda \gg M_{C,D}$. On the other hand, the monojet constraint is rather weak, $\kappa \lesssim 1$.

The most important bounds on the model are imposed by astrophysical observations, in particular, by FERMI and HESS searches for monochromatic gamma–ray lines. These exclude substantial regions of parameter space even for relatively heavy dark matter, $M_{C,D} \sim 1$ TeV. Analogous bounds from continuum gamma–ray emission are significantly weaker as the latter is subleading in our framework (unlike in other models [528]), while direct DM detection is inefficient due to loop suppression. These constraints still allow for thermal DM in the mass range 200–600 GeV (Fig. 58).

Finally, the model allows for an "optimistic" interpretation of the tentative 135 GeV gamma–ray line in the FERMI data. The line can be due to (non–thermal) dark matter annihilation with $M_C \simeq 135$ GeV for a range of the mediator mass M_D. This interpretation is consistent with the constraints coming from the continuum gamma–ray emission, direct DM detection and the LHC searches.

11.5 Conclusion on the hypercharge portal

We have considered the possibility that the hidden sector contains more than one massive vector fields. In this case, an additional *dim*–4 interaction structure of the Chern–Simons type becomes possible. It couples the hypercharge field strength to the antisymmetric combination of the massive vectors. If the latter are long–lived, the phenomenological signatures of such a coupling include missing energy in decays of various mesons and Z, as well as monojet and monophoton production at the LHC.

The hidden sector may possess a Z_2 symmetry, which would make the lighter vector field stable and a good dark matter candidate. The characteristic signature of this scenario is monochromatic gamma–ray emission from the Galactic Center, while the corresponding continuum contribution is suppressed. We find that this possibility is consistent with other constraints, including those from the LHC and direct DM detection. Large portions of the allowed parameter space can be probed both by indirect dark matter detection and the LHC monophoton searches.

Until now we have only discussed dark matter candidates which are in thermal equilibrium with the thermal bath. Which is a commonly done hypothesis. However, we now study in detail the scenario where the dark matter particle is not in kinetic equilibrium with the thermal bath i.e the dark matter is non thermal. We have introduced a new mechanism for the production of dark matter in the universe which does not rely on thermal equilibrium. Dark matter is populated from the thermal bath subsequent to inflationary reheating via a massive mediator whose mass is above the reheating scale, T_{RH}. To this end, we consider models with an extra U(1) gauge symmetry broken at some intermediate scale ($M_{int} \simeq 10^{10-12}$GeV). We show that not only does the model allow for gauge coupling unification (at a higher scale associated with grand unification) but can naturally provide a dark matter candidate which is a Standard Model singlet but charged under the extra U(1). The intermediate scale gauge boson(s) which are predicted in several E6/SO(10) constructions can be a natural mediator between dark matter and the thermal bath. We show that the dark matter abundance, while never having achieved thermal equilibrium, is fixed shortly after the reheating epoch by the relation T_{RH}^3/M_{int}^4. As a consequence, we show that the unification of gauge couplings which determines M_{int} also fixes the reheating temperature, which can be as high as $T_{RH} \simeq 10^{11}$GeV.

12 Non thermal dark matter and grand unification theory

12.1 Motivations

The Standard Model of particle physics is more than ever motivated by the recent discovery of the Higgs boson at both the ATLAS [457] and CMS [458] detectors. The SM, however, contains many free parameters, and the gauge couplings do not unify. Among the most elegant approaches to understand some of these parameters is the idea of a grand unified theory (GUT) in which the three gauge couplings $\alpha_{1,2,3}$ originate from a single gauge coupling associated to a grand unified gauge group [290]. This idea is supported by the fact that quantum numbers of quarks and leptons in the SM nicely fill representations of a GUT symmetry, e.g., the **10** and $\bar{\mathbf{5}}$ of $SU(5)$ or **16** of $SO(10)$.

Another issue concerning the SM is the lack of a candidate to account for Dark Matter (DM) which consists of 22% of the energy density of our universe. Stable Weakly Interacting Massive Particles are among the most popular candidates for DM. In most models, such as popular supersymmetric extensions of the SM [529,530], the annihilation of WIMPs in thermal equilibrium in the early universe determined the relic abundance of DM.

In this section, we will show that GUT gauge groups such as E_6 or SO(10) which contain additional U(1) gauge subgroups and are broken at an intermediate scale, can easily lead to gauge coupling unification [531] and may contain a new dark matter candidate which is charged under the extra U(1). However, unlike the standard equilibrium annihilation process, or complimentary process of freeze-in [434, 532–534], we propose an alternative mechanism for producing dark matter through interactions which are mediated by the heavy gauge bosons associated with the extra U(1). While being produced from the thermal bath, these dark matter particles never reach equilibrium. We will refer to dark matter produced with this mechanism as Non-Equilibrium Thermal Dark Matter or NETDM. The final relic abundance of NETDM is obtained shortly after the inflationary reheating epoch. This mechanism is fundamentally different from other non-thermal DM production mechanisms in the literature (to our knowledge). Assuming that none of the dark matter particles are directly produced by the decays of the inflaton during reheating, we compute the production of dark matter and relate the inflationary reheat temperature to the choice of the gauge group and the intermediate scale needed for gauge coupling unification. As an added benefit, the model naturally possesses the capability of producing a baryon asymmetry through leptogenesis, although that lies beyond of the scope of this work.

This section is organized as follows. After a summary of the unified models under consideration, we show how the presence of an intermediate scale allows for the possibility of producing a dark matter candidate which respects the WMAP constraint [535] and apply it to an explicit scenario. We then discuss our main results.

12.2 Unification in SO(10) models

The prototype of grand unification is based on the SU(5) gauge group. In an extension of SU(5) one can introduce SU(5) singlets as potential dark matter candidates. The simplest extension in which singlets are automatically incorporated is that of SO(10). There are, however, many ways to break SO(10) down to $SU(3) \times SU(2) \times U(1)$. This may happen in multiple stages, but here we are mainly concerned with the breaking of an additional U(1) (or SU(2)) factor at an intermediate scale M_{int}. Here, we will not go into the details of the breaking, but take some specific, well-known examples when needed. Assuming gauge coupling unification, the GUT mass scale, M_{GUT}, and the intermediate scale M_{int} can be predicted from the low–energy coupling constants with the use of the renormalisation group equation,

$$\mu \frac{d\alpha_i}{d\mu} = -b_i \alpha_i^2 \ . \tag{12.343}$$

The evolution of the three running coupling constants α_1, α_2 and α_3 from M_Z to the intermediate scale M_{int} is obtained from Eq. (12.343) using the β–functions of the Standard Model: $b_{1,2,3} = (-41/10, 19/6, 7)/2\pi$. We note that the gauge coupling, g_D, associated with $U'(1)$ is related at the GUT scale to g_1 of $U(1)_Y$ by $g_D = \sqrt{\frac{5}{3}} g_1$ and $\alpha_i = g_i^2/4\pi$. Between M_{int} and M_{GUT} (both to be determined) the running coupling constants are again obtained from Eq. (12.343), now using β–functions associated with the intermediate scale gauge group, which we will label $\tilde{b}_i$. The matching condition between the two different runnings at M_{int} can be written:

$$(\alpha_i^0)^{-1} + b_i(t_{int} - t_Z) = \alpha^{-1} + \tilde{b}_i(t_{int} - t_{GUT}) \tag{12.344}$$

with $t_{int} = \ln M_{int}$, $t_Z = \ln M_Z$, $t_{GUT} = \ln M_{GUT}$, $\alpha_i^0 = \alpha_i(M_Z)$ which is measured, and $\alpha = \alpha_i(M_{GUT})$ is the unified coupling constant at the GUT scale. This gives us a system of 3 equations, for 3 unknown parameters: α, t_{int}, t_{GUT}. Solving the Eq. (12.344), we obtain

$$t_{int} = \frac{1}{b_{32} - b_{21}} \left[\frac{(\alpha_3^0)^{-1} - (\alpha_2^0)^{-1}}{\tilde{b}_2 - \tilde{b}_3} - \frac{(\alpha_2^0)^{-1} - (\alpha_1^0)^{-1}}{\tilde{b}_1 - \tilde{b}_2} + (b_{32} - b_{21}) t_Z \right] , \tag{12.345}$$

where $b_{ij} \equiv (b_i - b_j)/(\tilde{b}_i - \tilde{b}_j)$.

To be concrete, we will consider a specific example to derive numerical results for the case of the breaking of $SO(10)$: $SO(10) \to SU(4) \times SU(2)_L \times U(1)_R \to_{M_{int}} SU(3)_C \times SU(2)_L \times U(1)_Y \to_{M_{EW}} SU(3)_C \times U(1)_{em}$. When the intermediate symmetry is broken by a **16** of Higgs bosons, the $\tilde{b}_i$ functions are given by $\tilde{b}_{1,2,3} = (5/2, 19/6, 63/6)/2\pi$ [531], where the computation was done at 1-loop level. For this case, we obtain $M_{int} = 7.8 \times 10^{12}$ GeV and $M_{GUT} = 1.3 \times 10^{15}$ GeV using $(\alpha_{1,2,3}^0)^{-1} \simeq (59.47, 29.81, 8.45)$. The evolution of the gauge couplings for this example is shown in Fig. 63.

12.3 Heavy Z' and dark matter

It has been shown in [536] and [537] that a stable dark matter candidate may arise in SO(10) models from an unbroken Z_2^{B-L} symmetry. If the dark matter is a fermion

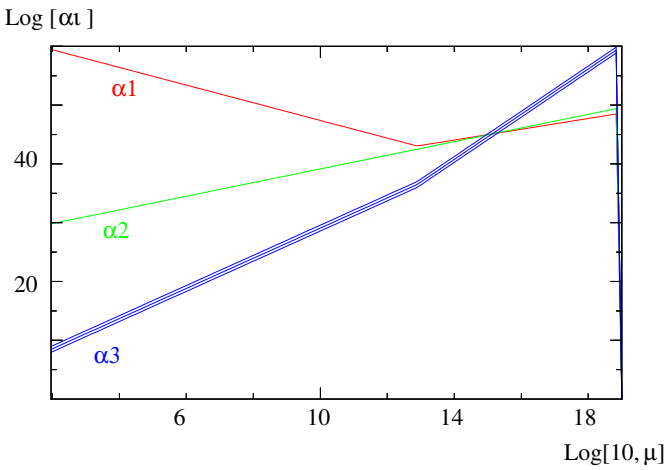

Figure 63: Example of the running of the SM gauge couplings for $SO(10) \to SU(4) \times SU(2)_L \times U(1)_R$.

(scalar) it should belong to a $3(B-L)$ even (odd) representation of SO(10). For example, the **126** or **144** contains a stable component χ which is neutral under the SM, yet charged under the extra U(1). As we have seen, to explain the unification of the gauge couplings in SO(10) one needs an intermediate scale M_{int} of order 10^{10} GeV. The dark matter candidate, χ, can be produced in the early Universe through s-channel Z' exchange: $SM\ SM \to Z' \to \chi\ \chi$. Since $M_{Z'} = \frac{5}{\sqrt{3}} g_D\ M_{int}$, the exchanged particle is so heavy (above the reheating scale, as we show below) that the DM production rate is very slow, and we can neglect the self annihilation process in the Boltzmann equation. Thus while the dark matter is produced from the thermal bath, we have a non–equilibrium production mechanism for dark matter, hence NETDM.

The evolution of the yield of χ, $Y_\chi = n_\chi/\mathbf{s}$ follows

$$\frac{dY_\chi}{dx} = \sqrt{\frac{\pi}{45}} \frac{g_s}{\sqrt{g_\rho}} m_\chi M_P \frac{\langle \sigma v \rangle}{x^2} Y_{eq}^2 \tag{12.346}$$

where n_χ is the number density of χ and $\mathbf{s}$ the entropy of the universe, g_ρ, g_s are the effective degrees of freedom for energy density and entropy, respectively; $x = m_\chi/T$, m_χ being the dark matter mass, M_P the Planck mass and

$$\langle \sigma v \rangle n_{eq}^2 \approx \frac{\kappa^2\ T}{2048\pi^6} \int_{4m_\chi^2}^{\infty} ds d\Omega \sqrt{s - 4m_\chi^2} |\mathcal{M}|^2 K_1(\sqrt{s}/T)\ . \tag{12.347}$$

Here n_{eq} is the equilibrium number density of the initial state (SM) particles; and K_1 is the first order modified Bessel function and κ the effective degrees of freedom of incoming particles.

Since the production of DM occurs mainly at $T_{RH} \gg m_\chi$, we can neglect m_χ in estimating the amplitude for production. In this case, assuming that both χ and the initial state, f, are fermions, we obtain

$$|\mathcal{M}_\chi|^2 \approx \frac{g_D^4 q_\chi^2 q_f^2 N_c^f}{(s - M_{Z'}^2)^2} \left[s^2 (1 + \cos^2\theta) \right] \tag{12.348}$$

where θ is the angle between the two outgoing DM particles, N_c^f is number of colors of the particle f, and q_i is the charge of the particle i under $U'(1)$ with a gauge coupling g_D. Here, q is an effective coupling which will ultimately depend on the specific intermediate gauge group chosen. With the approximations $m_\chi, m_f \ll \sqrt{s}$ and $M_{Z'} \gg T_{RH}$, and after integration over θ and sum over all incoming SM fermions in the thermal bath, we obtain

$$\frac{dY_\chi}{dx} = \sum_f \frac{g_D^4 q_\chi^2 q_f^2 N_c^f}{x^4} \left(\frac{45}{\pi}\right)^{3/2} \frac{1}{g_s\sqrt{g_\rho}} \frac{m_\chi^3 M_P}{M_{Z'}^4} \frac{\kappa_f^2}{2\pi^7} \tag{12.349}$$

Solving Eq. (12.349) between the reheating temperature and a temperature T gives

$$Y_\chi(T) = \sum_f q_\chi^2 q_f^2 N_c^f \left(\frac{45}{g_s\pi}\right)^{3/2} \frac{M_P}{M_{int}^4} \frac{3\ \kappa_f^2}{1250\pi^7} \left[T_{RH}^3 - T^3\right] \tag{12.350}$$

where we replaced the mass of the Z' by $M_{Z'} = \frac{5}{\sqrt{3}} g_D M_{int}$ and made the approximation $g_\rho = g_s$. We note that the effect of Z' decay on the abundance of χ is completely negligible due to its Boltzmann suppression in the Universe: the Z' is largely decoupled from the thermal bath already at the time of reheating.

We note several interesting features from Eq. (12.350). First of all, the number density of the dark matter does not depend at all on the strength of the $U'(1)$ coupling g_D but rather on the intermediate scale (that is determined by requiring gauge coupling unification as we demonstrated in the previous section). Second, the production of dark matter is mainly achieved at reheating. Thirdly, once the relic abundance is obtained, the number density per comoving frame (Y) is fixed, never having reached thermal equilibrium with the bath. And finally, upon applying the WMAP determination for the DM abundance, $\Omega h^2 = 0.1157$ [535], we obtain a tight constraint on T_{RH} once the pattern of $SO(10)$ breaking is known (and thus M_{int} fixed).

Thus, given a scheme of $SO(10)$ breaking we can determine the reheating temperature very precisely from the relic abundance constraint in the Universe. From

$$Y_0 = \frac{\Omega}{m_\chi} \frac{\rho_0^{crit}}{\mathbf{s}_0} = \left(\frac{\Omega h^2}{0.1}\right) \frac{13.5}{16\pi^3} \frac{H_0^2 M_P^2}{g_s^0 T_0^3 m_\chi} \tag{12.351}$$

where H is the Hubble parameter and the index "0" corresponds to present-day values. Combining Eq. (12.350) and Eq. (12.351) we find

$$T_{RH}^3 = \frac{5625\ \pi^4}{16 q_\chi^2 \sum_f \kappa_f^2 q_f^2 N_c^f} \left(\frac{\Omega h^2}{0.1}\right) \left(\frac{g_s \pi}{45}\right)^{3/2} \frac{M_P H_0^2}{T_0^3 m_\chi g_s^0} M_{int}^4 \tag{12.352}$$

or

$$T_{RH} \simeq 2 \times 10^8 \text{GeV} \left(\frac{\Omega h^2}{0.1}\right)^{1/3} \left(\frac{100\text{GeV}}{m_\chi}\right)^{1/3} \left(\frac{M_{int}}{10^{12}\text{GeV}}\right)^{4/3} \tag{12.353}$$

where we took for illustration $q_\chi^2 \sum_f \kappa_f^2 q_f^2 N_c^f = 1$. We show in Fig.(64) the evolution of T_{RH} as function of M_{int} for different values of the dark matter mass m_χ. We can thus determine the reheating temperature predicted by different symmetry breaking patterns[41]. We summarize them in Table 18, where the values of T_{RH} are given for $m_\chi = 100$GeV.

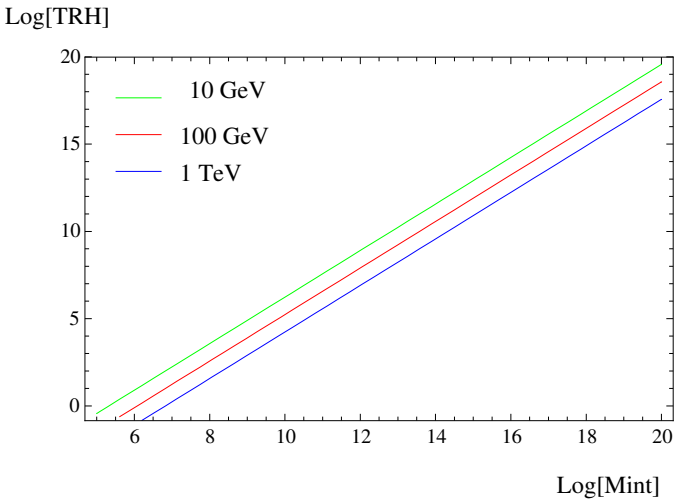

Figure 64: Reheating temperature as function of the SO(10) breaking scale for different mass of dark matter : 10, 100 and 1000 GeV

	$SO(10) \to \mathcal{G}\times$ [Higgs]	M_{int}(GeV)	T_{RH}(GeV)
A	$4 \times 2_L \times 1_R$ [**16**]	$10^{12.9}$	3×10^9
A	$4 \times 2_L \times 1_R$ [**126**]	$10^{11.8}$	1×10^8
B	$4 \times 2_L \times 2_R$ [**16**]	$10^{14.4}$	3×10^{11}
B	$4 \times 2_L \times 2_R$ [**126**]	$10^{13.8}$	5×10^{10}
C	$3_C \times 2_L \times 2_R \times 1_{B-L}$ [**16**]	$10^{10.6}$	3×10^6
C	$3_C \times 2_L \times 2_R \times 1_{B-L}$ [**126**]	$10^{8.6}$	6×10^3

Table 18: Possible breaking schemes of SO(10).

Finally, we must specify the identity of the NETDM candidate in the context described above. The dark matter can be in the **126** or **144** representations of SO(10). There are several mechanisms to render the DM mass light [537], one of which is through a fine-tuning of the SO(10) couplings contributing with different Clebsh-Gordan coefficients (see for example, [538] and [539]) to the masses of the various **126** components. For example, for the group $\mathcal{G}_A$:

$$\overline{\mathbf{126}}(M + y_{45}\mathbf{45}_H + y_{210}\mathbf{210}_H)\mathbf{126} \tag{12.354}$$

where $M \sim M_{GUT}$, and a $\mathcal{G}_A$ singlet in a linear combination of $\mathbf{210}_H$ and $\mathbf{45}_H$ has a vev at the GUT scale. m_χ is then given by a linear combination of M and the vev and can be tuned to small values, while all other particles inside the **126** live close to M_{GUT}.

12.4 Discussion

Unfortunately, the chance of detection (direct or indirect) of NETDM with a massive mediator Z' is nearly hopeless. Indeed, the diagram for the direct detection process,

[41] We note that the value obtained for the intermediate scale in different $SO(10)$ breaking schemes is not modified by the presence of a dark matter particle which is not charged under the SM gauge group.

measuring the elastic scattering off a nucleus, proceeds through the $t-$channel exchange of the Z' boson, and is proportional to $1/M_{Z'}^4$ yielding a negligible cross-section. In addition, due to the present low velocity of dark matter in our galaxy ($\simeq$ 200 km/s), the indirect detection prospects from $s-$channel Z' annihilation $\chi\chi \to Z' \to ff$ proportional to $s^2/M_{Z'}^4$ is also negligible.

As we have seen in Eq. (12.350), the production of dark matter occurs in the very early Universe at the epoch of reheating. A similar mechanism (though fundamentally completely different) where a dark matter candidate is produced close to the reheating time is the case of the gravitino [529, 530, 540, 541]. Indeed, in both cases equilibrium is never reached and the relic abundance is produced from the thermal background to attain the decoupling value Γ/H, with H the Hubble constant and $\Gamma = \langle\sigma v\rangle n_f$ the production rate. However, in the case of SO(10), the cross section decreases with the temperature like $\langle\sigma v\rangle_{Z'} \propto T^2/M_{Z'}^4$, whereas in the case of the gravitino the cross section is constant $\langle\sigma v\rangle_{3/2} \propto 1/M_P^2$ implying $Y(T) \propto T_{RH}$.

Finally, we note that cases B and C (in Table I) predict reheating temperatures which are larger (B) or smaller (C) than the case under consideration. Case A would also be compatible with successful thermal leptogenesis with a zero initial state abundance of right–handed neutrino [542–549]. However in the cases B and C, the persistence of the $SU(2)_R$ symmetry would imply that the cancelation in Eq. (12.354) would leave behind a light $SU(2)_R$ triplet (for DM inside a **126**) or doublet (for DM inside a **144**). These would affect somewhat the beta functions for the RGE's but more importantly leave behind a test of the model. In the triplet (doublet) case, we would expect three (at least two) nearly degenerate states: one with with charge 0, being the DM candidate, and also states with electric charge ±1 and ±2 (or ±1 in the doublet case).

In conclusion, we have shown that it is possible to produce dark matter through non–equilibrium thermal processes in the context of $SO(10)$ models which respect the WMAP constraints. Insisting on gauge coupling unification, we have demonstrated that there exists a tight link between the reheating temperature and the scheme of the $SO(10)$ breaking to the SM gauge group. Interestingly, the numerical values we obtained are quite high and very compatible with inflationary and leptogenesis-like models.

After having discussed the virtues of the NETDM model regarding mostly SM gauge couplings unification, we now study the genesis of dark matter in the primordial universe for representative classes of Z'-portals models (NETDM being included) [550].

13 Thermal and non-thermal production of dark matter via Z′-portal

13.1 Introduction

Even if PLANCK [397] confirmed recently the presence of dark matter in the universe with an unprecedented precision, its nature and its genesis are still unknown. The most popular scenario for the dark matter evolution is based on the mechanism of "thermal freeze-out" [551, 552]. In this scenario dark matter particles χ are initially in thermal equilibrium with respect to the thermal bath. When the temperature of the hot plasma T in the early universe dropped below the dark matter mass, its population decreased exponentially until the annihilation rate into lighter species Γ_χ could not overcome the expansion rate of the universe driven by the Hubble parameter $H(T)$. This defines the freeze-out temperature: $H(T_{\rm FO}) \gtrsim \Gamma_\chi$. The comoving number density of the dark matter particles[42] and thus its relic abundance are then fixed to the value that PLANCK [397] and WMAP [444,445] observe today, $\Omega h^2 = 0.1199 \pm 0.0027$ at 68% CL. In this scenario the stronger the interaction between dark matter and the rest of the thermal bath is, the more dark matter pairs annihilate, ending-up with smaller relic densities. The detection prospects for frozen-out WIMPs are remarkable, since they involve cross-sections which can be probed nowadays with different experimental strategies, as production at colliders [525, 553–558], Direct Detection and Indirect Detection experiments [559–566, 566, 567].

This popular freeze-out scenario is based on the assumption that the dark matter is initially produced at a democratic rate with the Standard Model particles. The so-called "WIMP miracle" can then be obtained if dark matter candidate has a mass of the electroweak scale and the dark sector and the Standard Model sector interact through electroweak strength coupling. Alternatively one can relax the hypothesis of democratic production rate and suppose that the initial abundance of dark matter has been negligibly small whether by hierarchical or gravitational coupling to the inflaton or others mechanisms. This is the case for gravitino dark matter [568], Feebly Interacting Massive Particle Dark Matter (FIMP) in generic scenarios [434, 532, 534], scalar portals [533, 569], decaying dark matter [570] or NETDM (Non Equilibrium Thermal Dark Matter) [571].

Alternatively to the freeze–out, in the freeze-in (FI) mechanism the dark matter gets populated through interactions and decays from particles of the thermal bath with such an extremely weak rate (that is why called FIMP) that it never reaches thermal equilibrium with the plasma. In this case, the dark matter population n_χ grows very slowly until the temperature of the universe drops below the mass m_χ. The production mechanism is then frozen by the expansion rate of the universe $H(T_{\rm FI})$. Contrary to the FO, in the FI scenario the stronger the interaction is, the larger the relic density results at the end, provided that the process never thermalises with the thermal bath. Due to the smallness of its coupling, the dark matter becomes very difficult to detect in colliders or direct detection experiments. However, one of the predictions of this scenario is that particles possibly decaying to dark matter need to have a long lifetime [532], so this peculiarity can be probed in principle in the LHC for example through the analysis of

[42] Proportional to the yield $Y_\chi = n_\chi/\mathbf{s}$, n_χ being the physical density of dark matter particles and $\mathbf{s}$ the entropy density.

displaced vertices.

In the previous section, we have analysed [571] a scenario where the dark matter was also produced out-of-equilibrium, but differing from the orthodox FI mechanism in an essential way. In this new NETDM proposal the DM-SM couplings can be large (as for FO case), whereas the particle mediating the interaction is very heavy, which caused the evolution of dark matter number density to be dominated mostly by very high temperatures, just after the reheating epoch. This situation is opposite to the FI scenario where the couplings are feeble, typically $\mathcal{O}(10^{-11})$, and the portal is either massless or at least has a mass smaller than dark matter mass m_χ, causing the process to be dominated by low temperatures ($T \lesssim m_\chi$) instead.

In this section we study the dark matter candidate χ populated by vector-like portals, whose masses lie in two different regimes: 1) A very heavy mediator, through the study of effective interactions of dark matter with the SM[43], and 2) An intermediate mediator, through the analysis of a kinetic-mixing model which contains a Z' acting as the portal. This study complements the case of massless vector-like mediators, studied in [434], showing distinct features concerning the evolution of the dark-sector independent thermalisation. On the other hand, we show the characteristics of the NETDM mechanism for a general vector-like interaction.

Let us give a brief overview of non-thermalised production of dark matter particles.

13.2 Boltzmann equation and production of dark matter out of equilibrium

If we consider that in the early stage of the universe the abundance of dark matter has been negligibly small whether by inflation or some other mechanism, the solution of the Boltzmann equation can be solved numerically in effective cases like in [532] or in the case of the exchange of a massless hidden photon as did the authors of [434]. Such an alternative to the classical freeze out thermal scenario was in fact proposed earlier in [533] in the framework of the Higgs-portal model [569] and denominated "freeze in" [532]. If one considers a massive field Z' coupling to the dark matter, the dominant processes populating the dark matter particle χ are given by the decay $Z' \to \bar{\chi}\chi$ and the annihilation $\overline{SM}\ SM \to \bar{\chi}\chi$ involving the massive particle Z' as a mediator, or "portal" between the visible (SM) sector and the invisible (dark matter) sector. Our study will be as generic as possible by taking into account both processes at the same time, although we will show that for very large mediator masses $m_{Z'}$, or if the Z' is not part of the thermal bath, the decay process is highly suppressed, and the annihilation clearly dominates[44]. Under the Maxwell–Boltzmann approximation[45] one can obtain an analytical solution of the DM yield adding the annihilation and decay processes:

[43]Note that in this analysis, the nature of the mediator (vector or scalar) is not fundamental and our result can apply for the exchange of heavy scalars or heavy Higgses present in unified models also.

[44]Note that in [532] the 2→2 annihilation process is considered subdominant with respect to the 1→2 decay process. However in the scenarios we will study, the annihilation dominates.

[45]We have checked that the Maxwell-Boltzmann approximation induces a 10% error in the solution which justifies it to understand the general result. See [572] for an explicit cross-check of this approximation.

$$
\begin{aligned}
Y_\chi &\approx \left[\left(\frac{45}{\pi}\right)^{3/2}\frac{M_{\rm p}}{4\pi^2}\right]\int_{T_0}^{T_{\rm RH}} dT \int_{4m_\chi^2}^{\infty} ds \frac{1}{\sqrt{g_*}g_*^s}\frac{1}{T^5} \\
&\times K_1\left(\frac{\sqrt{s}}{T}\right)\frac{1}{2048\pi^6}\sqrt{s-4m_\chi^2}|\tilde{\mathcal{M}}_{2\to 2}|^2 \\
&+ \left[\left(\frac{45}{\pi}\right)^{3/2}\frac{M_{\rm p}}{4\pi^2}\right]\int_{T_0}^{T_{\rm RH}} dT \frac{1}{\sqrt{g_*}g_*^s}\frac{1}{T^5} \\
&\times K_1\left(\frac{m_{Z'}}{T}\right)\frac{1}{128\pi^4}\sqrt{m_{Z'}^2-4m_\chi^2}|\tilde{\mathcal{M}}_{1\to 2}|^2 \ ,
\end{aligned}
\tag{13.355}
$$

where $M_{\rm p}$ is the Planck mass, $T_0 = 2.7$ K the present temperature of the universe, $T_{\rm RH}$ the reheating temperature, and K_1 is the 1st-order modified Bessel function of the second kind, g_*, g_*^s are the effective numbers of degrees of freedom of the thermal bath for the energy and entropy densities respectively. Finally, $|\tilde{\mathcal{M}}_{i\to 2}|^2 \equiv \int d\Omega |\mathcal{M}_{i\to 2}|^2$, where $\mathcal{M}_{i\to 2}$ is the squared amplitude of the process $i \to 2$ summed over all initial and final degrees of freedom, and Ω is the standard solid angle. Then, assuming a symmetric scenario for which the populations of χ and $\bar{\chi}$ are produced at the same rate, we can calculate the relic density

$$
\Omega_\chi h^2 \approx \frac{m_\chi Y_\chi^0}{3.6\times 10^{-9}{\rm GeV}} \ , \tag{13.356}
$$

where the super-index "0" refers to the value measured today. It turns out that the yield of the dark matter is actually sensitive to the temperature at which the dark matter is largely produced: at the beginning of the thermal history of the universe if the mediator mass lies above the reheating temperature $m_{Z'} > T_{\rm RH}$ (the so–called NETDM scenario [571]), or around the mass of the mediator if $2m_\chi < m_{Z'} < T_{RH}$ as the universe plasma reaches the pole of the exchanged particle, in a resonance–like effect. Note that in the case of massless hidden photon or effective freeze–in cases described respectively in [434] and [532] the effective temperature scale defining the nowadays relic abundance is given by the only dark scale accessible, i.e. the mass of the dark matter (like in the classical freeze out scenario). In the following sections we will describe the two microscopic frameworks ($m_{Z'} > T_{\rm RH}$ and $m_{Z'} < T_{\rm RH}$) in which we have done our analysis.

We now present the two models of study.

13.3 The models

13.3.1 $m_{Z'} > T_{\rm RH}$: effective vector-like interactions

If interactions between dark matter and SM particles involve very heavy particles with masses above the reheating temperature T_{RH}, we can describe them in the framework of effective field theory as a Fermi–like interaction can be a relatively accurate description of electroweak theories when energies involved in the interactions are below the electroweak scale. Several works studying effective interactions in very different contexts have been done by the authors of [573, 574] for accelerator constraints and [575, 576] for some

dark matter aspects. Depending on the nature of the dark matter we will consider the following effective operators, for complex scalar and Dirac fermionic dark matter [46]:

Fermionic dark matter:

$$\mathcal{O}_V^f = \frac{1}{\Lambda_f^2}(\bar{f}\gamma^\mu f)(\bar{\chi}\gamma_\mu \chi) \ , \tag{13.357}$$

leading to the squared-amplitude:

$$|\mathcal{M}_V^f|^2 = \frac{32N_c^f}{\Lambda_f^4}\left\{\frac{s^2}{8} + 2\left(\frac{s}{4} - m_f^2\right)\left(\frac{s}{4} - m_\chi^2\right)\cos^2\theta \right. \\ \left. + \frac{s}{2}(m_\chi^2 + m_f^2)\right\} \ . \tag{13.358}$$

Scalar dark matter:

$$\mathcal{O}_V^s = \frac{1}{\Lambda_f^2}(\bar{f}\gamma^\mu f)[(\partial_\mu\phi)\phi^* - \phi(\partial_\mu\phi)^*] \tag{13.359}$$

which leads to:

$$|\mathcal{M}_V^s|^2 = 4\frac{N_c^f}{\Lambda_f^4}\left[-8\left(\frac{s}{4} - m_f^2\right)\left(\frac{s}{4} - m_\phi^2\right)\cos^2\theta \right. \\ \left. + \left(\frac{s}{2} - m_f^2\right)(s - 4m_\phi^2) + m_f^2(s - 4m_\phi^2)\right] . \tag{13.360}$$

As we will show in section 13.4.1, the main contribution to the population of dark matter in this case occurs around the reheating time. At this epoch, all SM particles f and the dark matter candidate χ can be considered as massless relativistic species.[47] The expressions (13.358, 13.360) then become

$$|\mathcal{M}_V^f|^2 \approx 4\frac{N_c^f}{\Lambda_f^4}\ s^2(1 + \cos^2\theta), \\ |\mathcal{M}_V^s|^2 \approx 2\frac{N_c^f}{\Lambda_f^4}\ s^2(1 - \cos^2\theta), \tag{13.361}$$

where, for simplicity and without loss of generality, we have considered universal effective scale $\Lambda_f \equiv \Lambda$. Considering different scales in the hadronic and leptonic sectors as was done in [558] for instance won't change appreciably our conclusions.

[46] Other operators of the $\gamma_\mu\gamma^5$ pseudo-scalar types for instance can also appear for chiral fermionic dark matter, but we will neglect them as they bring similar contribution to the annihilation process.

[47] This is justified numerically by the fact that large s ($\gtrsim 4T^2 \gg m_\chi^2(T), m_f^2(T)$) dominates the first integration in Eq. (13.355).

13.3.2 $m_{Z'} < T_{\rm RH}$: extra Z' and kinetic mixing

Definition of the model

Neutral gauge sectors with an additional dark $U'(1)$ symmetry in addition to the SM hypercharge $U(1)_Y$ and an associated Z' are among the best motivated extensions of the SM, and give the possibility that a dark matter candidate lies within this new gauge sector of the theory. Extra gauge symmetries are predicted in most Grand Unified Theories (GUTs) and appear systematically in string constructions. Larger groups than $SU(5)$ or $SO(10)$ allow the SM gauge group and $U'(1)$ to be embedded into bigger GUT groups. Brane–world $U'(1)$s are special compared to GUT $U'(1)$'s because there is no reason for the SM particles to be charged under them; for a review of the phenomenology of the extra $U'(1)$s generated in such scenarios see e.g. [577]. In such framework, the extra Z' gauge boson would act as a portal between the "dark world" (particles not charged under the SM gauge group) and the "visible" sector.

Several papers considered that the "key" of the portal could be the gauge invariant kinetic mixing $(\delta/2)F_Y^{\mu\nu}F'_{\mu\nu}$ [428, 493, 578, 579, 579–586]. One of the first models of dark matter from the dark sector with a massive additional $U'(1)$, mixing with the SM hypercharge through both mass and kinetic mixings, can be found in [587]. The dark matter candidate χ could be the lightest (and thus stable) particle of this secluded sector. Such a mixing has been justified in recent string constructions [588–593], supersymmetry [594], SO(10) framework [595] but has also been studied within a model independent approach [579, 596–599] with vectorial dark matter [600] or extended extra-$U(1)$ sector [601]. For typical smoking gun signals in such models, like a monochromatic gamma-ray line, see [490, 602–605].

The matter content of any dark $U'(1)$ extension of the Standard Model can be decomposed into three families of particles:

- The *Visible sector* is made of particles which are charged under the SM gauge group $SU(3) \times SU(2) \times U_Y(1)$ but not charged under $U'(1)$.
- The *Dark sector* is composed of the particles charged under $U'(1)$ but neutral with respect to the SM gauge symmetries. The dark matter candidate, χ, is the lightest particle of the dark sector.
- The *Hybrid sector* contains states with SM and $U'(1)$ quantum numbers. These states are fundamental because they act as a portal between the two previous sectors through the kinetic mixing they induce at loop order.

From these considerations, it is easy to build the effective Lagrangian generated at one loop :

$$\begin{aligned}\mathcal{L} &= \mathcal{L}_{\rm SM} - \frac{1}{4}\tilde{B}_{\mu\nu}\tilde{B}^{\mu\nu} - \frac{1}{4}\tilde{X}_{\mu\nu}\tilde{X}^{\mu\nu} - \frac{\delta}{2}\tilde{B}_{\mu\nu}\tilde{X}^{\mu\nu} \\ &+ i\sum_i \bar{\psi}_i\gamma^\mu D_\mu\psi_i + i\sum_j \bar{\Psi}_j\gamma^\mu D_\mu\Psi_j\,, \end{aligned} \tag{13.362}$$

$\tilde{B}_\mu$ being the gauge field for the hypercharge, $\tilde{X}_\mu$ the gauge field of $U'(1)$ and ψ_i the particles from the hidden sector, Ψ_j the particles from the hybrid sector, $D_\mu = \partial_\mu -$

$i(q_Y\tilde{g}_Y\tilde{B}_\mu + q_D\tilde{g}_D\tilde{X}_\mu + gT^aW^a_\mu)$, T^a being the $SU(2)$ generators, and

$$\delta = \frac{\tilde{g}_Y\tilde{g}_D}{16\pi^2}\sum_j q^j_Y q^j_D \log\left(\frac{m^2_j}{M^2_j}\right) \tag{13.363}$$

with m_j and M_j being hybrid mass states [606]. It has been showed [586] that the value of δ may be as low as 10^{-14}, e.g. in the case of gauge-mediated SUSY-breaking models, where the typical relative mass splitting $|M_j - m_j|/M_j$ is extremely small.

Notice that the sum is on all the hybrid states, as they are the only ones which can contribute to the $\tilde{B}_\mu$, $\tilde{X}_\mu$ propagator. After diagonalising of the current eigenstates that makes the gauge kinetic terms of Eq. (13.362) diagonal and canonical, we can write after the $SU(2)_L \times U(1)_Y$ breaking[48]

$$\begin{aligned} A_\mu &= \sin\theta_W W^3_\mu + \cos\theta_W B_\mu \\ Z_\mu &= \cos\phi(\cos\theta_W W^3_\mu - \sin\theta_W B_\mu) - \sin\phi X_\mu \\ Z'_\mu &= \sin\phi(\cos\theta_W W^3_\mu - \sin\theta_W B_\mu) + \cos\phi X_\mu \end{aligned} \tag{13.364}$$

with, to first order in δ,

$$\begin{aligned} \cos\phi &= \frac{\alpha}{\sqrt{\alpha^2 + 4\delta^2\sin^2\theta_W}} \quad \sin\phi = \frac{2\delta\sin\theta_W}{\sqrt{\alpha^2 + 4\delta^2\sin^2\theta_W}} \\ \alpha &= 1 - m^2_{Z'}/M^2_Z - \delta^2\sin^2\theta_W \\ &\pm \sqrt{(1 - m^2_{Z'}/M^2_Z - \delta^2\sin^2\theta_W)^2 + 4\delta^2\sin^2\theta_W} \end{aligned} \tag{13.365}$$

and + (-) sign if $m_{Z'} < (>) M_Z$. The kinetic mixing parameter δ generates an effective coupling of SM states $\psi_{\rm SM}$ to Z', and a coupling of χ to the SM Z boson which induces an interaction on nucleons. Developing the covariant derivative on SM and χ fermions state, we computed the effective $\psi_{\rm SM}\psi_{\rm SM}Z'$ and $\chi\chi Z$ couplings to first order[49] in δ and obtained

$$\mathcal{L} = q_D\tilde{g}_D(\cos\phi\ Z'_\mu\bar{\chi}\gamma^\mu\chi + \sin\phi\ Z_\mu\bar{\chi}\gamma^\mu\chi). \tag{13.366}$$

In the rest of the analysis, we will use the notation $\tilde{g}_D \to g_D$. We took $q_D g_D = 1$ through our analysis, keeping in mind that for the $m_{Z'}$-regimes we consider here, our results stay completely general by a simple rescaling of the kinetic mixing δ if the dominant process transferring energy from SM to the dark sector is $\bar{f}f \to Z'^{(*)} \to \bar{\chi}\chi$; whereas if processes involving on-shell Z' dominate, the results become nearly independent of $q_D g_D$.

Processes of interest

As is clear from the model defined above, both dark matter and SM particles will interact via the standard Z or the extra Z' boson. Thus a priori there are four processes

[48] Our notation for the gauge fields are $(\tilde{B}^\mu, \tilde{X}^\mu)$ before the diagonalization, (B^μ, X^μ) after diagonalization and (Z^μ, Z'^μ) after the electroweak breaking.

[49] One can find a detailed analysis of the spectrum and couplings of the model in the appendix of Ref. [597–599]. The coupling g_D is the effective dark coupling $\tilde{g}_D$ after diagonalization.

contributing to the dark matter relic abundance: $\bar{f}f \to V \to \bar{\chi}\chi$, and $V \to \bar{\chi}\chi$, where V can be Z and/or Z', and in the $2 \to 2$ process both Z and Z' interfere to produce the total cross-section.[50] The amplitudes of those processes are:

$$|\mathcal{M}_{2\to2}|^2 = |\mathcal{M}_Z|^2 + |\mathcal{M}_{Z'}|^2 + (\mathcal{M}_Z\mathcal{M}^*_{Z'} + \text{h.c.}) \ , \tag{13.367}$$

where

$$\begin{aligned} |\mathcal{M}_Z|^2 &= \frac{(q_D g_D)^2 \sin^2\phi}{(s-M_Z^2)^2 + (M_Z\Gamma_Z)^2} \\ &\times \ \big\{(c_L^2 + c_R^2)\left[16m_\chi^2 m_f^2(\cos^2\theta - \sin^2\theta)\right. \\ &+ \ 8m_\chi^2 s\sin^2\theta - 8m_f^2 s\cos^2\theta + 2s^2(1+\cos^2\theta)\big] \\ &+ \ c_L c_R(32m_\chi^2 m_f^2 + 16m_f^2 s)\big\} \ , \end{aligned} \tag{13.368}$$

$$\begin{aligned} &|\mathcal{M}_{Z'}|^2 = |\mathcal{M}_Z|^2 \quad \text{with}: [\sin\phi \to \cos\phi, \\ &(M_Z, \Gamma_Z) \to (m_{Z'}, \Gamma_{Z'}), \quad (c_L, c_R) \to (c'_L, c'_R)] \ , \end{aligned} \tag{13.369}$$

and

$$\begin{aligned} &\mathcal{M}_Z\mathcal{M}^*_{Z'} + \text{h.c.} = \frac{2A\ (q_D g_D)^2 \sin\phi\cos\phi}{A^2 + B^2} \\ &\times \big\{(c_L c'_L + c_R c'_R)\left[16m_\chi^2 m_f^2(\cos^2\theta - \sin^2\theta)\right. \\ &+8m_\chi^2 s\sin^2\theta - 8m_f^2 s\cos^2\theta + 2s^2(1+\cos^2\theta)\big] \\ &+ (c_L c'_R + c_R c'_L)(16m_\chi^2 m_f^2 + 8m_f^2 s)\big\} \ , \end{aligned} \tag{13.370}$$

with

$$\begin{aligned} A &= s^2 - s(M_Z^2 + m_{Z'}^2) + M_Z^2 m_{Z'}^2 + M_Z m_{Z'}\Gamma_Z\Gamma_{Z'} \\ B &= s(\Gamma_Z M_Z - \Gamma_{Z'} m_{Z'}) + M_Z^2 m_{Z'}\Gamma_{Z'} - m_{Z'}^2 M_Z\Gamma_Z \ , \end{aligned} \tag{13.371}$$

whereas for the $1 \to 2$ process we have:

$$|\mathcal{M}_{1\to2}|^2 = \begin{cases} 4(q_D g_D)^2(\sin^2\phi)(M_Z^2 + 2m_\chi^2) & \text{if} \quad V = Z \\ 4(q_D g_D)^2(\cos^2\phi)(m_{Z'}^2 + 2m_\chi^2) & \text{if} \quad V = Z' \ . \end{cases} \tag{13.372}$$

Here the coefficients $c_{L,R}$ and $c'_{L,R}$ are the left and right couplings of the SM fermions to the Z and Z' bosons, respectively. The left (L) and right (R) couplings to the Z boson are:

$$\begin{aligned} (c_L)_f &= -\frac{(2g^2 T_{f_L} - g'^2 Y_{f_L})}{2\sqrt{g'^2 + g^2}}\cos\phi - \frac{g'}{2}Y_{f_L}\sin\phi\ \delta \ , \\ (c_R)_f &= \frac{1}{2}g' Y_{f_R}\left(\frac{g'}{\sqrt{g'^2 + g^2}}\cos\phi - \sin\phi\ \delta\right) \ , \end{aligned} \tag{13.373}$$

[50] There are additional processes, not written here, which can have non-negligible influence on the final dark matter number density; e.g. $\bar{f}f \to ZZ' \to Z\bar{\chi}\chi$, with a t-channel exchange of a fermion f. These processes have been taken into account in the full numerical solution of the coupled set of Boltzmann equations, as shown below.

for SM fermions f, and

$$c_\chi = q_D g_D \sin\phi \tag{13.374}$$

for the dark matter. Similarly, the couplings to the Z' boson to the SM fermions and dark matter χ are:

$$\begin{aligned}
(c_L)'_f &= -\frac{(2g^2 T_{f_L} - g'^2 Y_{f_L})}{2\sqrt{g'^2+g^2}} \sin\phi + \frac{g'}{2} Y_{f_L} \cos\phi\ \delta\ , \\
(c_R)'_f &= \frac{1}{2} g' Y_{f_R} \left(\frac{g'}{\sqrt{g'^2+g^2}} \sin\phi + \cos\phi\ \delta \right)\ , \\
c'_\chi &= q_D g_D \cos\phi\ .
\end{aligned} \tag{13.375}$$

Presently, we describe in details the results that we obtained for the previous models.

13.4 Results and discussion

13.4.1 In the case : $m_{Z'} > T_{\rm RH}$

In the case of production of dark matter through SM particle annihilation, the Boltzmann equation can be simplified

$$\begin{aligned}
\frac{dY}{dx} &= \frac{1}{16(2\pi)^8} \frac{1}{g_* \sqrt{g_*^s}} \left(\frac{45}{\pi}\right)^{3/2} \frac{M_p}{m_\chi} \\
&\times \int_{2x}^{\infty} z \left(z^2 - 4x^2\right)^{1/2} K_1(z) dz |\mathcal{M}(z)|^2 d\Omega
\end{aligned} \tag{13.376}$$

with $z = \sqrt{s}/T$, $x = m_\chi/T$ and Ω the solid angle of the outgoing dark matter particles. Using the expression for $|\mathcal{M}|^2$ obtained in Eq. (13.361) we can write an analytical expression of the relic yields present nowadays if we suppose (as we will check) that the non-thermal production of dark matter happens at temperatures (and thus s) much larger than the mass of dark matter or SM particles ($m_f, m_\chi \ll \sqrt{s}$). After integrating over the temperature (x to be precise) from T_{RH} to T, and considering that all the fermions of the SM contribute democratically ($\Lambda_f \equiv \Lambda$) one obtains[51]

$$\begin{aligned}
Y_V^f(T) &\simeq \frac{4}{3} \frac{384}{(2\pi)^7} \left(\frac{45}{\pi g_*^s}\right)^{3/2} \frac{M_p}{\Lambda^4} \left[T_{RH}^3 - T^3\right], \\
Y_V^s(T) &\simeq \frac{1}{3} \frac{384}{(2\pi)^7} \left(\frac{45}{\pi g_*^s}\right)^{3/2} \frac{M_p}{\Lambda^4} \left[T_{RH}^3 - T^3\right],
\end{aligned} \tag{13.377}$$

where $g_* \sim g_*^s$ has been used. We show in Fig. 65 the evolution of $Y(T)$ for a fermionic dark matter as a function of $x = m_\chi/T$ with $m_\chi = 100$ GeV for two different reheating

[51] Notice that the factor of difference corresponds to the different degrees of freedom for a real scalar and Dirac fermionic dark matter.

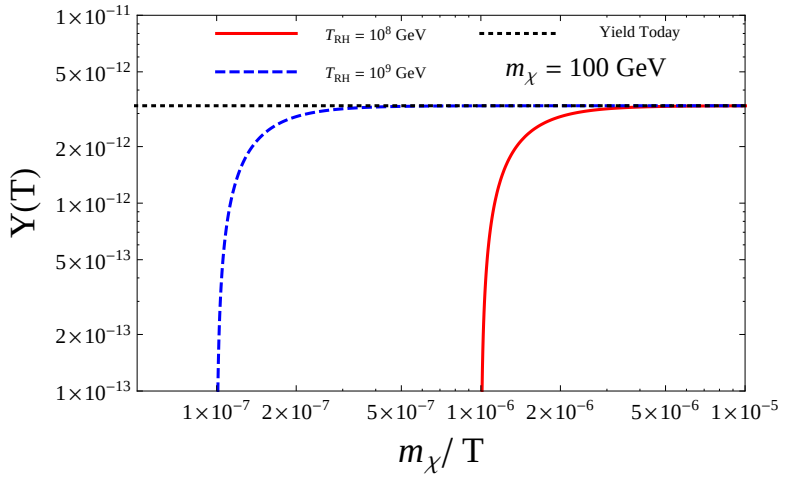

Figure 65: Evolution of the number density per comoving frame ($Y = n/\mathbf{s}$) for a 100 GeV fermionic dark matter as a function of m_χ/T for two reheating temperatures, $T_{RH} = 10^8$ (red) and 10^9 (blue) GeV in the case of vector interaction for fermionic a dark matter candidate. The value of the scale Λ has been chosen such that the nowadays yield Y corresponds to the nowadays value of $Y(T_0)$ measured by WMAP: $Y(T_0) \simeq 3.3 \times 10^{-12}$ represented by the horizontal black dashed line (see the text for details).

temperatures, $T_{\rm RH} = 10^8$ and 10^9 GeV. We note that to obtain analytical solution to the Boltzmann equation, we approximated the Fermi-Dirac/Bose-Einstein by Maxwell-Boltzmann distribution. This can introduce a 10% difference with respect to the exact case [572]. However, when performing our study we obviously solved numerically the complete set of Boltzmann equations. As one can observe in Fig. 65, the relic abundance of the dark matter is saturated very early in the universe history, around $T \simeq T_{\rm RH}$, confirming our hypothesis that we can consider all the particles in the thermal bath (as well as the dark matter) as massless in the annihilation process: $m_\chi, m_f \ll \sqrt{s}$. At $T \simeq T_{RH}/2$ the dark matter already reaches its asymptotical value.

Moreover, for a given value of the reheating temperature $T_{\rm RH}$, we compute the effective scale Λ such that the present dark matter yield $Y(T_0)$ respects the value measured by WMAP/PLANCK : $Y(T_0) \simeq 3.3 \times 10^{-12}$ for a 100 GeV dark matter. Imposing this constraint in Eq. (13.377), we obtain $\Lambda(T_{RH} = 10^8\text{GeV}) \simeq 3.9 \times 10^{12}$ GeV and $\Lambda(T_{RH} = 10^9\text{GeV}) \simeq 2.2 \times 10^{13}$ GeV for a fermionic dark matter.

As a consequence, we can derive the value of Λ respecting the WMAP/PLANCK constraint as a function of the reheating temperature $T_{\rm RH}$ for different masses of dark matter. This is illustrated in Fig. 66 where we solved numerically the exact Boltzmann equation. We observe that the values of Λ we obtained with our analytical solutions extracted from Eq. (13.377)- are pretty accurate and the dependence on the nature (fermion or scalar) of the dark matter is very weak. We also notice that the effective scale needed to respect WMAP constraint is very consistent with GUT–like SO(10) models which predict typical 10^{12-14} GeV as intermediate scale if one imposes unification [571]. Another interesting point is that $\Lambda \gg T_{RH}$ whatever is the nature of dark matter, ensuring the coherence of the effective approach. We have also plotted the result for very heavy dark matter candidates (PeV scale) to show that in such a scenario, there is

no need for the dark matter mass to lie within electroweak limits, avoiding any "mass fine tuning" as in the classical WIMP paradigm.

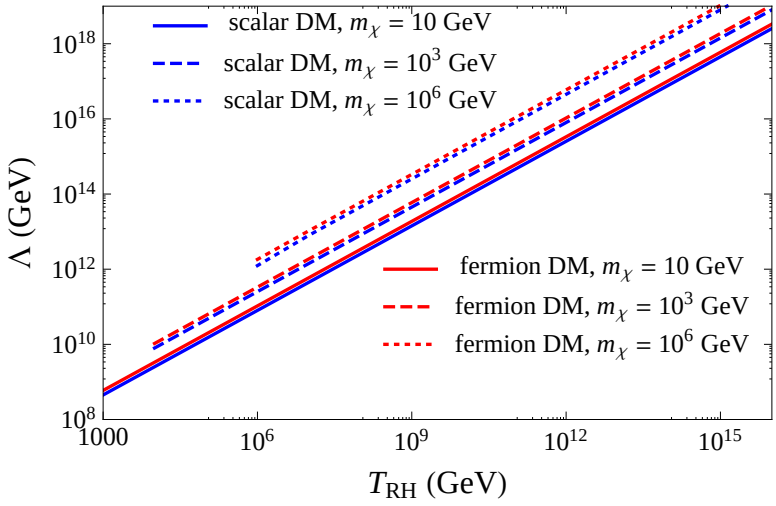

Figure 66: Values of the scale Λ for fermionic (red) and scalar (blue) dark matter, assuming good relic abundance ($\Omega_\chi h^2 = 0.12$) and dark matter mass of 10 GeV (solid), 1000 GeV (dashed) and 10^6 GeV (dotted), as a function of the reheating temperature.

We also want to underline the main difference with an infrared-dominated "freeze in" scenario, where the dark matter is also absent in the early universe. Indeed, in orthodox freeze-in, the relic abundance increases very slowly as a function of m_χ/T, and the process which populates the universe with dark matter is frozen at the time when the temperature drops below the mass of the dark matter, Boltzmann-suppressing its production by the thermal bath, which does not have sufficient energy to create it through annihilation. This can be considered as a fine tuning: the relic abundance should reach the WMAP value at a definite time, $T \simeq m_\chi/3$. In a sense, it is a common feature among freeze–in and freeze–out scenarios. In both cases the fundamental energy scale which stops the (de)population process is m_χ/T. When the mediator mass $m_{Z'}$ is larger than the reheating temperature, the fundamental scale which determines the relic abundance is $T_{\rm RH}/m_{Z'}$ or $T_{\rm RH}/\Lambda$ in the effective approach. The dark matter abundance is then saturated from the beginning, at the reheating time, and thus stays constant during the rest of the thermal history of the universe, and is nearly independent of the mass of the dark matter: no fine tuning is required, and no "special" freeze-in at $T \simeq m_\chi/3$. This is a particular case of the NETDM framework presented in [571]. Furthermore, the NETDM mecanism has the interesting properties to avoid large thermal corrections to dark matter mass. The reason is that all dark sector particles are approximately decoupled from the visible medium of the universe.[52]

13.4.2 In the case : $m_{Z'} < T_{\rm RH}$

Generalities

The case of light mediators (in comparison to the reheating temperature) is more

[52] While the thermal masses of visible particles may change the dark matter production rate, we have checked that this effect is negligible.

complex and rises several specific issues. We concentrate in this section on the computation of the dark matter relic abundance in the kinetic-mixing framework because it can be easily embedded in several ultraviolet completions. However, our analysis is valid for any kind of models with an extra $U(1)$ gauge group. The kinetic mixing δ is indeed completely equivalent to an extra $U(1)$ millicharge for the visible sector and one can think δ as the charge of the SM particles (visible world) to the Z'. Cosmological constraints allow us to restrict the parameter space of the model in the plane $(\delta, m_{Z'}, m_\chi)$. However we should consider two options for the mediator Z': either it is in thermal equilibrium with the SM plasma, or, in analogy with the dark matter, it has not been appreciably produced during the reheating phase.

The differential equation for the decay process $Z' \to \bar{\chi}\chi$, in the case where the dark matter annihilation is neglected, can be expressed as:

$$\frac{dY}{dx} = \frac{m_{Z'}^3 \Gamma_{Z'} g_{Z'}}{2\pi^2 H x^2 \mathbf{s}} K_1(x). \tag{13.378}$$

where $x \equiv m_{Z'}/T$, $\Gamma_{Z'}$ the decay width of Z' and $g_{Z'} = 3$ giving the degree of freedom of the massive gauge boson Z'. Expressing the entropy and Hubble parameter as:

$$\mathbf{s} = g_*^s \frac{2\pi^2}{45} \frac{m_{Z'}^3}{x^3}, \quad H = \sqrt{g_*} \sqrt{\frac{4\pi^3}{45}} \frac{m_{Z'}^2}{x^2 M_p}$$

we finally obtain the equation

$$Y_0 \approx \left(\frac{45}{\pi}\right)^{\frac{3}{2}} \frac{1}{g_*^s \sqrt{g_*}} \frac{M_p \Gamma_{Z'} g_{Z'}}{8\pi^4 m_{Z'}^2} \int_{\frac{m_{Z'}}{T_{RH}}}^{\infty} x^3 K_1(x) dx. \tag{13.379}$$

Approximating $\Gamma_{Z'} \simeq q_D^2 g_D^2 m_{Z'}/(16\pi)$, $q_D g_D$ being the effective gauge coupling of Z' and dark matter, and also taking $g_*^s \simeq g_*$ at the energies of interest, we can write

$$Y_0 \simeq \left(\frac{45}{\pi}\right)^{3/2} \frac{q_D^2 g_D^2 M_p}{128\pi^5 m_{Z'}} \int_{\frac{m_{Z'}}{T_{RH}}}^{\infty} x^3 K_1(x) dx. \tag{13.380}$$

Using $\int_0^\infty x^3 K_1(x) dx \simeq 4.7$ and Eq. (13.356) we obtain

$$\Omega_0 h^2 \simeq 2 \times 10^{22} q_D^2 g_D^2 \frac{m_\chi}{m_{Z'}}. \tag{13.381}$$

To respect WMAP/Planck data in a FIMP scenario one thus needs $g_D \simeq 10^{-11}$ if Z' is at TeV scale. For much higher values of g_D, the dark matter joins the thermal equilibrium at a temperature $T \gg m_\chi$ and then recovers the classical freeze out scenario.

Thus, a first important conclusion is that a Z' in thermal equilibrium with the plasma and decaying dominantly to dark matter would naturally overpopulate the dark matter which would thus thermalise with plasma, ending up with the standard freeze-out history. We then have no choice than to concentrate on the alternative scenario where Z', same as the dark matter, was not present after inflation. Thus the interaction of the SM bath (and the dark matter generated from it) could create it in a considerable amount. We now discus this alternative.

Chemical equilibrium of the dark sector

If Z' is generated largely enough at some point during the dark matter genesis, it will surely affect the dark matter final relic abundance through the efficient DM-Z' interactions. In the study of the evolution of the Z' population it may happen that Z' enters in a state of chemical equilibrium exclusively with dark matter, independently of the thermal SM bath, and thus with a different temperature. This "dark thermalisation" can have some effect on the final dark matter number density. The analysis we perform here is inspired from [434], which was however applied to a different model.

If the $Z'-$DM scattering rate is larger than the Hubble expansion rate of the universe[53], these two species naturally reach kinetic equilibrium, with a well defined temperature T', which a priori is different from (and is a function of) the thermal bath (photon) temperature, T. This temperature T' increases slowly (given the feeble couplings) due to the transfer of energy from the thermal bath, which determines the energy density ρ' and pressure P' of the dark sector. The Boltzmann equation governing the energy transfer in this case is:

$$\begin{aligned}
&\frac{d\rho'}{dt} + 3H(\rho' + P') = \int \prod_{i=1}^{4} d^3\bar{p}_i f_1(p_1) f_2(p_2) \\
&\times |\mathcal{M}|^2 (2\pi)^4 \delta^{(4)}(p_{\rm in} - p_{\rm out}) \cdot E_{\rm trans.} \\
&= \frac{1}{2048\pi^6} \int_{4m_\chi^2}^{\infty} ds K_2(\frac{\sqrt{s}}{T}) T \sqrt{(s-4m_\chi^2)s} |\tilde{\mathcal{M}}_{12\to\chi\bar{\chi}}|^2 \\
&+ \frac{1}{128\pi^4} K_2(\frac{m_{Z'}}{T}) m_{Z'} T \sqrt{m_{Z'}^2 - 4m_1^2} |\tilde{\mathcal{M}}_{Z'\to 12}|^2 \ ,
\end{aligned} \tag{13.382}$$

where 1 and 2 are the initial SM particles and $m_1 = m_2$, $|\tilde{\mathcal{M}}|^2$ have been defined below Eq. (13.355) summing over all initial and final degrees of freedom. For SM pair annihilation, the energy transfer per collision is $E_{\rm trans.} = E_1 + E_2$. It can be useful to write an analytical approximation for the solution $\rho'(T)$ in the early universe. Indeed for $T \gg m_{Z',\chi}$, it is easy to show that Eq. (13.382) reduces to

$$\begin{aligned}
&\frac{d(\rho'/\rho)}{dT} \simeq -640 \sqrt{\frac{45}{\pi}} \frac{\alpha \delta^2 M_p}{\pi^7 T^2 g_*^{3/2}} \\
&\Rightarrow \ \left(\frac{T'}{1\ \text{GeV}}\right) \simeq 3000\ \sqrt{\delta} \left(\frac{T}{1\ \text{GeV}}\right)^{3/4}
\end{aligned} \tag{13.383}$$

supposing that the dark bath is in kinetic equilibrium ($\rho' \propto (T')^4$) with $\alpha = g^2/4\pi$ (see next paragraph for more details). Even if all our analysis was made using the analytical solutions of the coupled Boltzmann system, we checked that this analytical solution is a quite good approximation to the exact numerical solution of Eq. (13.382) and will be very useful to understand the physical phenomena hidden by the numerical results.

[53] For a deeper analysis on this, see [572].

While presenting a detailed study of the visible-to-dark energy transfer is out of the scope of this section, we just want to point out that there is typically a moment at which the dark sector (i.e. dark matter plus Z') is sufficiently populated as for creating particles out of itself, e.g. in processes as a t-channelled $\chi\bar{\chi} \to Z'Z' \to 2\chi 2\bar{\chi}$. As this happens out of a total available energy ρ' at any given time, the net effect is to increase n_χ and $n_{Z'}$ at the cost of decreasing T'.

To quantify the effect of DM-Z' chemical equilibrium on the number densities of both particles, we solved the coupled set of their respective Boltzmann equations.

The relevant processes happening between the dark sector and SM[54], and with itself, are:

- a: $SM\overline{SM} \to Z'$, and $\bar{a}$: $SM\overline{SM} \leftarrow Z'$
- b: $\chi\overline{\chi} \to Z'$, and $\bar{b}$: $\chi\overline{\chi} \leftarrow Z'$
- c: $Z'Z' \to \chi\overline{\chi}$, and $\bar{c}$: $Z'Z' \leftarrow \chi\overline{\chi}$
- d: $\chi\overline{\chi} \to SM\overline{SM}$, and
  $\bar{d}$: $\chi\overline{\chi} \leftarrow SM\overline{SM}$.

The Boltzmann equations for the Z' and dark matter comoving number densities are:

$$\begin{aligned} \frac{dY_{Z'}}{dT} &= \frac{1}{HT}\left[\Gamma_{\bar{a}}(Y^{eq}_{Z'} - Y_{Z'}) - \Gamma_{\bar{b}} Y_{Z'}\right. \\ &+ \left.\langle\sigma\mathrm{v}\rangle_b Y_\chi^2 \mathbf{s} - \langle\sigma\mathrm{v}\rangle_c Y^2_{Z'}\mathbf{s} + 2\langle\sigma\mathrm{v}\rangle_{\bar{c}} Y_\chi^2 \mathbf{s}\right] \end{aligned} \tag{13.384}$$

$$\begin{aligned} \frac{dY_\chi}{dT} &= \frac{1}{HT}\left[\langle\sigma\mathrm{v}\rangle_d((Y^{eq}_\chi)^2 - Y_\chi^2)\mathbf{s} - \langle\sigma\mathrm{v}\rangle_b Y_\chi^2 \mathbf{s}\right. \\ &+ \left.\Gamma_{\bar{b}} Y_{Z'} - 2\langle\sigma\mathrm{v}\rangle_{\bar{c}} Y_\chi^2 \mathbf{s} + \langle\sigma\mathrm{v}\rangle_c Y^2_{Z'}\mathbf{s}\right]. \end{aligned} \tag{13.385}$$

Here in Eq. (13.385), in the very first term, we have made use of the chemical equilibrium condition for a process $A \leftrightarrow B\bar{B}$

$$\langle\sigma\mathrm{v}\rangle_{BB\to A}(Y^{eq}_B)^2\ \mathbf{s} = \Gamma_{A\to BB} Y^{eq}_A\ .$$

Besides, in Eq. (13.385), the term proportional to $\langle\sigma\mathrm{v}\rangle_d$ does not contain the contribution from on-shell Z', because it is already included in the term going with $\Gamma_{\bar{b}}$. The reason for this, is that the typical time the reaction $SM\overline{SM} \leftrightarrow \chi\overline{\chi}$ takes to happen, is $t_{\rm typ}$. This period, even if usually very short, is large enough as to consider $t_{\rm typ} \gtrsim dt$, where dt is the characteristic time interval when solving the Boltzmann equation. In other words, the evolution dictated by the Boltzmann equation is such that there are always physical (on-shell) Z' particles around, which effectively contribute to a Z' decay.

[54]Here we are not writting the contributions from processes like $SM\gamma \to SMZ'$ and $SM\overline{SM} \to \gamma Z'$; but they are taken into account for the numerical analysis.

The Boltzmann equation describing the evolution of the energy density transferred from the SM to the dark sector is Eq. (13.382). For SM pair annihilation, the energy transfer per collision $E_{\rm trans.} = E_1 + E_2$. The pressure P' is:

$$\begin{aligned} P' &= \rho'_{\rm rel}/3 \ , \\ \rho'_{\rm rel} &= \rho' - 2n_\chi m_\chi - n_{Z'} m_{Z'} \ , \end{aligned} \tag{13.386}$$

where $\rho'_{\rm rel}$ is the relativistic contribution to the energy density ρ'.

The relevant Z' production process is the scattering $\overline{\chi}\chi \to Z'Z'$ (as compared to $\overline{\chi}\chi \to Z'$), whereas the relevant Z' depletion process is the decay $Z' \to \overline{\chi}\chi$ (as compared to $Z'Z' \to \overline{\chi}\chi$), but of course we have considered all the processes when solving the Boltzmann equations. The results are shown in Fig. 67 for $m_{Z'} > 2m_\chi$ and in Fig. 68 for $m_{Z'} < 2m_\chi$.

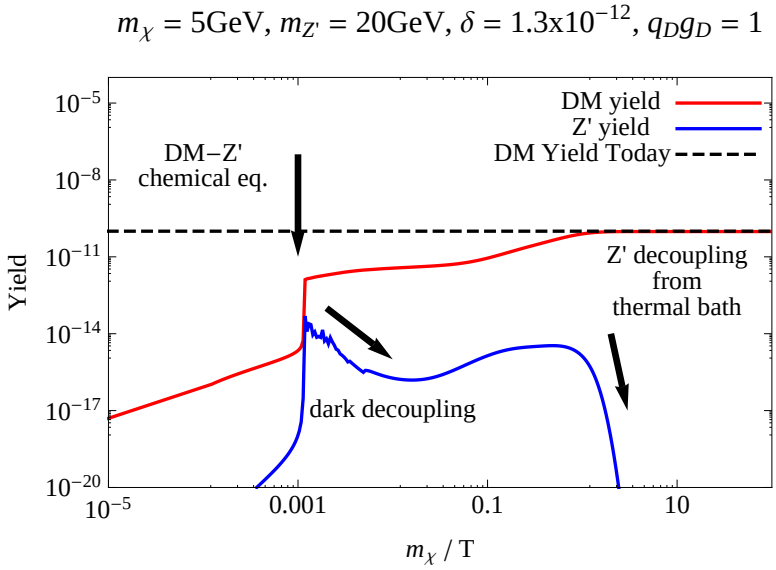

Figure 67: Evolution of the yield for dark matter (red) and Z' (blue) as a function of temperature for $m_{Z'} > 2m_\chi$. The set of parameters is given on the figure.

Figure 67 presents several original and interesting features. We can separate the thermal events in 4 phases that we detail below: dark kinetic equilibrium of the dark matter candidate, self exponential production of dark matter through its annihilation, decoupling of the Z' from the dark bath and then decoupling of χ and Z' from the thermal standard bath.

Indeed, we can notice a first kind of plateau for the dark matter yield Y_χ at $T \gg 10^3$ GeV. This corresponds to the time when the dark matter concentration is sufficient to enter equilibrium with itself through the exchange of a virtual Z' (s or t channel). Indeed, the condition $n_\chi \langle \sigma v \rangle > H(T)$ can be expressed as

$$\begin{aligned} &\left\{10^{-5} M_p g_*^s \delta^2 \alpha \ T^2\right\} \times \frac{(q_D g_D)^4}{(4\pi)^2 T^2} > \frac{1.66}{M_p} \sqrt{g_*} T^2 \\ &\Rightarrow T \lesssim 1.6 \times 10^{15} g_*^{1/4} \alpha^{1/2} \delta \ \ \text{GeV} \end{aligned} \tag{13.387}$$

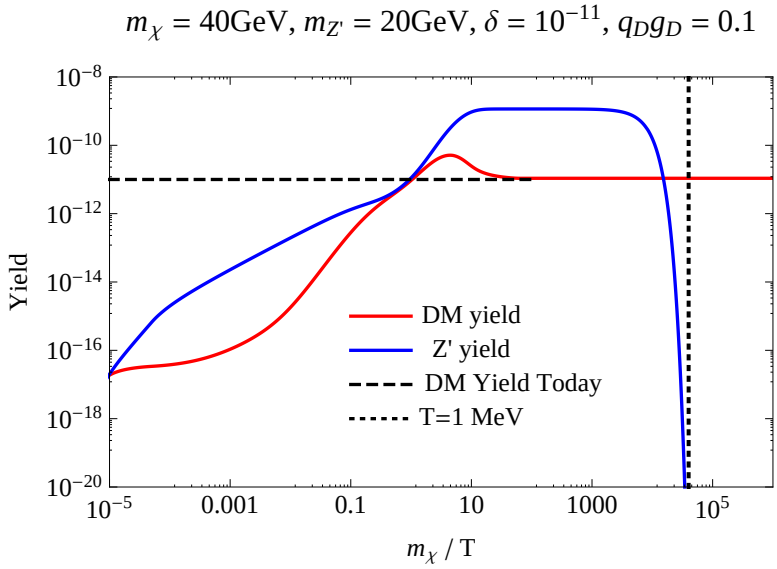

Figure 68: Same as Fig. 67 with $m_{Z'} < 2m_\chi$. Note here a smaller $q_D g_D$ is adopted to avoid too many dark matter annihilations.

where we have used an approximate solution of Eq. (13.355) at high temperatures:

$$Y_\chi \simeq \alpha\ \delta^2\ \frac{10^{14}\ \text{GeV}}{T} \tag{13.388}$$

with $\alpha = \frac{g^2}{4\pi}$. The result is then in accordance with what we observed numerically.

We then observe in a second phase, around $m_\chi/T = 10^{-3}$, a simultaneous and sharp rise in the number density of dark matter and Z'. This is because the dark sector enters in a phase of chemical equilibrium with itself, causing the population of both species to increase. Moreover, in the case $m_{Z'} > 2m_\chi$, we observe that the width of the Z' $\Gamma_{Z'}$ is much larger than the production rate through the t channel $\chi\chi \to Z'Z'$:

$$\begin{aligned} \Gamma_{Z'} &\simeq \frac{(q_D g_D)^2}{16\pi} m_{Z'} \simeq 0.4\ \text{GeV}\ , \\ n\langle\sigma v\rangle_{\chi\chi\to Z'Z'} &\simeq 10^{12} g_*^s\ \delta^2 \alpha\ (q_D g_D)^4 \\ &\simeq 10^{-12} \sqrt{\frac{T}{1\text{GeV}}}\ \text{GeV}. \end{aligned} \tag{13.389}$$

In other words, as soon as a Z' is produced, it automatically decays into two dark matter particles before having the time to thermalise or annihilate again. We then observe an exponential production of dark matter. Of course, each product of the Z' decay possesses half of the initial energy of the annihilating dark matter, this energy also decreasing exponentially. As a consequence, the temperature of the dark sector, T', typically drops below $m_{Z'}$ at a certain temperature T such that the dark sector does not have enough energy for maintaining an efficient Z' production[55]. This is illustrated as

[55]Strictly speaking one should not use the word *temperature* T' during this very short time but more express ourselves in terms of energy.

"dark decoupling" in Fig. 67, where the excess of Z' population decays mostly to dark matter particles. We can understand this phenomenon by looking more in details at the solution of the transfer of energy (13.383). Taking $T' \simeq m_{Z'}$ in Eq. (13.383), we can check that the decoupling of the Z' from the dark bath happens around a temperature $T \simeq 2$ TeV when the dark matter does not possess sufficiently energy to produce a Z' pair. This result is in accordance with the value observed in Fig. 67 along the arrow labelled *dark decoupling*.

However, the thermal (standard) bath is still able to slowly produce Z' after its decoupling from the dark bath but at a very slow rate (proportional to δ^2) up to the moment at which the temperature T drops below $m_{Z'}$, when the Z' population decays completely as we can also observe in Fig. 67. During this time the dark matter population increases also slowly due to the annihilation of SM particles through the exchange of a virtual Z' added to the product of the Z' decay until T reaches m_χ.

We also depict in Fig. 68 the evolution of the Z' and dark matter yields in the case $m_{Z'} < 2\ m_\chi$. We observe similar features, except that the Z' does not decouple from the dark bath and is not responsible anymore for the exponential production of dark matter. The dark matter decouples first from the plasma, and then the Z' continues to be produced at a slow rate, being also largely populated by the $t-$channel annihilation of the dark matter. However, it never reaches the thermal equilibrium with the thermal bath as it decays to SM particles (at a very low rate proportional to δ^2) at a temperature of about 1 MeV, not affecting the primordial nucleosynthesis (see below for details).

Cosmological constraints

The PLANCK collaboration [397] recently released its results and confirmed the WMAP [444, 445] non–baryonic content of the universe. It is then important to study in the $(m_\chi, m_{Z'}, \delta)$ parameter space the region which is still allowed by the cosmological WMAP/PLANCK constraint. As we discussed in the previous section, a small kinetic mixing can be sufficient to generate sufficient relic abundance. We show in Fig. 69 the plane (δ,$m_{Z'}$) compatible with WMAP/PLANCK data ($\Omega h^2 \simeq 0.12$) for different dark matter masses. Depending on the relative value between m_χ and $m_{Z'}$, we can distinguish four regimes clearly visible in Fig. 69:

(a) $m_{Z'} < 2m_\chi$. In this case, the dark matter is mainly produced from the plasma through $s-$channel exchange of the Z' and then decouples from the thermal bath at $T \simeq m_\chi$. Dark matter then annihilates into two Z' through $t-$channel process if kinetically allowed (see Fig. 68). For light Z', the amplitude of dark matter production[56] ($|\mathcal{M}|^2 \propto \delta^2 m_\chi^2/s \sim \delta^2 m_\chi^2/T^2$ from Eq.(13.369)) and the annihilating rate ($\chi\chi \to Z'Z'$) after the decoupling time are both independent of $m_{Z'}$. As a consequence, the relic abundance is also independent of $m_{Z'}$ (but strongly dependent of δ) as one can observe in the left region of Fig. 69.

(b) $2m_\chi < m_{Z'} < M_Z$. We notice a sharp decrease in the values of δ occurring around $m_{Z'} = 2m_\chi$. Indeed, for $m_{Z'} > 2m_\chi$ there exists a temperature in the plasma for which the resonant production of onshell Z' is abundant ($T \simeq m_{Z'}/2$). The Z'

[56] In this region the Z'-SM couplings (see 13.375) are roughly proportional to δ, since $\sin\phi \ll \delta$ for the values of δ and $m_{Z'}$ in consideration.

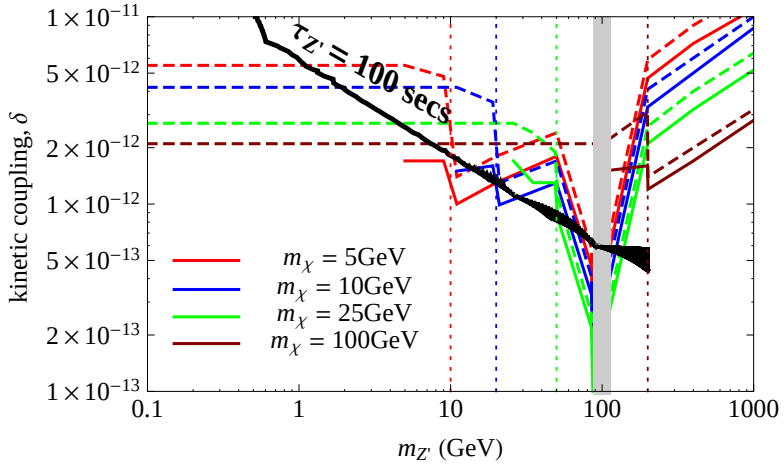

Figure 69: Kinetic-mixing coupling δ as a function of $m_{Z'}$ for different values of m_χ: 5, 10, 25 and 100 GeV for red, blue, green and brown curves, respectively. These lines are in agreement with WMAP: $\Omega_\chi h^2 \sim 0.12$. We have fixed $q_D g_D = 1$, as before. Solid lines are obtained taking into account the "dark thermalisation" effect (see text for details) whereas dashed lines are obtained without such an effect. The solid black line shows BBN constraints (see text details), which apply, for each dark matter mass (shown with dotted lines), to the region $m_{Z'} < 2m_\chi$.

being unstable, it immediately decays into 2 dark matter particles increasing its abundance. The rate of the dark matter production from the standard model bath around the pole $T \simeq m_{Z'}/2$ is proportional to $\delta^2 m_\chi^2 T^2/m_{Z'}^2\Gamma_{Z'}^2$ (Eq.(13.369)). This rate is higher than in the region $m_{Z'} < 2m_\chi$ where $|\mathcal{M}|^2 \propto \delta^2 m_\chi^2/T^2$: δ should then be smaller in order to still respect PLANCK/WMAP constraint.

(c) $m_{Z'} \approx M_Z$. This is the region of maximal mixing: $\phi \approx \pi/4$. The total amplitude of annihilation in Eq. (13.367) is maximised, driving δ toward very small values in order to respect PLANCK/WMAP constraint. However, this region is excluded by electroweak measurements because of large excess in the ρ parameter (see [597–599] for a complete analysis in this regime).

(d) $2m_\chi < M_Z < m_{Z'}$. For even larger values of $m_{Z'}$ the amplitude has a smooth tendency of decreasing with $m_{Z'}$ from its dependence on the width. The majority of the dark matter population is indeed created when the temperature of the universe, playing the role of a statistical accelerator with time dependent centre of mass energy, reaches $T \simeq m_{Z'}/2$ (or $m_Z/2$). The production cross section through $s-$channel exchange of Z' is then proportional to $\delta^2/m_{Z'}^2\Gamma_{Z'}^2 \propto \delta^2/m_{Z'}^4$. Keeping constant final relic abundance implies $\delta^2/m_{Z'}^4 =$ constant, which is observed in the right region of Fig. 69.

For the sake of completeness, we also show in Fig. 69 the effect of allowing the Z' and dark matter to enter in a phase of chemical equilibrium (solid lines), see Fig. 67 and compare it to the more naive case where no dark-thermalisation is taken into account (dashed lines). We observe that depending on the dark matter and Z' masses, the correction caused by the dark-thermalisation for $q_D g_D = 1$ is at most a factor 2.

Meanwhile, a general look at Fig. 69 tells us that the order of magnitude of δ to respect relic abundance data is generally in the range 10^{-12}–10^{-11}, which is in absolute value of the same order that typical FIMP couplings obtained in the literature for different frameworks [434, 532, 533, 569, 570] but with a much richer phenomenology due to the instability of the mediator and the existence of dark thermalisation. It is interesting to note that such tiny kinetic mixing, exponentially suppressed, is predicted by recent work on higher dimensional compactification and string phenomenology to lie within the range $10^{-12} \lesssim \delta \lesssim 10^{-10}$ [591, 592].

Finally, due to the feeble coupling δ, it is important to check constraints coming from Big Bang Nucleosynthesis (BBN) in the specific case $m_{Z'} < 2m_\chi$. Indeed, if Z' is lighter than the dark matter, the Z' will slowly decay to the particles of the thermal bath, potentially affecting the abundance of light elements. For the ranges of Z' masses we consider here, a naive bound from BBN can be obtained by simply requiring the Z' lifetime to be shorter than $\mathcal{O}(100)$ seconds. This is translated into a lower bound on the kinetic coupling δ, represented by the black solid line in Fig. 69, where the bound applies, for every m_χ (see dotted lines), to the region $m_{Z'} < 2m_\chi$. We see how the BBN bounds strongly constrain the region of the lightest Z', $m_{Z'} \lesssim 1$ GeV for the dark matter masses considered here. A more detailed study of nucleosynthesis processes in this framework can be interesting but is far beyond the scope of this present section.

Other constraints

In [597–599] several low-energy processes have been used in order to constrain the parameter space of the model we analysed. We refer the reader to that work in order to see the study in more details. In this section, we just want to extract one of the strongest bounds, which comes from Electroweak Precision Tests (EWPT). Indeed, since the model modifies the coupling of the Z to all fermions, the decay rate to leptons, for example, is in principle modified. It turns out that a model is compatible with EWPT under the condition

$$\left(\frac{\delta}{0.1}\right)^2 \left(\frac{250\text{GeV}}{m_{Z'}}\right)^2 \lesssim 1 \ . \tag{13.390}$$

For a very light Z' of $m_{Z'} \sim 1$ GeV, the EWPT constraints require $\delta \lesssim 10^{-4}$, which is well above the WMAP constraints shown in Fig. 69. Also, since the model modifies the Z mass, constraints coming from the deviation of the SM prediction for the parameter $\rho \equiv M_W^2/M_Z^2 c_W^2$ are also expected to appear; however, they turn out to be weaker or similar to those of EWPT.

Direct Detection experiments, leaded by XENON [447, 448, 607], are able to put much more stronger bounds on the model. The dark matter candidate can scatter off a nucleus through a t-channel exchange of Z or Z' bosons (see e.g. [597–599] [608]). It turns out that for the dark matter and Z' masses considered, the XENON1T analysis is expected to push δ to values $\delta \lesssim 10^{-4}$, to say the strongest. Again here those bounds are not competitive with those shown in Fig. 69.

As an example of constraints coming from indirect detection, we can use synchrotron data. The dark matter particles in the region of the Galactic Centre can annihilate to produce electrons and positrons, which will emit synchrotron radiation as they propagate

through the magnetic fields of the galaxy. In [609] the authors constrain the kinetic mixing in the framework of freeze-out. The synchrotron data is able to put bounds on the parameter space of the model, provided that m_χ and $m_{Z'}$ are light enough (less than $\mathcal{O}(100)$ GeV), and for values of δ compatible with a thermal relic which are much larger than those required to fit a WMAP with a froze-in dark matter. So given the small δ values considered here, the synchrotron bounds are unconstraining.

13.5 Conclusions for Z' portal

In this section we have studied the genesis of dark matter by a Z' portal for a spectrum of Z' mass from above the reheating temperature down to a few GeV. Specifically, we have distinguished two regimes: 1) a very massive portal whose mass is above the reheating temperature T_{RH}, illustrated by effective, vector-like interactions between the SM fermions and the dark matter, and 2) a weak-like portal, illustrated by a kinetic-mixing model with an extra $U(1)$ boson, Z', which couples feebly to the SM but with unsuppressed couplings to the dark matter, similar to a secluded dark sector.

In the situation of very massive portal we solved the system of Boltzmann equations and obtained the expected dependance of the dark matter production with the reheating temperature. By requiring consistency with the WMAP/PLANCK's measurements of the non–baryonic relic abundance, the scale of the effective interaction Λ should be approximatively $\Lambda \simeq 10^{12}$ GeV, for $T_{RH} \approx 10^9$ GeV.

For lighter Z' that couples to the standard model through its kinetic mixing with the standard model $U(1)$ gauge field, we considered Z' masses in the 1 GeV–1 TeV range. The values of the kinetic mixing δ compatible with the relic abundance we obtained are $10^{-12} \lesssim \delta \lesssim 10^{-11}$ depending on the value of the Z' mass. For such values, the constraints coming from other experimental fields like direct or indirect detection and LHC production, become meaningless. However the bounds coming from the Big Bang nucleosynthesis can be quite important. For the study of the dark matter number density evolution, we looked at the effect of chemical equilibrium between dark matter and Z' on the final dark matter population, which turns out for the parameter space we considered to give a correction of at most a factor of 2.

Conclusion

In this PhD thesis we have studied in detail the Higgs sector in many theories. We have hunted Beyond the Standard Model behavior of the new scalar resonance recently discovered by the ATLAS and CMS collaborations. Starting from the Standard Model, the first thing to check is the self-coupling of the Higgs boson, the only one elementary scalar field that we know. An important part of this thesis was devoted to the Higgs sector of supersymmetric theories in the hope to promote the observed scalar as the lightest SUSY Higgs boson. Finally, as a new object could bring other new things, we focussed on the possible invisible width of the Higgs. We underlined the interesting interplay between collider searches and astrophysical-cosmological experimental results which start to severely constrains simple extensions of the Standard Model. We summarize in the next lines the main results that we have obtained during these last three years:

- We have studied in detail the main Higgs pair production processes at the LHC, gluon fusion, vector boson fusion, double Higgs–strahlung and associated production with a top quark pair. They allow for the determination of the trilinear Higgs self–coupling which represents a first important step towards the reconstruction of the Higgs potential and thus the final verification of the Higgs mechanism as the origin of electroweak symmetry breaking. It turns out that the gluon initiated process to ZHH production which contributes at NNLO is sizable in contrast to the single Higgs-strahlung case. We have discussed in detail the various uncertainties of the different processes. It turns out that they are of the order of 40% in the gluon fusion channel while they are much more limited in the vector bosons fusion and double Higgs–strahlung processes, i.e. below 10%. Within the SM we also studied the sensitivities of the double Higgs production processes to the trilinear Higgs self–coupling in order to get an estimate of how accurately the cross sections have to be measured in order to extract the Higgs self–coupling with sufficient accuracy. Furthermore, we have performed analysis for the dominant Higgs pair production process through gluon fusion in different final states which are $b\bar{b}\gamma\gamma$, $b\bar{b}\tau\bar{\tau}$ and $b\bar{b}W^+W^-$ with the W bosons decaying leptonically. Due to the smallness of the signal and the large QCD backgrounds the analysis is challenging. The $b\bar{b}W^+W^-$ final state leads to a very small signal to background ratio after applying acceptance and selection cuts so that it is not promising. On the other hand, the significances obtained in the $b\bar{b}\gamma\gamma$ and $b\bar{b}\tau\bar{\tau}$ final states after cuts are extremely promising.

- We have explored the impact of a Standard Model–like Higgs boson with a mass $M_h \approx 125$ GeV on supersymmetric theories in the context of both unconstrained and constrained MSSM scenarios. We have shown that in the phenomenological MSSM, strong restrictions can be set on the mixing in the top sector and, for instance, the no–mixing scenario is excluded unless the supersymmetry breaking scale is extremely large, $M_S \gg 1$ TeV, while the maximal mixing scenario is disfavored for large M_S and $\tan\beta$ values. In constrained MSSM scenarios, the impact is even stronger. Several scenarios, such as minimal AMSB and GMSB are disfavored as they lead to a too light h particle. In the mSUGRA case, including

the possibility that the Higgs mass parameters are non–universal, the allowed part of the parameter space should have large stop masses and A_0 values. In more constrained versions of this model such as the "no–scale" and approximate "cNMSSM" scenarios, only a very small portion of the parameter space is allowed by the Higgs mass bound. Significant areas of the parameter space of models with large M_S values leading to very heavy supersymmetric particles, such as split SUSY or high–scale SUSY, can also be excluded as, in turn, they tend to predict a too heavy Higgs particle with $M_h \gtrsim 125$ GeV.

- We have considered the production of the heavier H, A and $H^\pm$ bosons of the MSSM at the LHC, focusing on the low $\tan\beta$ regime, $\tan\beta \lesssim 3$–5. We have first shown that this area of the MSSM parameter space, which was long thought to be excluded, is still viable provided that the SUSY scale is assumed to be very high, $M_S \gtrsim 10$ TeV. For such M_S values, the usual tools that allow to determine the masses and couplings of the Higgs and SUSY particles in the MSSM, including the higher order corrections, become inadequate. We have used a simple but not too inaccurate approximation to describe the radiative corrections to the Higgs sector, in which the unknown scale M_S and stop mixing parameter X_t are traded against the measured h boson mass, $M_h \approx 125$ GeV. In the low $\tan\beta$ region, there is a plethora of new search channels for the heavy MSSM Higgs bosons that can be analyzed at the LHC. The neutral H/A states can be still be produced in the gluon fusion mechanism with large rates, and they will decay into a variety of interesting final states such as $H \to WW, ZZ$, $H \to hh$, $H/A \to t\bar{t}$, $A \to hZ$. Interesting decays can also occur in the case of the charged Higgs bosons, e.g. $H^+ \to hW, c\bar{s}, c\bar{b}$. These modes come in addition to the two channels $H/A \to \tau^+\tau^-$ and $t \to bH^+ \to b\tau\nu$ which are currently being studied by ATLAS and CMS and which are very powerful in constraining the parameter space at high $\tan\beta$ values and, as is shown here, also at low $\tan\beta$ values. All this promises a very nice and exciting program for Higgs searches at the LHC in both the present and future runs. One could then cover the entire MSSM parameter space: from above (at high $\tan\beta$) by improving the $H/A \to \tau\tau$ searches but also from below (at low $\tan\beta$) by using the $WW, ZZ, tt, ..$ searches. The coverage of the $[\tan\beta, M_A]$ plane will be done in a model independent way, with no assumption on M_S and possibly on any other SUSY parameter.

- We have discussed the hMSSM, i.e. the MSSM that we seem to have after the discovery of the Higgs boson at the LHC that we identify with the lighter h state. The mass $M_h \approx 125$ GeV and the non–observation of SUSY particles, seems to indicate that the soft–SUSY breaking scale might be large, $M_S \gtrsim 1$ TeV. We have shown, using both approximate analytical formulae and a scan of the MSSM parameters, that the MSSM Higgs sector can be described to a good approximation by only the two parameters $\tan\beta$ and M_A if the information $M_h = 125$ GeV is used. One could then ignore the radiative corrections to the Higgs masses and their complicated dependence on the MSSM parameters and use a simple formula to derive the other parameters of the Higgs sector, α, M_H and $M_{H^\pm}$. In a second step, we have shown that to describe accurately the h properties when the direct radiative corrections are also important, the three couplings c_t, c_b and c_V are needed besides the h mass. We have performed a fit of these couplings using the

latest LHC data and taking into account properly the theoretical uncertainties. In the limit of heavy sparticles, the best fit point turns out to be at low $\tan\beta$, and with a not too high CP–odd Higgs mass, $M_A \approx 560$ GeV. The phenomenology of this particular point is quite interesting. First, the heavier Higgs particles will be accessible in the next LHC run at least in the channels $A, H \to t\bar{t}$ and presumably also in the modes $H \to WW, ZZ$.

- We have analyzed the implications of the recent LHC Higgs results for generic Higgs-portal models of scalar, vector and fermionic dark matter particles. Requiring the branching ratio for invisible Higgs decay to be less than 10%, we find that the DM–nucleon cross section for electroweak–size DM masses is predicted to be in the range $10^{-9} - 10^{-8}$ pb in almost all of the parameter space. Thus, the entire class of Higgs-portal DM models will be probed by the XENON100–upgrade and XENON1T direct detection experiments, which will also be able to discriminate between the vector and scalar cases. The fermion DM is essentially ruled out by the current data, most notably by XENON100. Furthermore, we find that light Higgs-portal DM $M_{\rm DM} \lesssim 60$ GeV is excluded independently of its nature since it predicts a large invisible Higgs decay branching ratio, which should be incompatible with the production of an SM–like Higgs boson at the LHC. Finally, it will be difficult to observe the DM effects by studying Higgs physics at the LHC. Such studies can be best performed in Higgs decays at the planned e^+e^- colliders. However, the DM particles have pair production cross sections that are too low to be observed at the LHC and eventually also at future e^+e^- colliders unless very high luminosities are made available.

- We have shown that monojet searches at the LHC already provide interesting limits on invisible Higgs decays, constraining the invisible rate to be less than the total SM Higgs production rate at the 95% CL. This provides an important constrain on the models where the Higgs production cross section is enhanced and the invisible branching fraction is significant. Monojets searches are sensitive mostly to the gluon–gluon fusion production mode and, thus, they can also probe invisible Higgs decays in models where the Higgs coupling to the electroweak gauge bosons is suppressed. The limits could be significantly improved when more data at higher center of mass energies are collected, provided systematic errors on the Standard Model contribution to the monojet background can be reduced. We also analyzed in a model–independent way the interplay between the invisible Higgs branching fraction and the dark matter scattering cross section on nucleons, in the context of effective Higgs portal models. The limit $\mathrm{BR}_{\rm inv} < 0.2$, suggested by the combination of Higgs data in the visible channels, implies a limit on the direct detection cross section that is stronger than the current bounds from XENON100, for scalar, fermionic, and vectorial dark matter alike. Hence, in the context of Higgs-portal models, the LHC is currently the most sensitive dark matter detection apparatus.

- We have considered the possibility that the hidden sector contains more than one massive vector fields. In this case, an additional *dim*–4 interaction structure becomes possible. It couples the hypercharge field strength to the antisymmetric

combination of the massive vectors. The phenomenological signatures of such a coupling include missing energy in decays of various mesons and Z, as well as monojet and monophoton production at the LHC. The hidden sector may possess a Z_2 symmetry, which would make the lighter vector field stable and a good dark matter candidate. The characteristic signature of this scenario is monochromatic gamma–ray emission from the Galactic Center, while the corresponding continuum contribution is suppressed. We find that this possibility is consistent with other constraints, including those from the LHC and direct DM detection. Large portions of the allowed parameter space can be probed both by indirect DM detection and the LHC monophoton searches.

- We have shown that it is possible to produce dark matter through non–equilibrium thermal processes in the context of $SO(10)$ models which respect the WMAP constraints. Insisting on gauge coupling unification, we have demonstrated that there exists a tight link between the reheating temperature and the scheme of the $SO(10)$ breaking to the SM gauge group. Interestingly, the numerical values we obtained are quite high and very compatible with inflationary and leptogenesis-like models.

- We have studied the genesis of dark matter by a Z' portal for a spectrum of Z' mass from above the reheating temperature down to a few GeV. Specifically, we have distinguished two regimes: a very massive portal whose mass is above the reheating temperature T_{RH}, illustrated by effective, vector-like interactions between the SM fermions and the dark matter, and a second regime with a weak-like portal, illustrated by a kinetic-mixing model with an extra $U(1)$ boson, Z', which couples feebly to the SM but with unsuppressed couplings to the dark matter, similar to a secluded dark sector. In the case of very massive portal we get the expected dependance of the dark matter production with the reheating temperature. By requiring consistency with the WMAP/PLANCK's measurements of the non–baryonic relic abundance, the scale of the effective interaction Λ should be approximatively $\Lambda \simeq 10^{12}$ GeV, for $T_{RH} \approx 10^9$ GeV. For lighter Z' that couples to the standard model through its kinetic mixing with the standard model $U(1)$ gauge field, we considered Z' masses in the 1 GeV–1 TeV range. The values of the kinetic mixing δ compatible with the relic abundance we obtained are $10^{-12} \lesssim \delta \lesssim 10^{-11}$ depending on the value of the Z' mass.

The ~ 125 GeV Higgs boson closes the first chapter of the probing of the mechanism that triggers the breaking of the electroweak symmetry and generates the fundamental particle masses. As shown by this thesis, we have now entered a new era and the Higgs, or something else should give us the direction to follow in order to transcend the Standard Model of particle physics.

A Dark matter pair production at colliders

The models

As discussed earlier in the text, we study the models defined by the following Lagrangian

$$\begin{aligned}
\Delta\mathcal{L}_S &= -\frac{1}{2}m_S^2 S^2 - \frac{1}{4}\lambda_S S^4 - \frac{1}{4}\lambda_{hSS} H^\dagger H S^2 \,, \\
\Delta\mathcal{L}_V &= \frac{1}{2}m_V^2 V_\mu V^\mu + \frac{1}{4}\lambda_V (V_\mu V^\mu)^2 + \frac{1}{4}\lambda_{hVV} H^\dagger H V_\mu V^\mu, \\
\Delta\mathcal{L}_f &= -\frac{1}{2}m_f \bar{\chi}\chi - \frac{1}{4}\frac{\lambda_{hff}}{\Lambda} H^\dagger H \bar{\chi}\chi \,.
\end{aligned} \tag{1.391}$$

From these different Lagrangian we can explicitly write the coupling of the Higgs to the dark matter candidate depending on its nature scalar, fermionic or vectorial

$$\begin{aligned}
g_{hSS} &= i\frac{v\lambda_{hSS}}{\sqrt{2}} \,, \\
g_{h\chi\chi} &= i\frac{v\lambda_{h\chi\chi}}{\sqrt{2}\Lambda} \,, \\
g_{hVV} &= -i\frac{v\lambda_{hVV}}{\sqrt{2}} \,.
\end{aligned} \tag{1.392}$$

We define in the following the convenient quantities called Q_i, that we will use for all the channels where we have to integrate over a phase space of two final state particles, i.e in gluon fusion at Leading Order (LO) and in vector boson fusion with the longitudinal approximation, these quantities read

$$\begin{aligned}
Q_S &= |g_{hSS}|^2 \,, \\
Q_\chi &= |g_{h\chi\chi}|^2 \sum_{s,s'} \left| \bar{u}^s(\chi) v^{s'}(\bar{\chi}) \right|^2 \,, \\
Q_V &= |g_{hVV}|^2 \sum_{s,s'} \left| \epsilon^s_\alpha(\chi) \epsilon^{s',\alpha}(\bar{\chi}) \right|^2 \,.
\end{aligned} \tag{1.393}$$

These quantities can be written in function of the velocity in the center of mass frame defined as $\beta_X = \sqrt{1 - 4M_X^2/s}$, they read

$$\begin{aligned}
Q_S &= |g_{hSS}|^2 \,, \\
Q_\chi &= |g_{h\chi\chi}|^2 \, 2s\beta_\chi^2, \\
Q_V &= |g_{hVV}|^2 \left[2 + \left(\frac{1+\beta_V^2}{1-\beta_V^2} \right)^2 \right] \,.
\end{aligned} \tag{1.394}$$

In the case where the dark matter is produced in association with a vector boson the final state contains three particles and we will use the equivalent of the Q_i functions that we will describe explicitly in the following.

Cross section at the LHC

Dark matter production in gluon fusion process

Leading order production

At leading order, dark matter pair production via gluon fusion is mediated by triangle diagrams of heavy quarks (top quark and b quark to a lesser extent). The partonic LO cross section can be expressed as

$$\hat{\sigma}_{\rm LO}(gg \to \chi\bar{\chi}) = \int_{\hat{t}_-}^{\hat{t}_+} d\hat{t}\, \frac{\alpha_s^2(\mu)}{2048(2\pi)^3} \left| \frac{F_\triangle}{\hat{s} - m_h^2 + i m_h \Gamma_h} \right|^2 Q_i. \tag{1.395}$$

The Mandelstam variables for the parton process are given by

$$\begin{aligned} \hat{s} &= Q^2, \\ \hat{t} &= -\frac{1}{2}\left[Q^2 - 2M_\chi^2 - \sqrt{\lambda(Q^2, M_\chi^2, M_\chi^2)}\cos\theta\right], \\ \hat{u} &= -\frac{1}{2}\left[Q^2 - 2M_\chi^2 + \sqrt{\lambda(Q^2, M_\chi^2, M_\chi^2)}\cos\theta\right], \end{aligned} \tag{1.396}$$

where θ is the scattering angle in the partonic c.m. system with invariant mass Q, and

$$\lambda(x, y, z) = (x - y - z)^2 - 4yz. \tag{1.397}$$

The integration limits of Eq. (1.395) read

$$\hat{t}_\pm = -\frac{1}{2}\left[Q^2 - 2M_\chi^2 \mp \sqrt{\lambda(Q^2, M_\chi^2, M_\chi^2)}\right] . \tag{1.398}$$

In term of the scattering angle θ, it corresponds to $\cos\theta = \pm 1$. The scale parameter μ is the renormalization scale. The form factor $F_\triangle$ is a function of the mass of the quark which enter the loop, m_Q, through the scaling variable $\tau_Q = 4m_Q^2/\hat{s}$, it reads

$$F_\triangle = \tau_Q \left[1 + (1 - \tau_Q) f(\tau_Q)\right] ,$$

with

$$f(\tau_Q) = \begin{cases} \arcsin^2 \dfrac{1}{\sqrt{\tau_Q}} & \tau_Q \geq 1 \\ -\dfrac{1}{4}\left[\log \dfrac{1 + \sqrt{1 - \tau_Q}}{1 - \sqrt{1 - \tau_Q}} - i\pi\right]^2 & \tau_Q < 1 \end{cases}$$

The total cross section for dark matter pair production through gluon fusion in proton collisions can be derived by integrating over the scattering angle and the gluon-gluon luminosity as written by the following equation

$$\sigma_{\rm LO}(pp \to gg \to \chi\bar{\chi}) = \int_{4M_\chi^2/s}^1 d\tau \frac{d\mathcal{L}^{gg}}{d\tau} \hat{\sigma}(\hat{s} = \tau s) . \tag{1.399}$$

Dark matter production with one jet in gluon fusion process

In the low-energy limit of vanishing Higgs four-momentum, the Higgs-field operator acts as a constant field. In this limit it is possible to derive an effective Lagrangian for the interactions of the Higgs bosons with gauge bosons, which is valid for a 125 GeV Higgs bosons. This effective Lagrangian has been successfully used to compute the QCD corrections to a number of processes, in particular to single-Higgs and double-Higgs production from gluon fusion at the LHC. In this case, the result of using the low-energy theorems has been shown to agree with the exact two-loop calculation to better than 10%. We will also make use of the low-energy theorems to compute QCD corrections to dark matter pair production via gluons fusion.

According to the Feynman rules for the effective interactions, the calculation has been carried out in dimensional regularization with $n = 4 - 2\epsilon$ dimensions. The strong coupling has been renormalized in the $\overline{\rm MS}$ scheme including five light-quark flavours, i.e. decoupling the top quark in the running of α_s.

The collinear initial-state singularities are left over in the partonic cross sections. Those divergences have been absorbed into the NLO parton densities, defined in the $\overline{\rm MS}$ scheme with five light-quark flavours. We end up with finite results, which can be cast into the form

$$\sigma_{\rm LO}(pp \to \chi\bar{\chi} + jet) = \Delta\sigma_{gg} + \Delta\sigma_{gq} \tag{1.400}$$

with the individual contributions

$$\begin{aligned}
\Delta\sigma_{gg} &= \frac{\alpha_s(\mu)}{\pi}\int_{\tau_0}^1 d\tau\,\frac{d\mathcal{L}^{gg}}{d\tau}\int_{\tau_0/\tau}^1\frac{dz}{z}\,\hat{\sigma}_{\rm LO}(Q^2 = z\tau s)\left\{-zP_{gg}(z)\log\frac{M^2}{\tau s}\right.\\
&\qquad\left. -\frac{11}{2}(1-z)^3 + 6[1+z^4+(1-z)^4]\left(\frac{\log(1-z)}{1-z}\right)_+\right\},\\
\Delta\sigma_{gq} &= \frac{\alpha_s(\mu)}{\pi}\int_{\tau_0}^1 d\tau\sum_{q,\bar{q}}\frac{d\mathcal{L}^{gq}}{d\tau}\int_{\tau_0/\tau}^1\frac{dz}{z}\,\hat{\sigma}_{\rm LO}(Q^2 = z\tau s)\left\{-\frac{z}{2}P_{gq}(z)\log\frac{M^2}{\tau s(1-z)^2}\right.\\
&\qquad\left. +\frac{2}{3}z^2 - (1-z)^2\right\}
\end{aligned} \tag{1.401}$$

where $\tau_0 = \frac{4M_\chi^2}{s}$. The objects $P_{gg}(z), P_{gq}(z)$ denote the Altarelli–Parisi splitting functions

$$\begin{aligned}
P_{gg}(z) &= 6\left\{\left(\frac{1}{1-z}\right)_+ + \frac{1}{z} - 2 + z(1-z)\right\} + \frac{33-2N_F}{6}\delta(1-z),\\
P_{gq}(z) &= \frac{4}{3}\frac{1+(1-z)^2}{z},
\end{aligned} \tag{1.402}$$

where $N_F = 5$ in our case. The factorization scale of the parton–parton luminosities $d\mathcal{L}^{ij}/d\tau$ is denoted by M.

In Fig.70,71,72 we show the cross section of this process for respectively a scalar, fermionic and vectorial dark matter.

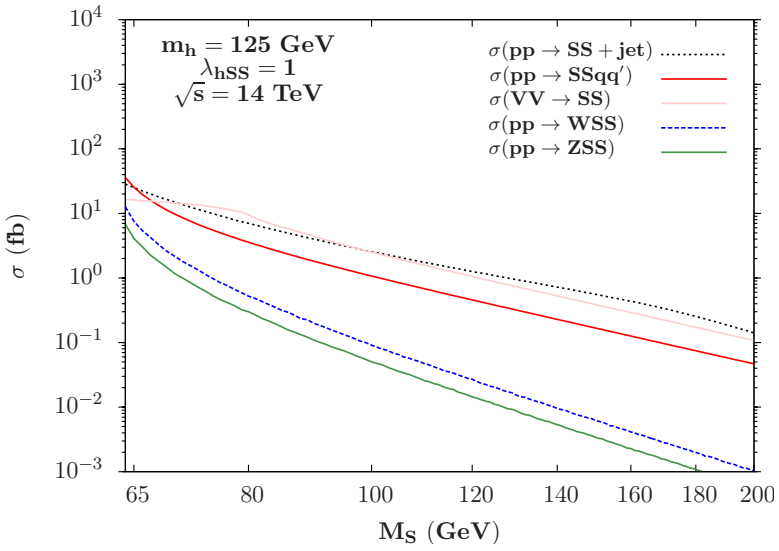

Figure 70: Scalar DM pair production cross sections at the LHC with $\sqrt{s} = 14$ TeV as a function of their mass for $\lambda_{hSS} = 1$. We consider the processes $pp \to ZSS, WSS$ (green,dotted blue) , $pp \to W^*W^* + Z^*Z^* \to SSqq$ in the longitudinal vector boson approximation (pink) and the exact result (red), and $pp \to SS + \text{jet}$ (dotted black).

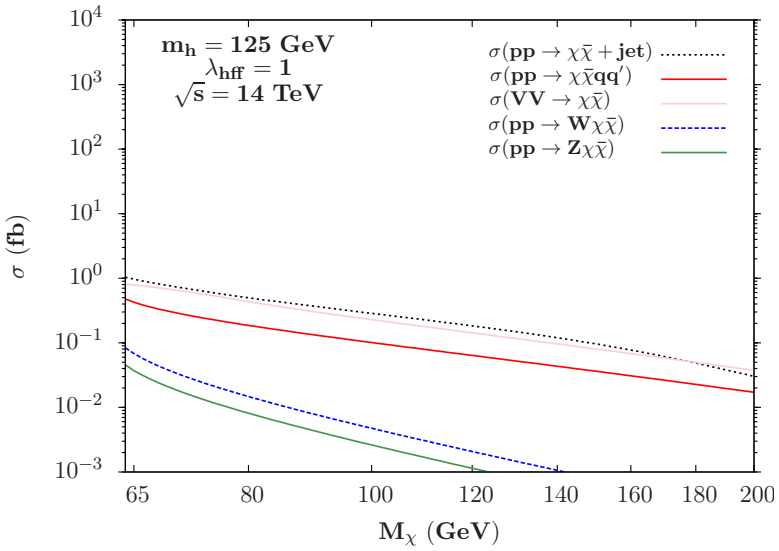

Figure 71: Fermion DM pair production cross sections at the LHC with $\sqrt{s} = 14$ TeV as a function of their mass for $\lambda_{hSS} = 1$. We consider the processes $pp \to ZSS, WSS$ (green,dotted blue) , $pp \to W^*W^* + Z^*Z^* \to SSqq$ in the longitudinal vector boson approximation (pink) and the exact result (red), and $pp \to SS + \text{jet}$ (dotted black).

Dark matter production in vector boson fusion processes

At high energies, one expects dark matter pair production in the vector boson fusion channel to have a substantial cross section since the longitudinal vector bosons have couplings to the Higgs which grow with energy. The cross section for $qq' \to V^*V^* \to \chi\bar{\chi}qq'$ is calculated in the longitudinal vector boson approximation in which one computes the

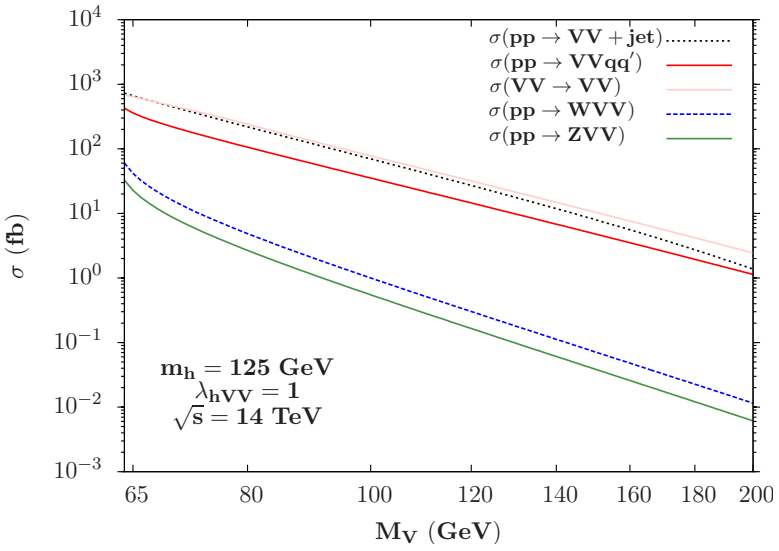

Figure 72: Vector DM pair production cross sections at the LHC with $\sqrt{s} = 14$ TeV as a function of their mass for $\lambda_{hSS} = 1$. We consider the processes $pp \to ZSS, WSS$ (green,dotted blue) , $pp \to W^*W^* + Z^*Z^* \to SSqq$ in the longitudinal vector boson approximation (pink) and the exact result (red), and $pp \to SS + \text{jet}$ (dotted black).

cross section for the $2 \to 2$ process $V_L V_L \to \chi\bar{\chi}$. Denoting by $\beta_{V,i}$ the velocities of V and the dark matter candidate in the VV c.m frame, one obtains

$$\hat{\sigma}_{V_L V_L} = \sigma(V_L^\star V_L^\star \to ii, \hat{s}) = \frac{G_F^2 M_V^4 v^2}{2\pi\hat{s}} \frac{\beta_i}{\beta_V} \left[\frac{1+\beta_V^2}{1-\beta_V^2} \frac{1}{(\hat{s}-m_h^2)} \right]^2 Q_i \tag{1.403}$$

with $V = Z, W^\pm$.

This last expression has to be folded with the longitudinal vector boson luminosity spectra 1.407 in order to obtain the $qq' \to \chi\bar{\chi}qq'$ cross section, which again has to be convoluted with the parton densities to obtain the full hadronic cross section

$$\sigma(pp \to V^\star V^\star \to iiqq') \simeq \int_{4M_i^2/s}^1 \mathrm{d}\tau \frac{\mathrm{d}\mathcal{L}}{\mathrm{d}\tau}\bigg|_{V_L V_L/pp} \sigma(V_L^\star V_L^\star \to ii, \hat{s} = \tau s) \tag{1.404}$$

with Q_i beeing Q_S, Q_χ or Q_V depending on the nature of the dark matter candidate as defined previously in 1.394. The longitudinal vector boson luminosity is defined as follow

$$\frac{\mathrm{d}\mathcal{L}}{\mathrm{d}\tau}\bigg|_{V_L V_L/pp} = \sum_{q,q'} \int_\tau^1 \frac{\mathrm{d}\tau'}{\tau'} \frac{\mathrm{d}\mathcal{L}^{\mathrm{qq}'}}{\mathrm{d}\tau'} \frac{\mathrm{d}\mathcal{L}}{\mathrm{d}\xi}\bigg|_{V_L V_L/qq'} \tag{1.405}$$

with $\xi = \tau/\tau'$ and the classical quark-quark luminosity

$$\frac{\mathrm{d}\mathcal{L}^{\mathrm{qq}'}}{\mathrm{d}\tau} = \int_\tau^1 \frac{\mathrm{dx}}{x} q(x;Q^2) q'(\tau/x;Q^2) \; . \tag{1.406}$$

About the scale, we make the typical choice $Q = m_h$. Then, the longitudinal vector boson luminosity reads

$$\left.\frac{\mathrm{d}\mathcal{L}}{\mathrm{d}\tau}\right|_{V_L V_L/qq'} = \frac{\alpha^2(\hat{a}_q^2+\hat{v}_q^2)^2}{\pi^2}\frac{1}{\tau}\left[(1+\tau)\ln(1/\tau) - 2(1-\tau)\right]. \tag{1.407}$$

$\hat{v}_f, \hat{a}_f$ are respectively the reduced vector and axial vector coupling of the fermion f to the V boson. In terms of the electric charge Q_f of the fermion f and with $I_f^3 = \pm\frac{1}{2}$ the left–handed weak isospin of the fermion and the weak mixing angle $s_W^2 \equiv \sin^2\theta_W$, one can write the reduced couplings of the fermion f to the Z boson as

$$\hat{v}_f = 2I_f^3 - 4Q_f s_W^2 \quad , \hat{a}_f = 2I_f^3 \,. \tag{1.408}$$

In the case of the W boson, its vector and axial–vector reduced couplings to fermions are simply

$$\hat{v}_f = \hat{a}_f = \sqrt{2} \tag{1.409}$$

(These results are only valid in the one–family approximation.)

In Fig.70,71,72 we show the cross section of this process for respectively a scalar, fermionic and vectorial dark matter.

Dark matter production in association with a gauge boson

In the case of dark matter pair production in association with a gauge boson the cross section reads

$$\sigma(pp \to V^\star \to Vii) = \int_{\frac{(2m_h^2+M_V)^2}{s}}^1 \mathrm{d}\tau \frac{\mathrm{d}\mathcal{L}^{\mathrm{qq}'}}{\mathrm{d}\tau}\hat{\sigma}(\mathrm{qq}' \to \mathrm{Vii}; \hat{\mathrm{s}} = \tau \mathrm{s}) \tag{1.410}$$

with

$$\hat{\sigma}(qq' \to Vii; \hat{s} = \tau s) = \int_0^1 \mathrm{d}x_1 \int_{1-x_1}^1 \mathrm{d}x_2 \frac{G_F^3 M_V^2 v^2}{192\sqrt{2}\pi^3 s}\frac{(\hat{a}_q^2+\hat{v}_q^2)}{(1-\mu_V)^2}\mathcal{Z}Q_i \tag{1.411}$$

since there is three particles in the final state, we define the adequate Q_i quantities as written in the following (we can check that in the limit $M_V = 0$ we re-obtain the Eq. (1.394))

$$\begin{aligned} Q_S &= |g_{hSS}|^2 \,, \\ Q_\chi &= |g_{h\chi\chi}|^2 \, 2s\left[(1-x_3) + \mu_Z - 4\mu_\chi\right], \\ Q_V &= |g_{hVV}|^2 \frac{1}{\mu_V^2}\left[2\mu_V^2 + \frac{1}{4}(1-x_3+\mu_Z-2\mu_V)^2\right] . \end{aligned} \tag{1.412}$$

We also used the parameter $\mathcal{Z}$ defined as

$$\mathcal{Z} = \frac{1}{4}\frac{\mu_Z(x_3^2+8\mu_Z)}{(1-x_3+\mu_Z-\mu_h)^2} \,. \tag{1.413}$$

In Fig.70,71,72 we show the cross section of this process for respectively a scalar, fermionic and vectorial dark matter.

Cross section at e^+e^- collider such as CLIC

We now concentrate on dark matter pair production through e^+e^- annihilations [610].

Dark matter production in Z boson fusion process

Concerning dark matter pair production in Z boson fusion process, the expression of the cross section reads

$$\sigma(e^+e^- \to Z^\star Z^\star \to ii\ell\ell) \simeq \int_{4M_i^2/s}^1 \mathrm{d}\tau \frac{\mathrm{d}\mathcal{L}}{\mathrm{d}\tau}\bigg|_{Z_L Z_L/ee} \hat{\sigma}_{Z_L Z_L} \tag{1.414}$$

using the longitudinal approximation, i.e the expression

$$\hat{\sigma}_{Z_L Z_L} = \sigma(e^+e^- \to Z_L^\star Z_L^\star \to ii\ell\ell, \hat{s} = \tau s) = \frac{G_F^2 M_Z^4 v^2}{2\pi\hat{s}} \frac{\beta_i}{\beta_V} \left[\frac{1+\beta_Z^2}{1-\beta_Z^2} \frac{1}{(\hat{s}-M_h^2)}\right]^2 Q_i \,. \tag{1.415}$$

and

$$\frac{\mathrm{d}\mathcal{L}}{\mathrm{d}\tau}\bigg|_{Z_L Z_L/ee} = \int_\tau^1 P_{Z_L/e}(z) P_{Z_L/e}(\tau/z) \frac{\mathrm{d}z}{z} \,, \tag{1.416}$$

$$\frac{\mathrm{d}\mathcal{L}}{\mathrm{d}\tau}\bigg|_{Z_L Z_L/ee} = \frac{\alpha^2(\hat{a}_e^2+\hat{v}_e^2)^2}{\pi^2} \frac{1}{\tau} \left[(1+\tau)\ln(1/\tau) - 2(1-\tau)\right], \tag{1.417}$$

and with $Q_i = Q_S, Q_\chi, Q_V$ defined as in the hadronic case 1.394.

In Fig.73 we show the cross section of this process for a scalar, fermionic and vectorial dark matter candidate.

Dark matter production in association with a gauge boson

The dark matter pair production in association with a gauge boson in lepton collider has a cross section which can be written as

$$\sigma(e^+e^- \to Z^\star \to Zii) = \int_0^1 \mathrm{d}x_1 \int_{1-x_1}^1 \mathrm{d}x_2 \frac{G_F^3 m_Z^2 v^2}{192\sqrt{2}\pi^3 s} \frac{(\hat{a}_e^2+\hat{v}_e^2)}{(1-\mu_Z)^2} \mathcal{Z} Q_i, \tag{1.418}$$

with $i = S, \chi, V$ corresponding to the Scalar, Majorana fermion or Vector Dark Matter case. Where the electron–Z couplings are defined as $\hat{a}_e = -1$ and $\hat{v}_e = -1 + 4\sin^2\theta_W$, $x_{1,2} = 2E_{1,2}/\sqrt{s}$ are the scaled energies of the two dark matter candidates, $x_3 = 2 - x_1 - x_2$ is the scaled energy of the Z boson; the scaled masses are denoted by $\mu_i = M_i^2/s$. In terms of these variables, the coefficient $\mathcal{Z}$ still reads as

$$\mathcal{Z} = \frac{1}{4} \frac{\mu_Z(x_3^2 + 8\mu_Z)}{(1 - x_3 + \mu_Z - \mu_h)^2} \,. \tag{1.419}$$

Since there is three particles in the final state, we use the following definitions

$$
\begin{aligned}
Q_S &= |g_{hSS}|^2 \ , \\
Q_\chi &= |g_{h\chi\chi}|^2 \, 2s \left[(1 - x_3) + \mu_Z - 4\mu_\chi \right] , \\
Q_V &= |g_{hVV}|^2 \, \frac{1}{\mu_V^2} \left[2\mu_V^2 + \frac{1}{4}(1 - x_3 + \mu_Z - 2\mu_V)^2 \right] \ .
\end{aligned} \tag{1.420}
$$

In Fig.73 we show the cross section of this process for a scalar, fermionic and vectorial dark matter candidate.

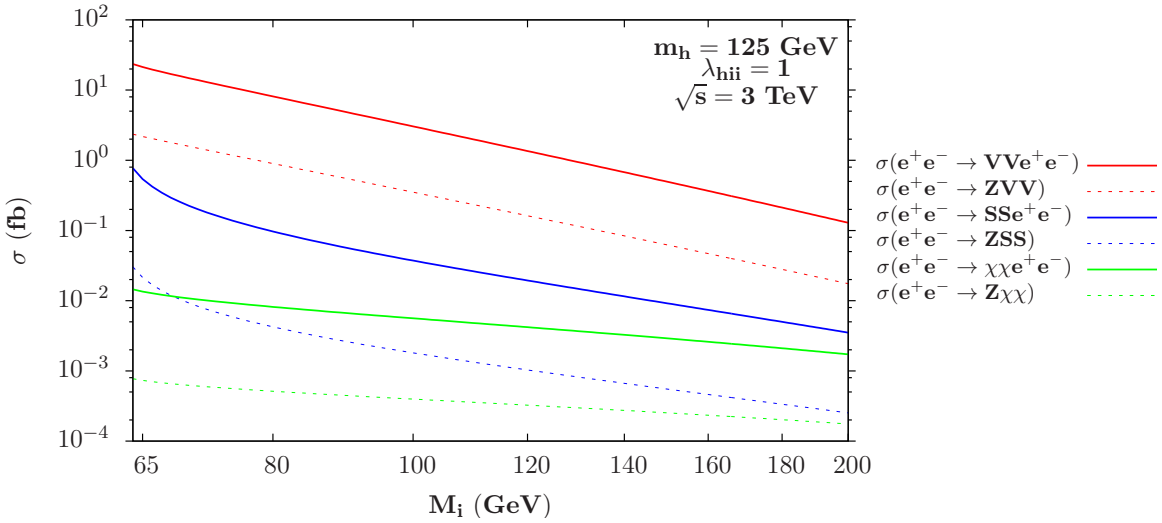

Figure 73: Scalar, fermion and vector DM pair production cross sections in the processes $e^+e^- \to Zii$ and $ZZ \to ii$ with $\sqrt{s} = 3$ TeV, as a function of their mass for $\lambda_{hii} = 1$.

B Synopsis

La brisure spontanée de la symétrie électro-faible est un pilier essentiel des théories modernes des interactions faibles. Dans le Modèle Standard, un seul doublet de champ scalaire est nécessaire pour briser la symétrie, donnant naissance à l'unique boson de Higgs de la théorie, témoin et relique de cette brisure. La découverte de cette particule par le LHC (Large Hadron Collider) et la détermination de ses propriétés fondamentales constituent de fait le test le plus crucial du Modèle Standard.

B.1 Le boson de Higgs dans le Modèle Standard

Dans ce prélude nous faisons un bref résumé de l'interaction forte, électro-faible et du mécanisme de brisure de la symétrie électro-faible du Modèle Standard (SM).

B.1.1 Le Modèle Standard avant la brisure de la symétrie électro-faible

La théorie électro-faible de Glashow-Weinberg-Salam décrit l'électromagnétisme et les interactions faibles par l'intermédiaire des quarks et des leptons. Il s'agit d'une théorie de Yang-Mills basée sur les groupes[57] de symétries $SU(2)_L \times U(1)_Y$. Lorsqu'on y ajoute le groupe de symétrie $SU(3)_C$ de la théorie de jauge QCD qui décrit l'interaction forte entre les quarks, nous obtenons une théorie décrivant trois des quatre forces de la Nature : c'est le Modèle Standard. Avant d'introduire la notion de brisure spontanée de la brisure électro-faible, le modèle possède deux types de champs :

- Les champs de matière, c'est-à-dire les trois générations de quarks et de leptons chiraux droits ou gauches, $f_{R,L} = \frac{1}{2}(1 \pm \gamma^5)f$. Les fermions gauches sont dans des isodoublets de l'interaction faible tandis que les fermions droits sont des isosingulets de l'interaction faible

$$I_f^{3L,3R} = \pm\frac{1}{2}, 0: \quad \begin{array}{lllll} L_1 = \begin{pmatrix}\nu_e \\ e^-\end{pmatrix}_L & , & e_{R_1} = e_R^- & , & Q_1 = \begin{pmatrix}u \\ d\end{pmatrix}_L \quad , \quad u_{R_1} = u_R, d_{R_1} = d_R \\ L_2 = \begin{pmatrix}\nu_\mu \\ \mu^-\end{pmatrix}_L & , & e_{R_2} = \mu_R^- & , & Q_2 = \begin{pmatrix}c \\ s\end{pmatrix}_L \quad , \quad u_{R_2} = c_R, d_{R_2} = s_R \\ L_3 = \begin{pmatrix}\nu_\tau \\ \tau^-\end{pmatrix}_L & , & e_{R_3} = \tau_R^- & , & Q_3 = \begin{pmatrix}t \\ b\end{pmatrix}_L \quad , \quad u_{R_3} = t_R, d_{R_3} = b_R \end{array}$$

  L'hypercharge des fermions est définie en fonction de la troisième composante de l'isospin faible I_f^3 et de la charge électrique Q_f (en unité de $+e$), pour $i = 1, 2, 3$ la relation de Gell-Mann-Nishijima s'écrit

$$Y_f = 2Q_f - 2I_f^3 \Rightarrow Y_{Li} = -1, Y_{e_{R_i}} = -2, \quad Y_{Q_i} = \frac{1}{3}, \quad Y_{u_{R_i}} = \frac{4}{3}, \quad Y_{d_{R_i}} = -\frac{2}{3}$$

  De plus les quarks sont des triplets du groupe $SU(3)_C$, alors que les leptons sont des singulets de couleur. Ce qui mène à la relation qui sert à annuler les anomalies

[57] Stricto sensu il s'agit des algèbres de Lie, mais nous ferons souvent cet abus en considérant plus généralement le groupe de Lie associé

de jauge

$$\sum_f Y_f = \sum_f Q_f = 0 \tag{2.421}$$

- Il y a les champs de jauge associés aux bosons de jauge de spin un, médiateurs des interactions. Dans le secteur électro-faible nous avons le champ B_μ qui correspond au générateur Y du groupe $U(1)_Y$ ainsi que les trois champs $W_\mu^{1,2,3}$ qui correspondent aux générateurs T^a (avec a=1,2,3) du groupe $SU(2)_L$. Ces générateurs sont en fait équivalents à la moitié des matrices 2×2 de Pauli

$$T^a = \frac{1}{2}\tau^a; \quad \tau_1 = \begin{pmatrix} 0 & 1 \\ 1 & 0 \end{pmatrix}, \quad \tau_2 = \begin{pmatrix} 0 & -i \\ i & 0 \end{pmatrix}, \quad \tau_3 = \begin{pmatrix} 1 & 0 \\ 0 & -1 \end{pmatrix} \tag{2.422}$$

et ces générateurs satisfont les relations de commutation

$$[T^a, T^b] = i\epsilon^{abc} T_c \quad \text{et} \quad [Y, Y] = 0 \tag{2.423}$$

où ϵ^{abc} est le tenseur complètement antisymétrique. Dans le secteur de l'interaction forte il y a un octet de champs de gluons $G_\mu^{1,\dots,8}$ qui correspondent aux huit générateurs du groupe $SU(3)_C$ (équivalents à la moitié des huit matrices 3×3 de Gell-Mann) qui vérifient

$$[K^a, K^b] = i f^{abc} K_c \quad \text{et} \quad Tr[K^a K^b] = \frac{1}{2}\delta_{ab} \tag{2.424}$$

où le tenseur f^{abc} regroupe les constantes de structure du groupe $SU(3)_C$. Les tenseurs de force sont donnés par

$$G^a_{\mu\nu} = \partial_\mu G^a_\nu - \partial_\nu G^a_\mu + g_s f^{abc} G^b_\mu G^c_\nu \tag{2.425}$$

$$W^a_{\mu\nu} = \partial_\mu W^a_\nu - \partial_\nu W^a_\mu + g_2 \epsilon^{abc} W^b_\mu W^c_\nu \tag{2.426}$$

$$B_{\mu\nu} = \partial_\mu B_\nu - \partial_\nu B_\mu \tag{2.427}$$

où g_s, g_2 et g_1 sont respectivement les constantes de couplage des groupes de jauge $SU(3)_C$, $SU(2)_L$ et $U(1)_Y$. A cause de la nature non abélienne des groupes $SU(2)$ et $SU(3)$, il y a des termes d'auto-interaction entre leur champs de jauge, $V_\mu = W_\mu$ ou G_μ, menant à des couplages entre trois voire quatre bosons de jauge. Les champs de matière Ψ sont couplés de manière minimale aux champs de jauge par l'intermédiaire de la dérivée covariante D_μ, qui est définie dans le cas des quarks par

$$D_\mu \Psi = \left(\partial_\mu - i g_s K_a G^a_\mu - i g_2 T_a W^a_\mu - i g_1 \frac{Y_q}{2} B_\mu\right)\Psi \tag{2.428}$$

menant à d'uniques couplages entre champs de matière et champs de jauge de la forme $g_i \bar{\Psi} V_\mu \gamma_\mu \Psi$.

Le Lagrangien du Modèle Standard, sans les termes de masses pour les fermions ni pour les bosons de jauge, s'écrit alors de la façon suivante

$$\begin{aligned} \mathcal{L}_{SM} = & -\frac{1}{4} G^a_{\mu\nu} G^{\mu\nu}_a - \frac{1}{4} W^a_{\mu\nu} W^{\mu\nu}_a - \frac{1}{4} B_{\mu\nu} B^{\mu\nu} \\ & + \bar{L}_i i D_\mu \gamma^\mu L_i + \bar{e}_{R_i} i D_\mu \gamma^\mu e_{R_i} + \bar{Q}_i i D_\mu \gamma^\mu Q_i + \bar{u}_{R_i} i D_\mu \gamma^\mu u_{R_i} + \bar{d}_{R_i} i D_\mu \gamma^\mu d_{R_i} \end{aligned}$$

Ce Lagrangien est invariant sous les transformations de jauge locales des champs fermioniques et de jauges. Par exemple dans le secteur électro-faible on a

$$L(x) \to L'(x) = e^{i\alpha_a(x)T^a + i\beta(x)Y} L(x), \quad R(x) \to R'(x) = e^{i\beta(x)Y} R(x) \quad (2.429)$$

$$\vec{W}_\mu(x) \to \vec{W}_\mu(x) - \frac{1}{g_2}\partial_\mu \vec{\alpha}(x) - \vec{\alpha}(x) \times \vec{W}_\mu(x), \quad B_\mu \to B_\mu(x) - \frac{1}{g_1}\partial_\mu \beta(x) \quad (2.430)$$

Jusqu'à maintenant les champs de jauge ainsi que les champs fermioniques sont gardés sans masse. Dans le cas de l'interaction forte, les gluons sont en effet sans masse et on peut fabriquer des termes de masse de la forme $m_q \bar{\Psi}\Psi$ pour les quarks et les leptons invariants sous les transformations de jauge du groupe $SU(3)$. Dans le cas du secteur électro-faible, la situation est bien plus délicate :

- Si nous ajoutons un terme de masse de la forme, $\frac{1}{2}M_V^2 W_\mu W^\mu$, pour les champs de jauge (ce que nous souhaitons, puisque expérimentalement il a été démontré qu'ils sont massifs) alors on viole l'invariance locales sous les transformations de jauge $SU(2) \times U(1)$. On peut mieux comprendre cela grâce à l'analogie avec le fait qu'en QED le photon est sans masse à cause de la symétrie locale $U(1)_Q$

$$\frac{1}{2}M_A^2 A_\mu A^\mu \to \frac{1}{2}M_A^2 \Big(A_\mu - \frac{1}{e}\partial_\mu \alpha\Big)\Big(A^\mu - \frac{1}{e}\partial^\mu \alpha\Big) \neq \frac{1}{2}M_A^2 A_\mu A^\mu \quad (2.431)$$

- De plus, si nous ajoutions explicitement un terme de masse de la forme $m_f \bar{\Psi}\Psi$ pour chaque fermion f du SM dans le Lagrangien, nous aurions par exemple pour l'électron

$$m_e \bar{e}e = m_e \bar{e}\Big(\frac{1}{2}(1-\gamma^5) + \frac{1}{2}(1+\gamma^5)\Big)e = m_e(\bar{e}_R e_L + \bar{e}_L e_R) \quad (2.432)$$

  ce qui est manifestement non-invariant sous les transformations de $SU(2)_L$ puisque e_L est un élément d'un doublet de $SU(2)_L$ alors que e_R est élément d'un singulet.

Ainsi, incorporer de manière brutale des termes de masse pour les bosons de jauge et pour les fermions brise automatiquement l'invariance sous les transformations de jauge locale associées à $SU(2)_L \times U(1)_Y$. En conséquence nous devons soit abandonner le fait que $M_Z \sim 90$ GeV et que $m_e \sim 0.5$ MeV soit abandonner l'idée que la symétrie de jauge imposée à la théorie soit exacte (non-brisée). La question qui s'est posée dans les années soixante est la suivante : est-il possible de fabriquer la masse des bosons de jauge ainsi que celle des fermions sans violer l'invariance de jauge $SU(2) \times U(1)$? La réponse est oui et s'explique grâce au mécanisme de brisure spontanée de symétrie (mécanisme de Higgs) proposé par Brout-Englert-Higgs. En introduisant un champ scalaire qui va acquérir une valeur moyenne non nulle dans le vide, un champ de jauge sans masse va acquérir une composante longitudinale de polarisation et donc une masse. Pour les fermions, leur masse peut apparaître en les couplant au champ scalaire de manière invariante sous les transformations de jauge.

B.1.2 Le mécanisme de Higgs dans le Modèle Standard

La faible portée de l'interaction faible implique qu'il faut générer une masse pour les trois bosons de jauge $W^\pm$ et Z^0 alors que le photon doit rester sans masse et la QED une

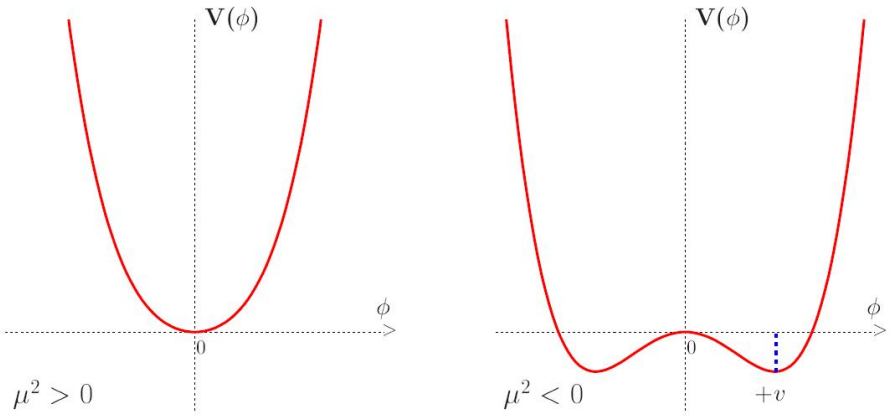

FIGURE 74 : Potentiel V du champ scalaire ϕ dans le cas $\mu^2 > 0$ (à gauche) et $\mu^2 < 0$ (à droite).

symétrie exacte. Ainsi, nous avons besoin de trois degrés de liberté, au moins, pour le champ scalaire. Le choix le plus simple est de considérer le champ Φ comme un doublet complexe de $SU(2)$

$$\Phi = \begin{pmatrix} \phi^+ \\ \phi^0 \end{pmatrix}, \quad Y_\Phi = +1 \tag{2.433}$$

Par simplicité nous ne considérons plus la partie due à l'interaction forte dans le Lagrangien du Modèle Standard et nous ne considérons que la première famille des leptons

$$\mathcal{L}_{SM} = -\frac{1}{4} W^a_{\mu\nu} W_a^{\mu\nu} - \frac{1}{4} B_{\mu\nu} B^{\mu\nu} + \bar{L}_i i D_\mu \gamma^\mu L_i + \bar{e}_{R_i} i D_\mu \gamma^\mu e_{R_i} + ... \tag{2.434}$$

Il nous faut ajouter la partie du champ scalaire invariante sous transformation de jauge

$$\mathcal{L}_S = (D^\mu \Phi)^\dagger (D_\mu \Phi) - V(\Phi), \quad V(\Phi) = \mu^2 \Phi^\dagger \Phi + \lambda (\Phi^\dagger \Phi)^2 \tag{2.435}$$

Si le terme de masse μ^2 est positif, le potentiel $V(\Phi)$ est aussi positif si l'auto-couplage λ est positif (nécessaire pour que le potentiel soit borné), ainsi le potentiel est minimum pour $\langle 0|\phi|0\rangle \equiv \phi_0 = 0$ comme montré sur la Fig. 74. $\mathcal{L}_S$ est donc simplement le Lagrangien d'une particule de spin 0 et de masse μ.

Si $\mu^2 < 0$, la composante neutre du doublet de champs Φ va acquérir une valeur moyenne non nulle dans le vide (état de plus basse énergie) :

$$\langle \Phi \rangle_0 \equiv \langle 0|\Phi|0\rangle = \begin{pmatrix} 0 \\ \frac{v}{\sqrt{2}} \end{pmatrix} \quad \text{avec} \quad v = \left(-\frac{\mu^2}{\lambda} \right)^{1/2} \tag{2.436}$$

On peut faire l'exercice suivant :

- écrire le champ Φ en termes des quatre champs $\theta_{1,2,3}(x)$ et $H(x)$ au premier ordre :

$$\Phi(x) = \begin{pmatrix} \theta_2 + i\theta_1 \\ \frac{1}{\sqrt{2}}(v + H) - i\theta_3 \end{pmatrix} = e^{i\theta_a \tau^a(x)/v} \begin{pmatrix} 0 \\ \frac{1}{\sqrt{2}}(v + H(x)) \end{pmatrix} \tag{2.437}$$

- passer en jauge unitaire (où seules restent les particules physiques dans le Lagrangien) par une transformation de jauge

$$\Phi(x) \to e^{-i\theta_a(x)\tau^a(x)/v}\Phi(x) = \frac{1}{\sqrt{2}}\begin{pmatrix} 0 \\ v + H(x) \end{pmatrix} \tag{2.438}$$

- développer le terme $|D_\mu\Phi|^2$ de $\mathcal{L}_S$

$$|D_\mu\Phi|^2 = \frac{1}{2}(\partial_\mu H)^2 + \frac{1}{8}g_2^2(v+H)^2|W_\mu^1 + iW_\mu^2|^2 + \frac{1}{8}(v+H)^2|g_2W_\mu^3 - g_1B_\mu|^2$$

- on définit les nouveaux champs $W^\pm$ et Z_μ (A_μ est le champ orthogonal à Z_μ)

$$W_\mu^\pm = \frac{1}{\sqrt{2}}(W_\mu^1 \mp iW_\mu^2), \quad Z_\mu = \frac{g_2W_\mu^3 - g_1B_\mu}{\sqrt{g_2^2+g_1^2}}, \quad A_\mu = \frac{g_2W_\mu^3 + g_1B_\mu}{\sqrt{g_2^2+g_1^2}} \tag{2.439}$$

- regrouper les termes bilinéaires des champs $W^\pm$,Z et A

$$M_W^2W_\mu^+W^{-\mu} + \frac{1}{2}M_Z^2Z_\mu Z^\mu + \frac{1}{2}M_A^2A_\mu A^\mu \tag{2.440}$$

On remarque que les bosons W et Z ont acquis une masse tandis que le photon est resté sans masse

$$M_W = \frac{1}{2}vg_2, \quad M_Z = \frac{1}{2}v\sqrt{g_2^2+g_1^2}, \quad M_A = 0 \tag{2.441}$$

La moitié de notre objectif a été atteinte, en brisant spontanément la symétrie $SU(2)_L \times U(1)_Y \to U(1)_Q$, trois bosons de Goldstone ont été absorbés par les bosons $W^\pm$ et Z pour former leur polarisation longitudinale responsable de leur masse. Comme la symétrie $U(1)_Q$ n'est toujours pas brisée, le photon, qui en est le générateur, reste sans masse, comme cela devrait être le cas.

A présent on peut générer la masse des fermions en utilisant le champ scalaire Φ d'hypercharge $Y = 1$ et l'isodoublet $\tilde{\Phi} = i\tau_2\Phi^*$, qui a une hypercharge $Y = -1$. On introduit le Lagrangien de Yukawa invariant sous $SU(2)_L \times U(1)_Y$

$$\mathcal{L}_F = -\lambda_e\bar{L}\Phi e_R - \lambda_d\bar{Q}\Phi d_R - \lambda_u\bar{Q}\tilde{\Phi}u_R + \text{h.c} \tag{2.442}$$

en considérant à titre d'exemple le cas de l'électron, on obtient

$$\begin{aligned} \mathcal{L}_F &= -\frac{1}{\sqrt{2}}\lambda_e(\bar{\nu}_e, \bar{e}_L)\begin{pmatrix} 0 \\ v+H \end{pmatrix} e_R + ... \\ &= -\frac{1}{\sqrt{2}}\lambda_e(v+H)\bar{e}_Le_R + ... \end{aligned} \tag{2.443}$$

Les constantes devant $\bar{f}_Lf_R$ (et h.c) sont identifiées avec la masse des fermions

$$m_e = \frac{\lambda_e v}{\sqrt{2}}, \quad m_u = \frac{\lambda_u v}{\sqrt{2}}, \quad m_d = \frac{\lambda_d v}{\sqrt{2}} \tag{2.444}$$

En conclusion de ce prélude, avec ce même isodoublet Φ de champ scalaire, nous avons généré la masse des bosons de jauge de l'interaction faible $W^\pm$,Z ainsi que la masse de fermions, tout en préservant la symétrie de jauge $SU(2) \times U(1)$ qui est à présent spontanément brisée. La symétrie électro-magnétique $U(1)_Q$ ainsi que la symétrie de couleur $SU(3)$ restent non-brisées. Le Modèle Standard est en fait l'invariance de jauge $SU(3) \times SU(2) \times U(1)$ combinée avec le mécanisme de brisure spontanée de symétrie, dont le Higgs est l'élément clé qu'il nous reste à étudier expérimentalement.

B.2 La production du boson de Higgs aux collisionneurs hadroniques.

B.2.1 Généralités sur les collisionneurs hadroniques

Le Higgs a tout d'abord été traqué au Tevatron du Fermilab (collisions $p\bar{p}$) qui a atteint une énergie dans le centre de masse de $\sqrt{s} = 1.96$ TeV et une luminosité intégrée de $\mathcal{L} = 12$ fb^{-1} de données par expérience (CDF et D0).

Depuis 2010 le LHC du CERN (collisions pp) acquiert des données. Il a fonctionné à $\sqrt{s} = 7,8$ TeV avec une luminosité intégrée de $\mathcal{L} \approx 20$ fb^{-1}. Mais il atteindra d'ici quelques mois l'énergie de $\sqrt{s} = 13$ TeV avec une luminosité prévue de $L = 10^{-2}$ pb^{-1}.s^{-1}.

Deux expériences, ATLAS et CMS, ont été conçues pour couvrir un large spectre de signatures. La recherche du Higgs et de la supersymétrie ont été les principaux guides pour construire les deux détecteurs.

La section efficace totale est extrêmement grande aux collisionneurs hadroniques. Elle est d'environ 100 mb au LHC, soit une fréquence d'interaction de 10^9 Hz. Dans le cas de la recherche du boson de Higgs le rapport signal sur bruit de fond est dans la plupart des voies de désintégration de l'ordre de 10^{-10}. Sa découverte a donc été un véritable challenge expérimental.

B.2.2 Modes de désintégration du boson de Higgs

Un boson de Higgs se désintègre principalement en $b\bar{b}, \tau\bar{\tau}, WW, ZZ, \gamma\gamma, Z\gamma$ lorsque sa masse est de l'ordre de 125 GeV cf. Fig. 75. De façon générale voici les critères recherchés pour extraire le signal :

- Dans la voie $H \to WW, ZZ$, au moins un des bosons W/Z doit être observé dans un de ses produits de désintégration leptonique, sachant que les rapports d'embranchement sont faibles $BR(W \to l\nu) \approx 20\%$ pour $l = \mu, e$, $BR(Z \to l^+l^-) \approx 6\%$ pour $l = \mu, e$ et $BR(Z \to \nu\nu) \approx 18\%$. Il est donc nécessaire de détecter avec précision des muons et électrons à grande impulsion transverse ainsi que de mesurer précisément l'énergie transverse manquante des neutrinos.
- Une bonne résolution sur la mesure de l'énergie des photons est nécessaire pour extraire du bruit de fond continu des $\gamma\gamma$ l'étroite résonance provenant de la désintégration $H \to \gamma\gamma$.
- le mode de désintégration principal est $H \to b\bar{b}$, il est important d'avoir d'excellents détecteurs de micro-vertex afin d'identifier les jets de quarks b.

B.2.3 Modes de production du boson de Higgs

Dans le Modèle Standard (SM) le Higgs se couple préférentiellement aux particules lourdes qui sont les bosons vecteurs W et Z, le quark top et dans une certaine mesure

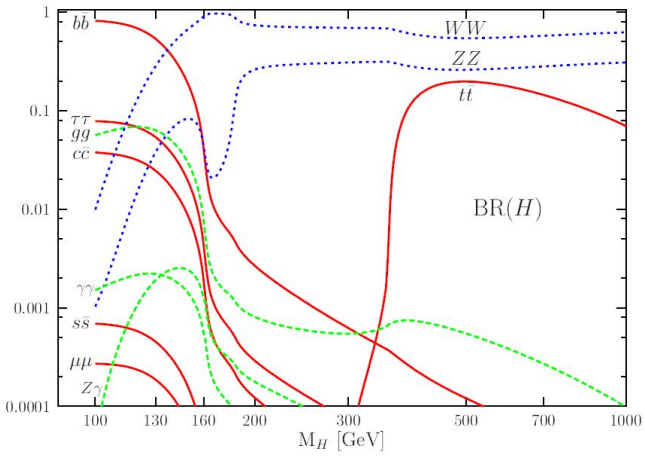

FIGURE 75 : Rapport d'embranchement du boson de Higgs du SM en fonction de sa masse.

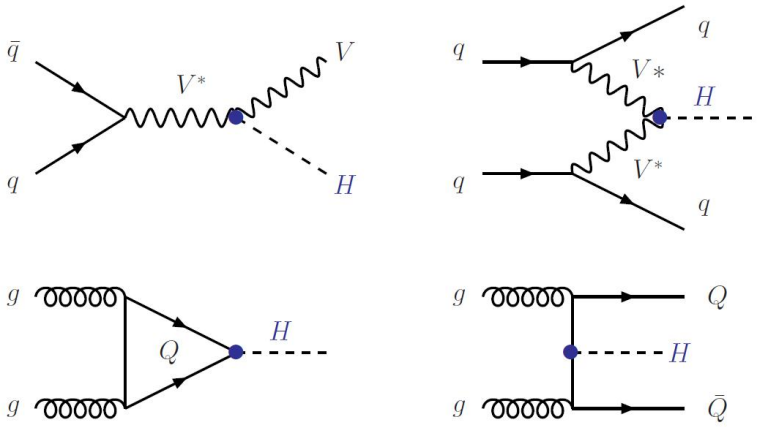

FIGURE 76 : Principaux modes de production du Higgs par le SM dans les collisionneurs hadroniques.

le quark b. Dans un collisionneur hadronique les quatre canaux principaux de création du Higgs sont par production associée avec un boson W/Z, par fusion de bosons vecteurs, par fusion de gluons et par production associée avec des quarks lourds, comme représentés par la Fig. 76.

Notons qu'il existe bien d'autres processus de production du Higgs mais leur section efficace est bien plus faible à cause des couplages électro-faibles en plus, ou à des couplages forts en plus (production du Higgs par fusion de gluons avec 0,1 ou 2 jets associés).

Pour calculer ces sections efficaces de production du Higgs il nous faut utiliser la théorie décrivant au mieux les interactions fortes, la QCD, à la fois dans son domaine perturbatif et dans son domaine non perturbatif. Le régime perturbatif de la QCD est à l'origine d'incertitudes théoriques sur la prédiction des sections efficaces des modes de production du Higgs, car les calculs sont fait jusqu'à un ordre donné du développement perturbatif. Le régime non perturbatif, représenté par les Fonctions de Distribution de

Parton (PDF), est aussi associé à une erreur théorique.

Concernant les corrections radiatives de la QCD, Il est bien connu que les processus faisant intervenir l'interaction forte ont des sections efficaces entachées d'une large incertitude si le calcul est fait à l'ordre le plus bas (LO pour Leading Order). Chaque ordre du développement perturbatif possède une dépendance en l'échelle de renormalisation μ_R (pour laquelle on défini la constante de couplage forte) et en l'échelle de factorisation (qui marque la séparation entre le domaine perturbatif de la théorie et le domaine non perturbatif décrit par les PDFs). Mais la section efficace, observable physique, ne peut dépendre de ces échelles de renormalisation et de factorisation qui sont non physiques. En pratique il s'avère donc nécessaire de considérer le plus haut ordre perturbatif (HO) dans la limite du possible afin de prendre en compte les corrections radiatives non négligeables. L'impact des corrections radiatives provenant des plus hauts ordres est souvent quantifié par le rapport K qui est définit comme le ratio entre la section efficace évaluée à HO (α_s et les PDFs calculées à HO) et la section efficace évaluée à LO (α_s et les PDFs calculé à LO)

$$K = \frac{\sigma_{HO}(pp \to H + X)}{\sigma_{LO}(pp \to H + X)} \tag{2.445}$$

B.3 Le mécanisme de fusion de gluons

B.3.1 Section efficace à LO

Les gluons n'ayant pas de masse (et de plus possèdent une couleur), ils ne peuvent pas se coupler directement avec le Higgs. La production du Higgs par le mécanisme de fusion de gluons se fait donc par l'intermédiaire d'une boucle de quarks lourds comme représenté par la Fig. 77. Dans le SM seulement le quark top et légèrement le quark bottom vont contribuer à cette amplitude. A l'ordre le plus bas (LO), la section efficace à l'échelle des partons peut s'exprimer à l'aide de la largeur de désintégration gluonique du Higgs $\sigma_0^H(H \to gg)$,

$$\hat{\sigma}_{LO}(gg \to H) = \sigma_0^H M_H^2 \delta(\hat{s} - M_H^2) = \frac{\pi^2}{8M_H}\Gamma_{LO}(H \to gg)\delta(\hat{s} - M_H^2) \tag{2.446}$$

où $\hat{s}$ est l'énergie dans le centre de masse au carré de la paire de gluon gg. Avec le résultat bien connu

$$\sigma_0^H(H \to gg) = \frac{G_\mu \alpha_s c(\mu_R^2)}{288\sqrt{2}\pi}\left|\frac{3}{4}\sum_q A_{1/2}^H(\tau_Q)\right|^2 \tag{2.447}$$

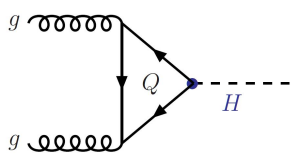

FIGURE 77 : Diagramme de création du Higgs par fusion de gluons, $gg \to H$.

Avec le facteur de forme $A_{1/2}^H$ fonction de $\tau_Q = M_H^2/4m_{Q^2}^2$ défini par

$$A_{1/2}^H(\tau) = 2[\tau + (\tau - 1)f(\tau)]\tau^{-2} \tag{2.448}$$

avec f défini comme

$$f(\tau) = \begin{cases} \arcsin^2 \sqrt{\tau} & \tau \leq 1 \\ -\frac{1}{4}\left[\ln \frac{1+\sqrt{1-\tau^{-1}}}{1-\sqrt{1-\tau^{-1}}} - i\pi\right]^2 & \tau > 1 \end{cases} \tag{2.449}$$

Dans cette approximation du premier ordre, on peut remplacer la distribution δ par une distribution de type Breit-Wigner

$$\delta(\hat{\sigma} - M_H^2) \to \frac{1}{\pi} \frac{\hat{s}\Gamma_H/M_H}{(\hat{s} - M_H^2)^2 + (\hat{s}\Gamma_H/M_H)^2} \tag{2.450}$$

Au premier ordre de la série perturbative et dans l'approximation de la largeur de désintégration étroite, la section efficace proton-proton s'écrit

$$\sigma_{LO}(pp \to H) = \sigma_0^H \tau_H \frac{d\mathcal{L}^{gg}}{d\tau_H} \quad \text{avec} \quad \frac{d\mathcal{L}^{gg}}{d\tau} = \int_\tau^1 \frac{dx}{x} g(x, \mu_F^2) g(\tau/x, \mu_F^2) \tag{2.451}$$

où classiquement $\tau_H = M_H^2/s$ est la variable de Drell-Yann et s l'énergie totale de la réaction dans le centre de masse.

B.3.2 Section efficace à NLO

Pour inclure les corrections de QCD à $\sigma(pp \to H + X)$, il faut prendre en compte, en plus des corrections virtuelles, les processus

$$gg \to Hg, \quad gq \to Hq \quad \text{et} \quad q\bar{q} \to Hg \tag{2.452}$$

Des diagrammes de Feynman typiques des corrections radiatives de QCD sont représentées Fig. 78.

Les corrections virtuelles modifient $\sigma_{LO}(pp \to H)$ par un coefficient proportionnel à α_s, tout comme les corrections réelles qui correspondent à la radiation de gluons ou

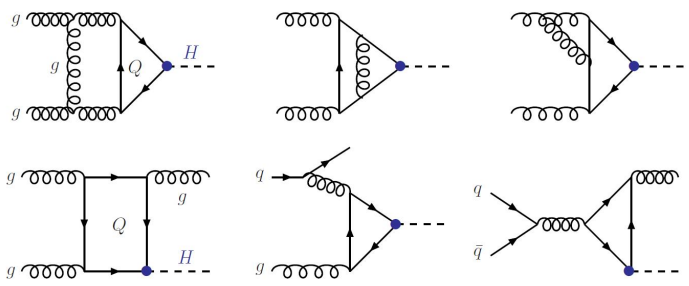

FIGURE 78 : Diagrammes caractéristiques de correction virtuelle et réelle à NLO de QCD pour $gg \to H$

de quarks dans l'état final. Ainsi le Higgs créé dans des collisions gluon-quark et quark-antiquark contribue à $\sigma_{NLO}(gg \to H)$ par des termes d'ordre α_s. On écrit alors la section efficace pour les sous-processus $ij \to H + X$, avec $i, j = g, q, \bar{q}$

$$\hat{\sigma}_{ij} = \sigma_0^H \Big\{ \delta_{ig}\delta_{jg} \Big[1 + C^H(\tau_Q)\frac{\alpha_s}{\pi} \Big] \delta(1-\hat{\tau}) + D_{ij}^H(\hat{\tau}, \tau_Q)\frac{\alpha_s}{\pi}\Theta(1-\hat{\tau}) \Big\} \tag{2.453}$$

où $\hat{\tau} = M_H^2/\hat{s}$ est la nouvelle variable d'échelle et Θ est la fonction de Heavyside. Si toutes les corrections sont présentes dans Eq. (2.453) alors les divergences ultraviolettes et infra-rouges s'annulent. Il reste cependant des singularités colinéaires qui sont absorbées dans la renormalisation des densités de partons, par exemple en adoptant le schéma de renormalisation $\overline{MS}$. La section efficace hadronique peut être mise sous la forme

$$\sigma(pp \to H + X) = \sigma_0^H \Big[1 + C^H \frac{\alpha_s}{\pi} \Big] \tau_H \frac{d\mathcal{L}^{gg}}{d\tau_H} + \Delta\sigma_{gg}^H + \Delta\sigma_{gq}^H + \Delta\sigma_{q\bar{q}}^H \tag{2.454}$$

La correction à deux boucles de quarks virtuelles régularisée par les singularités infrarouge dues aux émissions de gluons réels se trouve dans le coefficient C^H, qui se décompose de la façon suivante

$$C^H = \pi^2 + c^H + \frac{33 - 2N_f}{6} \ln \frac{\mu_R^2}{M_H^2} \tag{2.455}$$

avec

$$c^H = Re \sum_Q A_{1/2}^H(\tau_Q) c_Q^H(\tau_Q) / \sum_Q A_{1/2}^H(\tau_Q) \tag{2.456}$$

Les contributions non singulières provenant de la radiation de gluon lors de collisions gg et provenant des collisions gq et $q\bar{q}$ dépendent de l'échelle de renormalisation μ_R et de l'échelle de factorisation μ_F utilisées par les densités de partons.

$$\begin{aligned}
\Delta\sigma_{gg}^H &= \int_{\tau_H}^1 d\tau \frac{d\mathcal{L}^{gg}}{d\tau} \frac{\alpha_s(\mu_R)}{\pi} \sigma_0^H \Big\{ -zP_{gg}(z) \ln \frac{\mu_F c}{\tau s} + d_{gg}^H(z, \tau_Q) \\
&\quad + 12 \Big[\Big(\frac{ln(1-z)}{1-z} \Big)_+ - z[2 - z(1-z)\ln(1-z)] \Big] \Big\} \\
\Delta\sigma_{gq}^H &= \int_{\tau_H}^1 d\tau \sum_{q,\bar{q}} \frac{d\mathcal{L}^{gq}}{d\tau} \frac{\alpha_s(\mu_R)}{\pi} \sigma_0^H \Big\{ \Big[-\frac{1}{2} \ln \frac{\mu_F c}{\tau s} + \ln(1-z) \Big] zP_{gq}(z) + d_{gq}^H(z, \tau_Q) \Big\} \\
\Delta\sigma_{q\bar{q}}^H &= \int_{\tau_H}^1 d\tau \sum_q \frac{d\mathcal{L}^{q\bar{q}}}{d\tau} \frac{\alpha_s(\mu_R)}{\pi} \sigma_0^H d_{q\bar{q}}^H(z, \tau_Q)
\end{aligned} \tag{2.457}$$

avec $z = \tau_H/\tau$ et les fonctions de splitting d'Altarelli-Parisi

$$\begin{aligned}
P_{gg}(z) &= 6 \Big[\Big(\frac{1}{1-z} \Big)_+ + \frac{1}{z} - 2 + z(1-z) \Big] + \frac{33 - 2N_f}{6} \delta(1-z) \\
P_{gq}(z) &= \frac{4}{3} \frac{1 + (1-z)^2}{z}
\end{aligned} \tag{2.458}$$

où F_+ est l'usuelle "distribution +" telle que $F(\hat{\tau})_+ = F(\hat{\tau}) - \delta(1-\hat{\tau}) \int_0^1 d\hat{\tau}' F(\hat{\tau}')$. Dans la limite où le Higgs est très massif comparé à la masse des quarks (cas du quark bottom

par exemple), $\tau_Q = M_H^2/4m_Q \gg 1$

$$\begin{aligned}
c^H(\tau_Q) &\to \frac{5}{36}[\ln^2(4\tau_Q)_\pi^2] - \frac{4}{3}\ln(4\tau_Q) \\
d_{gg}^H(\hat{\tau},\tau_Q) &\to -\frac{2}{5}\ln(4\tau_Q)[7-7\hat{\tau}+5\hat{\tau}^2] - 6\ln(1-\hat{\tau})[1-\hat{\tau}+\hat{\tau}^2] \\
&\quad + 2\frac{\ln\hat{\tau}}{1-\hat{\tau}}[3-6\hat{\tau}-2\hat{\tau}^2+5\hat{\tau}^3-6\hat{\tau}^4] \\
d_{gq}^H(\hat{\tau},\tau_Q) &\to \frac{2}{3}\left[\hat{\tau}^2 - \left(1+(1-\hat{\tau})^2\right)\left(\frac{7}{15}\ln(4\tau_Q) + \ln\left(\frac{1-\hat{\tau}}{\hat{\tau}}\right)\right)\right] \\
d_{q\bar{q}}^H(\hat{\tau},\tau_Q) &\to 0
\end{aligned} \tag{2.459}$$

Dans la limite inverse (cas du quark top), $\tau_Q = M_H^2/4m_Q \ll 1$

$$c^H(\tau_Q) \to \frac{11}{2}, \quad d_{gg}^H \to -\frac{11}{2}(1-z)^3, \quad d_{gq}^H \to -1+2z-\frac{1}{3}z^2, \quad d_{q\bar{q}}^H \to \frac{32}{27}(1-z)^3 \tag{2.460}$$

B.4 La mesure de l'auto-couplage du boson de Higgs au LHC

Dans le chapitre 2 nous avons discuté en détail des principaux processus de production d'une paire de bosons de Higgs au LHC : par fusion de gluons, fusion de bosons vecteurs, double Higgs–strahlung et production associée avec une paire de quarks tops. Ils permettent la détermination du couplage trilinéaire du Higgs λ_{HHH}, qui est une étape importante afin de reconstruire le potentiel du boson de Higgs et ainsi fournir la preuve finale que le mécanisme du Higgs est à l'origine de la brisure de la symétrie électrofaible. Nous avons inclus les corrections importantes de la QCD à NLO au processus de fusion de gluons et de bosons vecteurs et nous avons calculé pour la première fois les corrections NNLO du processus de double Higgs–strahlung. Il s'avère que la contribution au processus de production ZHH initié par des gluons à NNLO est significative contrairement au cas où un seul Higgs est radié. Nous avons discuté en détail des différentes incertitudes sur les divers processus et nous avons fourni les valeurs des sections efficaces ainsi que leur incertitude totale pour des énergies de centre de masse de 8, 14, 33 et 100 TeV. Cette incertitude est de l'ordre de 40% dans le cas de la fusion de gluons tandis qu'elles sont bien plus réduites dans le cas de la fusion de vecteurs et de la double radiation de Higgs, i.e inférieure à 10%. Dans le cadre du modèle standard nous avons étudié la sensibilité du processus de production d'une paire de bosons de Higgs au couplage trilinéaire dans le but d'estimer la précision à laquelle nous devons le mesurer afin d'extraire ce couplage de manière suffisamment précise.

Dans une deuxième partie nous avons effectué une analyse au niveau des partons concernant le processus dominant de production d'une paire de bosons de Higgs, dans différents états finaux qui sont $b\bar{b}\gamma\gamma$, $b\bar{b}\tau\bar{\tau}$ and $b\bar{b}W^+W^-$ avec les bosons W qui se désintègrent en leptons. Dû au fait que le signal est faible et que les bruits de fond QCD sont larges, les analyses sont délicates. L'état final $b\bar{b}W^+W^-$ aboutit à un rapport signal sur bruit de fond extrêmement faible après avoir appliqué différentes coupures, ainsi cette possibilité n'est pas prometteuse. D'un autre côté, la sensibilité obtenue après coupures dans les états finaux $b\bar{b}\gamma\gamma$ et $b\bar{b}\tau\bar{\tau}$ sont de ~ 16 et ~ 9, respectivement avec un nombre d'événements qui n'est pas trop faible. Ces processus sont donc suffisamment

encourageants pour commencer de réelles analyses expérimentales qui tiennent compte des effets de détecteur et de l'hadronisation, qui sont largement en dehors du cadre de notre étude. Effectuant une première simulation au niveau du détecteur pour l'état final $b\bar{b}\gamma\gamma$ nous avons montré qu'à haute luminosité les résultats sont prometteurs. Prenant en compte les incertitudes théoriques et statistiques, nous pouvons nous attendre à mesurer le couplage trilinéaire d'auto-intéraction du boson de Higgs λ_{HHH}, à un facteur deux près. Afin d'améliorer la précision de cette mesure, il faudra très certainement avoir recour à de nouveaux collisionneurs.

B.5 Les implications d'un Higgs à 125 GeV pour les modèles supersymetriques

Au chapitre 6, nous avons étudié l'impact d'un boson de Higgs ayant une masse de l'ordre de 125 GeV, semblable à celui du modèle standard, pour les théories supersymétriques dans le contexte des scénarios non-contraints et contraints du Modèle Standard Supersymétrique Minimal (MSSM). En conclusion, nous avons montré que dans le modèle phénoménologique du MSSM, il existe de fortes restrictions sur le mélange dans le secteur du top et que, par example, le scénario avec mélange nul est exclu à moins que l'échelle de brisure de la supersymétrie soit extrêmement large, $M_S \gg 1$ TeV, tandis que le scénario à mélange maximal est défavorisé pour de larges valeurs de M_S et $\tan\beta$.

Dans les scénarios constraints du MSSM, l'impact est encore plus important. Plusieurs scénarios comme AMSB et GMSB sont défavorisés puisqu'ils mènent à une particule h trop légère. Dans le cas de mSUGRA, en incluant la possibilité que les paramètres de la masse du Higgs ne soient pas universels, la partie non-exclue de l'espace des paramètres correspond à la région où les masses de stop et A_0 sont larges. Dans des versions plus contraintes de ce modèle telles que les scénarios sans échelle et le cNMSSM approché, seulement une petite portion de l'espace des paramètres est autorisée par la contrainte sur la masse du boson de Higgs. Finalement, des parties importantes de l'espace des paramètres de modèles avec une large valeur M_S menant à des particules supersymétriques très lourdes, telles que "split SUSY" ou "high–scale SUSY", peuvent aussi être exclues puisqu'ils ont tendance à prédire un boson de Higgs trop lourd avec $M_h \gtrsim 125$ GeV.

B.6 Recherches de bosons de Higgs lourds dans la région des faibles $\tan\beta$

A la suite de l'observation d'un boson de 126 GeV par les collaborations d'ATLAS et CMS, ayant tout l'air d'un boson de Higgs tel qu'il est décrit par le modèle standard, l'un des prochains objectifs du LHC est de chercher de nouvelles particules non prédites par le modèle standard. Cela peut se faire en améliorant la précision sur les mesures des couplages du boson de Higgs en essayant d'isoler certaines déviations, mais cela peut aussi s'effectuer en cherchant directement la production de nouveaux états.

Dans le chapitre 7, nous avons considéré la production des bosons de Higgs lourds du MSSM : H, A et $H^{\pm}$ au LHC, en se concentrant sur le régime des faibles valeurs de $\tan\beta \lesssim 3$–5. Nous avons tout d'abord montré que cette zone de l'espace de phase du

MSSM, qui a été très longtemps considérée comme exclue, est toujours viable si nous supposons que l'échelle SUSY est très grande, $M_S \gtrsim 10$ TeV. Pour de telles valeurs de M_S, les outils classiques qui permettent de déterminer les masses et les couplages des particules supersymétriques, incluant les corrections d'ordres supérieures, deviennent obsolètes.

Ainsi nous avons utilisé une approximation simple mais pertinente pour décrire les corrections radiatives du secteur du Higgs, dans laquelle l'échelle inconnue M_S et le paramètre de mélange des stops X_t sont échangés pour la valeur mesurée de la masse du boson $M_h \approx 126$ GeV. En très bonne approximation, nous pouvons donc avec seulement deux paramètres, $\tan\beta$ et M_A, décrire le secteur du Higgs du MSSM en tenant compte des ordres supérieures. En supposant que M_S soit suffisamment large, ces deux paramètres peuvent avoir des valeurs faibles, i.e. $\tan\beta \approx 1$ et $M_A = \mathcal{O}(200)$ GeV.

Dans la région des faibles $\tan\beta$, il y a un grand nombre de canaux dans lesquels les bosons de Higgs lourds du MSSM pourraient être étudiés. Les états neutres H/A peuvent être produits abondamment par le mécanisme de fusion de gluons et peuvent se désintégrer dans un certain nombre d'états finaux telles que $H \to WW, ZZ$, $H \to hh$, $H/A \to t\bar{t}$, $A \to hZ$. D'intéressantes désintégrations peuvent aussi se produire dans le cas de l'étude des bosons de Higgs chargés e.g. $H^+ \to hW, c\bar{s}, c\bar{b}$. Tous ces derniers modes s'ajoutent aux deux canaux $H/A \to \tau^+\tau^-$ et $t \to bH^+ \to b\tau\nu$ qui sont étudiés par ATLAS et CMS et qui sont très contraignants pour l'espace des paramètres à hautes valeurs de $\tan\beta$ mais aussi à faibles valeurs de $\tan\beta$ comme nous l'avons montré.

Nous avons démontré que, déjà avec les données actuelles du LHC collectées à $\sqrt{s} =$ 7+8 TeV, nous sommes sensibles aux régions des faibles valeurs de $\tan\beta$ et M_A en extrapolant simplement dans le secteur du Higgs du MSSM les analyses disponibles sur la recherche à hautes masses de bosons de Higgs, c'est-à-dire les canaux WW, ZZ et $t\bar{t}$. Les sensibilités de ces recherches vont considérablement s'améliorer lorsque le LHC fonctionnera à 14 TeV et aura collecté 300 fb^{-1} de données. En l'absence de tout signal à cette énergie, le plan $[\tan\beta, M_A]$ peut être entièrement exclu pour toutes valeurs de $\tan\beta$ et jusqu'à une masse du pseudoscalaire de $M_A \approx 500$ GeV. Des recherches complémentaires peuvent aussi être faites dans des canaux du Higgs chargé qui n'ont pas été étudiés jusqu'à présent, tels que $H^+ \to Wh$.

Ainsi, tous les canaux qui ont été utilisés pour la recherche d'un boson du Higgs, de type modèle standard à haute masse, peuvent être recyclés pour la recherche de bosons de Higgs lourds du MSSM dans la région des faibles valeurs de $\tan\beta$. Tout cela promet un programme très excitant de recherche de ces bosons de Higgs au LHC dès à présent.

Nous pourrions alors couvrir entièrement l'espace des paramètres du MSSM : la région des grandes valeurs de $\tan\beta$ étant couverte par l'amélioration des recherches des canaux $H/A \to \tau\tau$, la région des faibles valeurs de $\tan\beta$ étant couverte par les canaux $WW, ZZ, tt, ...$ La couverture du plan $[\tan\beta, M_A]$ sera alors faite indépendamment du modèle choisi sous aucune hypothèse faite sur l'échelle M_S et sur tout autre paramètre supersymétrique. Les informations indirectes provenant de la masse du boson de Higgs léger ainsi que les informations sur ces couplages seront à ajouter à cela.

B.7 Le MSSM après la découverte du boson de Higgs

Dans le chapitre 8 nous avons étudié le "hMSSM", c'est à dire le MSSM que nous pensons avoir après la découverte du fameux boson de Higgs au LHC, que nous identifions avec l'état le plus léger. La valeur de la masse $M_h \approx 125$ GeV et le fait que nous n'observons pas (d'autres ?) de particules supersymétriques semblent indiquer que l'échelle de brisure douce de la supersymétrie doit être large $M_S \gtrsim 1$ TeV. Nous avons montré en utilisant à la fois une formule analytique approchée ainsi qu'un scan sur les paramètres du MSSM, que le secteur du Higgs du MSSM peut être décrit, en très bonne approximation, par seulement deux paramètres $\tan\beta$ et M_A si l'information $M_h = 125$ GeV est utilisée à bon escient. Nous pouvons alors ignorer les corrections radiatives aux masses des bosons de Higgs ainsi que leur dépendance compliqués aux autres paramètres du MSSM et utiliser une formule simple pour déduire les autres paramètres du secteur du Higgs, α, M_H et $M_{H^\pm}$.

Dans un deuxième temps, nous avons montré que pour décrire les propriétés de h lorsque les corrections radiatives directes sont importantes, les trois couplages c_t, c_b et c_V sont nécessaires en plus de la masse de l'état h. Nous avons effectué un fit de ces couplages en utilisant les dernières données du LHC et en prenant proprement en compte les incertitudes théoriques. Dans la limite où les particules supersymétriques sont lourdes, le point de meilleur fit s'avère être à basse valeur de $\tan\beta$, $\tan\beta \approx 1$ et avec une valeur pas trop grande pour la masse du pseudoscalaire, $M_A \approx 560$ GeV.

La phénoménologie de ce point particulier est très intéressante. Premièrement, les bosons de Higgs lourds seront accessibles lors du prochain programme du LHC, au moins par les canaux $A, H \to t\bar{t}$ et potentiellement aussi dans les modes $H \to WW, ZZ$ puisque les taux de production sont plutôt larges pour $\tan\beta \approx 1$. Cela est montré sur la Fig. 79 où nous avons représenté les sections efficaces multipliées par les taux de désintégrations de A et H en fonction de $\tan\beta$ et pour le choix particulier de $M_A = 557$ GeV et correspondant à une énergie dans le centre de masse de $\sqrt{s} = 14$ TeV.

De plus, une densité relique correcte de neutralinos peut être facilement obtenue par l'intermédiaire du processus d'annihilation $\chi_1^0\chi_1^0 \to A \to t\bar{t}$ en autorisant les paramètres μ et M_1 à être du même ordre de grandeur, la masse du neutralino étant proche du pôle du pseudoscalaire A, i.e. $m_{\chi_1^0} \approx \frac{1}{2}M_A$.

B.8 Lorsque le boson de Higgs interagit avec la matière noire

B.8.1 Contraintes sur des modèles simples

Dans le chapitre 10 nous avons analysé l'implication d'un boson de Higgs de 125 GeV pour des modèles génériques où ce boson se couple à un candidat de matière noire qui est de type scalaire, fermionique ou bien vectoriel. Exigeant que le boson de Higgs ait un rapport d'embranchement invisible inférieur à 10%, nous avons trouvé que la section efficace pour une matière noire avec une masse de l'ordre de l'échelle électrofaible est dans la gamme $10^{-9} - 10^{-8}$ pb dans presque tout l'espace des paramètres. Ainsi l'ensemble de ces modèles seront expérimentalement accessibles par l'expérience de détection directe XENON1T qui sera aussi capable de différencier le cas où la matière noire est scalaire ou vectorielle. La matière noire fermionique est actuellement exclue par

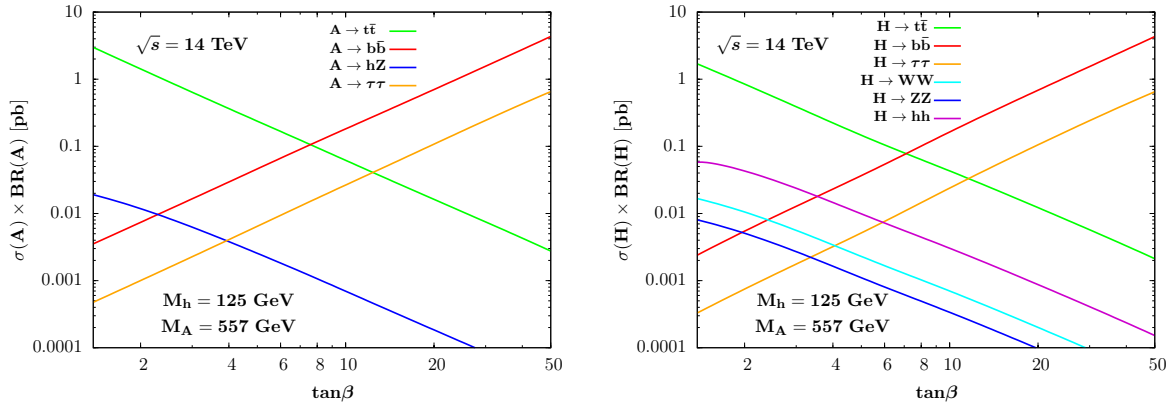

FIGURE 79 : Sections efficaces multipliées par les taux d'embranchements pour les bosons lourds du MSSM A (à gauche) et H (à droite) au LHC $\sqrt{s} = 14$ TeV en fonction de $\tan\beta$ pour $M_A = 557$ GeV et $M_h = 125$ GeV.

l'expérience XENON100. De plus, nous avons trouvé que la situation où la matière noire couplant au boson de Higgs est légère, $M_{\rm DM} \lesssim 60$ GeV, est exclue indépendamment de sa nature puisque la désintégration invisible du Higgs serait trop importante et serait donc incompatible avec les mesures de production du boson Higgs au LHC. Finalement, il sera difficile d'observer les effets de la matière noire au LHC dans la situation où $M_{\rm DM} \gtrsim 60$ GeV puisque les sections efficaces de production sont très faibles. De telles études nécessiteront très certainement un accélérateur de type e^+e^- avec une grande luminosité.

B.8.2 Les désintégrations invisibles du boson de Higgs

Nous avons montré que les recherches de simple jet au LHC fournissent déjà des limites très intéressantes sur la largeur de désintégration invisible du boson de Higgs, contraignant celle-ci à être plus petite que le taux de production du boson de Higgs dans le modèle standard à 95% de niveau de confiance. Cela apporte une contrainte importante sur les modèles où la section efficace de production du boson de Higgs est amplifiée et où le rapport d'embranchement en particules non détectables est significatif. Les recherches de monojets sont sensibles surtout au processus de fusion de gluons et ainsi elles peuvent contraindre la largeur invisible du boson de Higgs dans des modèles où le couplages du Higgs aux bosons de jauges sont réduits. Les limites obtenues pourront être largement améliorées lorsque plus de données seront collectées, en supposant que les erreurs systématiques sur les contributions du modèle standard au processus de simple jet seront réduits.

Nous avons aussi étudié, dans une approche qui ne dépend pas du modèle, la complémentarité entre le rapport d'embranchement du boson de Higgs en particule de matière noire et la section efficace de cette dernière sur les nucléons dans le contexte de théories effectives. La limite $\mathrm{BR}_{\rm inv} < 0.2$, suggérée par la combinaison des données du Higgs dans le secteur visible, implique une limite sur la section efficace de détection directe qui est bien plus forte que celle obtenue par l'expérience XENON100 pour un candidat de matière noire scalaire, fermionique ou vectoriel. Ainsi, dans le contexte des modèles

simples de couplage du boson de Higgs à un candidat de matière noire, le LHC est actuellement l'expérience la plus sensible pour une matière noire légère.

B.9 Lorsque le champ d'hypercharge interagit avec la matière noire

Dans le chapitre 11, nous avons considéré la possibilité qu'un secteur dit caché, contienne plus qu'un champ vectoriel massif. Dans ce cas, une nouvelle structure d'interaction de dimension 4 de type Chern–Simons devient possible. Cette dernière couple le champ associé à l'hypercharge à la combinaison antisymétrique des vecteurs massifs. Si ces derniers sont stables, de tels couplages se manifestent par de l'énergie manquante dans la désintégration de divers mésons et du boson de jauge Z ainsi que la production de simple jet et de simple photon au LHC. Si le secteur caché possède une symétrie Z_2, cela rendrait le champ vectoriel le plus léger stable et donc un bon candidat de matière noire. La signature caractéristique de ce scénario est l'émission mono-chromatique d'une raie gamma à partir du centre Galactique. Nous avons trouvé que cette possibilité est compatible avec d'autres contraintes qui incluent celles du LHC et celles de détection directe de matière noire. Une importante partie de l'espace des paramètres est expérimentalement accessible par la détection directe de matière noire ainsi que par les recherches de mono-photon au LHC.

B.10 Matière noire non thermique et théorie de grande unification

Le modèle standard de la physique des particules est plus que jamais justifié après la découverte du boson de Higgs. Cependant ce modèle possède beaucoup de paramètres et les couplages de jauge ne s'unifient pas à haute énergie. Parmi les approches les plus élégantes pour comprendre certains de ces paramètres, les théories de grande unification (GUT), dans lesquelles les couplages de jauge $\alpha_{1,2,3}$ proviennent d'un seul et même couplage de jauge qui est associé à un groupe de jauge plus général, permettent l'unification des couplages de jauge. Cette idée est confortée par le fait que les nombres quantiques des quarks et leptons dans le modèle standard possèdent une représentation simple dans une symétrie GUT , par exemple, le **10** et $\bar{\mathbf{5}}$ de $SU(5)$ ou le **16** de $SO(10)$.

Dans le chapitre 12 nous avons montré que des groupes de jauge de type GUT comme E_6 ou $SO(10)$, qui contiennent un sous-groupe additionnel $U(1)$ (à celui du modèle standard) et étant brisé à une échelle intermédiaire, peuvent facilement expliquer l'unification des couplages et peuvent contenir un nouveau candidat de matière noire qui est chargé sous le nouveau groupe de jauge $U(1)$. Cependant contrairement au processus standard d'annihilation à l'équilibre nous avons proposé un mécanisme alternatif pour produire la matière noire par l'intermédiaire de nouveaux bosons de jauge lourds associés au nouveau groupe $U(1)$. Tandis que la matière noire est bien produite à partir du bain thermique, celle-ci n'atteint jamais son équilibre : ce mécanisme de production a été baptisé Matière Noire Thermale en Non-Equilibre (NETDM). La densité relique de matière noire est obtenue juste après la période de réchauffement inflationnaire. Ce mécanisme est fondamentalement différent des autres mécanismes de production

de matière noire non-thermique. En supposant qu'aucune des particules de matière noire n'est produite par la désintégration de l'inflaton pendant le réchauffement, nous avons calculé la production de matière noire et nous avons relié la température de réchauffement à l'échelle intermédiaire associé à un certain groupe de jauge nécessaire pour obtenir l'unification des couplages de jauge. Dans le contexte des modèles $SO(10)$, nous avons démontré qu'il existe un lien étroit entre la température de réchauffement inflationnaire et le schéma de brisure de $SO(10)$ pour donner le groupe de jauge du modèle standard.

B.11 Lorsqu'un boson Z′ interagit avec la matière noire

Dans le chapitre 13 nous avons étudié la genèse de matière noire par l'intermédiaire d'un boson Z' ayant une masse de quelques GeV jusqu'à une masse supérieure à la température de réchauffement inflationnaire. Plus particulièrement nous avons distingué deux régimes : 1) un médiateur très lourd ayant une masse supérieure à la température de réchauffement T_{RH} et 2) un médiateur similaire à un boson électro-faible, illustré par un modèle avec un mélange cinétique avec un nouveau boson $U(1)$, i.e. un boson Z', qui couple faiblement au modèle standard a contrario de son couplage avec la matière noire.

Dans le cas d'un médiateur très massif, nous avons résolu le système d'équations de Boltzmann obtenant alors la dépendance de la production de matière en fonction de la température de réchauffement. En exigeant une bonne densité relique de matière non-baryonique, l'échelle de l'interaction effective Λ doit être approximativement de 10^{12} GeV, pour $T_{RH} \approx 10^9$ GeV.

Pour des Z' plus légers qui couplent avec le modèle standard par l'intermédiaire d'un mélange cinétique avec le groupe de jauge $U(1)$ du modèle standard, nous considérons une masse de Z' allant de 1 GeV à 1 TeV. Les valeurs du mélange cinétique δ, compatible avec l'abondance relique de matière noire, doivent vérifier $10^{-12} \lesssim \delta \lesssim 10^{-11}$ selon la masse du boson Z'. Pour de telles valeurs, les contraintes provenant d'autres expériences comme la détection directe et indirecte, la production direct au LHC sont sans incidences. Cependant les limites provenant de la nucléosynthèse primordiale peuvent être relativement importantes. Concernant l'étude de l'évolution de la densité en nombre de particule, nous avons vérifié les effets de l'équilibre chimique entre la matière noire et le boson Z' sur la population finale de matière noire qui s'avèrent donner une correction au maximum d'un facteur 2.

References

[1] E. Fermi, *An attempt of a theory of beta radiation. 1.*, *Z.Phys.* **88** (1934) 161–177.

[2] T. Lee and C.-N. Yang, *Question of Parity Conservation in Weak Interactions*, *Phys.Rev.* **104** (1956) 254–258.

[3] C. Wu, E. Ambler, R. Hayward, D. Hoppes, and R. Hudson, *Experimental Test of Parity Conservation in Beta Decay*, *Phys.Rev.* **105** (1957) 1413–1414.

[4] R. Feynman and M. Gell-Mann, *Theory of Fermi interaction*, *Phys.Rev.* **109** (1958) 193–198.

[5] N. Cabibbo, *Unitary Symmetry and Leptonic Decays*, *Phys.Rev.Lett.* **10** (1963) 531–533.

[6] **Gargamelle Neutrino** Collaboration, F. Hasert et al., *Observation of Neutrino Like Interactions Without Muon Or Electron in the Gargamelle Neutrino Experiment*, *Phys.Lett.* **B46** (1973) 138–140.

[7] T. Lee, M. Rosenbluth, and C.-N. Yang, *Interaction of Mesons With Nucleons and Light Particles*, *Phys.Rev.* **75** (1949) 905.

[8] S. Glashow, *Partial Symmetries of Weak Interactions*, *Nucl.Phys.* **22** (1961) 579–588.

[9] Y. Nambu, *Axial vector current conservation in weak interactions*, *Phys.Rev.Lett.* **4** (1960) 380–382.

[10] J. Goldstone, *Field Theories with Superconductor Solutions*, *Nuovo Cim.* **19** (1961) 154–164.

[11] J. Goldstone, A. Salam, and S. Weinberg, *Broken Symmetries*, *Phys.Rev.* **127** (1962) 965–970.

[12] P. W. Higgs, *Broken symmetries, massless particles and gauge fields*, *Phys.Lett.* **12** (1964) 132–133.

[13] F. Englert and R. Brout, *Broken Symmetry and the Mass of Gauge Vector Mesons*, *Phys.Rev.Lett.* **13** (1964) 321–323.

[14] G. Guralnik, C. Hagen, and T. Kibble, *Global Conservation Laws and Massless Particles*, *Phys.Rev.Lett.* **13** (1964) 585–587.

[15] P. W. Higgs, *Spontaneous Symmetry Breakdown without Massless Bosons*, *Phys.Rev.* **145** (1966) 1156–1163.

[16] T. Kibble, *Symmetry breaking in nonAbelian gauge theories*, *Phys.Rev.* **155** (1967) 1554–1561.

[17] Y. Nambu and G. Jona-Lasinio, *Dynamical Model of Elementary Particles Based on an Analogy with Superconductivity. 1.*, *Phys.Rev.* **122** (1961) 345–358.

[18] Y. Nambu and G. Jona-Lasinio, *Dynamical model of elementary particles based on an analogy with superconductivity. II*, *Phys.Rev.* **124** (1961) 246–254.

[19] J. S. Schwinger, *Gauge Invariance and Mass*, *Phys.Rev.* **125** (1962) 397–398.

[20] P. W. Anderson, *Plasmons, Gauge Invariance, and Mass*, *Phys.Rev.* **130** (1963) 439–442.

[21] S. Weinberg, *A Model of Leptons*, *Phys.Rev.Lett.* **19** (1967) 1264–1266.

[22] A. Salam, *Weak and Electromagnetic Interactions*, *Conf.Proc.* **C680519** (1968) 367–377.

[23] G. 't Hooft, *Renormalizable Lagrangians for Massive Yang-Mills Fields*, *Nucl.Phys.* **B35** (1971) 167–188.

[24] G. 't Hooft, *Renormalization of Massless Yang-Mills Fields*, *Nucl.Phys.* **B33** (1971) 173–199.

[25] J. Bjorken and S. Glashow, *Elementary Particles and SU(4)*, *Phys.Lett.* **11** (1964) 255–257.

[26] **E598** Collaboration, J. Aubert et al., *Experimental Observation of a Heavy Particle J*, *Phys.Rev.Lett.* **33** (1974) 1404–1406.

[27] S. Herb, D. Hom, L. Lederman, J. Sens, H. Snyder, et al., *Observation of a Dimuon Resonance at 9.5-GeV in 400-GeV Proton-Nucleus Collisions*, *Phys.Rev.Lett.* **39** (1977) 252–255.

[28] M. L. Perl, G. Abrams, A. Boyarski, M. Breidenbach, D. Briggs, et al., *Evidence for Anomalous Lepton Production in e+ e- Annihilation*, *Phys.Rev.Lett.* **35** (1975) 1489–1492.

[29] **CDF** Collaboration, F. Abe et al., *Search for the top quark decaying to a charged Higgs boson in $\bar{p}p$ collisions at $\sqrt{s} = 1.8$ TeV*, *Phys.Rev.Lett.* **73** (1994) 2667–2671.

[30] **CDF** Collaboration, F. Abe et al., *Observation of top quark production in $\bar{p}p$ collisions*, *Phys.Rev.Lett.* **74** (1995) 2626–2631, [hep-ex/9503002].

[31] **D0** Collaboration, S. Abachi et al., *Observation of the top quark*, *Phys.Rev.Lett.* **74** (1995) 2632–2637, [hep-ex/9503003].

[32] M. Kobayashi and T. Maskawa, *CP Violation in the Renormalizable Theory of Weak Interaction*, *Prog.Theor.Phys.* **49** (1973) 652–657.

[33] S. Dawson, A. Gritsan, H. Logan, J. Qian, C. Tully, et al., *Working Group Report: Higgs Boson*, arXiv:1310.8361.

[34] **ATLAS** Collaboration, *Updated ATLAS results on the signal strength of the Higgs-like boson for decays into WW and heavy fermion final states*, ATLAS-CONF-2012-162.

[35] **CMS** Collaboration, *Combination of standard model Higgs boson searches and measurements of the properties of the new boson with a mass near 125 GeV*, CMS-PAS-HIG-12-045.

[36] P. W. Higgs, *Broken Symmetries and the Masses of Gauge Bosons*, *Phys.Rev.Lett.* **13** (1964) 508–509.

[37] F. Boudjema and E. Chopin, *Double Higgs production at the linear colliders and the probing of the Higgs selfcoupling*, *Z.Phys.* **C73** (1996) 85–110, [hep-ph/9507396].

[38] A. Djouadi, W. Kilian, M. Muhlleitner, and P. Zerwas, *Testing Higgs selfcouplings at e+ e- linear colliders*, *Eur.Phys.J.* **C10** (1999) 27–43, [hep-ph/9903229].

[39] V. Barger, T. Han, P. Langacker, B. McElrath, and P. Zerwas, *Effects of genuine dimension-six Higgs operators*, *Phys.Rev.* **D67** (2003) 115001, [hep-ph/0301097].

[40] P. Osland and P. Pandita, *Measuring the trilinear couplings of MSSM neutral Higgs bosons at high-energy e+ e- colliders*, *Phys.Rev.* **D59** (1999) 055013, [hep-ph/9806351].

[41] E. Asakawa, D. Harada, S. Kanemura, Y. Okada, and K. Tsumura, *Higgs boson pair production in new physics models at hadron, lepton, and photon colliders*, *Phys.Rev.* **D82** (2010) 115002, [arXiv:1009.4670].

[42] A. Djouadi, W. Kilian, M. Muhlleitner, and P. Zerwas, *Production of neutral Higgs boson pairs at LHC*, *Eur.Phys.J.* **C10** (1999) 45–49, [hep-ph/9904287].

[43] A. Djouadi, W. Kilian, M. Muhlleitner, and P. Zerwas, *The Reconstruction of trilinear Higgs couplings*, hep-ph/0001169.

[44] M. M. Muhlleitner, *Higgs particles in the standard model and supersymmetric theories*, hep-ph/0008127.

[45] R. Grober and M. Muhlleitner, *Composite Higgs Boson Pair Production at the LHC*, *JHEP* **1106** (2011) 020, [arXiv:1012.1562].

[46] M. Spira, *QCD effects in Higgs physics*, *Fortsch.Phys.* **46** (1998) 203–284, [hep-ph/9705337].

[47] A. Djouadi, *The Anatomy of electro-weak symmetry breaking. I: The Higgs boson in the standard model*, *Phys.Rept.* **457** (2008) 1–216, [hep-ph/0503172].

[48] A. Djouadi, *The Anatomy of electro-weak symmetry breaking. II. The Higgs bosons in the minimal supersymmetric model*, *Phys.Rept.* **459** (2008) 1–241, [hep-ph/0503173].

[49] M. Gomez-Bock, M. Mondragon, M. Muhlleitner, R. Noriega-Papaqui, I. Pedraza, et al., *Rompimiento de la simetria electrodebil y la fisica del Higgs: Conceptos basicos*, *J.Phys.Conf.Ser.* **18** (2005) 74–135, [hep-ph/0509077].

[50] M. Gomez-Bock, M. Mondragon, M. Muhlleitner, M. Spira, and P. Zerwas, *Concepts of Electroweak Symmetry Breaking and Higgs Physics*, arXiv:0712.2419.

[51] O. J. Eboli, G. Marques, S. Novaes, and A. Natale, *TWIN HIGGS BOSON PRODUCTION*, *Phys.Lett.* **B197** (1987) 269.

[52] E. N. Glover and J. van der Bij, *Higgs boson pair production via gluon fusion*, *Nucl.Phys.* **B309** (1988) 282.

[53] D. A. Dicus, C. Kao, and S. S. Willenbrock, *Higgs Boson Pair Production From Gluon Fusion*, *Phys.Lett.* **B203** (1988) 457.

[54] T. Plehn, M. Spira, and P. Zerwas, *Pair production of neutral Higgs particles in gluon-gluon collisions*, *Nucl.Phys.* **B479** (1996) 46–64, [hep-ph/9603205].

[55] W.-Y. Keung, *Double Higgs From $W-W$ Fusion*, *Mod.Phys.Lett.* **A2** (1987) 765.

[56] D. A. Dicus, K. J. Kallianpur, and S. S. Willenbrock, *Higgs Boson Pair Production in the Effective W Approximation*, *Phys.Lett.* **B200** (1988) 187.

[57] K. J. Kallianpur, *Pair Production of Higgs Bosons via Heavy Quark Annihilation*, *Phys.Lett.* **B215** (1988) 392.

[58] A. Dobrovolskaya and V. Novikov, *On heavy Higgs boson production*, *Z.Phys.* **C52** (1991) 427–436.

[59] A. Abbasabadi, W. Repko, D. A. Dicus, and R. Vega, *Comparison of Exact and Effective Gauge Boson Calculations for Gauge Boson Fusion Processes*, *Phys.Rev.* **D38** (1988) 2770.

[60] V. D. Barger, T. Han, and R. Phillips, *Double Higgs Boson Bremsstrahlung From W and Z Bosons at Supercolliders*, *Phys.Rev.* **D38** (1988) 2766.

[61] M. Moretti, S. Moretti, F. Piccinini, R. Pittau, and A. Polosa, *Higgs boson self-couplings at the LHC as a probe of extended Higgs sectors*, *JHEP* **0502** (2005) 024, [hep-ph/0410334].

[62] G. Cynolter, E. Lendvai, and G. Pocsik, *Resonance production of three neutral supersymmetric Higgs bosons at LHC*, *Acta Phys.Polon.* **B31** (2000) 1749–1757, [hep-ph/0003008].

[63] T. Plehn and M. Rauch, *The quartic higgs coupling at hadron colliders*, *Phys.Rev.* **D72** (2005) 053008, [hep-ph/0507321].

[64] T. Binoth, S. Karg, N. Kauer, and R. Ruckl, *Multi-Higgs boson production in the Standard Model and beyond*, *Phys.Rev.* **D74** (2006) 113008, [hep-ph/0608057].

[65] E. Todesco and F. Zimmermann, *Proceedings, EuCARD-AccNet-EuroLumi Workshop: The High-Energy Large Hadron Collider, Malta, Republic of Malta, 14 - 16 Oct 2010*, arXiv:1111.7188.

[66] S. Dawson, S. Dittmaier, and M. Spira, *Neutral Higgs boson pair production at hadron colliders: QCD corrections*, *Phys.Rev.* **D58** (1998) 115012, [hep-ph/9805244].

[67] A. Djouadi, M. Spira, and P. Zerwas, *Production of Higgs bosons in proton colliders: QCD corrections*, *Phys.Lett.* **B264** (1991) 440–446.

[68] S. Dawson, *Radiative corrections to Higgs boson production*, *Nucl.Phys.* **B359** (1991) 283–300.

[69] D. Graudenz, M. Spira, and P. Zerwas, *QCD corrections to Higgs boson production at proton proton colliders*, *Phys.Rev.Lett.* **70** (1993) 1372–1375.

[70] R. P. Kauffman and W. Schaffer, *QCD corrections to production of Higgs pseudoscalars*, *Phys.Rev.* **D49** (1994) 551–554, [hep-ph/9305279].

[71] S. Dawson and R. Kauffman, *QCD corrections to Higgs boson production: nonleading terms in the heavy quark limit*, *Phys.Rev.* **D49** (1994) 2298–2309, [hep-ph/9310281].

[72] M. Spira, A. Djouadi, D. Graudenz, and P. Zerwas, *Higgs boson production at the LHC*, *Nucl.Phys.* **B453** (1995) 17–82, [hep-ph/9504378].

[73] M. Kramer, E. Laenen, and M. Spira, *Soft gluon radiation in Higgs boson production at the LHC*, *Nucl.Phys.* **B511** (1998) 523–549, [hep-ph/9611272].

[74] R. V. Harlander and W. B. Kilgore, *Next-to-next-to-leading order Higgs production at hadron colliders*, *Phys.Rev.Lett.* **88** (2002) 201801, [hep-ph/0201206].

[75] C. Anastasiou and K. Melnikov, *Higgs boson production at hadron colliders in NNLO QCD*, *Nucl.Phys.* **B646** (2002) 220–256, [hep-ph/0207004].

[76] V. Ravindran, J. Smith, and W. L. van Neerven, *NNLO corrections to the total cross-section for Higgs boson production in hadron hadron collisions*, *Nucl.Phys.* **B665** (2003) 325–366, [hep-ph/0302135].

[77] T. Han, G. Valencia, and S. Willenbrock, *Structure function approach to vector boson scattering in p p collisions*, *Phys.Rev.Lett.* **69** (1992) 3274–3277, [hep-ph/9206246].

[78] T. Figy, C. Oleari, and D. Zeppenfeld, *Next-to-leading order jet distributions for Higgs boson production via weak boson fusion*, *Phys.Rev.* **D68** (2003) 073005, [hep-ph/0306109].

[79] E. L. Berger and J. M. Campbell, *Higgs boson production in weak boson fusion at next-to-leading order*, *Phys.Rev.* **D70** (2004) 073011, [hep-ph/0403194].

[80] P. Bolzoni, F. Maltoni, S.-O. Moch, and M. Zaro, *Higgs production via vector-boson fusion at NNLO in QCD*, *Phys.Rev.Lett.* **105** (2010) 011801, [arXiv:1003.4451].

[81] R. V. Harlander, J. Vollinga, and M. M. Weber, *Gluon-Induced Weak Boson Fusion*, *Phys.Rev.* **D77** (2008) 053010, [arXiv:0801.3355].

[82] G. Altarelli, R. K. Ellis, and G. Martinelli, *Large Perturbative Corrections to the Drell-Yan Process in QCD*, *Nucl.Phys.* **B157** (1979) 461.

[83] J. Kubar-Andre and F. E. Paige, *Gluon Corrections to the Drell-Yan Model*, *Phys.Rev.* **D19** (1979) 221.

[84] T. Han and S. Willenbrock, *QCD correction to the p p → W H and Z H total cross-sections*, *Phys.Lett.* **B273** (1991) 167–172.

[85] R. Hamberg, W. van Neerven, and T. Matsuura, *A Complete calculation of the order $\alpha - s^2$ correction to the Drell-Yan K factor*, *Nucl.Phys.* **B359** (1991) 343–405.

[86] O. Brein, A. Djouadi, and R. Harlander, *NNLO QCD corrections to the Higgs-strahlung processes at hadron colliders*, *Phys.Lett.* **B579** (2004) 149–156, [hep-ph/0307206].

[87] B. A. Kniehl, *Associated Production of Higgs and Z Bosons From Gluon Fusion in Hadron Collisions*, *Phys.Rev.* **D42** (1990) 2253–2258.

[88] D. A. Dicus and C. Kao, *Higgs Boson - Z^0 Production From Gluon Fusion*, *Phys.Rev.* **D38** (1988) 1008.

[89] O. Brein, R. Harlander, M. Wiesemann, and T. Zirke, *Top-Quark Mediated Effects in Hadronic Higgs-Strahlung*, *Eur.Phys.J.* **C72** (2012) 1868, [arXiv:1111.0761].

[90] W. Beenakker, S. Dittmaier, M. Kramer, B. Plumper, M. Spira, et al., *NLO QCD corrections to t anti-t H production in hadron collisions*, *Nucl.Phys.* **B653** (2003) 151–203, [hep-ph/0211352].

[91] L. Reina and S. Dawson, *Next-to-leading order results for t anti-t h production at the Tevatron*, *Phys.Rev.Lett.* **87** (2001) 201804, [hep-ph/0107101].

[92] S. Dawson, L. Orr, L. Reina, and D. Wackeroth, *Associated top quark Higgs boson production at the LHC*, *Phys.Rev.* **D67** (2003) 071503, [hep-ph/0211438].

[93] A. Djouadi and P. Gambino, *Leading electroweak correction to Higgs boson production at proton colliders*, *Phys.Rev.Lett.* **73** (1994) 2528–2531, [hep-ph/9406432].

[94] A. Djouadi, P. Gambino, and B. A. Kniehl, *Two loop electroweak heavy fermion corrections to Higgs boson production and decay*, *Nucl.Phys.* **B523** (1998) 17–39, [hep-ph/9712330].

[95] U. Aglietti, R. Bonciani, G. Degrassi, and A. Vicini, *Two loop light fermion contribution to Higgs production and decays*, *Phys.Lett.* **B595** (2004) 432–441, [hep-ph/0404071].

[96] G. Degrassi and F. Maltoni, *Two-loop electroweak corrections to Higgs production at hadron colliders*, *Phys.Lett.* **B600** (2004) 255–260, [hep-ph/0407249].

[97] S. Actis, G. Passarino, C. Sturm, and S. Uccirati, *NLO Electroweak Corrections to Higgs Boson Production at Hadron Colliders*, *Phys.Lett.* **B670** (2008) 12–17, [arXiv:0809.1301].

[98] M. Ciccolini, A. Denner, and S. Dittmaier, *Strong and electroweak corrections to the production of Higgs + 2jets via weak interactions at the LHC*, *Phys.Rev.Lett.* **99** (2007) 161803, [arXiv:0707.0381].

[99] M. Ciccolini, A. Denner, and S. Dittmaier, *Electroweak and QCD corrections to Higgs production via vector-boson fusion at the LHC*, *Phys.Rev.* **D77** (2008) 013002, [arXiv:0710.4749].

[100] T. Figy, S. Palmer, and G. Weiglein, *Higgs Production via Weak Boson Fusion in the Standard Model and the MSSM*, *JHEP* **1202** (2012) 105, [arXiv:1012.4789].

[101] M. Ciccolini, S. Dittmaier, and M. Kramer, *Electroweak radiative corrections to associated WH and ZH production at hadron colliders*, *Phys.Rev.* **D68** (2003) 073003, [hep-ph/0306234].

[102] A. Denner, S. Dittmaier, S. Kallweit, and A. Muck, *Electroweak corrections to Higgs-strahlung off W/Z bosons at the Tevatron and the LHC with HAWK*, *JHEP* **1203** (2012) 075, [arXiv:1112.5142].

[103] **LHC Higgs Cross Section Working Group** Collaboration, S. Dittmaier et al., *Handbook of LHC Higgs Cross Sections: 1. Inclusive Observables*, arXiv:1101.0593.

[104] M. Gillioz, R. Grober, C. Grojean, M. Muhlleitner, and E. Salvioni, *Higgs Low-Energy Theorem (and its corrections) in Composite Models*, *JHEP* **1210** (2012) 004, [arXiv:1206.7120].

[105] S. Dawson, E. Furlan, and I. Lewis, *Unravelling an extended quark sector through multiple Higgs production?*, *Phys.Rev.* **D87** (2013) 014007, [arXiv:1210.6663].

[106] J. Baglio and A. Djouadi, *Higgs production at the lHC*, *JHEP* **1103** (2011) 055, [arXiv:1012.0530].

[107] U. Baur, T. Plehn, and D. L. Rainwater, *Probing the Higgs selfcoupling at hadron colliders using rare decays*, *Phys.Rev.* **D69** (2004) 053004, [hep-ph/0310056].

[108] U. Baur, T. Plehn, and D. L. Rainwater, *Measuring the Higgs boson self coupling at the LHC and finite top mass matrix elements*, *Phys.Rev.Lett.* **89** (2002) 151801, [hep-ph/0206024].

[109] U. Baur, T. Plehn, and D. L. Rainwater, *Determining the Higgs boson selfcoupling at hadron colliders*, *Phys.Rev.* **D67** (2003) 033003, [hep-ph/0211224].

[110] U. Baur, T. Plehn, and D. L. Rainwater, *Examining the Higgs boson potential at lepton and hadron colliders: A Comparative analysis*, *Phys.Rev.* **D68** (2003) 033001, [hep-ph/0304015].

[111] M. J. Dolan, C. Englert, and M. Spannowsky, *Higgs self-coupling measurements at the LHC*, *JHEP* **1210** (2012) 112, [arXiv:1206.5001].

[112] A. Papaefstathiou, L. L. Yang, and J. Zurita, *Higgs boson pair production at the LHC in the $b\bar{b}W^+W^-$ channel*, *Phys.Rev.* **D87** (2013) 011301, [arXiv:1209.1489].

[113] J. M. Butterworth, A. R. Davison, M. Rubin, and G. P. Salam, *Jet substructure as a new Higgs search channel at the LHC*, *Phys.Rev.Lett.* **100** (2008) 242001, [arXiv:0802.2470].

[114] **ATLAS** Collaboration, *Physics at a High-Luminosity LHC with ATLAS (Update)*, ATL-PHYS-PUB-2012-004.

[115] A. Djouadi, J. Kalinowski, and M. Spira, *HDECAY: A Program for Higgs boson decays in the standard model and its supersymmetric extension*, *Comput.Phys.Commun.* **108** (1998) 56–74, [hep-ph/9704448].

[116] A. Djouadi, M. Muhlleitner, and M. Spira, *Decays of supersymmetric particles: The Program SUSY-HIT (SUspect-SdecaY-Hdecay-InTerface)*, *Acta Phys.Polon.* **B38** (2007) 635–644, [hep-ph/0609292].

[117] M. Spira, tiger.web.psi.ch/proglist.html.

[118] K. Arnold, M. Bahr, G. Bozzi, F. Campanario, C. Englert, et al., *VBFNLO: A Parton level Monte Carlo for processes with electroweak bosons*, *Comput.Phys.Commun.* **180** (2009) 1661–1670, [arXiv:0811.4559].

[119] J. R. Ellis, M. K. Gaillard, and D. V. Nanopoulos, *A Phenomenological Profile of the Higgs Boson*, *Nucl.Phys.* **B106** (1976) 292.

[120] M. A. Shifman, A. Vainshtein, M. Voloshin, and V. I. Zakharov, *Low-Energy Theorems for Higgs Boson Couplings to Photons*, *Sov.J.Nucl.Phys.* **30** (1979) 711–716.

[121] B. A. Kniehl and M. Spira, *Low-energy theorems in Higgs physics*, *Z.Phys.* **C69** (1995) 77–88, [hep-ph/9505225].

[122] S. Catani, D. de Florian, M. Grazzini, and P. Nason, *Soft gluon resummation for Higgs boson production at hadron colliders*, *JHEP* **0307** (2003) 028, [hep-ph/0306211].

[123] D. de Florian and M. Grazzini, *Higgs production through gluon fusion: Updated cross sections at the Tevatron and the LHC*, *Phys.Lett.* **B674** (2009) 291–294, [arXiv:0901.2427].

[124] D. de Florian and M. Grazzini, *Higgs production at the LHC: updated cross sections at $\sqrt{s} = 8$ TeV*, *Phys.Lett.* **B718** (2012) 117–120, [arXiv:1206.4133].

[125] C. Anastasiou, R. Boughezal, and F. Petriello, *Mixed QCD-electroweak corrections to Higgs boson production in gluon fusion*, *JHEP* **0904** (2009) 003, [arXiv:0811.3458].

[126] S. Catani and M. Seymour, *A General algorithm for calculating jet cross-sections in NLO QCD*, *Nucl.Phys.* **B485** (1997) 291–419, [hep-ph/9605323].

[127] J. Alwall, P. Demin, S. de Visscher, R. Frederix, M. Herquet, et al., *MadGraph/MadEvent v4: The New Web Generation*, *JHEP* **0709** (2007) 028, [arXiv:0706.2334].

[128] T. Figy, *Next-to-leading order QCD corrections to light Higgs Pair production via vector boson fusion*, *Mod.Phys.Lett.* **A23** (2008) 1961–1973, [arXiv:0806.2200].

[129] T. Hahn, *Generating Feynman diagrams and amplitudes with FeynArts 3*, *Comput.Phys.Commun.* **140** (2001) 418–431, [hep-ph/0012260].

[130] T. Hahn and M. Perez-Victoria, *Automatized one loop calculations in four-dimensions and D-dimensions*, *Comput.Phys.Commun.* **118** (1999) 153–165, [hep-ph/9807565].

[131] T. Hahn and M. Rauch, *News from FormCalc and LoopTools*, *Nucl.Phys.Proc.Suppl.* **157** (2006) 236–240, [hep-ph/0601248].

[132] T. Hahn, *A Mathematica interface for FormCalc-generated code*, *Comput.Phys.Commun.* **178** (2008) 217–221, [hep-ph/0611273].

[133] A. Martin, W. Stirling, R. Thorne, and G. Watt, *Parton distributions for the LHC*, *Eur.Phys.J.* **C63** (2009) 189–285, [arXiv:0901.0002].

[134] H.-L. Lai, M. Guzzi, J. Huston, Z. Li, P. M. Nadolsky, et al., *New parton distributions for collider physics*, *Phys.Rev.* **D82** (2010) 074024, [arXiv:1007.2241].

[135] S. Alekhin, J. Blumlein, and S. Moch, *Parton Distribution Functions and Benchmark Cross Sections at NNLO*, *Phys.Rev.* **D86** (2012) 054009, [arXiv:1202.2281].

[136] M. Gluck, P. Jimenez-Delgado, E. Reya, and C. Schuck, *On the role of heavy flavor parton distributions at high energy colliders*, *Phys.Lett.* **B664** (2008) 133–138, [arXiv:0801.3618].

[137] **H1, ZEUS** Collaboration, V. Radescu, *Hera Precision Measurements and Impact for LHC Predictions*, arXiv:1107.4193.

[138] **NNPDF** Collaboration, A. Guffanti, *NNPDF2.1: Including heavy quark mass effects in NNPDF fits*, *AIP Conf.Proc.* **1369** (2011) 21–28.

[139] A. Martin, W. Stirling, R. Thorne, and G. Watt, *Uncertainties on alpha(S) in global PDF analyses and implications for predicted hadronic cross sections*, *Eur.Phys.J.* **C64** (2009) 653–680, [arXiv:0905.3531].

[140] **NNPDF** Collaboration, R. D. Ball et al., *Theoretical issues in PDF determination and associated uncertainties*, *Phys.Lett.* **B723** (2013) 330–339, [arXiv:1303.1189].

[141] J. Baglio and A. Djouadi, *Predictions for Higgs production at the Tevatron and the associated uncertainties*, *JHEP* **1010** (2010) 064, [arXiv:1003.4266].

[142] M. El-Kacimi and R. Lafaye, *Simulation of neutral Higgs pairs production processes in PYTHIA using HPAIR matrix elements*, ATL-PHYS-2002-015.

[143] A. Blondel, A. Clark, and F. Mazzucato, *Studies on the measurement of the SM Higgs self-couplings*, ATL-PHYS-2002-029.

[144] T. Sjostrand, S. Mrenna, and P. Z. Skands, *PYTHIA 6.4 Physics and Manual*, *JHEP* **0605** (2006) 026, [hep-ph/0603175].

[145] J. Alwall, M. Herquet, F. Maltoni, O. Mattelaer, and T. Stelzer, *MadGraph 5 : Going Beyond*, *JHEP* **1106** (2011) 128, [arXiv:1106.0522].

[146] M. Battaglia, E. Boos, and W.-M. Yao, *Studying the Higgs potential at the e+ e- linear collider*, *eConf* **C010630** (2001) E3016, [hep-ph/0111276].

[147] S. Ovyn, X. Rouby, and V. Lemaitre, *DELPHES, a framework for fast simulation of a generic collider experiment*, arXiv:0903.2225.

[148] A. Elagin, P. Murat, A. Pranko, and A. Safonov, *A New Mass Reconstruction Technique for Resonances Decaying to di-tau*, *Nucl.Instrum.Meth.* **A654** (2011) 481–489, [arXiv:1012.4686].

[149] J. M. Campbell and R. K. Ellis, *Radiative corrections to Z b anti-b production*, *Phys.Rev.* **D62** (2000) 114012, [hep-ph/0006304].

[150] P. Nason, S. Dawson, and R. K. Ellis, *The Total Cross-Section for the Production of Heavy Quarks in Hadronic Collisions*, *Nucl.Phys.* **B303** (1988) 607.

[151] P. Nason, S. Dawson, and R. K. Ellis, *The One Particle Inclusive Differential Cross-Section for Heavy Quark Production in Hadronic Collisions*, *Nucl.Phys.* **B327** (1989) 49–92.

[152] W. Beenakker, H. Kuijf, W. van Neerven, and J. Smith, *QCD Corrections to Heavy Quark Production in p anti-p Collisions*, *Phys.Rev.* **D40** (1989) 54–82.

[153] W. Beenakker, W. van Neerven, R. Meng, G. Schuler, and J. Smith, *QCD corrections to heavy quark production in hadron hadron collisions*, *Nucl.Phys.* **B351** (1991) 507–560.

[154] M. L. Mangano, P. Nason, and G. Ridolfi, *Heavy quark correlations in hadron collisions at next-to-leading order*, *Nucl.Phys.* **B373** (1992) 295–345.

[155] S. Frixione, M. L. Mangano, P. Nason, and G. Ridolfi, *Top quark distributions in hadronic collisions*, *Phys.Lett.* **B351** (1995) 555–561, [hep-ph/9503213].

[156] M. Beneke, I. Efthymiopoulos, M. L. Mangano, J. Womersley, A. Ahmadov, et al., *Top quark physics*, hep-ph/0003033.

[157] M. Cacciari, S. Frixione, M. L. Mangano, P. Nason, and G. Ridolfi, *Updated predictions for the total production cross sections of top and of heavier quark pairs at the Tevatron and at the LHC*, *JHEP* **0809** (2008) 127, [arXiv:0804.2800].

[158] N. Kidonakis and R. Vogt, *The Theoretical top quark cross section at the Tevatron and the LHC*, *Phys.Rev.* **D78** (2008) 074005, [arXiv:0805.3844].

[159] S. Moch and P. Uwer, *Theoretical status and prospects for top-quark pair production at hadron colliders*, *Phys.Rev.* **D78** (2008) 034003, [arXiv:0804.1476].

[160] S. Moch, P. Uwer, and A. Vogt, *On top-pair hadro-production at next-to-next-to-leading order*, *Phys.Lett.* **B714** (2012) 48–54, [arXiv:1203.6282].

[161] M. Cacciari, M. Czakon, M. Mangano, A. Mitov, and P. Nason, *Top-pair production at hadron colliders with next-to-next-to-leading logarithmic soft-gluon resummation*, *Phys.Lett.* **B710** (2012) 612–622, [arXiv:1111.5869].

[162] P. Bärnreuther, M. Czakon, and A. Mitov, *Percent Level Precision Physics at the Tevatron: First Genuine NNLO QCD Corrections to $q\bar{q} \to t\bar{t} + X$*, *Phys.Rev.Lett.* **109** (2012) 132001, [arXiv:1204.5201].

[163] S. R. Coleman and J. Mandula, *All Possible Symmetries of the S Matrix*, *Phys.Rev.* **159** (1967) 1251–1256.

[164] Y. Golfand and E. Likhtman, *Extension of the Algebra of Poincare Group Generators and Violation of p Invariance*, *JETP Lett.* **13** (1971) 323–326.

[165] P. Ramond, *Dual Theory for Free Fermions*, *Phys.Rev.* **D3** (1971) 2415–2418.

[166] A. Neveu and J. Schwarz, *Quark Model of Dual Pions*, *Phys.Rev.* **D4** (1971) 1109–1111.

[167] D. Volkov and V. Akulov, *Is the Neutrino a Goldstone Particle?*, *Phys.Lett.* **B46** (1973) 109–110.

[168] J. Wess and B. Zumino, *Supergauge Transformations in Four-Dimensions*, *Nucl.Phys.* **B70** (1974) 39–50.

[169] J. Iliopoulos and B. Zumino, *Broken Supergauge Symmetry and Renormalization*, *Nucl.Phys.* **B76** (1974) 310.

[170] S. Ferrara, J. Iliopoulos, and B. Zumino, *Supergauge Invariance and the Gell-Mann - Low Eigenvalue*, *Nucl.Phys.* **B77** (1974) 413.

[171] D. Z. Freedman, P. van Nieuwenhuizen, and S. Ferrara, *Progress Toward a Theory of Supergravity*, *Phys.Rev.* **D13** (1976) 3214–3218.

[172] S. Deser and B. Zumino, *Consistent Supergravity*, *Phys.Lett.* **B62** (1976) 335.

[173] R. Haag, J. T. Lopuszanski, and M. Sohnius, *All Possible Generators of Supersymmetries of the s Matrix*, *Nucl.Phys.* **B88** (1975) 257.

[174] L. O'Raifeartaigh, *Spontaneous Symmetry Breaking for Chiral Scalar Superfields*, *Nucl.Phys.* **B96** (1975) 331.

[175] P. Fayet and J. Iliopoulos, *Spontaneously Broken Supergauge Symmetries and Goldstone Spinors*, *Phys.Lett.* **B51** (1974) 461–464.

[176] L. E. Ibanez and G. G. Ross, *SU(2)-L x U(1) Symmetry Breaking as a Radiative Effect of Supersymmetry Breaking in Guts*, *Phys.Lett.* **B110** (1982) 215–220.

[177] L. Alvarez-Gaume, J. Polchinski, and M. B. Wise, *Minimal Low-Energy Supergravity*, *Nucl.Phys.* **B221** (1983) 495.

[178] J. R. Ellis, J. Hagelin, D. V. Nanopoulos, and K. Tamvakis, *Weak Symmetry Breaking by Radiative Corrections in Broken Supergravity*, *Phys.Lett.* **B125** (1983) 275.

[179] L. E. Ibanez and C. Lopez, *N=1 Supergravity, the Weak Scale and the Low-Energy Particle Spectrum*, *Nucl.Phys.* **B233** (1984) 511.

[180] L. E. Ibanez, C. Lopez, and C. Munoz, *The Low-Energy Supersymmetric Spectrum According to N=1 Supergravity Guts*, *Nucl.Phys.* **B256** (1985) 218–252.

[181] M. Drees, R. Godbole, and P. Roy, *Theory and phenomenology of sparticles: An account of four-dimensional N=1 supersymmetry in high energy physics*, .

[182] J. F. Gunion, H. E. Haber, G. L. Kane, and S. Dawson, *The Higgs Hunter's Guide*, *Front.Phys.* **80** (2000) 1–448.

[183] Y. Okada, M. Yamaguchi, and T. Yanagida, *Upper bound of the lightest Higgs boson mass in the minimal supersymmetric standard model*, *Prog.Theor.Phys.* **85** (1991) 1–6.

[184] Y. Okada, M. Yamaguchi, and T. Yanagida, *Renormalization group analysis on the Higgs mass in the softly broken supersymmetric standard model*, *Phys.Lett.* **B262** (1991) 54–58.

[185] J. R. Ellis, G. Ridolfi, and F. Zwirner, *Radiative corrections to the masses of supersymmetric Higgs bosons*, *Phys.Lett.* **B257** (1991) 83–91.

[186] H. E. Haber and R. Hempfling, *Can the mass of the lightest Higgs boson of the minimal supersymmetric model be larger than m(Z)?*, *Phys.Rev.Lett.* **66** (1991) 1815–1818.

[187] P. H. Chankowski, S. Pokorski, and J. Rosiek, *Charged and neutral supersymmetric Higgs boson masses: Complete one loop analysis*, *Phys.Lett.* **B274** (1992) 191–198.

[188] A. Brignole, *Radiative corrections to the supersymmetric neutral Higgs boson masses*, *Phys.Lett.* **B281** (1992) 284–294.

[189] A. Dabelstein, *The One loop renormalization of the MSSM Higgs sector and its application to the neutral scalar Higgs masses*, *Z.Phys.* **C67** (1995) 495–512, [hep-ph/9409375].

[190] D. M. Pierce, J. A. Bagger, K. T. Matchev, and R.-j. Zhang, *Precision corrections in the minimal supersymmetric standard model*, *Nucl.Phys.* **B491** (1997) 3–67, [hep-ph/9606211].

[191] A. Arbey, M. Battaglia, A. Djouadi, F. Mahmoudi, and J. Quevillon, *Implications of a 125 GeV Higgs for supersymmetric models*, *Phys.Lett.* **B708** (2012) 162–169, [arXiv:1112.3028].

[192] R. Hempfling and A. H. Hoang, *Two loop radiative corrections to the upper limit of the lightest Higgs boson mass in the minimal supersymmetric model*, *Phys.Lett.* **B331** (1994) 99–106, [hep-ph/9401219].

[193] S. Heinemeyer, W. Hollik, and G. Weiglein, *QCD corrections to the masses of the neutral CP - even Higgs bosons in the MSSM*, *Phys.Rev.* **D58** (1998) 091701, [hep-ph/9803277].

[194] S. Heinemeyer, W. Hollik, and G. Weiglein, *The Masses of the neutral CP - even Higgs bosons in the MSSM: Accurate analysis at the two loop level*, *Eur.Phys.J.* **C9** (1999) 343–366, [hep-ph/9812472].

[195] R. Barbieri, M. Frigeni, and F. Caravaglios, *The Supersymmetric Higgs for heavy superpartners*, *Phys.Lett.* **B258** (1991) 167–170.

[196] J. Espinosa and M. Quiros, *Two loop radiative corrections to the mass of the lightest Higgs boson in supersymmetric standard models*, *Phys.Lett.* **B266** (1991) 389–396.

[197] D. Pierce, A. Papadopoulos, and S. Johnson, *Limits on the CP even Higgs boson masses in the MSSM*, *Phys.Rev.Lett.* **68** (1992) 3678–3681.

[198] K. Sasaki, M. S. Carena, and C. Wagner, *Renormalization group analysis of the Higgs sector in the minimal supersymmetric standard model*, *Nucl.Phys.* **B381** (1992) 66–86.

[199] J. Kodaira, Y. Yasui, and K. Sasaki, *The Mass of the lightest supersymmetric Higgs boson beyond the leading logarithm approximation*, *Phys.Rev.* **D50** (1994) 7035–7041, [hep-ph/9311366].

[200] H. E. Haber and R. Hempfling, *The Renormalization group improved Higgs sector of the minimal supersymmetric model*, *Phys.Rev.* **D48** (1993) 4280–4309, [hep-ph/9307201].

[201] M. S. Carena, J. Espinosa, M. Quiros, and C. Wagner, *Analytical expressions for radiatively corrected Higgs masses and couplings in the MSSM*, *Phys.Lett.* **B355** (1995) 209–221, [hep-ph/9504316].

[202] M. S. Carena, P. M. Zerwas, E. Accomando, P. Bagnaia, A. Ballestrero, et al., *Higgs physics at LEP-2*, hep-ph/9602250.

[203] H. E. Haber, R. Hempfling, and A. H. Hoang, *Approximating the radiatively corrected Higgs mass in the minimal supersymmetric model*, *Z.Phys.* **C75** (1997) 539–554, [hep-ph/9609331].

[204] S. Li and M. Sher, *Upper Limit to the Lightest Higgs Mass in Supersymmetric Models*, *Phys.Lett.* **B140** (1984) 339.

[205] M. Drees and M. M. Nojiri, *One loop corrections to the Higgs sector in minimal supergravity models*, *Phys.Rev.* **D45** (1992) 2482–2492.

[206] J. Casas, J. Espinosa, M. Quiros, and A. Riotto, *The Lightest Higgs boson mass in the minimal supersymmetric standard model*, *Nucl.Phys.* **B436** (1995) 3–29, [hep-ph/9407389].

[207] J. R. Ellis, G. Ridolfi, and F. Zwirner, *On radiative corrections to supersymmetric Higgs boson masses and their implications for LEP searches*, *Phys.Lett.* **B262** (1991) 477–484.

[208] A. Brignole, J. R. Ellis, G. Ridolfi, and F. Zwirner, *The Supersymmetric charged Higgs boson mass and LEP phenomenology*, *Phys.Lett.* **B271** (1991) 123–132.

[209] R.-J. Zhang, *Two loop effective potential calculation of the lightest CP even Higgs boson mass in the MSSM*, *Phys.Lett.* **B447** (1999) 89–97, [hep-ph/9808299].

[210] J. R. Espinosa and R.-J. Zhang, *MSSM lightest CP even Higgs boson mass to O(alpha(s) alpha(t)): The Effective potential approach*, *JHEP* **0003** (2000) 026, [hep-ph/9912236].

[211] J. R. Espinosa and R.-J. Zhang, *Complete two loop dominant corrections to the mass of the lightest CP even Higgs boson in the minimal supersymmetric standard model*, *Nucl.Phys.* **B586** (2000) 3–38, [hep-ph/0003246].

[212] A. Brignole, G. Degrassi, P. Slavich, and F. Zwirner, *On the two loop sbottom corrections to the neutral Higgs boson masses in the MSSM*, *Nucl.Phys.* **B643** (2002) 79–92, [hep-ph/0206101].

[213] A. Brignole, G. Degrassi, P. Slavich, and F. Zwirner, *On the $O(\alpha(t)^2)$ two loop corrections to the neutral Higgs boson masses in the MSSM*, *Nucl.Phys.* **B631** (2002) 195–218, [hep-ph/0112177].

[214] M. S. Carena, S. Mrenna, and C. Wagner, *MSSM Higgs boson phenomenology at the Tevatron collider*, *Phys.Rev.* **D60** (1999) 075010, [hep-ph/9808312].

[215] **ATLAS** Collaboration, *Combination of Higgs Boson Searches with up to 4.9 fb^{-1} of pp Collisions Data Taken at a center-of-mass energy of 7 TeV with the ATLAS Experiment at the LHC*, ATLAS-CONF-2011-163.

[216] **CMS** Collaboration, CMS, *Combination of SM Higgs Searches*, CMS-PAS-HIG-11-032.

[217] "The LEP Electroweak Working Group and the SLD Heavy Flavour Group." lepewwg.web.cern.ch/LEPEWWG.

[218] **Particle Data Group** Collaboration, K. Nakamura et al., *Review of particle physics*, *J.Phys.* **G37** (2010) 075021.

[219] H. E. Haber and G. L. Kane, *The Search for Supersymmetry: Probing Physics Beyond the Standard Model*, *Phys.Rept.* **117** (1985) 75–263.

[220] S. Heinemeyer, W. Hollik, and G. Weiglein, *Electroweak precision observables in the minimal supersymmetric standard model*, *Phys.Rept.* **425** (2006) 265–368, [hep-ph/0412214].

[221] S. Heinemeyer, *MSSM Higgs physics at higher orders*, *Int.J.Mod.Phys.* **A21** (2006) 2659–2772, [hep-ph/0407244].

[222] **MSSM Working Group** Collaboration, A. Djouadi et al., *The Minimal supersymmetric standard model: Group summary report*, hep-ph/9901246.

[223] A. H. Chamseddine, R. L. Arnowitt, and P. Nath, *Locally Supersymmetric Grand Unification*, *Phys.Rev.Lett.* **49** (1982) 970.

[224] R. Barbieri, S. Ferrara, and C. A. Savoy, *Gauge Models with Spontaneously Broken Local Supersymmetry*, *Phys.Lett.* **B119** (1982) 343.

[225] L. J. Hall, J. D. Lykken, and S. Weinberg, *Supergravity as the Messenger of Supersymmetry Breaking*, *Phys.Rev.* **D27** (1983) 2359–2378.

[226] N. Ohta, *Grand unified theories based on local supersymmetry*, *Prog.Theor.Phys.* **70** (1983) 542.

[227] M. Dine and W. Fischler, *A Phenomenological Model of Particle Physics Based on Supersymmetry*, *Phys.Lett.* **B110** (1982) 227.

[228] L. Alvarez-Gaume, M. Claudson, and M. B. Wise, *Low-Energy Supersymmetry*, *Nucl.Phys.* **B207** (1982) 96.

[229] M. Dine and A. E. Nelson, *Dynamical supersymmetry breaking at low-energies*, *Phys.Rev.* **D48** (1993) 1277–1287, [hep-ph/9303230].

[230] M. Dine, A. E. Nelson, and Y. Shirman, *Low-energy dynamical supersymmetry breaking simplified*, *Phys.Rev.* **D51** (1995) 1362–1370, [hep-ph/9408384].

[231] G. Giudice and R. Rattazzi, *Theories with gauge mediated supersymmetry breaking*, *Phys.Rept.* **322** (1999) 419–499, [hep-ph/9801271].

[232] L. Randall and R. Sundrum, *Out of this world supersymmetry breaking*, *Nucl.Phys.* **B557** (1999) 79–118, [hep-th/9810155].

[233] G. F. Giudice, M. A. Luty, H. Murayama, and R. Rattazzi, *Gaugino mass without singlets*, *JHEP* **9812** (1998) 027, [hep-ph/9810442].

[234] J. A. Bagger, T. Moroi, and E. Poppitz, *Anomaly mediation in supergravity theories*, *JHEP* **0004** (2000) 009, [hep-th/9911029].

[235] N. Arkani-Hamed and S. Dimopoulos, *Supersymmetric unification without low energy supersymmetry and signatures for fine-tuning at the LHC*, *JHEP* **0506** (2005) 073, [hep-th/0405159].

[236] G. Giudice and A. Romanino, *Split supersymmetry*, *Nucl.Phys.* **B699** (2004) 65–89, [hep-ph/0406088].

[237] J. D. Wells, *PeV-scale supersymmetry*, *Phys.Rev.* **D71** (2005) 015013, [hep-ph/0411041].

[238] L. J. Hall and Y. Nomura, *A Finely-Predicted Higgs Boson Mass from A Finely-Tuned Weak Scale*, *JHEP* **1003** (2010) 076, [arXiv:0910.2235].

[239] M. S. Carena, S. Heinemeyer, C. Wagner, and G. Weiglein, *Suggestions for improved benchmark scenarios for Higgs boson searches at LEP-2*, hep-ph/9912223.

[240] A. Djouadi, J.-L. Kneur, and G. Moultaka, *SuSpect: A Fortran code for the supersymmetric and Higgs particle spectrum in the MSSM*, *Comput.Phys.Commun.* **176** (2007) 426–455, [hep-ph/0211331].

[241] B. Allanach, *SOFTSUSY: a program for calculating supersymmetric spectra*, *Comput.Phys.Commun.* **143** (2002) 305–331, [hep-ph/0104145].

[242] B. Allanach, A. Djouadi, J. Kneur, W. Porod, and P. Slavich, *Precise determination of the neutral Higgs boson masses in the MSSM*, *JHEP* **0409** (2004) 044, [hep-ph/0406166].

[243] P. Kant, R. Harlander, L. Mihaila, and M. Steinhauser, *Light MSSM Higgs boson mass to three-loop accuracy*, *JHEP* **1008** (2010) 104, [arXiv:1005.5709].

[244] F. Brummer, S. Kraml, and S. Kulkarni, *Anatomy of maximal stop mixing in the MSSM*, *JHEP* **1208** (2012) 089, [arXiv:1204.5977].

[245] B. Dumont, J. F. Gunion, and S. Kraml, *The phenomenological MSSM in view of the 125 GeV Higgs data*, *Phys.Rev.* **D89** (2014) 055018, [arXiv:1312.7027].

[246] S. Heinemeyer, W. Hollik, and G. Weiglein, *FeynHiggs: A Program for the calculation of the masses of the neutral CP even Higgs bosons in the MSSM*, *Comput.Phys.Commun.* **124** (2000) 76–89, [hep-ph/9812320].

[247] A. Arbey, M. Battaglia, and F. Mahmoudi, *Constraints on the MSSM from the Higgs Sector: A pMSSM Study of Higgs Searches, $B_s^0 \to \mu^+\mu^-$ and Dark Matter Direct Detection*, *Eur.Phys.J.* **C72** (2012) 1906, [arXiv:1112.3032].

[248] J. R. Ellis, A. Lahanas, D. V. Nanopoulos, and K. Tamvakis, *No-Scale Supersymmetric Standard Model*, *Phys.Lett.* **B134** (1984) 429.

[249] J. R. Ellis, C. Kounnas, and D. V. Nanopoulos, *Phenomenological SU(1,1) Supergravity*, *Nucl.Phys.* **B241** (1984) 406.

[250] A. Benhenni, J.-L. Kneur, G. Moultaka, and S. Bailly, *Revisiting No-Scale Supergravity Inspired Scenarios: Updated Theoretical and Phenomenological Constraints*, *Phys.Rev.* **D84** (2011) 075015, [arXiv:1106.6325].

[251] T. Li, J. A. Maxin, D. V. Nanopoulos, and J. W. Walker, *Profumo di SUSY: Suggestive Correlations in the ATLAS and CMS High Jet Multiplicity Data*, arXiv:1111.4204.

[252] A. Djouadi, U. Ellwanger, and A. Teixeira, *The Constrained next-to-minimal supersymmetric standard model*, *Phys.Rev.Lett.* **101** (2008) 101802, [arXiv:0803.0253].

[253] A. Djouadi, U. Ellwanger, and A. Teixeira, *Phenomenology of the constrained NMSSM*, *JHEP* **0904** (2009) 031, [arXiv:0811.2699].

[254] A. Djouadi, M. Drees, U. Ellwanger, R. Godbole, C. Hugonie, et al., *Benchmark scenarios for the NMSSM*, *JHEP* **0807** (2008) 002, [arXiv:0801.4321].

[255] S. AbdusSalam, B. Allanach, H. Dreiner, J. Ellis, U. Ellwanger, et al., *Benchmark Models, Planes, Lines and Points for Future SUSY Searches at the LHC*, *Eur.Phys.J.* **C71** (2011) 1835, [arXiv:1109.3859].

[256] J. R. Ellis, T. Falk, K. A. Olive, and Y. Santoso, *Exploration of the MSSM with nonuniversal Higgs masses*, *Nucl.Phys.* **B652** (2003) 259–347, [hep-ph/0210205].

[257] H. Baer, A. Mustafayev, S. Profumo, A. Belyaev, and X. Tata, *Neutralino cold dark matter in a one parameter extension of the minimal supergravity model*, *Phys.Rev.* **D71** (2005) 095008, [hep-ph/0412059].

[258] J. R. Ellis, K. A. Olive, and P. Sandick, *Varying the Universality of Supersymmetry-Breaking Contributions to MSSM Higgs Boson Masses*, *Phys.Rev.* **D78** (2008) 075012, [arXiv:0805.2343].

[259] L. Roszkowski, R. Ruiz de Austri, R. Trotta, Y.-L. S. Tsai, and T. A. Varley, *Global fits of the Non-Universal Higgs Model*, *Phys.Rev.* **D83** (2011) 015014, [arXiv:0903.1279].

[260] **CMS** Collaboration, S. Chatrchyan et al., *Search for Neutral MSSM Higgs Bosons Decaying to Tau Pairs in pp Collisions at* $\sqrt{s} = 7$ *TeV*, *Phys.Rev.Lett.* **106** (2011) 231801, [arXiv:1104.1619].

[261] A. Arbey, M. Battaglia, and F. Mahmoudi, *Implications of LHC Searches on SUSY Particle Spectra: The pMSSM Parameter Space with Neutralino Dark Matter*, *Eur.Phys.J.* **C72** (2012) 1847, [arXiv:1110.3726].

[262] A. Akeroyd, F. Mahmoudi, and D. M. Santos, *The decay* $Bs \to mu + mu-$*: updated SUSY constraints and prospects*, *JHEP* **1112** (2011) 088, [arXiv:1108.3018].

[263] A. Arbey and F. Mahmoudi, *SUSY Constraints, Relic Density, and Very Early Universe*, *JHEP* **1005** (2010) 051, [arXiv:0906.0368].

[264] F. Mahmoudi, *SuperIso v2.3: A Program for calculating flavor physics observables in Supersymmetry*, *Comput.Phys.Commun.* **180** (2009) 1579–1613, [arXiv:0808.3144].

[265] A. Arbey and F. Mahmoudi, *SuperIso Relic: A Program for calculating relic density and flavor physics observables in Supersymmetry*, *Comput.Phys.Commun.* **181** (2010) 1277–1292, [arXiv:0906.0369].

[266] G. Kane, P. Kumar, R. Lu, and B. Zheng, *Higgs Mass Prediction for Realistic String/M Theory Vacua*, *Phys.Rev.* **D85** (2012) 075026, [arXiv:1112.1059].

[267] D. Feldman, G. Kane, E. Kuflik, and R. Lu, *A new (string motivated) approach to the little hierarchy problem*, *Phys.Lett.* **B704** (2011) 56–61, [arXiv:1105.3765].

[268] M. Ibe and T. T. Yanagida, *The Lightest Higgs Boson Mass in Pure Gravity Mediation Model*, *Phys.Lett.* **B709** (2012) 374–380, [arXiv:1112.2462].

[269] N. Bernal, A. Djouadi, and P. Slavich, *The MSSM with heavy scalars*, *JHEP* **0707** (2007) 016, [arXiv:0705.1496].

[270] G. F. Giudice and A. Strumia, *Probing High-Scale and Split Supersymmetry with Higgs Mass Measurements*, *Nucl.Phys.* **B858** (2012) 63–83, [arXiv:1108.6077].

[271] M. S. Carena and H. E. Haber, *Higgs boson theory and phenomenology*, *Prog.Part.Nucl.Phys.* **50** (2003) 63–152, [hep-ph/0208209].

[272] **ATLAS** Collaboration, *Combined coupling measurements of the Higgs-like boson with the ATLAS detector using up to 25 fb^{-1} of proton-proton collision data*, ATLAS-CONF-2013-034.

[273] H. E. Haber, *Challenges for nonminimal Higgs searches at future colliders*, hep-ph/9505240.

[274] R. Barbieri and G. Giudice, *Upper Bounds on Supersymmetric Particle Masses*, *Nucl.Phys.* **B306** (1988) 63.

[275] **ALEPH, DELPHI, L3, OPAL , LEP Working Group for Higgs Boson Searches** Collaboration, S. Schael et al., *Search for neutral MSSM Higgs bosons at LEP*, *Eur.Phys.J.* **C47** (2006) 547–587, [hep-ex/0602042].

[276] A. Delgado and G. Giudice, *On the tuning condition of split supersymmetry*, *Phys.Lett.* **B627** (2005) 155–160, [hep-ph/0506217].

[277] E. Arganda, J. L. Diaz-Cruz, and A. Szynkman, *Decays of H^0/A^0 in supersymmetric scenarios with heavy sfermions*, *Eur.Phys.J.* **C73** (2013) 2384, [arXiv:1211.0163].

[278] E. Arganda, J. L. Diaz-Cruz, and A. Szynkman, *Slim SUSY*, *Phys.Lett.* **B722** (2013) 100, [arXiv:1301.0708].

[279] H. Baer, F. E. Paige, S. D. Protopopescu, and X. Tata, *ISAJET 7.48: A Monte Carlo event generator for p p, anti-p, p, and e+ e- reactions*, hep-ph/0001086.

[280] W. Porod, *SPheno, a program for calculating supersymmetric spectra, SUSY particle decays and SUSY particle production at e+ e- colliders*, *Comput.Phys.Commun.* **153** (2003) 275–315, [hep-ph/0301101].

[281] E. Bagnaschi, N. Bernal, A. Djouadi, J. Quevillon, and P. Slavich *in preparation.*

[282] L. Maiani, A. Polosa, and V. Riquer, *Probing Minimal Supersymmetry at the LHC with the Higgs Boson Masses*, *New J.Phys.* **14** (2012) 073029, [arXiv:1202.5998].

[283] L. Maiani, A. Polosa, and V. Riquer, *Heavier Higgs Particles: Indications from Minimal Supersymmetry*, *Phys.Lett.* **B718** (2012) 465–468, [arXiv:1209.4816].

[284] F. Zwirner, *The quest for low-energy supersymmetry and the role of high-energy e+ e- colliders*, hep-ph/9203204.

[285] G. Degrassi, P. Slavich, and F. Zwirner, *On the neutral Higgs boson masses in the MSSM for arbitrary stop mixing*, *Nucl.Phys.* **B611** (2001) 403–422, [hep-ph/0105096].

[286] A. Arbey, M. Battaglia, A. Djouadi, and F. Mahmoudi, *The Higgs sector of the phenomenological MSSM in the light of the Higgs boson discovery*, *JHEP* **1209** (2012) 107, [arXiv:1207.1348].

[287] A. Arbey, M. Battaglia, A. Djouadi, and F. Mahmoudi, *An update on the constraints on the phenomenological MSSM from the new LHC Higgs results*, *Phys.Lett.* **B720** (2013) 153–160, [arXiv:1211.4004].

[288] M. S. Carena, S. Heinemeyer, C. Wagner, and G. Weiglein, *Suggestions for benchmark scenarios for MSSM Higgs boson searches at hadron colliders*, *Eur.Phys.J.* **C26** (2003) 601–607, [hep-ph/0202167].

[289] M. Carena, S. Heinemeyer, O. Stål, C. Wagner, and G. Weiglein, *MSSM Higgs Boson Searches at the LHC: Benchmark Scenarios after the Discovery of a Higgs-like Particle*, *Eur. Phys. J.* **C73** (2013) 2552, [arXiv:1302.7033].

[290] **Particle Data Group** Collaboration, J. Beringer et al., *Review of Particle Physics (RPP)*, *Phys.Rev.* **D86** (2012) 010001.

[291] S. Alekhin, A. Djouadi, and S. Moch, *The top quark and Higgs boson masses and the stability of the electroweak vacuum*, *Phys.Lett.* **B716** (2012) 214–219, [arXiv:1207.0980].

[292] J. L. Feng, K. T. Matchev, and T. Moroi, *Multi - TeV scalars are natural in minimal supergravity*, *Phys.Rev.Lett.* **84** (2000) 2322–2325, [hep-ph/9908309].

[293] J. L. Feng, K. T. Matchev, and T. Moroi, *Focus points and naturalness in supersymmetry*, *Phys.Rev.* **D61** (2000) 075005, [hep-ph/9909334].

[294] J. L. Feng, *Naturalness and the Status of Supersymmetry*, *Ann.Rev.Nucl.Part.Sci.* **63** (2013) 351–382, [arXiv:1302.6587].

[295] S. Akula, B. Altunkaynak, D. Feldman, P. Nath, and G. Peim, *Higgs Boson Mass Predictions in SUGRA Unification, Recent LHC-7 Results, and Dark Matter*, *Phys.Rev.* **D85** (2012) 075001, [arXiv:1112.3645].

[296] B. S. Acharya, G. Kane, and P. Kumar, *Compactified String Theories – Generic Predictions for Particle Physics*, *Int.J.Mod.Phys.* **A27** (2012) 1230012, [arXiv:1204.2795].

[297] G. Kane, R. Lu, and B. Zheng, *Review and Update of the Compactified M/string Theory Prediction of the Higgs Boson Mass and Properties*, *Int.J.Mod.Phys.* **A28** (2013) 1330002, [arXiv:1211.2231].

[298] M. S. Carena, D. Garcia, U. Nierste, and C. E. Wagner, *Effective Lagrangian for the $\bar{t}bH^+$ interaction in the MSSM and charged Higgs phenomenology*, *Nucl.Phys.* **B577** (2000) 88–120, [hep-ph/9912516].

[299] D. Noth and M. Spira, *Higgs Boson Couplings to Bottom Quarks: Two-Loop Supersymmetry-QCD Corrections*, *Phys.Rev.Lett.* **101** (2008) 181801, [arXiv:0808.0087].

[300] E. Boos, A. Djouadi, M. Muhlleitner, and A. Vologdin, *The MSSM Higgs bosons in the intense coupling regime*, *Phys.Rev.* **D66** (2002) 055004, [hep-ph/0205160].

[301] E. Boos, A. Djouadi, and A. Nikitenko, *Detection of the neutral MSSM Higgs bosons in the intense coupling regime at the LHC*, *Phys.Lett.* **B578** (2004) 384–393, [hep-ph/0307079].

[302] D. A. Dicus and S. Willenbrock, *Higgs Boson Production from Heavy Quark Fusion*, *Phys.Rev.* **D39** (1989) 751.

[303] M. Spira, *HIGLU: A program for the calculation of the total Higgs production cross-section at hadron colliders via gluon fusion including QCD corrections*, hep-ph/9510347.

[304] J. M. Campbell, R. K. Ellis, F. Maltoni, and S. Willenbrock, *Higgs-Boson production in association with a single bottom quark*, *Phys.Rev.* **D67** (2003) 095002, [hep-ph/0204093].

[305] F. Maltoni, Z. Sullivan, and S. Willenbrock, *Higgs-boson production via bottom-quark fusion*, *Phys.Rev.* **D67** (2003) 093005, [hep-ph/0301033].

[306] R. V. Harlander and W. B. Kilgore, *Higgs boson production in bottom quark fusion at next-to-next-to leading order*, *Phys.Rev.* **D68** (2003) 013001, [hep-ph/0304035].

[307] R. V. Harlander, S. Liebler, and H. Mantler, *SusHi: A program for the calculation of Higgs production in gluon fusion and bottom-quark annihilation in the Standard Model and the MSSM*, *Computer Physics Communications* **184** (2013) 1605–1617, [arXiv:1212.3249].

[308] S. Dittmaier, . Kramer, Michael, and M. Spira, *Higgs radiation off bottom quarks at the Tevatron and the CERN LHC*, *Phys.Rev.* **D70** (2004) 074010, [hep-ph/0309204].

[309] S. Dawson, C. Jackson, L. Reina, and D. Wackeroth, *Exclusive Higgs boson production with bottom quarks at hadron colliders*, *Phys.Rev.* **D69** (2004) 074027, [hep-ph/0311067].

[310] A. Arbey, M. Battaglia, and F. Mahmoudi, *Supersymmetric Heavy Higgs Bosons at the LHC*, *Phys.Rev.* **D88** (2013), no. 1 015007, [arXiv:1303.7450].

[311] S. Dawson, A. Djouadi, and M. Spira, *QCD corrections to SUSY Higgs production: The Role of squark loops*, *Phys.Rev.Lett.* **77** (1996) 16–19, [hep-ph/9603423].

[312] R. V. Harlander and M. Steinhauser, *Supersymmetric Higgs production in gluon fusion at next-to-leading order*, *JHEP* **0409** (2004) 066, [hep-ph/0409010].

[313] R. Harlander and M. Steinhauser, *Effects of SUSY QCD in hadronic Higgs production at next-to-next-to-leading order*, *Phys.Rev.* **D68** (2003) 111701, [hep-ph/0308210].

[314] M. Muhlleitner, H. Rzehak, and M. Spira, *MSSM Higgs Boson Production via Gluon Fusion: The Large Gluino Mass Limit*, *JHEP* **0904** (2009) 023, [arXiv:0812.3815].

[315] N. Liu, L. Wu, P. W. Wu, and J. M. Yang, *Complete one-loop effects of SUSY QCD in $b\bar{b}h$ production at the LHC under current experimental constraints*, *JHEP* **1301** (2013) 161, [arXiv:1208.3413].

[316] **ATLAS** Collaboration, *Search for Supersymmetry in final states with two same-sign leptons, jets and missing transverse momentum with the ATLAS detector in pp collisions at sqrts=8 TeV*, ATLAS-CONF-2012-105.

[317] **ATLAS** Collaboration, *Search for supersymmetry using events with three leptons, multiple jets, and missing transverse momentum with the ATLAS detector*, ATLAS-CONF-2012-108.

[318] **CMS** Collaboration, S. Chatrchyan et al., *Search for supersymmetry in events with opposite-sign dileptons and missing transverse energy using an artificial neural network*, *Phys.Rev.* **D87** (2013) 072001, [arXiv:1301.0916].

[319] **CMS** Collaboration, S. Chatrchyan et al., *Search for supersymmetry in pp collisions at $\sqrt{s} = 7$ TeV in events with a single lepton, jets, and missing transverse momentum*, *Eur.Phys.J.* **C73** (2013) 2404, [arXiv:1212.6428].

[320] **ATLAS** Collaboration, *Search for a Standard Model Higgs boson in $H \to \mu\mu$ decays with the ATLAS detector.*, ATLAS-CONF-2013-010.

[321] **CMS** Collaboration, CMS, *Search for Neutral MSSM Higgs Bosons in the mu+mu- final state with the CMS experiment in pp Collisions at sqrt s =7 TeV*, CMS-PAS-HIG-12-011.

[322] **CMS** Collaboration, R. Salerno, *Higgs searches at CMS*, arXiv:1301.3405.

[323] M. Spira, A. Djouadi, D. Graudenz, and P. Zerwas, *SUSY Higgs production at proton colliders*, *Phys.Lett.* **B318** (1993) 347–353.

[324] R. V. Harlander and W. B. Kilgore, *Production of a pseudoscalar Higgs boson at hadron colliders at next-to-next-to leading order*, *JHEP* **0210** (2002) 017, [hep-ph/0208096].

[325] A. Bawa, C. Kim, and A. D. Martin, *Charged Higgs production at hadron colliders*, *Z.Phys.* **C47** (1990) 75–82.

[326] V. D. Barger, R. Phillips, and D. Roy, *Heavy charged Higgs signals at the LHC*, *Phys.Lett.* **B324** (1994) 236–240, [hep-ph/9311372].

[327] S. Moretti and K. Odagiri, *Production of charged Higgs bosons of the minimal supersymmetric standard model in b quark initiated processes at the large hadron collider*, *Phys.Rev.* **D55** (1997) 5627–5635, [hep-ph/9611374].

[328] J. Gunion, *Detecting the t b decays of a charged Higgs boson at a hadron supercollider*, *Phys.Lett.* **B322** (1994) 125–130, [hep-ph/9312201].

[329] F. Borzumati, J.-L. Kneur, and N. Polonsky, *Higgs-Strahlung and R-parity violating slepton-Strahlung at hadron colliders*, *Phys.Rev.* **D60** (1999) 115011, [hep-ph/9905443].

[330] T. Plehn, *Charged Higgs boson production in bottom gluon fusion*, *Phys.Rev.* **D67** (2003) 014018, [hep-ph/0206121].

[331] S. Moretti, *Improving the discovery potential of charged Higgs bosons at the Tevatron and Large Hadron Collider*, *Pramana* **60** (2003) 369–376, [hep-ph/0205104].

[332] A. Djouadi, J. Kalinowski, and P. Zerwas, *Two and three-body decay modes of SUSY Higgs particles*, *Z.Phys.* **C70** (1996) 435–448, [hep-ph/9511342].

[333] S. Moretti and W. J. Stirling, *Contributions of below threshold decays to MSSM Higgs branching ratios*, *Phys.Lett.* **B347** (1995) 291–299, [hep-ph/9412209].

[334] F. Borzumati and A. Djouadi, *Lower bounds on charged Higgs bosons from LEP and Tevatron*, *Phys.Lett.* **B549** (2002) 170–176, [hep-ph/9806301].

[335] **ATLAS** Collaboration, *Combined measurements of the mass and signal strength of the Higgs-like boson with the ATLAS detector using up to 25 fb^{-1} of proton-proton collision data*, ATLAS-CONF-2013-014.

[336] **CMS** Collaboration, *Updated measurements of the Higgs boson at 125 GeV in the two photon decay channel*, CMS-PAS-HIG-13-001.

[337] **ATLAS** Collaboration, *Measurements of the properties of the Higgs-like boson in the four lepton decay channel with the ATLAS detector using 25 fb^{-1} of proton-proton collision data*, ATLAS-CONF-2013-013.

[338] **CMS** Collaboration, *Properties of the Higgs-like boson in the decay H to ZZ to 4l in pp collisions at $\sqrt{s} = 7$ and 8 TeV*, CMS-PAS-HIG-13-002.

[339] **ATLAS** Collaboration, *Measurements of the properties of the Higgs-like boson in the $WW^{(*)} \to \ell\nu\ell\nu$ decay channel with the ATLAS detector using 25 fb^{-1} of proton-proton collision data*, ATLAS-CONF-2013-030.

[340] **CMS** Collaboration, *Update on the search for the standard model Higgs boson in pp collisions at the LHC decaying to W + W in the fully leptonic final state*, CMS-PAS-HIG-13-003.

[341] **ATLAS** Collaboration, *Search for the Standard Model Higgs boson in produced in association with a vector boson and decaying to bottom quarks with the ATLAS detector*, ATLAS-CONF-2012-161.

[342] **CMS** Collaboration, *Search for the standard model Higgs boson produced in association with W or Z bosons, and decaying to bottom quarks for HCP 2012*, CMS-PAS-HIG-12-044.

[343] **ATLAS** Collaboration, *Search for Neutral MSSM Higgs bosons in sqrts = 7 TeV pp collisions at ATLAS*, ATLAS-CONF-2012-094.

[344] **ATLAS** Collaboration, G. Aad et al., *Search for the neutral Higgs bosons of the Minimal Supersymmetric Standard Model in pp collisions at $\sqrt{s} = 7$ TeV with the ATLAS detector*, *JHEP* **1302** (2013) 095, [arXiv:1211.6956].

[345] **CMS** Collaboration, *Search for MSSM Neutral Higgs Bosons Decaying to Tau Pairs in pp Collisions*, CMS-PAS-HIG-12-050.

[346] A. Djouadi, *Precision Higgs coupling measurements at the LHC through ratios of production cross sections*, *Eur.Phys.J.* **C73** (2013) 2498, [arXiv:1208.3436].

[347] **ATLAS** Collaboration, *Search for charged Higgs bosons decaying via $H^+ \to \tau\nu$ in ttbar events using 4.6 fb^{-1} of pp collision data at sqrt(s) = 7 TeV with the ATLAS detector*, ATLAS-CONF-2012-011.

[348] **ATLAS** Collaboration, G. Aad et al., *Search for charged Higgs bosons decaying via $H^+ \to \tau\nu$ in top quark pair events using pp collision data at $\sqrt{s} = 7$ TeV with the ATLAS detector*, *JHEP* **1206** (2012) 039, [arXiv:1204.2760].

[349] **CMS** Collaboration, S. Chatrchyan et al., *Search for a light charged Higgs boson in top quark decays in pp collisions at $\sqrt{s} = 7$ TeV*, *JHEP* **1207** (2012) 143, [arXiv:1205.5736].

[350] M. Carena, P. Draper, T. Liu, and C. Wagner, *The 7 TeV LHC Reach for MSSM Higgs Bosons*, *Phys.Rev.* **D84** (2011) 095010, [arXiv:1107.4354].

[351] N. D. Christensen, T. Han, and S. Su, *MSSM Higgs Bosons at The LHC*, *Phys.Rev.* **D85** (2012) 115018, [arXiv:1203.3207].

[352] J. Chang, K. Cheung, P.-Y. Tseng, and T.-C. Yuan, *Implications on the Heavy CP-even Higgs Boson from Current Higgs Data*, *Phys.Rev.* **D87** (2013), no. 3 035008, [arXiv:1211.3849].

[353] **ATLAS** Collaboration, *Search for Higgs bosons in Two-Higgs-Doublet models in the $H \to WW \to e\nu\mu\nu$ channel with the ATLAS detector*, ATLAS-CONF-2013-027.

[354] **CMS** Collaboration, S. Chatrchyan et al., *Search for a standard-model-like Higgs boson with a mass in the range 145 to 1000 GeV at the LHC*, *Eur.Phys.J.* **C73** (2013) 2469, [arXiv:1304.0213].

[355] **ATLAS** Collaboration, G. Aad et al., *A search for $t\bar{t}$ resonances in lepton+jets events with highly boosted top quarks collected in pp collisions at $\sqrt{s} = 7$ TeV with the ATLAS detector*, *JHEP* **1209** (2012) 041, [arXiv:1207.2409].

[356] **CMS** Collaboration, S. Chatrchyan et al., *Search for Z' resonances decaying to $t\bar{t}$ in dilepton+jets final states in pp collisions at $\sqrt{s} = 7$ TeV*, *Phys.Rev.* **D87** (2013) 072002, [arXiv:1211.3338].

[357] T. Plehn, G. P. Salam, and M. Spannowsky, *Fat Jets for a Light Higgs*, *Phys.Rev.Lett.* **104** (2010) 111801, [arXiv:0910.5472].

[358] J. Baglio, A. Djouadi, R. Gröber, M. Mühlleitner, and J. Quevillon, *The measurement of the Higgs self-coupling at the LHC: theoretical status*, *JHEP* **1304** (2013) 151, [arXiv:1212.5581].

[359] R. Gröber, *Aspects of Higgs Physics and New Physics at the LHC*, PhD thesis.

[360] **ATLAS** Collaboration, *A Search for a light charged Higgs boson decaying to cs in pp collisions at $\sqrt{s} = 7$ TeV with the ATLAS detector*, ATLAS-CONF-2011-094.

[361] **ATLAS** Collaboration, G. Aad et al., *Search for a light charged Higgs boson in the decay channel $H^+ \to c\bar{s}$ in $t\bar{t}$ events using pp collisions at $\sqrt{s} = 7$ TeV with the ATLAS detector*, *Eur.Phys.J.* **C73** (2013) 2465, [arXiv:1302.3694].

[362] U. Ellwanger, C. Hugonie, and A. M. Teixeira, *The Next-to-Minimal Supersymmetric Standard Model*, *Phys.Rept.* **496** (2010) 1–77, [arXiv:0910.1785].

[363] M. Maniatis, *The Next-to-Minimal Supersymmetric extension of the Standard Model reviewed*, *Int.J.Mod.Phys.* **A25** (2010) 3505–3602, [arXiv:0906.0777].

[364] S. King, M. Muhlleitner, and R. Nevzorov, *NMSSM Higgs Benchmarks Near 125 GeV*, *Nucl.Phys.* **B860** (2012) 207–244, [arXiv:1201.2671].

[365] G. Branco, P. Ferreira, L. Lavoura, M. Rebelo, M. Sher, et al., *Theory and phenomenology of two-Higgs-doublet models*, *Phys.Rept.* **516** (2012) 1–102, [arXiv:1106.0034].

[366] W. Altmannshofer, S. Gori, and G. D. Kribs, *A Minimal Flavor Violating 2HDM at the LHC*, *Phys.Rev.* **D86** (2012) 115009, [arXiv:1210.2465].

[367] Y. Bai, V. Barger, L. L. Everett, and G. Shaughnessy, *General two Higgs doublet model (2HDM-G) and Large Hadron Collider data*, *Phys.Rev.* **D87** (2013), no. 11 115013, [arXiv:1210.4922].

[368] A. Drozd, B. Grzadkowski, J. F. Gunion, and Y. Jiang, *Two-Higgs-Doublet Models and Enhanced Rates for a 125 GeV Higgs*, *JHEP* **1305** (2013) 072, [arXiv:1211.3580].

[369] B. Grinstein and P. Uttayarat, *Carving Out Parameter Space in Type-II Two Higgs Doublets Model*, *JHEP* **1306** (2013) 094, [arXiv:1304.0028].

[370] A. Djouadi, L. Maiani, G. Moreau, A. Polosa, J. Quevillon, et al., *The post-Higgs MSSM scenario: Habemus MSSM?*, *Eur.Phys.J.* **C73** (2013) 2650, [arXiv:1307.5205].

[371] J. Quevillon, *Simplified description of the MSSM Higgs sector*, arXiv:1405.2241.

[372] A. Djouadi and J. Quevillon, *The MSSM Higgs sector at a high M_{SUSY}: reopening the low tanβ regime and heavy Higgs searches*, arXiv:1304.1787.

[373] A. Djouadi, *Squark effects on Higgs boson production and decay at the LHC*, *Phys.Lett.* **B435** (1998) 101–108, [hep-ph/9806315].

[374] A. Arvanitaki and G. Villadoro, *A Non Standard Model Higgs at the LHC as a Sign of Naturalness*, *JHEP* **1202** (2012) 144, [arXiv:1112.4835].

[375] A. Delgado, G. F. Giudice, G. Isidori, M. Pierini, and A. Strumia, *The light stop window*, *Eur.Phys.J.* **C73** (2013) 2370, [arXiv:1212.6847].

[376] A. Djouadi, V. Driesen, W. Hollik, and J. I. Illana, *The Coupling of the lightest SUSY Higgs boson to two photons in the decoupling regime*, *Eur.Phys.J.* **C1** (1998) 149–162, [hep-ph/9612362].

[377] L. Maiani, A. Polosa, and V. Riquer, *Bounds to the Higgs Sector Masses in Minimal Supersymmetry from LHC Data*, *Phys.Lett.* **B724** (2013) 274–277, [arXiv:1305.2172].

[378] A. Djouadi and G. Moreau, *The couplings of the Higgs boson and its CP properties from fits of the signal strengths and their ratios at the 7+8 TeV LHC*, arXiv:1303.6591.

[379] G. Moreau, *Constraining extra-fermion(s) from the Higgs boson data*, *Phys.Rev.* **D87** (2013) 015027, [arXiv:1210.3977].

[380] S. Heinemeyer, O. Stal, and G. Weiglein, *Interpreting the LHC Higgs Search Results in the MSSM*, *Phys.Lett.* **B710** (2012) 201–206, [arXiv:1112.3026].

[381] M. Frank, L. Galeta, T. Hahn, S. Heinemeyer, W. Hollik, et al., *Charged Higgs Boson Mass of the MSSM in the Feynman Diagrammatic Approach*, *Phys.Rev.* **D88** (2013) 055013, [arXiv:1306.1156].

[382] M. Carena, S. Gori, N. R. Shah, and C. E. Wagner, *A 125 GeV SM-like Higgs in the MSSM and the $\gamma\gamma$ rate*, *JHEP* **1203** (2012) 014, [arXiv:1112.3336].

[383] G. F. Giudice, P. Paradisi, A. Strumia, and A. Strumia, *Correlation between the Higgs Decay Rate to Two Photons and the Muon g - 2*, *JHEP* **1210** (2012) 186, [arXiv:1207.6393].

[384] A. Djouadi, A. Falkowski, Y. Mambrini, and J. Quevillon, *Direct Detection of Higgs-Portal Dark Matter at the LHC*, *Eur.Phys.J.* **C73** (2013) 2455, [arXiv:1205.3169].

[385] B. Batell, S. Jung, and C. E. Wagner, *Very Light Charginos and Higgs Decays*, *JHEP* **1312** (2013) 075, [arXiv:1309.2297].

[386] G. Bélanger, G. Drieu La Rochelle, B. Dumont, R. M. Godbole, S. Kraml, et al., *LHC constraints on light neutralino dark matter in the MSSM*, *Phys.Lett.* **B726** (2013) 773–780, [arXiv:1308.3735].

[387] L. Calibbi, J. M. Lindert, T. Ota, and Y. Takanishi, *Cornering light Neutralino Dark Matter at the LHC*, *JHEP* **1310** (2013) 132, [arXiv:1307.4119].

[388] G. Belanger, B. Dumont, U. Ellwanger, J. Gunion, and S. Kraml, *Global fit to Higgs signal strengths and couplings and implications for extended Higgs sectors*, *Phys.Rev.* **D88** (2013) 075008, [arXiv:1306.2941].

[389] R. Barbieri, D. Buttazzo, K. Kannike, F. Sala, and A. Tesi, *Exploring the Higgs sector of a most natural NMSSM*, *Phys.Rev.* **D87** (2013), no. 11 115018, [arXiv:1304.3670].

[390] D. Carmi, A. Falkowski, E. Kuflik, T. Volansky, and J. Zupan, *Higgs After the Discovery: A Status Report*, *JHEP* **1210** (2012) 196, [arXiv:1207.1718].

[391] P. P. Giardino, K. Kannike, M. Raidal, and A. Strumia, *Reconstructing Higgs boson properties from the LHC and Tevatron data*, *JHEP* **1206** (2012) 117, [arXiv:1203.4254].

[392] J. R. Espinosa, C. Grojean, V. Sanz, and M. Trott, *NSUSY fits*, *JHEP* **1212** (2012) 077, [arXiv:1207.7355].

[393] A. Azatov, S. Chang, N. Craig, and J. Galloway, *Higgs fits preference for suppressed down-type couplings: Implications for supersymmetry*, *Phys.Rev.* **D86** (2012) 075033, [arXiv:1206.1058].

[394] Orsay and Rome collaboration *in preparation.*

[395] K. Begeman, A. Broeils, and R. Sanders, *Extended rotation curves of spiral galaxies: Dark haloes and modified dynamics*, *Mon.Not.Roy.Astron.Soc.* **249** (1991) 523.

[396] D. Clowe, M. Bradac, A. H. Gonzalez, M. Markevitch, S. W. Randall, et al., *A direct empirical proof of the existence of dark matter*, *Astrophys.J.* **648** (2006) L109–L113, [astro-ph/0608407].

[397] **Planck** Collaboration, P. Ade et al., *Planck 2013 results. XVI. Cosmological parameters*, arXiv:1303.5076.

[398] M. Viel, J. Lesgourgues, M. G. Haehnelt, S. Matarrese, and A. Riotto, *Constraining warm dark matter candidates including sterile neutrinos and light gravitinos with WMAP and the Lyman-alpha forest*, *Phys.Rev.* **D71** (2005) 063534, [astro-ph/0501562].

[399] D. Hooper, *TASI 2008 Lectures on Dark Matter*, arXiv:0901.4090.

[400] V. Silveira and A. Zee, *Scalar phantoms*, *Phys.Lett.* **B161** (1985) 136.

[401] R. E. Shrock and M. Suzuki, *Invisible Decays of Higgs Bosons*, *Phys.Lett.* **B110** (1982) 250.

[402] G. Belanger, B. Dumont, U. Ellwanger, J. Gunion, and S. Kraml, *Higgs Couplings at the End of 2012*, *JHEP* **1302** (2013) 053, [arXiv:1212.5244].

[403] S. Kanemura, S. Matsumoto, T. Nabeshima, and N. Okada, *Can WIMP Dark Matter overcome the Nightmare Scenario?*, *Phys.Rev.* **D82** (2010) 055026, [arXiv:1005.5651].

[404] O. Lebedev, H. M. Lee, and Y. Mambrini, *Vector Higgs-portal dark matter and the invisible Higgs*, *Phys.Lett.* **B707** (2012) 570–576, [arXiv:1111.4482].

[405] J. McDonald, *Gauge singlet scalars as cold dark matter*, *Phys.Rev.* **D50** (1994) 3637–3649, [hep-ph/0702143].

[406] C. Burgess, M. Pospelov, and T. ter Veldhuis, *The Minimal model of nonbaryonic dark matter: A Singlet scalar*, *Nucl.Phys.* **B619** (2001) 709–728, [hep-ph/0011335].

[407] H. Davoudiasl, R. Kitano, T. Li, and H. Murayama, *The New minimal standard model*, *Phys.Lett.* **B609** (2005) 117–123, [hep-ph/0405097].

[408] B. Patt and F. Wilczek, *Higgs-field portal into hidden sectors*, hep-ph/0605188.

[409] X.-G. He, T. Li, X.-Q. Li, J. Tandean, and H.-C. Tsai, *Constraints on Scalar Dark Matter from Direct Experimental Searches*, *Phys.Rev.* **D79** (2009) 023521, [arXiv:0811.0658].

[410] X.-G. He, T. Li, X.-Q. Li, J. Tandean, and H.-C. Tsai, *The Simplest Dark-Matter Model, CDMS II Results, and Higgs Detection at LHC*, *Phys.Lett.* **B688** (2010) 332–336, [arXiv:0912.4722].

[411] V. Barger, Y. Gao, M. McCaskey, and G. Shaughnessy, *Light Higgs Boson, Light Dark Matter and Gamma Rays*, *Phys.Rev.* **D82** (2010) 095011, [arXiv:1008.1796].

[412] V. Barger, P. Langacker, M. McCaskey, M. J. Ramsey-Musolf, and G. Shaughnessy, *LHC Phenomenology of an Extended Standard Model with a Real Scalar Singlet*, *Phys.Rev.* **D77** (2008) 035005, [arXiv:0706.4311].

[413] T. Clark, B. Liu, S. Love, and T. ter Veldhuis, *The Standard Model Higgs Boson-Inflaton and Dark Matter*, *Phys.Rev.* **D80** (2009) 075019, [arXiv:0906.5595].

[414] R. N. Lerner and J. McDonald, *Gauge singlet scalar as inflaton and thermal relic dark matter*, *Phys.Rev.* **D80** (2009) 123507, [arXiv:0909.0520].

[415] O. Lebedev and H. M. Lee, *Higgs Portal Inflation*, *Eur.Phys.J.* **C71** (2011) 1821, [arXiv:1105.2284].

[416] S. Andreas, T. Hambye, and M. H. Tytgat, *WIMP dark matter, Higgs exchange and DAMA*, *JCAP* **0810** (2008) 034, [arXiv:0808.0255].

[417] A. Goudelis, Y. Mambrini, and C. Yaguna, *Antimatter signals of singlet scalar dark matter*, *JCAP* **0912** (2009) 008, [arXiv:0909.2799].

[418] C. E. Yaguna, *Gamma rays from the annihilation of singlet scalar dark matter*, *JCAP* **0903** (2009) 003, [arXiv:0810.4267].

[419] Y. Cai, X.-G. He, and B. Ren, *Low Mass Dark Matter and Invisible Higgs Width In Darkon Models*, *Phys.Rev.* **D83** (2011) 083524, [arXiv:1102.1522].

[420] A. Biswas and D. Majumdar, *The Real Gauge Singlet Scalar Extension of Standard Model: A Possible Candidate of Cold Dark Matter*, *Pramana* **80** (2013) 539–557, [arXiv:1102.3024].

[421] M. Farina, M. Kadastik, D. Pappadopulo, J. Pata, M. Raidal, et al., *Implications of XENON100 and LHC results for Dark Matter models*, *Nucl.Phys.* **B853** (2011) 607–624, [arXiv:1104.3572].

[422] T. Hambye, *Hidden vector dark matter*, *JHEP* **0901** (2009) 028, [arXiv:0811.0172].

[423] T. Hambye and M. H. Tytgat, *Confined hidden vector dark matter*, *Phys.Lett.* **B683** (2010) 39–41, [arXiv:0907.1007].

[424] J. Hisano, K. Ishiwata, N. Nagata, and M. Yamanaka, *Direct Detection of Vector Dark Matter*, *Prog.Theor.Phys.* **126** (2011) 435–456, [arXiv:1012.5455].

[425] C. Englert, T. Plehn, D. Zerwas, and P. M. Zerwas, *Exploring the Higgs portal*, *Phys.Lett.* **B703** (2011) 298–305, [arXiv:1106.3097].

[426] C. Englert, T. Plehn, M. Rauch, D. Zerwas, and P. M. Zerwas, *LHC: Standard Higgs and Hidden Higgs*, *Phys.Lett.* **B707** (2012) 512–516, [arXiv:1112.3007].

[427] S. Andreas, C. Arina, T. Hambye, F.-S. Ling, and M. H. Tytgat, *A light scalar WIMP through the Higgs portal and CoGeNT*, *Phys.Rev.* **D82** (2010) 043522, [arXiv:1003.2595].

[428] R. Foot, H. Lew, and R. Volkas, *A Model with fundamental improper space-time symmetries*, *Phys.Lett.* **B272** (1991) 67–70.

[429] A. Melfo, M. Nemevsek, F. Nesti, G. Senjanovic, and Y. Zhang, *Inert Doublet Dark Matter and Mirror/Extra Families after Xenon100*, *Phys.Rev.* **D84** (2011) 034009, [arXiv:1105.4611].

[430] Y. Mambrini, *Higgs searches and singlet scalar dark matter: Combined constraints from XENON 100 and the LHC*, *Phys.Rev.* **D84** (2011) 115017, [arXiv:1108.0671].

[431] M. Raidal and A. Strumia, *Hints for a non-standard Higgs boson from the LHC*, *Phys.Rev.* **D84** (2011) 077701, [arXiv:1108.4903].

[432] X.-G. He and J. Tandean, *Hidden Higgs Boson at the LHC and Light Dark Matter Searches*, *Phys.Rev.* **D84** (2011) 075018, [arXiv:1109.1277].

[433] Y. Mambrini, *Invisible Higgs and Scalar Dark Matter*, *J.Phys.Conf.Ser.* **375** (2012) 012045, [arXiv:1112.0011].

[434] X. Chu, T. Hambye, and M. H. Tytgat, *The Four Basic Ways of Creating Dark Matter Through a Portal*, *JCAP* **1205** (2012) 034, [arXiv:1112.0493].

[435] K. Ghosh, B. Mukhopadhyaya, and U. Sarkar, *Signals of an invisibly decaying Higgs in a scalar dark matter scenario: a study for the Large Hadron Collider*, *Phys.Rev.* **D84** (2011) 015017, [arXiv:1105.5837].

[436] A. Greljo, J. Julio, J. F. Kamenik, C. Smith, and J. Zupan, *Constraining Higgs mediated dark matter interactions*, *JHEP* **1311** (2013) 190, [arXiv:1309.3561].

[437] J. McDonald and N. Sahu, *Z(2)-Singlino Dark Matter in a Portal-Like Extension of the Minimal Supersymmetric Standard Model*, *JCAP* **0806** (2008) 026, [arXiv:0802.3847].

[438] G. Belanger, F. Boudjema, A. Pukhov, and A. Semenov, *micrOMEGAs: A Tool for dark matter studies*, *Nuovo Cim.* **C033N2** (2010) 111–116, [arXiv:1005.4133].

[439] G. Belanger, F. Boudjema, A. Pukhov, and A. Semenov, *Dark matter direct detection rate in a generic model with micrOMEGAs 2.2*, *Comput.Phys.Commun.* **180** (2009) 747–767, [arXiv:0803.2360].

[440] G. Belanger, F. Boudjema, A. Pukhov, and A. Semenov, *micrOMEGAs 2.0.7: A program to calculate the relic density of dark matter in a generic model*, *Comput.Phys.Commun.* **177** (2007) 894–895.

[441] R. Young and A. Thomas, *Octet baryon masses and sigma terms from an SU(3) chiral extrapolation*, *Phys.Rev.* **D81** (2010) 014503, [arXiv:0901.3310].

[442] **MILC** Collaboration, D. Toussaint and W. Freeman, *The Strange quark condensate in the nucleon in 2+1 flavor QCD*, *Phys.Rev.Lett.* **103** (2009) 122002, [arXiv:0905.2432].

[443] **QCDSF** Collaboration, G. Bali et al., *A lattice study of the strangeness content of the nucleon*, *Prog.Part.Nucl.Phys.* **67** (2012) 467–472, [arXiv:1112.0024].

[444] **WMAP** Collaboration, D. Spergel et al., *Wilkinson Microwave Anisotropy Probe (WMAP) three year results: implications for cosmology*, *Astrophys.J.Suppl.* **170** (2007) 377, [astro-ph/0603449].

[445] **WMAP** Collaboration, E. Komatsu et al., *Five-Year Wilkinson Microwave Anisotropy Probe (WMAP) Observations: Cosmological Interpretation*, *Astrophys.J.Suppl.* **180** (2009) 330–376, [arXiv:0803.0547].

[446] **XENON100** Collaboration, E. Aprile et al., *Implications on Inelastic Dark Matter from 100 Live Days of XENON100 Data*, *Phys.Rev.* **D84** (2011) 061101, [arXiv:1104.3121].

[447] **XENON100** Collaboration, E. Aprile et al., *Dark Matter Results from 100 Live Days of XENON100 Data*, *Phys.Rev.Lett.* **107** (2011) 131302, [arXiv:1104.2549].

[448] **XENON100** Collaboration, E. Aprile et al., *Dark Matter Results from 225 Live Days of XENON100 Data*, *Phys.Rev.Lett.* **109** (2012) 181301, [arXiv:1207.5988].

[449] **LUX Collaboration** Collaboration, D. Akerib et al., *First results from the LUX dark matter experiment at the Sanford Underground Research Facility*, *Phys.Rev.Lett.* **112** (2014) 091303, [arXiv:1310.8214].

[450] A. De Simone, G. F. Giudice, and A. Strumia, *Benchmarks for Dark Matter Searches at the LHC*, arXiv:1402.6287.

[451] **ECFA/DESY LC Physics Working Group** Collaboration, J. Aguilar-Saavedra et al., *TESLA: The Superconducting electron positron linear collider with an integrated x-ray laser laboratory. Technical design report. Part 3. Physics at an e+ e- linear collider*, hep-ph/0106315.

[452] **ILC** Collaboration, G. Aarons et al., *International Linear Collider Reference Design Report Volume 2: Physics at the ILC*, arXiv:0709.1893.

[453] D. Choudhury and D. Roy, *Signatures of an invisibly decaying Higgs particle at LHC*, *Phys.Lett.* **B322** (1994) 368–373, [hep-ph/9312347].

[454] R. Godbole, M. Guchait, K. Mazumdar, S. Moretti, and D. Roy, *Search for 'invisible' Higgs signals at LHC via associated production with gauge bosons*, *Phys.Lett.* **B571** (2003) 184–192, [hep-ph/0304137].

[455] **Higgs Working Group** Collaboration, D. Cavalli et al., *The Higgs working group: Summary report*, hep-ph/0203056.

[456] **ATLAS** Collaboration, G. Aad et al., *Expected Performance of the ATLAS Experiment - Detector, Trigger and Physics*, arXiv:0901.0512.

[457] **ATLAS** Collaboration, G. Aad et al., *Observation of a new particle in the search for the Standard Model Higgs boson with the ATLAS detector at the LHC*, *Phys.Lett.* **B716** (2012) 1–29, [arXiv:1207.7214].

[458] **CMS** Collaboration, S. Chatrchyan et al., *Observation of a new boson at a mass of 125 GeV with the CMS experiment at the LHC*, *Phys.Lett.* **B716** (2012) 30–61, [arXiv:1207.7235].

[459] A. Djouadi and A. Lenz, *Sealing the fate of a fourth generation of fermions*, *Phys.Lett.* **B715** (2012) 310–314, [arXiv:1204.1252].

[460] E. Kuflik, Y. Nir, and T. Volansky, *Implications of Higgs Searches on the Four Generation Standard Model*, *Phys.Rev.Lett.* **110** (2013) 091801, [arXiv:1204.1975].

[461] A. Drozd, B. Grzadkowski, and J. Wudka, *Multi-Scalar-Singlet Extension of the Standard Model - the Case for Dark Matter and an Invisible Higgs Boson*, *JHEP* **1204** (2012) 006, [arXiv:1112.2582].

[462] A. Djouadi, O. Lebedev, Y. Mambrini, and J. Quevillon, *Implications of LHC searches for Higgs–portal dark matter*, *Phys.Lett.* **B709** (2012) 65–69, [arXiv:1112.3299].

[463] H. Georgi, S. Glashow, M. Machacek, and D. V. Nanopoulos, *Higgs Bosons from Two Gluon Annihilation in Proton Proton Collisions*, *Phys.Rev.Lett.* **40** (1978) 692.

[464] R. K. Ellis, I. Hinchliffe, M. Soldate, and J. van der Bij, *Higgs Decay to tau+ tau-: A Possible Signature of Intermediate Mass Higgs Bosons at the SSC*, *Nucl.Phys.* **B297** (1988) 221.

[465] D. de Florian, G. Ferrera, M. Grazzini, and D. Tommasini, *Higgs boson production at the LHC: transverse momentum resummation effects in the H- -> 2 gamma, H–> WW–> nu lnu and H–> ZZ–> 4l decay modes*, *JHEP* **1206** (2012) 132, [arXiv:1203.6321].

[466] Y. Bai, P. Draper, and J. Shelton, *Measuring the Invisible Higgs Width at the 7 and 8 TeV LHC*, *JHEP* **1207** (2012) 192, [arXiv:1112.4496].

[467] C. Englert, J. Jaeckel, E. Re, and M. Spannowsky, *Evasive Higgs Maneuvers at the LHC*, *Phys.Rev.* **D85** (2012) 035008, [arXiv:1111.1719].

[468] **ATLAS** Collaboration, *Search for New Phenomena in Monojet plus Missing Transverse Momentum Final States using 10fb^{-1} of pp Collisions at sqrts=8 TeV with the ATLAS detector at the LHC*, ATLAS-CONF-2012-147.

[469] **CMS** Collaboration, S. Chatrchyan et al., *Search for dark matter and large extra dimensions in monojet events in pp collisions at $\sqrt{s} = 7$ TeV*, *JHEP* **1209** (2012) 094, [arXiv:1206.5663].

[470] O. J. Eboli and D. Zeppenfeld, *Observing an invisible Higgs boson*, *Phys.Lett.* **B495** (2000) 147–154, [hep-ph/0009158].

[471] H. Davoudiasl, T. Han, and H. E. Logan, *Discovering an invisibly decaying Higgs at hadron colliders*, *Phys.Rev.* **D71** (2005) 115007, [hep-ph/0412269].

[472] A. Alves, *Observing Higgs Dark Matter at the CERN LHC*, *Phys.Rev.* **D82** (2010) 115021, [arXiv:1008.0016].

[473] **ATLAS** Collaboration, G. Aad et al., *Search for new phenomena with the monojet and missing transverse momentum signature using the ATLAS detector in $\sqrt{s} = 7$ TeV proton-proton collisions*, *Phys.Lett.* **B705** (2011) 294–312, [arXiv:1106.5327].

[474] M. Drees and M. Nojiri, *Neutralino - nucleon scattering revisited*, *Phys.Rev.* **D48** (1993) 3483–3501, [hep-ph/9307208].

[475] S. Alioli, P. Nason, C. Oleari, and E. Re, *NLO Higgs boson production via gluon fusion matched with shower in POWHEG*, *JHEP* **0904** (2009) 002, [arXiv:0812.0578].

[476] E. Bagnaschi, G. Degrassi, P. Slavich, and A. Vicini, *Higgs production via gluon fusion in the POWHEG approach in the SM and in the MSSM*, *JHEP* **1202** (2012) 088, [arXiv:1111.2854].

[477] **CMS** Collaboration, *Combination of standard model Higgs boson searches and measurements of the properties of the new boson with a mass near 125 GeV*, CMS-PAS-HIG-13-005.

[478] **ATLAS** Collaboration, *Search for invisible decays of a Higgs boson produced in association with a Z boson in ATLAS*, ATLAS-CONF-2013-011.

[479] J. F. Kamenik and C. Smith, *Could a light Higgs boson illuminate the dark sector?*, *Phys.Rev.* **D85** (2012) 093017, [arXiv:1201.4814].

[480] T. Nabeshima, *Higgs portal dark matter at a linear collider*, arXiv:1202.2673.

[481] L. Lopez-Honorez, T. Schwetz, and J. Zupan, *Higgs portal, fermionic dark matter, and a Standard Model like Higgs at 125 GeV*, *Phys.Lett.* **B716** (2012) 179–185, [arXiv:1203.2064].

[482] **WMAP** Collaboration, E. Komatsu et al., *Seven-Year Wilkinson Microwave Anisotropy Probe (WMAP) Observations: Cosmological Interpretation*, *Astrophys.J.Suppl.* **192** (2011) 18, [arXiv:1001.4538].

[483] D. J. Gross, J. A. Harvey, E. J. Martinec, and R. Rohm, *The Heterotic String*, *Phys.Rev.Lett.* **54** (1985) 502–505.

[484] W. Buchmuller, K. Hamaguchi, O. Lebedev, and M. Ratz, *Supersymmetric standard model from the heterotic string*, *Phys.Rev.Lett.* **96** (2006) 121602, [hep-ph/0511035].

[485] T. Asaka, S. Blanchet, and M. Shaposhnikov, *The nuMSM, dark matter and neutrino masses*, *Phys.Lett.* **B631** (2005) 151–156, [hep-ph/0503065].

[486] O. Lebedev and A. Westphal, *Metastable Electroweak Vacuum: Implications for Inflation*, *Phys.Lett.* **B719** (2013) 415–418, [arXiv:1210.6987].

[487] C. Coriano, N. Irges, and E. Kiritsis, *On the effective theory of low scale orientifold string vacua*, *Nucl.Phys.* **B746** (2006) 77–135, [hep-ph/0510332].

[488] P. Anastasopoulos, M. Bianchi, E. Dudas, and E. Kiritsis, *Anomalies, anomalous U(1)'s and generalized Chern-Simons terms*, *JHEP* **0611** (2006) 057, [hep-th/0605225].

[489] I. Antoniadis, A. Boyarsky, S. Espahbodi, O. Ruchayskiy, and J. D. Wells, *Anomaly driven signatures of new invisible physics at the Large Hadron Collider*, *Nucl.Phys.* **B824** (2010) 296–313, [arXiv:0901.0639].

[490] E. Dudas, Y. Mambrini, S. Pokorski, and A. Romagnoni, *(In)visible Z-prime and dark matter*, *JHEP* **0908** (2009) 014, [arXiv:0904.1745].

[491] I. Antoniadis, *Motivation for weakly interacting SubeV particles*, .

[492] Y. Farzan and A. R. Akbarieh, *Natural explanation for 130 GeV photon line within vector boson dark matter model*, *Phys.Lett.* **B724** (2013) 84–87, [arXiv:1211.4685].

[493] B. Holdom, *Two U(1)'s and Epsilon Charge Shifts*, *Phys.Lett.* **B166** (1986) 196.

[494] L. Chang, O. Lebedev, and J. Ng, *On the invisible decays of the Upsilon and J / Psi resonances*, *Phys.Lett.* **B441** (1998) 419–424, [hep-ph/9806487].

[495] **BaBar** Collaboration, B. Aubert et al., *A Search for Invisible Decays of the Upsilon(1S)*, *Phys.Rev.Lett.* **103** (2009) 251801, [arXiv:0908.2840].

[496] **ALEPH, DELPHI, L3, OPAL, SLD, LEP Electroweak Working Group, SLD Electroweak Group, SLD Heavy Flavour Group** Collaboration, S. Schael et al., *Precision electroweak measurements on the Z resonance*, *Phys.Rept.* **427** (2006) 257–454, [hep-ex/0509008].

[497] S. Andreas, O. Lebedev, S. Ramos-Sanchez, and A. Ringwald, *Constraints on a very light CP-odd Higgs of the NMSSM and other axion-like particles*, *JHEP* **1008** (2010) 003, [arXiv:1005.3978].

[498] T. Inami and C. Lim, *Effects of Superheavy Quarks and Leptons in Low-Energy Weak Processes k(L) –> mu anti-mu, K+ –> pi+ Neutrino anti-neutrino and K0 –> anti-K0*, *Prog.Theor.Phys.* **65** (1981) 297.

[499] B. Grinstein, M. J. Savage, and M. B. Wise, *B –> X(s) e+ e- in the Six Quark Model*, *Nucl.Phys.* **B319** (1989) 271–290.

[500] G. Buchalla, *Precision flavour physics with $B \to K\nu\bar{\nu}$ and $B \to Kl^+l^-$*, *Nucl.Phys.Proc.Suppl.* **209** (2010) 137–142, [arXiv:1010.2674].

[501] **BaBar** Collaboration, P. del Amo Sanchez et al., *Search for the Rare Decay $B \to K\nu\bar{\nu}u$*, *Phys.Rev.* **D82** (2010) 112002, [arXiv:1009.1529].

[502] **BaBar** Collaboration, P. del Amo Sanchez et al., *Search for Production of Invisible Final States in Single-Photon Decays of $\Upsilon(1S)$*, *Phys.Rev.Lett.* **107** (2011) 021804, [arXiv:1007.4646].

[503] **L3** Collaboration, P. Achard et al., *Single photon and multiphoton events with missing energy in e^+e^- collisions at LEP*, *Phys.Lett.* **B587** (2004) 16–32, [hep-ex/0402002].

[504] G. Raffelt and A. Weiss, *Red giant bound on the axion - electron coupling revisited*, *Phys.Rev.* **D51** (1995) 1495–1498, [hep-ph/9410205].

[505] G. Vertongen and C. Weniger, *Hunting Dark Matter Gamma-Ray Lines with the Fermi LAT*, *JCAP* **1105** (2011) 027, [arXiv:1101.2610].

[506] N. Jarosik, C. Bennett, J. Dunkley, B. Gold, M. Greason, et al., *Seven-Year Wilkinson Microwave Anisotropy Probe (WMAP) Observations: Sky Maps, Systematic Errors, and Basic Results*, *Astrophys.J.Suppl.* **192** (2011) 14, [arXiv:1001.4744].

[507] **Planck** Collaboration, P. Ade et al., *Planck 2013 results. I. Overview of products and scientific results*, arXiv:1303.5062.

[508] **LAT** Collaboration, M. Ackermann et al., *Fermi LAT Search for Dark Matter in Gamma-ray Lines and the Inclusive Photon Spectrum*, *Phys.Rev.* **D86** (2012) 022002, [arXiv:1205.2739].

[509] J. Conrad, *Searches for Particle Dark Matter with gamma-rays*, *AIP Conf.Proc.* **1505** (2012) 166–176, [arXiv:1210.4392].

[510] **Fermi-LAT** Collaboration, M. Ackermann et al., *Search for Gamma-ray Spectral Lines with the Fermi Large Area Telescope and Dark Matter Implications*, *Phys.Rev.* **D88** (2013) 082002, [arXiv:1305.5597].

[511] **H.E.S.S.** Collaboration, A. Abramowski et al., *Search for photon line-like signatures from Dark Matter annihilations with H.E.S.S*, *Phys.Rev.Lett.* **110** (2013) 041301, [arXiv:1301.1173].

[512] **LAT** Collaboration, M. Ackermann et al., *Constraints on the Galactic Halo Dark Matter from Fermi-LAT Diffuse Measurements*, *Astrophys.J.* **761** (2012) 91, [arXiv:1205.6474].

[513] D. Hooper, C. Kelso, and F. S. Queiroz, *Stringent and Robust Constraints on the Dark Matter Annihilation Cross Section From the Region of the Galactic Center*, *Astropart.Phys.* **46** (2013) 55–70, [arXiv:1209.3015].

[514] **Fermi LAT** Collaboration, A. Drlica-Wagner, *Constraints on Dark Matter and Supersymmetry from LAT Observations of Dwarf Galaxies*, arXiv:1210.5558.

[515] C. Weniger, *A Tentative Gamma-Ray Line from Dark Matter Annihilation at the Fermi Large Area Telescope*, *JCAP* **1208** (2012) 007, [arXiv:1204.2797].

[516] T. Bringmann, X. Huang, A. Ibarra, S. Vogl, and C. Weniger, *Fermi LAT Search for Internal Bremsstrahlung Signatures from Dark Matter Annihilation*, *JCAP* **1207** (2012) 054, [arXiv:1203.1312].

[517] E. Tempel, A. Hektor, and M. Raidal, *Fermi 130 GeV gamma-ray excess and dark matter annihilation in sub-haloes and in the Galactic centre*, *JCAP* **1209** (2012) 032, [arXiv:1205.1045].

[518] G. Chalons and A. Semenov, *Loop-induced photon spectral lines from neutralino annihilation in the NMSSM*, *JHEP* **1112** (2011) 055, [arXiv:1110.2064].

[519] G. Chalons, *Gamma-ray lines constraints in the NMSSM*, arXiv:1204.4591.

[520] S. Profumo and T. Linden, *Gamma-ray Lines in the Fermi Data: is it a Bubble?*, *JCAP* **1207** (2012) 011, [arXiv:1204.6047].

[521] A. Ibarra, S. Lopez Gehler, and M. Pato, *Dark matter constraints from box-shaped gamma-ray features*, *JCAP* **1207** (2012) 043, [arXiv:1205.0007].

[522] **XENON100** Collaboration, E. Aprile et al., *Limits on spin-dependent WIMP-nucleon cross sections from 225 live days of XENON100 data*, *Phys.Rev.Lett.* **111** (2013), no. 2 021301, [arXiv:1301.6620].

[523] **XENON** Collaboration, P. Beltrame, *Direct Dark Matter search with the XENON program*, arXiv:1305.2719.

[524] **CMS** Collaboration, *Search for new physics in monojet events in pp collisions at sqrt(s)= 8 TeV*, CMS-PAS-EXO-12-048.

[525] P. J. Fox, R. Harnik, J. Kopp, and Y. Tsai, *Missing Energy Signatures of Dark Matter at the LHC*, *Phys.Rev.* **D85** (2012) 056011, [arXiv:1109.4398].

[526] **CMS** Collaboration, S. Chatrchyan et al., *Search for Dark Matter and Large Extra Dimensions in pp Collisions Yielding a Photon and Missing Transverse Energy*, *Phys.Rev.Lett.* **108** (2012) 261803, [arXiv:1204.0821].

[527] **ATLAS** Collaboration, G. Aad et al., *Search for dark matter candidates and large extra dimensions in events with a photon and missing transverse momentum in pp collision data at $\sqrt{s} = 7$ TeV with the ATLAS detector*, *Phys.Rev.Lett.* **110** (2013) 011802, [arXiv:1209.4625].

[528] W. Buchmuller and M. Garny, *Decaying vs Annihilating Dark Matter in Light of a Tentative Gamma-Ray Line*, *JCAP* **1208** (2012) 035, [arXiv:1206.7056].

[529] H. Goldberg, *Constraint on the Photino Mass from Cosmology*, *Phys.Rev.Lett.* **50** (1983) 1419.

[530] J. R. Ellis, J. Hagelin, D. V. Nanopoulos, K. A. Olive, and M. Srednicki, *Supersymmetric Relics from the Big Bang*, *Nucl.Phys.* **B238** (1984) 453–476.

[531] M. Fukugita and T. Yanagida, *Physics of neutrinos*, .

[532] L. J. Hall, K. Jedamzik, J. March-Russell, and S. M. West, *Freeze-In Production of FIMP Dark Matter*, *JHEP* **1003** (2010) 080, [arXiv:0911.1120].

[533] J. McDonald, *Thermally generated gauge singlet scalars as selfinteracting dark matter*, *Phys.Rev.Lett.* **88** (2002) 091304, [hep-ph/0106249].

[534] C. E. Yaguna, *An intermediate framework between WIMP, FIMP, and EWIP dark matter*, *JCAP* **1202** (2012) 006, [arXiv:1111.6831].

[535] **WMAP** Collaboration, G. Hinshaw et al., *Nine-Year Wilkinson Microwave Anisotropy Probe (WMAP) Observations: Cosmological Parameter Results*, *Astrophys.J.Suppl.* **208** (2013) 19, [arXiv:1212.5226].

[536] M. Kadastik, K. Kannike, and M. Raidal, *Dark Matter as the signal of Grand Unification*, *Phys.Rev.* **D80** (2009) 085020, [arXiv:0907.1894].

[537] M. Frigerio and T. Hambye, *Dark matter stability and unification without supersymmetry*, *Phys.Rev.* **D81** (2010) 075002, [arXiv:0912.1545].

[538] R. Slansky, *Group Theory for Unified Model Building*, *Phys.Rept.* **79** (1981) 1–128.

[539] T. Fukuyama, A. Ilakovac, T. Kikuchi, S. Meljanac, and N. Okada, *SO(10) group theory for the unified model building*, *J.Math.Phys.* **46** (2005) 033505, [hep-ph/0405300].

[540] M. Bolz, A. Brandenburg, and W. Buchmuller, *Thermal production of gravitinos*, *Nucl.Phys.* **B606** (2001) 518–544, [hep-ph/0012052].

[541] V. S. Rychkov and A. Strumia, *Thermal production of gravitinos*, *Phys.Rev.* **D75** (2007) 075011, [hep-ph/0701104].

[542] G. Giudice, A. Notari, M. Raidal, A. Riotto, and A. Strumia, *Towards a complete theory of thermal leptogenesis in the SM and MSSM*, *Nucl.Phys.* **B685** (2004) 89–149, [hep-ph/0310123].

[543] S. Antusch and A. Teixeira, *Towards constraints on the SUSY seesaw from flavour-dependent leptogenesis*, *JCAP* **0702** (2007) 024, [hep-ph/0611232].

[544] S. Davidson and A. Ibarra, *A Lower bound on the right-handed neutrino mass from leptogenesis*, *Phys.Lett.* **B535** (2002) 25–32, [hep-ph/0202239].

[545] E. Nardi, Y. Nir, E. Roulet, and J. Racker, *The Importance of flavor in leptogenesis*, *JHEP* **0601** (2006) 164, [hep-ph/0601084].

[546] A. Abada, S. Davidson, A. Ibarra, F.-X. Josse-Michaux, M. Losada, et al., *Flavour Matters in Leptogenesis*, *JHEP* **0609** (2006) 010, [hep-ph/0605281].

[547] R. Barbieri, P. Creminelli, A. Strumia, and N. Tetradis, *Baryogenesis through leptogenesis*, *Nucl.Phys.* **B575** (2000) 61–77, [hep-ph/9911315].

[548] M. Raidal, A. Strumia, and K. Turzynski, *Low-scale standard supersymmetric leptogenesis*, *Phys.Lett.* **B609** (2005) 351–359, [hep-ph/0408015].

[549] A. Pilaftsis and T. E. Underwood, *Resonant leptogenesis*, *Nucl.Phys.* **B692** (2004) 303–345, [hep-ph/0309342].

[550] X. Chu, Y. Mambrini, J. Quevillon, and B. Zaldivar, *Thermal and non-thermal production of dark matter via Z'-portal(s)*, *JCAP* **1401** (2014) 034, [arXiv:1306.4677].

[551] L. Bergstrom, *Nonbaryonic dark matter: Observational evidence and detection methods*, *Rept.Prog.Phys.* **63** (2000) 793, [hep-ph/0002126].

[552] G. Bertone, D. Hooper, and J. Silk, *Particle dark matter: Evidence, candidates and constraints*, *Phys.Rept.* **405** (2005) 279–390, [hep-ph/0404175].

[553] H. Dreiner, D. Schmeier, and J. Tattersall, *Contact Interactions Probe Effective Dark Matter Models at the LHC*, *Europhys.Lett.* **102** (2013) 51001, [arXiv:1303.3348].

[554] H. Dreiner, M. Huck, M. Krämer, D. Schmeier, and J. Tattersall, *Illuminating Dark Matter at the ILC*, *Phys.Rev.* **D87** (2013), no. 7 075015, [arXiv:1211.2254].

[555] J. Kopp, E. T. Neil, R. Primulando, and J. Zupan, *From gamma ray line signals of dark matter to the LHC*, *Phys.Dark Univ.* **2** (2013) 22–34, [arXiv:1301.1683].

[556] M. T. Frandsen, F. Kahlhoefer, A. Preston, S. Sarkar, and K. Schmidt-Hoberg, *LHC and Tevatron Bounds on the Dark Matter Direct Detection Cross-Section for Vector Mediators*, *JHEP* **1207** (2012) 123, [arXiv:1204.3839].

[557] J. Goodman and W. Shepherd, *LHC Bounds on UV-Complete Models of Dark Matter*, arXiv:1111.2359.

[558] Y. Mambrini and B. Zaldivar, *When LEP and Tevatron combined with WMAP and XENON100 shed light on the nature of Dark Matter*, *JCAP* **1110** (2011) 023, [arXiv:1106.4819].

[559] K. Cheung, P.-Y. Tseng, Y.-L. S. Tsai, and T.-C. Yuan, *Global Constraints on Effective Dark Matter Interactions: Relic Density, Direct Detection, Indirect Detection, and Collider*, *JCAP* **1205** (2012) 001, [arXiv:1201.3402].

[560] C. R. Das, O. Mena, S. Palomares-Ruiz, and S. Pascoli, *Determining the Dark Matter Mass with DeepCore*, *Phys.Lett.* **B725** (2013) 297–301, [arXiv:1110.5095].

[561] C.-L. Shan, *Effects of Residue Background Events in Direct Dark Matter Detection Experiments on the Estimation of the Spin-Independent WIMP-Nucleon Coupling*, arXiv:1103.4049.

[562] M. Pato, L. Baudis, G. Bertone, R. Ruiz de Austri, L. E. Strigari, et al., *Complementarity of Dark Matter Direct Detection Targets*, *Phys.Rev.* **D83** (2011) 083505, [arXiv:1012.3458].

[563] G. Bertone, D. G. Cerdeno, M. Fornasa, R. R. de Austri, and R. Trotta, *Identification of Dark Matter particles with LHC and direct detection data*, *Phys.Rev.* **D82** (2010) 055008, [arXiv:1005.4280].

[564] N. Bernal, A. Goudelis, Y. Mambrini, and C. Munoz, *Determining the WIMP mass using the complementarity between direct and indirect searches and the ILC*, *JCAP* **0901** (2009) 046, [arXiv:0804.1976].

[565] O. Mena, S. Palomares-Ruiz, and S. Pascoli, *Reconstructing WIMP properties with neutrino detectors*, *Phys.Lett.* **B664** (2008) 92–96, [arXiv:0706.3909].

[566] S. Palomares-Ruiz and J. M. Siegal-Gaskins, *Annihilation vs. Decay: Constraining dark matter properties from a gamma-ray detection*, *JCAP* **1007** (2010) 023, [arXiv:1003.1142].

[567] P. Konar, K. Kong, K. T. Matchev, and M. Perelstein, *Shedding Light on the Dark Sector with Direct WIMP Production*, *New J.Phys.* **11** (2009) 105004, [arXiv:0902.2000].

[568] T. Moroi, H. Murayama, and M. Yamaguchi, *Cosmological constraints on the light stable gravitino*, *Phys.Lett.* **B303** (1993) 289–294.

[569] C. E. Yaguna, *The Singlet Scalar as FIMP Dark Matter*, *JHEP* **1108** (2011) 060, [arXiv:1105.1654].

[570] G. Arcadi and L. Covi, *Minimal Decaying Dark Matter and the LHC*, *JCAP* **1308** (2013) 005, [arXiv:1305.6587].

[571] Y. Mambrini, K. A. Olive, J. Quevillon, and B. Zaldivar, *Gauge Coupling Unification and Nonequilibrium Thermal Dark Matter*, *Phys.Rev.Lett.* **110** (2013), no. 24 241306, [arXiv:1302.4438].

[572] M. Blennow, E. Fernandez-Martinez, and B. Zaldivar, *Freeze-in through portals*, arXiv:1309.7348.

[573] Y. Bai, P. J. Fox, and R. Harnik, *The Tevatron at the Frontier of Dark Matter Direct Detection*, *JHEP* **1012** (2010) 048, [arXiv:1005.3797].

[574] Y. J. Chae and M. Perelstein, *Dark Matter Search at a Linear Collider: Effective Operator Approach*, *JHEP* **1305** (2013) 138, [arXiv:1211.4008].

[575] X. Gao, Z. Kang, and T. Li, *Origins of the Isospin Violation of Dark Matter Interactions*, *JCAP* **1301** (2013) 021, [arXiv:1107.3529].

[576] P. Gondolo, J. Hisano, and K. Kadota, *The Effect of quark interactions on dark matter kinetic decoupling and the mass of the smallest dark halos*, *Phys.Rev.* **D86** (2012) 083523, [arXiv:1205.1914].

[577] P. Langacker, *The Physics of Heavy Z' Gauge Bosons*, *Rev.Mod.Phys.* **81** (2009) 1199–1228, [arXiv:0801.1345].

[578] R. Foot and X.-G. He, *Comment on Z Z-prime mixing in extended gauge theories*, *Phys.Lett.* **B267** (1991) 509–512.

[579] D. Feldman, Z. Liu, and P. Nath, *The Stueckelberg Z-prime Extension with Kinetic Mixing and Milli-Charged Dark Matter From the Hidden Sector*, *Phys.Rev.* **D75** (2007) 115001, [hep-ph/0702123].

[580] S. P. Martin, *Implications of supersymmetric models with natural R-parity conservation*, *Phys.Rev.* **D54** (1996) 2340–2348, [hep-ph/9602349].

[581] T. G. Rizzo, *Gauge kinetic mixing and leptophobic Z' in E(6) and SO(10)*, *Phys.Rev.* **D59** (1998) 015020, [hep-ph/9806397].

[582] F. del Aguila, M. Masip, and M. Perez-Victoria, *Physical parameters and renormalization of U(1)-a x U(1)-b models*, *Nucl.Phys.* **B456** (1995) 531–549, [hep-ph/9507455].

[583] B. A. Dobrescu, *Massless gauge bosons other than the photon*, *Phys.Rev.Lett.* **94** (2005) 151802, [hep-ph/0411004].

[584] T. Cohen, D. J. Phalen, A. Pierce, and K. M. Zurek, *Asymmetric Dark Matter from a GeV Hidden Sector*, *Phys.Rev.* **D82** (2010) 056001, [arXiv:1005.1655].

[585] Z. Kang, T. Li, T. Liu, C. Tong, and J. M. Yang, *Light Dark Matter from the $U(1)_X$ Sector in the NMSSM with Gauge Mediation*, *JCAP* **1101** (2011) 028, [arXiv:1008.5243].

[586] K. R. Dienes, C. F. Kolda, and J. March-Russell, *Kinetic mixing and the supersymmetric gauge hierarchy*, *Nucl.Phys.* **B492** (1997) 104–118, [hep-ph/9610479].

[587] D. Feldman, B. Kors, and P. Nath, *Extra-weakly Interacting Dark Matter*, *Phys.Rev.* **D75** (2007) 023503, [hep-ph/0610133].

[588] M. Cicoli, M. Goodsell, J. Jaeckel, and A. Ringwald, *Testing String Vacua in the Lab: From a Hidden CMB to Dark Forces in Flux Compactifications*, *JHEP* **1107** (2011) 114, [arXiv:1103.3705].

[589] J. Kumar, A. Rajaraman, and J. D. Wells, *Probing the Green-Schwarz Mechanism at the Large Hadron Collider*, *Phys.Rev.* **D77** (2008) 066011, [arXiv:0707.3488].

[590] M. Goodsell, S. Ramos-Sanchez, and A. Ringwald, *Kinetic Mixing of U(1)s in Heterotic Orbifolds*, *JHEP* **1201** (2012) 021, [arXiv:1110.6901].

[591] M. Goodsell, J. Jaeckel, J. Redondo, and A. Ringwald, *Naturally Light Hidden Photons in LARGE Volume String Compactifications*, *JHEP* **0911** (2009) 027, [arXiv:0909.0515].

[592] S. Abel, M. Goodsell, J. Jaeckel, V. Khoze, and A. Ringwald, *Kinetic Mixing of the Photon with Hidden U(1)s in String Phenomenology*, *JHEP* **0807** (2008) 124, [arXiv:0803.1449].

[593] S. Cassel, D. Ghilencea, and G. Ross, *Electroweak and Dark Matter Constraints on a Z-prime in Models with a Hidden Valley*, *Nucl.Phys.* **B827** (2010) 256–280, [arXiv:0903.1118].

[594] S. Andreas, M. Goodsell, and A. Ringwald, *Dark Matter and Dark Forces from a Supersymmetric Hidden Sector*, *Phys.Rev.* **D87** (2013) 025007, [arXiv:1109.2869].

[595] M. E. Krauss, W. Porod, and F. Staub, *SO(10) inspired gauge-mediated supersymmetry breaking*, *Phys.Rev.* **D88** (2013), no. 1 015014, [arXiv:1304.0769].

[596] M. Pospelov, *Secluded U(1) below the weak scale*, *Phys.Rev.* **D80** (2009) 095002, [arXiv:0811.1030].

[597] Y. Mambrini, *The ZZ' kinetic mixing in the light of the recent direct and indirect dark matter searches*, *JCAP* **1107** (2011) 009, [arXiv:1104.4799].

[598] Y. Mambrini, *The Kinetic dark-mixing in the light of CoGENT and XENON100*, *JCAP* **1009** (2010) 022, [arXiv:1006.3318].

[599] E. J. Chun, J.-C. Park, and S. Scopel, *Dark matter and a new gauge boson through kinetic mixing*, *JHEP* **1102** (2011) 100, [arXiv:1011.3300].

[600] F. Domingo, O. Lebedev, Y. Mambrini, J. Quevillon, and A. Ringwald, *More on the Hypercharge Portal into the Dark Sector*, *JHEP* **1309** (2013) 020, [arXiv:1305.6815].

[601] J. Heeck and W. Rodejohann, *Kinetic and mass mixing with three abelian groups*, *Phys.Lett.* **B705** (2011) 369–374, [arXiv:1109.1508].

[602] E. Dudas, Y. Mambrini, S. Pokorski, and A. Romagnoni, *Extra U(1) as natural source of a monochromatic gamma ray line*, *JHEP* **1210** (2012) 123, [arXiv:1205.1520].

[603] Y. Mambrini, *A Clear Dark Matter gamma ray line generated by the Green-Schwarz mechanism*, *JCAP* **0912** (2009) 005, [arXiv:0907.2918].

[604] C. Jackson, G. Servant, G. Shaughnessy, T. M. Tait, and M. Taoso, *Gamma-ray lines and One-Loop Continuum from s-channel Dark Matter Annihilations*, *JCAP* **1307** (2013) 021, [arXiv:1302.1802].

[605] C. Jackson, G. Servant, G. Shaughnessy, T. M. Tait, and M. Taoso, *Higgs in Space!*, *JCAP* **1004** (2010) 004, [arXiv:0912.0004].

[606] M. Baumgart, C. Cheung, J. T. Ruderman, L.-T. Wang, and I. Yavin, *Non-Abelian Dark Sectors and Their Collider Signatures*, *JHEP* **0904** (2009) 014, [arXiv:0901.0283].

[607] **XENON100** Collaboration, E. Aprile et al., *First Dark Matter Results from the XENON100 Experiment*, *Phys.Rev.Lett.* **105** (2010) 131302, [arXiv:1005.0380].

[608] G. Arcadi, Y. Mambrini, M. H. G. Tytgat, and B. Zaldivar, *Invisible Z' and dark matter: LHC vs LUX constraints*, *JHEP* **1403** (2014) 134, [arXiv:1401.0221].

[609] Y. Mambrini, M. H. Tytgat, G. Zaharijas, and B. Zaldivar, *Complementarity of Galactic radio and collider data in constraining WIMP dark matter models*, *JCAP* **1211** (2012) 038, [arXiv:1206.2352].

[610] A. Djouadi, *Higgs particles at future hadron and electron - positron colliders*, *Int.J.Mod.Phys.* **A10** (1995) 1–64, [hep-ph/9406430].